



HAL
open science

Coupling microwaves with a CO₂ desorption process from amine solvent : experimental and modeling approaches

Ali Hajj

► **To cite this version:**

Ali Hajj. Coupling microwaves with a CO₂ desorption process from amine solvent : experimental and modeling approaches. Chemical and Process Engineering. Ecole nationale supérieure Mines-Télécom Atlantique, 2024. English. NNT : 2024IMTA0412 . tel-04771116

HAL Id: tel-04771116

<https://theses.hal.science/tel-04771116v1>

Submitted on 7 Nov 2024

HAL is a multi-disciplinary open access archive for the deposit and dissemination of scientific research documents, whether they are published or not. The documents may come from teaching and research institutions in France or abroad, or from public or private research centers.

L'archive ouverte pluridisciplinaire **HAL**, est destinée au dépôt et à la diffusion de documents scientifiques de niveau recherche, publiés ou non, émanant des établissements d'enseignement et de recherche français ou étrangers, des laboratoires publics ou privés.

COLLEGES SCIENCES
BRETAGNE POUR L'INGENIEUR
LOIRE ET LE NUMERIQUE



THESE DE DOCTORAT DE

L'ÉCOLE NATIONALE SUPERIEURE
MINES-TELECOM ATLANTIQUE BRETAGNE PAYS DE LA LOIRE
– IMT ATLANTIQUE

Ecole Doctorale N° 648
Sciences pour l'Ingénieur et le Numérique
Spécialité : **Génie des Procédés et Bioprocédés**

Par

Ali HAJJ

Coupling microwaves with a CO₂ desorption process from amine solvent: experimental and modeling approaches

Thèse présentée et soutenue à l'IMT Atlantique, Nantes, 29/08/2024
Unité de recherche : GEPEA-UMR CNRS 6144
Thèse N° : 2024IMTA0412

Rapporteurs avant soutenance :

Christophe CASTEL	Professeur	ENSIC-LRGP
Cédric QUENDO	Professeur	Université de Bretagne Occidentale

Composition du Jury :

Président :	Isabelle POLAERT	Professeure, LSPC-INSA Rouen-Normandie
	Christophe CASTEL	Professeur, ENSIC-LRGP
	Cédric QUENDO	Professeur, Université de Bretagne Occidentale
Examineurs :	Elise EL AHMAR	Maitre-assistante (HDR), CTP- Mines Paris PSL
	Louis LATRASSE	Directeur R&D, SAIREM
Directeur de la thèse :	Pascaline PRÉ	Professeure, IMT Atlantique
Co-directeur de la thèse :	Sébastien CURET	Professeur, Oniris

Invité(s) :

Etienne SAVARY	Maître de conférences, ADEME
Jean-Marie JACOMINO	SAIREM

Author's word

At the end of my thesis I cannot but feel overjoyed by the many beautiful souls that stood by me. And so, I extend my gratitude:

To Myself

I was my biggest ally and my strongest support and if it weren't for my intrinsic self-motivation, I'd be in a very different place now. In first place I thank myself.

To my Friends

To Tahriri my most loyal friend and companion, to Rida for providing council in hard times, to Maarouf for being kind, to Moeen and Anwar being decent people that you can rely on, for Yasser shri and dubon and the good times we spent, and to all my friends whose names I did not mention.

I love you and wish you all the best

From Sairem

To Louis Latrassé for being the coolest and smartest guy I met, to Etienne for being the toughest but most understanding guy, to Jean-Marie the father of sairem and its employees. To all the team of sairem whom I failed to mention, i thank you and wish you more happiness and money, practically the same thing no?

From IMT & Oniris

To my supervisors Pascaline and Sebastien, we had our difficult moments, but we were mature enough to pull through it and not get drawn into conflict. I wasn't the best student but you were patient (most of the time) and continually helped me with your guidance. I appreciate everything and I will always be in your debt.

To my family

Spending 4 year away from you was the greatest hardship, but I had no choice but to push on. Perhaps you didn't realize how difficult it was as nothing compares. I hope to make up for lost time, for those laughs, meals, joys, cries, fights, excitements, jokes that we never had in these 4 years. I hope this happens before death does us apart. I love you issa, rida, karkoobe, 5eero, abo 7meed.

To my mother

I know that from the first time you held me, you aspired to make me into a good man, that I would become something or somebody to make you proud. I have yet to fulfill your wish, be patient, it's coming no doubt about that.

Ali HAJJ

Nantes 29/08/2024



Résumé du manuscrit

Le manuscrit suivant est divisé en cinq chapitres principaux. L'auteur a jugé opportun d'accorder à chaque chapitre de cet ouvrage sa propre section « préambule » où figurent les principes fondamentaux et les prérequis pour la lecture du chapitre. De plus, chaque chapitre s'est vu attribué sa propre nomenclature, annexes et références. On pense que cela facilitera la tâche du lecteur dans la recherche d'informations supplémentaires.

Le premier chapitre est l'état de l'art en matière de captage du carbone. Il présente la problématique du réchauffement climatique et les tendances à venir. À partir de là, il devient clair que le captage et le stockage du carbone sont un défi essentiel pour atteindre les objectifs de zéro émission nette. La technologie d'absorption des amines est discutée ainsi que ses problèmes et ses améliorations récentes. Parmi celles-ci, nous nous concentrons sur les membranes d'absorption gaz-solvant et la technologie micro-ondes pour la régénération. Le chapitre deux décrit la caractérisation diélectrique du solvant de référence sélectionné – l'éthanolamine aqueuse à différentes concentrations de dioxyde de carbone, températures et fréquences. Ce travail est important pour les trois chapitres suivants où la régénération thermique par irradiation micro-ondes est investiguée. Dans le troisième chapitre, la régénération de l'éthanolamine aqueuse chargée en CO₂ a été expérimentalement étudiée dans différentes conditions opératoires en utilisant une membrane à fibre creuse. La modélisation du système expérimental est présentée au chapitre quatre et montre plutôt un bon accord avec les résultats expérimentaux. Le dernier chapitre aborde la conception et l'exploitation d'un prototype expérimental d'unité de désorption permettant d'opérer la régénération micro-onde à l'échelle d'un module membranaire.

1 État de l'art

Introduction et contexte

Ces dernières années, les émissions de gaz à effet de serre (GES) ont continué d'augmenter à l'échelle mondiale, principalement en raison des activités industrielles, des transports, de la déforestation et de la production d'énergie à partir de combustibles fossiles. Malgré les efforts internationaux tels que l'Accord de Paris, les émissions n'ont pas encore atteint leur pic, avec des augmentations significatives observées dans les économies en développement rapide. Cependant, des voies d'atténuation prometteuses sont recherchées pour freiner cette tendance. Les sources d'énergie renouvelables telles que l'énergie éolienne, solaire et hydroélectrique sont de plus en plus adoptées, tandis que les innovations en matière d'efficacité énergétique et de technologies vertes gagnent du terrain. Des technologies de captage et de stockage du carbone (CSC) sont également en cours de développement pour réduire les émissions des processus industriels existants.

Technologies de captage du carbone

Les technologies de captage du dioxyde de carbone sont cruciales pour atténuer le changement climatique et peuvent être classées en trois grands types : l'oxycombustion, la pré-combustion et la post-combustion. L'oxycombustion consiste à brûler des combustibles fossiles dans de l'oxygène pur plutôt que dans de l'air, ce qui produit des gaz de combustion composés principalement de vapeur d'eau et de CO_2 , ce qui facilite le captage du CO_2 . Le captage avant combustion, couramment utilisé dans les usines à cycle combiné de gazéification intégrée (IGCC), convertit les combustibles fossiles en un mélange d'hydrogène et de CO_2 avant la combustion, permettant ainsi au CO_2 d'être capté du flux riche en hydrogène. Le captage post-combustion, la méthode la plus largement utilisée, consiste à éliminer le CO_2 des gaz d'échappement après la combustion des combustibles fossiles, généralement en utilisant des solvants chimiques comme les amines pour absorber le CO_2 des gaz de combustion. Chaque méthode offre des avantages distincts et est adaptée à différentes applications et étapes du processus de production d'énergie.

Absorption du CO_2 dans les solvants aminés

L'absorption du CO_2 par les solvants aminés est une méthode largement utilisée pour capturer le dioxyde de carbone provenant des émissions industrielles, en particulier dans les processus de post-combustion. Dans cette méthode, les gaz de combustion contenant du CO_2 passent à travers une solution de solvants aminés, tels que l'éthanolamine, qui réagissent chimiquement avec le CO_2 pour former un composé pouvant être séparé du flux gazeux. La solution d'amine riche en CO_2 est ensuite chauffée dans une unité de régénération, libérant du CO_2 pur pour le stockage ou l'utilisation et régénérant le solvant aminé pour sa réutilisation. Ce procédé est très efficace et peut capter jusqu'à 90 % du CO_2 des gaz de combustion. Malgré son efficacité, la méthode nécessite une énergie importante pour l'étape de régénération et pose des défis liés à la dégradation des solvants et à la corrosion. Les recherches en cours visent à améliorer l'efficacité, à réduire les coûts et à améliorer la durabilité de cette technologie vitale de captage du carbone.

Avancées dans le captage post-combustion par absorption chimique

Plusieurs voies sont explorées pour améliorer l'efficacité et la rentabilité de l'absorption des amines pour le captage du CO₂. Une piste majeure est le développement de nouveaux solvants dotés d'une capacité d'absorption de CO₂ plus élevée et de vitesses de réaction plus rapides, susceptibles de réduire l'énergie requise pour la régénération du solvant et de minimiser sa dégradation. De plus, l'utilisation de contacteurs membranaires gagne du terrain ; ces dispositifs facilitent le transfert efficace du CO₂ des gaz de combustion vers la solution d'amine en offrant une grande surface et en réduisant l'encombrement de l'équipement. Cela peut améliorer les taux de transfert de masse et réduire la consommation d'énergie. Une autre approche innovante implique l'application de l'irradiation par micro-ondes dans l'étape de régénération du solvant. Le chauffage par micro-ondes peut chauffer sélectivement et rapidement la solution d'amine, accélérant ainsi la libération de CO₂ et réduisant potentiellement la demande énergétique globale par rapport aux méthodes de régénération thermique conventionnelles. Ensemble, ces avancées sont prometteuses pour rendre la capture du CO₂ à base d'amines plus durable et économiquement viable.

2 Caractérisation diélectrique d' une solution de 30% d'éthanolamine riche en CO₂

Introduction

La connaissance des propriétés diélectriques est cruciale pour modéliser correctement le phénomène de chauffage par micro-ondes. Les travaux existants sur la caractérisation diélectrique des alcanolamines se limitent à des échantillons soit d'alcanolamines pures, soit d'alcanolamines aqueuses exemptes de CO₂. À notre connaissance, la littérature existante sur la caractérisation diélectrique des alcanolamines aqueuses riches en CO₂ est insuffisante pour permettre des études de modélisation approfondies. Cela dit, l'objectif principal de ce chapitre est la caractérisation diélectrique de 30 % en poids d'éthanolamine aqueuse, dans la gamme de fréquences [915-2450] MHz et à différentes températures et concentrations de CO₂. Les propriétés diélectriques obtenues ont été ajustées avec le modèle diélectrique Cole-Cole et les paramètres de dispersion obtenus ont été interprétés à l'aide de la spéciation chimique obtenue à partir du modèle d'équilibre vapeur-liquide de Kent-Eisenberg.

La présentation de ce chapitre est la suivante :

Préambule sur les interactions matériaux micro-ondes

Cette partie aborde brièvement les principes fondamentaux de l'interaction micro-ondes-matériau, nous définissons les paramètres qui caractérisent cette interaction sous la forme de la constante diélectrique complexe composée de la permittivité relative et du facteur de perte diélectrique. De plus, ce sous-chapitre aborde les ondes électromagnétiques planes non guidées et leurs caractéristiques, à partir de là, la propagation électromagnétique dans un diélectrique avec

perle a été explorée pour atteindre les concepts de profondeur de pénétration. Plus loin dans ce sous-chapitre, nous modélisons les propriétés diélectriques avec des modèles de dispersion diélectrique tels que ceux de Debye, Cole-Cole, Davidson-Cole et Havriliak-Negami . Les différences fondamentales entre les modèles de relaxation diélectrique ont été mises en évidence en traçant la courbe de dispersion diélectrique dans un diagramme de Cole-Cole.

Caractérisation diélectrique des solvants chargés en CO₂ : matériaux et méthodes

Dans cette partie, la caractérisation diélectrique d'une solution aqueuse d'éthanolamine à 30% en poids avec une concentration en CO₂ dissous. Nous commençons par fournir un bref aperçu des techniques de mesure diélectrique tout en mettant davantage l'accent sur la sonde de mesure coaxiale à extrémité ouverte, la technique utilisée dans cette étude. Pour fournir une interprétation plus approfondie des propriétés diélectriques expérimentales, les données diélectriques expérimentales ont été adaptées à un modèle de relaxation diélectrique. Enfin, le modèle d'équilibre vapeur-liquide de Kent-Eisenberg a été présenté ainsi que sa méthode de résolution.

Propriétés diélectriques et paramètres de dispersion en fonction des conditions de fonctionnement

Dans cette partie, les propriétés diélectriques expérimentales et extrapolées d'une solution aqueuse à 30% d'éthanolamine libre et chargée en CO₂ ont été présentées sous forme de diagrammes de Bode ou de diagrammes de dispersion de Cole-Cole. La perte diélectrique de la solution a été divisée en pertes par conduction ionique ou par mécanismes de rotation dipolaire. Les effets de la fréquence, de la température et de la charge de CO₂ sur la dispersion diélectrique ont été discutés. Dans la suite, les paramètres de relaxation diélectrique du modèle Cole-Cole - obtenus en ajustant le modèle aux données expérimentales - ont été tracés en fonction de la température et à différentes concentrations de CO₂, et interprétés à l'aide de la spéciation chimique obtenue par résoudre le modèle d'équilibre vapeur-liquide de Kent-Eisenberg.

Résultats : propriétés de l'éthanolamine aqueuse exempte de CO₂

Les propriétés diélectriques d'une solution d'éthanolamine à 30 % en poids sans teneur en CO₂ sont inférieures à celles de l'eau dans la plage de fréquence de mesure. Les raisons étant que l'éthanolamine pure a une constante diélectrique statique plus faible et un mécanisme de relaxation plus faible que l'eau distillée. L'augmentation de la température a diminué la constante diélectrique mesurée et le facteur de perte en raison respectivement d'une liaison hydrogène plus faible et d'un mécanisme de relaxation plus rapide.

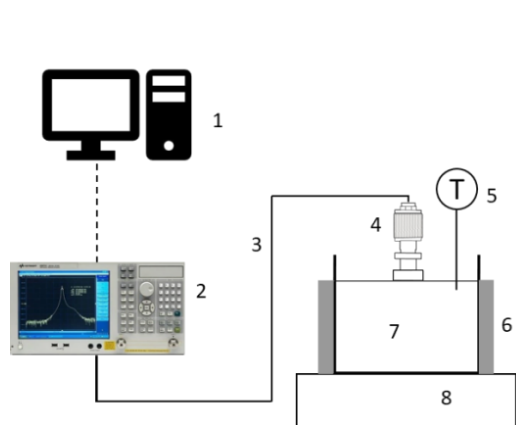
Résultats : propriétés de l'éthanolamine aqueuse enrichie en CO₂

Les propriétés diélectriques de solutions d'éthanolamine à 30 % avec du CO₂ chimiquement dissous ont été mesurées et adaptées au modèle Cole-Cole. Dans toutes les données expérimentales, le facteur de perte était élevé et augmentait avec des températures et des taux de carbonatation plus élevés. La perte diélectrique par conduction ionique

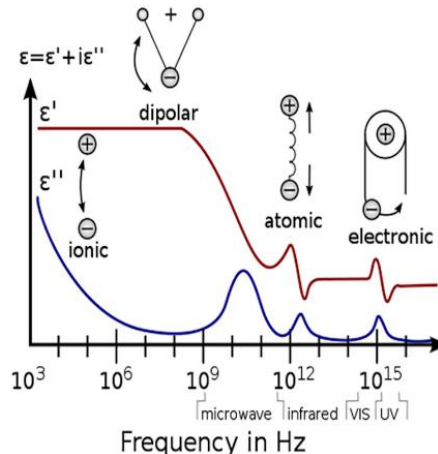
s'est avérée être le mécanisme de perte dominant sur la plage de fréquences de mesure, bien que les extrapolations du modèle Cole-Cole aient montré que la perte par rotation dipolaire dominait à la fréquence de relaxation. Compte tenu de l'absorbance élevée de la solution chargée en CO₂, les profondeurs de pénétration calculées étaient de l'ordre de quelques millimètres et diminuaient avec l'augmentation de la fréquence, de la température et des taux de carbonatation.

Résultats : Analyse du modèle de dispersion Cole-Cole ajusté aux propriétés de l'éthanolamine aqueuse enrichie en CO₂

En ce qui concerne les paramètres de dispersion ajustés, les résultats indiquent que la constante diélectrique statique diminue avec la température, mais augmente avec le taux de carbonatation. Cela se produit malgré la diminution de la concentration dipolaire avec une teneur en CO₂ plus élevée, comme le montre le modèle d'équilibre vapeur-liquide ; les raisons suspectées sont soit le déficit des points de mesure à des fréquences suffisamment inférieures à la fréquence de relaxation de la solution, soit que les espèces ioniques sont capables de se détendre sous le mécanisme de polarisation ionique. Le temps de relaxation apparent de la solution diminue avec la température mais augmente avec la charge de CO₂ par action de l'augmentation de la viscosité et des interactions ion-dipôle. Il est démontré que la solution connaît une distribution plus large des temps de relaxation avec une charge croissante de CO₂ tandis qu'un comportement non monotone est observé en ce qui concerne la température. Il a été démontré que la conductivité CC ajustée de la solution était supérieure d'au moins un ordre de grandeur à celle des 30 % en poids. Solution ETA sans charge de CO₂ et augmentée avec des températures et des taux de carbonatation plus élevés.



Mesure des propriétés diélectriques avec la technique de la sonde coaxiale ouverte. 1 : ordinateur, 2 : analyseur de réseau vectoriel, 3 : câble coaxial ; 4 : sonde de mesure ; 5 : fibre optique ; 6 : conteneur isotherme ; 7 : échantillon testé ; 8 : chauffe-eau double enveloppe.



Propriétés diélectriques (ϵ' , ϵ'') en fonction de la fréquence de l'irradiation électromagnétique. Les milieux interagissent avec l'irradiation par l'un des quatre mécanismes suivants : ionique, dipolaire, atomique et électronique.

3 Étude expérimentale du processus de désorption du CO₂ sous micro-ondes

Introduction

Le chapitre précédent s'est concentré sur la caractérisation des interactions micro-ondes - solvant en mesurant les propriétés diélectriques de l'éthanolamine aqueuse dans différentes conditions. Comme le solvant a été considéré comme un puissant absorbant de l'irradiation des micro-ondes, l'étape suivante consiste à étudier le processus de désorption assistée par les micro-ondes à l'échelle locale. Comme indiqué précédemment, l'un des principaux objectifs de ce travail est d'opérer la désorption de solvants riches en CO₂ sous irradiation micro-ondes à travers un contacteur membranaire à l'échelle d'un module membranaire à fibres creuses. Cette dernière étant composée d'une multitude de capillaires à fibres creuses, il est jugé nécessaire de comprendre la désorption à l'échelle d'une seule fibre pour avoir une idée du fonctionnement d'un faisceau de fibres, c'est-à-dire d'un module membranaire. Cela implique d'étudier expérimentalement l'influence des variables de fonctionnement sur le flux de désorption et de modéliser le processus de désorption sous irradiation micro-ondes. Alors que le chapitre suivant traite de l'aspect modélisation de l'étude, ce chapitre aborde la caractérisation expérimentale de la désorption du CO₂ à partir d'un solvant circulant du côté lumière d'une membrane à fibres creuses poreuses en Téflon d'un seul millimètre sous irradiation micro-ondes. Les effets du taux de carbonatation, de la température, du débit de solvant et du débit de gaz sur les flux de désorption ont été étudiés et quantifiés. Les données expérimentales de désorption générées dans ce chapitre servent également à valider l'approche de modélisation numérique du chapitre suivant.

La présentation de ce chapitre est la suivante :

Préambule

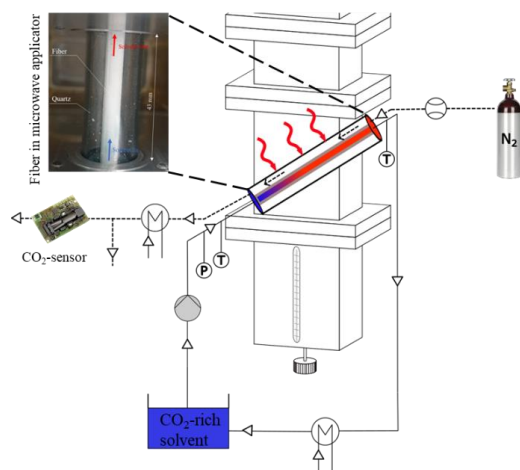
Les principes fondamentaux de la propagation des micro-ondes dans un guide d'ondes rectangulaire sont résumés. Nous partons des équations de Maxwell pour dériver les modes possibles de propagation des micro-ondes et les équations de champ électrique et magnétique correspondantes. Des exemples sont donnés pour les deux modes de propagation, magnétique transverse et électrique transverse.

Opérer la désorption du CO₂ sous micro-ondes à l'échelle d'une fibre

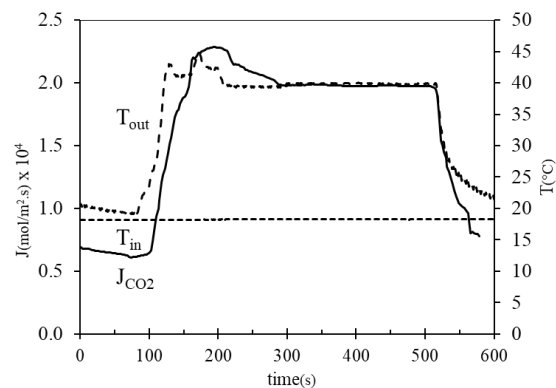
Le dispositif utilisé pour étudier la désorption du CO₂ à l'échelle d'une seule fibre sous irradiation micro-ondes est présenté, l'accent étant mis sur la conception de l'applicateur micro-ondes. La méthodologie de conception du plan expérimental est présentée ainsi que l'équation de régression correspondante qui corrèle les performances de désorption aux conditions opératoires.

Résultats

L'effet de l'irradiation micro-ondes sur le flux de désorption à partir de 30 % en poids. Le solvant éthanolamine a été étudié dans différentes conditions opératoires dans le cadre d'une conception de plan expérimental. Il a été conclu que parmi les conditions opératoires, la température de sortie avait l'effet le plus important sur le flux de désorption, suivie du débit de solvant. L'effet de l'interaction entre la température et l'augmentation du débit de solvant a amélioré les performances de régénération. Le gaz de balayage avait très peu d'effet sur le flux de désorption car la concentration de CO_2 mesurée du côté de la coque était faible, de sorte que toute augmentation du gaz de balayage avait peu d'effet sur l'augmentation de la force motrice. Les flux de désorption obtenus dans ce travail ont été comparés à ceux obtenus dans la littérature par différents modes de régénération : balayage de N_2 ou régénération sous vide. Les résultats expérimentaux actuels sont du même ordre de grandeur que ceux de la littérature utilisant du gaz de balayage N_2 , mais ceux employant la décompression sous vide du solvant présentent des performances de régénération inférieures à celles de ces travaux, malgré un fonctionnement à des températures plus élevées.



Montage expérimental pour la désorption assistée par micro-ondes de solutions d'éthanolamine riches en CO_2 dans une fibre creuse millimétrique



Résultats expérimentaux d'essais de désorption par micro-ondes : flux de désorption du CO_2 (J), température d'entrée du solvant (T_{in}) et température de sortie du solvant (T_{out}) en fonction du temps.

4 Modélisation numérique de la désorption chimique sous irradiation micro-ondes – Echelle fibre creuse

Introduction

Les chapitres précédents ont traité de la caractérisation diélectrique d'une solution aqueuse d'éthanolamine à différentes températures et taux de carbonatation, ainsi que de la caractérisation expérimentale de la désorption du dioxyde de carbone sous irradiation micro-ondes à travers une fibre creuse millimétrique poreuse. Le chapitre actuel traite de la modélisation numérique du processus de désorption.

Dans ce chapitre, nous présentons la conception d'un modèle multi-physique simulant la désorption chimique du CO₂ d'une solution d'alkanolamine dans une fibre creuse millimétrique exposée à une irradiation micro-ondes. Nous commençons par modéliser la propagation des champs électromagnétiques dans l'applicateur micro-ondes. Ensuite, les transferts de chaleur et de quantité de mouvement ont été intégrés dans le modèle 3D pour simuler le processus de chauffage par micro-ondes d'un flux laminaire de solvant dans une fibre creuse. Les phénomènes de transfert de masse et de réaction chimique ont été décrits selon la théorie du double film, prenant en compte les variables dépendantes de la température et le mouillage partiel de la matrice poreuse. La présentation de ce chapitre est la suivante :

Modélisation des champs EM dans un applicateur monomode

Dans cette section, les champs électromagnétiques ont été modélisés dans l'applicateur micro-ondes et les niveaux de puissance réfléchie ont été comparés à ceux obtenus expérimentalement. La distribution du champ électrique dans le solvant permet d'estimer la puissance micro-onde dissipée ici.

Couplage de la propagation EM à la mécanique des fluides et à la physique des transferts thermiques :

Les équations de transfert de chaleur et de transfert de quantité de mouvement ont été résolues pour obtenir les cartes de température dans le solvant déchargé. Après validation du modèle numérique, la sensibilité des cartes de température a été testée par rapport à plusieurs conditions opératoires et propriétés des fibres.

Modélisation de la désorption du CO₂ à travers une seule fibre creuse

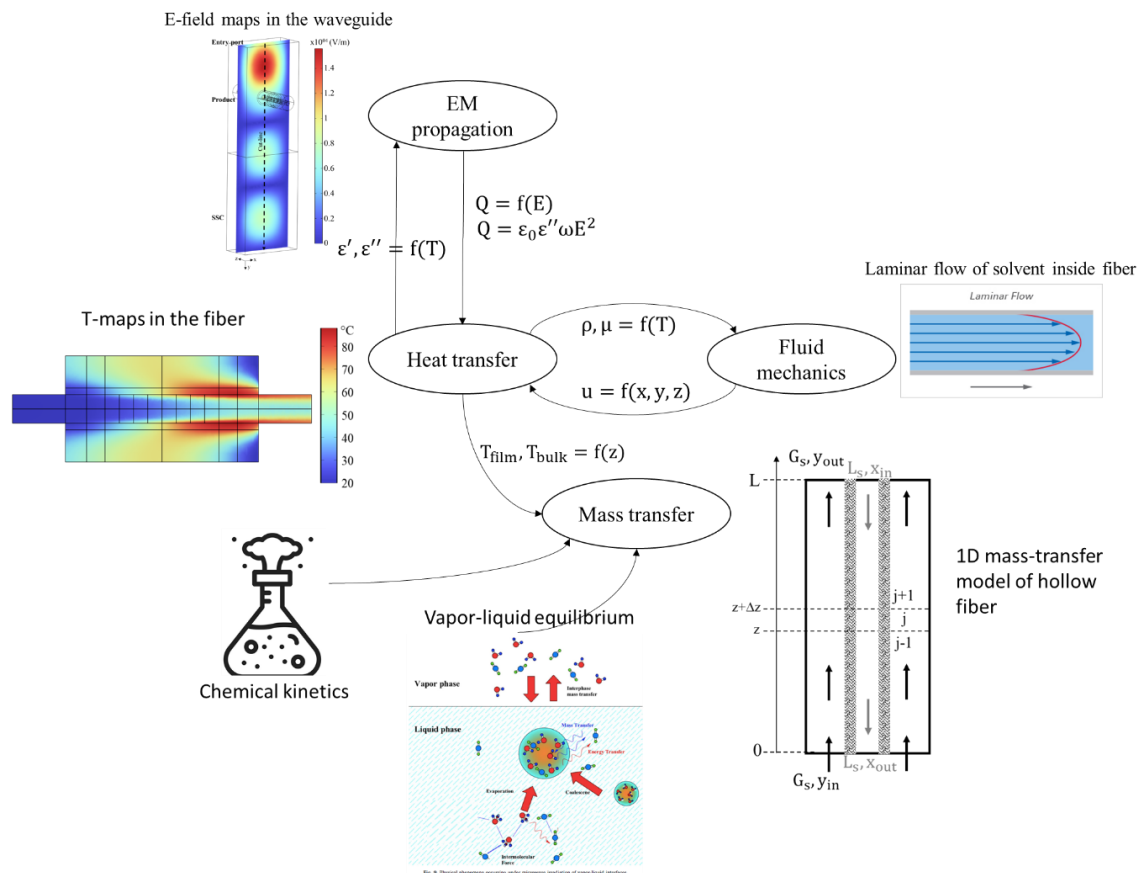
Pour simuler la désorption sous champs micro-ondes, les cartes de température obtenues précédemment ont été intégrées dans un modèle de transfert 1D, en supposant que l'effet de l'enthalpie de réaction est négligeable. Cette dernière est basée sur l'approche de résistance en série avec un facteur d'amélioration pour tenir compte de la réaction chimique lors de la désorption. Les principaux résultats incluent les profils de flux de désorption le long de la direction axiale de la fibre. Des études complémentaires ont également été réalisées pour explorer l'effet des conditions opératoires et de la géométrie des fibres sur le flux de désorption.

Analyse de sensibilité des taux de désorption du CO₂

Dans la dernière partie de ce chapitre, une analyse de sensibilité a été entreprise vis-à-vis des propriétés de la membrane poreuse, des propriétés physiques et d'équilibre du solvant, ainsi que des conditions opératoires. Une telle étude était importante pour déterminer la précision de l'estimation des propriétés du solvant, ainsi que pour mettre en évidence les principaux facteurs d'amélioration des performances de désorption.

Résultats

Le modèle simule les taux de désorption locaux dans la direction axiale de la fibre creuse lorsque les niveaux de température varient axialement et radialement dans tout le solvant circulant à l'intérieur de la fibre. Pour simuler la désorption par micro-ondes, les cartes de température tridimensionnelles obtenues dans la cavité micro-ondes ont été transformées en deux profils de température unidimensionnels qui représentent les variations de température le long de la longueur de la fibre, à la fois dans le film liquide et dans la masse. Les flux de désorption dans la direction axiale de la fibre montrent que la désorption commence à des températures élevées, conduisant à des taux de désorption négligeables sur 60 % de la surface de la fibre. Des études supplémentaires suggèrent que contrairement aux procédés conventionnels, le mode de fonctionnement à co-courant est plus avantageux que le mode de fonctionnement à contre-courant en raison de l'absorption de CO₂ dans les régions froides de la fibre. Pour tenter de caractériser les performances de la régénération micro-onde, elle est comparée aux données numériques de désorption en mode isotherme. La régénération micro-onde s'avère plus efficace du côté « chaud » de la fibre, cependant le mode isotherme est globalement plus efficace.



Modèle multi-physique de la désorption chimique du CO₂ à partir d'un solvant éthanolamine dans une fibre creuse, et sous irradiation micro-ondes.

5 Régénération assistée par micro-ondes dans un contacteur à membrane

Introduction

Jusqu'à présent dans ce travail, la désorption chimique a été étudiée à l'échelle d'une seule fibre, expérimentalement et numériquement. L'étude a été réalisée en utilisant une fibre de dimensions assez grandes par rapport aux tailles courantes. De plus, le champ électrique responsable du chauffage du solvant dans la fibre creuse était uniforme dans la région de la lumière de la fibre, ce qui n'est qu'un cas particulier. L'utilisation de modules de fibres contenant un grand nombre de fibres dans une cavité au lieu d'une seule fibre conduira très probablement à des non-uniformités dans les répartitions du champ électrique, ce qui peut mettre en danger sa stabilité opérationnelle à long terme.

Dans ce chapitre, nous discutons de l'évolution de la régénération d'une fibre unique à l'échelle d'un module membranaire à travers la conception d'un prototype d'unité pour la régénération de solvant assistée par micro-ondes dans un module membranaire à fibres creuses. Le cœur de ce processus est constitué de deux cavités micro-ondes conçues sur mesure pour la régénération isotherme et non isotherme (assistée par micro-ondes) du solvant. Une cavité micro-ondes a été utilisée pour préchauffer le solvant avant d'entrer dans le module membranaire, tandis que le mode non isotherme repose sur le chauffage du solvant pendant qu'il traverse le module membranaire, c'est-à-dire que ce dernier est logé à l'intérieur de la cavité micro-ondes conçue sur mesure. La majeure partie de ce chapitre étant consacrée à la conception des cavités micro-ondes nommées - en particulier pour la régénération non isotherme - et au fonctionnement de l'unité prototype, les performances du prototype n'ont pas été entièrement explorées et restent l'objectif de travaux futurs. La présentation de ce chapitre est la suivante :

Modélisation numérique et conception d'applicateurs micro-ondes

Une brève introduction de la conception des applicateurs cylindriques monomodes, les principales considérations doivent être données à l'orientation du produit par rapport au champ électrique incident, à la longueur et au diamètre de la cavité, ainsi qu'à la longueur de l'iris pour une impédance optimale. correspondant à.

Cavité micro-ondes pour préchauffage du solvant

Dans cette partie nous exposons la méthodologie, les résultats numériques et expérimentaux associés à la cavité utilisée pour préchauffer le solvant avant d'effectuer la désorption chimique dans le module membranaire. Les principaux résultats sont présentés sous forme de spectres S_{11} et de cartes de dissipation de puissance dans le flux de solvant.

Cavité micro-ondes pour régénération non isotherme du solvant

Une deuxième cavité a été conçue pour chauffer le solvant par micro-ondes alors qu'il circule directement à l'intérieur du module membranaire. Ceci nécessite de loger le module membranaire à l'intérieur de la cavité. La méthodologie de conception de la cavité est similaire à celle de la cavité de préchauffage, mais l'objectif principal de cette partie est l'évaluation correcte des propriétés diélectriques du module à membrane rempli de solvant, qui influencent largement l'analyse des cartes de dissipation de puissance du champ E.

Conception de l'unité prototype

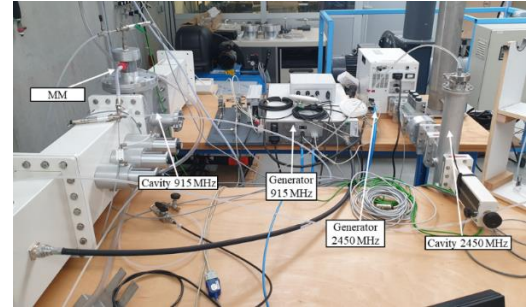
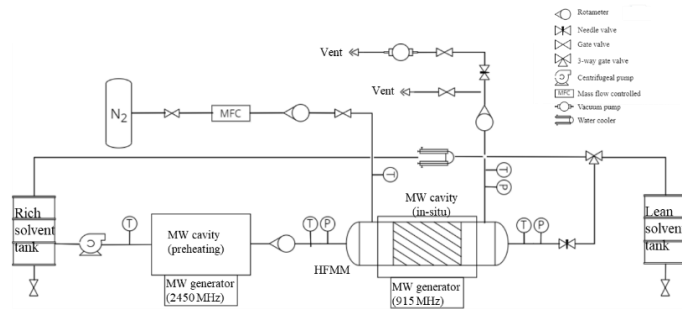
Un processus à l'échelle prototype de désorption assistée par micro-ondes dans un module à membrane a été conçu. Le prototype permet la régénération du solvant dans des conditions isothermes ou non isothermes dans le module membranaire. Le côté gaz du module à membrane peut en revanche être occupé par une configuration de balayage gazeux ou peut être placé sous vide.

Résultats

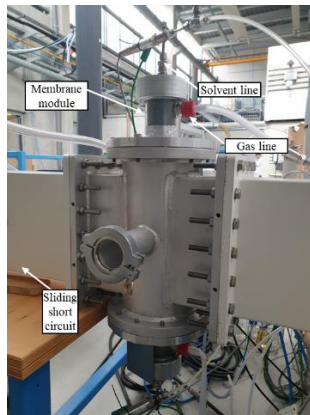
Le prototype de processus réalisé se concentre uniquement sur l'étape de désorption, il permet différents schémas temporels et différents modes de régénération, balayage gaz vs régénération sous vide ou modes isotherme vs non isotherme. Bien que la condition côté gaz du module à membrane puisse être facilement mise en œuvre, atteindre la condition de température n'est pas simple, c'est pourquoi la majeure partie de ce chapitre a traité de cette problématique.

La régénération isotherme dans le module membranaire est réalisée en préchauffant le solvant avant son entrée dans le contacteur gaz-liquide. La cavité, appelée cavité de préchauffage, a été conçue selon une méthodologie empirique visant à minimiser la puissance réfléchie en micro-ondes. La cavité a été conçue pour s'adapter à un large éventail de propriétés diélectriques du produit, c'est-à-dire que les niveaux simulés de puissance réfléchie sont de l'ordre de quelques pour cent, comme cela a également été vérifié expérimentalement.

La régénération non isotherme peut être obtenue en chauffant le solvant in situ dans le module de membrane de désorption. Cela est donc jugé possible en plaçant ce dernier à l'intérieur de la cavité micro-ondes personnalisée – appelée cavité in situ. La conception de cet équipement était moins simple car le principal défi était la valeur inconnue des propriétés diélectriques des 30 % en poids. Module à membrane rempli d'ETA. Nous avons donc utilisé la méthode inverse pour adapter le spectre S_{11} simulé à celui expérimental ce qui révèle les propriétés diélectriques apparentes du module membranaire. Les cartes de dissipation de puissance associées montrent une très bonne homogénéité suivant une section radiale, ce qui promet une bonne stabilité des performances sur le long terme.



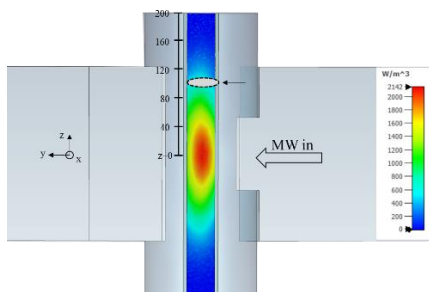
Unité pilote de régénération d'une solution aqueuse d'éthanolamine riche en CO_2 à l'échelle d'un module à fibres creuses. Le module membranaire est placé à l'intérieur de la cavité micro-ondes pour permettre une régénération assistée par micro-ondes. Le préchauffage du solvant avant son entrée dans le module membranaire permet une régénération isotherme.



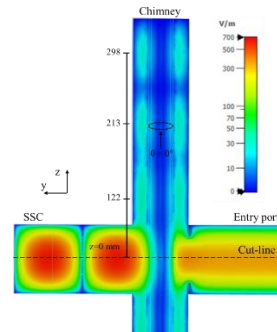
Cavité micro-ondes accueillant le module à membrane à fibres creuses pour un chauffage direct in situ pendant la régénération



Cavité micro-ondes pour préchauffage du solvant avant entrée dans le module de régénération



Distribution modélisée du champ électrique à l'intérieur du module à membrane à fibres creuses (915 MHz). La région de la lumière du module est occupée par un solvant aqueux éthanolamine enrichi en CO_2



Champs électriques modélisés à l'intérieur de la cavité pour préchauffer le solvant éthanolamine enrichi en CO_2 (2450 MHz).

Table of contents

Table of figures.....	25
List of Tables.....	37
1 State of the art.....	1
1.1 Introduction and Context.....	1
1.1.1 Dangers of global warming.....	1
1.1.2 GHG emissions: Trends and sources.....	2
1.1.3 Carbon capture utilization and storage.....	5
1.2 Carbon Capture technologies.....	6
1.2.1 Oxy-fuel combustion.....	7
1.2.2 Pre-combustion.....	9
1.2.3 Post-combustion carbon capture.....	11
1.2.3.1 Membrane separation.....	11
1.2.3.2 Adsorption on a solid.....	12
1.2.3.3 Absorption in a liquid.....	12
1.2.4 Carbon capture by amine absorption.....	13
1.2.4.1 Operation.....	13
1.2.4.2 Process disadvantages.....	14
1.2.4.3 Post-combustion capture by amine absorption: demonstrators world-wide.....	16
1.3 Absorption of CO ₂ in aminated solvents.....	19
1.3.1 Reaction kinetics.....	19
1.3.2 Modeling transfer phenomenon with chemical reaction: resistance in series approach.....	21
1.3.3 Modelling chemical equilibrium in CO ₂ -amine-H ₂ O system.....	22
1.4 Advances in post-combustion capture by chemical absorption.....	23
1.4.1 Alternative alkanolamine solvents.....	24
1.4.1.1 Primary alkanolamines.....	25
1.4.1.2 Secondary alkanolamines.....	26

1.4.1.3	Tertiary alkanolamines	26
1.4.1.4	Industrial solvents.....	27
1.4.1.5	Other considerations for solvent choice	28
1.4.2	CO ₂ absorption using hollow fiber membranes	30
1.4.2.1	A novel gas-liquid contactor.....	30
1.4.2.2	Application in chemical absorption of CO ₂	30
1.4.2.3	Operation in chemical desorption.....	32
1.4.2.4	Membrane materials	34
1.4.2.5	Membrane wetting: a barrier to industrial deployment	36
1.4.3	Novel regeneration method in chemical absorption using Microwave technology.....	37
1.4.3.1	Basics of microwave heating	37
1.4.3.2	Microwave applications in Food and Chemical industries	39
1.4.3.3	Microwave applications to carbon capture	39
1.5	Thesis objectives.....	41
1.6	Annex.....	43
1.6.1	Abbreviations.....	43
1.7	References	44
2	Dielectric characterization of CO ₂ -rich 30% ethanolamine solution.....	56
2.1	Introduction	56
2.2	Preamble: microwave-material interaction.....	58
2.2.1	Dielectric polarizability and electrostatic potential	58
2.2.2	Plane waves in lossy dielectrics.....	60
2.2.3	Penetration depth	62
2.2.4	The complex dielectric constant	63
2.2.5	Dielectric properties function of frequency	65
2.2.6	Dielectric relaxation models	67
2.2.6.1	Debye model.....	67

2.2.6.2	Cole-Cole model.....	69
2.2.6.3	Asymmetric models.....	71
2.2.6.4	Relaxation of a dielectric with ionic content	72
2.3	Dielectric characterization of CO ₂ -loaded solvents: materials and methods.....	73
2.3.1	Dielectric measurement techniques	73
2.3.2	Dielectric characterization of aqueous 30% wt. ETA with CO ₂	75
2.3.3	Generation of CO ₂ loaded 30% wt. ETA solutions	76
2.3.4	Cole-Cole relaxation model and fitting procedure.....	77
2.3.5	Solvent chemical speciation: vapor-liquid equilibrium	77
2.3.5.1	Brief review of vapor-liquid equilibrium modelling	77
2.3.5.2	Application of Kent-Eisenberg model: equations and resolution	78
2.4	Results	79
2.4.1	Chemical speciation profiles.....	79
2.4.2	Validation of dielectric measurements.....	80
2.4.3	Dielectric dispersion of non-loaded 30% ETA.....	81
2.4.4	Dielectric Dispersion of CO ₂ -loaded 30% wt. ETA aqueous solution	85
2.4.4.1	Dielectric dispersion diagram.....	86
2.4.4.2	Penetration depth of MW in 30% wt. ETA loaded with CO ₂	90
2.4.5	Dielectric dispersion parameters.....	91
2.4.5.1	Static permittivity (ϵ_0).....	91
2.4.5.2	Relaxation time (τ).....	93
2.4.5.3	Relaxation time distribution parameter (n).....	94
2.4.5.4	DC electrical conductivity (σ)	95
2.5	Summary.....	96
2.6	Appendix	98
2.6.1	Symbols	98
2.6.2	Abbreviations.....	98

2.6.3	Subscripts.....	98
2.6.4	Kent-Eisenberg VLE model.....	99
2.7	References	99
3	Experimental study of the CO ₂ desorption process under microwaves.....	104
3.1	Introduction	104
3.2	Preamble: electromagnetic propagation in a rectangular waveguide	105
3.2.1	TM mode	106
3.2.2	TE mode.....	109
3.3	Operating CO ₂ desorption under MW at the scale of a porous fiber	110
3.3.1	Experimental set-up	110
3.3.2	Applicator design: fiber orientation.....	115
3.3.2.1	Geometry and boundary conditions.....	115
3.3.3	Numerical results	117
3.3.4	Experimental design analysis.....	119
3.3.5	Energy balance on a circulating liquid.....	122
3.4	Results	123
3.4.1	Energy balance on a circulating liquid.....	123
3.4.2	System dynamics: desorption rates and temperature profiles.....	124
3.4.3	Influence of operating parameters on desorption flux	126
3.4.3.1	Temperature influence.....	127
3.4.3.2	Carbonation-ratio influence	128
3.4.3.3	Solvent flow rate influence	129
3.4.3.4	N ₂ flow rate influence.....	129
3.4.4	Regression of Experimental desorption flux.....	130
3.4.5	Comparative analysis of desorption performances with literature.....	131
3.4.5.1	N ₂ -gas sweeping regeneration	132
3.4.5.2	Vacuum regeneration.....	134

3.5	Conclusion.....	134
3.6	Annex.....	136
3.6.1	Abbreviations.....	136
3.6.2	Symbols	136
3.6.3	Effect of controlled variables and their interactions:.....	137
3.6.4	Complementary data: Influence of operating parameters on desorption	137
3.7	References	140
4	Numerical modeling of chemical desorption under MW irradiation – Hollow fiber scale	144
4.1	Introduction	144
4.2	Modeling EM fields in a mono-mode applicator.....	146
4.2.1	Maxwell’s Equations	146
4.2.2	Geometry and Boundary condition.....	146
4.2.3	Meshing and resolution scheme.....	147
4.2.4	Results.....	148
4.2.4.1	Model validation: comparison of reflected power spectra.....	148
4.2.5	Sensitivity analysis of power reflection.....	150
4.2.6	Simulation of EM fields: case of 30% wt. ETA enriched with CO ₂	151
4.2.6.1	Optimal SSC position	152
4.2.6.2	Electric-field maps.....	153
1.1	Coupling EM wave propagation to energy and momentum balances	155
4.2.7	Energy and momentum conservation equations	155
4.2.8	Boundary conditions	157
4.2.9	Resolution and Meshing	157
4.3	Numerical results.....	159
4.3.1	Validation of MW-heating model.....	159
4.3.1.1	MW-heating of distilled water (DW)	159
4.3.2	MW-heating of 30% wt. ETA enriched with CO ₂	160

4.3.2.1	2D/3D temperature maps in the fiber	160
4.3.2.2	Radial and tangential temperature profiles in the fiber.....	162
4.3.2.3	Dielectric property maps.....	162
4.3.2.4	Effect of operating conditions on temperature distributions	163
4.3.2.5	Effect of heat losses across the membrane	164
4.4	Modeling of CO ₂ desorption across a single hollow fiber.....	165
4.4.1	Resistance in series for modeling mass-transfer.....	165
4.4.1.1	Liquid phase mass-transfer coefficient.....	167
4.4.1.2	Membrane mass-transfer coefficient	167
4.4.1.3	Effect of chemical reaction on liquid phase mass-transfer coefficient.....	168
4.4.2	Modeling chemical desorption along a porous fiber at isothermal conditions	170
4.4.2.1	Model equations: analytical form	170
4.4.3	Coupling MW heating with chemical desorption of CO ₂	173
4.4.4	Resolution and boundary conditions.....	176
1.2	Results	179
4.4.5	Model Validation: chemical desorption in a hollow fiber at isothermal conditions	179
4.4.6	Results: MW-assisted chemical desorption	180
4.4.6.1	Effect of temperature profile assumptions.....	180
4.4.6.2	Effect of partial membrane wetting	182
4.4.6.3	Local desorption flux.....	183
4.4.6.4	Overall mass-transfer coefficient and enhancement factor.....	185
4.4.6.5	Driving force for mass-transfer	186
4.4.6.6	Power consumption for chemical desorption reaction.....	187
4.4.7	MW-assisted desorption versus isothermal desorption.....	188
4.4.8	Effect of solvent preheating on desorption	189
4.4.9	Effect of fiber radius on desorption flux.....	191
4.4.10	Effect of sliding short circuit (SSC) on temperature maps	193

4.4.11	Co-current versus Counter-current operation	194
4.5	Sensitivity analysis of CO ₂ desorption rates.....	195
4.5.1	Objectives and motivation	195
4.5.2	Methodology and equations.....	196
4.5.3	Desorption Sensitivity	197
4.5.3.1	Membrane properties.....	197
4.5.3.2	Transfer and equilibrium properties	197
4.5.3.3	Operating conditions.....	198
4.5.3.4	Recommendations	199
4.6	Conclusion.....	199
4.7	Annex: correlations used for the estimation of properties of the simulated systems.....	201
4.7.1	Notations.....	201
4.7.2	Abbreviations.....	201
4.7.3	Subscripts / Superscripts.....	201
4.7.3.1	Dielectric properties of porous PTFE fiber.....	202
4.7.3.2	Dielectric properties of distilled water	202
4.7.3.3	Dielectric properties of 30% wt.ETA.....	203
4.7.3.4	Thermal conductivity of 30% wt. ETA	203
4.7.3.5	Specific heat of 30% wt. ETA solution	204
4.7.3.6	Density of 30% wt. ETA solution.....	204
4.7.3.7	Viscosity of 30% wt. ETA solution.....	205
4.7.4	Model parameters: Mass-transfer modeling	206
1.2.1.1	CO ₂ diffusivity in 30% wt. ETA.....	206
4.7.4.1	ETA diffusivity in 30% wt. ETA solution.....	206
4.7.4.2	Solubility of CO ₂ in aqueous ETA solution.....	207
1.2.1.2	Diffusivity of CO ₂ in N ₂ gas	208
4.7.4.3	Evaluating the Knudsen diffusivity	209

4.7.5	References.....	210
5	MW-assisted regeneration in membrane contactor	214
5.1	Introduction	214
5.2	Design of single-mode microwave applicators.....	216
5.3	MW cavity for solvent preheating	217
5.3.1	Methodology: empirical approach for cavity design	217
5.3.2	Geometry, meshing and boundary conditions	218
5.3.3	Numerical results	219
1.2.1.3	Simulation run #1	219
5.3.3.1	Simulation run #2	222
5.3.3.2	E-field and power-loss maps	223
5.3.4	Experimental validation of reflected power spectra	224
5.3.4.1	Materials and methods.....	224
5.3.4.2	Simulating the dielectric properties of 30% wt. ETA.....	224
5.3.4.3	Results	225
5.4	MW cavity for non-isothermal regeneration of solvent.....	227
5.4.1	Challenges.....	227
5.4.1.1	Performance stability	227
5.4.1.2	Difficulty in cavity optimization	227
5.4.2	Apparent dielectric properties of membrane contactor.....	228
5.4.3	Geometry, meshing and boundary conditions	230
5.5	Results: cavity for non-isothermal regeneration.....	231
5.5.1	MW reflected power: Simulation run #1	231
5.5.2	MW reflected power: Simulation run #2	232
5.5.3	Power dissipation fields in membrane module	233
5.5.3.1	Case of low dielectric properties of the membrane module	234
5.5.3.2	Case of elevated properties of the membrane module.....	234

5.5.4	Experimental validation of reflected power profiles	236
5.5.4.1	Materials and methods.....	236
5.5.4.2	Results	237
5.5.5	Dielectric characterization of membrane module through reverse technique.....	237
5.5.6	Power dissipation maps in membrane module.....	240
5.6	Prototype for MW-assisted regeneration	240
5.6.1	MW-assisted regeneration at the desorption stage.....	241
5.7	Conclusion.....	242
5.8	Annex.....	243
5.8.1	Nomenclature.....	243
5.8.2	Symbols	243
5.8.3	Operation of prototype unit for mixed absorption/desorption operation	243
5.8.3.1	Operating modes:.....	244
5.8.3.2	Isothermal Vs non-isothermal regeneration:.....	244
5.8.3.3	Vacuum versus sweeping gas regeneration:	244
5.9	References	245
6	General conclusions.....	248
7	Perspectives	250

Table of figures

Figure 1-1: Change of temperature extremes and soil moisture levels at different global temperature rise (Source: IPCC 6th assessment report [4])2

Figure 1-2: Global greenhouse gas emissions are presented as equivalent quantities of CO₂ [3]. Emissions over the period (2015-2022) are estimated global emissions. For upcoming years different emission paths are traced: SSP_{1-1.9} that limits warming to (1.5°C) with a 50% chance, SSP_{1-2.4} that limits warming to 2°C with a (67%) chance, projections based upon implemented policies in 2022.....3

Figure 1-3: global estimates of greenhouse gas emissions from major sectors [16]4

Figure 1-4: Global generation of electricity from different sources[15]5

Figure 1-5: Committed CO₂ emissions from existing fossil fuel infrastructure, compared with carbon budgets reflecting the long-term temperature goal of the Paris Agreement6

Figure 1-6: Global energy sector CO₂ emissions reductions by measure in the Sustainable Development Scenario 2019-70 [17]6

Figure 1-7: Concentration of CO₂ in flue gas stream from different processes [23].....7

Figure 1-8: Operation of carbon using Oxy/fuel combustion technology in a pulverized coal power plant [26]8

Figure 1-9: Process flow diagram for an IGCC process with carbon capture [35]10

Figure 1-10: Post-combustion capture of CO₂ [50]11

Figure 1-11: PolarCapTM process by MTR for carbon capture from flue gases12

Figure 1-12: Footprint of PolarCapTM process for treatment of 20ton/day flue gas at the NCCC.....12

Figure 1-13: Demonstration of the operating range of physical and chemical absorption.....13

Figure 1-14: Process flow diagram for post-combustion capture by chemical absorption [64].....14

Figure 1-15: Repartitioning of power in an electrical power plant with CO₂ capture and compression [71].16

Figure 1-16: Map of the CCS projects worldwide [19].....16

Figure 1-17: photo of Boundary dam CCs project operated by SaskPower.....17

Figure 1-18: Photo of MHI’s KM-CDR carbon capture unit at Alabama power plant in Mobile county.19

Figure 1-19: Process flow diagram for MHI’s KM-CDR carbon capture process by chemical absorption in KS-1 solvent.....19

Figure 1-20: Different modeling schemes for gas-liquid reactive systems [86]20

Figure 1-21: Concentration profiles of components different cases of reaction regimes: (a)-pseudo first order regime, (b)-fast intermediate regime, (c)-instantaneous regime22

Figure 1-22: Equipment cost in chemical absorption process using (ETA) solvent [105].....24

Figure 1-23: Results of the ecotoxicity testing, shown as concentration where compounds inhibited algal growth by 50% (EC-50). The blue line shows the lowest acceptable value (10 mg/l) for a chemical to be released in the marine environment [139]29

Figure 1-24: Figure 1: The biodegradability of all the chemicals tested, results shown as percent degraded with regards to the theoretical oxygen demand (ThOD). The red line shows the lowest acceptable value for a chemical to be released in the marine environment, while the green line is the lower limit for a chemical to be released independent of the ecotoxicity [139].....29

Figure 1-25: Hollow fiber bundles with potted ends [149]. The fibers are porous as show by the Scanning electron microscope (SEM) image.31

Figure 1-26: Operation of hollow fiber module for CO₂ capture from flue gases [151]31

Figure 1-27: Advantages and drawbacks of membrane contactors in gas absorption [143]32

Figure 1-28: Experimental setup of solvent regeneration in a hollow fiber module while using N₂ sweeping gas-used by [97]34

Figure 1-29: Experimental set-up of open-loop solvent regeneration in a hollow fiber membrane module using vacuum regeneration with steam as sweeping gas - used by [173]34

Figure 1-30: Literature survey of gas absorption experiments in hydrophobic porous membranes37

Figure 1-31: Conductive heat transfer in comparison to microwave heating [206]38

Figure 1-32: Representation of microwave heating in a multi-mode MW cavity [207]39

Figure 1-33: Representation of a microwave heating in a mono-mode cavity [207]39

Figure 1-34: Comparison of microwave (MW) and conventional heating (CH) to regenerate the CO₂-loaded 30%wt. ETA solution after an initial absorption step of 20 min with 20% CO₂ [219].40

Figure 1-35: Experimental setup used for CO₂ absorption and regeneration of aqueous ethanolamine solution by microwave [220].....40

Figure 2-1: Polarization of dielectric material in a capacitor under a static potential difference – taken from [12]59

Figure 1-2: Plane transverse electromagnetic wave60

Figure 1-3: Penetration depth of a TEM wave in a lossy dielectric as a function distance (z)63

Figure 1-5: Dominating relaxation mechanisms in a dielectric as a function of the frequency of the E-field – taken from [13].....65

Figure 1-6: Mechanisms for EM dissipation into heat66

Figure 1-7: Bode plot of dielectric properties of distilled water at T=20°C.....68

Figure 1-8: Dielectric dispersion diagram of Debye relaxation model of distilled water at 20°C69

Figure 1-9: Effect of parameter (n) on the relative dielectric constant (ϵ')71

Figure 1-10: Effect of parameter (n) on the relative dielectric loss factor (ϵ'').....71

Figure 1-11: Effect of the parameter (n) on the dielectric dispersion of a polar liquid	71
Figure 1-12: Dielectric dispersion diagram of the Cole-Davidson relaxation.....	72
Figure 1-13: Total, dipolar and ionic dielectric dispersion curves for saline water at $T=20^{\circ}\text{C}$ and $C_{\text{NaCl}}=20\text{g/l}$...	73
Figure 1-14: One-port coaxial line or waveguide method.....	74
Figure 1-15: Electric-field lines in a cross-sectional view of a dielectric probe dipped in a sample	74
Figure 1-16: Measurement of dielectric properties with open-ended coaxial probe technique. 1: computer, 2: vector network analyzer, 3: coaxial cable; 4: measurement probe; 5: optical fiber; 6: thermally insulated container; 7: sample under test; 8: double envelope water heater.	76
Figure 1-17: Apparatus for generating CO_2 loaded 30% wt. ETA aqueous solutions	76
Figure 1-18: Kent-Eisenberg chemical speciation model and experimental values obtained by NMR spectroscopy for 30% wt. ETA from Poplsteinova [55].	80
Figure 1-19: Total dipolar and ionic concentrations in 30% wt. ETA solution at different carbonation ratios.	80
Figure 1-20: Measured (\square) and calculated (—) relative dielectric constant of deionized water at different temperatures.....	81
Figure 1-21: Measured (\square) and calculated (—) relative dielectric loss factor of deionized water at different temperatures.....	81
Figure 1-22: Dielectric dispersion diagram of distilled water, 30% ETA (Experimental) and 30% ETA (Cole-Cole) at 20°C	82
Figure 1-23: Dielectric dispersion diagram of distilled water, 30% ETA (Experimental) and 30% ETA (Cole-Cole) at 60°C	82
Figure 1-24: Bode plot of relative dielectric constant for distilled water and 30% wt. ETA solution at 20°C and 60°C	84
Figure 1-25: Bode plot of dielectric loss factor for distilled water and 30% wt. ETA solution at 20°C and 60°C . ..	84
Figure 1-26: Modeled and experimental relative permittivity of 30% wt. ETA solution at 915MHz (blue) and 2450MHz (orange): \times , $\alpha=0.22$; \square , $\alpha=0.33$; Δ , $\alpha=0.44$; \circ , $\alpha=0.55$	86
Figure 1-27: Modeled and experimental relative dielectric loss factor of 30% wt. ETA solution at 915MHz (blue) and 2450MHz (orange): \times , $\alpha=0.22$; \square , $\alpha=0.33$; Δ , $\alpha=0.44$; \circ , $\alpha=0.55$	86
Figure 1-28: Dielectric dispersion of 30%wt. ETA at $\alpha=0.22$ and $T=20^{\circ}\text{C}$	87
Figure 1-29: Dielectric dispersion of 30%wt. ETA at $\alpha=0.55$ and $T=80^{\circ}\text{C}$	87
Figure 1-30: Dielectric loss factor of 30% wt. ETA function of frequency at $T=20^{\circ}\text{C}$ and at different values of α	89
Figure 1-31: Dielectric loss factor by dipolar rotation and ionic conduction of 30% wt. ETA function of frequency for $\alpha=0.22$ and at different temperatures	89

Figure 1-32: Dielectric dispersion of 30% ETA over the frequency range [915-2450 MHz] at T=20°C and $\alpha \in [0.22-0.55]$ 90

Figure 1-33: Dielectric dispersion of 30% ETA over the frequency range [915-2450 MHz] at $\alpha=0.22$ for T $\in [20-80$ °C].....90

Figure 1-34: MW penetration depth in 30%wt. ETA function of temperature at different CO₂ loadings at f=915MHz91

Figure 1-35: MW penetration depth in 30%wt. ETA function of temperature at different CO₂ loadings at f=2450 MHz.....91

Figure 1-36: Static dielectric constant of 30%wt. ETA as a function of T α . (symbols), experimental; (lines), polynomial fittings.....93

Figure 1-37: Apparent relaxation time (τ) of 30%wt. ETA as a function of T at different (α). (symbols), experimental; (lines), polynomial fittings.....94

Figure 1-38: Distribution parameter of relaxation time function of T at different (α). (symbols), experimental; (lines), polynomial fittings95

Figure 1-39: DC electrical conductivity of 30%wt. ETA solution function of T at different (α). (symbols), experimental; (lines), polynomial fittings.....96

Figure 2-1: EM propagation following (ak) parallel to the z-axis in a rectangular waveguide of dimensions (a x b)105

Figure 2-2: instantaneous E-field plot in a XY-plane of rectangular waveguide (WR340) for a TM₁₁ propagation at 5GHz.....109

Figure 2-3: instantaneous E-field plot in a XZ-plane of rectangular waveguide (WR340) for a TM₁₁ propagation at 5GHz, y=b/2.109

Figure 2-4: E-field plot in a XY-plane of rectangular waveguide for the propagation mode TE₁₀.....110

Figure 2-5: E-field plot in a XZ-plane of rectangular waveguide for the propagation mode TE₁₀110

Figure 2-6: Experimental set-up for MW-assisted CO₂ desorption from 30%ETA solvent in a hollow fiber. 1: microwave generator; 2: coaxial cable; 3: coaxial line - waveguide transition; 4: automatic three-stub impedance tuner; 5: microwave applicator; 6: sliding short circuit; 7: N₂ bottle; 8: flow meter; 9: condenser; 10: CO₂ sensor; 11: solvent reservoir; 12: peristaltic pump; 13: heat exchanger.....112

Figure 2-7: MW applicator containing hollow fiber placed concentrically with respect to the quartz tube and parallel with respect to the incident E-field.....113

Figure 2-8: Schematic of the CO₂ desorption in the liquid phase, gas phase, and the porous membrane.....113

Figure 2-9: Fiber orientation parallel with respect to the polarization of incident E-field (E) with a direction of propagation (k)115

Figure 2-10: Fiber orientation perpendicular with respect to the polarization of incident E-field (E) with a direction of propagation (k).....115

Figure 2-11: Microwave reflected power function of the internal diameter of the fiber filled with 30%wt. ETA at [0.55, 80°C]. (□): parallel orientation; (Δ): perpendicular orientation118

Figure 2-12: E-field map at 2450MHz in a hollow fiber (di= 3mm) at optimal SSC adaptation, 30%wt. ETA at [0.55 ,80°C]118

Figure 2-13: E-field map at 2450MHz in a hollow fiber (di= 13mm) at optimal SSC adaptation, 30%wt. ETA at [0.55 ,80°C]118

Figure 2-14: Reflected power fraction function of sliding short circuit position at 2450 MHz; (di=3mm) and parallel orientation. Simulated liquids are: distilled water (DW), 30%wt. ETA [0.22, 20°C], 30%wt. ETA [0.55, 80°C].119

Figure 2-15: Reflected power fraction function of frequency at optimal SSC positions; (di=3mm) and parallel orientation. Simulated liquids are: distilled water (DW), 30%wt. ETA [0.22, 20°C], 30%wt. ETA [0.55, 80°C].119

Figure 2-16: 2^k experimental design cube for a system-response dependent on three variables (X1, X2, X3). Each sphere designates the conditions on that experimental point under the form (X1X2X3) with (H) and (L) accounting for “high” and “low” levels respectively.....120

Figure 2-17: Representation of a six-port reflectometer122

Figure 2-18:Representation of a dual directional coupler as a 4-port network device with ports 3, and 4 being 122

Figure 2-19: Different measurements of absorbed MW power by DW circulating in a hollow fiber at different mass flow rates. Automatic impedance 3-stub tuner (AI3S); MW generator; thermal balance on DW.124

Figure 2-20: Different measurements of absorbed MW power by pure ETA circulating in a hollow fiber at different mass flow rates. Automatic impedance 3-stub tuner (AI3S); MW generator; thermal balance on ETA.124

Figure 2-21: CO₂ desorption flux under MW irradiation from 30%wt. ETA circulating in a hollow fiber. For all figures, T_{in}=20°C, α=0.55, and v_{N2}=3.33mL/s. The couple [T_{out} (°C); v_{liq} (mL/s)] varies for each figure. (a)- [40; 0.2], (b)- [60; 0.2], (c)- [40; 0.59], (d)- [60; 0.59].126

Figure 2-22: CO₂ desorption flux at (α=0.55), represented according to the 2^k Experimental design scheme. ...127

Figure 2-23: CO₂ desorption flux at (α=0.44), represented according to the 2^k Experimental design scheme. ...127

Figure 2-24: vapor-liquid Equilibrium for 30%wt. ETA function of carbonation ratio at different temperatures: (□)-40°C; (x)-60°C; (Δ)-80°C; (○)-100°C. [23, 24, 26, 32, 33]129

Figure 2-25: CO₂ concentration in outlet gas stream at different Experimental conditions and carbonation ratio (α=0.55)130

Figure 2-26: CO₂ concentration in outlet gas stream at different Experimental conditions and carbonation ratio (α=0.44)130

Figure 2-27: Regression coefficients based on the Experimental data of (α=0.55)131

Figure 2-28: Regression coefficients based on the Experimental data of ($\alpha=0.44$)	131
Figure 2-29: CO ₂ desorption flux from 30% wt. ETA circulating in a hollow fiber under MW irradiation, $T_{in}=20^{\circ}\text{C}$, $\alpha=0.55$. The Experimental conditions of [$T_{out}(^{\circ}\text{C})$, v_l (ml/s), v_g (ml/s)] are as follows: a-[40, 0.2, 33.3], b-[60, 0.2, 33.3], c-[40, 0.59, 33.3], d-[60, 0.59, 33.3]	138
Figure 2-30: CO ₂ desorption flux from 30% wt. ETA circulating in a hollow fiber under MW irradiation, $T_{in}=20^{\circ}\text{C}$, $\alpha=0.44$. The Experimental conditions of [$T_{out}(^{\circ}\text{C})$, v_l (ml/s), v_g (ml/s)] are as follows: a-[50, 0.2, 3.33], b-[60, 0.2, 3.33], c-[50, 0.59, 3.33], d-[60, 0.59, 3.33], E-[50, 0.2, 6.66], f-[60, 0.2, 6.66], g-[50, 0.59, 6.66], h-[60, 0.59, 6.66].	140
Figure 1-1: Representation of MW-assisted desorption set-up in Comsol multi-physics.	148
Figure 1-2: Meshed geometry of waveguide, and the solvent domain in the fiber lumen region.	148
Figure 1-3: (S_{11}) spectrum with distilled water ($T=20^{\circ}\text{C}$) occupying the lumen region.	149
Figure 1-4: Reflected power spectrum with distilled water ($T=20^{\circ}\text{C}$) occupying the lumen region.	149
Figure 1-5: S_{11} spectrum with 30% wt. ETA (25°C) in the lumen region: experimental results using the VNA, simulated data at the real position of the SCC, and simulated data at the simulated optimal SSC position	150
Figure 1-6: S_{11} spectrum with 30% wt. ETA (25°C) in the lumen region: experimental results using the VNA, simulated data at the real position of the SCC, and simulated data at the simulated optimal SSC position	150
Figure 1-7: sensitivity of reflected power with respect to the relative permittivity (ϵ') of distilled water. Base value of relative permittivity at $f=2450$ MHz is set as ($\epsilon_{H2O}'=78.67$).....	151
Figure 1-8: Sensitivity of reflected power with respect to the dielectric loss factor of distilled water. Base value of dielectric loss factor at $f=2450$ MHz is set as ($\epsilon_{H2O}''=10$).....	151
Figure 1-9: Sensitivity of reflected power to the internal radius of the fiber. Base value of fiber radius is set at 2.15 mm.	151
Figure 1-10: Sensitivity of optimal reflected power at $f=2450$ MHz	151
Figure 1-11: Simulated reflected power (% Pr) function of SSC position at 2540MHz - SSC step size (10 mm). Solvent used is 30% wt. ETA at ($\alpha=0.44$) and $T=20,60,80^{\circ}\text{C}$	152
Figure 1-12: Simulated reflected power (% Pr) function of SSC position at 2540MHz - SSC step size (2 mm). Solvent used is 30% wt. ETA at ($\alpha=0.44$) and $T=20,60,80^{\circ}\text{C}$	152
Figure 1-13: E-field maps in waveguide ($f=2450$ MHz) - case of 30% wt.ETA, $\alpha=0.44$, $T=60^{\circ}\text{C}$	154
Figure 1-14: Plot of E-field norm on cut-line along the length of the waveguide ($f=2450\text{MHz}$). Case 30% wt. ETA ($\alpha=0.44$), $T=20^{\circ}\text{C}$, 60°C , 80°C	154
Figure 1-15: E-field map in the MW cavity ($f=2450$ MHz). Case of 30% wt. ETA, $\alpha=0.44$, $T=60^{\circ}\text{C}$	154
Figure 1-16: E-field in the longitudinal cross-section of the solvent domain at different conditions [T , α]: [20°C , 0.44], [60°C , 0.44], [80°C , 0.44].	155
Figure 1-17: E-field in the radial cross-section of the solvent at mid-cavity	155

Figure 1-18: Schematic of the equation coupling to model solvent heating by microwave irradiation at steady state.	156
Figure 1-19: Meshing of the fiber lumen domain using two different configurations: (a)-Extremely Fine; (b)- Custom 2.....	158
Figure 1-20: Comparison of simulated and experimental outlet temperatures of MW heating of distilled water.	159
Figure 1-21: Comparison of simulated and experimental outlet temperatures of MW heating of 30%wt. ETA – unloaded.	159
Figure 1-22: Simulated temperature maps on the longitudinal (ZY) cross-section of the fiber for different experiments [v_1, T_{out}]: Exp 9 - [0.2, 50]; Exp 10 - [0.2, 60]; Exp 11 – [0.6, 50]; Exp 12- [0.6, 60]	160
Figure 1-23: Velocity map in fiber lumen at operating conditions of Exp 12: $v_1= 0.6\text{mL/s}$, $T_{out}=60^\circ\text{C}$, $\alpha=0.44$.	161
Figure 1-24: Electric field map in fiber lumen at operating conditions of Exp 12: $v_1= 0.6\text{mL/s}$, $T_{out}=60^\circ\text{C}$, $\alpha=0.44$	161
Figure 1-26: Radial temperature profiles at “mid-cavity” position for experiments (9-12).....	162
Figure 1-27: Tangential temperature profiles at $r=r_i$ and for $0<\Theta<360^\circ$ at operating conditions of experiment 12 [0.6 mL/s, $T_{out}=60^\circ\text{C}$].	162
Figure 1-28: Schematic showing the paths over which temperature was evaluated.	162
Figure 1-29: Relative permittivity (ϵ') in fiber lumen at $f=2450$ MHz and at conditions of experiment (12), [$\alpha, v_1,$ T_{out}] = [0.44, 0.6mL/s, 60°C].....	163
Figure 1-30: Dielectric loss factor (ϵ'') in fiber lumen at conditions of experiment 12, [α, v_1, T_{out}] = [0.44, 0.6mL/s, 60°C].....	163
Figure 1-32: Influence of solvent vl rate on T_{max} inside the fiber. [α, T_{out}] = [0.44, 60°C].....	163
Figure 1-33: Influence of carbonation ratio (α) on T_{max} inside the fiber. [v_1, T_{out}] = [0.6 mL/s, 60°C].....	163
Figure 1-34: Influence of the outlet temperature of the solvent on T_{max} inside the fiber. [v_1, α] = [0.6 mL/s, 0.44]	163
Figure 1-35: Temperature distribution in the gas, membrane and solvent regions. Operating conditions of experiment (12) were used: $T_{out}=60^\circ\text{C}$, solvent $v_1=0.6$ mL/s, $v_g=3.33$ mL/s, $\alpha_{in}=0.44$	165
Figure 1-36: Temperature distribution in the gas, membrane and solvent regions. Operating conditions of experiment (16) were used: $T_{out}=60^\circ\text{C}$, solvent $v_1=0.6$ mL/s, $v_g=6.66$ mL/s, $\alpha_{in}=0.44$	165
Figure 1-39: Schematic of the resistance in series model for mass-transfer, gas filled membrane.....	165
Figure 1-40: Schematic of the resistance in series model for mass-transfer, partially wetted mode of operation.	165
Figure 1-41: Schematic of a chemical desorption across a single hollow fiber	170
Figure 1-42: Mass balance across a differential element of the hollow fiber.....	170

Figure 1-43: Vapor-liquid equilibrium plot of CO₂ with 30%wt. ETA as a function of the carbonation ratio at different temperatures: (x)-40°C, (Δ)-60°C, (□)-80°C; (◇)-100°C. Colors indicate the source of each data set: Red-[34], Violet-[33], orange-[35], green-[36].....172

Figure 1-44: Transformation of a 3D T-maps into bulk and film T-profiles.....174

Figure 1-45: Longitudinal temperature profiles of the bulk region at operating conditions [mass flow-rate, T_{out}] of experiments (9-12): Exp(9)-[0.2, 50]; Exp(10)-[0.6, 50]; Exp(11)-[0.2, 60]; Exp(12)-[0.6, 60].175

Figure 1-46: Longitudinal temperature profiles of the film region at operating conditions [mass flow-rate, T_{out}] of experiments (9-12): Exp(9)-[0.2, 50]; Exp(10)-[0.6, 50]; Exp(11)-[0.2, 60]; Exp(12)-[0.6, 60].175

Figure 1-47: Schematic of mass-transfer coupling to MW heating to simulate MW-assisted chemical desorption175

Figure 1-48: Resolution of microwave-assisted CO₂ desorption model.....178

Figure 1-49: Isothermal regeneration of 15% wt. ETA at varying temperatures and liquid velocities: comparing the simulated results to experimental data of [29]. (Lines)- predictions from numerical model; (symbols)- experimental data.179

Figure 1-50: Isothermal regeneration of 15% wt. ETA at varying liquid and gas velocities: comparing the simulated results to experimental data of [29]. (Lines)- predictions from numerical model; (symbols)- experimental data.179

Figure 1-51: Comparison of experimental desorption flux with the numerical model utilizing the “film” temperature profile and F=0%181

Figure 1-52: Desorption flux with model utilizing “film” T-profile at different wetting fractions.....181

Figure 1-53: Comparison of experimental desorption flux with the numerical model utilizing Bulk T-profile..182

Figure 1-54: Comparison of experimental desorption flux with the numerical model utilizing both bulk and film T-profiles.182

Figure 1-55: Fitting numerical desorption flux to experimental values by adjusting the wetted fraction (F) of the membrane.183

Figure 1-56: Evolution of the resistance in the membrane and the liquid phase at different wetting fractions (F).183

Figure 1-57: Experimental and simulated desorption flux at different experiments. Used wetting fraction in numerical model is (F=0.01%)183

Figure 1-58: CO₂ desorption profile as a function of the fiber position184

Figure 1-59: Accumulated desorption rate function of the area for mass-transfer184

Figure 1-60: Schematic representation of the evolution of the direction of mass-transfer in counter-current mode of operation.....185

Figure 1-61: Profile of overall transfer coefficient (K_L) function of the fiber length, (F=0.01%)186

Figure 1-62: Simulated profiles of transfer coefficients of liquid (k_l), membrane (k_m) and enhancement factor of experiment (12), ($F=0.01\%$)186

Figure 1-63: Driving force for mass transfer ($x_{f,l} - x_{f,g}^*$) function of fiber length. Wetting fraction $F=0.01\%$ 186

Figure 1-64: Bulk temperature profile, experiments (9-12)186

Figure 1-65: Driving force diagram, case of isothermal regeneration at operating conditions of experiment (12), ($F=0.01\%$).....187

Figure 1-66: Driving force diagram, case of microwave regeneration at operating conditions of experiment (12), ($F=0.01\%$).....187

Figure 1-67: Profile of MW power used for chemical desorption reaction, experiments (9-12).188

Figure 1-68: Percentage of incident MW power used for chemical desorption reaction, experiments (9-16).....188

Figure 1-69: Comparison of desorption flux under isothermal and non-isothermal regeneration. Wetting fraction ($F=0.01\%$).....189

Figure 1-70: Simulated desorption profile: isothermal vs non-isothermal regeneration. Operating conditions of experiment 12. Wetting fraction ($F=0.01\%$).....189

Figure 1-71: Film T-profiles along the fiber for 30%wt. ETA solvent flow rate (0.6mL/s) at different entry temperature $T_{in} = [10, 50]$, and $T_{out}=60^\circ\text{C}$190

Figure 1-72: Film T-profiles along the fiber for 30%wt.ETA solvent flow rate (0.6mL/s) for different entry temperature $T_{in} = [10,50]$, and $T_{out}=60^\circ\text{C}$190

Figure 1-73: Average desorption flux function of solvent entry temperature (T_{in}). $F= 0.01\%$, $T_{out}= 60^\circ\text{C}$, solvent $v_l= 0.6\text{mL/s}$191

Figure 1-74: Variations of local desorption rates along the fiber length for different entry temperature. $F = 0.01\%$, $T_{out} = 60^\circ\text{C}$, solvent $v_l = 0.6\text{mL/s}$191

Figure 1-75: T-maps in fiber lumen for different internal radii of the hollow fiber. For all cases, $T_{in}=20^\circ\text{C}$, $T_{out}=60^\circ\text{C}$ and solvent mass-flux= $4.9\text{g/cm}^2.\text{s}$191

Figure 1-76: Bulk and film temperature profiles for different internal radii of the fiber. For all cases, $T_{in}=20^\circ\text{C}$, $T_{out}=60^\circ\text{C}$, mass-flux = $4.9 \text{ g/cm}^2.\text{s}$ 192

Figure 1-77: Maximal solvent temperature for different internal radii of the fiber. $T_{in}=20^\circ\text{C}$, $T_{out}=60^\circ\text{C}$, mass-flux = $4.9 \text{ g/cm}^2.\text{s}$ 192

Figure 1-78: Average desorption flux function of the internal radius of the fiber. For all cases, $T_{in}=20^\circ\text{C}$, $T_{out}=60^\circ\text{C}$, mass-flux = $4.9 \text{ g/cm}^2.\text{s}$, and $F=0.01\%$ 193

Figure 1-79: Height of transfer unit function of the internal radius of the fiber. For all cases, $T_{in}=20^\circ\text{C}$, $T_{out}=60^\circ\text{C}$, mass-flux = $4.9 \text{ g/cm}^2.\text{s}$, and $F=0.01\%$, $\phi=0.85$193

Figure 1-80: Electric and temperature field maps at different SSC positions. Solvent 30%wt. ETA ($\alpha=0.44$), $T_{in}=20^{\circ}C$, mass flow=0.6mL/s, $r_i=2.15mm$.	194
Figure 1-81: Evolution of desorption flux along fiber length, co-current Vs counter-current mode at operating conditions of experiment 12. $T_{out}=60^{\circ}C$, solvent vl=0.6mL/s, $\alpha_{in}=0.44$, gas flow=3.33 mL/s.	195
Figure 1-82: Evolution of driving force for mass transfer along fiber length, Co-current Vs counter-current mode at operating conditions of experiment 12. $T_{out}=60^{\circ}C$, solvent vl=0.6mL/s, $\alpha_{in}=0.44$, gas flow=3.33 mL/s.	195
Figure 1-83: Comparison of desorption performance between two modes of operation: co-current vs counter-current operation for solvent and sweeping gas flows.	195
Figure 1-84: Sensitivity curves of the desorption flux with respect to the change in membrane properties.	198
Figure 1-85: Sensitivity curves of the desorption flux with respect to the change in physical or equilibrium properties.	198
Figure 1-86: Sensitivity curves of the global desorption flux with respect to operating conditions.	199
Figure 1-87: mean sensitivity of the desorption flux with respect to quantities pertaining to membrane properties, physical properties of the solvent, and operating conditions.	199
Figure 1-88: collision integral for CO ₂ -N ₂ mixture (Ω).	209
Figure 1-1: The susceptibility (Y_0) of the capacitive iris for impedance matching.	216
Figure 1-2: The susceptibility (Y_0) of an inductive iris for impedance matching.	216
Figure 1-3: Perpendicular orientation of the product with respect to the incident E-field.	217
Figure 1-4: Parallel orientation of the product with respect to the incident E-field.	217
Figure 1-5: Longitudinal orientation of the product in the waveguide.	217
Figure 1-6: Cross-section view of the 2.45 GHz MW cavity for preheating 30%wt. ETA. drawn in CST Studio Suite®.	219
Figure 1-7 : Average optimal power reflection coefficients as a function of iris aperture for all tested diameters.	221
Figure 1-8: Comparison of optimal (S_{11}) at two cavity configurations for different dielectric properties [ϵ' , ϵ''].	221
Figure 1-9: Comparison of optimal (S_{11}) at two cavity configurations for different dielectric properties [ϵ' , ϵ''] – a perturbation of 1.5mm was applied at the optimal SSC position.	221
Figure 1-10: Average (S_{11}) value as a function of the iris dimension for a cavity diameter (70 mm).	222
Figure 1-11: Average E-field distribution in the preheating cavity at ($f=2.4699$ GHz), optimal SSC position (48 mm), [ϵ' , ϵ''] of the solvent are [55, 70].	223
Figure 1-12: Average E-field plot along the waveguide length at ($f=2.4699$ GHz), optimal SSC position, [ϵ' , ϵ''] of the solvent are [55, 70].	223

Figure 1-13: Power loss density over a circular path on the outer surface of the solvent, and at different heights (z). The values of (θ) at 90° and 260° represent the sides facing the entry port and the sliding short circuit respectively.	223
Figure 1-14: Dielectric dispersion diagram showing the design properties, those of 30%wt.ETA over $\alpha= [0.22-0.55]$ and $T= [20-80^\circ\text{C}]$, and the tested properties	225
Figure 1-15: Microwave cavity for solvent preheating	226
Figure 1-16: Microwave entry port of the solvent preheating cavity	226
Figure 1-17 Experimental and simulated S_{11} spectra for case of pure Ethanol.	226
Figure 1-18 Experimental and simulated S_{11} spectra for case of Saline water (2) - 68g/L NaCl.	226
Figure 1-19: comparison of optimal SSC position (min S_{11} at 2450).	226
Figure 1-20: Damaged membrane module after placing it in a microwave cavity (center)	227
Figure 1-21: Hollow fibers of membrane module after stripping the PVC shell material	227
Figure 1-22: Prediction of the apparent dielectric properties of the membrane module by the dielectric mixing laws, $f= 915\text{MHz}$. Module is filled with 30% wt. ETA at ($\alpha=0.44$), and ($T=60^\circ\text{C}$)	230
Figure 1-23: Cross-section view of the in-situ MW cavity that operates at a frequency 915MHz. Drawn in CST microwave-studio.	231
Figure 1-24: Average power reflection coefficient as a function of the size of the iris, and at different cavity diameters.	232
Figure 1-25: optimal (S_{11}) parameter as a function of the iris dimension	233
Figure 1-26: optimal reflected power and its sensitivity for different dielectric properties of the membrane module, $D=160\text{mm}$, iris dimension= 74 mm	233
Figure 1-27: Power loss distributions in the hollow fiber module. Dielectric properties of the membrane module are $[\epsilon', \epsilon''] = [5, 10]$	234
Figure 1-28: Power loss distributions in the hollow fiber module. Dielectric properties of the membrane module are $[\epsilon', \epsilon''] = [5, 10]$	234
Figure 1-29: Power loss distributions along the hollow fiber module. Dielectric properties of the membrane module are $[\epsilon', \epsilon''] = [35, 50]$	235
Figure 1-30: Power loss distribution at radial sections of the membrane module at different heights.	235
Figure 1-31: Power loss density in the membrane module at different heights. Dielectric properties of membrane are $[\epsilon', \epsilon''] = [5, 10]$, absolute average deviation presented in right axis	236
Figure 1-32: Power loss density in the membrane module at different heights. Dielectric properties of membrane are $[\epsilon', \epsilon''] = [35, 50]$, absolute average deviation presented in right axis	236
Figure 1-33: mechanical drawing of the microwave cavity at 915 MHz	236
Figure 1-34: Experimental characterization of reflected power in the in-situ desorption cavity	236

Figure 1-35: Experimental reflected power spectrum for different tested liquids: 30%wt. ETA, Distilled water, saline water (48g/L NaCl) and (68g/L NaCl) circulating through the lumen of the membrane module.237

Figure 1-36: Simulated power reflection spectra whilst using different dielectric mixing laws to represent the properties of the membrane module. The latter is filled with saline water (48g/L) at 20°C to simulate 30%wt. ETA ($\alpha=0.44$, $T=60^\circ\text{C}$)238

Figure 1-37: Dielectric dispersion diagram for the simulated dielectric properties of the membrane module. Data are divided into groups based on the value of the resulting (S11). (x): $-3 \text{ dB} < S_{11}$; (Δ): $-6 \text{ dB} < S_{11} < -3 \text{ dB}$; (\circ): $-9 \text{ dB} < S_{11} < -6 \text{ dB}$; (+): $-12 \text{ dB} < S_{11} < -9 \text{ dB}$; (\diamond): $S_{11} < -12 \text{ dB}$ 239

Figure 1-38: Comparison between the experimental spectrum of saline water (48g/L NaCl) and those obtained numerically at different dielectric properties of the membrane239

Figure 1-39: Power dissipation along a longitudinal cross-section of the membrane module. Dielectric properties of MM are $[\epsilon', \epsilon''] = [4, 0.708]$ 240

Figure 1-40: Power dissipation on different radial cross-sections of the membrane module. Dielectric properties taken of MM are $[\epsilon', \epsilon''] = [4, 0.708]$ 240

Figure 1-41: Averaged MW absorbed power and deviation at different radial cross sections of the membrane module. Dielectric properties of the MM are $[\epsilon', \epsilon''] = [4, 0.708]$ 240

Figure 1-42: Process flow diagram for microwave-assisted regeneration of amine solution in hollow fiber module.241

Figure 1-43: Experimental set-up for MW-assisted desorption in a HFMM242

Figure 1-44: HFMM fixed inside the MW cavity (915 MHz)242

Figure 1-45: Process flow diagram for regeneration of amine rich solutions using hollow fiber membrane modules245

List of Tables

Table 1-1: Worldwide projects for oxy-fuel combustion technology for carbon capture [33].....	8
Table 1-2: Most commonly used alkanolamines for chemical capture of CO ₂ [79]	25
Table 1-3: Industrial solvents currently in use. Taken from [71].....	28
Table 1-4: properties of common hydrophobic polymer materials used for gas-liquid contactors [163]	35
Table 1.1: Penetration depth and wavenumber of EM radiation in some particular mediums.....	63
Table 1.2: Fitted Cole-Cole dispersion properties of 30%wt. ETA, and those of DW at T=20°C and 60°C.....	82
Table 1.4: Dielectric dispersion properties for Cole-Cole model at different temperatures and CO ₂ loadings	88
Table 1.3: Parameters for polynomial fits for the dispersion parameters of the Cole-Cole relaxation model	91
Table 2-1: Characteristics of (TE ₁₀) mode in a WR340 waveguide at 2.45GHz.....	110
Table 2-2: Hollow fiber characteristics. Note: (m) denotes measured characteristics while (s) denotes those specified by the supplier	112
Table 2-3: Dielectric properties at 2450MHz of different materials	116
Table 2-4: tested mesh types	117
Table 2-5: Contrast coefficients of the 2 ^k experimental design plan on the CO ₂ desorption rates at constant (α). Controlled variables are [T, νl , νg]	121
Table 2-6: Determination of absorbed microwave power and the associated uncertainty	123
Table 2-7: Average desorption flux obtained at operating conditions within the framework of the (2 ^k) experimental design approach	127
Table 2-8: Comparison of the CO ₂ desorption flux from this work with those from literature	132
Table 1.1: complex permittivity of materials used in the simulation environment at 2450MHz.	147
Table 1.2: Characteristics of different mesh types on the solvent domain	147
Table 1.3: Boundary conditions for fluid mechanics and heat transfer applied on fiber lumen.....	157
Table 1.4: Meshing configuration of the fiber lumen domain (solvent).....	158
Table 1.5: Averaged quantities over the fiber domain at different fiber configurations for the case of microwave heating of distilled water	158
Table 1.7: Operating conditions at experiments (9-16) of the experimental design	160
Table 1.6: Choice of T-profile in calculating physical and equilibrium properties in the non-isothermal chemical desorption model	176
Table 1.7: Operating conditions at experiments (9-16) of plan of experimental design	180
Table 1.8: quantities used to evaluate the sensitivity of the desorption flux	196
Table 1.10: relative permittivity (ϵ') and loss factor (ϵ'') of 30%wt. ETA at 2.45GHz.	203
Table 1.9: parameters for the calculation of specific heat of aqueous ethanolamine solutions.....	204

Table 1.11: constants for calculation of molar and excess volumes	205
Table 1.12: fitting constants for the viscosity of amine solvents	206
Table 1.13: Coefficients for solubility of N ₂ O in pure alkanolamines	207
Table 1-1: Ranges of geometrical parameters, frequency and dielectric properties simulated	220
Table 1-2: Refined ranges of the parameters to optimize the solvent preheating MW cavity	222
Table 1-3: Dielectric properties of the liquids used to validate the performance of the preheating cavity (f=2450 MHz).....	225
Table 1-4: Preheating cavity characterization using a VNA at f=2450 MHz.....	226
Table 1-5: Dielectric mixing laws for the estimation of the dielectric properties of the solvent filled membrane module. Subscript (1) and (2) stand for both the dispersed and continuous phases respectively	229
Table 1-6: characteristics of membrane module (Hydroblue, China)	229
Table 1-7: varied parameters for the design of in-situ cavity.....	232
Table 1-8: varied parameters for in-situ cavity design, simulation run #2.....	233
Table 1-9: Estimations of the dielectric properties of the membrane module using dielectric mixing laws. Membrane module is assumed to be filled with saline water (48g/L NaCl) at T=20°C which simulates the properties of 30% wt. ETA at $\alpha=0.44$ and T=60°C.	238

1 State of the art

1.1 Introduction and Context

Since the industrial revolution in the 19th century, human activity has caused an increase of greenhouse gases (GHG) that entailed the rise in global temperature. The intensity of GHG has been growing ever since due to population increase, increase in industrial activity and improvements in the quality of life. In an effort to combat greenhouse gas (GHG) emissions, the United Nations Framework Convention on Climate Change (UNFCCC) was created in 1992 by the United Nations (UN) to organize global efforts in reducing GHG emissions [1] through yearly meetings entitled “conference of parties” (COP). Perhaps one of the most important actions taken in these conferences is the establishment of the Paris Agreement in 2015 at COP 21 [2]. The Paris Agreement, with 195 participating signatories, aims to limit levels of warming to below ($<2^{\circ}\text{C}$) with the best-case scenario of limiting warming at levels ($<1.5^{\circ}\text{C}$). The agreement is based on the principle of just differentiated responsibility among its participants to combat global emissions. Repartitioning of responsibility among members is governed by criteria of economic development, national context that privileges a package of mitigative actions unique to that member, or even its historic cumulative emissions. Historically the G20 group is responsible for 80% cumulated greenhouse gas emissions between (1850-2021), of which the United States is responsible for (17%) of global accumulated emissions despite representing only (4%) of the global population in 2021 [3]. This goes to show the severe inequality of emissions, and the consequent risks on peoples with acute vulnerabilities to climate change due to limited resources for climate adaptation, or the lack of long-term inclusive governmental policies.

1.1.1 Dangers of global warming

The Intergovernmental Panel on Climate Change (IPCC) states in its 6th assessment report - summary for policy makers [4] – states that the increase of global temperature would have dire consequences on human life ranging from heat-related mortality to mental health challenges, biodiversity loss in ecosystems (forests, coral reefs, arctic regions), decrease in food production and freshwater sources, and mass waves of immigration from coastal cities due to sea level rise. Under the scenario of unabated greenhouse-gas emissions it is expected that global average temperature would increase by (4°C) by the end of the century relative to preindustrial levels (relative to year 1850). Under such conditions rare weather events such as heavy precipitation, droughts, or extreme heat-waves would become much more frequent: as an example, extreme heat waves previously occurring once every 50 years would occur roughly once per year [5]. For a scenario of a (4°C) increase of global temperature, thawing of permafrost and arctic sheets accelerates leading to a rise sea level by at least ($\sim 100\text{ cm}$) by the end of the century. Resulting consequences would be the flooding of coastal

cities which places roughly (630) million people at the risk [6], or the disappearance of certain regions such as the Tuvalu archipelago in the Asian pacific [7], or the Greenland permafrost sheet over the span of multiple millennia.

Figure 1-1 presents the changes in the annual hottest day in the year and the change in the annual total mean soil moisture content at different levels of global warming. It can be seen that annual hottest days increase everywhere in the globe, with the regions experiencing hotter days being particular to severe droughts as in regions of south America and Mediterranean Basin. Consequences on human health are translated by the onset of dangerous heat-humidity conditions that would occur daily in certain regions if warming surpasses the (4°C) mark. In certain regions, particularly along the equator, roughly all animal and seagrass species would be exposed to potentially dangerous temperature conditions.

Graphic removed to respect copyright

Figure 1-1: Change of temperature extremes and soil moisture levels at different global temperature rise (Source: IPCC 6th assessment report [4])

1.1.2 GHG emissions: Trends and sources

The IPCC has defined certain scenarios called “shared socioeconomic paths” (SSP) that trace the climate response as a function of GHG emissions, the associated impacts and risks, in addition to opportunities for mitigation and adaptation as subject to socio-economic variables. The IPCC highlights many scenarios or shared socioeconomic pathways (SSP_{x-y}) with (x) being the scenario number and (y) being the level of radiative forcing (W/m²) – the net heating rate per unit surface of earth. Of these scenarios distinguish the following: (SSP_{1-1.9}) where warming is limited to 1.5°C with more than 50% likelihood, and SSP_{1-2.4} where warming is limited to 2°C with more than 67% likelihood. Figure 1-2 shows the emission pathways under current policies to diverge greatly from those required to limit global temperature rise to 1.5°C and 2°C- considered as the safe limits to which ecosystems can naturally adapt. To achieve

greater emission reductions, countries employ the concept of naturally determined contributions of countries (NDC) [8] as per the Paris agreement [9]. NDCs are milestones in GHG emission cuts that it strives to achieve and can be: conditional where international assistance is needed (technical or financial) or non-conditional i.e. each country is capable of achieving with its current available means. Figure 1-2 shows that even under implementation of all NDCs, the emissions gap at 2030 remains large at 19 and 11 GtCO₂ equivalent from the pathways that limit warming to 1.5°C and 2°C respectively. The required yearly emission cuts are 5.3 and 8.7 percentage points to remain consistent with the 1.5 and 2°C warming pathways [3]. For reference the COVID-19 pandemic caused a dip in GHG emissions 2020 by 4.7% relative to the precedent year mainly due to the decrease of road transport emissions [10].

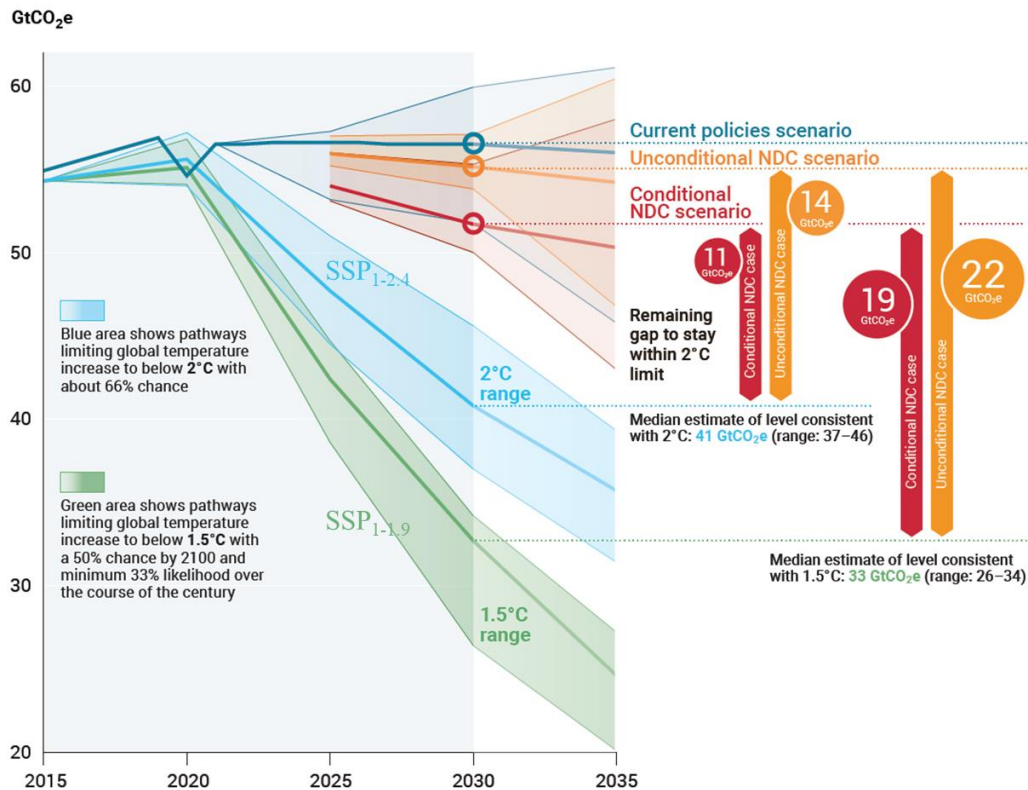


Figure 1-2: Global greenhouse gas emissions are presented as equivalent quantities of CO₂ [3]. Emissions over the period (2015-2022) are estimated global emissions. For upcoming years different emission paths are traced: SSP_{1-1.9} that limits warming to (1.5°C) with a 50% chance, SSP_{1-2.4} that limits warming to 2°C with a (67%) chance, projections based upon implemented policies in 2022. (CC-by 4.0)

The IPCC in its report entitled “Guidelines for GHG inventories” categorizes emissions to result from five main sectors: energy systems, industry, transport, buildings, and agriculture forestry and land use (AFOLU). Global estimates of CO₂ emissions are shown in Figure 1-3 show that the “energy systems” sector the major emitter of global GHGs (34%). This sector encompasses all fugitive emissions for mining coal and for the extraction and refining of oil and natural gas (10% of global GHG emissions in total), and includes generation of heat and electricity representing (24.2% of global GHG emissions in total) to be used mostly in the industry and buildings sector [10]. Figure 1-3 shows

emissions from south Asia (India) and eastern Asia (China, Japan, Republic of Korea) to rise steadily due to the wide deployment of fossil fuel power plants to meet the growth in their energy needs. The (EU) has shown decreasing CO₂ emissions annual decrease of (2%) in its GHG emissions to reach a (48%) reduction relative to the 1990 emission levels [11].

World-wide emission mitigation measures include deployment of wind turbines and solar PV panels for the production of electricity as motivated by an ever lower levelized cost of electricity (LCOE) with respect to coal fired power plants [12]. It is worth emphasizing that governmental actions under the form of production/investment tax credits, taxation on emissions, or a cap and trade systems help shape investments in energy production systems and incentivize flow of capital to limit emissions [13].

Another major driver of emissions mitigation is switching to lower carbon-intensity energy sources such as natural gas instead of Coal. While the European Union (EU) and the United States (US) have cut down their coal consumption (-202 Mt), this was offset through increased demand of China and India (+318 Mt) which increased global consumption. It is expected for coal consumption to peak during 2024 due to onset of renewables and natural gas as a fossil fuel source [14].

Currently, Solar and wind power have shown markable increases in the period (2010-2022) to account for 12% of the global electric power generation (Figure 1-3), however in meeting the global energetic requirements they still account for less than (3%) [15]. On the other hands fossil fuels continue to be the biggest energy source for the generation of electricity as seen in Figure 1-4, and will continue to play a vital role in meeting the energy needs of economies, while the transition to more sustainable energy systems takes place.

Graphic removed to respect copyright

Figure 1-3: global estimates of greenhouse gas emissions from major sectors [16]

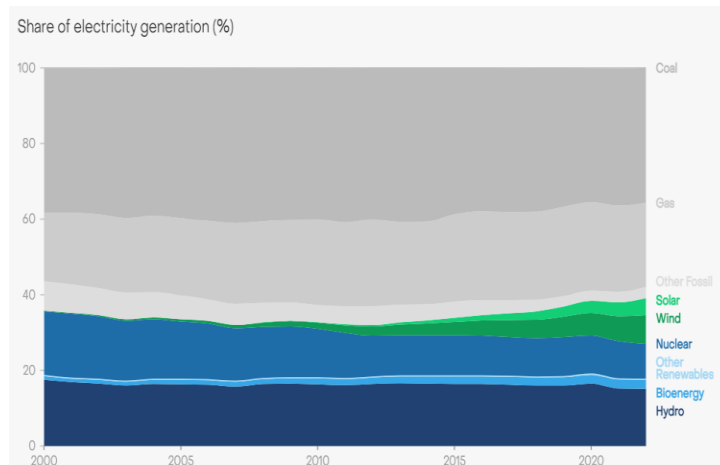


Figure 1-4: Global generation of electricity from different sources [15]. (CC-by 4.0)

1.1.3 Carbon capture utilization and storage

The matter of dismantling GHG emitting systems has to be done over many decades all while taking into consideration matters of energetic security for countries, economic competitiveness, and maintaining high living standards. Still it remains clear that economies of developed and developing nations will continue to rely on carbonaceous energy sources in the short and medium terms. In this sense the International Energy Agency (IEA) has defined carbon capture utilization and storage (CCUS) to be indispensable in bridging the transition to clean sustainable energy sources. CCUS when CO₂ is captured from large emitting point source (power plants, or an industrial site), then conditioned and compressed to be transported through pipelines into deep geological formations where it stored for long durations. Alternatively, the captured carbon could be used directly in a given application such as the production of synthetic fuels, injected into producing wells for EOR or the production of low-carbon hydrogen. The necessity of CCUS is demonstrated in Figure 1-5. The projected fossil production from existing wells and coal mines and the existing infrastructure would produce cumulative emissions that exceed the estimated carbon budget that limit warming to 1.5°C.

The main advantage of CCS is that it decouples emissions from the fuel type, i.e. regardless of the fuel used little to no CO₂ gas is emitted. Perhaps another reason is that it would allow the continual use of fossil fuel infrastructure and assets while conforming to net-zero emission goals, which prevents the risk of transforming into stranded assets. The IEA has set predicted the role of CCUS based on current policies and nationally determined contributions for a target net-zero emissions for energy system in the year 2070. CCS is expected to play an important role in reducing the CO₂ emissions by 10 GtCO₂/annum in the year of 2070 only to reach a cumulative mitigation of 15% CO₂ emissions. Main targets of CCS are large point sources from coal and gas fired power plants, chemical processes such as methanol and ammonia production, cement production, BACCS (bioenergy with carbon capture and storage) which is a carbon negative technology, metal industry and so on. DAC (direction air capture) is a relatively new technology that sequesters CO₂ from the atmosphere.

Costs of transport can be reduced by concentrating large point source emissions (power plants, cement, or chemical plants) in a limited region denoted as an industrial hub which promotes cooperation to erect a common infrastructure for the transport of captured CO₂ emissions [17, 18].

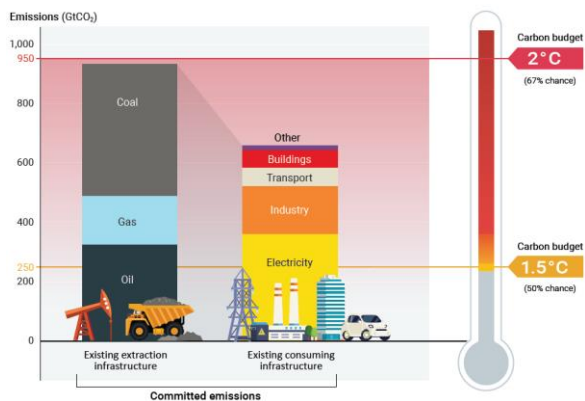


Figure 1-5: Committed CO₂ emissions from existing fossil fuel infrastructure, compared with carbon budgets reflecting the long-term temperature goal of the Paris Agreement

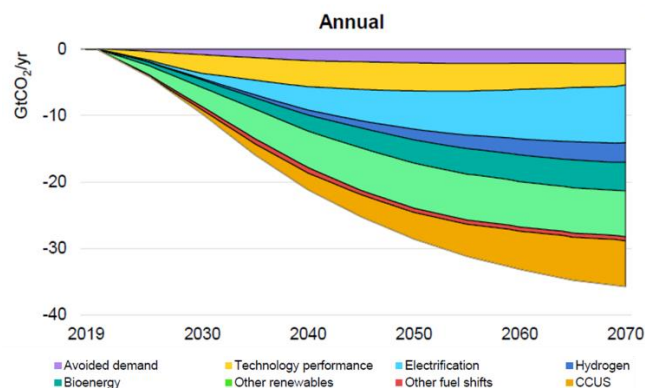


Figure 1-6: Global energy sector CO₂ emissions reductions by measure in the Sustainable Development Scenario 2019-70 [17] (CC-by 4.0)

1.2 Carbon Capture technologies

In 2021, 135 facilities exist for CO₂ capture with a total capture capacity of (~149.3 Mt per annum) [19], however most existing facilities are intended for upstream natural gas processing or in the chemical industry (production of ethanol, syn-gas, and fertilizer...). In 2023, the CC projects implemented in the energy generation sector account for (~16%) from the total CO₂ sequestered by CCS [20].

Large-scale deployment of CCS is hindered by the elevated capital operating costs which risk doubling the levelized cost of electricity (LCOE)- the specific cost of electricity unit (€/kWh) leads to zero net-present value of the project at the its end of life. In a more specific manner, that stage of separation of CO₂ from the gas stream accounts of 70-80% of the incurred cost of CCS [18, 21, 22] while the balance is for transport and storage. It is for this reason that R&D-focus ranges from incremental improvements in carbon capture to breakthrough novelties that promise high cost-reductions.

Carbon capture is a group of technologies with the purpose of separating CO₂ from its balance. The conditions in which the CO₂ will vary depending on the sector from which it is emitted as shown in Figure 1-7 [23], and will guide the usage of one capture technology over the other. The concentration and temperature of the CO₂-containing stream are essential in determining the minimum thermodynamic work necessary [24]. This would translate to greater energetic consumption as has been concluded by [25] where a decrease of 50% in the CO₂ concentration causes (~90%) increase in capture costs. Overall the real work required for the separation will depend on the technique used.

In the following subsection we discuss the main technologies for carbon capture (CC): Oxy-fuel combustion, Pre-combustion capture, and Post-combustion. Discussions in this part highlight the general operation of each capture technology, its characteristics and axes of improvement.

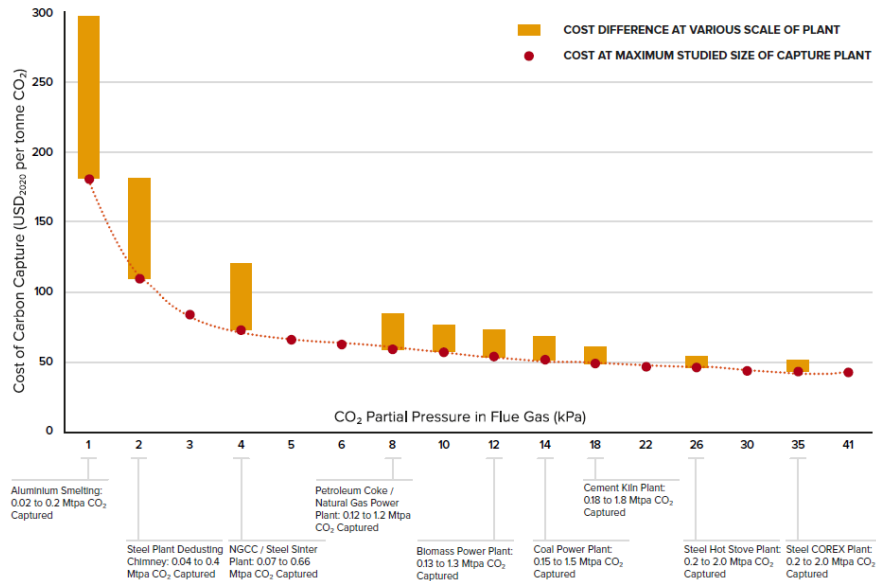


Figure 1-7: Concentration of CO₂ in flue gas stream from different processes [23] (CC-by 4.0)

1.2.1 Oxy-fuel combustion

This capture technology is based on the combustion of fuel combustion in an oxygen-enriched environment to create a CO₂-rich flue gas. The flow sheet diagram of the process is depicted in Figure 1-8 [26]. In the air separation unit (ASU), oxygen is separated from nitrogen to achieve a purity level (~95%) [26, 27]. Currently, the production of oxygen from air is achieved through cryogenic distillation with a duty of 200kWh/tCO₂. The produced oxygen stream enters the boiler along with a flue gas recycle-stream representing (~70%) of the outlet flue gas from the reboiler [28]. This is done in order to dilute the incident oxygen to levels that replicate that in air and control the flame temperature in the boiler to safe levels; otherwise the flame temperature may reach (3500°C) [22]. The exiting stream from the reboiler is composed mostly of (~80% CO₂) with the balance being mostly water [29]. The stream is then passed to the compression and purification unit (CPU) where much of the water vapor is condensed, and impurities (NO_x and SO_x) are removed using a low-temperature cryogenic flash (LTF) unit. The purity of the produced CO₂ depends on the end-of-pipe application, as an example, EOR requires CO₂ concentration to be higher than (>95%).

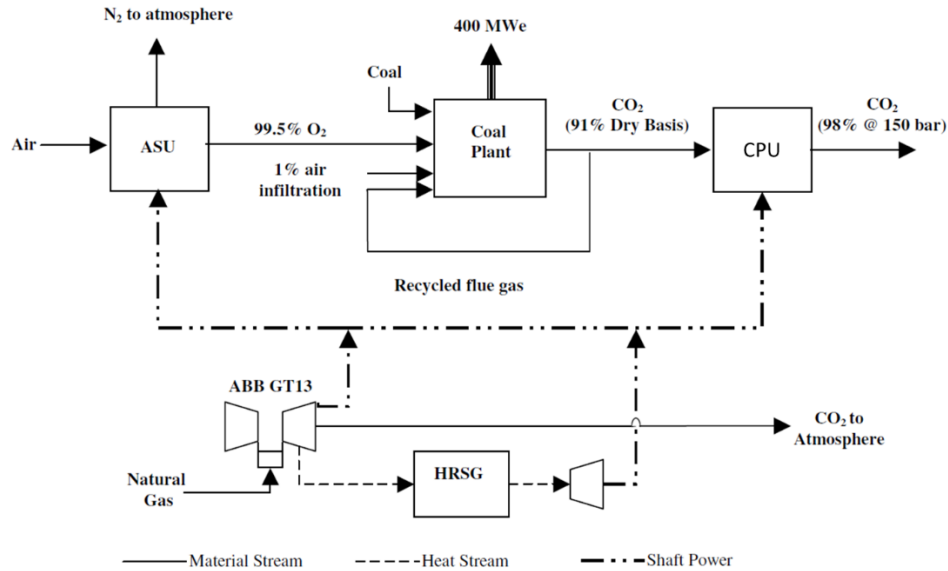


Figure 1-8: Operation of carbon using Oxy/fuel combustion technology in a pulverized coal power plant [26]. (reproduced with permission from Singh 2003)

Oxy-fuel combustion is considered to present a feasible technology to achieve deep-reductions of CO₂ emissions. Among its principle advantages is that it can be retrofitted to existing power plants with minimum adjustments [30], and the flue gas volumes are reduced to a fifth of those encountered in coal fired plants [31]. Another its characteristic is the low NO_x concentration in the flue gas [28] which signifies a lower capital cost of gas-cleaning devices [32]. Despite its strengths, the high energetic consumption of the ASU obstructs its wide-spread deployment followed by risks of damaging the boiler material at elevated combustion temperatures [27, 31]. The effectiveness and scalability of oxy-fuel combustion to capture CO₂ has been studied through a series of 13 projects shown in Table 1-1 [33], which allocates (OFC) a technology readiness level (TRL) of 7 [34].

Project Name	Overall Status	Country Location	Plant power (MW)	Project Start Date	Cost	Currency Name
SaskPower Oxyfuel	Terminated	Canada	300	01/01/2012	1 500 000 000	Canadian Dollar
South Korea CCS2	Active	South Korea	300	16/10/2009	-	US Dollar
FutureGen 2.0	Terminated	United States	200	01/01/2010	1 650 000 000	US Dollar
ZENG Worsham-Steed	Potential	United States	70	01/01/2007	-	US Dollar
Hydrogen Energy California Project	Terminated	United States	400	01/12/2019	4 028 136 691	US Dollar
Aviva Corp Coolimba Oxyfuel Project	Terminated	Australia	400	01/01/2010	1 000 000 000	Australian Dollar
Datang Daqing CCS Project	Hold	China	350	01/01/2020	-	US Dollar
Shanxi International Energy Oxyfuel Project	Potential	China	350	01/01/2020	-	US Dollar
OXYCFB300 Compostilla Project	Active	Spain	323	01/01/2009	180 000 000	Euros
Petrom Zero Emissions Plant (ZEP)	Potential	Romania	15	01/01/2009	-	US Dollar
White Rose CCS Project	Potential	United Kingdom	450	01/09/2014	-	US Dollar
Total Lacq Project	Completed	France	0.90	01/01/2009	60 000 000	Euros
Schwarze Pumpe (Vattenfall CO ₂ -Free Oxyfuel Plant)	Terminated	Germany	30	01/05/2008	120 000 000	Euros

Table 1-1: Worldwide projects for oxy-fuel combustion technology for carbon capture [33] (CC-by 4.0)

1.2.2 Pre-combustion

Pre-combustion capture involves the application of carbon capture technology before combustion takes place. The process transformation of hydrocarbon fuel into syngas either by gasification of coal or steam methane reforming [34] as shown in Figure 1-9 for flow sheet diagram of an integrated gasification combined cycle (IGCC) [35]. The process consists of four main sections: the oxygen island where pure oxygen stream is generated, syngas island where gasification and water-gas shift (WGS) reaction take place, the syngas purification island to remove H₂S, HCl, COS, and capture CO₂ [36], and the power island which has the combined Brayton/Rankine power cycles. The gasifier operates at a temperature above 1260°C and at elevated pressure in the order of (3-7 MPa) [24, 35]. The gasifier is operated above the ash melting temperature, hence ash is collected as a sludge [35]. Oxygen from the air separation unit (ASU) (95% O₂, 2%N₂, 3%Ar) [37] partially oxidizes the fuel as shown in reaction (1.1) to produce (CO) [38].



The heat generated from oxidation of fuel provides the necessary energy for the endothermic steam reforming reaction, with steam being bled from an intermediate pressure turbine, grossly represented. Such a configuration is called an auto-thermal reforming, other operating schemes exists such as with heat exchange reformer, and non-catalytic partial oxidation among others.



After dedusting and desulfurization, the produced syngas is composed mainly of CO, H₂, and CO₂ [39]. CO is reduced to CO₂ the water-gas shift (WGS) reactor where it reacts with steam as shown (1.3).



The equilibrium WGS reaction is exothermic, hence product formation is favored by lower temperatures. For this reason WGS reaction occurs in more than one reactor with a progressive decrease in temperature and pressure to favor conversion and avoid sintering of the catalyst (Iron-Chromium, or Copper-Zinc) [35].

The CO₂ in the treated syngas is in the range of (15-60%) [22] and at a sufficiently high pressure to justify the use of physical absorbents that require extensively less amounts for separation [40]. Of the most commonly used solvents are methanol, dimethyl ether of polyethylene glycol, or n-methyl pyrrolidone used in the Rectisol[®], Purisol[®] and Selexol[™] processes. In some of those processes, absorption occurs at very low temperatures (-45°C) for Rectisol and (0-5°C) for Selexol[™] which increases the refrigeration duty of these units [41]. Chemical solvents could be used for carbon capture, although they outperformed by physical solvents at high CO₂ pressures [35].

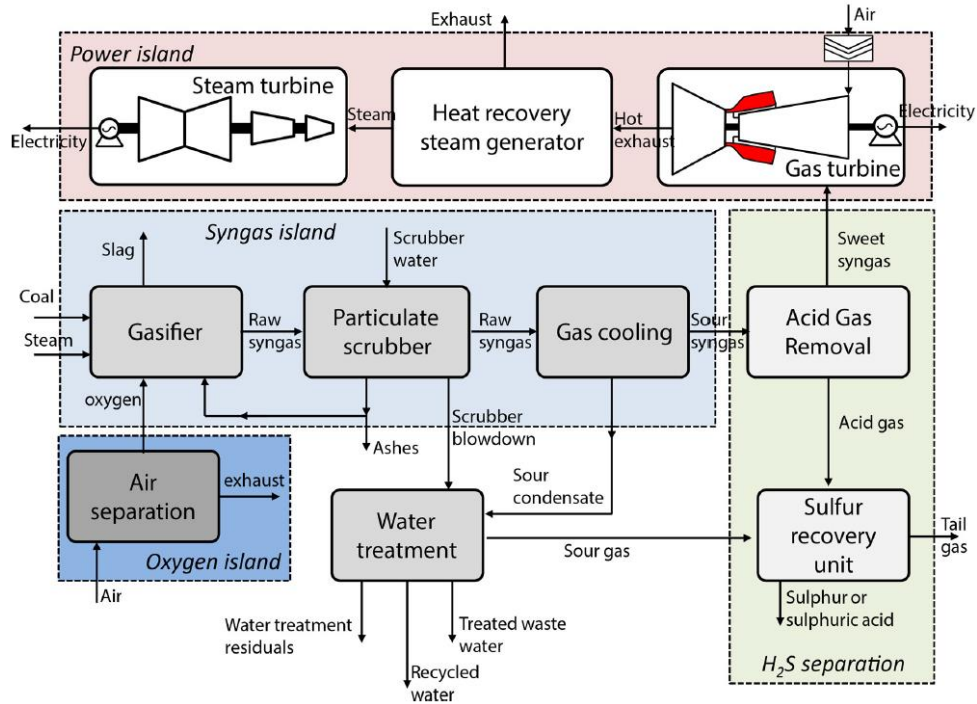


Figure 1-9: Process flow diagram for an IGCC process with carbon capture [35]. (reproduced with permission from Jansen 2015)

Pre-combustion capture incurs a low penalty on the power-plant in comparison to other capture technologies [22]. Pre-combustion literature studies report loss of efficiencies for coal fired plants in the order of (~10%) [37, 42, 43] similar to commercialization attempts by multinationals such as General Electric (GE) or Shell that report similar penalties [44]. A very big advantage of pre-combustion capture is the flexibility of choice: for periods of low electricity demand, the plant can produce syngas to produce high valued chemicals, or H₂ for fuel cells or as a low carbon fuel or in the transport sector [45]. Principle disadvantages of the process include difficulty in retrofitting existing power plants [46] as the power island would require a syngas plant in front. The greater number of unit operations to generate syngas increases the frequency of unplanned maintenance.

Currently pre-combustion capture in an IGCC is at a TRL level 7, however for CCS in a “conventional” power cycle using natural gas (NG) the TRL level is 9 meaning that the technology is matured and commercialized. To date the total number of projects - whether completed, active, or in the planning stage - amount to 61 and are concentrated in north America, China, and Australia [33]. Future efforts in pre-combustion capture focus on improvements of the WGS catalysis [47] as this operation accounts for 55% of the incurred penalty loss on the power output of the plant [46], improvements in CO₂ separation techniques using ionic liquids [48] or in conventional processes such as the Rectisol® [49], adsorption using metal organic frameworks (MOF) or separation using membrane processes among others.

1.2.3 Post-combustion carbon capture

Perhaps the category of carbon capture that is the most advanced is the Post-combustion capture technologies [50]. The difference from Oxy-fuel or pre-combustion techniques is that CO₂ is captured after combustion of the flue gas as shown in Figure 1-10. Post-combustion capture using amine solvents is most developed commercial-scale process, such that this process is responsible for capturing 860Mt CO₂ in 2023 [22]. Its greatest advantage is that it could be easily retrofitted to any large point source emission which requires little to no adjustment upstream of the capture process. As mentioned earlier, this capture technology englobes a portfolio of capture techniques can cover a wide range of operating conditions. Membrane separation, adsorption on a solid, and absorption in a liquid are the most common separation techniques and are briefly discussed below [46]. The separation technique of “chemical absorption” is to be discussed more thoroughly, and hence was accorded its section.

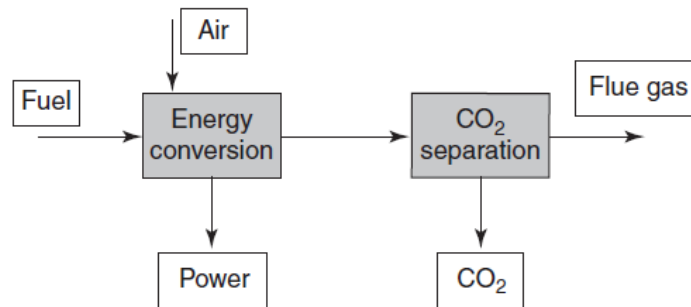


Figure 1-10: Post-combustion capture of CO₂ [50].

1.2.3.1 Membrane separation

Membrane techniques represent an innovative approach to separating CO₂ from flue gas mixtures. This method relies on a symmetric or asymmetric membrane that separates a gas medium when a driving force, such as a pressure difference, or temperature is applied on both sides. The membrane splits the gas stream (feed) into a permeate gas stream and a retained stream (retentate) [51]. Different membranes rely on different mechanisms for the separation of components of a gaseous phase [52]. Separation can be achieved by varying mechanisms which depend on the membrane types. Micro and mesoporous membranes separate the gaseous components by size sieving, or surface diffusion. Dense polymeric membranes rely on solution-diffusion mechanism to achieve separation.

Currently membrane separation is at a TRL level 7 [23, 53], i.e. it is being tested at the pilot plant scale. One example of a commercialization attempt membrane processes for carbon capture is by Membrane Technology and Research (MTR) [54]. MTR has implemented its proprietary PolarCap™ process - Figure 1-11 - which uses the Polaris™ membrane to treat 20 tons/day of flue gas at the National Center for Carbon Capture (NCCC) in Alabama [55]. Figure 1-12 is a glaring example of membrane process in comparison to chemical absorption processes having a similar treatment capacity.

Graphic removed to respect copyright

Graphic removed to respect copyright

Figure 1-11: PolarCap™ process by MTR for carbon capture from flue gases [55].

Figure 1-12: Footprint of PolarCap™ process for treatment of 20ton/day flue gas at the NCCC [55].

1.2.3.2 Adsorption on a solid

Selective adsorption is the adherence of a gas component on the outer surface of a material; this can be contrasted to absorption which entails the entire volume of the material. Adsorption technology involves two key processes: adsorption and regeneration. During the adsorption phase, a gas mixture passes over an adsorbent bed under specific operating conditions, allowing the target component to be adsorbed. This is followed by the regeneration phase, where the trapped gas is separated from the adsorbent, allowing the adsorbent to be reused in another cycle [56]. Regeneration techniques involve the manipulation of the operating conditions which leads to the techniques of: temperature swing adsorption (TSA), pressure swing adsorption (PSA), vacuum swing adsorption (VSA), pressure-temperature swing adsorption (PTSA) [46].

The purification process involves the adsorption of a component due to the affinity of the adsorbate onto the adsorbent [57]. Physical adsorption involves weak interactions between the adsorbate and the material pores [46] usually under the form of Van Der Waals forces which leading to low adsorption enthalpies [58] and consequently small regeneration requirement of the adsorbent [59]. Chemical adsorption or chemisorption occurs due to the formation of chemical bond between the adsorbent and the adsorbate resulting in higher enthalpies of adsorption compared to physisorption [58].

Common used adsorbents are broadly divided into two categories carbonaceous and non-carbonaceous materials. Carbonaceous materials include activated carbons which can be produced from inexpensive biomass (potato peels or barley waste) by pyrolysis [60] to attain high surface-area densities in the adsorbent ($\sim 1000 \text{ m}^2/\text{g}$) [61]. Other commonly used adsorbents include organometallic frameworks or zeolites [62]. The choice of adsorbent material should be subject to the criteria of high selectivity, good thermal and electrical conductivities, high durability, and good adsorption/desorption kinetics.

1.2.3.3 Absorption in a liquid

Absorption is dissolution of a gaseous compound in the volume of a liquid (absorbent). Absorption can either be physical and would then be based on the inter-molecular interactions between the dissolving compound and the absorbent media. Usually physical solubility is expressed with Henry's law which linearly relates the partial pressure of the overhead gas to its concentration in the absorbent phase [22, 46]. Physical solvents can be regenerated at reduced pressures, by the addition of heat, by using a sweeping gas, or a mixture of these techniques [63]. An ideal solvent is

defined by its availability, low cost, low volatility, low corrosion rates, low degradation rate, and good absorption/regeneration kinetics. Physical absorbents have found application in carbon-free power generation by separating CO₂ from H₂-rich steam in pre-combustion capture technologies. Processes used to achieve this separation are the well-known Rectisol, Purisol, Selexol, and Fluor processes among others [35, 40, 41].

Chemical absorption involves the dissolution of a gaseous component by chemically reacting with the absorbent. Contrary to the physical solvents, the chemical solubility generates many ionic species that are in equilibrium with another. The resulting complex interactions in the medium are described by vapor-liquid equilibrium laws. Chemical absorption finds utility when the partial pressure of soluble gas is low, such conditions can lead to appreciable concentration in the liquid phase. Figure 1-13 [35] demonstrates that the operating conditions of the soluble gas determine the appropriate separation method.

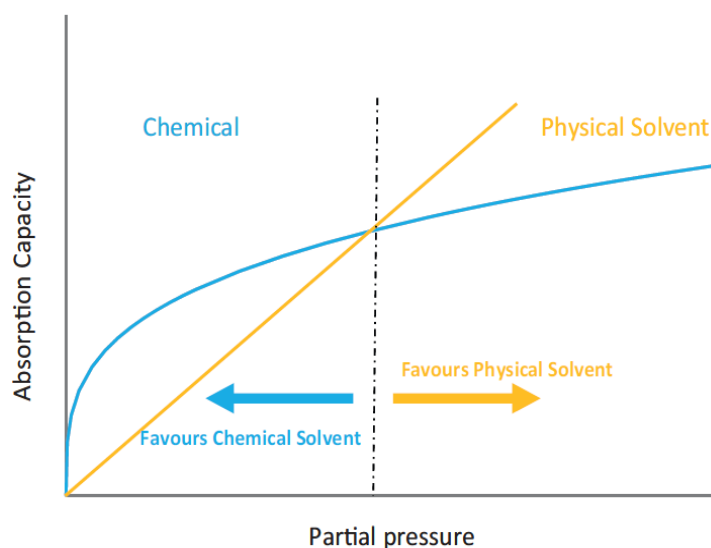


Figure 1-13: Demonstration of the operating range of physical and chemical absorption

1.2.4 Carbon capture by amine absorption

1.2.4.1 Operation

The operation of a classical post-combustion chemical absorption process is demonstrated in Figure 1-14 [64]. The process employs the industry standard aqueous ethanolamine (ETA) [41] to attain CO₂ recovery-rate of around 80-95% [26, 65]. The carbon capture train is composed of a flue gas pretreatment unit, SO₂ pre-scrubber unit, packed column for gas absorption (absorber), stripping tower, solvent recovery unit and other auxiliaries such as pumps, blowers, and heat exchangers among others [66]. In an operation of a coal fired plant the flue gas exiting the boiler is passed by a flue gas desulfurization unit (FGD), and a selective catalytic converter to reduce SO_x and NO_x to below (10 ppmv) to avoid solvent degradation [67, 68]. The flue gas is then passed direct contact cooler (DCC) to reduce its temperature to [40 – 50] °C further reduce SO_x content, and a blower to counteract the downstream pressure drop. In

the absorber, the low-temperature lean 30% wt. ETA solvent is made to flow counter-currently with respect to the flue gas. The exiting solvent stream is enriched in CO₂ expressed by the high carbonation ratio (0.4 - 0.5 molCO₂ / mol ETA). The CO₂ lean flue gas at the top of the absorber is washed to lower its temperature and condensate solvent fumes prior to its release.

The “cold” rich solvent stream exchanges heat with the “hot” lean solvent stream to raise its temperature to (~100 °C) before entering the stripper. The stripper operates at pressure (1.5 - 2 bar) [26] and a reboiler generates steam at a temperature of 120°C [69] that travels counter-currently with respect to the liquid solvent and liberates the chemically dissolved CO₂. The steam and solvent vapors of the overhead stream are condensed by cooling water at T = 40°C [26] then separated in the accumulator. CO₂-rich gas is conditioned for further purity then transported for its end-of-the-pipe application such for enhanced oil recovery (EOR) at a purity of (95 vol%), or for underground sequestration (90 vol%). The hot lean solvent at the bottom of the stripper with a carbonation ratio $\alpha \in [0.2, 0.3]$ [65] is recycled to the absorber subsequently to cooling to the temperature range $\in [30 - 50]$ °C as lower [70]. The lower limit of lean solvent temperature is superior by 10°C than that of cooling water at 20°C, otherwise lower absorber temperatures are more efficient.

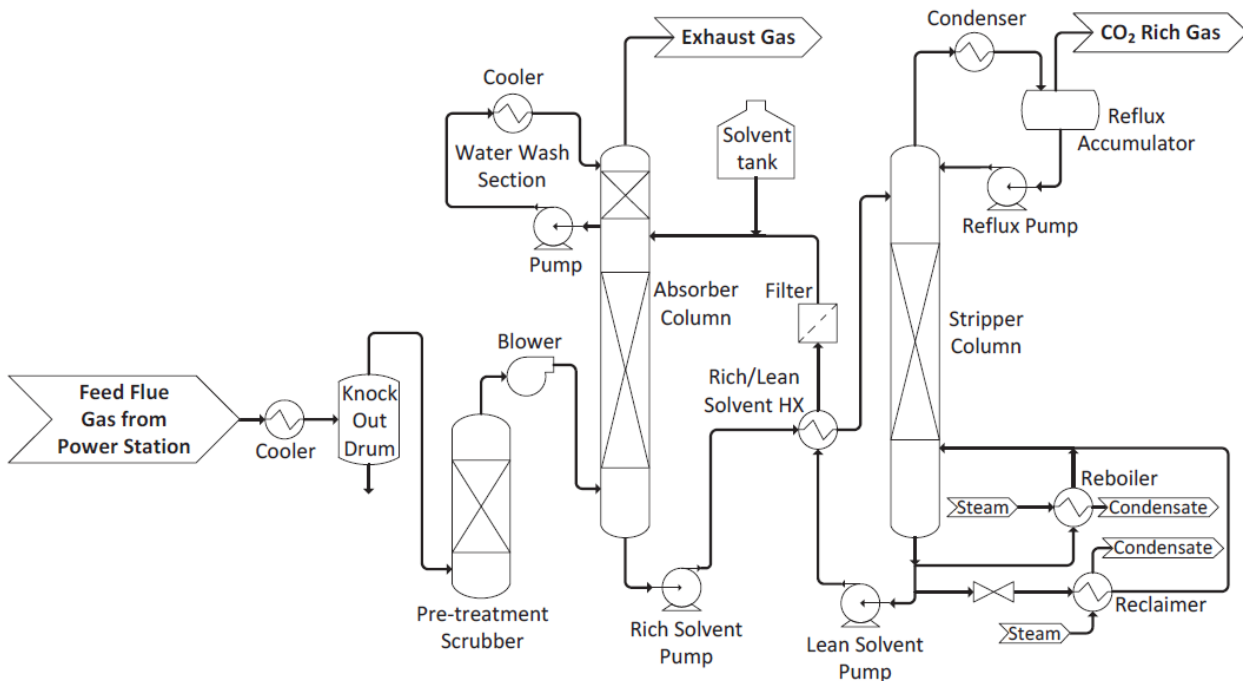


Figure 1-14: Process flow diagram for post-combustion capture by chemical absorption [64]. (Reproduced with permission from Bui 2013)

1.2.4.2 Process disadvantages

High energetic penalty

Implementation of post-combustion capture by amine absorption entails losses in the energetic efficiency of any emitting process. In the case of a power plant (PC or NG), the efficiency penalty leads to a decrease of the net electrical power that is available for consumer use (E_{net}). Figure 1-15 [71] demonstrates the repartitioning of the gross electrical power (E_{gross}). Auxiliary power (E_{aux}) is used by the power generation process to run itself, power is diverted to pumps and flue gas blowers in the capture plant (E_{cap}) [72], and finally the power to run the compression train of CO₂-rich stream. Moreover the reboiler of the stripping column is run by low pressure steam that is extracted from the power generation process [68]. A coal-fired power plant would have an efficiency of about (41-48%) [66, 73] depending on type of the power cycle [71]. When amine post-combustion is implemented, drops in the efficiency levels of 14% [74], 13% [75], 9% [73], and 11% [66] were reported.

Elevated capital expenditure

The high capital expenditures (CAPEX) for the treatment of the large volumes of flue gas streams. The presence of nitrogen in combustion-air leads to flue gases with diluted CO₂ concentrations. That decrease in driving force for capture, for a coal-fired power plant CO₂ content approaches (7-15%) while for a gas-fired one it is in the range of (4%) [23]. Consequently, implementing capture under such conditions entails high capital costs due to exaggerated equipment size necessary for the treatment of these volumes [67].

Solvent degradation and process corrosion

ETA can degrade due to a variety of reasons such as thermal degradation, or oxidation. Thermal degradation of ETA activates at 205 °C [76] and thus it is more likely to occur in the solvent regeneration unit. It is deemed of small effect but nonetheless leads to the formation of ammonia and N-(2-hydroxyethyl) ethylenediamine (HEEDA) in the presence of CO₂ [77]. The main degradation pathway of ETA is oxidative degradation, which occurs due to the presence of appreciable concentrations of oxygen in the absorber (~7 %). The Oxidative degradation of ETA yields a variety of products from which we mention those of corrosive character, i.e. acidic compounds: formic, glycolic and carboxylic, oxalic acids among others [77]. The subsequent reactions with ethanolamine causes the formation of non-regenerable heat stable salts [78]. A rule popular rule of thumb in natural gas purification is that ETA should not exceed 30% by weight in the aqueous solvent, as this prevents excessive equipment corrosion [79]. Increased concentration of ETA in of itself is not corrosive, rather it is the increased yield of acidic concentrations as a result from degradation reactions [80].

Studies through literature all report very consistent ETA losses/degradation, estimated to be in the order of (~1.5 kg) of ETA per ton of CO₂ captured [66, 72, 73]. Cost-wise, this represents around (~26.8 %) from all operating and maintenance costs (O&M). It was found that (ETA) solvents are caused a uniform corrosion rate of (~ 1 μm / yr) carbon steel equipment, whereas stainless steel vessels were much more resistant [69].

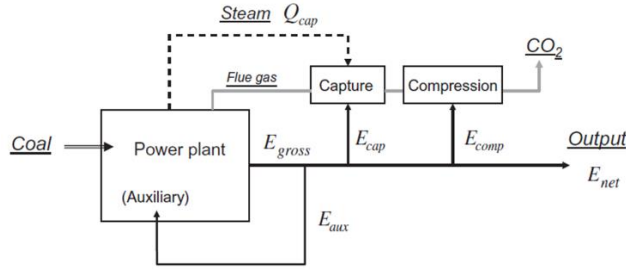


Figure 1-15: Repartitioning of power in an electrical power plant with CO₂ capture and compression [71]. (Reproduced with permission from Goto 2013)

1.2.4.3 Post-combustion capture by amine absorption: demonstrators world-wide

In 2021, the number of commercial CCUS facilities in the world increased to 135 according to the report published by the Global CCS Institute dating to September 2021 (27 are operational, 4 are in construction, 58 in advanced development (“Global CCS Institute. (2021)). These numbers can be contrasted with 2020 and 2019, where large-scale CCUS facilities numbered 65 and 51, with at a maximum CO₂ capture capacity of around 114.3 MtCO₂ [81] and 96 MtCO₂ [82]. To achieve Paris Agreement climate targets by 2050 (>2000) facilities will be required as outlined in the IEA’s Sustainable Development Scenario, between 70 and 100 new facilities need to be built every year. Figure 1-16 shows the CCS facilities around the world in late development at end of 2021[19]. It can be particularly distinguished that CC is not exclusive to power generation, as only 26 facilities (62.51 MtCO₂/year) are deployed in power plants, the share of natural gas processing is 20 facilities (42.95 MtCO₂/year), chemical production 9 facilities at 13.72 (MtCO₂/year), hydrogen production 16 facilities at 13.45 Mt CO₂/year, ethanol production 39 facilities at 10.85 MtCO₂/year, fertilizer production 7 facilities at 7.45 MtCO₂/year, and cement 3 facilities with 3.2 MtCO₂/year. The progress in a few CCS projects is discussed in the next section.



Figure 1-16: Map of the CCS projects worldwide [19]. (CC-by 4.0)

BD3 CCUS project

The project was initiated by SaskPower to allow continued operation of coal-fired power-generating stations, while mitigating the climate change impact of associated air emissions. A CCS unit (Figure 1-17) of a theoretical capacity of

1 MtCO₂/annum was installed at the boundary dam power station in Canada (section 3 of the power plant) [83, 84]. The capture facility cost was \$0.75 billion Canadian dollar, with a rated capture efficiency of 90%, with the necessary infrastructure to allow for utilization of the produced CO₂ in enhanced oil recovery (EOR) at the Weyburn oilfield (70 km away). The excess CO₂ was transported by a 2 km pipeline to the Aquistore site for injection and long-term geological storage at 3.4 km of depth, while captured SO₂ from flue gases was sent to a Sulphuric Acid Plant. The plant required a tuning and refining period of one year to reach optimum performance, capture efficiency during first year was 50% then it rose to (80-90 %) throughout the rest of its life. This plant was important in solving challenges that are crucial not only for improving for establishing and strengthening global perception and confidence in CCS as a CO₂ mitigation solution.

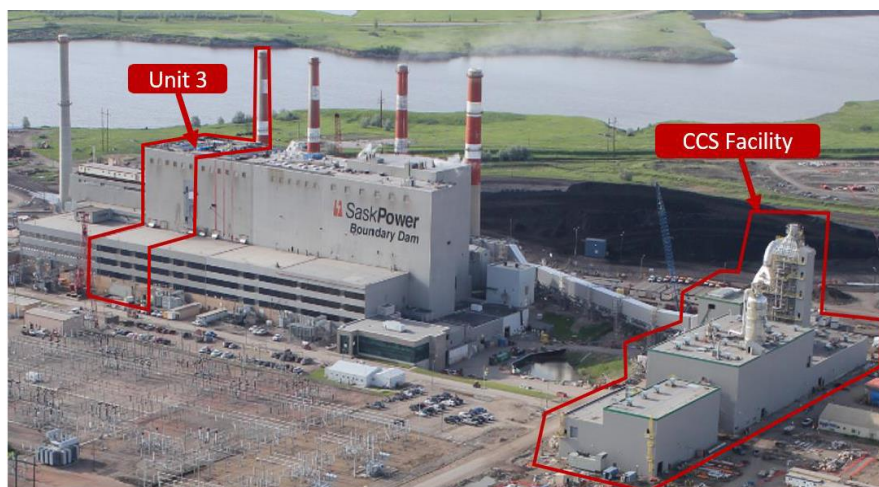


Figure 1-17: photo of Boundary dam CCs project operated by SaskPower. (Reproduced with permission from stephenne 2014)

CCS project in Power Plant in Mobile County, Alabama

Mitsubishi heavy industries (MHI) collaborated with Southern Company, which is a major electric power company in the southern eastern U.S., and the Electric Power Research Institute (EPRI) to construct a demonstration facility for the capture of CO₂ from the flue gas of a coal-fired plant [85] (with a capacity of 500 tons per day) at Southern Company subsidiary Alabama Power Plant in Mobile County, Alabama. MHI adopts the KM CDR Process[®] (Figure 1-19), a CO₂ capture process that uses the unique “KS-1” solvent developed together with the Kansai Electric Power. The carbon storage was conducted as part of the regional carbon sequestration partnership of the Department of Energy (DOE) and the southeast regional carbon sequestration partnership.

This demonstration facility started the capture of CO₂ from the plant in June 2011 and subsequently the underground storage of captured CO₂ in August 2012. The CO₂ capture plant attained a CO₂ capture amount of 500 tons per day and a CO₂ capture ratio of 90 percent, according to the initial plan, and verified its energy saving performance requiring steam consumption of 1 ton per CO₂ ton, and by the end of October 2013 and the cumulative CO₂ capture amount reached approximately 200,000 tons.

Important takeaways from this project for MHI are the validation of an automatic load-following control-system that maintains capture efficiency as the flue gas flow and composition change with varying power boiler duty following electric power production. Other activities revolved around testing the solvent-emission reduction technology developed by MHI which reduced emissions by 90% with the original process of MHI, along with other heat integration process schemes to reduce lower the efficiency penalty on power generation.

Graphic removed to respect copyright

Graphic removed to respect copyright

Figure 1-18: Photo of MHI's KM-CDR carbon capture unit at Alabama power plant in Mobile county [85].

Figure 1-19: Process flow diagram for MHI's KM-CDR carbon capture process by chemical absorption in KS-1 solvent [85].

1.3 Absorption of CO₂ in aminated solvents

Up to this point, discussions of amine absorption has been treated from an ergonomic manner where operation, performance and problems were treated. In this section we briefly the kinetic and thermodynamic models that describe the reaction of CO₂ with alkanolamines.

1.3.1 Reaction kinetics

An important characteristic of reactive absorption processes is the broad spectrum of reaction rates they demonstrate, ranging from very slow (sluggish reactions) to nearly instantaneous (fast reactions). This variability presents a challenge in attaining an optimal process design, as conventional models may not possess the required level of precision and scalability while rigorous depictions of gas-liquid contactors results in complex systems of equations that are often difficult to solve reliably and efficiently [86]. Therefore, correctly hierarchizing the impact of different parameters on reactive absorption allows to draw out assumptions that simplify the model with little loss of accuracy.

General modeling approaches are presented in Figure 1-20 and are ordered in the range of increasing complexity that vary in light of different depictions of mass-transport and reaction modeling. Model number 1 is the simplest where the gas-liquid reactor is modeled as an ideal tray column where no limitations to mass transfer, and reaction kinetics are infinitely fast (instantaneous). Model 2 on the other hand considers the liquid bulk reactions. In models 3-4-5 a rate-based approach adopted where the resistance to transport is taken into consideration. Model 3 assumes chemical equilibrium while model 4 depicts reaction kinetics inside a perfectly mixed bulk, while the enhancement factor accounts for kinetics in the liquid film. Model number 5 is of greatest complexity hence kinetics in the bulk and film are rate-based, although the assumption of a perfectly mixed liquid bulk may fall short under certain hydrodynamic conditions of the solvent.

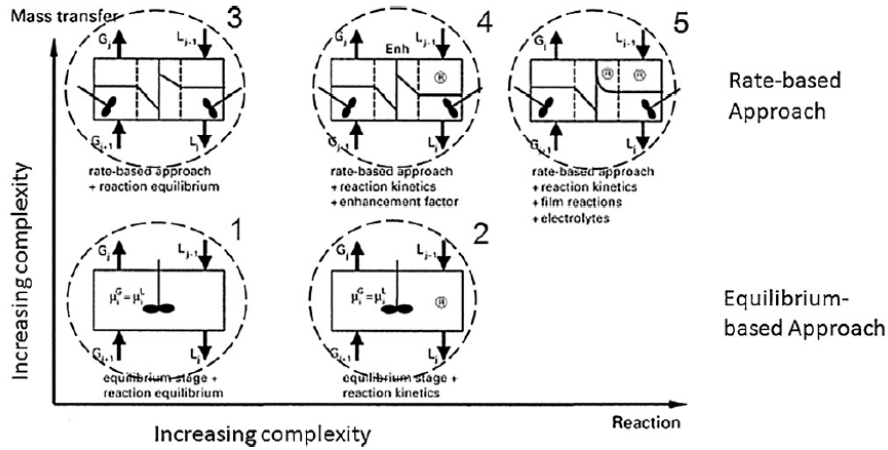


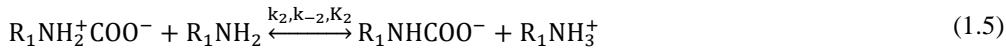
Figure 1-20: Different modeling schemes for gas-liquid reactive systems [86]. (Reproduced with permission from Kenig 2001)

CO₂ reactions with aqueous amines have been interpreted either by the zwitterion mechanism, which was first proposed by [87], or by the base-catalyzed hydration reaction mechanism, also known as termolecular mechanism [88]. According to the Zwitterion Mechanism, CO₂ in the liquid phase reacts with a primary or secondary amine to form a zwitterion intermediate that is subsequently deprotonated by any base in the solution. The zwitterion mechanism unfolds as follows: CO₂ combines with ethanolamine (R₁NH₂) to produce the zwitterion as shown in (1.4) the reactions that CO₂ undergoes with secondary amine di-ethanolamine (DEA) and the primary one 2-amino-2-methylpropanol) (AMP) are similar in nature.

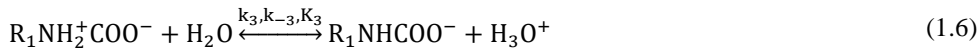


Once formed, the zwitterion proceeds to be deprotonated by any base in the solution (ETA, OH⁻, H₂O) as shown in (1.5), (1.6), and (1.7) respectively with (k), (k₋₁) and (K) being the forward, backward rates and the equilibrium constant of the reaction respectively.

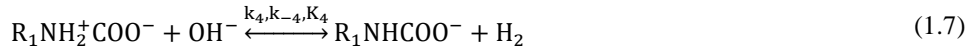
Zwitterion deprotonation by ethanolamine:



Zwitterion deprotonation by water:



Zwitterion deprotonation by hydroxide ions:



Therefore for reaction between CO₂ and ETA solution, total rate is expressed analytically in (1.8) by [89].

$$r_{\text{CO}_2} = \frac{-k_1[\text{R}_1\text{NH}_2]([\text{CO}_2] - [\text{CO}_2]_e)}{1 + \frac{k_{-1}}{k_2[\text{R}_1\text{NH}_2] + k_3[\text{H}_2\text{O}] + k_4[\text{OH}^-]}} \quad (1.8)$$

Application of process conditions assumptions may lead to different expressions of the reaction rates [90], as an example, the widely known pseudo-first order reaction rate is based on the assumptions of the solvent being free of CO₂, constant amine concentration, zwitterion deprotonation by ETA molecule is dominant and is much slower than

the zwitterion formation step [91]. With these assumptions, the rate of reaction would resemble a first order reaction rate with respect to CO₂. It is worthy to note that pseudo first order rate does not find utility in modeling reactive absorption at absorber or stripper conditions due to elevated loading levels $\alpha \in [0.2-0.5]$ [92], instead it is used to obtain reaction kinetic data in gas-liquid contactors of very well-defined hydrodynamic conditions and transfer phenomena [93].

$$r_{\text{CO}_2} = -\frac{k_1 k_2}{k_{-1}} [\text{R}_1\text{NH}_2]^2 [\text{CO}_2] = k_{\text{app}} [\text{CO}_2] \quad (1.9)$$

1.3.2 Modeling transfer phenomenon with chemical reaction: resistance in series approach

The resistance-in-series is an analytical model first proposed by [94] which models mass-transfer in a circuit-like approach. In a gas-liquid transfer operation, the transported molecule encounters two resistances, that in the stagnant liquid film, and that in the stagnant gas film. The transfer flux that originates between the gas and liquid bulks, for a transfer with chemical reaction can be expressed as follows, with (C_{lb}) and (C_{gb}) designating both the bulk molecular concentrations in the liquid and gas phases respectively, (k_{l}) and (k_{g}) designate the mass-transfer coefficients across the stagnant liquid and gas films, while (E) is the enhancement factor and (H_{e}) is the Henry's law.

$$J = \frac{(C_{\text{lb}} - C_{\text{gb}})}{\left(\frac{1}{E k_{\text{l}}} + \frac{1}{k_{\text{g}} H_{\text{e}}}\right)} \quad (1.10)$$

The driving force for mass-transfer [$C_{\text{lb}} - C_{\text{gb}}$] is positive for a desorption operation, and negative for an absorption operation. The transfer coefficients can be either empirically determined, or may be an expression resulting from resolving the equation of mass-transport over the geometry of the gas-liquid contactor. Enhancement factor is quantified as the ratio between the absorption rate of a gas component in a liquid when a chemical reaction is present and the absorption rate when no reaction occurs, both at identical concentration driving forces. This definition is advantageous as it sums up all the impacts of chemical reactions on the absorption rate into a single quantity. However, there isn't a universal analytical expression and it is very much dependent on the gas absorption conditions. Technically, this quantity accounts for the consumption of the diffusing molecule in the case of absorption or the generation of the latter for the case of chemical desorption, in any case it is strictly positive and greater than unity. Assuming the reaction between the soluble gas (A) and the absorbent (B) we distinguish different regimes as shown in Figure 1-21.

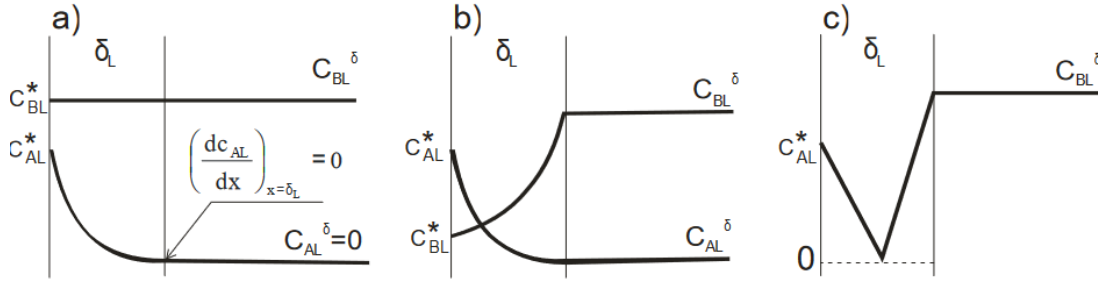


Figure 1-21: Concentration profiles of components different cases of reaction regimes: (a)-pseudo first order regime, (b)-fast intermediate regime, (c)-instantaneous regime

The case of fast pseudo first order (subfigure-a) occurs at low concentrations of absorbing gas in the liquid film, coupled with fast reaction absorption reaction rate, this case is especially useful when measuring kinetic reaction data. At higher gas concentrations in the film, the soluble gas is able to diffuse deeper into the absorbent and thus the liquid film increases in thickness as shown in subfigure (b). At very high concentrations of dissolved gas coupled with instantaneous reaction rates, the absorption is limited by the diffusion of the reactant molecules to the gas film as shown in subfigure (c) in Figure 1-21. At instantaneous rate the enhancement factor (E_∞) is defined as shown in (1.11). Here the rate of reaction is strictly determined by the diffusion rate of the reactant (B) from the bulk to the liquid. Distinguishing between different reaction regimes is dependent on the value of the Hatta number (Ha) shown in (1.12).

$$E_\infty = 1 + \frac{D_B C_{B,b}}{v_B D_A C_A^*} \quad (1.11)$$

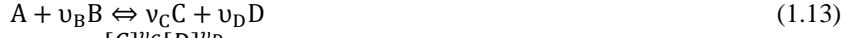
$$Ha = \frac{\sqrt{k_2 D_A C_{B,b}}}{k_1} \quad (1.12)$$

Perhaps the case of gas absorption was best covered by [95] for reversible reaction with instantaneous rate. The author solved Fick's equation for diffusion over the reactive liquid film in the absorbent to give the analytical expression of the enhancement factor (E). This expression has found its usefulness in modeling gas desorption from alkanolamines as the high temperatures usually employed allow the reaction to be very rapid and thus assume instantaneous character [96–98].

1.3.3 Modelling chemical equilibrium in CO₂-amine-H₂O system

Main categories of model include empirical, semi-empirical, and rigorous models all of which rely on experimentation to correlate VLE data. Example of empirical model is found in the work of [99]. Semi-empirical models are not rigorously defined and in consequence exhibit considerable errors when correlating equilibrium data of very low carbon dioxide loadings and high temperatures [100]. Yet due to their inherent simplicity, they find extensive applications in correlating the VLE of carbon dioxide loaded aqueous alkanolamines. Semi-empirical models employ published apparent equilibrium values for the system reactions, one or more of the equilibrium properties are adjusted to obtain best fits with the experimental data. In this manner Kent-Eisenberg Model is a prime example of such a modeling approaches [101], although lacking in theoretical background it is popular in correlating vapor-liquid equilibrium (VLE)

data of carbon dioxide loaded aqueous alkanolamine solutions. Other derivations of the model exist such as those by [102] or [103]. In the semi-empirical model of Kent-Eisenberg, each chemical reaction provides an algebraic equation due to chemical equilibrium as shown in (1.13) and (1.14).



$$K = \frac{[C]^{\nu_C} [D]^{\nu_D}}{[A][B]^{\nu_B}} \quad (1.14)$$

We enumerate below the reactions occurring for a system of CO₂-H₂O and a primary amine:

Carbamate reversion to bicarbonate:



Dissociation of protonated amine:



Dissociation of carbon dioxide:



Dissociation of bicarbonate:



Dissociation of water:



The resulting algebraic equations are complemented by electroneutrality balance, amine balance, and balance of CO₂ content in the solution. It should be noted that water and amine components are considered to be non-volatile materials.

The electroneutrality of the solution dictates the following:

$$\sum z_i \square_i = 0 \quad (1.20)$$

At a given loading (α) the alkanolamine can be present under its initial form, or under its derivatives:

$$[\text{RNH}_2]_{|\alpha=0} = [\text{RNH}_3^+] + [\text{RNHCOO}^-] + [\text{RNH}_2] \quad (1.21)$$

The total dissolved CO₂ is balanced as follows:

$$\alpha[\text{RNH}_2]_{|\alpha=0} = [\text{RNHCOO}^-] + [\text{HCO}_3^-] + [\text{CO}_3^{2-}] + [\text{HCO}_3^-] \quad (1.22)$$

For greater ruggedness in thermodynamic modeling, the Dishmukh-mather model [104] can be used which includes the activity coefficients (γ) in the calculation of the equilibrium constants as shown in (1.23).

$$K = \frac{[C]^{\nu_C} \gamma^{\nu_C} [D]^{\nu_D} \gamma^{\nu_D}}{[A] \gamma^{\nu_A} [B]^{\nu_B} \gamma^{\nu_B}} \quad (1.23)$$

With the activity coefficient being calculated from the Debye-Hückle equation (1.24), the first term accounts for long range electrostatic forces while the second accounts for short range Van-der-Walls forces. The parameter (A) is related to the dielectric constant of the mixture, (b) is a constant, (I) is the ionic strength, (z) is charge of the molecule, while (β_{ij}) the binary interaction parameter.

$$\ln \gamma_i = \frac{-Az_i^2 I^{0.5}}{1 + b_k I^{0.5}} + 2 \sum_{j=1}^n \beta_{ij} \square_j \quad (1.24)$$

1.4 Advances in post-combustion capture by chemical absorption

In order to achieve wide-spread implementation of carbon capture, cost-reduction and economic feasibility should be targeted. A quick examination of Figure 1-22 shows major costs reside in steam generation, capital costs of plant, solvent make-up and fixed operating and maintenance. In this part we explore recent improvements in chemical capture which includes: alternative solvents to alleviate solvent make-up and steam duty, membrane contactors as a more

economical and compact replacement to packed columns, and microwave technology as a novel method that promises reduction in regeneration energy.

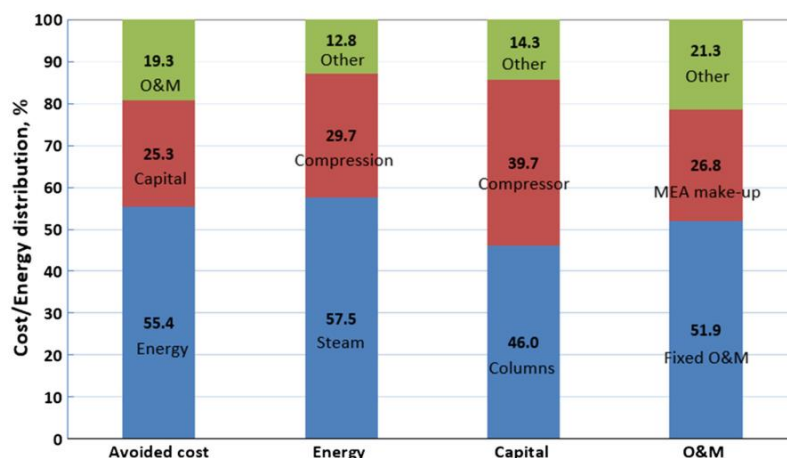


Figure 1-22: Equipment cost in chemical absorption process using (ETA) solvent [105]. (Reproduced with permission from Li 2016)

1.4.1 Alternative alkanolamine solvents

A good solvent is characterized by many of qualities the most important of which are: high loading rate (defined as the molar ratio CO₂ to the solvent), fast reaction kinetics, and environmentally friendly [106]. The cyclic capacity is of utmost importance of a solvent, it is the difference between the rich loading at the absorber conditions, and lean CO₂ loading ($\alpha_{rich}-\alpha_{lean}$) after regeneration [107]. Therefore, a higher cyclic capacity would decrease the solvent circulation rate, and increase the thermodynamic efficiency of the stripping column [108]. Fast kinetics is an important feature hence this leads to smaller column sizes reductions and operating costs. The task of finding the best solvent for post-combustion capture is no easy one, due to high count of possible solvents and the corresponding necessity of experimental knowledge of physical, transfer, thermal, chemical and CO₂-solubility properties at a wide range of operating conditions. This motivates the development of rigorous thermodynamic models that are able to predict those properties [109]. The three main classes for thermodynamic modeling are empirical models, equations of state, and excess Gibbs energy models [110]. Alkanolamines is the most studied group of solvents for CO₂ capture in chemical absorption, we proceed to briefly discuss common alkanolamine solvents for chemical absorption.

Alkanolamines are characterized by the presence of a hydroxyl group (-OH) which decreases their volatility by hydrogen bonding. The amino group provides the necessary alkalinity for the acid-gas reaction with CO₂ [79]. Broadly speaking, alkanolamines are divided into three groups: primary, secondary, and tertiary amines. Primary alkanolamines are characterized by the nitrogen atom of the amino group being substituted only once, i.e. it has two bonds with Hydrogen and one bond with an alkyl group. Secondary alkanolamines experience double substitution, while tertiary alkanolamines have a fully substituted [93]. The most common alkanolamines for carbon capture are presented in Table

1-2 which includes: primary amines such as ethanolamine also known as (MEA) and diglycolamine (DGA); secondary amines like di-ethanolamine (DEA) and di-isopropanolamine (DIPA); tertiary amines such methyldiethanolamine (MDEA) and triethanolamine (TEA).

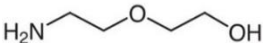
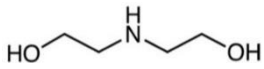
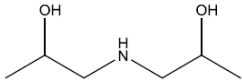
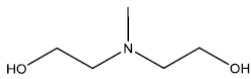
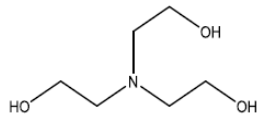
Secondary name	Abbrev.	CAS number	Chemical structure	MW (g/mol)	pKa
Ethanolamine	ETA	141-43-5		61.08	9.44 [111]
Diglycolamine	DGA	929-06-6		105.13	---
Diethanolamine	DEA	111-42-2		105.14	8.92[111]
Diisopropanolamine	DIPA	110-97-4		133.19	8.84 [112]
N-Methyldiethanolamine	MDEA	105-59-9		119.16	8.65 [113]
Triethanolamine	TEA	102-71-6		149.19	7.85 [113]

Table 1-2: Most commonly used alkanolamines for chemical capture of CO₂ [79]. (Reproduced with permission from Nielsen 1997)

1.4.1.1 Primary alkanolamines

Primary alkanolamines are characterized by high reactivity with CO₂ and low to intermediate absorption capacities [41]. The reaction of primary amines with CO₂ is modeled by the zwitterion mechanism first proposed by [87, 89]. The latter is composed of a two-step mechanism:

- step-1: Formation of a neutral compound called “zwitterion” by reaction of amine group with CO₂.
- step-2: Deprotonation of the zwitterion by a base to form the carbamate anion.

What defines primary amines is their ability to produce very stable carbamate anions. The carbamate stability is quantified with the equilibrium constant (k_c) of the hydrolysis reaction shown in (1.25), with (R) and (R') being alkyl or alkanol groups [114]. As a consequence, two amine molecules will react with CO₂ to achieve a theoretical loading limit of (0.5 mol CO₂/ mol amine). At low CO₂ partial pressures, the CO₂ content that is physically absorbed is negligible with respect to the chemically absorbed one.



Historically, ETA was used as a stand-alone absorber at concentrations (< 20% wt.) however in other cases it was blended with di or tri-glycol amine. The blended solvent was used for acid-gas removal, dehydrating agent, and was

characterized by a lower steam consumption in comparison to aqueous systems. Its main disadvantage includes a higher stripping temperature which leads to severe corrosivity in the heat-exchanger and the stripper [79].

Recently, sterically hindered amines such as 2-amino-2-methyl-1-Propanol (AMP) have been receiving a great deal of focus. Sterically hindered is a category of primary or secondary amines, characterized by a primary amino group attached to a tertiary carbon atom, or a secondary amino group attached to a secondary or tertiary amino group. Although having a higher cyclic capacities than aqueous ETA, their low rate of reaction necessitates mixing them with fast-reacting alkanolamines such as ethanolamine [115] or piperazine (PZ) [116, 117].

1.4.1.2 Secondary alkanolamines

Secondary alkanolamines have intermediate reaction kinetics, but experience a higher equilibrium loading than primary amines [41]. Reaction with CO₂ is modeled by the zwitterion mechanism. The lower carbamate stability allows its dissolution to form bicarbonate (HCO₃⁻) which increases the free concentration of alkanolamines and helps maintain the alkalinity of the solution. The lower carbamate stability is a result of the steric hindrance due to the extra bond with the alkanol group [118]. Most widely used secondary amine is (DEA) which was used historically to treat refinery flue gases due to its resistance to carbonyl sulfide (COS) and ethenethione (CS₂). They also have advantages of low vaporization losses and low corrosivity. Main concerns when using (DEA) is that it tends to undergo irreversible reactions with CO₂ and difficulty in reclaiming the degradation products [79]. Modeling results of [119] show that aqueous DEA achieved a lower energy penalty for CO₂ capture than aqueous ETA.

As mentioned, the task of choosing a good solvent for CO₂-capture is extremely complicated. To remedy this, authors in literature usually rely on solvent screening apparatuses to obtain data on their general behavior: kinetics of absorption/desorption, CO₂ solubility, physical properties among other simultaneously obtained. Screening tests of [120, 121] have shown that the secondary amines: 2-(propylamino)ethanol (PAE) and 2-(isopropylamino)ethanol (IPAE) have superior cyclic capacities to DEA - 67.8, 51.2 and 41.9 g/kg of solvent respectively.

1.4.1.3 Tertiary alkanolamines

Tertiary alkanolamines have very good absorption capacity to their base-catalyzed hydration mechanism but have very poor kinetic performance [79]. It was proposed that tertiary alkanolamines are incapable of directly reacting with CO₂. Instead, these amines exhibit a base-catalytic effect on the hydration of CO₂ [122] as shown in equation (1.26) which leads to a theoretical loading of (1 mol CO₂/mol amine).



Methyldiethanolamine (MDEA) has been used for the selective absorption of sour gas (H₂S) from non-hydrocarbon gases (Coal gasification). Data from used sweetening processes in the 1980s - such as that used by the (Fluor Daniel) or (Dow Chemicals, USA) - report levels as low as 5 ppmv of H₂S while the leaving CO₂ relatively unabsorbed. The major advantage of MDEA is that it could be used at high concentrations (up to 60% wt.), it is highly resistance to thermal and chemical degradation, and essentially non-corrosive. These desirable properties motivated

blending it with fast-reacting amines such as PZ or ETA for a reduced energy penalty for post-combustion capture as demonstrated by many authors [123, 124]. Literature screening tests keep shedding light on new solvents such as diethylaminoethanol (DEAE) , or 3-pyrrolidino-1,2-propandiol (3PP-1,2-PD) among others [113, 125].

1.4.1.4 Industrial solvents

We cite in Table 1-3 commercialized solvents currently in use by FLUOR[®], Mitsubishi heavy industries, Shell, and HITACHI.

Econamine-FG+SM is a proprietary carbon capture solution of FLUOR[®], currently operating in more than 30 licensed plants worldwide at power plants, refineries, and chemical facilities. The technology builds on Fluor's more than 400 CO₂ removal units in natural gas and synthesis gas processing [126]. Main advantages of the Econamine FG+SM solvent include: low make-up cost, and high flexibility - capture as low as 3% vol. carbon dioxide. Power generation penalty is in the order of 9 percentage points [127].

KS-1TM/KS-2TM are CO₂ solvents comprised of a sterically hindered amine that has shown much resistance degradation compared to conventional ETA [118, 128], reduced efficiency penalty (~9%) [127, 129] in electric power plants. With the aim of achieving carbon neutrality in 2040, Mitsubishi has recently successfully tested its new solvent of KS-21TM at the Mongstad technology center in Norway with a capture efficiency of (95-98%).

Shell's CANSOLVTM CO₂ Capture System employs a regenerable solvent. Shell Catalysts & Technologies has used its experience to develop a patented CO₂ capture technology that offers cutting-edge performance, including low parasitic energy consumption, fast kinetics and extremely low volatility. Reported efficiency losses for power generation are in the order of (~8.2%).

H3 is a proprietary solvent of Shell[®] that was developed in the 1990s by Babcock-Hitachi K.K. – one of Hitachi group companies. The solvent is amine-based has a high CO₂ absorption capacity and requires a lower regeneration energy (~30%) relative to the 30%wt. ETA solution. Recent developments include improved stability against degradation by chemical additives [130]. Reported losses in efficiency are in the order of (~7.8%) [131, 132].

Solvent	Regeneration Energy (GJ/t-CO ₂)	Efficiency penalty (%)	References
Commercial			
Econamine FG+ SM	3.12	9.2	[127]
KS-1 TM	3.08	8.4	[127]
KS-2 TM	3.0	9.3	[129]
CANSOLV	2.33	8.2	[128, 133]
H3	2.8	7.8	[131],[132]

Table 1-3: Industrial solvents currently in use. Taken from [71]. (Reproduced from Goto 2013)

1.4.1.5 Other considerations for solvent choice

We deemed it necessary to shed light on two aspects that are rarely at the forefront of criteria for novel solvents: the heat of absorption of the solvent, and the environmental considerations associated.

Heat of absorption and stripper duty

Generally speaking, solvents with faster reaction kinetics are associated with higher carbamate stability, and to the enthalpy of reaction [74]. In general, primary alkanolamines have the highest heats of reaction (80-90 kJ/mol CO₂) followed by secondary alkanolamines (80-90 kJ/mol CO₂) then the tertiary ones (55 kJ/mol CO₂) [134, 135]. The heat of reaction is a fundamental property to be considered when choosing a solvent for chemical absorption. Higher reaction heat increases the regeneration energy in the stripper as evident from (1.27) [105], moreover it also increases the cooling duty in the condenser as the two are inextricably linked. It would therefore make sense to choose solvents with low reaction enthalpies. This is not completely true as decreasing heats of absorption lead to higher boil-up ratio in the stripper column [108, 135].

$$Q_{Reb} = \underbrace{(n_{CO_2} \Delta H_{CO_2})}_{\text{Heat of desorption}} + \underbrace{(\bar{m}_{soln} \bar{C}_p (T_{in} - T_{out}))}_{\text{Sensible heat}} + \underbrace{(n_{vap,H_2O} H_{vap,H_2O})}_{\text{Heat of vaoprisation}} \quad (1.27)$$

The heat of absorption is directly related to the temperature-sensitivity of vapor-liquid equilibrium by the Gibbs-Helmholtz equation [135]. This equation is used by many researchers [136, 137] to estimate (ΔH_{abs}) starting from measurements of vapor-liquid equilibrium.

$$\left[\frac{\partial(G/T)}{\partial(1/T)} \right] = \frac{-\Delta H_{rxn}}{R} \quad (1.28)$$

The said equation reduces to the expression shown in (1.29) under assumptions of constant activity coefficients and chemical speciation. Equation (1.29) relates the sensitivity of equilibrium pressure of CO₂ to the heat of reaction (ΔH_{rxn}). It implies that with increased heat of absorption, the equilibrium partial pressure of CO₂ at stripper conditions increases. In turn this decreases the boil-up ratio and the reboiler duty.

$$\frac{\partial(\ln p_{CO_2})}{\partial(1/T)} = -\frac{\Delta H_{rxn}}{R} \quad (1.29)$$

Environmental considerations

It is often found in literature that not much attention is given to the environmental aspect of a solvent, i.e. solvents are judged by the decrease in the cost of avoided CO₂ emissions. However, in treating an environmental problem such as global warming, one should not create another one.

Amines can leak from a capture plant by way of the exhaust gas, and the CO₂-rich stream. Perhaps amine leakage is mainly found due to and can be reduced by water washing of the exiting flue gas [135]. From an environmental perspective, solvents are judged by their biodegradability and their ecotoxicity. Ecotoxicity is the concentration of pollutant (mg/L) that prevents the growth of algae by 50% relative to the control cultures (EC50). Biodegradability is the difference between the biological oxygen demand (BOD) and the theoretical oxygen demand (ThOD) after a period of 28 days (BOD28). Marine ecotoxicity and biodegradability were measured for more than 40 amines [138] and results are shown in Figure 1-23 and Figure 1-24 respectively. Ecotoxicity results show that many of the most popular amines for carbon capture (ETA, DEA, MDEA, PZ, AMP) pass the ecotoxicity tests - (>10 mg/L). The mentioned amines however, appear have little biodegradable which motivates phasing them out [135].

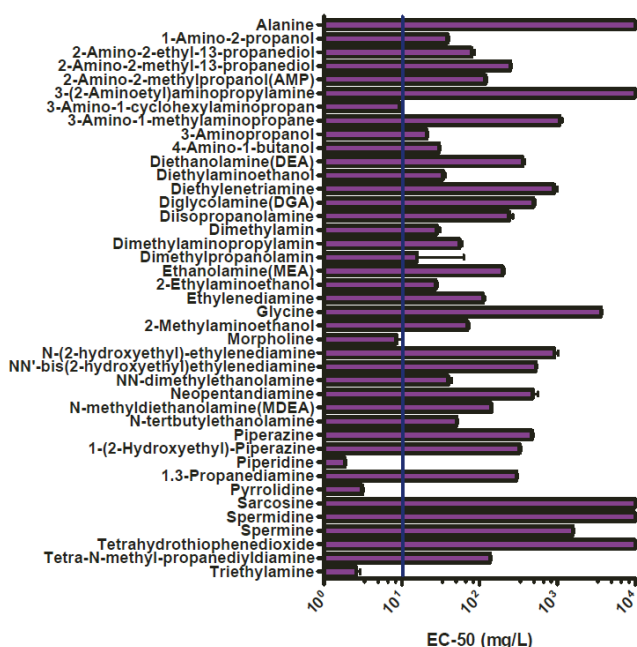


Figure 1-23: Results of the ecotoxicity testing, shown as concentration where compounds inhibited algal growth by 50% (EC-50). The blue line shows the lowest acceptable value (10 mg/l) for a chemical to be released in the marine environment [139]. (CC-by 4.0)

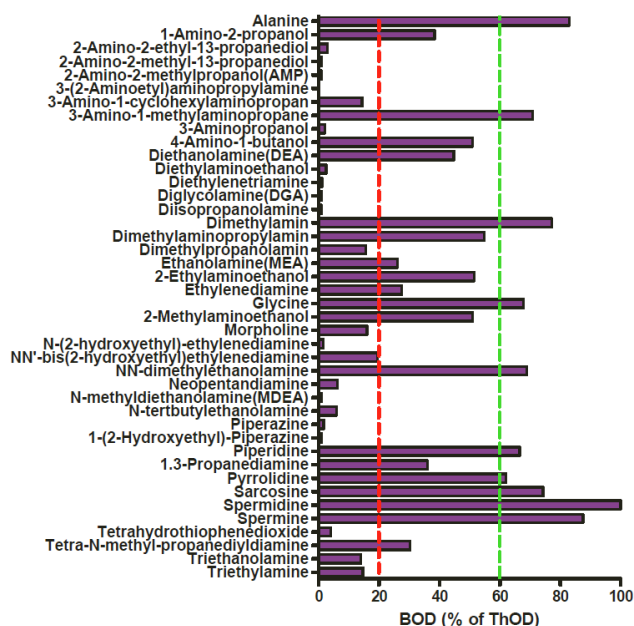


Figure 1-24: Figure 1: The biodegradability of all the chemicals tested, results shown as percent degraded with regards to the theoretical oxygen demand (ThOD). The red line shows the lowest acceptable value for a chemical to be released in the marine environment, while the green line is the lower limit for a chemical to be released independent of the ecotoxicity [139]. (CC-by 4.0)

1.4.2 CO₂ absorption using hollow fiber membranes

1.4.2.1 A novel gas-liquid contactor

Membrane processes have been finding applications in many industries such as the food industry with applications of water treatment for beer production, wine filtration, or removal of microorganisms [140]. Applications in the pharmaceutical industry include the production of ultra-pure and injectable-grade water for drugs [141]. Classical employment of membrane consist of filtration applications, however membranes have been finding use in chemical industry and in processes such as gas absorption [142]. This process involves the membrane playing the role of a gas-liquid contactor between a gas stream and a suitable solvent [143].

CO₂ removal through packed column absorption and stripping has been a longstanding technique widely employed for gases characterized by low oxygen content. While new column packings are constantly being tested for increased transfer area and rates and lower pressure drops [144, 145], the application of membranes as a gas-liquid contactor has received much attention. Post-combustion capture using hollow fiber membranes was first proposed in 1980s for the absorption of CO₂ in sodium hydroxide solution [146, 147]. Since then considerable progress has been made in incorporating hollow fibers in chemical desorption.

1.4.2.2 Application in chemical absorption of CO₂

In the context of post-combustion capture by absorption, the solvent contacts the CO₂-rich gas stream across a membrane contactor, usually a hollow fiber membrane. Usually, porous hollow fibers (Figure 1-25) provide very high interfacial surface to volume ratios, even among other membrane systems such as flat-sheet membranes [148]. The membrane acts as a non-dispersive barrier between the phase circulating inside the hollow fiber tubes (lumen region), and the one that occupy the outer shell region. CO₂ from the gas stream travels through the pores of the membrane and gets absorbed in the solvent. Usually, hollow fibers are assembled in bundles of great numbers, with their ends potted together. A typical operation of a CO₂ absorption is shown in Figure 1-26, in this example the flue gas stream is made to circulate counter-currently on the lumen side of the fiber while the solvent circulated on the shell side. Solvent circulation in the fiber lumen translates to a greater efficiency of separation due to reduced thickness of stagnant liquid film [149, 150].

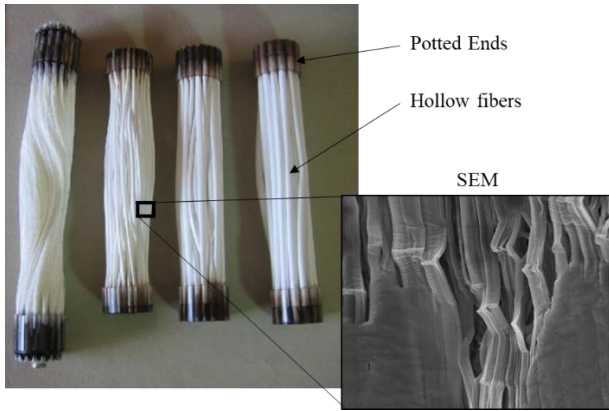


Figure 1-25: Hollow fiber bundles with potted ends [149]. The fibers are porous as show by the Scanning electron microscope (SEM) image. (reproduced with permission from Demontagny 2006)

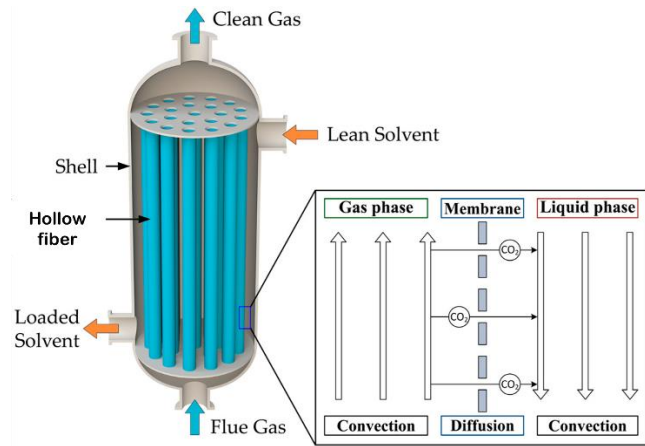


Figure 1-26: Operation of hollow fiber module for CO₂ capture from flue gases [151]. (CC-by 4.0)

Usage of hollow fibers is associated to many advantages that are expressed in Figure 1-27 [143]. Unlike packed columns, they have great operational flexibility: the liquid and gas phases flow independently, in addition this prevents issues such as column flooding or liquid entrainment [97, 152]. Another advantage is their potential for process intensification. Hollow fibers are reported to have interfacial surface densities that four [153, 154] to thirty [155] times greater than packed columns. The interfacial density was found to be influenced mainly by the packing factor (volume fraction occupied by the fibers in the module), and the outer diameter of the hollow fiber (d_o) [154, 156]. Moreover, hollow fiber modules are characterized by their ease of scale up/down, such that a greater capacity can be obtained when placing the modules in parallel [157], while a greater efficiency of capture can be achieved when the modules are placed in series [149]. Despite their advantages, the main barrier to wide-scale deployment of membrane gas absorption systems is wetting of the porous media by the solvent [158].

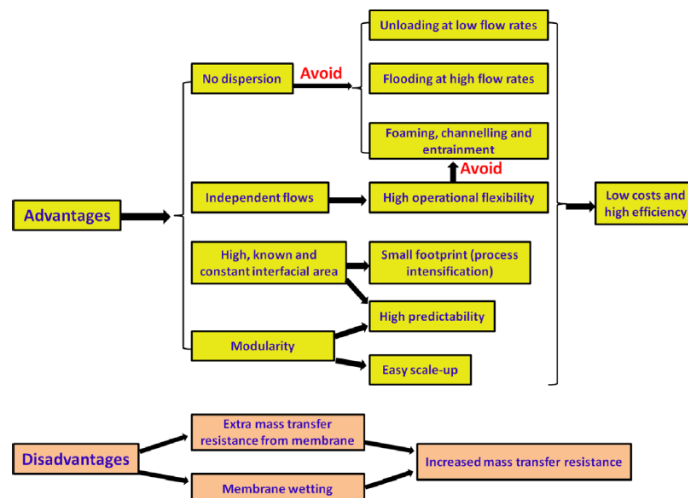


Figure 1-27: Advantages and drawbacks of membrane contactors in gas absorption [143]. (Reproduced with permission from Zhao 2016)

1.4.2.3 Operation in chemical desorption

The integration of gas absorption membranes (GAMs) in Carbon capture involves employing membrane modules for the absorption of CO₂ into the solvent of choice, and the subsequent regeneration of the latter. Concerning the absorption step, many authors were successful in implementing hollow fibers for carbon capture. Long-term stability of performance was conditioned by usage of robust membranes having a high hydrophobicity such as Polytetrafluoroethylene (PTFE) [149, 154, 159–161] or Polyetheretherketone (PEEK) [162]. This however must not imply that results are satisfactory for industrial-scale application. Robust membranes are orders of magnitude more expensive than other membrane counterparts [163]. With regards integrating membrane systems for solvent regeneration, we are inclined to believe that there is yet to be a satisfactory long-term performance as wetting of the membrane remains the main issue. A literature survey shows that most regeneration studies membranes are conducted following two modes: sweeping-gas regeneration with a non-condensable gas and vacuum membrane regeneration.

Sweeping gas regeneration

In this configuration an inert gas stream is made to circulate on the opposite side from the hot solvent phase [164]. The sweeping gas plays the role of decreasing the partial pressure of the volatile component by “sweeping” it away from the solvent surface. For chemical desorption of CO₂, this allows maintaining a concentration which permits desorption to take place. A typical example of sweeping gas regeneration is shown in Figure 1-28 where the preheated solvent flows in the lumen counter-currently to a pure N₂ stream in the shell side of the module. Inside CO₂ is desorbed from the solvent and evacuated by the gas stream. [97] tested surface modified alumina membranes to regenerate 15%wt. ETA solvent in a sweeping gas configuration with N₂ gas. He observed that higher temperatures and lower solvent velocities increase the regeneration rate ($\Delta\alpha = \alpha_{\text{rich}} - \alpha_{\text{lean}}$) of the solvent. The use of inorganic membranes (Al₂O₃, ZrO₂, or SiO₂) is motivated by their outstanding thermal and chemical stabilities [165], although their hydrophilic nature necessitates surface treatments to render them hydrophobic. [96] used N₂ sweeping-gas to study the

effect of operating parameters on the regeneration performance of aqueous ETA solvent in a PTFE hollow fiber module. [166] performed continuous absorption-regeneration cycles of the multi-amine (polyamidoamine) coupled with a polypropylene (PP) membrane, he also studied the regeneration of aqueous ETA solution used with a poly(4-methyl-1-pentene) (PMP) membrane. [167] studied desorption from a mixed solvent of potassium glycinate (PG) and 2-amin-2-mehtyl-1-propanol (AMP). The author was able to achieve a very low lean loading of his solvent while using steam as a sweeping gas. [168] tested the regeneration of 30% wt. potassium carbonate in a PTFE flat sheet membrane but was victim to wetting. An alternative asymmetric membrane from polyether sulfone (PES) supported on a microporous layer proved to be a cheaper and better alternative.

Sweeping gas, while easy enough to implement, and despite its utility for desorption studies, is not viable solution. Inert sweeping gas regeneration translates to separating CO₂ from an inert stream of nitrogen - during absorption - only to release into another inert stream – the non-codnsable sweping gas. Its use is motivated by the ease of implementation to conduct laboratory-scale studies although from a practical point of view it is non-existent.

Vacuum regeneration

Vacuum regeneration consists of applying a vacuum on the gas-side of the membrane module to promote desorption. It is well known that the severe temperature levels for solvent regeneration accentuate thermal and chemical attacks on the membrane [161, 169, 170]. Therefor a vacuum is applied on gaseous side promises a reduction in the regeneration temperature below that of the boiling point [171] of the solvent and a subsequent savings in energy. Vacuum regeneration can be rendered more attractive by integrating low-grade heat from a process to heat the solvent [172]. A typical operation of a vacuum regeneration is shown in Figure 1-29 [173]. In this example, the preheated-solvent circulates through the fiber lumen, while vacuum is applied on the shell side. Low-pressure steam is generated by ohmic heater and acts as a sweeping gas. It should be kept in mind that energy savings by avoiding the vaporization of the solvent, can be countered by the duty of the vacuum pump, the additional compression work of the CO₂ stream, and heat duty for low-pressure steam generation [150, 174].

It was reported that the use of vacuum without any heating for solvent regeneration had a very poor reperformance with the (PG+AMP) mixed solvent [167]. [175] reported using aqueous DEA in a membrane flashing process, during operation the solvent would intentionally penetrate hollow fibers into the shell side where a vacuum is applied to regenerate CO₂. [171] studied the regeneration of 30% wt. ETA using with low pressure steam as a sweeping gas. He concluded that to achieve intensification with respect packed columns, the solvent should operate at 90-95°C. [174] studied the vacuum regeneration of 20% wt. ETA using (PP) membrane at 70°C. He found that optimal vacuum pressure to be around (~35 kPa): higher vacuum pressures lead to energy expenditure to generate saturated steam, while lower pressures vacuum pressure increase the duty of the vacuum pump. [173] screened 13 different amines (primary, secondary, tertiary, multi-amines) in a continuous absorption - vacuum regeneration scheme. He observed the best regeneration performance in tertiary amines while primary amines had the outperformed during absorption performance. [176] studied the vacuum regeneration of 30% wt. ETA in inorganic membranes whose surface was

modified to be hydrophobic with a highly fluorinated compound. The author reports regeneration flux ($\text{mol/m}^2/\text{s}$) to be (2-40) times higher than in N_2 -sweeping studies. Asymmetric membrane of PDMS dense thin-film coated on a polyethylene (PE) support was used for high-vacuum regeneration of 30% wt. ETA [177].

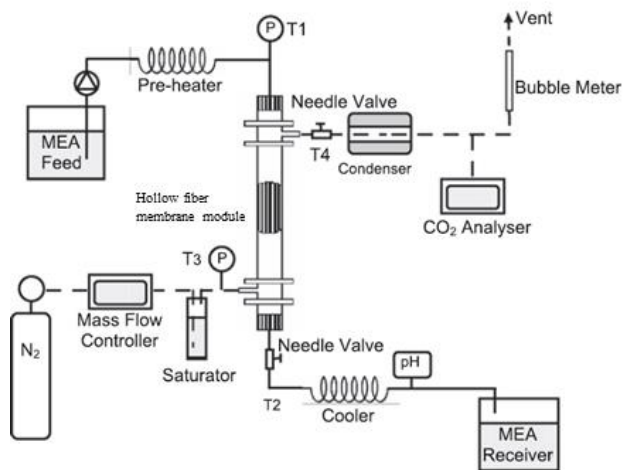


Figure 1-28: Experimental setup of solvent regeneration in a hollow fiber module while using N_2 sweeping gas- used by [97]. (Reproduced with permission from koonaphadeelert 2009).

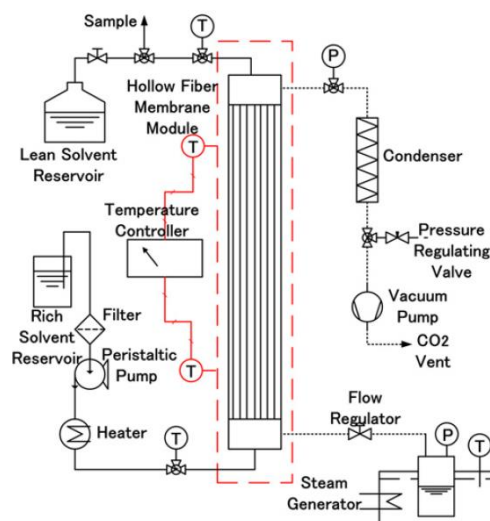


Figure 1-29: Experimental set-up of open-loop solvent regeneration in a hollow fiber membrane module using vacuum regeneration with steam as sweeping gas - used by [173]. (Reproduced with permission from Wang 2013).

1.4.2.4 Membrane materials

Most commonly used membranes for gas-absorption application are porous membranes. Given that most absorption process occur in hydrophilic aqueous solvents, membranes are preferred to have a high hydrophobicity [163]. This restricts the choice of materials to: polyethylene (PE), polypropylene (PP), polydivinylfluoride (PVDF), polytetrafluoroethylene (PTFE), polysulfone (PSF) and polyetheretherketone (PEEK) [178]. The main characteristics of these porous membranes are shown in Table 1-4. Membranes made from (PE) and (PP) are very cheap (0.01\$/m) which makes them very attractive candidates for gas-absorption [160]. They do however suffer from chemical attacks, thermal attacks, and alteration of their surface properties by alkanolamines [169]. This penalizes their performance due to subsequent membrane wetting [179, 180]. To remedy their poor performance, they are being tested as a support for a dense thin film ($\sim 1\mu\text{m}$) to prevent liquid intrusion [181]. However, dense film comes at a price of higher membrane resistance [166]. (PVDF) is a well-known polymeric membrane that offers ease of fabrication due to its solubility in common solvents [182], and ease of adjusting membrane morphology with additives such as lithium chloride (LiCl) and phosphoric acid (PA). (PVDF) membranes have low wetting-resistance against aqueous alkanolamines [169], it was reported however that the addition of sodium chloride (NaCl) or sodium glycinate (SG) to the solvent allowed for a stable absorption performance [183]. PTFE and PEEK are most robust materials used for chemical absorption of CO_2 in amine solvents. The presence of the four fluoride groups on the PTFE polymer backbone leads to a greater structural integrity, or in an equivalent manner, to a greater resistance to changes in its morphology [184]. It is partly due to this

reason that stable-operation and integrity of surface properties are reported for gas absorption with alkanolamines [96, 154, 159, 169, 185]. PEEK is perhaps the most mechanically robust and performing polymer [186]. Superhydrophobic PEEK was tested for CO₂ absorption with alkanolamines [187]. Results show a stable performance over 120 hours of operation; the levelized cost electricity was 28% than in a packed column for CO₂ capture from a power plant. High price and difficulty of fabrication are the main barriers to its widespread deployment.

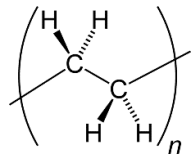
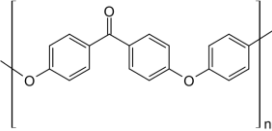
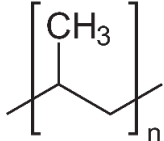
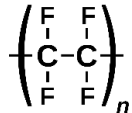
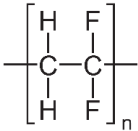
Polymer	Polyethylene (PE)	Polyether ether ketone (PEEK)	Polypropylene (PP)	Polytetrafluoroethylene (PTFE)	Polyvinylidene fluoride (PVDF)
Structure of the repeating unit					
Type of thermoplastic polymer	Semi-crystalline	Semi-crystalline	Semi-crystalline	Semi-crystalline	Semi-crystalline
Density (g/cm ³)	0.960	1.32	0.946	2.20	1.78
Melting Point (C°)	135	343	160	327	177
Glass Transition Temperature (C°)	- 110 to 115	140 to 145	- 20 to 10	115 to 130	- 42 to 25
Merits	<ul style="list-style-type: none"> • Cheap Stable membrane performance if absorbents with lower wettability are used. 	<ul style="list-style-type: none"> • High solvent and chemical resistance. • Superior mechanical properties. • High melting point indicates its ability to withstand desorption temperature (100 - 150°C). 	<ul style="list-style-type: none"> • Cheap (US\$ 0.01/m)[160] • Commercially available (under trade name Liqui-Cel) • Stable membrane performance if absorbents with lower wettability are used. 	<ul style="list-style-type: none"> • High hydrophobicity • Low surface energy • High resistance to wetting by aqueous solution • High melting point indicates its ability to withstand desorption temperature (100 - 150°C). 	<ul style="list-style-type: none"> • Cheap (US\$ 0.36/m) [160] • Membrane performance are intermediate (between PP and PTFE) • PVDF hollow fiber membranes can be obtained through phase inversion
Limitations	<ul style="list-style-type: none"> • Membrane degradation can occur if alkanolamine solutions are used. • Difficult to withstand desorption temperature (100 - 150 °C) due to the low melting point. 	<ul style="list-style-type: none"> • Creation of porous PEEK membranes via concentrated acids creates difficulty in scaling up for commercial use. • Creation of porous PEEK via melt spinning requires an extraordinary operating condition (370 °C and 17,000 kPa). • High temperature is required to dissolve PEEK polymer. 	<ul style="list-style-type: none"> • Severe membrane wetting if alkanolamine solutions are used. • Difficult to withstand desorption temperature (100 - 150°C) due to the low melting point. 	<ul style="list-style-type: none"> • Expensive (US\$ 11.50/m) • Difficult to fabricate PTFE hollow fibers with small diameter (high interfacial area). • Insoluble in common organic solvents (conventional phase inversion method is not feasible). 	<ul style="list-style-type: none"> • Difficult to withstand desorption temperature (100 - 150 °C) due to the low melting point. Weaker chemical resistance than PTFE

Table 1-4: properties of common hydrophobic polymer materials used for gas-liquid contactors [163]. (CC-by 4.0)

1.4.2.5 Membrane wetting: a barrier to industrial deployment

To achieve the highest possible mass transfer rate, the gas phase should fill the membrane pores completely. When the membrane pores become wetted (liquid phase is filling membrane pores), the membrane mass transfer resistance starts to build up, making membrane applications unjustified economically [188]. However, having gas-filled pores is not likely to occur. Realistically, membrane pores become partially or in a worst-case scenario fully wetted by the absorbent over a long operation period. Wetting can occur when the transmembrane pressure is superior to the liquid entry pressure (LEP) as expressed by the Laplace-Young equation [158] (1.30) with (γ) being the surface tension, (Θ) the contact angle between the solvent and the membrane, (d_{\max}) is the maximum pore diameter, and B is a factor that adjust the LEP for non-cylindrical pores.

$$\text{LEP} = -\frac{4B\gamma \cos\theta}{d_{\max}} \quad (1.30)$$

Wetting in some instances may occur at some time after the start of the operation process, this is due to interactions with solvent molecules which causes the alteration of their surface properties and their morphological structure. Examples in literature demonstrate this phenomenon as [169] who author found that upon prolonged exposures to aqueous DEA solution, different membranes of Nylon, PVDF, and PP and PTFE experienced large decrements of their hydrophobicity as presented by the wetting angle with the solvent. [150, 179, 189] noticed through scanning electron microscope the change of the structural morphology of the porous structure leading eventually to membrane wetting. Goniometric measurements indicate that the contact angle made with a droplet decreased with exposure time [169, 189].

In the context of classical solvent choice for carbon capture, to decrease the likelihood of wetting the solvent should possess high surface tension which is achieved by careful choice of the alkanolamine and its mass fraction [109, 189]. Operating conditions should also be checked, high temperatures increases the risk of wetting by alteration of surface properties of the solvent [190], fluctuating pressures may cause a momentary increase in the trans-membrane pressure leading to membrane wetting [191]. For a counter-current operation, wetting is more likely to occur at the solvent entry due to a relatively higher pressure [192]. Another possible mechanism for wetting is called condensation or capillary wetting, it is incentivized when the vapor pressure of the solvent is elevated, and occurs when the temperature gradient inside the membrane has been lost such as for cases of shutdown or intermittent operation [190]. [158] did a literature survey and found 23 studies that used common hydrophobic porous membranes for carbon capture. Of these studies 21 authors reported the onset of membrane wetting while 2 reported non-wetted operation.

Another crucial consideration is the selection of potting glue used to seal the modules, as failures commonly arise at the interface between the adhesive and membrane or the housing [169]. For the majority of polymeric membranes, the adhesives employed necessitate chemical cross-linking facilitated by curing agents. Epoxy or polyurethane-based adhesives are extensively utilized both in laboratory settings and in industry [170,171]. Additionally, acrylic,

polyaromatic, or silicon adhesives can be compatible with specific membrane materials. However, many of these adhesives lack resistance to amine solvents, which can result in the rapid disintegration of the modules.

Solvent		Contact angle (Θ°)	Operation time	Immersion time	Status	Reference
Water	PVDF	100°	15 days	-	Wetted	[193]
		92°	-	30 days	Wetted	[194]
		109.8 ± 1.20	-	-	Not wetted	[195]
	PTFE	113	-	-	-	[196]
		111.3	-	-	Wetted	[197]
	PP	126.1°	-	60 days	Wetted	(46)
		104°	-	-	-	[196]
		128 ± 0.7°	-	-	-	[198]
	PSF	64 ± 1.3°	-	-	-	[199]
2 M NaOH	PVDF	90°	15 days	-	Wetted	[193]
20 wt% MEA	PP	120 ± 1.3°	-	-	-	[198]
30 wt% MEA	PP	121.6°	-	60 days	Wetted	(46)
0.1 MEA	PVDF	91.50°	12 days	-	Wetted	[183]
0.5 MEA	PVDF	91.27°	-	-	Wetted	
1M MEA	PVDF	90.12°	-	-	Wetted	
		-	60 hours	-	Wetted	[160]
	PP	110°	-	-	Not wetted	[200]
	PTEF	-	60 hours	-	Not wetted	[160]
2 M MEA	PVDF	82°	15 days	-	Wetted	[193]
3 M MEA	PP	107°	-	-	Not wetted	[200]
5 M MEA	PE	84°	-	-	Wetted	[154]
	PTFE	101°	6600 hours	-	Wetted	
1 MDEA	PVDF	87.92°	12 days	-	Wetted	[183]
20% wt% DEA	PP	103.7°	-	10 days	Wetted	[170]
30 wt% MDEA	PP	121.6°	-	60 days	Wetted	[201]
0.5 M MDEA	PP	97°	-	-	Wetted	[202]

Figure 1-30: Literature survey of gas absorption experiments in hydrophobic porous membranes [158]. (CC-by 4.0)

1.4.3 Novel regeneration method in chemical absorption using Microwave technology

1.4.3.1 Basics of microwave heating

Microwaves are electromagnetic radiation having a frequency in the range (300MHz - 300GHz), of this band, only two frequencies are allocated for industrial use and are restricted to 915 MHz ± 13MHz and 2450 MHz ± 50 MHz [203, 204]. Dielectrics are materials that experience a tendency to dissipate electromagnetic irradiation, they are neither complete insulators, nor are highly conductive, but rather possess intermediate electrical properties [205]. In classical heat-transfer by conduction or convection, energy is transferred from the outside surface due to the presence of a temperature gradient. In microwave heating, electromagnetic dissipation occurs in a volumetric manner as shown in

Figure 1-31. Electromagnetic waves are able to penetrate inside the material and then heat it which liberates this technology from many of the constraints of classical heat transfer.

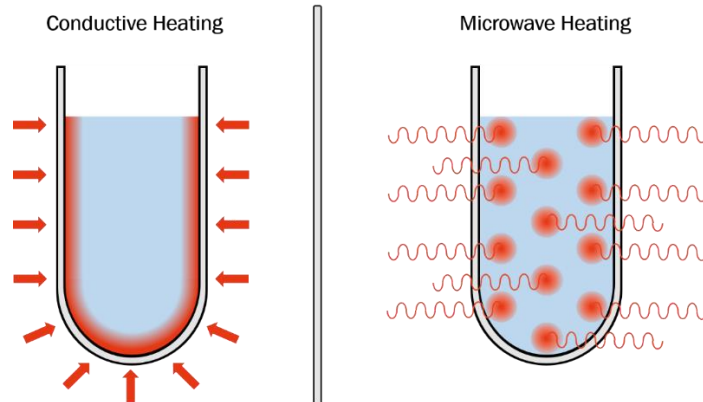


Figure 1-31: Conductive heat transfer in comparison to microwave heating [206]

The interaction between microwaves and dielectrics is governed by the complex dielectric constant (ϵ^*) as shown in (1.31), with (ϵ') is the relative permittivity of the material with respect to free space, and (ϵ'') being the dielectric loss factor. The dielectric properties of a medium are dependent on the frequency of the irradiation, composition, and its temperature among others. The relative permittivity represents the polarization in a unit volume of the material. The loss factor is directly related to the specific energy loss as shown in the classical equation (1.32), with (ω) being the angular velocity of the electromagnetic radiation, (ϵ_0^*) being the permittivity of free space, (ϵ'') being the dielectric loss factor, and (E_{rms}) is the root mean square value of the electric field.

$$\epsilon^* = \epsilon' - j\epsilon'' \quad (1.31)$$

$$P_{loss} = \omega\epsilon_0^*\epsilon''E_{rms}^2 \text{ (W/m}^3\text{)} \quad (1.32)$$

The transfer of microwave energy to the product takes place in the applicator which can be either multimode or mono-mode. Multimode applicators (Figure 1-32) are most commonly used and range from domestic ovens to large-scale industrial dryers. Typically, they are shaped like a rectangular, closed metal box (referred to as a "cavity") - a Faraday cage with at least two dimensions longer than half of the wavelength. Within the cavity, numerous resonance modes exist due to the microwaves reflecting off the cavity walls. These reflections cause wave interference, resulting in a highly non-uniform microwave field applied to the heated material (load), even when a mode stirrer or rotating disk is used. Despite this nonuniformity, the advantage of these applicators is their ability to be constructed large enough to accommodate significant volumes of materials for processing. Conversely, mono-mode applicators (Figure 1-33) generate a relatively stable single-standing wave inside the cavity. The material to be irradiated is usually placed at one of the electromagnetic field's maxima. This characteristic means that mono-mode applicators have strict limitations on the size of the volume and material load they can process.

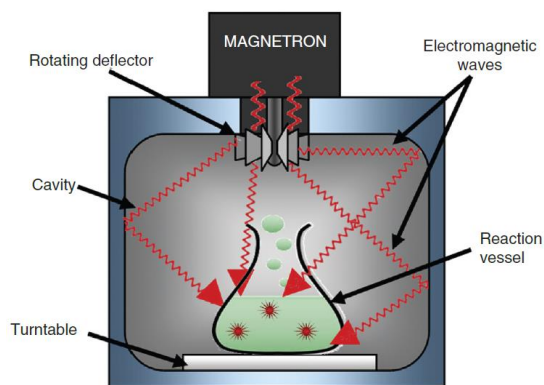


Figure 1-32: Representation of microwave heating in a multi-mode MW cavity [207]. (CC-by 4.0)

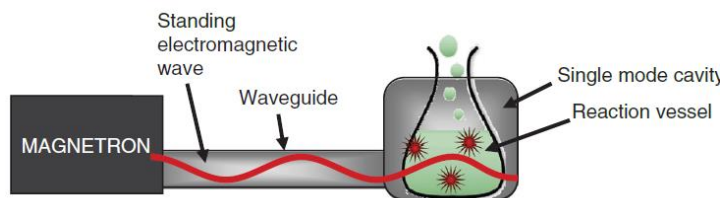


Figure 1-33: Representation of a microwave heating in a mono-mode cavity [207]. (CC-by 4.0)

1.4.3.2 Microwave applications in Food and Chemical industries

Microwave (MW) heating uses electromagnetic waves to heat materials. This method is highly efficient as it directly transfers energy to the molecules within the material, causing them to vibrate and generate heat. Key characteristics of microwave heating include rapid heating, selective heating of polar molecules, and the ability to penetrate materials to heat them from the inside out. These microwave heating has found many industrial applications, in the food industry we present the classical examples of drying, backing, pasteurization etc... [208]. Advantages include higher energetic efficiency [209, 210], shortening the treatment time (up to 50%) [208], and maintaining a high nutritional value due to the rapidity of the process. MWs have also found many applications in the chemical industry [207]. In organic synthesis, there has been reports of accelerations of reaction by a factor of 1000 relative to conventional processes in addition to greater yields [211, 212]. Heterogenous catalysis report higher reaction rates due to selective heating by microwaves of the supported catalyst particles [213]. Others report an 18-fold reduction in the specific energy consumption for the MW-assisted extraction process compared to hydrodistillation [214]. In the field of gas separation, thermal regeneration of adsorbent bed by microwaves has received considerable attention. This is due to the fact that microwave heating provides a much faster regeneration by exploiting the microwave hot-spots [204]. The concept is based on the fact that microwaves are selective towards polar adsorbates as shown for the dehydration of a 13X zeolite bed [215]. Similar conclusions were made by studies that employed a adsorbate mixtures of a polar and non-polar components where the selective regeneration of the polar compound was observed [216].

1.4.3.3 Microwave applications to carbon capture

So far, only a few studies have focused exclusively on microwave regeneration for CO₂ capture and recovery. Conducted studies integrate microwaves in adsorption, or in chemical absorption.

Adsorption process

Studies regarding CO₂ capture by adsorption highlight the chemical selectivity of microwaves, faster desorption rates, and potential energy savings compared to conventional thermal heating. One study employed microwave-assisted vacuum regeneration of zeolite 13X to recover CO₂ from wet flue gas [217]. More recently, research on CO₂ adsorption and desorption from amine-functionalized mesoporous silica using microwave heating demonstrated that CO₂ load, dielectric response, and heating rates increased proportionally with amine functionalization [218]. In another study, alkanolamine (ETA, or DEA) droplets of size (80µm) were coated with silicate nanoparticles to create a “dry” alkanolamine and achieve substantial contact surfaces (~75 000 m²/ m³). Microwave regeneration of a 10 g sample of the “dry” alkanolamines decreased the regeneration time to (1h) in comparison to conventional hot-plate heating (2h).

Absorption process

With regards to carbon capture by solvents, only a very small handful of research papers exist on the subject. [219] studied the regeneration of a 5 mL sample of 30% wt. ETA at 70°C, either with microwaves or by conventional heating, while using a N₂ stream as a sweeping gas [219]. The desorption rates (Figure 1-34) show microwave heating to be superior to conventional heating despite having very similar temperature profiles. Consequent cyclic regeneration tests reveal that regeneration at 90°C would lead to regeneration efficiencies ($\alpha_h - \alpha_i$) similar to those encountered in classical absorption in ETA (0.25). Following the work of [219], a more expanded study on microwave regeneration for chemical absorption was performed [220]. The author studied the regeneration of a 5 mL sample in the set-up shown in (Figure 1-35) at varying temperatures and amine mass-fraction of the solvent. Results show that regeneration at 90 °C of 50% wt. ETA had the lowest energy consumption per unit of CO₂ captured (2000 kJ/ mol). The same author then studied microwave regeneration of 5 mL samples of non-aqueous ethanolamine solutions [221]. Results show that 20-40% wt. of ETA in diethylene glycol monoethylether (DEGEE) would lead to a 78% reduction of capture energy (kJ / mol CO₂) in comparison to the aqueous 30% wt. ETA.

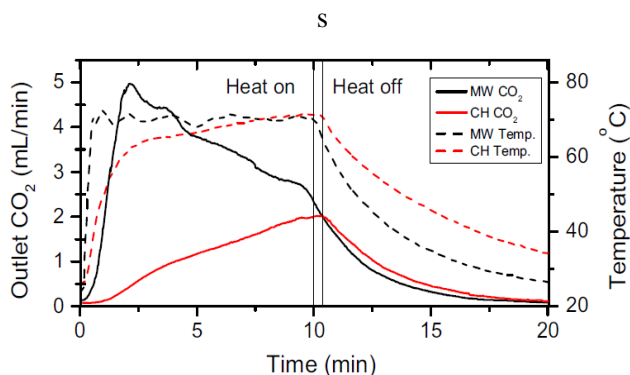


Figure 1-34: Comparison of microwave (MW) and conventional heating (CH) to regenerate the CO₂-loaded 30%wt. ETA solution after an initial absorption step of 20 min with 20% CO₂ [219]. (CC-by 4.0)

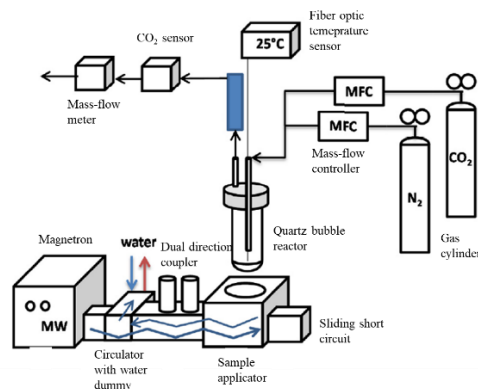


Figure 1-35: Experimental setup used for CO₂ absorption and regeneration of aqueous ethanolamine solution by microwave [220]. (CC-by 4.0)

1.5 Thesis objectives

The bibliographical review highlights the intention of the entire world is shifting its focus on reducing greenhouse emissions. While renewable energy and alternative fuels are gaining momentum, fossil fuels will continue to play the bigger part in meeting energetic needs of economies. This entails the installation of carbon capture and storage technologies to decarbonize fossil fuel emission sources until they are phased out.

Much work in research and development is being poured into three capture techniques of oxy fuel combustion, pre-combustion, and post-combustion. Usually the superiority of one technology over another is settled by comparing the increase in electricity cost.

The greatest focus is perhaps on the post-combustion capture with chemical absorption in amine. It is perhaps in view of its long-standing history in natural gas processing and the resulting technological maturity. It is plagued however by a high energy penalty to regenerate the solvent, extensive absorber size, elevated solvent make-up rates due to degradation, equipment corrosion, and low biodegradability of the solvent among others.

Improvements to these problems involve searching for new solvents, other alkanolamines, alkylamines, ionic liquids, organic solvents. Membrane technology is currently being researched as a non-selective gas-liquid contactor to replace the conventional packed column of the amine process. The advantage of coupling membranes to amine absorption are gains in operational and process flexibility, elevated interfacial density, and decreased solvent degradation by operating at lower temperatures especially in vacuum regeneration mode. Despite the moderate number of studies on membranes, unstable long-term performance still due to membrane wetting still persists.

Microwave regeneration of absorbents/adsorbents (usually amines) recently received some interest by no more than a few authors. These studies report very fast heating rates, regeneration efficiency higher with respect to conventional heating, lower processing times, and a better energetic efficiency per unit of CO₂ regenerated.

Having said all of the above, the main objectives of this thesis is to:

- 1) Reinforce the existing literature on the application of membrane processes to chemical desorption. The author believes that due to the compactness of membranes, they have the potential to expand carbon capture to small and medium point source emissions. In addition, coupling membranes to chemical desorption would transfer all the advantages of the former technology.

- 2) Examine the feasibility of coupling microwave technology to membrane processes: this allows microwave regeneration from the batch to the continuous scale.
- 3) Examine the intensification of microwave regeneration performance which translates to high regeneration efficiencies at lower operating temperatures.
- 4) Generate dielectric data of aqueous alkanolamines: to the best of our knowledge, dielectric data of aqueous alkanolamines loaded with CO₂ has not been loaded. Such data are necessary prerequisite to any numerical modeling approach of microwave-assisted desorption.
- 5) Develop a numerical model that accounts for the plethora of physical phenomenon involved

The following manuscript is divided into five main chapters. The author found it appropriate to accord to each chapter of this work its own “preamble” section where the necessary fundamentals and prerequisites are presented. Moreover, each chapter was accorded its own nomenclature, annex and references. This is thought to facilitate to the reader the task of searching for supplementary information. Besides the “state of the art” the manuscript counts four other chapters (2 to 5). Chapter two outlines the dielectric characterization of the solvent of choice – aqueous ethanolamine at varying carbon dioxide concentrations, temperatures, and frequencies. This work is important for all three following chapters where electromagnetic modeling is involved. In the chapter three the experimental regeneration of aqueous ethanolamine was studied at different operating conditions while using a hollow fiber membrane. The experimental system was consequently modeled in chapter four and the agreement with experimental regeneration results was rather good. The final chapter tackles the design and operation of a prototype unit to operate microwave regeneration at the scale of membrane module.

1.6 Annex

1.6.1 Abbreviations

AMP	Aminomethylpropanol	PEEK	Polyetheretherketone
ASU	Air separation unit	PES	Polyethersulfone
BECCS	Bioenergy carbon capture and storage	PMP	polymethylpentene
BOD	Biological oxygen demand	PP	Polypropylene
CAPEX	Capital expenditure	PSA	Pressure swing adsorption
CC	Carbon capture	PTFE	Polytetrafluoroethylene
CCS	Carbon capture and storage	PVDF	Polyvinylidene difluoride
CCUS	Carbon capture utilization and storage	PZ	Piperizine
COP	Conference of parties	SEM	Scanning electron microscope
CPU	Compression pressurization unit	SG	Sodium glycinate
DAC	Direct air capture	SSP	Shared socio-economic pathways
DEA	Diethanolamine	TEA	Triethanolamine
DGA	Diethylene glycol	TEA	Triethanolamine
DIPA	Diisopropanolamine	ThoD	Theoretical oxygen demand
DOE	Department of energy	TRL	Technology readiness level
Econamine	Proprietary solvent of Fluor	TSA	Temperature swing adsorption
EOR	Enhanced oil recovery	UN	United nations
EPRI	Electric power research institute	UNFCCC	United nations framework convention on climate change
ETA	Ethanolamine	US	United states
EU	European Union	VSA	Vacuum swing adsorption
FGD	Flue gas desulfurization	WGS	Water has shift
G20	G20 group	NG	Natural gas
GE	General electric		
GHG	Greenhouse gas		
IEA	International energy agency		
IGCC	Integrated gasification combined cycle		
IPCC	Intergovernmental panel on climate change		
KS	proprietary solvent of Mitsubishi industries		
LCOE	Levelized cost of electricity		
LTF	Low temperature flash		
MDEA	Methyldiethanolamine		
MHI	Mitsubishi heavy industries		
MOF	Metal organic framework		
NDC	Nationally determined contributions		
NG	Natural gas		

1.7 References

1. What is the UNFCCC, the United Nations Framework Convention on Climate Change? | UNFCCC. (n.d.). Retrieved May 27, 2024, from <https://unfccc.int/fr/processus-et-reunions/qu-est-ce-que-la-ccnucc-la-convention-cadre-des-nations-unies-sur-les-changements-climatiques>
2. Paris agreement. (2018, November 29). UNFCCC. Retrieved from https://unfccc.int/sites/default/files/english_paris_agreement.pdf
3. United Nations Environment Programme. (2023). *Emissions Gap Report 2023: Broken Record – Temperatures hit new highs, yet world fails to cut emissions (again)*. United Nations Environment Programme. <https://doi.org/10.59117/20.500.11822/43922>
4. Calvin, K., Dasgupta, D., Krinner, G., Mukherji, A., Thorne, P. W., Trisos, C., ... Péan, C. (2023). *IPCC, 2023: Climate Change 2023: Synthesis Report. Contribution of Working Groups I, II and III to the Sixth Assessment Report of the Intergovernmental Panel on Climate Change [Core Writing Team, H. Lee and J. Romero (eds.)]*. IPCC, Geneva, Switzerland. (First.). Intergovernmental Panel on Climate Change (IPCC). <https://doi.org/10.59327/IPCC/AR6-9789291691647>
5. Intergovernmental Panel On Climate Change (Ippc). (2023). *Climate Change 2021 – The Physical Science Basis: Working Group I Contribution to the Sixth Assessment Report of the Intergovernmental Panel on Climate Change* (1st ed.). Cambridge University Press. <https://doi.org/10.1017/9781009157896>
6. Kulp, S. A., & Strauss, B. H. (2019). New elevation data triple estimates of global vulnerability to sea-level rise and coastal flooding. *Nature Communications*, *10*(1), 4844. <https://doi.org/10.1038/s41467-019-12808-z>
7. Farbotko, C. (2010). Wishful sinking: Disappearing islands, climate refugees and cosmopolitan experimentation. *Asia Pacific Viewpoint*, *51*(1), 47–60. <https://doi.org/10.1111/j.1467-8373.2010.001413.x>
8. Global Climate Action. (n.d.). Nationally determined contributions. Retrieved from <https://climateaction.unfccc.int/>
9. UNFCCC. (2023). *Nationally determined contributions under the Paris Agreement. Synthesis report by the secretariat*. United Arab Emirates. Retrieved from <https://unfccc.int/documents/632334>
10. Lamb, W. F., Wiedmann, T., Pongratz, J., Andrew, R., Crippa, M., Olivier, J. G. J., ... Minx, J. (2021). A review of trends and drivers of greenhouse gas emissions by sector from 1990 to 2018. *Environmental Research Letters*, *16*(7), 073005. <https://doi.org/10.1088/1748-9326/abee4e>
11. Total net greenhouse gas emission trends and projections in Europe. (n.d.).
12. Emissions of Carbon Dioxide in the Electric Power Sector. (n.d.).
13. Bandilla, K. W. (n.d.). 31 - Carbon Capture and Storage.
14. Coal 2023 - Analysis and forecast to 2026. (2023).
15. Jones, D., Broadbent, H., Fulghum, N., Bruce-Lockhart, C., Dizon, R., MacDonald, P., ... Myllyvirta, L. (2023). *Global Electricity Review 2023*, 163.
16. Intergovernmental Panel On Climate Change (Ippc) (Ed.). (2023). Emissions Trends and Drivers. In *Climate Change 2022 - Mitigation of Climate Change* (1st ed., pp. 215–294). Cambridge University Press. <https://doi.org/10.1017/9781009157926.004>
17. CCUS in clean energy transitions. (2020). *Energy Technology Perspectives*.
18. CCS institute. (2011). *The costs of CO2 capture, transport and storage*. Retrieved from <https://www.globalccsinstitute.com/resources/publications-reports-research/the-costs-of-co2-capture-transport-and-storage-post-demonstration-ccs-in-the-eu/>
19. Global CCS Institute. (2021). *The Global Status of CCS Report 2021*. Australia. (n.d.).
20. A worldwide database of CCUS projects. (n.d.). Retrieved from <https://www.iea.org/data-and-statistics/data-tools/ccus-projects-explorer>
21. Nataly Echevarria Huaman, R., & Xiu Jun, T. (2014). Energy related CO2 emissions and the progress on CCS projects: A review. *Renewable and Sustainable Energy Reviews*, *31*, 368–385. <https://doi.org/10.1016/j.rser.2013.12.002>
22. Dziejarski, B., Krzyżyńska, R., & Andersson, K. (2023). Current status of carbon capture, utilization, and storage technologies in the global economy: A survey of technical assessment. *Fuel*, *342*, 127776. <https://doi.org/10.1016/j.fuel.2023.127776>
23. *Technology Readiness and Costs of CCS*. (2021). Retrieved from <https://www.globalccsinstitute.com/resources/publications-reports-research/technology-readiness-and-costs-of-ccs/>
24. Wilcox, J. (2012). *Carbon Capture*. Springer New York, NY. Retrieved from <https://doi.org/10.1007/978-1-4614-2215-0>

25. Nuchitprasittichai, A., & Cremaschi, S. (2013). Sensitivity of amine-based CO₂ capture cost: The influences of CO₂ concentration in flue gas and utility cost fluctuations. *International Journal of Greenhouse Gas Control*, *13*, 34–43. <https://doi.org/10.1016/j.ijggc.2012.12.012>
26. Singh, D., Croiset, E., Douglas, P. L., & Douglas, M. A. (2003). Techno-economic study of CO₂ capture from an existing coal-fired power plant: MEA scrubbing vs. O₂/CO₂ recycle combustion. *Energy Conversion and Management*, *44*(19), 3073–3091. [https://doi.org/10.1016/S0196-8904\(03\)00040-2](https://doi.org/10.1016/S0196-8904(03)00040-2)
27. Wei, X., Manovic, V., & Hanak, D. P. (2020). Techno-economic assessment of coal- or biomass-fired oxy-combustion power plants with supercritical carbon dioxide cycle. *Energy Conversion and Management*, *221*, 113143. <https://doi.org/10.1016/j.enconman.2020.113143>
28. Cormos, C.-C. (2016). Oxy-combustion of coal, lignite and biomass: A techno-economic analysis for a large scale Carbon Capture and Storage (CCS) project in Romania. *Fuel*, *169*, 50–57. <https://doi.org/10.1016/j.fuel.2015.12.005>
29. Rubin, E., Abanades, J. C., Akai, M., Benson, S., Keith, D., Mazzotti, M., ... Soltanieh, M. (n.d.). Carbon Dioxide Capture and Storage : technical summery. Retrieved from <https://www.ipcc.ch/report/carbon-dioxide-capture-and-storage/>
30. Adam, R., & Ozarisoy, B. (2023). Techno-Economic Analysis of State-of-the-Art Carbon Capture Technologies and Their Applications: Scient Metric Review. *Encyclopedia*, *3*(4), 1270–1305. <https://doi.org/10.3390/encyclopedia3040092>
31. Mondal, M. K., Balsora, H. K., & Varshney, P. (2012). Progress and trends in CO₂ capture/separation technologies: A review. *Energy*, *46*(1), 431–441. <https://doi.org/10.1016/j.energy.2012.08.006>
32. Wienchol, P., Szlęk, A., & Ditaranto, M. (2020). Waste-to-energy technology integrated with carbon capture – Challenges and opportunities. *Energy*, *198*, 117352. <https://doi.org/10.1016/j.energy.2020.117352>
33. Carbon Capture and Storage Database of National Energy Technology Laboratory (NETL). (n.d.). Retrieved from <https://netl.doe.gov/carbon-management/carbon-storage/worldwide-ccs-database>
34. Bui, M., Adjiman, C. S., Bardow, A., Anthony, E. J., Boston, A., Brown, S., ... Mac Dowell, N. (2018). Carbon capture and storage (CCS): the way forward. *Energy & Environmental Science*, *11*(5), 1062–1176. <https://doi.org/10.1039/C7EE02342A>
35. Jansen, D., Gazzani, M., Manzolini, G., Dijk, E. V., & Carbo, M. (2015). Pre-combustion CO₂ capture. *International Journal of Greenhouse Gas Control*, *40*, 167–187. <https://doi.org/10.1016/j.ijggc.2015.05.028>
36. Cao, M., Zhao, L., Xu, D., Ciora, R., Liu, P. K. T., Manousiouthakis, V. I., & Tsotsis, T. T. (2020). A carbon molecular sieve membrane-based reactive separation process for pre-combustion CO₂ capture. *Journal of Membrane Science*, *605*, 118028. <https://doi.org/10.1016/j.memsci.2020.118028>
37. Pettinau, A., Ferrara, F., Tola, V., & Cau, G. (2017). Techno-economic comparison between different technologies for CO₂-free power generation from coal. *Applied Energy*, *193*, 426–439. <https://doi.org/10.1016/j.apenergy.2017.02.056>
38. Theo, W. L., Lim, J. S., Hashim, H., Mustaffa, A. A., & Ho, W. S. (2016). Review of pre-combustion capture and ionic liquid in carbon capture and storage. *Applied Energy*, *183*, 1633–1663. <https://doi.org/10.1016/j.apenergy.2016.09.103>
39. Osman, A. I., Abu-Dahrieh, J. K., Cherkasov, N., Fernandez-Garcia, J., Walker, D., Walton, R. I., ... Rebrov, E. (2018). A highly active and synergistic Pt/Mo₂C/Al₂O₃ catalyst for water-gas shift reaction. *Molecular Catalysis*, *455*, 38–47. <https://doi.org/10.1016/j.mcat.2018.05.025>
40. Figueroa, J. D., Fout, T., Plasynski, S., McIlvried, H., & Srivastava, R. D. (2008). Advances in CO₂ capture technology—The U.S. Department of Energy’s Carbon Sequestration Program. *International Journal of Greenhouse Gas Control*, *2*(1), 9–20. [https://doi.org/10.1016/S1750-5836\(07\)00094-1](https://doi.org/10.1016/S1750-5836(07)00094-1)
41. Vega, F., Cano, M., Camino, S., Fernández, L. M. G., Portillo, E., & Navarrete, B. (2018). Solvents for Carbon Dioxide Capture. In I. Karamé, J. Shaya, & H. Srour (Eds.), *Carbon Dioxide Chemistry, Capture and Oil Recovery*. InTech. <https://doi.org/10.5772/intechopen.71443>
42. Cormos, C.-C. (2011). Evaluation of power generation schemes based on hydrogen-fuelled combined cycle with carbon capture and storage (CCS). *International Journal of Hydrogen Energy*, *36*(5), 3726–3738. <https://doi.org/10.1016/j.ijhydene.2010.12.042>
43. Descamps, C., Bouallou, C., & Kanniche, M. (2008). Efficiency of an Integrated Gasification Combined Cycle (IGCC) power plant including CO₂ removal. *Energy*, *33*(6), 874–881. <https://doi.org/10.1016/j.energy.2007.07.013>
44. NETL. (n.d.). IGCC Efficiency. Retrieved from <https://netl.doe.gov/research/Coal/energy-systems/gasification/gasifipedia/igcc-efficiency>
45. Osman, A. I., Deka, T. J., Baruah, D. C., & Rooney, D. W. (2023). Critical challenges in biohydrogen production processes from the organic feedstocks. *Biomass Conversion and Biorefinery*, *13*(10), 8383–8401. <https://doi.org/10.1007/s13399-020-00965-x>

46. Osman, A. I., Hefny, M., Abdel Maksoud, M. I. A., Elgarahy, A. M., & Rooney, D. W. (2021). Recent advances in carbon capture storage and utilisation technologies: a review. *Environmental Chemistry Letters*, 19(2), 797–849. <https://doi.org/10.1007/s10311-020-01133-3>
47. Zhao, K., Jia, C., Li, Z., Du, X., Wang, Y., Li, J., ... Yao, J. (2023). Recent Advances and Future Perspectives in Carbon Capture, Transportation, Utilization, and Storage (CCTUS) Technologies: A Comprehensive Review. *Fuel*, 351, 128913. <https://doi.org/10.1016/j.fuel.2023.128913>
48. Zhou, T., Shi, H., Ding, X., & Zhou, Y. (2021). Thermodynamic modeling and rational design of ionic liquids for pre-combustion carbon capture. *Chemical Engineering Science*, 229, 116076. <https://doi.org/10.1016/j.ces.2020.116076>
49. Gatti, M., Martelli, E., Marechal, F., & Consonni, S. (2014). Review, modeling, Heat Integration, and improved schemes of Rectisol®-based processes for CO₂ capture. *Applied Thermal Engineering*, 70(2), 1123–1140. <https://doi.org/10.1016/j.applthermaleng.2014.05.001>
50. Feron, P. H. M., & Hendriks, C. A. (2005). CO₂ Capture Process Principles and Costs. *Oil & Gas Science and Technology*, 60(3), 451–459. <https://doi.org/10.2516/ogst:2005027>
51. Strathmann, H. (2000). Membranes and membrane separation processes. In *Ullmann's encyclopedia of industrial chemistry*. John Wiley & Sons, Ltd. https://doi.org/10.1002/14356007.a16_187
52. Ji, G., & Zhao, M. (2017). Membrane Separation Technology in Carbon Capture. In Y. Yun (Ed.), *Recent Advances in Carbon Capture and Storage*. InTech. <https://doi.org/10.5772/65723>
53. Hou, R., Fong, C., Freeman, B. D., Hill, M. R., & Xie, Z. (2022). Current status and advances in membrane technology for carbon capture. *Separation and Purification Technology*, 300, 121863. <https://doi.org/10.1016/j.seppur.2022.121863>
54. MTR's PolarCap™ process. (n.d.). Retrieved from <https://www.mtrinc.com/coal-fired-power-plants/>
55. Membrane Technology and Research, Inc. (2015). *PILOT TESTING OF A MEMBRANE SYSTEM FOR POSTCOMBUSTION CO₂ CAPTURE: Operational History at NCCC for the 20 TPD Small-Pilot System*. Retrieved from <https://www.nationalcarboncapturecenter.com/wp-content/uploads/2021/01/Membrane-Technology-and-Research-Operational-History-at-NCCC-for-the-20-TPD-Small-Pilot-System-2015.pdf>
56. Shah, G., Ahmad, E., Pant, K. K., & Vijay, V. K. (2021). Comprehending the contemporary state of art in biogas enrichment and CO₂ capture technologies via swing adsorption. *International Journal of Hydrogen Energy*, 46(9), 6588–6612. <https://doi.org/10.1016/j.ijhydene.2020.11.116>
57. Abd, A. A., Othman, M. R., & Kim, J. (2021). A review on application of activated carbons for carbon dioxide capture: present performance, preparation, and surface modification for further improvement. *Environmental Science and Pollution Research*, 28(32), 43329–43364. <https://doi.org/10.1007/s11356-021-15121-9>
58. Samanta, A., Zhao, A., Shimizu, G. K. H., Sarkar, P., & Gupta, R. (2012). Post-Combustion CO₂ Capture Using Solid Sorbents: A Review. *Industrial & Engineering Chemistry Research*, 51(4), 1438–1463. <https://doi.org/10.1021/ie200686q>
59. Abd, A. A., Naji, S. Z., Hashim, A. S., & Othman, M. R. (2020). Carbon dioxide removal through physical adsorption using carbonaceous and non-carbonaceous adsorbents: A review. *Journal of Environmental Chemical Engineering*, 8(5), 104142. <https://doi.org/10.1016/j.jece.2020.104142>
60. Kosheleva, R. I., Mitropoulos, A. C., & Kyzas, G. Z. (2019). Synthesis of activated carbon from food waste. *Environmental Chemistry Letters*, 17(1), 429–438. <https://doi.org/10.1007/s10311-018-0817-5>
61. Osman, A. I., Blewitt, J., Abu-Dahrieh, J. K., Farrell, C., Al-Muhtaseb, A. H., Harrison, J., & Rooney, D. W. (2019). Production and characterisation of activated carbon and carbon nanotubes from potato peel waste and their application in heavy metal removal. *Environmental Science and Pollution Research*, 26(36), 37228–37241. <https://doi.org/10.1007/s11356-019-06594-w>
62. Singh, G., Lee, J., Karakoti, A., Bahadur, R., Yi, J., Zhao, D., ... Vinu, A. (2020). Emerging trends in porous materials for CO₂ capture and conversion. *Chemical Society Reviews*, 49(13), 4360–4404. <https://doi.org/10.1039/D0CS00075B>
63. Jimoh, T. A., Omoarukhe, F. O., Epelle, E. I., Okoye, P. U., Oke Olusola, E., Mukherjee, A., & Okolie, J. A. (2023). Introduction to carbon capture by solvent-based technologies. In *Reference module in earth systems and environmental sciences*. Elsevier. <https://doi.org/10.1016/B978-0-323-93940-9.00003-7>
64. Bui, M., Gunawan, I., Verheyen, V., Artanto, Y., Meuleman, E., & Feron, P. (2013). Dynamic Modeling and Validation of Post-combustion CO₂ Capture Plants in Australian Coal-fired Power Stations. *Energy Procedia*, 37, 2694–2702. <https://doi.org/10.1016/j.egypro.2013.06.154>
65. Alie, C., Backham, L., Croiset, E., & Douglas, P. L. (2005). Simulation of CO₂ capture using MEA scrubbing: a flowsheet decomposition method. *Energy Conversion and Management*, 46(3), 475–487. <https://doi.org/10.1016/j.enconman.2004.03.003>

66. Bostick, D., Stoffregen, T., & Rigby, S. (n.d.). Final techno-economic analysis of 550 mwe supercritical PC power plant CO₂ capture with linde-BASF advanced PCC technology.
67. Maliz, C. L. (1995). Carbon Dioxide Recovery: Large Scale Design Trends. In *Technical Meeting / Petroleum Conference of The South Saskatchewan Section*. Presented at the Technical Meeting / Petroleum Conference of The South Saskatchewan Section, Regina: Petroleum Society of Canada. <https://doi.org/10.2118/95-160>
68. Hendriks, C. (1994). *Carbon Dioxide Removal from Coal-Fired Power Plants*. Springer Dordrecht. Retrieved from <https://doi.org/10.1007/978-94-011-0301-5>
69. Kittel, J., Idem, R., Gelowitz, D., Tontiwachwuthikul, P., Parrain, G., & Bonneau, A. (2009). Corrosion in MEA units for CO₂ capture: Pilot plant studies. *Energy Procedia*, 1(1), 791–797. <https://doi.org/10.1016/j.egypro.2009.01.105>
70. Desideri, U., & Paolucci, A. (1999). Performance modelling of a carbon dioxide removal system for power plants. *Energy Conversion*.
71. Goto, K., Yogo, K., & Higashii, T. (2013). A review of efficiency penalty in a coal-fired power plant with post-combustion CO₂ capture. *Applied Energy*, 111, 710–720. <https://doi.org/10.1016/j.apenergy.2013.05.020>
72. Abu-Zahra, M. R. M., Niederer, J. P. M., Feron, P. H. M., & Versteeg, G. F. (2007). CO₂ capture from power plants. *International Journal of Greenhouse Gas Control*, 1(2), 135–142. [https://doi.org/10.1016/S1750-5836\(07\)00032-1](https://doi.org/10.1016/S1750-5836(07)00032-1)
73. Davison, J. (2007). Performance and costs of power plants with capture and storage of CO₂. *Energy*, 32(7), 1163–1176. <https://doi.org/10.1016/j.energy.2006.07.039>
74. Abu Zahra, M. R. M., Fernandez, E. S., & Goetheer, E. L. V. (2011). Guidelines for process development and future cost reduction of CO₂ post-combustion capture. *Energy Procedia*, 4, 1051–1057. <https://doi.org/10.1016/j.egypro.2011.01.154>
75. Freund, P. (2003). Making deep reductions in CO₂ emissions from coal- red power plant using capture and storage of CO₂, 217.
76. Wang, M., Lawal, A., Stephenson, P., Sidders, J., & Ramshaw, C. (2011). Post-combustion CO₂ capture with chemical absorption: A state-of-the-art review. *Chemical Engineering Research and Design*, 89(9), 1609–1624. <https://doi.org/10.1016/j.cherd.2010.11.005>
77. Gouedard, C., Picq, D., Launay, F., & Carrette, P.-L. (2012). Amine degradation in CO₂ capture. I. A review. *International Journal of Greenhouse Gas Control*, 10, 244–270. <https://doi.org/10.1016/j.ijggc.2012.06.015>
78. Supap, T., Idem, R., & Tontiwachwuthikul, P. (2011). Mechanism of formation of heat stable salts (HSSs) and their roles in further degradation of monoethanolamine during CO₂ capture from flue gas streams. *Energy Procedia*, 4, 591–598. <https://doi.org/10.1016/j.egypro.2011.01.093>
79. Nielsen, R. B., Irvine, M. D., & McCullough, J. G. (1997). Controlling corrosion in amine treating plants. Retrieved from <https://api.semanticscholar.org/CorpusID:25336552>
80. Lawal, A. O., & Idem, R. O. (2006). Kinetics of the Oxidative Degradation of CO₂ Loaded and Concentrated Aqueous MEA-MDEA Blends during CO₂ Absorption from Flue Gas Streams. *Industrial & Engineering Chemistry Research*, 45(8), 2601–2607. <https://doi.org/10.1021/ie050560c>
81. Global CCS Institute. (2020). The Global Status of CCS Report 2020. (n.d.).
82. Global CCS Institute. (2019). The Global Status of CCS Report 2019. (n.d.).
83. Giannaris, S., Janowczyk, D., Ruffini, J., Hill, K., Jacobs, B., Bruce, C., ... Srisang, W. (2021). SaskPower's Boundary Dam Unit 3 Carbon Capture Facility - The Journey to Achieving Reliability. *SSRN Electronic Journal*. <https://doi.org/10.2139/ssrn.3820191>
84. Stéphenne, K. (2014). Start-up of World's First Commercial Post-combustion Coal Fired CCS Project: Contribution of Shell Cansolv to SaskPower Boundary Dam ICCS Project. *Energy Procedia*, 63, 6106–6110. <https://doi.org/10.1016/j.egypro.2014.11.642>
85. Kamijo, T., Yonekawa, T., Inui, M., Hirata, T., Tsujiuchi, T., & Miyamoto, O. (2015). Deployment of World's Largest Post-combustion Carbon Capture Plant for Coal-fired Power Plants, 52(1).
86. Kenig, E. Y., Schneider, R., & Górak, A. (2001). Reactive absorption: Optimal process design via optimal modelling. *Chemical Engineering Science*, 56(2), 343–350. [https://doi.org/10.1016/S0009-2509\(00\)00234-7](https://doi.org/10.1016/S0009-2509(00)00234-7)
87. Caplow, M. (1968). Kinetics of carbamate formation and breakdown. *Journal of the American Chemical Society*, 90(24), 6795–6803. <https://doi.org/10.1021/ja01026a041>
88. Kierzkowska-Pawlak, H. (2012). Determination of Kinetics in Gas-Liquid Reaction Systems. An Overview. *Ecological Chemistry and Engineering S*, 19(2), 175–196. <https://doi.org/10.2478/v10216-011-0014-y>

89. Danckwerts, P. V. (1979). The reaction of CO₂ with ethanolamines. *Chemical Engineering Science*, 34(4), 443–446. [https://doi.org/10.1016/0009-2509\(79\)85087-3](https://doi.org/10.1016/0009-2509(79)85087-3)
90. Jamal, A., Meisen, A., & Jim Lim, C. (2006). Kinetics of carbon dioxide absorption and desorption in aqueous alkanolamine solutions using a novel hemispherical contactor—I. Experimental apparatus and mathematical modeling. *Chemical Engineering Science*, 61(19), 6571–6589. <https://doi.org/10.1016/j.ces.2006.04.046>
91. Versteeg, G. F., & van Swaaij, W. P. M. (1988). On the kinetics between CO₂ and alkanolamines both in aqueous and non-aqueous solutions—II. Tertiary amines. *Chemical Engineering Science*, 43(3), 587–591. [https://doi.org/10.1016/0009-2509\(88\)87018-0](https://doi.org/10.1016/0009-2509(88)87018-0)
92. Freguia, S., & Rochelle, G. T. (2003). Modeling of CO₂ capture by aqueous monoethanolamine. *AIChE Journal*, 49(7), 1676–1686. <https://doi.org/10.1002/aic.690490708>
93. Vaidya, P. D., & Kenig, E. Y. (2007). CO₂-Alkanolamine Reaction Kinetics: A Review of Recent Studies. *Chemical Engineering & Technology*, 30(11), 1467–1474. <https://doi.org/10.1002/ceat.200700268>
94. Lewis, W. K., & Whitman, W. G. (1924). Principles of Gas Absorption. *Industrial & Engineering Chemistry*, 16(12), 1215–1220. <https://doi.org/10.1021/ie50180a002>
95. Astarita, G., & Savage, D. W. (1980). Gas absorption and desorption with reversible instantaneous chemical reaction. *Chemical Engineering Science*, 35(8), 1755–1764. [https://doi.org/10.1016/0009-2509\(80\)85011-1](https://doi.org/10.1016/0009-2509(80)85011-1)
96. Khaisri, S. (2011). CO₂ stripping from monoethanolamine using a membrane contactor. *Journal of Membrane Science*, 9.
97. Koonaphaddeert, S., Wu, Z., & Li, K. (2009). Carbon dioxide stripping in ceramic hollow fibre membrane contactors. *Chemical Engineering Science*, 64(1), 1–8. <https://doi.org/10.1016/j.ces.2008.09.010>
98. Weiland, R. H., Rawal, M., & Rice, R. G. (1982). Stripping of carbon dioxide from monoethanolamine solutions in a packed column. *AIChE Journal*, 28(6), 963–973. <https://doi.org/10.1002/aic.690280611>
99. Plesu Valentin, Bonet Jordi, Bonet-Ruiz Alexandra E., Chavarria Alan, Iancu Petrica, & Llorens Joan. (2018). Surrogate model for carbon dioxide equilibrium absorption using aqueous monoethanolamine. *Chemical Engineering Transactions*, 70, 919–924. <https://doi.org/10.3303/CET1870154>
100. Suleman, H., Maulud, A. S., Fosbøl, P. L., Nasir, Q., Nasir, R., Shahid, M. Z., ... Abunowara, M. (2021). A review of semi-empirical equilibrium models for CO₂-alkanolamine-H₂O solutions and their mixtures at high pressure. *Journal of Environmental Chemical Engineering*, 9(1), 104713. <https://doi.org/10.1016/j.jece.2020.104713>
101. Kent, R. L., & Eisenberg, B. (1976). Better data for amine treating, 87–90.
102. Jou, F.-Y., Mather, A. E., & Otto, F. D. (1995). The solubility of CO₂ in a 30 mass percent monoethanolamine solution. *The Canadian Journal of Chemical Engineering*, 73(1), 140–147. <https://doi.org/10.1002/cjce.5450730116>
103. Haji-Sulaiman, M. Z., Aroua, M. K., & Benamor, A. (1998). Analysis of Equilibrium Data of CO₂ in Aqueous Solutions of Diethanolamine (DEA), Methyldiethanolamine (MDEA) and Their Mixtures Using the Modified Kent Eisenberg Model. *Chemical Engineering Research and Design*, 76(8), 961–968. <https://doi.org/10.1205/026387698525603>
104. Deshmukh, D., & Mather, A. E. (n.d.). A MATHEMATICAL MODEL FOR EQUILIBRIUM SOLUBILITY OF HYDROGEN SULFIDE AND CARBON DIOXIDE IN AQUEOUS ALKANOLAMINE SOLUTIONS, 8.
105. Li, K., Leigh, W., Feron, P., Yu, H., & Tade, M. (2016). Systematic study of aqueous monoethanolamine (MEA)-based CO₂ capture process: Techno-economic assessment of the MEA process and its improvements. *Applied Energy*, 165, 648–659. <https://doi.org/10.1016/j.apenergy.2015.12.109>
106. Liang, Z. (Henry), Rongwong, W., Liu, H., Fu, K., Gao, H., Cao, F., ... Tontiwachwuthikul, P. (Pt). (2015). Recent progress and new developments in post-combustion carbon-capture technology with amine based solvents. *International Journal of Greenhouse Gas Control*, 40, 26–54. <https://doi.org/10.1016/j.ijggc.2015.06.017>
107. Bernhardsen, I. M., & Knuutila, H. K. (2017). A review of potential amine solvents for CO₂ absorption process: Absorption capacity, cyclic capacity and pK_a. *International Journal of Greenhouse Gas Control*, 61, 27–48. <https://doi.org/10.1016/j.ijggc.2017.03.021>
108. Rochelle, G., Chen, E., Freeman, S., Van Wagener, D., Xu, Q., & Voice, A. (2011). Aqueous piperazine as the new standard for CO₂ capture technology. *Chemical Engineering Journal*, 171(3), 725–733. <https://doi.org/10.1016/j.cej.2011.02.011>
109. Pereira, L. M. C., Llovel, F., & Vega, L. F. (2018). Thermodynamic characterisation of aqueous alkanolamine and amine solutions for acid gas processing by transferable molecular models. *Applied Energy*, 222, 687–703. <https://doi.org/10.1016/j.apenergy.2018.04.021>

110. Boot-Handford, M. E., Abanades, J. C., Anthony, E. J., Blunt, M. J., Brandani, S., Mac Dowell, N., ... Fennell, P. S. (2014). Carbon capture and storage update. *Energy Environ. Sci.*, 7(1), 130–189. <https://doi.org/10.1039/C3EE42350F>
111. Hamborg, E. S., & Versteeg, G. F. (2009). Dissociation Constants and Thermodynamic Properties of Amines and Alkanolamines from (293 to 353) K. *Journal of Chemical & Engineering Data*, 54(4), 1318–1328. <https://doi.org/10.1021/je800897v>
112. Hartono, A., Vevelstad, S. J., Ciftja, A., & Knuutila, H. K. (2017). Screening of strong bicarbonate forming solvents for CO₂ capture. *International Journal of Greenhouse Gas Control*, 58, 201–211. <https://doi.org/10.1016/j.ijggc.2016.12.018>
113. Chowdhury, F. A., Yamada, H., Higashii, T., Goto, K., & Onoda, M. (2013). CO₂ Capture by Tertiary Amine Absorbents: A Performance Comparison Study. *Industrial & Engineering Chemistry Research*, 52(24), 8323–8331. <https://doi.org/10.1021/ie400825u>
114. Gupta, M., & Svendsen, H. F. (2020). Modeling temperature dependent and absolute carbamate stability constants of amines for CO₂ capture. *International Journal of Greenhouse Gas Control*, 98, 103061. <https://doi.org/10.1016/j.ijggc.2020.103061>
115. Choi, W.-J., Seo, J.-B., Jang, S.-Y., Jung, J.-H., & Oh, K.-J. (2009). Removal characteristics of CO₂ using aqueous MEA/AMP solutions in the absorption and regeneration process. *Journal of Environmental Sciences*, 21(7), 907–913. [https://doi.org/10.1016/S1001-0742\(08\)62360-8](https://doi.org/10.1016/S1001-0742(08)62360-8)
116. Hassankiadeh, M. N., & Jahangiri, A. (2018). Application of aqueous blends of AMP and piperazine to the low CO₂ partial pressure capturing: New experimental and theoretical analysis. *Energy*, 165, 164–178. <https://doi.org/10.1016/j.energy.2018.09.160>
117. Tong, D., Maitland, G. C., Trusler, M. J. P., & Fennell, P. S. (2013). Solubility of carbon dioxide in aqueous blends of 2-amino-2-methyl-1-propanol and piperazine. *Chemical Engineering Science*, 101, 851–864. <https://doi.org/10.1016/j.ces.2013.05.034>
118. Mimura, T., Shimojo, S., Suda, T., Iijima, M., & Mitsuoka, S. (1995). Research and development on energy saving technology for flue gas carbon dioxide recovery and steam system in power plant. *Energy Conversion and Management*, 36(6–9), 397–400. [https://doi.org/10.1016/0196-8904\(95\)00029-D](https://doi.org/10.1016/0196-8904(95)00029-D)
119. Xue, B., Yu, Y., Chen, J., Luo, X., & Wang, M. (2017). A comparative study of MEA and DEA for post-combustion CO₂ capture with different process configurations. *International Journal of Coal Science & Technology*, 4(1), 15–24. <https://doi.org/10.1007/s40789-016-0149-7>
120. Yamada, H., Chowdhury, F. A., Goto, K., & Higashii, T. (2013). CO₂ solubility and species distribution in aqueous solutions of 2-(isopropylamino)ethanol and its structural isomers. *International Journal of Greenhouse Gas Control*, 17, 99–105. <https://doi.org/10.1016/j.ijggc.2013.03.027>
121. Chowdhury, F. A., Yamada, H., Matsuzaki, Y., Goto, K., Higashii, T., & Onoda, M. (2014). Development of novel synthetic amine absorbents for CO₂ capture. *Energy Procedia*, 63, 572–579. <https://doi.org/10.1016/j.egypro.2014.11.062>
122. Donaldson, T. L., & Nguyen, Y. N. (1980). Carbon dioxide reaction kinetics and transport in aqueous amine membranes. *Industrial & Engineering Chemistry Fundamentals*, 19, 260–266.
123. Aroonwilas, A., & Veawab, A. (2007). Integration of CO₂ capture unit using single- and blended-amines into supercritical coal-fired power plants: Implications for emission and energy management. *International Journal of Greenhouse Gas Control*, 1(2), 143–150. [https://doi.org/10.1016/S1750-5836\(07\)00011-4](https://doi.org/10.1016/S1750-5836(07)00011-4)
124. Ding, X., Chen, H., Li, J., & Zhou, T. (2023). Comparative techno-economic analysis of CO₂ capture processes using blended amines. *Carbon Capture Science & Technology*, 9, 100136. <https://doi.org/10.1016/j.ccst.2023.100136>
125. Rayer, A. (2013). Solubility of CO₂ in reactive solvents for post-combustion CO₂ capture (pp. 58–77). <https://doi.org/10.4155/9781909453340>
126. FLUOR. (2022). Econamine FG Plus. Retrieved from <https://a.fluor.com/f/1014770/x/a744f915e1/econamine-fg-plus-brochure.pdf>
127. IEAGHG. (2004). *Improvement in power generation with post-combustion capture of CO₂* (No. PH4/33).
128. Mimura, T., Simayoshi, H., Suda, T., Iijima, M., & Mitsuoka, S. (1997). Development of energy saving technology for flue gas carbon dioxide recovery in power plant by chemical absorption method and steam system. *Energy Conversion and Management*, 38, S57–S62. [https://doi.org/10.1016/S0196-8904\(96\)00246-4](https://doi.org/10.1016/S0196-8904(96)00246-4)
129. Gibbins, J. R., & Crane, R. I. (2004). Scope for reductions in the cost of CO₂ capture using flue gas scrubbing with amine solvents. *Proceedings of the Institution of Mechanical Engineers, Part A: Journal of Power and Energy*, 218(4), 231–239. <https://doi.org/10.1243/0957650041200678>

130. Honoki, M., Yokoyama, K., Takamoto, S., Kikkawa, H., Katsube, T., Kawasaki, T., ... Morton, F. C. (2013). Hitachi's carbon dioxide scrubbing technology with H3-1 absorbent for coal-fired power plants. *Energy Procedia*, 37, 2188–2195. <https://doi.org/10.1016/j.egypro.2013.06.098>
131. Stöver, B., Bergins, C., & Klebes, J. (2011). Optimized post combustion carbon capturing on coal fired power plants. *Energy Procedia*, 4, 1637–1643. <https://doi.org/10.1016/j.egypro.2011.02.035>
132. *Technology options for clean coal power generation with CO2 capture*. (2010). Montreal, Canada.
133. Shaw, D. (2009). Cansolv CO2 capture: The value of integration. *Greenhouse Gas Control Technologies* 9, 1(1), 237–246. <https://doi.org/10.1016/j.egypro.2009.01.034>
134. Kim, I., & Svendsen, H. F. (2011). Comparative study of the heats of absorption of post-combustion CO2 absorbents. *International Journal of Greenhouse Gas Control*, 5(3), 390–395. <https://doi.org/10.1016/j.ijggc.2010.05.003>
135. Svendsen, H. F., Hessen, E. T., & Mejdell, T. (2011). Carbon dioxide capture by absorption, challenges and possibilities. *Chemical Engineering Journal*, 171(3), 718–724. <https://doi.org/10.1016/j.cej.2011.01.014>
136. Jou, F.-Y., Otto, F. D., & Mather, A. E. (1994). Vapor-Liquid Equilibrium of Carbon Dioxide in Aqueous Mixtures of Monoethanolamine and Methyldiethanolamine. *Industrial & Engineering Chemistry Research*, 33(8), 2002–2005. <https://doi.org/10.1021/ie00032a016>
137. MATHONAT, C. (1995). *Calorimetrie de melange, a ecoulement, a temperatures et pressions elevees. Application a l'etude de l'elimination du dioxyde de carbone a l'aide de solutions aqueuses d'alcanolamines* (phd). Retrieved from <http://www.theses.fr/1995CLF21756>
138. Eide-Haugmo, I., Brakstad, O. G., Hoff, K. A., Sørheim, K. R., Da Silva, E. F., & Svendsen, H. F. (2009). Environmental impact of amines. *Energy Procedia*, 1(1), 1297–1304. <https://doi.org/10.1016/j.egypro.2009.01.170>
139. Novatech. (2005). *Supplementary Guidance for the completing of Harmonised Offshore Chemical Notification Format (HOCNF) 2000 for Norwegian sector*.
140. Charcosset, C. (2021). Classical and Recent Applications of Membrane Processes in the Food Industry. *Food Engineering Reviews*, 13(2), 322–343. <https://doi.org/10.1007/s12393-020-09262-9>
141. Ma, R., Li, J., Zeng, P., Duan, L., Dong, J., Ma, Y., & Yang, L. (2024). The Application of Membrane Separation Technology in the Pharmaceutical Industry. *Membranes*, 14(1), 24. <https://doi.org/10.3390/membranes14010024>
142. Klaassen, R., Feron, P. H. M., & Jansen, A. E. (2005). Membrane Contactors in Industrial Applications. *Chemical Engineering Research and Design*, 83(3), 234–246. <https://doi.org/10.1205/cherd.04196>
143. Zhao, S., Feron, P. H. M., Deng, L., Favre, E., Chabanon, E., Yan, S., ... Qi, H. (2016). Status and progress of membrane contactors in post-combustion carbon capture: A state-of-the-art review of new developments. *Journal of Membrane Science*, 511, 180–206. <https://doi.org/10.1016/j.memsci.2016.03.051>
144. Wang, C., Perry, M., Seibert, F., & Rochelle, G. T. (2013). Characterization of novel structured packings for CO2 capture. *Energy Procedia*, 37, 2145–2153. <https://doi.org/10.1016/j.egypro.2013.06.093>
145. Zhao, X., Smith, K. H., Simioni, M. A., Tao, W., Kentish, S. E., Fei, W., & Stevens, G. W. (2011). Comparison of several packings for CO2 chemical absorption in a packed column. *International Journal of Greenhouse Gas Control*, 5(5), 1163–1169. <https://doi.org/10.1016/j.ijggc.2011.07.006>
146. Qi, Z., & Cussler, E. L. (1985). Microporous hollow fibers for gas absorption: I. Mass transfer in the liquid. *Journal of Membrane Science*, 23(3), 321–332. [https://doi.org/10.1016/S0376-7388\(00\)83149-X](https://doi.org/10.1016/S0376-7388(00)83149-X)
147. Qi, Z., & Cussler, E. L. (1985). Microporous hollow fibers for gas absorption: II. Mass transfer across the membrane. *Journal of Membrane Science*, 23(3), 333–345. [https://doi.org/10.1016/S0376-7388\(00\)83150-6](https://doi.org/10.1016/S0376-7388(00)83150-6)
148. Wang, F., Zhao, J., Miao, H., Zhao, J., Zhang, H., Yuan, J., & Yan, J. (2018). Current status and challenges of the ammonia escape inhibition technologies in ammonia-based CO2 capture process. *Applied Energy*, 230, 734–749. <https://doi.org/10.1016/j.apenergy.2018.08.116>
149. Demontigny, D., Tontiwachwuthikul, P., & Chakma, A. (2006). Using polypropylene and polytetrafluoroethylene membranes in a membrane contactor for CO2 absorption. *Journal of Membrane Science*, 277(1–2), 99–107. <https://doi.org/10.1016/j.memsci.2005.10.024>
150. Fang, M., Wang, Z., Yan, S., Cen, Q., & Luo, Z. (2012). CO2 desorption from rich alkanolamine solution by using membrane vacuum regeneration technology. *International Journal of Greenhouse Gas Control*, 9, 507–521. <https://doi.org/10.1016/j.ijggc.2012.05.013>

151. Bozonc, A.-C., Sandu, V.-C., Cormos, C.-C., & Cormos, A.-M. (2024). 3D-CFD modeling of hollow-fiber membrane contactor for CO₂ absorption using MEA solution. *Membranes*, *14*(4). <https://doi.org/10.3390/membranes14040086>
152. Vogt, M., Goldschmidt, R., Bathen, D., Epp, B., & Fahlenkamp, H. (2011). Comparison of membrane contactor and structured packings for CO₂ absorption. *Energy Procedia*, *4*, 1471–1477. <https://doi.org/10.1016/j.egypro.2011.02.013>
153. Kumar, P. S., Hogendoorn, J. A., Feron, P. H. M., & Versteeg, G. F. (2002). New absorption liquids for the removal of CO₂ from dilute gas streams using membrane contactors. *Chemical Engineering Science*, *57*(9), 1639–1651. [https://doi.org/10.1016/S0009-2509\(02\)00041-6](https://doi.org/10.1016/S0009-2509(02)00041-6)
154. Nishikawa, N., Ishibashi, M., Ohta, H., Akutsu, N., Matsumoto, H., Kamata, T., & Kitamura, H. (1995). CO₂ removal by hollow-fiber gas-liquid contactor. *Energy Conversion and Management*, *36*(6–9), 415–418. [https://doi.org/10.1016/0196-8904\(95\)00033-A](https://doi.org/10.1016/0196-8904(95)00033-A)
155. Gabelman, A., & Hwang, S.-T. (1999). Hollow fiber membrane contactors. *Journal of Membrane Science*, *46*.
156. Albarracin Zaidiza, D., Belaissaoui, B., Rode, S., & Favre, E. (2017). Intensification potential of hollow fiber membrane contactors for CO₂ chemical absorption and stripping using monoethanolamine solutions. *Separation and Purification Technology*, *188*, 38–51. <https://doi.org/10.1016/j.seppur.2017.06.074>
157. Wang, Z., Fang, M., Yu, H., Ma, Q., & Luo, Z. (2013). Modeling of CO₂ Stripping in a Hollow Fiber Membrane Contactor for CO₂ Capture. *Energy & Fuels*, *27*(11), 6887–6898. <https://doi.org/10.1021/ef401488c>
158. Ibrahim, M. H., El-Naas, M. H., & Zhang, Z. (n.d.). CO₂ Capture using Hollow Fiber Membranes: A review of membrane wetting, 58.
159. Falk-Pedersen, O., Grønvold, M. S., Nøkleby, P., Bjerve, F., & Svendsen, H. F. (2005). CO₂ Capture with Membrane Contactors. *International Journal of Green Energy*, *2*(2), 157–165. <https://doi.org/10.1081/GE-200058965>
160. Khaisri, S., deMontigny, D., Tontiwachwuthikul, P., & Jiratananon, R. (2009). Comparing membrane resistance and absorption performance of three different membranes in a gas absorption membrane contactor. *Separation and Purification Technology*, *65*(3), 290–297. <https://doi.org/10.1016/j.seppur.2008.10.035>
161. Chabanon, E., Kimball, E., Favre, E., Lorain, O., Goetheer, E., Ferre, D., ... Broutin, P. (2014). Hollow Fiber Membrane Contactors for Post-Combustion CO₂ Capture: A Scale-Up Study from Laboratory to Pilot Plant. *Oil & Gas Science and Technology – Revue d'IFP Energies nouvelles*, *69*(6), 1035–1045. <https://doi.org/10.2516/ogst/2012046>
162. Li, S., Pyrzyński, T. J., Klinghoffer, N. B., Tamale, T., Zhong, Y., Aderhold, J. L., ... Bikson, B. (2017). Scale-up of PEEK hollow fiber membrane contactor for post-combustion CO₂ capture. *Journal of Membrane Science*, *527*, 92–101. <https://doi.org/10.1016/j.memsci.2017.01.014>
163. Chuah, C. Y., Kim, K., Lee, J., Koh, D.-Y., & Bae, T.-H. (2020). CO₂ Absorption Using Membrane Contactors: Recent Progress and Future Perspective. *Industrial & Engineering Chemistry Research*, *59*(15), 6773–6794. <https://doi.org/10.1021/acs.iecr.9b05439>
164. Alkhudhiri, A., Darwish, N., & Hilal, N. (2012). Membrane distillation: A comprehensive review. *Desalination*, *287*, 2–18. <https://doi.org/10.1016/j.desal.2011.08.027>
165. Tan, X., Liu, S., & Li, K. (2001). Preparation and characterization of inorganic hollow fiber membranes. *Journal of Membrane Science*, *188*(1), 87–95. [https://doi.org/10.1016/S0376-7388\(01\)00369-6](https://doi.org/10.1016/S0376-7388(01)00369-6)
166. Kosaraju, P., Kovvali, A. S., Korikov, A., & Sirkar, K. K. (2005). Hollow Fiber Membrane Contactor Based CO₂ Absorption–Stripping Using Novel Solvents and Membranes. *Industrial & Engineering Chemistry Research*, *44*(5), 1250–1258. <https://doi.org/10.1021/ie0495630>
167. Lu, J.-G. (2013). CO₂ capture by membrane absorption coupling process Experiments and coupling process evaluation. *Journal of Membrane Science*, *10*.
168. Simioni, M., Kentish, S. E., & Stevens, G. W. (2011). Membrane stripping: Desorption of carbon dioxide from alkali solvents. *Journal of Membrane Science*, *378*(1–2), 18–27. <https://doi.org/10.1016/j.memsci.2010.12.046>
169. Porcheron, F., Ferré, D., Favre, E., Nguyen, P. T., Lorain, O., Mercier, R., & Rougeau, L. (2011). Hollow fiber membrane contactors for CO₂ capture: From lab-scale screening to pilot-plant module conception. *Energy Procedia*, *4*, 763–770. <https://doi.org/10.1016/j.egypro.2011.01.117>
170. Wang, R., Li, D. F., Zhou, C., Liu, M., & Liang, D. T. (2004). Impact of DEA solutions with and without CO₂ loading on porous polypropylene membranes intended for use as contactors. *Journal of Membrane Science*, *229*(1–2), 147–157. <https://doi.org/10.1016/j.memsci.2003.10.022>
171. Scholes, C. A. (2019). Membrane contactors modelled for process intensification post combustion solvent regeneration. *International Journal of Greenhouse Gas Control*, *87*, 203–210. <https://doi.org/10.1016/j.ijggc.2019.05.025>

172. Gibbins, J. R., Crane, R. I., Lambropoulos, D., Booth, C., Roberts, C. A., & Lord, M. (2005). - Maximising the effectiveness of post combustion CO₂ capture systems. In E. S. Rubin, D. W. Keith, C. F. Gilboy, M. Wilson, T. Morris, J. Gale, & K. Thambimuthu (Eds.), *Greenhouse gas control technologies 7* (pp. 139–146). Oxford: Elsevier Science Ltd. <https://doi.org/10.1016/B978-008044704-9/50015-X>
173. Wang, Z., Fang, M., Pan, Y., Yan, S., & Luo, Z. (2013). Amine-based absorbents selection for CO₂ membrane vacuum regeneration technology by combined absorption–desorption analysis. *Chemical Engineering Science*, *93*, 238–249. <https://doi.org/10.1016/j.ces.2013.01.057>
174. Wang, Z., Fang, M., Ma, Q., Zhao, Z., Wang, T., & Luo, Z. (2014). Membrane Stripping Technology for CO₂ Desorption from CO₂-rich Absorbents with Low Energy Consumption. *Energy Procedia*, *63*, 765–772. <https://doi.org/10.1016/j.egypro.2014.11.085>
175. Okabe, K., Mano, H., & Fujioka, Y. (2008). Separation and recovery of carbon dioxide by a membrane flash process. *International Journal of Greenhouse Gas Control*, *2*(4), 485–491. <https://doi.org/10.1016/j.ijggc.2008.06.004>
176. Lee, H. J., Kim, M. K., & Park, J. H. (2020). Decompression stripping of carbon dioxide from rich monoethanolamine through porous hydrophobic modified ceramic hollow fiber membrane contactor. *Separation and Purification Technology*, *236*, 116304. <https://doi.org/10.1016/j.seppur.2019.116304>
177. Ahn, H., Kim, J., & Kim, J.-H. (2013). Low-temperature vacuum stripping of CO₂ from aqueous amine solutions using thin-film silicalite-filled PDMS composite membranes. *International Journal of Greenhouse Gas Control*, *18*, 165–172. <https://doi.org/10.1016/j.ijggc.2013.07.004>
178. Bazhenov, S. D., & Lyubimova, E. S. (2016). Gas–liquid membrane contactors for carbon dioxide capture from gaseous streams. *Petroleum Chemistry*, *56*(10), 889–914. <https://doi.org/10.1134/S0965544116100029>
179. Wang, R., Zhang, H. Y., Feron, P. H. M., & Liang, D. T. (2005). Influence of membrane wetting on CO₂ capture in microporous hollow fiber membrane contactors. *Separation and Purification Technology*, *46*(1–2), 33–40. <https://doi.org/10.1016/j.seppur.2005.04.007>
180. Mosadegh-Sedghi, S., Brisson, J., Rodrigue, D., & Iliuta, M. C. (2012). Morphological, chemical and thermal stability of microporous LDPE hollow fiber membranes in contact with single and mixed amine based CO₂ absorbents. *Separation and Purification Technology*, *96*, 117–123. <https://doi.org/10.1016/j.seppur.2012.05.025>
181. Kreulen, H., Smolders, C. A., Versteeg, G. F., & van Swaaij, W. P. M. (1993). Microporous hollow fibre membrane modules as gas-liquid contactors. Part 1. Physical mass transfer processes. *Journal of Membrane Science*, *78*(3), 197–216. [https://doi.org/10.1016/0376-7388\(93\)80001-E](https://doi.org/10.1016/0376-7388(93)80001-E)
182. Mansourizadeh, A., & Mousavian, S. (2013). Structurally developed microporous polyvinylidene fluoride hollow-fiber membranes for CO₂ absorption with diethanolamine solution. *Journal of Polymer Research*, *20*(3), 99. <https://doi.org/10.1007/s10965-013-0099-3>
183. Rongwong, W., Jiratananon, R., & Atchariyawut, S. (2009). Experimental study on membrane wetting in gas–liquid membrane contacting process for CO₂ absorption by single and mixed absorbents. *Separation and Purification Technology*, *69*(1), 118–125. <https://doi.org/10.1016/j.seppur.2009.07.009>
184. Mansourizadeh, A., & Ismail, A. F. (2009). Hollow fiber gas–liquid membrane contactors for acid gas capture: A review. *Journal of Hazardous Materials*, *171*(1), 38–53. <https://doi.org/10.1016/j.jhazmat.2009.06.026>
185. Chabanon, E., Roizard, D., & Favre, E. (2011). Membrane Contactors for Postcombustion Carbon Dioxide Capture: A Comparative Study of Wetting Resistance on Long Time Scales. *Industrial & Engineering Chemistry Research*, *50*(13), 8237–8244. <https://doi.org/10.1021/ie200704h>
186. Ding, Y., & Bikson, B. (2010). Preparation and characterization of semi-crystalline poly(ether ether ketone) hollow fiber membranes. *Journal of Membrane Science*, *357*(1), 192–198. <https://doi.org/10.1016/j.memsci.2010.04.021>
187. Li, S., Rocha, D. J., James Zhou, S., Meyer, H. S., Bikson, B., & Ding, Y. (2013). Post-combustion CO₂ capture using superhydrophobic, polyether ether ketone, hollow fiber membrane contactors. *Journal of Membrane Science*, *430*, 79–86. <https://doi.org/10.1016/j.memsci.2012.12.001>
188. Kreulen, H., Smolders, C. A., Versteeg, G. F., & Van Swaaij, W. P. M. (1993). Determination of mass transfer rates in wetted and non-wetted microporous membranes. *Chemical Engineering Science*, *48*(11), 2093–2102. [https://doi.org/10.1016/0009-2509\(93\)80084-4](https://doi.org/10.1016/0009-2509(93)80084-4)
189. Lv, Y., Yu, X., Tu, S.-T., Yan, J., & Dahlquist, E. (2010). Wetting of polypropylene hollow fiber membrane contactors. *Journal of Membrane Science*, *362*(1–2), 444–452. <https://doi.org/10.1016/j.memsci.2010.06.067>

190. Rezaei, M., Warsinger, D. M., Lienhard V, J. H., Duke, M. C., Matsuura, T., & Samhaber, W. M. (2018). Wetting phenomena in membrane distillation: Mechanisms, reversal, and prevention. *Water Research*, *139*, 329–352. <https://doi.org/10.1016/j.watres.2018.03.058>

191. Colin A. Scholes, G. W. S., Abdul Qader, & Kentish, S. E. (2014). Membrane gas-solvent contactor pilot plant trials of CO₂ absorption from flue gas. *Separation Science and Technology*, *49*(16), 2449–2458. <https://doi.org/10.1080/01496395.2014.937499>

192. Chabanon, E., Roizard, D., & Favre, E. (2013). Modeling strategies of membrane contactors for post-combustion carbon capture: A critical comparative study. *Chemical Engineering Science*, *87*, 393–407. <https://doi.org/10.1016/j.ces.2012.09.011>

193. Atcharyawut, S., Jiratananon, R., & Wang, R. (2007). Separation of CO₂ from CH₄ by using gas–liquid membrane contacting process. *Journal of Membrane Science*, *304*(1), 163–172. <https://doi.org/10.1016/j.memsci.2007.07.030>

194. Zhao, Y.-H., Qian, Y.-L., Zhu, B.-K., & Xu, Y.-Y. (2008). Modification of porous poly(vinylidene fluoride) membrane using amphiphilic polymers with different structures in phase inversion process. *Journal of Membrane Science*, *310*(1), 567–576. <https://doi.org/10.1016/j.memsci.2007.11.040>

195. Mansourizadeh, A., Jazebizadeh, M. H., Vaseghi, M. R., & Aghili, A. (2015). A comparative study on the structure of developed porous PVDF and PEI hollow fiber membrane contactors for CO₂ absorption. *Journal of Polymer Research*, *23*(1), 4. <https://doi.org/10.1007/s10965-015-0881-5>

196. Extrand, C. W. (2003). A Thermodynamic Model for Wetting Free Energies from Contact Angles. *Langmuir*, *19*(3), 646–649. <https://doi.org/10.1021/la0259609>

197. Marzouk, S. A. M., Al-Marzouqi, M. H., Abdullatif, N., & Ismail, Z. M. (2010). Removal of percentile level of H₂S from pressurized H₂S–CH₄ gas mixture using hollow fiber membrane contactors and absorption solvents. *Journal of Membrane Science*, *360*(1), 436–441. <https://doi.org/10.1016/j.memsci.2010.05.046>

198. Franco, J. A., deMontigny, D., Kentish, S. E., Perera, J. M., & Stevens, G. W. (2009). Effect of amine degradation products on the membrane gas absorption process. *Chemical Engineering Science*, *64*(18), 4016–4023. <https://doi.org/10.1016/j.ces.2009.06.012>

199. Ismail, A. F., & Mansourizadeh, A. (2010). A comparative study on the structure and performance of porous polyvinylidene fluoride and polysulfone hollow fiber membranes for CO₂ absorption. *Journal of Membrane Science*, *365*(1), 319–328. <https://doi.org/10.1016/j.memsci.2010.09.021>

200. Comite, A., Costa, C., Demartini, M., Di Felice, R., & Rotondi, M. (2016). Rate of CO₂ transfer to loaded MEA solutions using a membrane contactor device. *International Journal of Greenhouse Gas Control*, *52*, 378–386. <https://doi.org/10.1016/j.ijggc.2016.07.029>

201. Li, Y., Gao, J., Li, J., Li, Y., Bernards, M. T., Tao, M., ... Shi, Y. (2020). Screening and Performance Evaluation of Triethylenetetramine Nonaqueous Solutions for CO₂ Capture with Microwave Regeneration. *Energy & Fuels*, *34*(9), 11270–11281. <https://doi.org/10.1021/acs.energyfuels.0c02006>

202. Lu, J.-G., Zheng, Y.-F., & Cheng, M.-D. (2008). Wetting mechanism in mass transfer process of hydrophobic membrane gas absorption. *Journal of Membrane Science*, *308*(1), 180–190. <https://doi.org/10.1016/j.memsci.2007.09.051>

203. Federal Communications comission. 2018. Office of Engineering and Technology Policy and Rules Division. (2018).

204. Cherbański, R., & Molga, E. (2009). Intensification of desorption processes by use of microwaves—An overview of possible applications and industrial perspectives. *Chemical Engineering and Processing: Process Intensification*, *48*(1), 48–58. <https://doi.org/10.1016/j.cep.2008.01.004>

205. Sadiku, M. N. O. (2001). *Elements of electromagnetics* (3rd ed.). New York: Oxford University Press New York.

206. Microwave heating, mechanism and theory. (n.d.). Retrieved from https://cem.com/fr/microwave-heating-mechanism-and-theory?__store=fr&__from_store=en

207. Stefanidis, G. D., Muñoz, A. N., Sturm, G. S. J., & Stankiewicz, A. (2014). A helicopter view of microwave application to chemical processes: reactions, separations, and equipment concepts. *Reviews in Chemical Engineering*, *30*(3). <https://doi.org/10.1515/revce-2013-0033>

208. Guzik, P., Kulawik, P., Zajac, M., & Migdał, W. (2022). Microwave applications in the food industry: an overview of recent developments. *Critical Reviews in Food Science and Nutrition*, *62*(29), 7989–8008. <https://doi.org/10.1080/10408398.2021.1922871>

209. Zhao, D., An, K., Ding, S., Liu, L., Xu, Z., & Wang, Z. (2014). Two-Stage Intermittent Microwave Coupled with Hot-Air Drying of Carrot Slices: Drying Kinetics and Physical Quality. *Food and Bioprocess Technology*, *7*(8), 2308–2318. <https://doi.org/10.1007/s11947-014-1274-1>

210. Zhang, J. P., Wu, Y. H., Liu, E. Q., Song, H., & Li, Y. (2014). Comparison of storage characteristics and quality of semi-dry fermented sausage using microwave vacuum drying and hot air drying. In *Environmental protection and resources exploitation II* (Vol. 1010, pp. 1783–1788). Trans Tech Publications Ltd. <https://doi.org/10.4028/www.scientific.net/AMR.1010-1012.1783>
211. Kranjc, K., & Kocevar, M. (2013). From conventional reaction conditions to microwave-assisted catalytic transformations of various substrates. State of the art in 2012 (part B: Catalysis). *Current Organic Chemistry*, *17*, 457–473. <https://doi.org/10.2174/1385272811317050004>
212. Kranjc, K., & Kocevar, M. (2013). From conventional reaction conditions to microwave-assisted catalytic transformations of various substrates. State of the art in 2012 (part B: Catalysis). *Current Organic Chemistry*, *17*, 457–473. <https://doi.org/10.2174/1385272811317050004>
213. Chemat-Djenni, Z., Hamada, B., & Chemat, F. (2007). Atmospheric pressure microwave assisted heterogeneous catalytic reactions. *Molecules (Basel, Switzerland)*, *12*(7), 1399–1409. <https://doi.org/10.3390/12071399>
214. Filly, A., Fernandez, X., Minuti, M., Visinoni, F., Cravotto, G., & Chemat, F. (2014). Solvent-free microwave extraction of essential oil from aromatic herbs: From laboratory to pilot and industrial scale. *Food Chemistry*, *150*, 193–198. <https://doi.org/10.1016/j.foodchem.2013.10.139>
215. Roussy, G., & Chenot, P. (1981). Selective energy supply to adsorbed water and nonclassical thermal process during microwave dehydration of zeolite. *The Journal of Physical Chemistry*, *85*(15), 2199–2203. <https://doi.org/10.1021/j150615a013>
216. Kim, K.-J., & Ahn, H.-G. (2012). The effect of pore structure of zeolite on the adsorption of VOCs and their desorption properties by microwave heating. *Microporous and Mesoporous Materials*, *152*, 78–83. <https://doi.org/10.1016/j.micromeso.2011.11.051>
217. Webley, P. A., & Zhang, J. (2014). Microwave assisted vacuum regeneration for CO₂ capture from wet flue gas. *Adsorption*, *20*(1), 201–210. <https://doi.org/10.1007/s10450-013-9563-y>
218. Nigar, H., Garcia-Baños, B., Peñaranda-Foix, F. L., Catalá-Civera, J. M., Mallada, R., & Santamaría, J. (2016). Amine-functionalized mesoporous silica: A material capable of CO₂ adsorption and fast regeneration by microwave heating. *AIChE Journal*, *62*(2), 547–555. <https://doi.org/10.1002/aic.15118>
219. McGurk, S. J., Martín, C. F., Brandani, S., Sweatman, M. B., & Fan, X. (2017). Microwave swing regeneration of aqueous monoethanolamine for post-combustion CO₂ capture. *Applied Energy*, *192*, 126–133. <https://doi.org/10.1016/j.apenergy.2017.02.012>
220. Bougie, F., & Fan, X. (2018). Microwave regeneration of monoethanolamine aqueous solutions used for CO₂ capture. *International Journal of Greenhouse Gas Control*, *79*, 165–172. <https://doi.org/10.1016/j.ijggc.2018.10.008>
221. Bougie, F., Pokras, D., & Fan, X. (2019). Novel non-aqueous MEA solutions for CO₂ capture. *International Journal of Greenhouse Gas Control*, *86*, 34–42. <https://doi.org/10.1016/j.ijggc.2019.04.013>

Page left intentionally black

2 Dielectric characterization of CO₂-rich 30% ethanolamine solution

2.1 Introduction

Microwave incorporation in carbon capture techniques is a subject of novelty and promises many advancements such as intensification and improvements in process economy. Recently microwaves were applied to regenerate CO₂-rich solvents in the context of carbon capture by chemical absorption. Till now, few studies have attempted to study microwave regeneration of CO₂-rich amine solutions, the scale of which is limited to few milliliters of solvent [1–3]. It is evident however that any attempt of modeling, or scaling-up the process of microwave-assisted solvent regeneration will require knowledge of the dielectric properties of the solvent.

Existing works on the dielectric characterization of alkanolamines are limited to samples either of pure alkanolamines, or aqueous alkanolamines that are free of CO₂ content. Patil [4] measured and fitted the dielectric properties of a binary mixture of ethanolamine and di-ethanolamine. Jadhavpatil [5] used the Havriliak-Negami model to fit the dielectric dispersion of aqueous ethanolamine solutions at different temperatures and proportions, but the solutions under test were free of CO₂. Hsieh [6] measured the static dielectric constant of some aqueous alkanolamines that are free of CO₂.

As far as we can tell, the existing literature on dielectric characterization of CO₂-rich aqueous alkanolamines is far from being exhaustive. Having said that, the main focus of this chapter is the dielectric characterization of 30% by weight aqueous ethanolamine, at the frequency range [915-2450] MHz and at different temperatures and CO₂ loadings.

The obtained dielectric properties were fitted with the Cole-Cole dielectric model, and the obtained dispersion parameters were interpreted with the help of the chemical speciation obtained from the vapor-liquid equilibrium model of Kent-Eisenberg. The organization of this chapter is such that it is divided into three main subchapters:

-2.2 Preamble: microwave-material interaction

This part discusses briefly the fundamentals of microwave-material interaction, we define the parameters that characterize this interaction in the form of the complex dielectric constant composed of the relative permittivity and the dielectric loss factor. The latter was derived from Maxwell's equations and alternatively by using the equivalent circuit approach. In addition, this subchapter discusses unguided plane electromagnetic waves and their characteristics, from there on out electromagnetic propagation in a lossy dielectric was explored to reach the concepts of the penetration depth and Poynting's vector. The dielectric properties of a lossy medium were characterized as a function of frequency with the help of dielectric dispersion models such as those of Debye, Cole-Cole, Davidson-Cole and Havriliak-Negami models. Differences between the dielectric relaxation models were highlighted by plotting the dielectric dispersion curve in a Cole-Cole diagram.

-2.3 Dielectric characterization of CO₂-loaded solvents: materials and methods

The chapter discusses the dielectric characterization of 30% by weight aqueous ethanolamine solution with dissolved CO₂ concentration. We start by providing a brief review of the dielectric measurement techniques while putting greater focus on the open-ended coaxial measurement probe, the technique used in this study. To provide a deeper interpretation of the experimental dielectric properties, the experimental dielectric data were fitted to a dielectric relaxation model. Lastly, Kent-Eisenberg vapor-liquid equilibrium model was presented along with its resolution method.

-2.4 Dielectric properties and dispersion parameters function of operating conditions

In this part, the experimental and extrapolated dielectric properties of 30% aqueous ethanolamine free and loaded with CO₂ were presented under the form of Bode plots or Cole-Cole dispersion diagrams. The dielectric loss of the solution was divided into losses by ionic conduction or dipolar rotation mechanisms. The effects of frequency, temperature, and CO₂ loading on the dielectric dispersion were discussed. In the sequel, the dielectric relaxation parameters of the Cole-Cole model - obtained by fitting the model to the experimental data - were plotted as a function of temperature and at different CO₂ concentrations, and interpreted with the help of the chemical speciation obtained by solving the Kent-Eisenberg vapor-liquid equilibrium model.

2.2 Preamble: microwave-material interaction

2.2.1 Dielectric polarizability and electrostatic potential

Materials can broadly be classified into conductors, semi-conductors and dielectrics. Applications of microwave heating are adapted to dielectric materials instead of conductors that are inert to microwaves. A dielectric material consists of permanent or instantaneous dipoles, a dipole is a covalently bonded molecule which has an unequal charge distribution: while protons are bound in the nucleus, the electrons move around more freely and spend - on average - more time in a particular region of the molecule creating a partial negative charge on that region and partial positive charge on the opposite side. Dipolar rotation takes place when the external E-field exerts a torque on the dipoles of the medium which forces them to “relax” by rotating to seek the position that minimizes the former [7]. The equilibrium position has been widely accepted to be that of parallel alignment with the E-field [4, 5, 8–10].

A dipole can be characterized through its dipole moment μ expressed in (C.m) and shown in equation (2.1) with (Q) being the charge of a monopole, and (d) the distance separating them. A dipole when subjected to an external E-field, experiences a torque (2.2) that rotates it to reduce its potential energy by achieving parallel alignment with the E-field.

$$\vec{\mu} = Q * \vec{d} \quad (2.1)$$

$$\vec{T} = \vec{\mu} \times \vec{E} \quad (2.2)$$

In a dielectric medium, dipole concentrations are great therefor the polarizability (\vec{P}) was defined as the average dipole moment per unit volume of the material expressed in (C/m²) and shown in (2.3), and (Δv) being an infinitesimal volume element. It is the sum of all the individual dipole moment vectors divided by the volume occupied by the formers. The polarizability of liquids is generally considered as anisotropic, and being linearly dependent on the E-field strength.

$$\vec{P} = \lim_{\Delta v \rightarrow 0} \frac{\sum_i \vec{\mu}_i}{\Delta v} \quad (2.3)$$

In order to understand the link between dielectric constant and the polarizability of the material we start by considering the electrostatic potential on a point in vacuum at a distance (R) from an elementary volume of dielectric material under an external E-field. The resulting potential (dV) due to an infinitesimal volume (dv) is expressed in equation (2.4), with (ϵ_0^*) being the vacuum permittivity (F/m), (R) and (\vec{a}_r) are the distance and the unit vector between the dipole element and the point of interest.

$$dV = \frac{\vec{P} \cdot \vec{a}_r}{4\pi\epsilon_0^* R^2} dv \quad (2.4)$$

The electrostatic potential due to the entire dielectric volume is expressed in the form of an integral over the surface and volume of the dielectric as shown in equation (2.5). The first term on the righthand side is the electrostatic potential due to a surface charge density (ρ_{bs}), the second is the electrostatic potential due to a volumetric charge density (ρ_{bv}), (ϵ_0^*) is the permittivity of free space in (F/m), (R) is the distance between the elementary volume (dv) and the point of

interest in vacuum. The obtained charge distributions occur due to dipole displacements on the molecular scale, these charges are immobile and hence they are called “bound charges” as opposed to free charges that can displace under the influence of an external E-field. Therefore, a dielectric under an external E-field possesses a superficial and volumetric charge densities, all while remaining globally neutral. The surface and volumetric charge densities are expressed in terms of polarizability as shown in the equations (2.6) and (2.7) respectively [11], with (\vec{a}_n) is the unit vector that is normal to the surface of the dielectric.

$$V = \iint_S \frac{\rho_{bs}}{4\pi\epsilon_0^*R} dS + \iiint_V \frac{\rho_{bv}}{4\pi\epsilon_0^*R} dv \quad (2.5)$$

$$\rho_{bs} = \vec{P} \cdot \vec{a}_n \quad (2.6)$$

$$\rho_{bv} = -\nabla \cdot \vec{P} \quad (2.7)$$

The existence of a surface bound charge is demonstrated as follows. If we consider that the dielectric material was placed in a capacitor (Figure 2-1), the E-field between the armatures of the latter will polarize the dielectric material. The capacitor plates would accumulate two types of charges, free charges from the electrochemical cell as well as bound charges due to molecular displacements. The bulk of the dielectric has a global net charge of zero but has nonetheless a bound charge that depends on the spatial variations of the polarizability as expressed in (2.7).

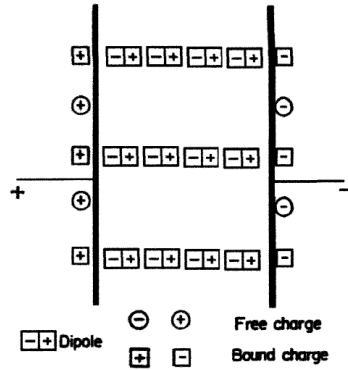


Figure 2-1: Polarization of dielectric material in a capacitor under a static potential difference – taken from [12]

Gauss’s law is the first one of Maxwell’s equations, it states that an electrical charge produces a certain amount of electric field lines, i.e. the integral of the normal component of the electrical flux - denoted by \vec{D} (C/m²) - over a closed Gaussian surface is equal to the net electrical charge inside that surface. Gauss’s law on an elementary volume is expressed in equation (2.8) with (ρ_t) being the total volumetric charge density (C/m³).

$$\rho_t = \nabla \cdot \vec{D} \quad (2.8)$$

For a dielectric material containing free charges and under an external E-field, the total volumetric charge density is calculated from the free and bound charge densities as expressed in equation (2.9).

$$\rho_t = \rho_{bv} + \rho_v \quad (2.9)$$

Upon substituting equations (2.7), (2.8) into (2.9) and rearranging we get the expression of the total volumetric charge density function of the electric field and the polarizability of the dielectric – equation (2.10).

$$\rho_t = \nabla \cdot (\epsilon_0^* \vec{E} + \vec{P}) \quad (2.10)$$

If the polarizability of the material (\vec{P}) is assumed to be isotropic and linear with respect to the E-field as is the case with many materials, it can be expressed as shown in equation (2.11) with (χ) being labeled as the dielectric susceptibility of the material.

$$\vec{P} = \chi \epsilon_0^* \vec{E} \quad (2.11)$$

Replacing (2.11) in (2.10) and rearranging we get the expression of the total charge as a function of the relative static dielectric constant (ϵ_r) as shown in (2.12) and expressed in equation (2.13) with (ϵ) being the medium permittivity in (F/m).

$$\rho_t = \nabla \cdot (\epsilon_0^* \epsilon_r \vec{E}) \quad (2.12)$$

$$\epsilon_r = (1 + \chi) = \epsilon / \epsilon_0^* \quad (2.13)$$

2.2.2 Plane waves in lossy dielectrics

An electromagnetic (EM) wave is composed of an electric field and a magnetic field, having perpendicular polarizations (directions) relative to one another. Unguided communications operate using transverse electromagnetic (TEM) waves, here the E-field and the H-field (magnetic field intensity) are perpendicular to one another and occupy a plane that is orthogonal to the direction of propagation as seen in figure (Figure 2-2). An EM propagating in a medium is characterized by its polarization, magnitude, phase, frequency (Hz), and wavelength that changes depending on the medium.

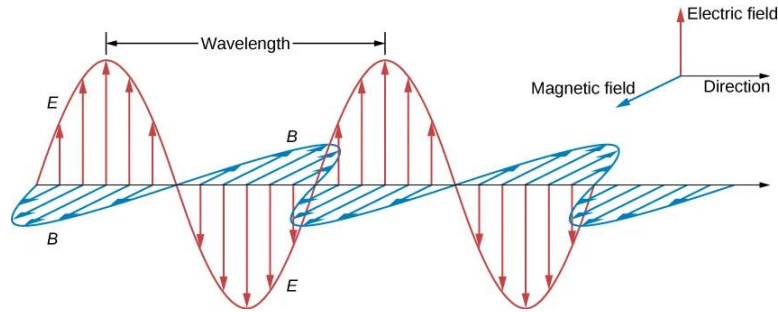


Figure 2-2: Plane transverse electromagnetic wave

The phase of an EM wave can change with respect to time at a given position, or with respect to position at a given instant. This dynamic is expressed by the wave equation, a second order partial differential equation as shown in equation (2.14) linking temporal variations of the wave to spatial ones. The magnitude of the wave is $M(t, z)$, with a velocity (u), and a direction of propagation along the z-axis.

$$\frac{\partial^2 M}{\partial t^2} - u^2 \frac{\partial^2 M}{\partial z^2} = 0 \quad (2.14)$$

This form can be obtained by analytical manipulations of Maxwell's equations (2.15)-(2.18) in vacuum. Below are cited Maxwell's equations in a lossy dielectric, the electric and magnetic fields are assumed to be time harmonic; therefor equations are presented below in phasor domain. Expressions in phasor domain are distinguished from the time form by a subscript (s). The phasor form of the E-field can be written as: $\vec{E}_s = |\vec{E}_s| \angle \theta \vec{a}_r$ (V/m): $|\vec{E}_s|$ being the phasor

magnitude, (θ) being the phase of the EM wave, and (\vec{a}_r) being the direction of the E-field having a magnitude of unity; a similar definition can be made for the magnetic field intensity (\vec{H}_s) expressed in (A/m).

$$\text{Gauss's law:} \quad \nabla \cdot \vec{E}_s = 0 \quad (2.15)$$

$$\text{Magnetic monopole:} \quad \nabla \cdot \vec{H}_s = 0 \quad (2.16)$$

$$\text{Faraday's law:} \quad \nabla \times \vec{E}_s = -j\omega\mu\vec{H}_s \quad (2.17)$$

$$\text{Ampere-Maxwell law:} \quad \nabla \times \vec{H}_s = (\sigma + j\omega\epsilon)\vec{E}_s \quad (2.18)$$

In Maxwell's equations, ω is the angular frequency (rd/s) of the EM field, ϵ is the dielectric constant (F/m), μ the magnetic permeability of the medium (H/m), and σ is the static electrical conductivity (S/m). In simplified terms, (2.15) and (2.16) respectively imply that the entering and exiting electric field intensity (E) and the magnetic flux density (H) entering and exiting a closed surface are conserved. Faraday's law (2.17) states that a closed path integral of the electric field intensity (E) equals the time rate-change of electric flux passing through that path, while (2.18) states that the closed path integral of the magnetic flux density equals the sum of the induction current (σE) and the displacement current traversing a surface linked to that path. The displacement current is the time rate change of the Electric flux density ($D = \epsilon E$) with D having the unit of (C/m²).

Upon performing several analytical manipulations, the classical wave equation for the electric field and the magnetic fields can be obtained as shown in equations (2.19) and (2.20) respectively. The real and imaginary parts of the complex coefficient ($\alpha + j\beta$) was represented in terms of the medium properties (ϵ, σ, μ) in equations (2.21), and (2.22). ϵ is the dielectric constant at the particular frequency of the E-field, and while we have till now considered it as a constant quantity, reality is that it varies drastically depending on the frequency of the E-field. The dependency of the dielectric properties on frequency will be discussed in more details in section (2.2.5).

$$\nabla^2 E_s - (\alpha + j\beta)E_s = 0 \quad (2.19)$$

$$\nabla^2 H_s - (\alpha + j\beta)H_s = 0 \quad (2.20)$$

$$\alpha = \omega \sqrt{\frac{\mu\epsilon}{2} \left[\sqrt{1 + \left[\frac{\sigma}{\omega\epsilon}\right]^2} - 1 \right]} \quad (2.21)$$

$$\beta = \omega \sqrt{\frac{\mu\epsilon}{2} \left[\sqrt{1 + \left[\frac{\sigma}{\omega\epsilon}\right]^2} + 1 \right]} \quad (2.22)$$

To simplify our discussion of EM fields, we will consider the E-field to be polarized only along (\vec{a}_x) which gives in phasor form: $\vec{E}_{sx} = |\vec{E}_{sx}| \angle \theta_E \vec{a}_x$ with $|\vec{E}_{sx}|$ the magnitude of the E-field (V/m). In addition, if we assume that the propagation takes place only along \vec{a}_z , then the wave equation of the E-field would become as shown in equation (2.23). The solution of the latter is expressed in equation (2.24) in terms of the constants (α, β). This expression describes the E-field magnitude for a plane wave propagating in the positive (z) direction, as a function of time and position. (β) – expressed in (rd/m) – is the phase constant (or wave number) given in (2.25), it is expressed in terms of the wavelength (λ) of the EM in that medium, or in terms of the angular frequency and the wave velocity in the medium. (β) relates the change in phase as a function of the distance separating any two points along the direction of propagation. The phase

of the E-field is dependent both on time and distance, where a lower phase of the EM wave could be obtained when considering downstream points at a given instant. Plane waves are commonly encountered in unguided propagation at the far-field region relative to the emitting antenna.

$$\frac{\partial^2 \vec{E}_{sx}}{\partial z^2} - (\alpha + j\beta)\vec{E}_{sx} = 0 \quad (2.23)$$

$$\vec{E}(z, t) = E_0 e^{-\alpha z} \cos(\omega t - \beta z) \vec{a}_x \quad (2.24)$$

$$\beta = \frac{2\pi}{\lambda} = \frac{\omega}{v} \quad (2.25)$$

The magnetic field intensity can be calculated from the expression of the E-field in conjunction with Faraday's law - equation (2.17). The ratio of the electric to magnetic field intensity gives the complex intrinsic impedance of the medium (η), it relates the magnitudes of the electric and the magnetic fields as well as their phase difference at a particular position as shown in equation (2.26). The expression of the magnetic field intensity in the time domain is given by (2.27).

$$\eta = \frac{\vec{E}_s}{\vec{H}_s} = \sqrt{\frac{j\omega\mu}{\sigma + j\omega\epsilon}} = |\eta| e^{j\theta_\eta} \quad (2.26)$$

$$H(z, t) = \frac{E_0}{|\eta|} e^{-\alpha z} \cos(\omega t - \beta z - \theta_\eta) \quad (2.27)$$

2.2.3 Penetration depth

The magnitude of the electric field, as seen in (2.24), is denoted by $|\vec{E}_x| = E_0 e^{-\alpha z}$ is a decreasing function of (z) – the distance that the EM wave has propagated in the material. This happens on account of the lossy dielectric dissipating the EM energy into heat; therefor an EM wave propagating in a lossy dielectric cannot travel indefinitely. The distance traveled by an EM wave into a material is denoted by the penetration depth - D_p (m) given by the inverse of the constant (α) and expressed in equation (2.28). The latter is defined as the distance where the E-field magnitude reaches a value of 37% of (E_0) as shown in Figure 2-3 and is the inverse of the constant (α) in equation (2.28). It is worth noting that the remaining EM power at the penetration depth ($z = D_p$) is 13.5% relative to that at the entry point of the wave at ($z = 0$).

$$D_p = \frac{1}{\alpha} \quad (2.28)$$

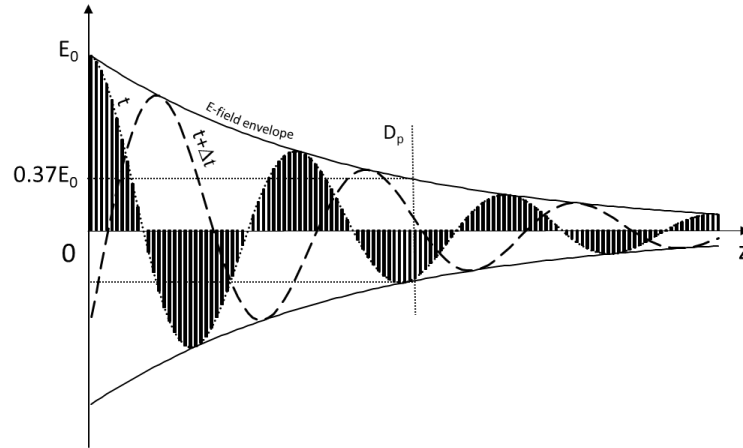


Figure 2-3: Penetration depth of a TEM wave in a lossy dielectric as a function distance (z)

EM propagation in a lossy dielectric is the general case of wave behavior in a medium, from which many special cases can be derived. Propagation in other types of mediums such as: free space, lossless dielectrics, or in electrical conductors can be obtained by adjusting the electric and magnetic properties (ϵ, μ, σ) of equations (2.20) and (2.21). Table 2.1 gives the penetration depth and the wave number (β) for EM propagation in different mediums. The penetration depth is infinite for the cases of lossless materials such as free space or lossless dielectrics, for electrical conductors the penetration depth is inversely dependent on frequency implying that higher frequencies have a smaller penetrating depth. The wavenumber (β) increases with frequency for free space due to the decrease of the wavelength, but for lossless dielectrics it increases with the dielectric constant (ϵ). The dielectric constant and the magnetic permeability determine the wave velocity in the medium, i.e. the higher the latter quantities the lower the velocity in that particular medium ($v = 1/\sqrt{\mu\epsilon}$)

Medium	$\epsilon(\text{F/m})$	$\mu(\text{H/m})$	$\sigma(\text{S/m})$	$D_p(\text{m})$	$\beta(\text{rd/m})$
Free space	1	1	0	∞	ω/c
Lossless dielectric	$\epsilon_r\epsilon_0$	$\mu_r\mu_0$	0	∞	$\omega\sqrt{\mu\epsilon}$
Electrical Conductors	1	$\mu_r\mu_0$	∞	$1/\sqrt{\pi f\mu\sigma}$	$\sqrt{\pi f\mu\sigma}$

Table 2.1: Penetration depth and wavenumber of EM radiation in some particular mediums

2.2.4 The complex dielectric constant

Ampere-Maxwell's law of equation (2.18), can be manipulated to reach equation (2.29) expressed in phasor form. The complex permittivity (ϵ^*) as expressed in (2.30) characterizes the macroscopic interactions between the EM wave and the material. The real part ($\epsilon_0^*\epsilon_r$) describes the energy storage capacity of the dielectric through its polarization by different mechanisms, with (ϵ_r) being the relative dielectric constant with respect to vacuum. The imaginary part denoted as ($\frac{\sigma}{\omega} = \epsilon_0^*\epsilon''$) – with ϵ'' being the dielectric loss factor - describes the lossy character of the dielectric that is responsible for dissipating EM energy into heat which can also be achieved through different mechanisms. In other

words, higher dielectric loss leads to greater dissipation of EM energy in the form of heat. To ensure homogeneity of nomenclature with literature the symbol (ϵ') will be used from here on out to denote (ϵ_r).

The complex dielectric constant (ϵ^*) is the sole most important number for characterizing the macroscopic interactions of EM irradiations and materials. Another popular and useful number is the loss tangent denoted by $\tan(\delta)$ presented in equation (2.31). The loss tangent is defined as the ratio of the displacement current density ($J_{ds} = \omega \epsilon' E_s$) to the conduction current density ($J_s = \sigma E_s$), both corresponding to the two right-hand side terms of Ampere-Maxwell's equation (2.18). Equivalently, the loss tangent can be expressed as the ratio of the dielectric loss factor to the dielectric constant. The loss angle (δ) is related to the phase difference between the electric and the magnetic fields (θ_η) by the equation: $\delta = 2\theta_\eta$.

$$\nabla \times \vec{H}_s = j\omega \left(\epsilon - \frac{j\sigma}{\omega} \right) \vec{E}_s = j\omega \epsilon^* \vec{E}_s \quad (2.29)$$

$$\epsilon^* = \epsilon - \frac{j\sigma}{\omega} = \epsilon_0^* (\epsilon' - j\epsilon'') \quad (2.30)$$

$$\tan \delta = \frac{J_s}{J_{ds}} = \frac{|\sigma \vec{E}_s|}{|j\omega \epsilon \vec{E}_s|} = \frac{\sigma}{\omega \epsilon} = \frac{\epsilon''}{\epsilon'} \quad (2.31)$$

The expression for the volumetric dissipation rate of energy (Q) in (W/m³) is shown in (2.32). It is very important to mention that required energy to heat the solvent depends purely on its thermal properties. The dielectric properties influence the distribution of the electric fields inside the dielectric, and hence the EM dissipation rates.

$$Q = \frac{1}{2} \omega \epsilon_0 \epsilon'' E_0^2 \quad (2.32)$$

2.2.5 Dielectric properties function of frequency

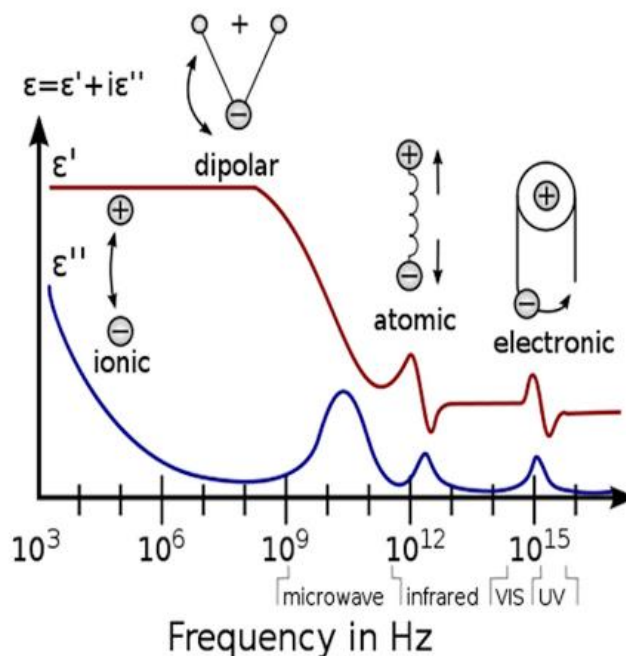


Figure 2-4: Dominating relaxation mechanisms in a dielectric as a function of the frequency of the E-field – taken from [13].
(CC-by 4.0)

Till now relative permittivity (ϵ') was assumed to be a constant function of frequency, but in reality, dielectrics can undergo different types of polarizations depending on the applied frequency of the EM wave. Polarization is defined as the ordering in space of an electrically charged units as dipoles. In a dielectric medium there exists different polarizations that contribute to the overall dielectric constant or dielectric loss factor, from those polarization mechanisms we mention: electronic, atomic, dipolar, and ionic among others. Electronic polarization occurs due to the displacement of the electrons with respect to the nucleus under an E-field, its contribution to the total dielectric constant is minimal at microwave and infrared frequencies, but it relaxes in the region of visible light and UV irradiation [14]. Atomic polarization occurs when the bonds in a molecule undergo stretching under an applied E-field, this polarization mechanism relaxes in the infrared region [15]. At much lower frequencies such as in the MW region, “slower” polarization mechanisms persist mainly dipolar rotation and ionic conduction [16].

At MW frequencies, dipoles form networks that minimize the potential energy of the system; for example, n-alcohols are suspected to form chain-like structures [10, 17] while water molecules align in different shapes of clusters such as spherical or parallel sheets [7]. The static dielectric constant represents the maximum polarization a material can undergo, i.e. at static E-field the dipoles of a dielectric have infinite time to reorganize their structure in the configuration that allows for maximum energy storage in the system. However, at increasing frequencies of the external E-field, the magnitude and direction (also known as polarization) of the latter may change faster than the rate at which the dipoles can polarize. Consequently, with a lower population of dipoles aligned with the E-field, the dielectric

constant is lower than at static conditions. It can therefore be concluded that the dielectric constant is a monotone function that decreases with frequency.

One way to anticipate the decrease of the dielectric constant is through comparison of the applied frequency to the relaxation frequency of the dielectric medium. The relaxation frequency is the frequency at which the polarizability of the medium by dipolar rotation reaches 63% relative to that reached at static (invariant) condition of E-field. If the relaxation time – derived from the relaxation frequency, and defined as the time needed by the dielectric to reach 63% polarizability– is much lower than the rate-change of the applied E-field, the dipoles need considerably lower time to polarize and thus can easily keep up with the E-field, the dielectric constant in this case is almost identical to the static dielectric constant. At the other extreme, if the relaxation time is much higher than the period of the E-field, then the latter would change polarization and magnitude at a much greater rate than what the medium can follow, the resulting dielectric constant would be very low in comparison to that at static conditions. Temperature-increase decreases the dielectric constant as well by increasing the thermal energy of the dipoles which makes it more difficult for them to organize into clusters [12].

Previously the dielectric loss factor was assumed to be dependent solely on ionic conduction as shown in (2.30). In reality, many pure dielectrics with no ionic content dissipate MW energy into heat. We take the example of distilled water, it is considered to be very lossy dielectric despite it having minimal content of dissolved metals and salts. The lossy character of water is owed to the polarization mechanism of dipolar rotation: the continuous polarization of dipoles with successive establishment and dissolution of preferentially oriented hydrogen bonded clusters creates intermolecular friction which leads to heat dissipation. The total power dissipation under MW irradiation in a dielectric containing dissolved ionic content is accounted for by the combined mechanisms of dipolar polarization and ionic conduction as demonstrated in Figure 2-5.

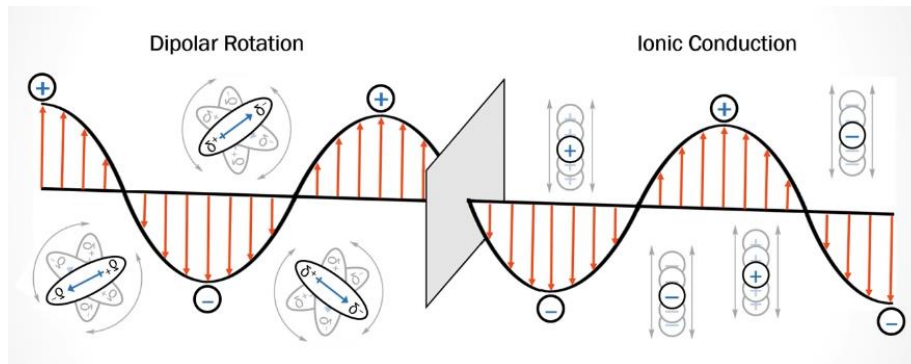


Figure 2-5: Mechanisms for EM dissipation into heat

Dielectric relaxation models describe the behavior of the relaxation mechanism at different E-field frequencies. The relaxation mechanism represents to what point the medium is able to “relax” or for the dipoles to reach equilibrium position, as well as the ability of the latter to dissipate EM energy. Some key factors that influence the relaxation mechanism are: phase of the dielectric (liquid, solid...), its temperature, and composition among others. Dielectric relaxation models are semi-empirical, such that they are made to fit experimental dielectric data through an error

minimization procedure on the dielectric constant (ϵ') or the dielectric loss factor (ϵ'') as a function of frequency. Some advantages of using such relaxation models is that medium behavior can be summarized by a few parameters, moreover they allow extrapolation of dielectric properties to frequency ranges that require expensive equipment to measure.

2.2.6 Dielectric relaxation models

2.2.6.1 Debye model

The dielectric relaxation of Debye is a classical semi-empirical model for representing the dielectric properties as a function of frequency, it is the base model from which many other relaxation models have been derived, therefore it warrants to be well understood before moving to more complex ones. The model is based on the concept of polarization build-up in the dielectric as a function of the applied E-field, and the rotational diffusion of spherical polar molecules in a viscous medium having a single relaxation time [12, 14]. Despite its assumptions, the Debye model has proven to be able to produce good quality fits for dielectric data of many polar and organic liquids [4, 10, 15, 17, 19–21]. The expression of the complex dielectric constant according to the Debye model is presented in (2.33). The Debye model contains three parameters that define the relaxation mechanism of the medium under an external E-field: the relative static dielectric constant (ϵ_0), the relative optical dielectric constant (ϵ_∞), and the relaxation time (τ).

$$(\epsilon' - j\epsilon'') = \epsilon_\infty + \frac{\epsilon_0 - \epsilon_\infty}{1 - j\omega\tau} \quad (2.33)$$

Separating the real and the imaginary parts we get the expressions for the relative dielectric constant (ϵ') and the dielectric loss factor (ϵ'') in (2.34) and (2.35) respectively.

$$\epsilon' = \epsilon_\infty + \frac{\epsilon_0 - \epsilon_\infty}{1 + \omega^2\tau^2} \quad (2.34)$$

$$\epsilon'' = \frac{(\epsilon_0 - \epsilon_\infty)\omega\tau}{1 + \omega^2\tau^2} \quad (2.35)$$

The maximum dielectric loss factor can be found by deriving (ϵ'') as a function of ($\omega\tau$) and equating to zero; (ϵ''_{\max}) is obtained when ($\omega\tau = 1$). Therefore the maximum loss is obtained when the angular frequency of the E-field is equal to the relaxation frequency of the medium.

$$\text{at } \omega\tau = 1 \text{ we get : } \begin{cases} \epsilon''_{\max} = \frac{(\epsilon_0 - \epsilon_\infty)}{2} \\ \epsilon' = \frac{(\epsilon_0 + \epsilon_\infty)}{2} \end{cases} \quad (2.36)$$

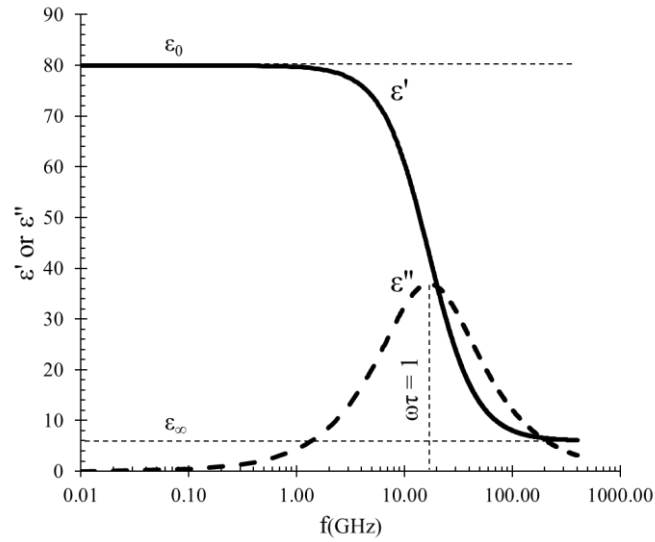


Figure 2-6: Bode plot of dielectric properties of distilled water at $T=20^{\circ}\text{C}$

Usually the dielectric properties are presented in either a Bode plot or a dielectric dispersion diagram otherwise known as the Cole-Cole diagram. The Bode plot displays the relative dielectric constant and the dielectric loss factor as a function of logarithm of frequency. Presented in Figure 2-6 is an example of the dielectric properties of distilled water at $T=20^{\circ}\text{C}$. The dielectric data were obtained by using the Debye model in conjunction with the dielectric dispersion parameters obtained from literature [16] which can be found in the annex of this chapter. The relative dielectric constant (ϵ') experiences a monotone decrease with frequency as discussed in the previous section. At the frequency region much lower than the relaxation frequency ($\omega\tau \ll 1$) the dielectric constant is identical to the static dielectric constant. In this region the dipoles are able to reach equilibrium under the E-field faster than the rate of polarization change of the latter. At relatively low frequencies, water has no lossy character as can be inferred from the null loss factor (ϵ''). When the E-field has a low frequency, the dissociation and structuring does not occur at high enough rates to appreciably dissipate EM irradiation. In the neighborhood of the relaxation region ($\omega\tau \sim 1$), (ϵ') decreases sharply because the time needed for the dipoles of the dielectric to reach equilibrium becomes comparable with the period of the applied E-field, therefore less and less dipoles would achieve polarization under the oscillating E-field translating to a lower dielectric constant. On the other hand, the dielectric loss factor in the relaxation region increases sharply to reach its maximum at the relaxation frequency. In the relaxation region, a considerable quantity of dipoles undergoes dipolar rotation that allows for the highest dissipation rates of EM energy. When the frequency of the E-field increases to values higher than the relaxation frequency, the dipoles are unable to polarize with the E-field at the rate at which it changes; the dipoles are motionless where neither polarization nor intermolecular friction occurs knowing that the latter is a consequence of the former. The only remaining polarization is the electronic polarization that can be linked to the refractive index of the dielectric by Maxwell's equations (2.48).

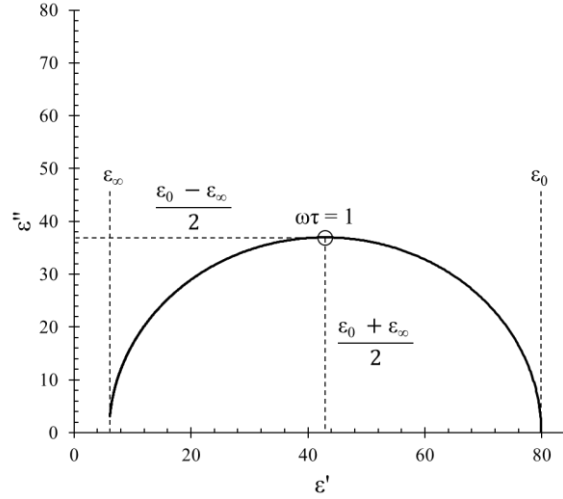


Figure 2-7: Dielectric dispersion diagram of Debye relaxation model of distilled water at 20°C

Another method for presenting the dielectric properties of materials is through a dielectric dispersion diagram - also known as the Cole-Cole diagram. The dielectric loss factor is plotted as a function of the associated relative dielectric constant. The shape of the dielectric properties curve can indicate which relaxation model is most suitable to represent the dielectric properties of the material. If the dielectric follows the Debye relaxation mechanism then the dielectric dispersion curve follows a semi-circular shape as the dielectric properties satisfy the equation (2.37)- derived from (2.33). The dielectric dispersion of distilled water at 20°C is plotted in Figure 2-7. The frequency is not shown on this diagram but can rather be inferred by the intersection of the dispersion curve with the horizontal axis at (ϵ_0) marking the low frequency region. The highest point on the semicircle corresponds to the point of maximal dissipation by the medium at the relaxation frequency (f_r). At very high frequencies the dispersion intersects the horizontal axis at the optical dielectric constant (ϵ_∞).

$$\left[\epsilon' - \frac{\epsilon_0 + \epsilon_\infty}{2} \right]^2 + [\epsilon'']^2 = \left[\frac{\epsilon_0 - \epsilon_\infty}{2} \right]^2 \quad (2.37)$$

2.2.6.2 Cole-Cole model

The Debye relaxation model has several main assumptions, one of which is the discrete nature of the relaxation time, i.e all the dipoles in the medium have a single relaxation time. The Cole-Cole model is a semi-empirical model first proposed by Cole [22] for the electrical impedance of membranes in biological systems. It is very similar to the Debye model with an empirical adjustment on the formula. Still, it has been able to produce better fits than with dielectric models that consider a Gaussian distribution of relaxation times [23]. In a similar way to the Debye model, the Cole-Cole model describes a symmetrical dielectric dispersion as a function of frequency, and while most materials follow this symmetrical distribution, non-symmetrical models or multiple relaxation mechanisms are suggested to fit materials that display an asymmetrical dispersion. The rigorous character of the Cole-Cole model has made it adept in

replicating the properties of non-ideal systems such as that of saline water with high concentrations of saccharose [24], and more rigorous such as to be able to fit those of near ideal systems such as mixtures of n-alcohol and water [17, 25].

The expression of the complex permittivity of the Cole-Cole model as a function of frequency is presented in (2.38). The main difference from the Debye equation is the inclusion of a term (n) denoting the distribution of relaxation times, such that the more (n) decreases the broader is the distribution of relaxation times. It is worth noting that Debye relaxation is a special case of the Cole-Cole relaxation obtained for (n=1). As with the Debye model, relaxation occurs when the condition ($\omega\tau = 1$) is satisfied.

$$\varepsilon^* = \varepsilon_\infty + \frac{\varepsilon_0 - \varepsilon_\infty}{1 - (j\omega\tau)^n} \quad (2.38)$$

The real and the imaginary parts were separated to give the expressions in (2.39) and (2.40) respectively.

$$\varepsilon' = \varepsilon_\infty + (\varepsilon_0 - \varepsilon_\infty) \frac{1 + (\omega\tau)^n \cos\left(\frac{n\pi}{2}\right)}{1 + 2(\omega\tau)^n \cos\left(\frac{n\pi}{2}\right) + (\omega\tau)^{2n}} \quad (2.39)$$

$$\varepsilon'' = (\varepsilon_0 - \varepsilon_\infty) \frac{(\omega\tau)^n \sin\left(\frac{n\pi}{2}\right)}{1 + 2(\omega\tau)^n \cos\left(\frac{n\pi}{2}\right) + (\omega\tau)^{2n}} \quad (2.40)$$

In a practical manner, the constant (n) affects the allure of the dielectric constant and loss factor as a function of frequency. We consider the dielectric properties of a polar dielectric in Figure 2-8 and Figure 2-9 respectively where the dispersion parameter (n) was varied, while the remaining parameters ($\varepsilon_0, \varepsilon_\infty, \tau$) were kept constant. Figure 2-8 shows that when (n) decreases, the spread of the relaxation times increases leading to a flatter profile of (ε') as a function of frequency. Therefore with decreasing (n) the dielectric constant becomes smaller at frequencies lower than the relaxation frequency. For frequencies greater than the relaxation frequency, the dielectric constant is greater due to the presence of dipole groups having very low relaxation times (high relaxation frequencies). Such fast-relaxing dipoles permit the medium to maintain greater values of dielectric constant at high frequencies in contrast to the case of a unique relaxation time.

Similarly, the dielectric loss factor experiences a wider spread with increasing (n) as shown in Figure 2-9. This happens on account of a considerable population of the dipoles having very low or very high relaxation frequencies all while the apparent relaxation time remains constant. Consequently, dielectrics with lower values of (n) tend to have a lower dielectric loss factor in the neighborhood of the relaxation frequency but higher values at the low and high frequency extremes (example of n=0.25 against n=0.75).

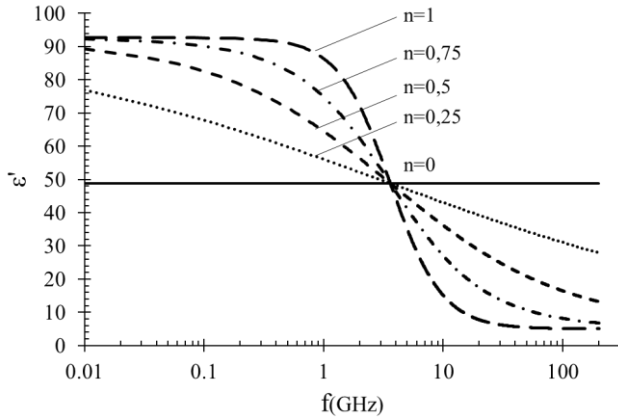


Figure 2-8: Effect of parameter (n) on the relative dielectric constant (ϵ')

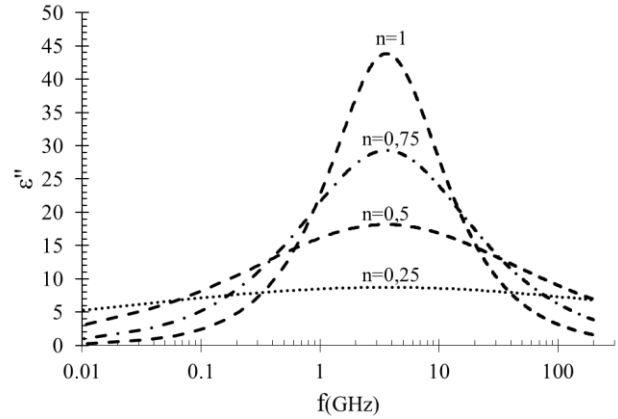


Figure 2-9: Effect of parameter (n) on the relative dielectric loss factor (ϵ'')

The effect of (n) on the dielectric dispersion can be examined on a Cole-Cole diagram as shown in Figure 2-10. For (n=1) we find that the dielectric dispersion follows a semi-circular shape similar to Debye model. When the value of (n) decreases, the curve is no longer a semi-circle but rather a circular arc intersecting the horizontal axis at (ϵ_0) and (ϵ_∞) but with a depressed maximal dielectric loss. The dielectric dispersion is a circular arc with its center depressed vertically and having the following coordinates $\left[\frac{\epsilon_s + \epsilon_\infty}{2}, -\frac{\epsilon_s - \epsilon_\infty}{2} \cot(n\pi/2) \right]$.

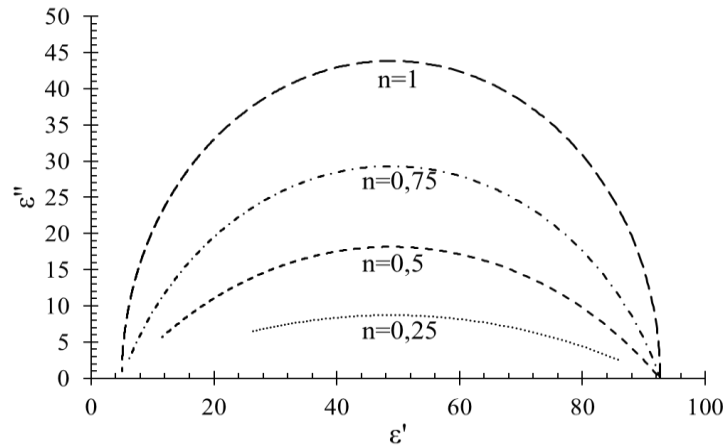


Figure 2-10: Effect of the parameter (n) on the dielectric dispersion of a polar liquid

2.2.6.3 Asymmetric models

So far, we have cited the dielectric relaxation models of Debye and Cole, both of which describe symmetrical dielectric dispersions. There exist however other variations of the Debye model to account for asymmetric dielectric dispersions. Davidson-Cole [26] is an example of such variations and represented in equation (2.41). The dielectric dispersion curve is such that it intersects the horizontal axis at ϵ_0 and ϵ_∞ at the low and high frequency extremes respectively. The dispersion curve forms a skewed arc, where at the low frequency extreme the dielectric dispersion is semi-circular while at the high frequency extreme the dispersion curve is a straight line. The constant (β) controls the degree of skewness, i.e as $\beta \rightarrow 1$ the dielectric dispersion will be a semi-circle as with the Debye model.

$$\varepsilon^* = \varepsilon_\infty + \frac{\varepsilon_0 - \varepsilon_\infty}{(1 - j\omega\tau)^\beta} \quad (2.41)$$

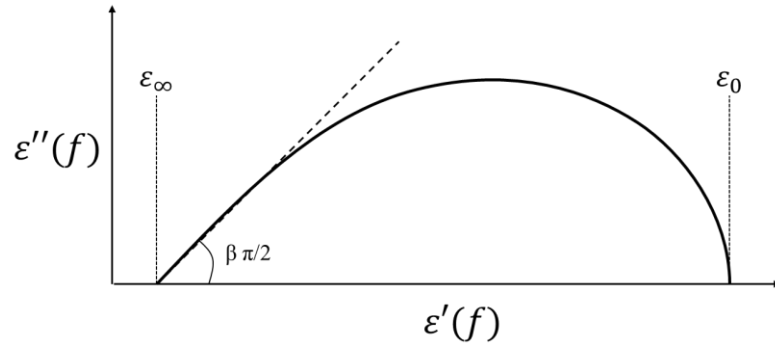


Figure 2-11: Dielectric dispersion diagram of the Cole-Davidson relaxation

Another variation of the dielectric relaxation model is the Havriliik-Nagami relaxation model [27] represented in equation (2.42) and is characterized by two adjustable parameters: (n, β) values of ($0 < n < 1, 0 < \beta < 1$) respectively. The terms (n) and (β) account for the existence of a distribution of relaxation times [23] and for the asymmetrical dielectric dispersions respectively. Notice that we can get the Debye, Cole-Cole, and Cole-Davidson relaxation expressions for the pair values of [n, β]: [$1, 1$]; [$n, 1$]; and [$1, \beta$] respectively. In the Havriliik-Nagami model the dielectric dispersion curve is a circular arc in the low frequency range (a characteristic of the Cole-Cole model), and a straight line at the high frequency end in a similar manner to the Davidson-Cole model.

$$\varepsilon^* = \varepsilon_\infty + \frac{\varepsilon_0 - \varepsilon_\infty}{(1 - (j\omega\tau)^n)^\beta} \quad (2.42)$$

The description of the complex dielectric dispersions can be achieved by the relatively simple Debye model, however with the consideration of several relaxation mechanisms that activate at different frequency ranges [28]. The complex permittivity with multiple Debye relaxation mechanisms would have the form shown in (2.43), with $\Delta\varepsilon_i$ is the dielectric decrement defined as $(\varepsilon_0 - \varepsilon_\infty)_i$ and (τ_i) is the relaxation time of that relaxation time.

$$\varepsilon^* = \varepsilon_\infty + \sum_{i=1}^k \frac{\Delta\varepsilon_i}{1 + j\omega\tau_i} \quad (2.43)$$

2.2.6.4 Relaxation of a dielectric with ionic content

Ionic presence is consequential to the dielectric behavior of the medium. The most notable effect is through the increased dissipation of EM power by the ionic conduction mechanism [29]. The relaxation models, as seen earlier, account only for losses by dipolar relaxation, the addition of the dielectric loss term - (2.30) - can allow the model to take into account the losses by ionic species as has been done by many authors [24, 30–32]. A general form of the modified dielectric relaxation model is given in (2.44) where the previously discussed relaxation models can be obtained for different values of [α, β], while accounting for losses by ionic conduction.

$$\varepsilon^* = \varepsilon_\infty + \frac{\varepsilon_0 - \varepsilon_\infty}{(1 - (j\omega\tau)^n)^\beta} + j \frac{\sigma}{\omega\varepsilon_0^*} \quad (2.44)$$

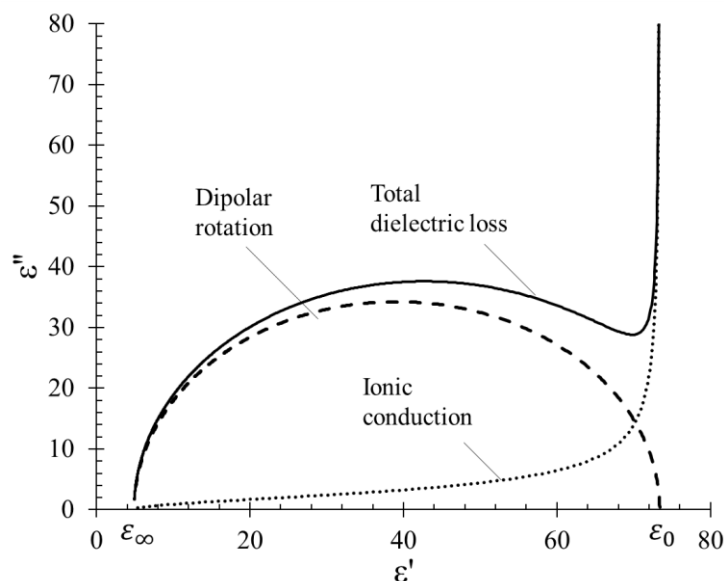


Figure 2-12: Total, dipolar and ionic dielectric dispersion curves for saline water at $T=20^{\circ}\text{C}$ and $C_{\text{NaCl}}=20\text{g/l}$

The presence of ionic species impacts the dielectric dispersion curve, instead of intersecting the ϵ' -axis at ϵ_0 , the curve tilts upward because at low frequencies the contribution of ionic conduction is high which pulls the dispersion curve upwards. This is demonstrated in Figure 2-12 for a solution of saline water, here the dielectric dispersion has been decomposed into its two components: dipolar relaxation, and ionic conduction. The dipolar relaxation of water follows a semi-circular shape where virtually no loss originates from this mechanism at very low frequencies, while loss by ionic conduction dominates in this range. In the neighborhood of the relaxation region, the contribution of ionic conduction virtually disappears while that of dipolar rotation reaches its maximum. It is worth noting that it might be difficult to distinguish from the experimental dielectric dispersion which model is well adapted to fit the properties of dielectric mediums containing ionic species. This difficulty is further accentuated when the relaxation frequency of the medium is low enough as to greatly coincide with the region where ionic conduction is most active.

2.3 Dielectric characterization of CO_2 -loaded solvents: materials and methods

2.3.1 Dielectric measurement techniques

There exists a multitude of techniques to measure the dielectric properties, they fall into three main categories: reflectometric, transmission methods - both of which depend on the measurement of the S-parameters - and resonance methods that depend on the measurement of the Q-factor [33]. The reflectometric techniques are the most widely used as demonstrated by the large amounts of data that were generated based on this technique. The one-port coaxial line/waveguide method and the coaxial sensors are shown in Figure 2-13 and Figure 2-14 respectively.

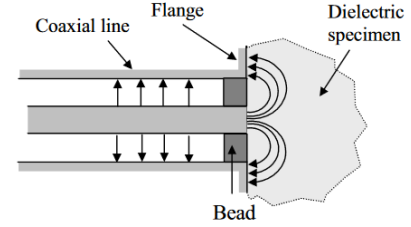
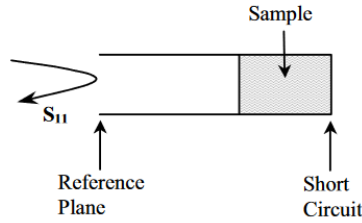


Figure 2-13: One-port coaxial line or waveguide method [33]. (CC-by 4.0) Figure 2-14: Electric-field lines in a cross-sectional view of a dielectric probe dipped in a sample [33]. (CC-by 4.0)

In the one-port method, the sample is placed at the end of the waveguide followed by a short circuit. The sample under test is machined or placed as to avoid geometric discontinuities with the waveguide. The incident electromagnetic wave (EM)- propagates under the fundamental mode and meets the sample: part of it is absorbed, the other is reflected back to the entry port and towards the vector network analyzer (VNA). The ratio of the incident to the reflected wave is called the (S_{11}) parameter. We define it in equation (2.45) with the subscripts (i) and (r) denoted the incident and reflected waves respectively.

$$S_{11} = \frac{E_r \angle \theta_r}{E_i \angle \theta_i} \quad (2.45)$$

The coaxial sensor is a cut-off section of a coaxial cable with a probe on its end, it is connected to a VNA through a phase-constant coaxial line. The design of the sensor tip as shown in Figure 2-14 is such that the outer conductor is made into a wide flange that minimizes the E-field at the flange boundary. A dielectric material is fixed between the inner and outer conductors of the probe to prevent the ingress of the liquid. It has been mentioned that to achieve good measurement accuracy, the outer diameter of the flange should be chosen to be at least a few times that of the outer conductor of the coaxial cable [34]. The (S_{11}) parameter – measured by the VNA – is the image of the complex permittivity of the sample, still the treatment of the (S_{11}) data is important in determining the dielectric properties. Several techniques can be used to infer the complex permittivity from the (S_{11}) spectrum, this includes: iterative modal analysis, numerical techniques such as finite-element method (FEM) or finite difference time-domain method (FDTD), or even empirical correlations between (S_{11}) and complex permittivity of the sample under test. Before starting any measurement, the VNA is calibrated by a three-step procedure that defines the reference plane of the (S_{11}) factor to that in probe surface dipped in the sample under test, it also eliminates any impedance mismatching throughout the circuit. The calibration is performed measuring complex reflection coefficient by: (i)-leaving the probe to open-air, (ii)-shorting the inner and outer conductor of the probe (shorting block, aluminum foil, liquid mercury), (iii)-probe is dipped in a reference liquid with traceable dielectric properties.

This technique is considered to be of low accuracy and low repeatability relative to others such as the resonant cavity method [13]. Causes of low accuracy can be related to errors in calibration procedure such as: uncertainty in the dielectric properties of the reference liquid, or the treatment method of the S_{11} data to obtain the complex permittivity. Despite its low accuracy in comparison with other techniques, it presents many advantages that render it the most used technique for dielectric characterization of materials. The sensor once calibrated provides continuous on-line

measurements by simply dipping the probe in the sample. This makes a very suitable technique for monitoring continuous industrial processes, and it therefore outperforms many other techniques that require the sample to be machined to specific geometries [13]. Another important advantage of the coaxial sensor technique is that it is capable of instantly obtaining the complex permittivity of a material over a very wide frequency spectrum (500 MHz - 110 GHz); this can be contrasted to many resonant techniques that produce dielectric data on a unique frequency. The above advantages make it suitable for monitoring industrial processes, and versatile enough to measuring the properties of material ranging from foods and beverages to in-situ biological tissues [35]. Care should be taken in achieving a good contact between the probe head and the sample, although easily achievable in liquid samples, it can present a source of errors with solid ones.

2.3.2 Dielectric characterization of aqueous 30% wt. ETA with CO₂

In this work, the open-ended coaxial probe method was used to measure the dielectric properties of the 30% wt. ETA solution free or loaded with CO₂ over the frequency spectrum of 915-2450MHz. Our main interest is to characterize the dielectric behavior at the two main frequencies allocated for high power microwave applications: 915 MHz and 2450 MHz. The dielectric properties are obtained from the readings of the two ports network parameter (S_{11}) that vary with: frequency, complex permittivity and the probe geometry [36]. The dielectric probe (Agilent 85070E: high temperature configuration) was linked by an SMA connector to a metallic coaxial cable incoming from the VNA (Agilent E5062A ENA-L, 300kHz-3GHz). The probe calibration was done by measuring the reflecting signal through a three-step procedure: leaving the probe to open-air, connecting a metallic shorting block, and dipping it in reference liquid such as deionized water at 20°C. Measurements were triggered via a software provided by the probe manufacturer and results were obtained in a few seconds time. In order to measure the complex permittivity at different temperatures, the sample was placed in a beaker of volume (125mL) on top of a heating plate similarly to other works [35]. The lateral surface of the sample holder was thermally insulated, and the height of sample is one order of magnitude higher than the minimal value set by the probe manufacturer [37]. Before triggering the measurements, the temperature at the level of probe was verified using an optical fiber connected to a data logger (H201, Rugged Monitoring). Measurements were repeated three times and the results were averaged. Drift errors were evaluated by measuring the dielectric properties of DW once per day for three days. Results show good reproducibility with the maximum relative standard deviation of [ϵ' , ϵ''], at each frequency of the spectrum over three days, being 0.83% and 3.24% respectively.

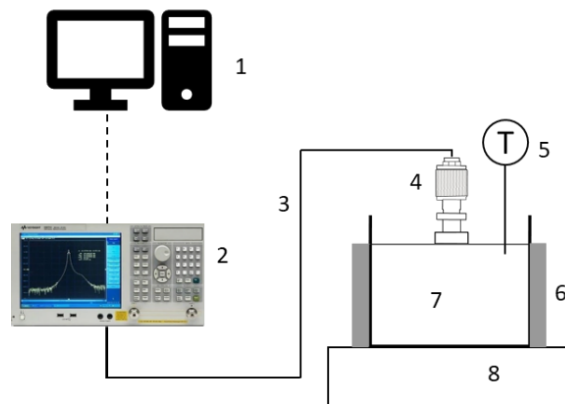


Figure 2-15: Measurement of dielectric properties with open-ended coaxial probe technique. 1: computer, 2: vector network analyzer, 3: coaxial cable; 4: measurement probe; 5: optical fiber; 6: thermally insulated container; 7: sample under test; 8: double envelope water heater.

2.3.3 Generation of CO₂ loaded 30% wt. ETA solutions

Ethanolamine (C₂H₇NO) (Sigma-Aldrich >98%) and deionized water (DW) were weighed to prepare a 30% wt. by weight aqueous Ethanolamine solution (30% wt. ETA). The apparatus shown in Figure 2-16, and adopted by many [38, 39], was then used to load the aqueous solution with CO₂. The inlet gas stream, composed of 80 by 20% CO₂ and N₂ respectively, was introduced by two mass-flow controllers. The stream was first saturated with water, then bubbled into a reactor containing 1 liter of 30% wt. ETA solution where the CO₂ in the gas stream reacts with ETA. Outlet stream was analyzed using gas chromatography (INFICON-Fusion, column type U-bond at 60°C with Helium 186 kPa) and equilibrium was reached when successive readings by the chromatograph showed no variations. Given the exothermic nature of CO₂ chemical absorption [40], the bubbling reactor was placed in a water bath that serves as a heat sink.

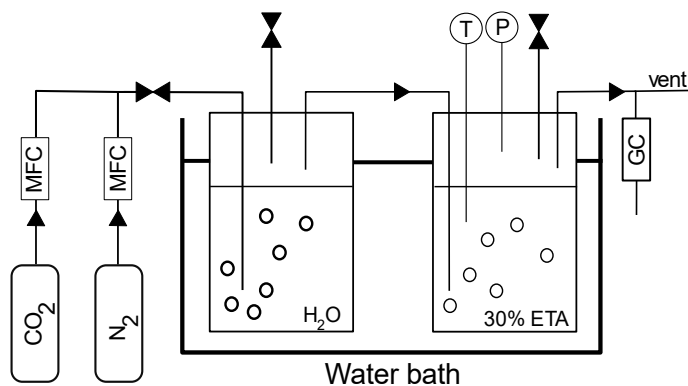


Figure 2-16: Apparatus for generating CO₂ loaded 30% wt. ETA aqueous solutions

When the loading procedure is over, the charge of the solution was determined using Barium chloride (BaCl₂) titration method. This is a classical method for determination of acid gas content first proposed by Weiland [41] and applied widely by others [38, 42, 43]. In this method, 5mL of the sample under test is mixed with 10mL hot aqueous BaCl₂ solution (1.4 M). CO₂ is then precipitated under the form of barium carbonate salt (BaCO₃) according to (2.46).



After aging for one day in a cooled environment, the precipitate was separated from the liquid by filtration using a filter paper (Whitman 1440-150mm grade 40). The filter paper and precipitate were dried in an oven for 2 days at 100°C. Gravimetric measurement allows calculation of the CO₂ content by subtracting the mass of the dried filter paper (measured separately). To validate the experimental procedure, 2g of sodium bicarbonate (NaHCO₃) (Sigma Aldrich ≥99.7%) were dissolved in 100 mL of DW, and the solution was tested for its acid gas content (CO₂ under the form of HCO₃⁻) with the described method. The obtained result is within 5% the true value. Aqueous ETA solutions with different CO₂ loadings were prepared by diluting CO₂-loaded 30%wt. ETA with unloaded ones.

2.3.4 Cole-Cole relaxation model and fitting procedure

The Cole-Cole relaxation model accounting for ionic conduction was chosen to fit the experimental dielectric properties of 30% wt. ETA with varying CO₂ concentrations (2.47). In the case of non-loaded 30%wt. ETA solution we chose account for ionic conduction in the dielectric dispersion model even though solution has no dissolved ionic content. It should be kept in mind that ETA is a weak base, therefore it would dissociate to produce [H⁺], [OH⁻], and [ETAH⁺] ionic species that contribute to ionic conduction. The fitting was performed simultaneously to both the real and the imaginary parts of the experimental complex dielectric constant using a complex nonlinear least square (CNLS) routine. The objective function is shown in (2.48), and the Levenberg-Marquart optimization algorithm [44] was coded in MATLAB® to find the solution set (ε₀, τ, n, σ) that allows for this minimization. Initial guess of the solution vector was chosen intuitively but carefully. For a lack of better estimation, the optical dielectric constant of the mixture (ε_{∞,m}) was calculated from Maxwell's equations (2.49) where (n_∞) is the refractive index of 30%wt. ETA with no dissolved CO₂ at 20°C measured by Ju [45] - (2.49).

$$\epsilon^* = \epsilon_\infty + \frac{\epsilon_0 - \epsilon_\infty}{(1 - (j\omega\tau)^n)^\beta} + j \frac{\sigma}{\omega\epsilon_0^*} \quad (2.47)$$

$$\text{Error}^2 = \frac{1}{n} \sum_{i=1}^n [(\epsilon'_{i,e} - \epsilon'_{i,m})^2 + (\epsilon''_{i,e} - \epsilon''_{i,m})^2] \quad (2.48)$$

$$\epsilon_{\infty,\text{mix}} = n_\infty^2 \quad (2.49)$$

2.3.5 Solvent chemical speciation: vapor-liquid equilibrium

2.3.5.1 Brief review of vapor-liquid equilibrium modelling

A vapor-liquid equilibrium (VLE) model predicts the chemical speciation in a multicomponent multiphase system. For the case of absorption or desorption of CO₂ or H₂S from alkanolamines, having an accurate vapor-liquid model is essential in sizing the equipment and predicting the outlet streams compositions. VLE models in general are divided into two broad categories: non-rigorous thermodynamic models such as Kent-Eisenberg, modified Kent-Eisenberg; and rigorous ones such as: Deshmukh-Mather [46], e-NRTL, and UNIQUAQ among others [42]. While the non-rigorous models have some theoretical background, they do employ many assumptions such as an infinitely dilute liquid or the applicability of Henry's law. VLE predictions following these models depend largely on empirical correction factors

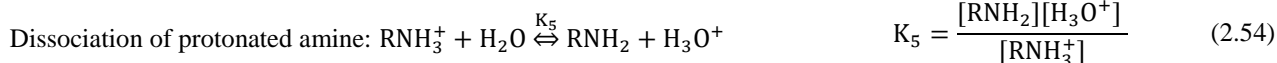
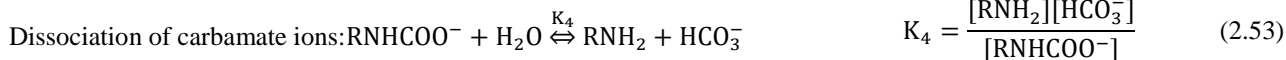
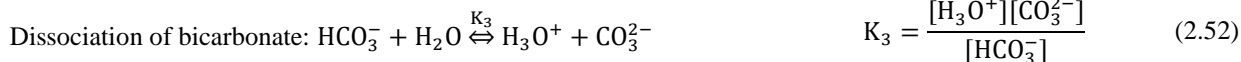
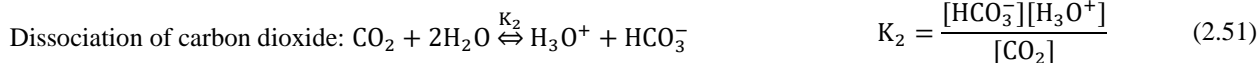
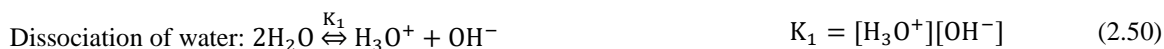
such as the fitted chemical equilibrium constants. This is contrary to the rigorous models, although semi-empirical in nature, employ activity coefficients to account for the non-idealities of the system [47].

The Kent-Eisenberg (KE) model owes its popularity to being the easiest to implement with good accuracy levels. Aboudheir [48] studied the kinetics of CO₂ absorption in highly loaded aqueous ETA systems, he used the KE model to calculate the chemical composition of loaded solutions before the start of the reaction. Similarly, Edali [49] and Jamal [50] used this model to calculate the initial concentrations for kinetic absorption into mixed amine system and desorption from 30% wt. ETA respectively. There exists some other variants such as the modified Kent-Eisenberg model as implemented by Jou [43] and Chakma [51] to correlate the vapor-liquid equilibrium of CO₂/H₂S in aqueous solvent MDEA and DGA respectively. The main difference of the modified KE from the base model is that the fitted equilibrium constants are dependent on the carbonation ratio (α).

As far as we can tell, introducing a VLE model in the frame of analysis of dielectric properties has never been performed before. The main advantage of such a methodology is that it would provide predictions of the chemical speciation in the liquid phase with a reasonable accuracy, so as to explain the variations of the dielectric properties at different levels of CO₂ charges.

2.3.5.2 Application of Kent-Eisenberg model: equations and resolution

Model input parameters are the total ETA concentration, the carbonation ratio (α), and the temperature. The model is constituted of five equations that describe the equilibrium relations in the system in addition to three balance equations. The apparent equilibrium constants for the involved chemical reactions are provided in the appendix. A total of eight equations are used to solve for the concentrations of eight chemical species: ETA denoted by RNH₂, ETAH⁺ denoted by RNH₃⁺, ETACOO⁻ denoted by RNHCOO⁻, in addition to other chemical species such as OH⁻, H⁺, HCO₃⁻, CO₃²⁻, and CO₂. The model assumes no interaction between the different chemical species [47], thus the apparent equilibrium constants of the dissociation reactions of: CO₂, H₂O, and HCO₃⁻ are taken directly from literature for an infinitely diluted solution [52]. Those related to ETA - (2.53) and (2.54) - were fitted to experimental VLE data by Kent-Eisenberg [53] employing a least-squared error procedure which lumps the model's errors from its assumptions into two equilibrium constants. The chemical equilibrium of the system is presented by the following reactions:



The equilibrium equations are complemented by the balance equations:

-Amine balance

$$[\text{RNH}_2]_0 = [\text{RNH}_2] + [\text{RNHCOO}^-] + [\text{RNH}_3^+] \quad (2.55)$$

-Carbon balance

$$\alpha[\text{RNH}_2]_0 = [\text{RNHCOO}^-] + [\text{HCO}_3^-] + [\text{CO}_3^{2-}] + [\text{CO}_2] \quad (2.56)$$

-Electroneutrality of solution

$$[\text{RNH}_3^+] + [\text{H}^+] = [\text{RNHCOO}^-] + [\text{HCO}_3^-] + [\text{OH}^-] + [\text{CO}_3^{2-}] \quad (2.57)$$

The non-linear system, composed of eight algebraic equations were solved using finite-element method (FEM) in COMSOL® Multiphysics (6.1). The coefficient-form partial differential equation module (PDE) was used to solve the system. The non-linear equations were written as residual terms and solved over a 1D geometry representing the CO₂ loading for $\alpha \in [0-0.8]$. Uniform meshing was used for a total of 30 points over the domain, and zero flux boundary condition was used at $\alpha=0$ and $\alpha=0.8$. Initial values of the variables were chosen intuitively to have the same order of magnitude as the expected solution at condition of no CO₂ loading. It should be noted that H₂O concentration was determined after solving the system of equations by performing an atomic balance on hydrogen before and after CO₂ loading as shown in (2.58). An underlying condition of this equation is the isochoric nature of the solution as a function of the CO₂ loading; an observation that can easily be drawn when regarding the density values reported by Weiland [54] for 30%wt. ETA.

$$2[\text{H}_2\text{O}]_\alpha + [\text{H}^+]_\alpha + [\text{OH}^-]_\alpha + 7[\text{RNH}_2]_\alpha + 8[\text{RNH}_3^+]_\alpha + 6[\text{RNHCOO}^-]_\alpha + [\text{HCO}_3^-]_\alpha = 2[\text{H}_2\text{O}]_{\alpha=0} + 7[\text{RNH}_2]_{\alpha=0} \quad (2.58)$$

2.4 Results

2.4.1 Chemical speciation profiles

The VLE model of Kent-Eisenberg was solved for $\alpha \in [0-0.8]$ and for T variation from 20 to 80°C; the molar fractions (x) of chemical components are plotted in Figure 2-17. Results show that speciation is overwhelmingly dependent on the CO₂ loading instead of the temperature (not presented here), consequently we will consider the chemical speciation at 20°C on the aforementioned range of (α). In order to evaluate the accuracy of the model, calculated mole fractions are compared to those obtained experimentally by Poplsteinova [55] using NMR spectroscopy; both data sets are plotted in Figure 2-17. It is clear that there is a good quantitative agreement between experimental and predicted chemical speciation which validates the KE model.

Figure 2-17 shows that with increased carbonation ratio (α), concentration of ETA decreases as it's being consumed to produce ionic species, mainly ETAH⁺ and ETACOO⁻ for the region ($\alpha < 0.5$) while other ionic species have negligible concentrations. Theoretically, the highest possible loading that can be reached in a primary or secondary amine solutions is ($\alpha=0.5$), but at higher loadings, carbamate ions (ETACOO⁻) dissociate to produce more ETA that reacts with CO₂ and H₂O to produce HCO₃⁻; it is for this reason that loadings higher than ($\alpha=0.5$) are possible [56]. The concentration of H₂O is not plotted in Figure 2-17 to preserve the current scale because of the comparatively high molar fraction ($x_{\text{H}_2\text{O}} > 0.8$) than the other chemical species. Still, the concentration of H₂O experiences some decrease with

increasing (α); a drop of 7% – using equation (2.58) - was calculated over the between ($\alpha=0$) and ($\alpha=0.8$). The total dipolar and ionic mole fractions were also calculated according to equations (2.59) and (2.60) respectively. The species considered to participate in the polarization mechanism are: H_2O and ETA, while the main species considered to participate in ionic conduction: ETAH^+ , ETACOO^- , HCO_3^- . Figure 2-18 shows how the dipolar content of the solution decreases (mainly by the decrease of ETA) with increasing carbonation ratio; on the other hand, the solution experiences a linear increase of its ionic content with increasing carbonation ratios (α).

$$X_{\text{dipoles}} = X_{\text{H}_2\text{O}} + X_{\text{ETA}} \quad (2.59)$$

$$X_{\text{ions}} = X_{\text{ETAH}^+} + X_{\text{ETACOO}^-} + X_{\text{HCO}_3^-} \quad (2.60)$$

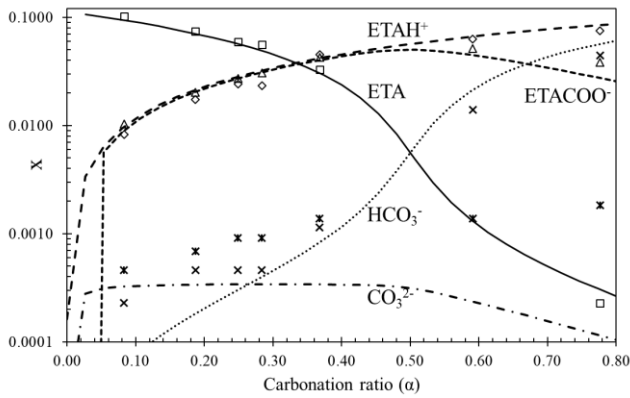


Figure 2-17: Kent-Eisenberg chemical speciation model and experimental values obtained by NMR spectroscopy for 30% wt. ETA from Poplsteinova [55].

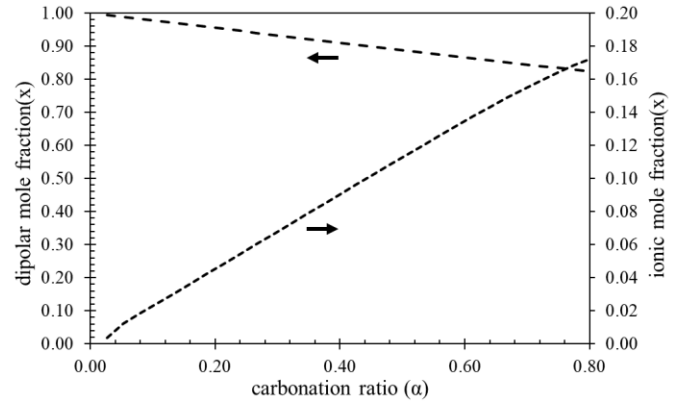


Figure 2-18: Total dipolar and ionic concentrations in 30% wt. ETA solution at different carbonation ratios.

2.4.2 Validation of dielectric measurements

To validate the measurement technique, the relative permittivity and the dielectric loss factor of DW were measured over the frequency range [915-2450MHz] for the temperatures [20-60°C] by steps of 10°C. Experimental results are plotted along with those of DW calculated from the Debye relaxation model in Figure 2-19 and Figure 2-20 respectively. The Debye model was used for calculation of the dielectric properties of distilled water. The dispersion parameters function of temperature were obtained from Buchner[16]; validity of these parameters are for the temperature range [0, 55] °C and in the frequency range $f < 20.05\text{GHz}$.

$$\epsilon_0 = 87.8 \exp(-0.00456 T(^{\circ}\text{C})) \quad (2.61)$$

$$\tau(\text{ps})^{-1} = 5.63 \cdot 10^{-02} + 2.12 \cdot 10^{-03} T(^{\circ}\text{C}) + 1.86 \cdot 10^{-05} T^2(^{\circ}\text{C}) \quad (2.62)$$

$$\epsilon_{\infty} = 6.49 - 0,025 T(^{\circ}\text{C}) \quad (2.63)$$

With regards to ϵ' , the two sets of experimental data agree almost perfectly where AARD is less than 2% for all temperatures. ϵ'' displays good agreement with the model, but considerable deviations persist where the max encountered AARD $< 10\%$ due to the low equipment sensitivity in this range of (ϵ''). The lower limit of measurement on the dielectric loss should be greater than (5% ϵ') of the liquid under test [37]. Gadani [57] observed similar %AARD when validating his measurement technique with DW for the frequency range [0.2-1.4] GHz.

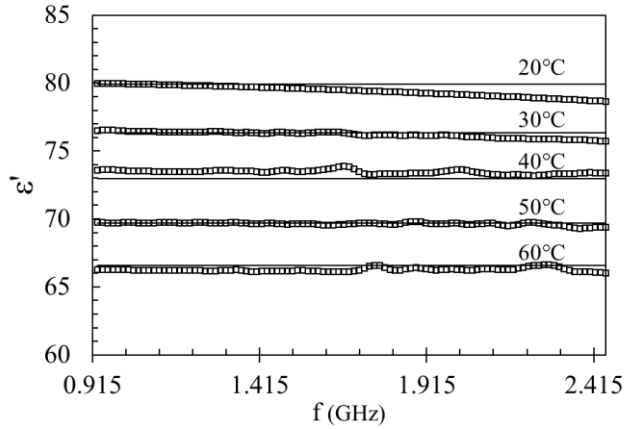


Figure 2-19: Measured (\square) and calculated ($—$) relative dielectric constant of deionized water at different temperatures

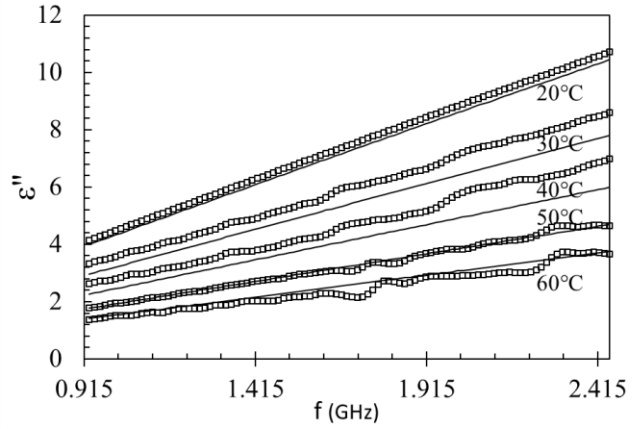


Figure 2-20: Measured (\square) and calculated ($—$) relative dielectric loss factor of deionized water at different temperatures

2.4.3 Dielectric dispersion of non-loaded 30% ETA

The dielectric properties of 30%wt. ETA free of CO_2 , were fitted with the Cole-Cole relaxation model; experimental results as well as extrapolations of the Cole-Cole model are plotted in the dielectric dispersion diagrams in Figure 2-21 and Figure 2-22 for $T=20^\circ\text{C}$ and $T=60^\circ\text{C}$ respectively. The fitting error on the dielectric properties of 30%wt. ETA at 20 and 60°C is 0.04 and 0.01 respectively - obtained from (2.48). The accuracy of the Cole-Cole dispersion model for correlating the properties of a medium is subject to the response of the latter to a varying electric field: the implicit assumptions of a model can be very well obeyed by one medium while disobeyed by another. While the experimental frequency measurement range is [915-2450 MHz], the Cole-Cole model was extrapolated to reach the relaxation frequency of both solutions. The properties of distilled water were also plotted to serve as a reference; the latter were calculated from the Debye model in conjunction with the dispersion parameters $[\epsilon_0, \epsilon_\infty, \tau]$ provided by Buchner [16]. The Cole-Cole dispersion parameters $[\epsilon_0, \tau, n, \sigma]$, as well as the relaxation frequency (f_r) and the fitting error for non-loaded 30%wt. ETA are displayed in Table 2.2.

	30% wt. ETA		H2O	
	20 °C	60 °C	20 °C	60 °C
T(°C)	20 °C	60 °C	20 °C	60 °C
ϵ_0	69.10	58.27	79.93	66.58
n	0.93	0.98	1	1
ϵ_∞	1.88	1.88	5.99	4.99
τ (ps)	19.2	8.8	9.42	3.99
σ (S/m)	0.079	0.177	—	—
f_r (GHz)	8.28	18.08	16.89	39.84
Error ²	0.04	0.01	—	—

Table 2.2: Fitted Cole-Cole dispersion properties of 30% wt. ETA, and those of DW at T=20°C and 60°C

Figure 2-21 shows that for the experimental 30% wt. ETA properties as well as for distilled water there is a decrease in the relative dielectric constant (ϵ') with frequency. With increasing frequency lower number of dipoles are able to polarize, this leads to a monotonous decrease of the dielectric constant. On the hand, the loss factor (ϵ'') increases at higher frequencies indicating that the frequency range of measurement is lower than the relaxation frequency (f_r) of the solution. The extrapolation of the Cole-Cole model until the relaxation frequency shows that the dispersion curve of 30% wt. ETA follows a near perfect semi-circular shape indicating that 30% wt. ETA follows a Debye relaxation. Still, ETA and DW have a large disparity in their relaxation times (102 ps) and (6.52 ps) respectively at 35°C [4], the reason which is responsible for the deviation from the Debye model. It is worth noting that the parameter of distribution of relaxation times nears unity ($n=0.93$) which is another indicator of a near-Debye relaxation.

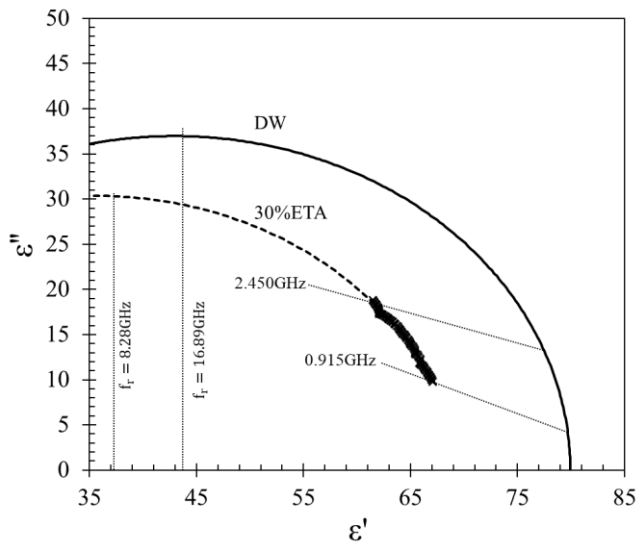


Figure 2-21: Dielectric dispersion diagram of distilled water, 30% ETA (Experimental) and 30% ETA (Cole-Cole) at 20°C

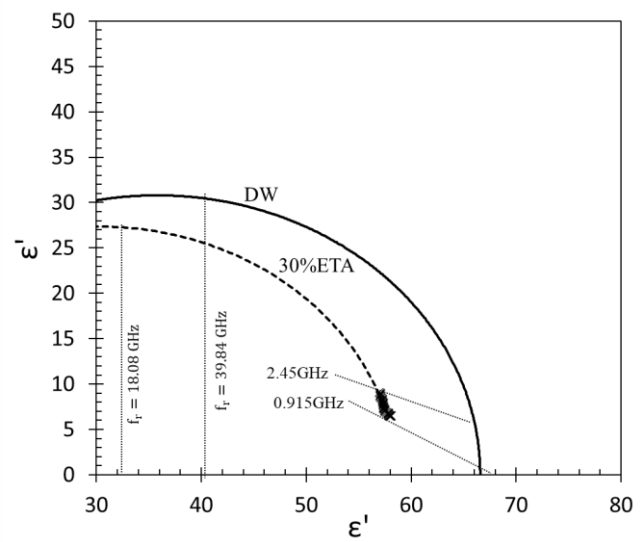


Figure 2-22: Dielectric dispersion diagram of distilled water, 30% ETA (Experimental) and 30% ETA (Cole-Cole) at 60°C

The dispersion curve of 30% wt. ETA is shifted leftwards with respect to that of DW due to a lower dielectric constant that influences the shape of the dispersion curve. It is also depressed downwards with respect to that of distilled water due to the decrease in maximal loss factor (ϵ'' at $f = f_r$). Pure ethanolamine has lower static dielectric constant (~ 31.94) [9] than DW (~ 80) at 20°C [30]. Although ETA has two hydrogen bonds ($\text{NH}_2 \dots \text{H}/\text{OH} \dots \text{H}$) per molecule,

and has a greater dipole moment than that of water - 2.37D [9] and 1.8D [14] respectively - DW ultimately has the greater effective dipole moment. The effective dipole moment being the normalized dipole moment per unit of the medium and is proportional to the static dielectric constant of a medium. It is suspected that lower dielectric constant of ETA results from the steric hindrance which would shut down the formation contrary of large H-bonded clusters as in H₂O or n-alcohols [7, 9]. Jadhavpatil [5] fitted the dielectric properties of 30%wt. ETA with the model of Havriliik-Negami [27] and obtained ($\epsilon_0 = 69$) at 25°C, a value that is in very good agreement with this work ($\epsilon_0=69.1$ at 20°C). This serves to indicate that despite the lack of wide experimental dataset for dielectric properties, the dispersion parameters obtained in this work are comparable to those obtained by others.

Although no experimental data on the loss factor of pure ETA at relaxation frequency exist, we note that pure ETA follows a Debye relaxation [4]. The dielectric loss factor of ETA at the relaxation frequency is proportional to the static dielectric constant as shown in (2.36). Therefore, while pure ETA has a lower static dielectric constant than that of DW so will it have a lower loss factor at relaxation. Another speculation with regards to the weaker relaxation of 30%wt. ETA relative to DW is that ETA and H₂O have different relaxation times. At 35°C, ETA has a higher relaxation time of 102ps [4], than that of DW is 6.52ps; The larger molecular size and stronger hydrogen bonding strength [10, 58] of ETA are the reasons for this disparity. This leads to higher relaxation times of 30%wt. ETA – 19.2ps at 20°C than water. Figure 2-23 shows that the relaxation time increases between H₂O and 30% ETA from 9.42ps to 19.2ps at 20°C respectively, and decreases with temperature from 20°C to 60°C for both liquids. The relaxation time of 30%wt. ETA measured by Jadhavpatil [5] is 37ps and may be accorded good credibility considering that it was fitted on a more inclusive data set [10MHz-20GHz] than ours [915MHz-2.45GHz]. Still the relaxation values obtained by this author show considerable spread and may therefore put in question the stability of his results. Another very important reason for this discrepancy is due to the fact that Jadhavpatil [5] did not account for loss by ionic conduction mechanism in his dispersion model. Consequently, the fitted relaxation time would be higher than the true value in order to make the solution relax at lower frequencies thus compensating for the contribution of the ionic species on the dielectric loss factor (ϵ'').

Figure 2-22 shows the experimental as well as the Cole-Cole dielectric dispersion of 30%wt. ETA and DW at T=60°C. Similar observations can be made as with Figure 2-21, the dispersion curve has a semi-circular form which points at a Debye relaxation. In addition, the dispersion curve of 30%wt. ETA has the same relative position relative to that of distilled water as with Figure 2-21. One interesting observation is that the measured dielectric properties at 60°C cover a smaller segment of the dispersion curve in comparison to the dielectric measurements at 20°C. The reason behind is that the temperature-increase pushes the relaxation frequency of 30%wt. ETA to higher values and further away from our measurement spectrum. As the frequency range of measurement is constant [915-2450MHz], it would be more situated in the region of high dielectric constant and low dielectric loss factor. The greater proximity to the relaxation frequency at 20°C than at 60°C allows for a greater range of variations of (ϵ'') as with (ϵ') as well. It is for

this reason that our experimental data correspond to a greater portion of the dielectric dispersion curve at 20°C than that at 60°C (Figure 2-22).

The relative dielectric constant (ϵ') and loss factor (ϵ'') of DW, and 30% wt. ETA are plotted as a function of the logarithm of frequency in Figure 2-23, and Figure 2-24 respectively. Figure 2-23 shows that at a given temperature, water has a greater dielectric constant than 30% wt. ETA as discussed earlier. When the temperature increases from 20°C to 60°C the dielectric constant depresses - as can be seen for both liquids - which translates into a downwards shift of the graphs. With temperature increase, hydrogen bonding strength decreases giving way to smaller H-bonded clusters, and thus a lower relaxation time [12] and the relaxation curve is shifted to the right to higher relaxation frequencies. The relative dielectric constant of 30% wt. ETA at 20°C reaches the optical dielectric constant (ϵ_∞) at lower frequencies than at 60°C due to its slower relaxation mechanism at 60°C (lower relaxation time) – (fitted values of τ at 20 °C and 60 °C in Table 2.2 reveal this).

The dielectric loss factors as a function of frequency for DW and 30% wt. ETA are shown in Figure 2-24. It can be observed that at a given temperature, DW has a higher relaxation frequency than 30% ETA. At higher temperatures, the 30% wt. ETA curves for (ϵ'') as a function of frequency are shifted to the right, such that relaxation happens at higher frequencies. Although a lower number of dipoles are participating in the relaxation at higher temperatures, the fact that these dipoles “relax” at higher frequencies allows the dielectric loss values of 60°C to be superior to those at 20°C in the high frequency range.

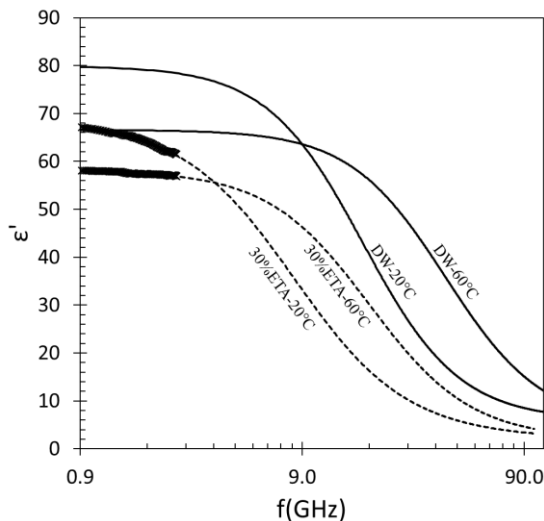


Figure 2-23: Bode plot of relative dielectric constant for distilled water and 30% wt. ETA solution at 20°C and 60°C

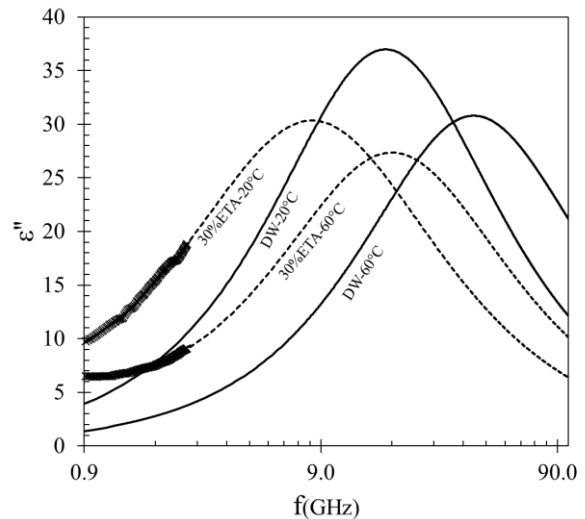


Figure 2-24: Bode plot of dielectric loss factor for distilled water and 30% wt. ETA solution at 20°C and 60°C

The Kirkwood correlation factor (g_{eff}) was evaluated for 30% ETA system at 20°C using the Kirkwood formula shown in (2.64) [59]. The Kirkwood correlation factor is the ratio of the effective dipole moment in condensed phase (liquid, solid...) relative to that calculated at vacuum and is a good general indicator of the nature of the dipole interactions. We distinguish the following cases:

$-g_{\text{eff}} > 1$: The dipoles in the medium are in a parallel alignment. The effective dipole moment is enhanced relative to that in vacuum.

$-g_{\text{eff}} = 1$: The dipoles do not interact with another. The effective dipole moment is identical to sum of the moments of the dielectric molecules in the gaseous phase.

$-g_{\text{eff}} < 1$: The dipoles are in anti-alignment with one another causing them to have a lower effective dipole moment relative to vacuum condition.

$$\frac{4\pi N}{9kT} \left(\frac{\mu_1^2 \rho_1}{M_1} \varphi_1 + \frac{\mu_2^2 \rho_2}{M_2} \varphi_2 \right) g_{\text{eff}} = \frac{(\epsilon_0 - \epsilon_\infty)(2\epsilon_0 + \epsilon_\infty)}{\epsilon_0(\epsilon_\infty + 2)^2} \quad (2.64)$$

In (2.64) μ is the dipole moment in the gaseous phase, ρ is the pure-component density obtained from Weiland[54], M the molar mass, N is Avogadro's number, k is the Boltzmann constant, φ the volume fraction. The calculated Kirkwood correlation (g_{eff}) coefficients at 20°C and 60°C are 2.69 and 2.65. Given that (g_{eff}) is greater than unity, dipoles are in parallel alignment resulting in an increase of the effective dipole moment. It appears that (g_{eff}) maintains an almost constant value with temperature increase from 20°C to 60°C, the result of a proportional decrease of both the liquid phase and vacuum effective moment of the dielectric. The result is in accordance with that of Jadhavpatil [5] who obtained constant (g_{eff}) with temperature for 30% wt. ETA (~2.7 units at 25°C). Nonetheless, care needs to be taken in the interpretation of (g_{eff}) in light of its high sensitivity to the optical dielectric constant (ϵ_∞) [10], with the latter not being obtained accurately from dielectric measurements in the MW frequency range.

Table 2.2 shows that 30% wt. ETA solution possesses a non-negligible electrical conductivity at 20°C and 60°C. The protonation reaction of ETA molecules is the cause as shown in (2.65). Therefor the dielectric loss factor is augmented by losses from ionic species through the ionic conduction mechanism. The ionic species in the 30% ETA solution contribute to the dielectric loss factor by 1.55 and 3.2 units at 915 MHz for 20°C and 60°C respectively with an expected decrease in their contribution at higher frequencies [29]. The increased contribution of ionic conduction with temperature is brought about by an augmentation of the conductivity. The latter increases at 60°C and is almost double that at 20°C, due to higher ion mobility [60] on one hand, and the increase of the dissociation constant of ETA on another [45]. It is worth mentioning that ETA is a weak base having $\text{pK}_a=9.5$ at $T=25^\circ\text{C}$ [39]. It follows that the electrical conductivity of the 30% wt. ETA solution is low ($\sim 0.72 \text{ mS}\cdot\text{cm}^{-1}$) at 20°C [45]; a value in agreement with the one obtained in this work through fitting the dielectric relaxation model ($0.79 \text{ mS}\cdot\text{cm}^{-1}$).



2.4.4 Dielectric Dispersion of CO₂-loaded 30% wt. ETA aqueous solution

The dielectric properties of 30% ETA solution were measured over the frequency range [915- 2450] MHz at temperatures ranging from 20 to 80 by steps of 10°C, and α was varied over [0.22-0.55] by steps $\Delta\alpha=0.11$. The Debye and Cole-Cole dielectric dispersion models were fitted to the experimental dielectric data by finding the set of parameters [ϵ_0 , τ , n , σ] that minimizes the squared errors as per (2.48). Both dispersion models provided good fitting results, but those from Cole-Cole model were privileged due to the greater accuracy in modeling the experimental data.

Figure 2-25, and Figure 2-26 present the parity plots for the calculated and experimentally obtained relative permittivity and dielectric loss factor respectively at 915MHz and 2450MHz. It can be observed that deviations between both sets of data is minimal highlighting the quality of the fit and the suitability of the Cole-Cole dispersion to model the dielectric properties of the solutions.

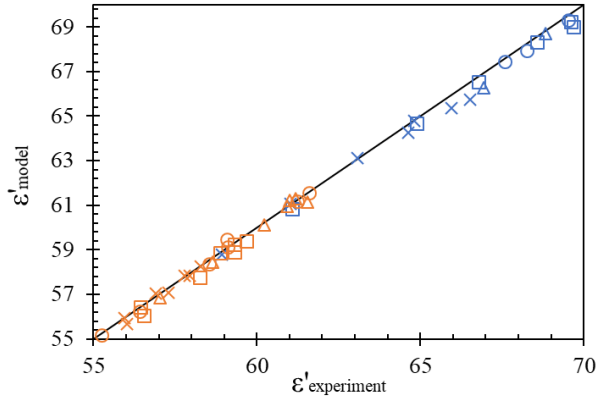


Figure 2-25: Modeled and experimental relative permittivity of 30% wt. ETA solution at 915MHz (blue) and 2450MHz (orange): x, $\alpha=0.22$; \square , $\alpha=0.33$; Δ , $\alpha=0.44$; \circ , $\alpha=0.55$.

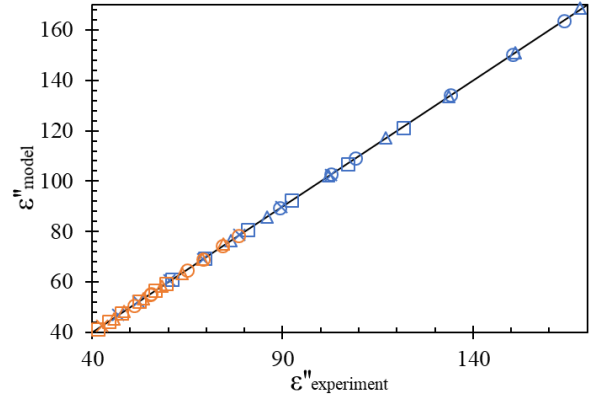


Figure 2-26: Modeled and experimental relative dielectric loss factor of 30% wt. ETA solution at 915MHz (blue) and 2450MHz (orange): x, $\alpha=0.22$; \square , $\alpha=0.33$; Δ , $\alpha=0.44$; \circ , $\alpha=0.55$.

2.4.4.1 Dielectric dispersion diagram

Figure 2-27 and Figure 2-28 show the experimental dielectric data of 30%wt. ETA at ($\alpha=0.22$, $T=20^{\circ}\text{C}$) and ($\alpha=0.55$, $T=80^{\circ}\text{C}$) respectively. The fitted Cole-Cole model was extrapolated to frequencies that approach the optical relaxation frequency. The total dielectric loss (ϵ''_t) was decomposed into its two contributions: loss by dipolar polarization (ϵ''_{DR}) - presented in (2.67), and loss by ionic conduction (ϵ''_{IC}) - presented in (2.68). We note that the expression of (2.67) was calculated from Cole-Cole relaxation model by separating the real and the imaginary parts.

$$\epsilon''_t = \epsilon''_{DR} + \epsilon''_{IC} \quad (2.66)$$

$$\epsilon''_{DR} = (\epsilon_0 - \epsilon_{\infty}) \frac{(f * T)^n \sin\left(\frac{n\pi}{2}\right)}{1 + 2(f * T)^n \cos\left(\frac{n\pi}{2}\right) + (f * T)^{2n}} \quad (2.67)$$

$$\epsilon''_{IC} = \sigma / \omega \epsilon_0^* \quad (2.68)$$

The dielectric dispersion of the solvent ($\alpha=0.22$, $T=20^{\circ}\text{C}$) seems to approach the semi-circular behavior indicating a Debye behavior and further observed by (n) having a value of 0.84 Figure 2-27. The figure shows that both mechanisms have different contributions to the dielectric loss depending on the frequency of the E-field: at 915 MHz the ionic conduction overtakes the dipolar rotation because ionic conduction is most active at low frequencies. This changes at 2450 MHz where ionic conduction is hindered contrary to the dipolar rotation which is incentivized by the greater proximity to the relaxation frequency. The increasing contribution of dipolar rotation observed in the experimental data shows that the relaxation frequency of the solution is superior to the spectrum of measurement in this study.

Figure 2-28 shows that the contribution of the ionic conduction to the overall dielectric loss is immense with respect to the preceding case. Although it is not displayed on the figure for the purpose of preserving the scale, ionic conduction contributes to the dielectric loss by 179.45 units contrary to dipole rotation which 8.71 units at 915 MHz respectively. This can be explained by the concentration surge of ETACOO^- and ETAH^+ with higher CO_2 loading. The increased concentration of the chemically dissolved CO_2 reduces the molecular concentration of ETA and increases those of ionic species as indicated by Figure 2-17. Another reason is that higher temperatures lead to higher ion mobilities and consequently greater interactivity of the ions with the E-field. The observed decrease of the ionic conduction contribution from 915 to 2450 MHz could be explained with the Falkenhagen theorem [29]: the central ion - when subjected to a harmonic external E-field - experiences a certain mobility but the surrounding ionic cloud lags behind, thus exerting an opposite relaxation force on the former and reducing its mobility with higher frequencies. At very high E-field frequencies, the displacement of the central ion from its equilibrium position is negligible; at this point both the central ion and the ionic cloud are considered motionless and the loss mechanism loses its effect. The relaxation frequency in Figure 2-27 - case of ($\alpha=0.22$ and $T=20^\circ\text{C}$) - is lower than that of ($\alpha=0.55$ and $T=80^\circ\text{C}$) by action of the higher temperatures decreasing the viscosity on one hand and the size of the H-bonded clusters on another, this is discussed in greater detail in section 2.4.5.2.

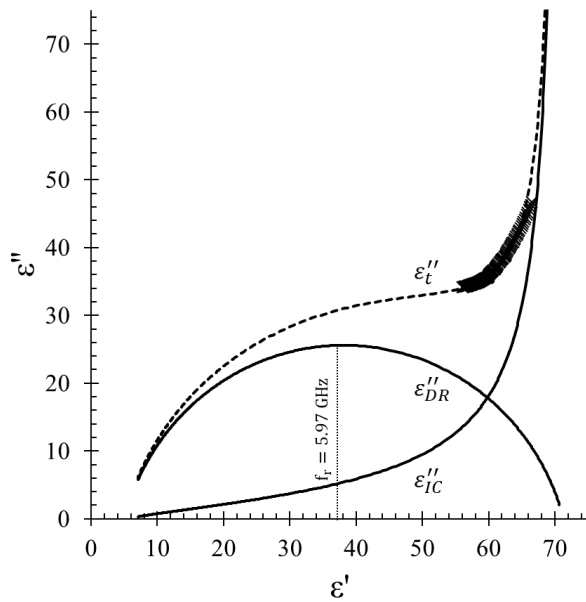


Figure 2-27: Dielectric dispersion of 30%wt. ETA at $\alpha=0.22$ and $T=20^\circ\text{C}$

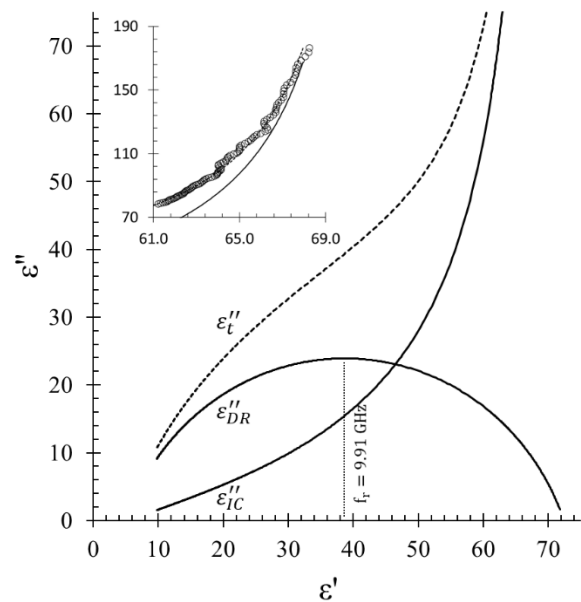


Figure 2-28: Dielectric dispersion of 30%wt. ETA at $\alpha=0.55$ and $T=80^\circ\text{C}$

The dielectric loss factor as a function of frequency at 20°C for different values of (α), and at $\alpha=0.22$ for different temperatures were plotted in Figure 2-29 and Figure 2-30. These plots aim at highlighting the effect of the temperature and CO_2 loading on the dielectric loss of 30%wt. ETA loaded with CO_2 . The loss factor has been decomposed into its two contributions: dipolar rotation and ionic conduction.

Figure 2-29 shows that the dielectric loss factor at 20°C and at different carbonation ratios (α); as expected, loss by ionic conduction has a greater effect than dipolar rotation, one that increases with greater carbonation ratios. At low frequencies ionic conduction overtakes loss by dipolar rotation as opposed to higher frequencies where the latter dominates and the former vanishes. It can be observed that with increasing (α) the dielectric loss profile by dipolar rotation is shifted to lower frequencies, indicating a slower relaxation mechanism (greater relaxation time), this can be related to the increase of viscosity associated with higher CO₂ content. Another interesting observation is that for higher values of (α), the loss by dipolar rotation is less pronounced at the relaxation frequency but more pronounced at relatively higher and lower frequencies. Several reasons are at work, we mention as main contributor the broader distribution of relaxation times marked by lower values of (n) [0.84, 0.73, 0.67, 0.66] for greater carbonation ratios [0.22 ,0.33, 0.44 ,0.55] respectively.

T(°C)	ϵ_0	τ (ps)	σ (S/m)	n	fr(GHz)	Error ²
$\alpha=0,22$						
20	71,3	26,7	1,8	0,84	5,97	0,1
30	70,1	21,9	2,2	0,82	7,27	0,1
40	67,8	17,7	2,7	0,83	8,99	0,1
50	69,7	15,4	3,1	0,75	10,36	0,0
60	66,8	13,1	3,6	0,77	12,14	0,0
70	63,6	11,3	4,3	0,80	14,10	0,0
80	60,1	11,1	5,0	0,88	14,29	0,0
$\alpha=0,33$						
20	80,5	32,0	2,3	0,73	4,97	0,1
30	80,9	27,5	2,8	0,70	5,78	0,1
40	79,5	23,0	3,5	0,69	6,92	0,1
50	76,6	19,4	4,1	0,70	8,19	0,1
60	72,4	16,4	5,0	0,74	9,70	0,0
70	68,6	14,3	5,8	0,78	11,10	0,1
80	63,4	13,0	6,4	0,82	12,24	0,1
$\alpha=0,44$						
20	89,6	38,7	3,0	0,67	4,11	0,1
30	90,6	35,5	3,5	0,64	4,49	0,0
40	88,3	28,9	4,4	0,64	5,50	0,0
50	84,1	23,5	5,3	0,66	6,78	0,0
60	79,3	19,1	6,2	0,69	8,31	0,0
70	74,7	16,2	7,2	0,74	9,83	0,0
80	68,8	15,3	8,2	0,86	10,43	0,2
$\alpha=0,55$						
20	92,7	44,1	3,6	0,66	3,61	0,0
30	92,7	38,5	4,3	0,65	4,13	0,0
40	82,7	31,9	4,8	0,65	4,99	0,0
50	84,2	26,6	6,1	0,66	5,98	0,0
60	87,2	25,1	6,9	0,58	6,35	0,1
70	75,2	17,1	7,8	0,75	9,29	0,0
80	72,4	16,1	8,5	0,79	9,91	0,0

Table 2.3: Dielectric dispersion properties for Cole-Cole model at different temperatures and CO₂ loadings

The dielectric loss factors displayed in Figure 2-30 shows that ionic conduction (IC) is the dominant loss mechanism at low frequencies where the values of the latter can be greater by one to two orders of magnitude than that

of dipolar rotation (DR), and increase with temperature. Figure 2-30 highlights that the relaxation is strictly faster with higher temperatures as translated by a shift of the loss curve by dipolar rotation in towards higher frequencies.

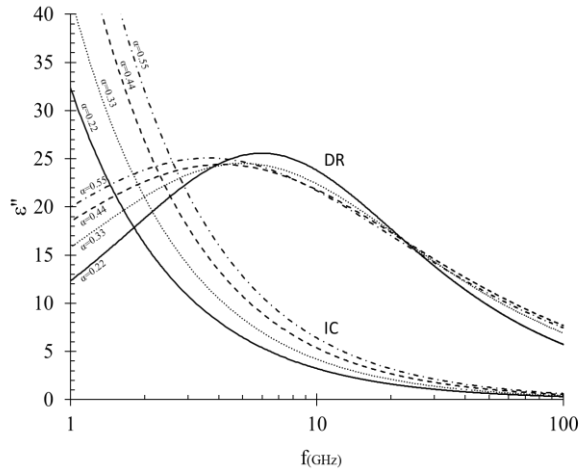


Figure 2-29: Dielectric loss factor of 30% wt. ETA function of frequency at T=20°C and at different values of α

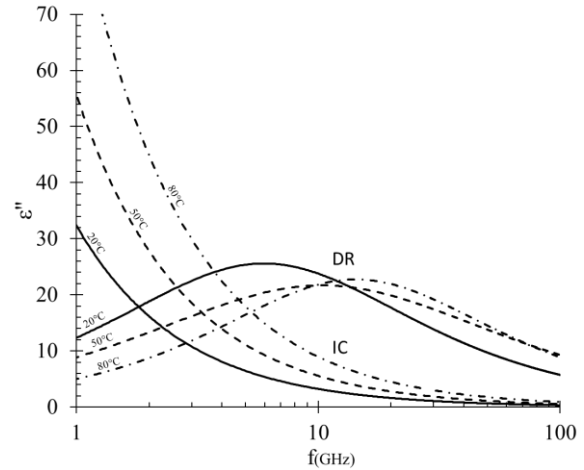


Figure 2-30: Dielectric loss factor by dipolar rotation and ionic conduction of 30% wt. ETA function of frequency for $\alpha=0.22$ and at different temperatures

The effect of α on the dielectric dispersion was studied by plotting the Cole-Cole fit in Figure 2-31 at T=20 °C, $\alpha \in [0.22, 0.55]$, and over the measurement frequency range [915-2450 MHz]. The values of (ϵ') at 915 MHz are in the range [65-72] units: values that are in the same range as those of water, but lower owing to ETA possessing a weaker static dielectric constant than water - 31.94 [9] and 79.93 at 20°C respectively. It can be observed that with increased (α) the curve is shifted upwards and stretches to cover a greater range of (ϵ') . The upwards shift is caused by an increased lossy character due to increased ionic concentration in the liquid as observed in Figure 2-17. It is accompanied by a slightly greater steepness; the latter originates from greater sensitivity of ionic conduction to frequency decrease with higher ionic concentrations. The stretching of the dispersion curve with increasing (α) is due to the decrease of the relaxation frequency which would have a greater proximity to the measured frequency spectrum in this study [0.915 - 2.45 GHz]. This can be contrasted to measurement frequencies that are infinitely lower or higher relative to the relaxation frequency where (ϵ') plateaus to the single value of (ϵ_0) or (ϵ_∞) respectively.

The effect of temperature on the dielectric dispersion is studied in Figure 2-32 where temperature is varied along the range [20-80 °C] while fixing (α) to 0.22. The figure shows that greater temperature leads to a steeper curve with lower range on (ϵ') . The reasons are similar to what was discussed in the previous paragraph: the ionic conduction producing higher values of (ϵ'') thus a greater sensitivity to the frequency of applied E-field, and the shift of the relaxation frequency away from the measurement spectrum producing a narrower range of (ϵ') . At 915MHz, (ϵ') decreases monotonously with higher temperatures, although at 2450MHz this does not hold true

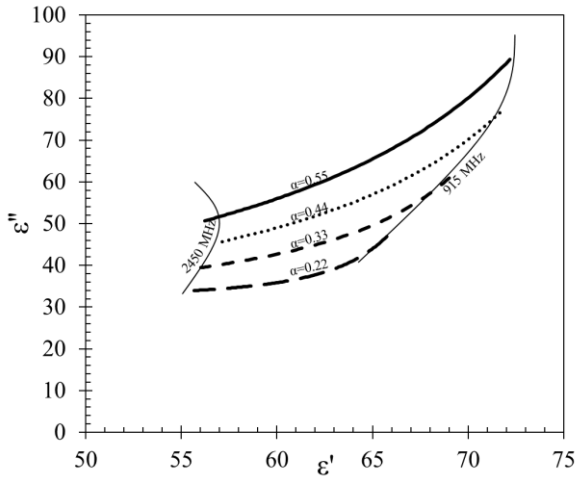


Figure 2-31: Dielectric dispersion of 30% ETA over the frequency range [915-2450 MHz] at T=20°C and $\alpha \in [0.22-0.55]$

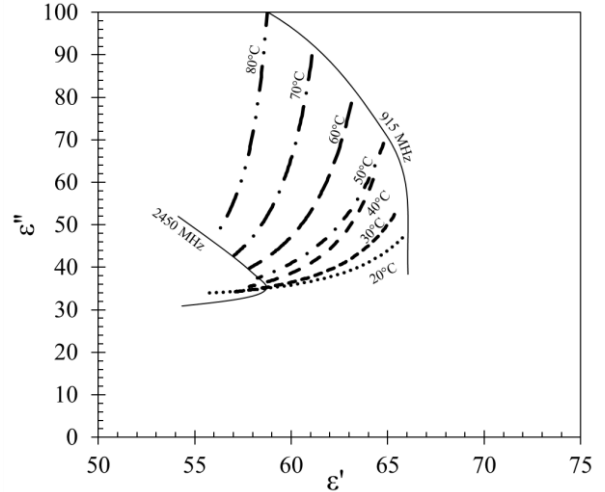


Figure 2-32: Dielectric dispersion of 30% ETA over the frequency range [915-2450 MHz] at $\alpha=0.22$ for T $\in [20-80^\circ\text{C}]$

2.4.4.2 Penetration depth of MW in 30% wt. ETA loaded with CO₂

The penetration depth of the E-field in the solution was calculated at different temperatures and carbonation ratios (α) as per the expression given in (2.69) – more on this in (2.2.3). D_p (mm) being the penetration depth, c (m/s) is the speed of light in vacuum, and f (Hz) is the frequency of the E-field; (ϵ'') is the loss factor resulting from combined dipolar rotation and ionic conduction was used.

$$D_p = (c/2\pi f\sqrt{2\epsilon'}) \left[\sqrt{1 + (\epsilon''/\epsilon')^2} - 1 \right]^{-1/2} \quad (2.69)$$

Figure 2-33 presents the penetration depths at 915MHz. The calculated values are in the order of a few millimeters which are small in comparison to that of DW (11.4 mm at 915MHz and 20°C). The nature of 30% wt. ETA loaded with CO₂ as a very strong absorbent of MW irradiation leads to the rapid absorption of incident MW irradiation, consequently the resulting penetration depths are rather small. One consequence is that in such cases MW heating of a body would be marked by a high degree of non-homogeneity in the volumetric heating rate. Figure 2-33 shows that the penetration depth (D_p) decreases with increasing temperature and carbonation ratio. The change of the dielectric loss factor (ϵ'') is responsible: although the increase of temperature and (α) influences both dielectric constant and loss factor, the latter increases radically as opposed to the relatively gentle changes of the former as seen in Figure 2-31 and Figure 2-32. As a result, the increase in the dielectric loss with temperature and carbonation ratio is mainly responsible for the decreased penetration depths.

Figure 2-34 presents the penetration depth at 2450MHz, (D_p) is in the order of a few millimeters as with the case of 915MHz but has even lower values. The obvious reason is that (D_p) is inversely proportional to frequency, and so MWs with higher frequencies penetrate less as shown in (2.21). It remains important to be taken into consideration that the dielectric properties are also frequency-dependent with decreasing trends of both dielectric constant and loss factor (for our case of an ionic solution).

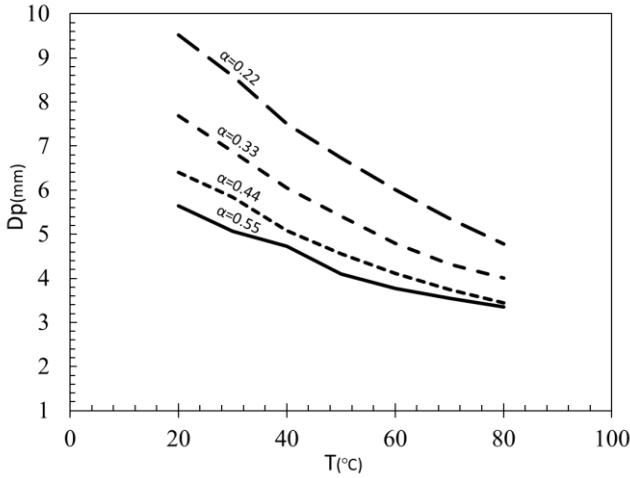


Figure 2-33: MW penetration depth in 30% wt. ETA function of temperature at different CO₂ loadings at f=915MHz

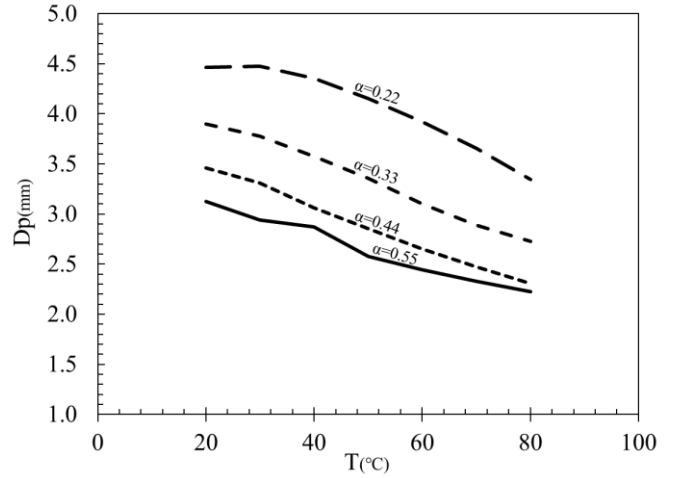


Figure 2-34: MW penetration depth in 30% wt. ETA function of temperature at different CO₂ loadings at f=2450 MHz

2.4.5 Dielectric dispersion parameters

The fitted dielectric dispersion parameters (ϵ_0 , τ , n , σ) of the Cole-Cole model are presented in Figure 2-35, Figure 2-36, Figure 2-37, and Figure 2-38 respectively as a function of temperature [20-80°C] and at different CO₂ loadings $\alpha=[0.22, 0.33, 0.44, 0.55]$. They were approximated by a polynomial of the form shown in equation (2.70) whose parameters are given in Table 2.4. The polynomial was provided to obtain better reproducibility of the experimental results and a better interpolation at experimental conditions not accounted for in this work. The polynomial form was chosen arbitrarily to well represent the dispersion properties. The variations of the dispersion parameters are discussed in the ensuing paragraphs.

$$f(T, \alpha) = (aT^2 + bT + c)(d\alpha^3 + e\alpha^2 + f\alpha + g) \quad (2.70)$$

	ϵ_0	$\tau(\text{ps})$	$\sigma(\text{S/m})$	n
a	-0.0155	0.0136	0.00145	0.000576
b	0.418	-2,87	0.324	-0.0486
c	319	197	9,60	4,99
d	-3,47	-3,83	-3,71	-1,21
e	3,12	3,78	3,46	1,56
f	-0.643	-0.724	-0.675	-0.727
g	0.258	0.205	0.134	0.285
Error ²	4,21	0,80	0,02	0,00

Table 2.4: Parameters for polynomial fits for the dispersion parameters of the Cole-Cole relaxation model

2.4.5.1 Static permittivity (ϵ_0)

The values of static relative permittivity for 30% wt. ETA with CO₂ are shown in Figure 2-36. (ϵ_0) appears to decrease with temperature at all tested values of α . It is expected hence higher temperatures contribute to higher thermal energies that counteract formation of H-bonded clusters [21]. This behavior is able to justify the one observed in Figure 2-32 where (ϵ') at 915 and 2450 MHz decreases with increasing temperatures. The decrement of the static permittivity ($\Delta\epsilon_0$)

over the temperature range in this study (60°C) is in the range of [15.36 - 19.24]; values that are comparable to that of pure water: $\Delta\epsilon_0 = 19.22$ [16], or to that of 30% wt. aqueous ETA - $\Delta\epsilon_0=18$ [5] over the same temperature range.

Figure 2-36 also shows that (ϵ_0) has an increasing trend with α . One would expect that with increasing (α) the molecular ETA concentration would decrease as shown in Figure 2-17, translating to a decrease of the total dipole concentration in the solution. In addition, the augmentation of ionic concentration evokes greater dipole-ion short-range interactions. This leads to irrotational bonding of dipoles by their neighboring ions [61], or through the long-range kinetic depolarization described by the Hubbard-Onsanger [62] theorem. It can therefore be assumed that static permittivity of 30% wt. ETA with no CO₂ content would be higher than that which contains CO₂. The static permittivity of 30% wt. ETA free of CO₂ measured by Jadhavpatil [5] and verified locally nears 69 units at 25°C, a value that is inferior to all the obtained values in this work at the same temperature.

One explanation as to why our results are difficult to interpret is that the measurement spectrum does not extend to sufficiently low frequencies, i.e. the relaxation frequency of the solution is comparable to that spectrum of measurement; accordingly, not enough experimental points are presented at the low frequency region to accurately portray the static dielectric behavior. This is particularly true with lower temperatures and higher α ; as an example, the relaxation frequency of the solution at 20°C and $\alpha=0.55$ is 3.61 GHz (taken from Table 2.3), a value not so far from the upper limit of the measurement spectrum 2.45GHz. Still the possibility of ionic polarization contributing to the static dielectric constant cannot be ruled out; while many authors have studied the dielectric relaxation of electrolyte solutions and concluded the decrease of the static dielectric constant with ionic concentrations, these studies were centered around simple salts. Dielectric studies focusing on electrolyte solutions with more complex ions such as those of ETA are not so common, and therefore it is difficult to form decisive interpretations.

Nevertheless, discussions on the behavior of the static permittivity does not undermine in any way the model's ability to accurately replicate the solutions' dielectric properties on this frequency range. The model will be accurate enough for practical ends such as microwave equipment design and EM modeling; this is clearly demonstrated by the excellent fits of the Cole-Cole model to the experimental data shown in Figure 2-25 and Figure 2-26.

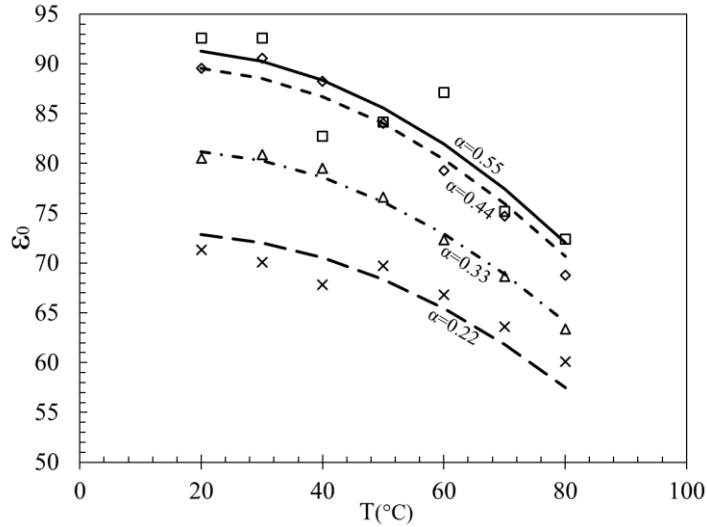


Figure 2-35: Static dielectric constant of 30% wt. ETA as a function of T α . (symbols), experimental; (lines), polynomial fittings

2.4.5.2 Relaxation time (τ)

The relaxation time of the solution is shown in Figure 2-36 as a function of temperature and at different values of (α). Figure 2-36 shows that with increasing temperature the relaxation time decreases to reach values in the neighborhood of 10 picoseconds – the relaxation time of DW at 20°C [28]. While increasing temperatures decrease the number of dipoles under the influence of the E-field – translating to lower static permittivity, the ones that are under this influence are able to relax faster and would ultimately have a lower relaxation time (higher relaxation frequency).

Figure 2-36 also reveals the increase of the relaxation time of the solution with increasing α , indicating a slower relaxation mechanism; the result of two effects at play. The first is the rise of the solution's viscosity, i.e. the latter increases by 31% when (α) increases from 0.22 to 0.55 at 25°C [54], hence increased viscosity hinders dynamic relaxation rendering it slower [24], and increasing of the relaxation time of the solution. The second contributing effect is the interaction of ionic species with the molecular dipoles of the system (ETA, H₂O): molecular dipoles in the neighborhood of ionic species, - solvated dipoles - experience an increase/decrease of relaxation time compared to those in the bulk of the ion-free dielectric. This happens to be the case of aqueous solution of NaCl where the relaxation time of H₂O dipoles in solvation shell of the anionic species (Cl⁻) is lower than that of pure water, contrary to that of Na⁺ where it's higher. The result is a slight reduction in the apparent relaxation time as a function of the salt concentration [16] as has been observed by Engenho [24] for aqueous saline solutions. Figure 2-36 shows the increase of the relaxation time with α ; so, either the viscosity increase had a greater effect on the relaxation time than ion-dipole interactions, or both effects contributed to hindering the dipolar movement and ultimately led to a slower relaxation mechanism. Results support the behavior of the dielectric loss factor in Figure 2-29 and Figure 2-30 where the dipolar relaxation gets shifted to lower relaxation frequencies with higher carbonation ratios and lower temperatures.

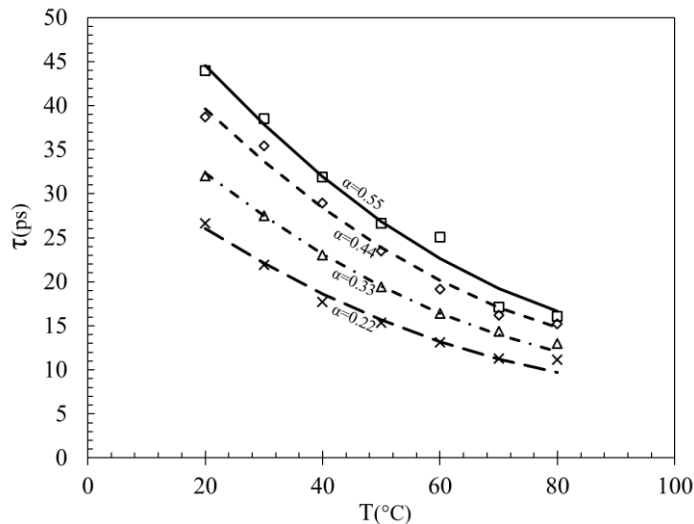


Figure 2-36: Apparent relaxation time (τ) of 30%wt. ETA as a function of T at different (α). (symbols), experimental; (lines), polynomial fittings

2.4.5.3 Relaxation time distribution parameter (n)

Parameter (n) is plotted in Figure 2-37 as a function of temperature and at different (α) for 30%wt. ETA loaded with CO_2 . It appears that (n) is inferior to unity over all conditions, implying the existence of a distribution of relaxation times of the solution [23]. Another observation is that (n) displays a parabola-like trend as a function of temperature, with the lowest value occurring at $40^\circ\text{C} < T < 50^\circ\text{C}$, and higher values at the T extremes. Buchner [16] observed a similar non-monotonous trend as a function of temperature for saline solutions over the range of 5 to 35°C .

Figure 2-37 reveals the monotonous decrease of (n) with greater carbonation ratios; the chemical absorption of CO_2 produces many ionic species, mainly ETACOO^- and ETAH^+ as predicted by the speciation model in Figure 2-17. The produced ionic species interact differently with the dipoles of the solution (water and ETA) resulting in broader distributions of relaxation times. Values of (n) obtained in this study are not uncommon, Nguenouhou [19] obtained values in the order of 0.8 for water and saccharose at 25°C , also Peyman [31] obtained a value of 0.83 for an aqueous saline solution (NaCl) having a molarity 4.44 M.

It appears that the general trend is a broader distribution of relaxation times with increasing solute concentration in the solvent phase. This trend is not respected when different dipolar species are mixed. Bao [44] observed an almost parabolic profile of (n) for an ethanol/water mixture as a function of the mole fraction of water with a value of unity at the pure component extremes. Kaatz [10] on the other hand instead of using the Cole-Cole model, used a Debye model with two relaxation mechanisms to fit the dielectric properties of binary mixtures of organic solvents at different compositions. He observed that the existence of several relaxation times was most pronounced at equimolar composition of the medium.

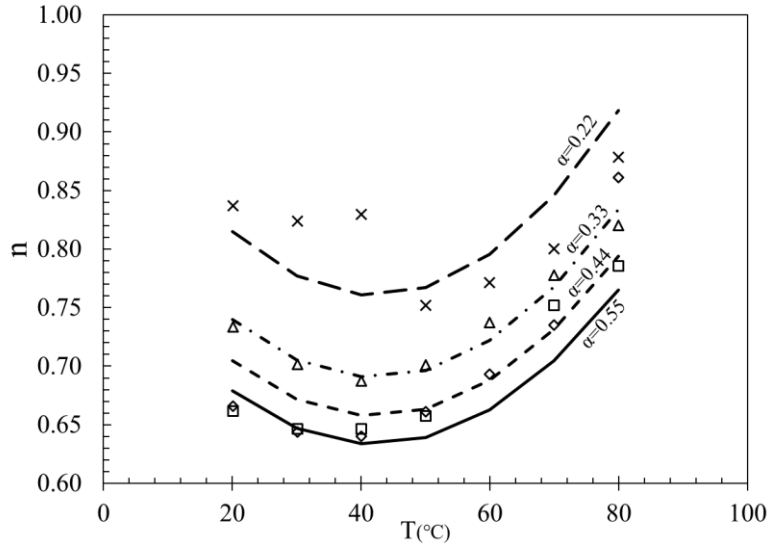


Figure 2-37: Distribution parameter of relaxation time function of T at different (α). (symbols), experimental; (lines), polynomial fittings

2.4.5.4DC electrical conductivity (σ)

The electrical conductivity of 30% wt. ETA solution is displayed in Figure 2-38 as a function of T and α . The electrical conductivity of loaded solutions are one to two orders of magnitude greater than for non-loaded ones (0.072 S/m at 20°C) [45] owing to ionic presence from the absorption reaction. It appears that (σ) increases linearly with temperature. Temperature rise decreases the viscosity of the solution [54] translating to greater ion mobility as per the Walden equation [60]. Additionally, increasing temperatures counteract the ion-pair association; the latter phenomenon occurs when the interionic distance decreases by the action of increased ionic concentrations, leading to creation of neutral ion pairs that are inert to the external E-field [63].

(σ) increases with CO₂ charge from $\alpha=0.22$ up to 0.44. The reason is the consumption of ETA dipoles to produce ionic species (ETAH⁺ and ETACOO⁻). For an increase of (α) from 0.44 to 0.55, σ experiences a lower increment of conductivity which suggests the commencement of ion-pair association. The effects of α and T on the electrical conductivity justify the experimental results in Figure 2-31 and Figure 2-32 respectively, where the dielectric dispersion curve tilts upward to higher values of ϵ'' - especially at 915MHz - with the increase of these two conditions.

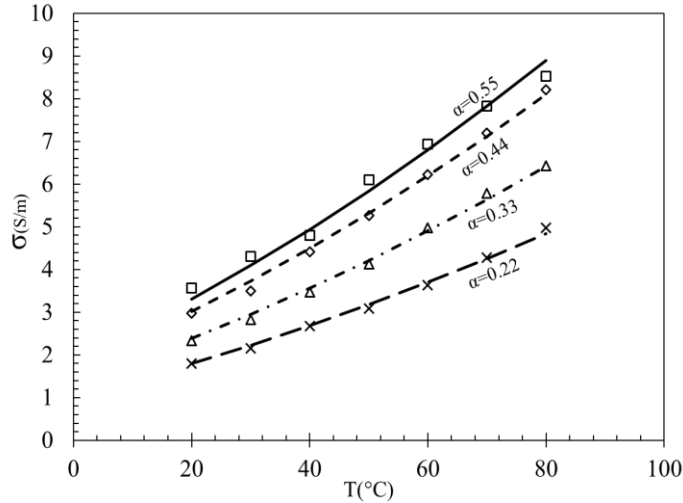


Figure 2-38: DC electrical conductivity of 30% wt. ETA solution function of T at different (α). (symbols), experimental; (lines), polynomial fittings

2.5 Summary

In this chapter the dielectric properties of 30% by weight aqueous ethanolamine solution were measured on the frequency range [915-2450] MHz at different temperatures and carbonation ratios using the open-ended coaxial probe technique. The dielectric dispersion parameters of the liquid were obtained by fitting the Cole-Cole relaxation model with a term to account for ionic conduction. Experimental and dielectric dispersion parameters were interpreted with the help of the chemical speciation obtained from the Kent-Eisenberg vapor liquid equilibrium model.

The dielectric properties (ϵ' , ϵ'') of 30% ETA solution with no CO₂ content are lower than those of water in the frequency range of measurement. The reasons being that pure ETA has a lower static dielectric constant and a weaker relaxation mechanism than distilled water. Temperature increase decreased the measured dielectric constant and loss factor by reason of weaker hydrogen bonding and faster relaxation mechanism respectively. The fitted Cole-Cole dispersion parameters were used to calculate the Kirkwood correlation factor. Obtained values are greater than unity indicating a reinforcement of the effective dipole moment of the solution. The fitted DC conductivity was almost identical to data from literature and it emphasizes the need to account for ionic conduction in relaxation model.

Dielectric properties of 30% ETA solutions with chemically dissolved CO₂ were measured and fitted with the Cole-Cole model. Across all experimental data the loss factor was elevated, and increased with greater temperatures and carbonation ratios. Dielectric loss by ionic conduction was found to be the dominating loss mechanism over the frequency range of measurement, although extrapolations of the Cole-Cole model showed that loss by dipolar rotation dominated at the relaxation frequency. In light of the high absorbance of the CO₂-loaded solution, the calculated penetration depths were in the order of a few millimeters and decreased with increasing frequency, temperature and carbonation ratios.

With regards to the fitted dispersion parameters, results indicate that the static dielectric constant (ϵ_0) decreases with temperature, but increases with the carbonation ratio. This happens despite decreases of dipolar concentration with higher CO₂ content as shown by the vapor liquid equilibrium model; the suspected reasons are either the deficit of the measurement points at frequencies that are sufficiently lower than the relaxation frequency of the solution or that the ionic species are able to relax under the ionic polarization mechanism. The apparent relaxation time of the solution decreases with temperature but increases with CO₂ loading by action of viscosity increase and ion-dipole interactions. The solution is shown to experience a broader distribution of relaxation times with increasing CO₂ loading while a non-monotonous behavior is observed with respect to temperature. The fitted DC conductivity of the solution was showed to be greater by at least one order of magnitude than for the 30%wt. ETA solution with no CO₂ loading, and increased with greater temperatures and carbonation ratios.

2.6 Appendix

2.6.1 Symbols

ϵ^*	Complex permittivity
ϵ'	Relative permittivity
ϵ''	Dielectric loss factor
f	Frequency (Hz)
f_r	Relaxation frequency (Hz)
ϵ_∞	Optical dielectric constant
ω	Angular Frequency (rd/s)
ϵ_0	Static dielectric constant (F/m)
τ	Relaxation time (s)
n	Cole-Cole Fitting parameter
β	Davidson-Cole model
σ	Electric conductivity (S/m)
n_∞	Refractive index
x	Mole fraction
χ	Susceptibility of medium
μ	Dipole moment (Debye)
M	Molar mass (g/mol)
ρ	Density (g/l)
k	Boltzmann constant
N	Avogadro's number (mol^{-1})
φ	Volume fraction
ϵ_0^*	Vacuum permittivity (F/m)
T	Temperature ($^\circ\text{C}$)
α	Carbonation ratio
c	Speed of light in vacuum (m/s)
K	Equilibrium constant
g_{eff}	Kirkwood correlation factor

2.6.2 Abbreviations

EM	Electromagnetic
ETA	Ethanolamine
DEA	Diethanolamine
HCO_3^-	Bicarbonate
CO_3^{2-}	Carbonate
DW	Deionized water
BaCl_2	Barium Chloride
BaCO_3	Barium Carbonate
AARD	Absolute Average Relative Deviation
CC	Cole-Cole dispersion model
KE	Kent-Eisenberg
VLE	Vapor-Liquid Equilibrium
MFC	Mass flow controller

2.6.3 Subscripts

e	Experimental
m	Model
mix	Mixture
t	Total
IC	Ionic Conduction
DR	Dipolar Rotation

2.6.4 Kent-Eisenberg VLE model

The equilibrium constants used in the K.E VLE model are presented in the equation below with the corresponding parameters for each equation.

$$\text{Equation form: } \ln(K) = \frac{a_1}{T} + a_2 \ln T + a_3$$

	a_1	a_2	a_3	T-Validity(K)	Reference
$K_1(\text{mol}/\text{dm}^3)^2$	-13445.9	-22.4773	140.932	273-498	[52]
$K_2(\text{mol}/\text{dm}^3)$	-12092.1	-36.7816	235.482	273-498	[52]
$K_3(\text{mol}/\text{dm}^3)$	-12431.7	-35.4819	220.067	273-498	[52]
$K_4(\text{mol}/\text{dm}^3)$	-3090.83	0	6.69425	298-413	[53]
$K_5(\text{mol}/\text{dm}^3)$	-5851.11	0	-3.3636	298-413	[53]

2.7 References

- McGurk, Stephen J., Claudia F. Martín, Stefano Brandani, Martin B. Sweatman, and Xianfeng Fan. 2017. Microwave swing regeneration of aqueous monoethanolamine for post-combustion CO₂ capture. *Applied Energy* 192: 126–133. <https://doi.org/10.1016/j.apenergy.2017.02.012>.
- Bougie, Francis, and Xianfeng Fan. 2017. Analysis of the Regeneration of Monoethanolamine Aqueous Solutions by Microwave Irradiation. *Energy Procedia* 142: 3661–3666. <https://doi.org/10.1016/j.egypro.2017.12.259>.
- Yang, J., H. Y. Tan, Q. X. Low, B. P. Binks, and J. M. Chin. 2015. CO₂ capture by dry alkanolamines and an efficient microwave regeneration process. *Journal of Materials Chemistry A* 3: 6440–6446. <https://doi.org/10.1039/C4TA06273F>.
- Patil, A.V., G.N. Shinde, and V.P. Pawar. 2012. Dielectric relaxation study of hydrogen bonded structures in ethanolamine with diethanolamine using TDR technique. *Journal of Molecular Liquids* 168: 42–46. <https://doi.org/10.1016/j.molliq.2012.01.017>.
- Jadhavpatil, Vandana, Prabhakar Undre, and Sangram Helambe. 2019. Dielectric Relaxation in Water-Ethanolamine Mixtures as a Function of Composition and Temperature. *Integrated Ferroelectrics* 202: 112–121. <https://doi.org/10.1080/10584587.2019.1674829>.
- Hsieh, Chi-Jui, Ji-Miao Chen, and Meng-Hui Li. 2007. Dielectric Constants of Aqueous Diisopropanolamine, Diethanolamine, N-Methyldiethanolamine, Triethanolamine, and 2-Amino-2-methyl-1-propanol Solutions. *Journal of Chemical & Engineering Data* 52: 619–623. <https://doi.org/10.1021/jc600515j>.
- Kemp, Daniel D., and Mark S. Gordon. 2008. An Interpretation of the Enhancement of the Water Dipole Moment Due to the Presence of Other Water Molecules. *The Journal of Physical Chemistry A* 112: 4885–4894. <https://doi.org/10.1021/jp801921f>.
- Undre, Prabhakar, P W Khirade, and S C Mehrotra. 2012. Microwave dielectric characterization of 1,2-diaminopropane, 1,3-diaminopropane and 3,3'-diaminodipropylamine. *Asian Journal of Spectroscopy*.
- Ikada, Eiji... [et al.]. 1969. Dielectric properties of ethanolamines. *Bulletin of the Institute for Chemical Research, Kyoto University* 46. Institute for Chemical Research, Kyoto University.
- Kaatze, U., and V. Lönnecke-Gabel. 1991. Dielectric spectroscopy on binary mixtures of organic solvents. *Journal of Molecular Liquids* 48: 45–60. [https://doi.org/10.1016/0167-7322\(91\)80025-Y](https://doi.org/10.1016/0167-7322(91)80025-Y).
- Sadiku, Matthew N. O. 2001. *Elements of electromagnetics*. 3rd ed. Oxford Series in Electrical and Computer Engineering. New York: Oxford University Press New York.
- Raju, G.G. 2003. *Dielectrics in electric fields*. Power Engineering. Taylor & Francis.
- 6 techniques for measuring dielectric properties. 2016. In *An introduction for agriculturalists and engineers*, 52–77. Warsaw, Poland: De Gruyter Open Poland. <https://doi.org/doi:10.1515/9783110455403-007>.
- Popov, Ivan, Paul Ben Ishai, Airat Khamzin, and Yuri Feldman. 2016. The mechanism of the dielectric relaxation in water. *Physical Chemistry Chemical Physics* 18: 13941–13953. <https://doi.org/10.1039/C6CP02195F>.
- Kaatze, U, and V Uhlendorf. The Dielectric Properties of Water at Microwave Frequencies By.

16. Buchner, Richard, Glenn T. Hefter, and Peter M. May. 1999. Dielectric Relaxation of Aqueous NaCl Solutions. *The Journal of Physical Chemistry A* 103: 1–9. <https://doi.org/10.1021/jp982977k>.
17. Bao, Jian-Zhong, Mays L. Swicord, and Christopher C. Davis. 1996. Microwave dielectric characterization of binary mixtures of water, methanol, and ethanol. *The Journal of Chemical Physics* 104: 4441–4450. <https://doi.org/10.1063/1.471197>.
18. Reynolds, J A, and J M Hough. 1957. Formulae for Dielectric Constant of Mixtures. *Proceedings of the Physical Society. Section B* 70: 769–775. <https://doi.org/10.1088/0370-1301/70/8/306>.
19. Kaatze, Udo. 1989. Complex permittivity of water as a function of frequency and temperature. *Journal of Chemical & Engineering Data* 34: 371–374. <https://doi.org/10.1021/jc00058a001>.
20. Lou, Jianfeng, T. Alan Hatton, and Paul E. Laibinis. 1997. Effective Dielectric Properties of Solvent Mixtures at Microwave Frequencies. *The Journal of Physical Chemistry A* 101: 5262–5268. <https://doi.org/10.1021/jp970731u>.
21. Winsor, Paul, and Robert H. Cole. 1982. Dielectric properties of electrolyte solutions. 1. Sodium iodide in seven solvents at various temperatures. *The Journal of Physical Chemistry* 86: 2486–2490. <https://doi.org/10.1021/j100210a049>.
22. Cole, Kenneth S. 1928. Electric impedance of suspensions of spheres. *Journal of General Physiology* 12: 29–36. <https://doi.org/10.1085/jgp.12.1.29>.
23. Cole, Robert H. 1955. On the Analysis of Dielectric Relaxation Measurements. *The Journal of Chemical Physics* 23: 493–499. <https://doi.org/10.1063/1.1742017>.
24. Bakam Nguenouho, O. S., A. Chevalier, B. Potelon, J. Benedicto, and C. Quendo. 2022. Dielectric characterization and modelling of aqueous solutions involving sodium chloride and sucrose and application to the design of a bi-parameter RF-sensor. *Scientific Reports* 12: 7209. <https://doi.org/10.1038/s41598-022-11355-w>.
25. Rodríguez-Moré, Zail Omán. Complex dielectric permittivity of rum and its mixtures with methanol, ethanol, and water at frequencies up to 15 GHz. *JOURNAL OF MICROWAVE POWER AND ELECTROMAGNETIC ENERGY*.
26. Davidson, D. W., and R. H. Cole. 2004. Dielectric relaxation in glycerol, propylene glycol, and n-Propanol. *The Journal of Chemical Physics* 19: 1484–1490. <https://doi.org/10.1063/1.1748105>.
27. Havriliak, S., and S. Negami. 2007. A complex plane analysis of α -dispersions in some polymer systems. *Journal of Polymer Science Part C: Polymer Symposia* 14: 99–117. <https://doi.org/10.1002/polc.5070140111>.
28. Buchner, R., J. Barthel, and J. Stauber. 1999. The dielectric relaxation of water between 0°C and 35°C. *Chemical Physics Letters* 306: 57–63. [https://doi.org/10.1016/S0009-2614\(99\)00455-8](https://doi.org/10.1016/S0009-2614(99)00455-8).
29. Falkenhagen, H. 1931. The Principal Ideas in the Interionic Attraction Theory of Strong Electrolytes. *Reviews of Modern Physics* 3: 412–426. <https://doi.org/10.1103/RevModPhys.3.412>.
30. STOGRYN, A. 1971. Equations for Calculating the Dielectric Constant of Saline Water 19: 733–736. <https://doi.org/10.1109/TMTT.1971.1127617>.
31. Peyman, A., C. Gabriel, and E.H. Grant. 2007. Complex permittivity of sodium chloride solutions at microwave frequencies. *Bioelectromagnetics* 28: 264–274. <https://doi.org/10.1002/bem.20271>.
32. Klein, Lawrence A, and Calvin T Swift. An Improved Model for the Dielectric Constant of Sea Water at Microwave Frequencies.
33. Gregory, A.P., and R.N. Clarke. 2006. A review of RF and microwave techniques for dielectric measurements on polar liquids. *IEEE Transactions on Dielectrics and Electrical Insulation* 13: 727–743. <https://doi.org/10.1109/TDEI.2006.1667730>.
34. Okoniewski, M., J. Anderson, E. Okoniewska, K. Caputa, and S.S. Stuchly. 1995. Further analysis of open-ended dielectric sensors. *IEEE Transactions on Microwave Theory and Techniques* 43: 1986–1989. <https://doi.org/10.1109/22.402291>.
35. Cilia, Federico, Simona Di Meo, Lourdes Farrugia, Julian Bonello, Iman Farhat, Evan Joe Dimech, Marco Pasian, and Charles V Sammut. 2022. Techniques for temperature-dependent dielectric measurements: a review. In *2022 Microwave Mediterranean Symposium (MMS)*, 1–4. Pizzo Calabro, Italy: IEEE. <https://doi.org/10.1109/MMS55062.2022.9825550>.
36. Misra, D., M. Chhabra, B.R. Epstein, M. Microtznik, and K.R. Foster. 1990. Noninvasive electrical characterization of materials at microwave frequencies using an open-ended coaxial line: test of an improved calibration technique. *IEEE Transactions on Microwave Theory and Techniques* 38: 8–14. <https://doi.org/10.1109/22.44150>.
37. Keysight 85070E: Dielectric Probe kit 200 MHz to 50 GHz. 2017. Keysight Technologies.
38. Shen, Keh Perng, and Meng Hui Li. 1992. Solubility of carbon dioxide in aqueous mixtures of monoethanolamine with methyldiethanolamine. *Journal of Chemical & Engineering Data* 37: 96–100. <https://doi.org/10.1021/jc00005a025>.

39. Evjen, Sigvart, Iris Renate Krokvik, Anne Fiksahl, and Hanna Knuutila. 2017. Analysis of the Protonation Constant (pKa) and Absorption Properties of Non-alkanolamines. *Energy Procedia* 114: 2590–2598. <https://doi.org/10.1016/j.egypro.2017.03.1416>.
40. Kim, Inna, and Hallvard F. Svendsen. 2007. Heat of Absorption of Carbon Dioxide (CO₂) in Monoethanolamine (MEA) and 2-(Aminoethyl)ethanolamine (AEEA) Solutions. *Industrial & Engineering Chemistry Research* 46: 5803–5809. <https://doi.org/10.1021/ie0616489>.
41. Weiland, Ralph H., and Olev. Trass. 1969. Titrimetric determination of acid gases in alkali hydroxides and amines. *Analytical Chemistry* 41: 1709–1710. <https://doi.org/10.1021/ac60281a024>.
42. Aronu, Ugochukwu E., Shahla Gondal, Erik T. Hessen, Tore Haug-Warberg, Ardi Hartono, Karl A. Hoff, and Hallvard F. Svendsen. 2011. Solubility of CO₂ in 15, 30, 45 and 60 mass% MEA from 40 to 120°C and model representation using the extended UNIQUAC framework. *Chemical Engineering Science* 66: 6393–6406. <https://doi.org/10.1016/j.ces.2011.08.042>.
43. Jou, Fang Yuan, Alan E. Mather, and Frederick D. Otto. 1982. Solubility of hydrogen sulfide and carbon dioxide in aqueous methyldiethanolamine solutions. *Industrial & Engineering Chemistry Process Design and Development* 21: 539–544. <https://doi.org/10.1021/i200019a001>.
44. Bao, J.-Z., C.C. Davis, and R.E. Schmukler. 1993. Impedance spectroscopy of human erythrocytes: system calibration, and nonlinear modeling. *IEEE Transactions on Biomedical Engineering* 40: 364–378. <https://doi.org/10.1109/10.222329>.
45. Ju, Huitian, Walid ElMoudir, Ahmed Aboudheir, and Nader Mahinpey. 2018. Density, Viscosity, Refractive Index, and Electrical Conductivity of Degraded Monoethanolamine Solutions at Standard Temperatures. *Journal of Chemical & Engineering Data* 63: 1969–1976. <https://doi.org/10.1021/acs.jced.7b01101>.
46. Deshmukh, D, and A E Mather. A MATHEMATICAL MODEL FOR EQUILIBRIUM SOLUBILITY OF HYDROGEN SULFIDE AND CARBON DIOXIDE IN AQUEOUS ALKANOLAMINE SOLUTIONS: 8.
47. Suleman, Humbul, Abdulhalim Shah Maulud, Philip Loldrup Fosbøl, Qazi Nasir, Rizwan Nasir, Muhammad Zubair Shahid, Muhammad Nawaz, and Mustafa Abunowara. 2021. A review of semi-empirical equilibrium models for CO₂-alkanolamine-H₂O solutions and their mixtures at high pressure. *Journal of Environmental Chemical Engineering* 9: 104713. <https://doi.org/10.1016/j.jece.2020.104713>.
48. Aboudheir, Ahmed, Paitoon Tontiwachwuthikul, Amit Chakma, and Raphael Idem. 2003. Kinetics of the reactive absorption of carbon dioxide in high CO₂-loaded, concentrated aqueous monoethanolamine solutions. *Chemical Engineering Science* 58: 5195–5210. <https://doi.org/10.1016/j.ces.2003.08.014>.
49. Edali, Mohamed, Ahmed Aboudheir, and Raphael Idem. 2009. Kinetics of carbon dioxide absorption into mixed aqueous solutions of MDEA and MEA using a laminar jet apparatus and a numerically solved 2D absorption rate/kinetics model. *International Journal of Greenhouse Gas Control* 3: 550–560. <https://doi.org/10.1016/j.ijggc.2009.04.006>.
50. Jamal, Aqil, Axel Meisen, and C. Jim Lim. 2006. Kinetics of carbon dioxide absorption and desorption in aqueous alkanolamine solutions using a novel hemispherical contactor—I. Experimental apparatus and mathematical modeling. *Chemical Engineering Science* 61: 6571–6589. <https://doi.org/10.1016/j.ces.2006.04.046>.
51. Hu, W, and A Chakma. zyzxy Modelling of Equilibrium Solubility of CO, and H₂S in Aqueous Diglycolamine (DGA) Solutions: 3.
52. Edwards, Thomas J., G. Maurer, John Newman, and John M. Prausnitz. 1978. Vapor-Liquid Equilibria in a Multicomponent Aqueous Solutions of Volatile Weak Electrolytes: 966–976.
53. Kent, R.L., and B. Eisenberg. 1976. Better data for amine treating: 87–90.
54. Weiland, Ralph H., John C. Dingman, D. Benjamin Cronin, and Gregory J. Browning. 1998. Density and Viscosity of Some Partially Carbonated Aqueous Alkanolamine Solutions and Their Blends. *Journal of Chemical & Engineering Data* 43: 378–382. <https://doi.org/10.1021/je9702044>.
55. Jakobsen, Jana Poplsteinova, Jostein Krane, and Hallvard F. Svendsen. 2005. Liquid-Phase Composition Determination in CO₂-H₂O-Alkanolamine Systems: An NMR Study. *Industrial & Engineering Chemistry Research* 44: 9894–9903. <https://doi.org/10.1021/ie048813+>.
56. Sartori, Guido, and David W. Savage. 1983. Sterically hindered amines for carbon dioxide removal from gases. *Industrial & Engineering Chemistry Fundamentals* 22: 239–249. <https://doi.org/10.1021/i100010a016>.
57. Gadani, D H, V A Rana, S P Bhatnagar, A N Prajapati, and A D Vyas. 2012. Effect of salinity on the dielectric properties of water. *APPL PHYS* 50: 7.

58. Solsona, F J Arcega, and J M Fornies-Marquina. 1982. Dielectric properties of ten primary amines at microwave frequencies as a function of temperature. *Journal of Physics D: Applied Physics* 15: 1783–1793. <https://doi.org/10.1088/0022-3727/15/9/024>.
59. Kirkwood, John G. 2004. The dielectric polarization of polar liquids. *The Journal of Chemical Physics* 7: 911–919. <https://doi.org/10.1063/1.1750343>.
60. Subbiah, Balaji, and Ken R. Morison. 2018. Electrical conductivity of viscous liquid foods. *Journal of Food Engineering* 237: 177–182. <https://doi.org/10.1016/j.jfoodeng.2018.05.037>.
61. Schwartz, Arnold C. 1976. J. B. Hasted, aqueous dielectrics (serie: Studies in chemical physics). VII, 302 S., 113 abb., 31 tab., london 1973: Chapman and hall. £ 5.75. *Journal of Basic Microbiology* 16: 567–567.
62. Hubbard, J B, L Onsager, W M van Beek, and M Mandel. 1977. Kinetic polarization deficiency in electrolyte solutions. *Proceedings of the National Academy of Sciences* 74: 401–404. <https://doi.org/10.1073/pnas.74.2.401>.
63. Zhang, Weitao, Xia Chen, Yan Wang, Lianying Wu, and Yangdong Hu. 2020. Experimental and Modeling of Conductivity for Electrolyte Solution Systems. *ACS Omega* 5: 22465–22474. <https://doi.org/10.1021/acsomega.0c03013>.

3 Experimental study of the CO₂ desorption process under microwaves

3.1 Introduction

The previous chapter focused on characterizing the MW-solvent interactions by performing measurements of dielectric properties at different conditions. As the solvent has been deemed a strong absorber of MW irradiation, the next step is to study the process of MW-assisted desorption at the local scale. As stated before, one of the main objectives of this work is to operate desorption from CO₂ rich solvents under MW irradiation at the scale of hollow fiber membrane module. The latter is composed of a multitude of hollow fiber capillaries, so it is deemed necessary to understand the desorption at the scale of a single fiber to have insights into the operation of a bundle of fibers, i.e. membrane module. This entails studying experimentally the influence of the operating variables on the desorption flux, and modeling the desorption process under MW irradiation. While the next chapter treats the modeling aspect of the study, this chapter focuses on the experimental characterization of CO₂ desorption from a solvent circulating in the lumen side of a single millimetric PTFE porous hollow fiber membrane under MW irradiation. The effects of carbonation ratio, temperature, and solvent flow rate, and gas flow rate on desorption fluxes were studied and quantified within the framework of a plan of experimental design. The experimental desorption data generated in this chapter also serve in validating the numerical modeling approach of the next chapter. The layout of this chapter is as follows:

3.2- Preamble: electromagnetic propagation in a rectangular waveguide: The fundamentals of MW propagation in a rectangular waveguide are summarized, we start from Maxwell's equations to derive the possible modes of MW propagation and the corresponding electric and magnetic field equations. Examples are given for both modes of propagation, transverse magnetic and transverse electric.

3.3- Operating CO₂ desorption under MW at the scale of a porous fiber: The set-up used to study the CO₂ desorption at the single fiber scale under MW irradiation is presented, with great emphasis being placed on the design of the MW applicator. The methodology of design of experimental plan is presented along with the corresponding regression equation that correlates the desorption performance to the operating conditions.

3.4- Results: Desorption flux and the outlet temperature profiles of the solvent are presented as a function of time, for different experimental conditions under quasi-steady state condition. After obtain the average desorption fluxes, experimental data were regressed which allows obtaining the regression coefficients. Coefficients representing the effect of the controlled variables and their interactions on the response, were plotted against one another to quantify the degree of influence on the desorption flux. In the last subsection, experimental desorption

rates data obtained locally under microwave irradiation were compared to those derived from literature studies reporting isothermal desorption performances using membrane contactors.

3.2 Preamble: electromagnetic propagation in a rectangular waveguide

Waveguides are metallic structures that come in different shapes and size, they are used to guide electromagnetic waves from one point to another with minimal losses and wave distortion. Waveguides are a form of transmission lines but have the advantage of having very low losses with respect to typical coaxial cables. This advantage is further highlighted as the frequency of the electromagnetic irradiation increases and the skin effect in the coaxial cable starts to pose very high resistive losses. The source of what follows in this section is the book (elements of electromagnetics) [1].

As with unguided propagations, EM irradiation propagating in a waveguide is described by Maxwell’s equations - be found in section (2.2.2) of this manuscript. These equations can be rearranged to obtain the partial differential equations designated as the “wave equation” for the electric field, as presented in (3.1) and (3.2) respectively. The subscript “s” denotes a phasor quantity i.e. ($\vec{E}_s = E_0 \angle \theta_E \vec{a}_E$) while ($\vec{H}_s = H_0 \angle \theta_H \vec{a}_H$). If the medium inside the waveguide is taken to be a lossless dielectric, then the wavenumber (k) can be expressed as shown in equation (3.3), with (ω) being the angular frequency, (μ) permeability, and (ϵ) the permittivity of the dielectric medium. We note that this expression of (k) – Wavenumber (rd/m) - can be obtained by substituting ($\sigma = 0$) in equations (2.21) and (2.22).()

$$\nabla^2 \vec{E}_s + k^2 \vec{E}_s = 0 \tag{3.1}$$

$$\nabla^2 \vec{H}_s + k^2 \vec{H}_s = 0 \tag{3.2}$$

$$k = \omega \sqrt{\mu \epsilon} \tag{3.3}$$

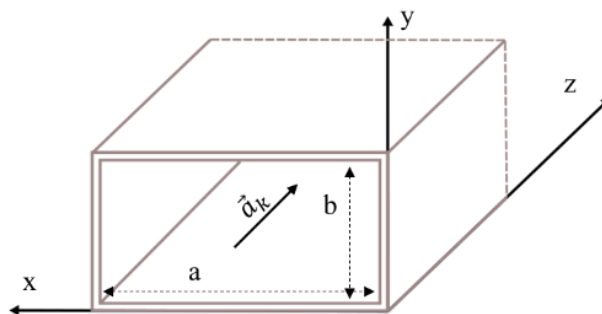


Figure 3-1: EM propagation following (\vec{a}_k) parallel to the z-axis in a rectangular waveguide of dimensions (a x b). Vacuum is assumed inside ($\epsilon'' = 0$)

We consider the case of EM propagation in lossless vacuum - ($\epsilon'' = 0$) - in a rectangular waveguide following the the z-direction - Figure 3-1. The wave equations for the E-field and the H-field along the z-axis are expressed in Cartesian coordinates in (3.4) and (3.5) respectively.

$$\frac{\partial^2 E_{zs}}{\partial x^2} + \frac{\partial^2 E_{zs}}{\partial y^2} + \frac{\partial^2 E_{zs}}{\partial y^2} + k^2 E_{zs} = 0 \quad (3.4)$$

$$\frac{\partial^2 H_{zs}}{\partial x^2} + \frac{\partial^2 H_{zs}}{\partial y^2} + \frac{\partial^2 H_{zs}}{\partial y^2} + k^2 H_{zs} = 0 \quad (3.5)$$

Given that E_{zs} and H_{zs} are both functions of (x, y, z) , and upon applying a separation of spatial variables, we get the general solutions of both (3.4) and (3.5) as shown in (3.6) and (3.7) respectively; with (A_i) , (B_i) , (k_i) , and (γ) being constants to be determined.

$$E_{zs}(x, y, z) = [A_1 \cos(k_x x) + A_2 \sin(k_x x)][A_3 \cos(k_y y) + A_4 \sin(k_y y)]e^{-\gamma z} \quad (3.6)$$

$$H_{zs}(x, y, z) = [B_1 \cos(k_x x) + B_2 \sin(k_x x)][B_3 \cos(k_y y) + B_4 \sin(k_y y)]e^{-\gamma z} \quad (3.7)$$

As the general expressions of both (E_{zs}) and (H_{zs}) have been determined, the remaining components of the electric field (E_{xs}, E_{ys}) and the magnetic field (H_{xs}, H_{ys}) can be expressed in terms of these two by applying Faraday's law and Ampere-Maxwell's law. The remaining field components are expressed in (3.8)-(3.11) with the constants (h, k, k_x, k_y) being related as per (3.12) with (k_x) and (k_y) being the wavenumber projection on the (x) and (y) direction.

$$E_{xs} = -\frac{\gamma}{h^2} \frac{\partial E_{zs}}{\partial x} - \frac{j\omega\mu}{h^2} \frac{\partial H_{zs}}{\partial y} \quad (3.8)$$

$$E_{ys} = -\frac{\gamma}{h^2} \frac{\partial E_{zs}}{\partial y} - \frac{j\omega\mu}{h^2} \frac{\partial H_{zs}}{\partial x} \quad (3.9)$$

$$H_{xs} = \frac{j\omega\varepsilon}{h^2} \frac{\partial E_{zs}}{\partial y} - \frac{\gamma}{h^2} \frac{\partial H_{zs}}{\partial x} \quad (3.10)$$

$$H_{ys} = \frac{j\omega\varepsilon}{h^2} \frac{\partial E_{zs}}{\partial x} - \frac{\gamma}{h^2} \frac{\partial H_{zs}}{\partial y} \quad (3.11)$$

$$h^2 = k^2 + \gamma^2 = k_x^2 + k_y^2 \quad (3.12)$$

Given that all field components can be expressed in terms of (H_{zs}) and (E_{zs}) we distinguish the different possible values of these two quantities that produce different EM field mappings in the waveguide. The transverse electromagnetic (TEM) mode of propagation requires that the E-field and the H-field have no components on the direction of propagation – taken as \vec{a}_z in this case – therefor (E_{zs}) and (H_{zs}) would be required to have null values. Substituting these values in equations (3.9)-(3.11), we realize that all E-field components vanish, therefor we conclude that TEM propagation in a rectangular waveguide is not possible. We move on to enumerate the other possible propagation modes in the next sections.

3.2.1 TM mode

The transverse magnetic mode (TM) occurs when the magnetic field has no projection along the direction of propagation, i.e. $(H_{zs} = 0 \ \& \ E_{zs} \neq 0)$. (E_{zs}) being tangential to the waveguide walls at $(x=0, x=a)$ and $(y=0, y=b)$, it follows that it is null at regions of proximity to the waveguide walls. This is due to the fact that an E-field cannot exist in metallic conductors which forces the tangential component of the E-field to vanish in the interior of the waveguide. Applying the boundary conditions to (3.6) leads to the expression of the E-field propagation in a

rectangular waveguide (3.13) with (E_0) being the magnitude of the E-field. The expression is similar to that for the case of non-guided EM propagation where the phase of the E-field varies as a function of distance (z) .

$$E_{zs}(x, y, z) = E_0 \sin(k_x x) \sin(k_y y) e^{-\gamma z} \quad (3.13)$$

Similarly, the wavenumbers (k_x) and (k_y) were determined by utilizing the boundary conditions, and are presented in (3.14) and (3.15). (m) and (n) are positive integers, they represent the number of half cycles of the electric field in the waveguide across the x -axis and the y -axis respectively. The combination of (m,n) denote a different spacial patterns of the electric field and magnetic field.

$$k_x = m\pi/a \quad (3.14)$$

$$k_y = n\pi/b \quad (3.15)$$

(TM_{mn}) denotes a transverse magnetic propagation in a waveguide with mode (m,n) - or patterns of the E-field and magnetic field, (E_{zs}) may therefore be expressed as shown in (3.16).

$$E_{zs}(x, y, z) = E_0 \sin\left(\frac{m\pi x}{a}\right) \sin\left(\frac{n\pi y}{b}\right) e^{-\gamma z} \quad (3.16)$$

The mode through which the EM waves propagate is determined by the $[m, n]$ constants. It is worth noting that for $[m, n]$ values being: $[0, 0]$; $[m, 0]$; and $[0, n]$ EM propagation is not possible hence (E_{zs}) vanishes while (H_{zs}) is already taken as null. For the case where both (m) and (n) are different from zero, we obtain expressions for the remaining components of the E-field and H-field in (3.17)-(3.20) respectively.

$$E_{xs} = -\frac{\gamma}{h^2} \left(\frac{m\pi}{a}\right) E_0 \cos\left(\frac{m\pi x}{a}\right) \sin\left(\frac{n\pi y}{b}\right) e^{-\gamma z} \quad (3.17)$$

$$E_{ys} = -\frac{\gamma}{h^2} \left(\frac{m\pi}{a}\right) E_0 \sin\left(\frac{m\pi x}{a}\right) \cos\left(\frac{n\pi y}{b}\right) e^{-\gamma z} \quad (3.18)$$

$$H_{xs} = \frac{j\omega\epsilon}{h^2} \left(\frac{n\pi}{b}\right) E_0 \sin\left(\frac{m\pi x}{a}\right) \cos\left(\frac{n\pi y}{b}\right) e^{-\gamma z} \quad (3.19)$$

$$H_{ys} = -\frac{j\omega\epsilon}{h^2} \left(\frac{m\pi}{a}\right) E_0 \cos\left(\frac{m\pi x}{a}\right) \sin\left(\frac{n\pi y}{b}\right) e^{-\gamma z} \quad (3.20)$$

In the expressions of the E-field components in (3.17)-(3.20), we notice that the only ambiguity remaining pertains to the constant (γ) . We distinguish the different of cases of (γ) expressed in (3.21) – also derived from (3.12).

$$\gamma = \sqrt{(m\pi/a)^2 + (n\pi/b)^2 - \omega^2\mu\epsilon} \quad (3.21)$$

The nature of (γ) as being either null, a positive decimal, or a complex number is what determines whether propagation happens or not. For clarification, propagation is defined by the ability of the EM wave to traverse the rectangular waveguide, or for EM energy to propagate. In mathematical terms, this leads to a phase difference between two points along the z -direction that are separated. If we start by assuming the numbers of half-cycles (m) and (n) , the value of (γ) is then dependent on the angular frequency (ω) . The first case of (γ) is when it vanishes by equating (3.21) to zero. This allows the calculation of what is called the cut-off frequency (f_c) as expressed in (3.22), and the cut-off wavelength (λ_c) expressed in (3.23).

$$f_c = \frac{1}{2\sqrt{\mu\epsilon}} \sqrt{(m/a)^2 + (n/b)^2} \quad (3.22)$$

$$\lambda_c = \frac{2}{\sqrt{(m/a)^2 + (n/b)^2}} \quad (3.23)$$

From here on out (γ) can be expressed in terms of the cut-off frequency (f_c) as shown below in (3.24).

$$\gamma = (2\pi\sqrt{\mu\epsilon})\sqrt{f_c^2 - f^2} \quad (3.24)$$

For the case of γ being a positive decimal, this requires that ($f_c > f$), hence when considering (3.16) to (3.20), all E-field and H-field components would vanish following the exponential ($e^{-\gamma z}$). However, we have already assumed the lossless character of the dielectric inside the waveguide ($\epsilon'' = 0$) - for a detailed discussion refer to chapter (2) - so it is not possible for the wave to be attenuated by dissipation, rather, the attenuation is caused by the inability of the wave to propagate in the waveguide. We conclude that if the frequency of the wave is lower than the cut-off frequency the wave cannot propagate.

The last case is for (γ) being a purely imaginary number when the condition ($f_c < f$) is replaced in (3.24). In this case the EM field components do not vanish but experience a change in phase as a function of (z) similar to the case of unguided propagation in a lossless dielectric (3.16). The constant (γ) equals the guided wavenumber (β), which is expressed in (3.25) with (β') being the wavenumber for unguided EM propagation – i.e. waves propagating in free space. As a small recap, the cutoff frequency is the limit where EM irradiation with with frequency ($f < f_c$) cannot propagate, while those having ($f > f_c$) can propagate.

$$\beta = \beta' \sqrt{1 - (f_c/f)^2} \quad (3.25)$$

Other wave characteristics as the guided velocity (u) and the guided wavelength (λ) can be calculated from (3.26).

$$u = \frac{\omega}{\beta} \quad , \quad \lambda = \frac{2\pi}{\beta} \quad (3.26)$$

As an example, the instantaneous E-field magnitude for an EM wave propagating in the TM_{11} mode was plotted in Figure 3-2 and Figure 3-3 for the XY and XZ planes respectively. EM waves propagate at a frequency ($f=5\text{GHz}$), higher than the cut-off frequency ($f_c=3.9\text{GHz}$) for the chosen classical waveguide (WR340) with dimensions ($a \times b = 87 \times 43\text{mm}$). Figure 3-2 shows that the E-field peaks at the middle of the waveguide section, hence (E_{zs}) peaks at ($x = a/2$) and at ($y = b/2$), while both (E_{xs}) and (E_{ys}) vanish at this point. The E-field norm - defined as $\left[\sqrt{\|E_{xs}\|^2 + \|E_{ys}\|^2 + \|E_{zs}\|^2} \right]$ - vanishes at corners of the waveguide hence all of the E-field components vanish at these locations. Figure 3-3 shows the cyclic variation as a function of the distance (z) the distance between 2 peaks being equal to ($\lambda/2$).

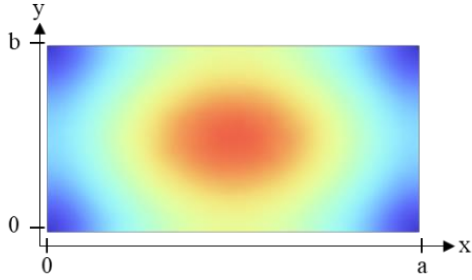


Figure 3-2: E-field norm in a XY-plane of rectangular waveguide (WR340) for a TM_{11} propagation at 5GHz

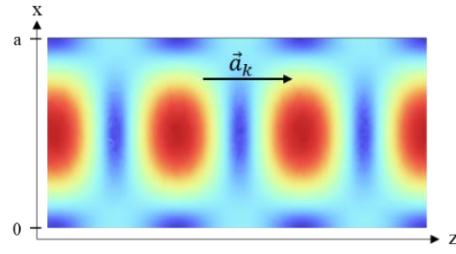


Figure 3-3: E-field norm in a XZ-plane of rectangular waveguide (WR340) for a TM_{11} propagation at 5GHz, $y=b/2$.

3.2.2 TE mode

Besides the TM mode, the transverse electric mode (TE) is the other possible propagation mode characterized by the conditions of ($E_{zs} = 0$ & $H_{zs} \neq 0$). Following a similar methodology as in section (3.2.1), we can obtain the expressions of the E-field and the H-field components in (3.27) - (3.28) and (3.29) - (3.31) respectively. The guided velocity (u), wavenumber (β) and the wavelength (λ) are expressed in an identical manner to those obtained for the TM mode.

$$E_{xs} = \frac{j\omega\mu}{h^2} \left(\frac{n\pi}{b}\right) H_0 \cos\left(\frac{m\pi x}{a}\right) \sin\left(\frac{n\pi y}{b}\right) e^{-\gamma z} \quad (3.27)$$

$$E_{ys} = \frac{j\omega\mu}{h^2} \left(\frac{n\pi}{b}\right) H_0 \sin\left(\frac{m\pi x}{a}\right) \cos\left(\frac{n\pi y}{b}\right) e^{-\gamma z} \quad (3.28)$$

$$H_{zs} = H_0 \cos\left(\frac{m\pi x}{a}\right) \cos\left(\frac{n\pi y}{b}\right) e^{-\gamma z} \quad (3.29)$$

$$H_{xs} = \frac{j\beta}{h^2} \left(\frac{m\pi}{a}\right) H_0 \sin\left(\frac{m\pi x}{a}\right) \cos\left(\frac{n\pi y}{b}\right) e^{-\gamma z} \quad (3.30)$$

$$H_{ys} = \frac{j\beta}{h^2} \left(\frac{n\pi}{b}\right) H_0 \cos\left(\frac{m\pi x}{a}\right) \sin\left(\frac{n\pi y}{b}\right) e^{-\gamma z} \quad (3.31)$$

For the case of propagating EM irradiation, the lowest possible mode – also called fundamental mode – occurs when ($m=1$) and ($n=0$); this mode has the lowest cut-off frequency (f_c). The field components (E_{xs}) and (H_{ys}) vanish in this mode, while (E_{ys}) and (H_{xs}) both have a single half-cycle variation following the y-axis and x-axis respectively.

EM applications are not limited to telecommunication, but extend to industrial [2], food and home use [3] as well as chemical processes [4]. The main frequencies assigned to these applications are the (433, 896, 915, 2375, 2450 MHz). For the case of industrial or home use of MWs, waveguide dimensions are fixed so as to allow for the exclusive propagation of the fundamental mode (TE_{10}) as is the case with the (WR340) standard waveguide that is compatible with the 2375 and 2450 MHz frequencies. The characteristics of MW irradiation propagating in the fundamental (TE_{10}) at 2450MHz are given in Table 3-1. Note that primed quantities represent unguided characteristics of MW irradiation.

a (mm)	86
b (mm)	43
f_c (GHz)	1.74
u' (m/s) $\times 10^8$	3
u (m/s) $\times 10^8$	4.269
β' (rd/m)	51.31
β (rd/m)	36.05
λ' (cm)	12.24
λ (cm)	17.42

Table 3-1: Characteristics of (TE₁₀) mode in a WR340 waveguide at 2.45GHz

To visualize this mode, the E-field magnitude – composed exclusively of (E_{ys}) – is represented in Figure 3-4 and Figure 3-5 in the XY-plane and the XZ-plane respectively. Figure 3-4 shows the single half-cycle of the instantaneous E-field across the x-axis where the E-field vanishes near the waveguide boundaries and peaks at ($x = a/2$) - hence the half-cycle ($m=1$). The instantaneous E-field shows no variation as a function of the y-coordinate, that is because there is not a single half-cycle across this dimension ($n=0$). Figure 3-5 shows that instantaneous E-field norm as cyclic as a function of (z) where each two peaks are separated by a distance of ($\lambda/2=87.1$ mm).

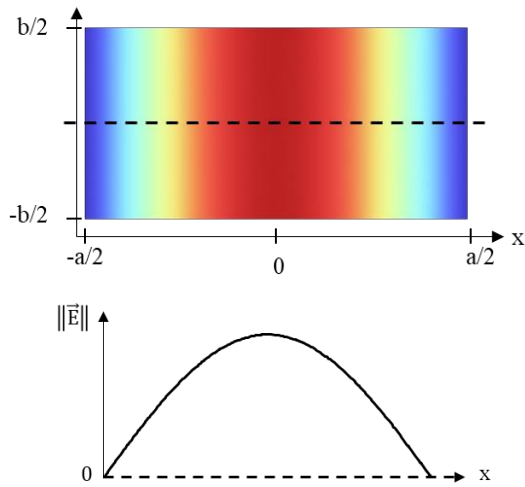


Figure 3-4: E-field plot in a XY-plane of rectangular waveguide for the propagation mode TE₁₀

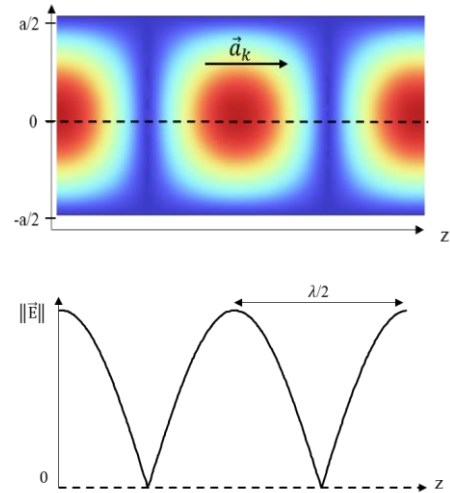


Figure 3-5: E-field plot in a XZ-plane of rectangular waveguide for the propagation mode TE₁₀

3.3 Operating CO₂ desorption under MW at the scale of a porous fiber

3.3.1 Experimental set-up

CO₂ desorption tests were carried out at the scale of a single porous fiber using the set-up shown in Figure 3-6. The set-up is composed of a solid-state microwave generator (MKS Alter® products - model SG524, P_{max}-450W,

2400-2500MHz, Italy) which produces MWs that are transmitted through a coaxial cable. Microwaves propagate in the waveguide exclusively under the fundamental mode (TE_{10}), passing by an automatic impedance three-stub tuner (AI3S) (HOMER-Series STHT 2.45-GHz Autotuner, S-Team, Slovakia) that can be used for impedance matching and minimization of reflected power, but here it was used exclusively to provide measurements of the incident and reflected microwave powers within the waveguide. The microwave applicator is composed of a standard WR340 standard waveguide section that is drilled to allow for a porous fiber to be inserted following the small dimension of the waveguide ($b=43\text{mm}$). The characteristics of the hollow fiber are shown Table 3-2 of which the porosity and the mean pore size were determined using the technique of mercury porosimetry. The fiber was placed concentrically in a quartz tube of the following dimensions (length x inner diameter x outer diameter = 57 x 16 x 20 mm) and the ensemble (fiber + quartz shell) was placed parallel to the small dimension of the waveguide ($b=43\text{ mm}$)- more details on cavity design in section (3.3.2). A sliding short circuit piston (SSC) (PCCMWR340L130, Sairem) was used for impedance matching to decrease the microwave reflected power from the load towards the generator.

Material ^s	PTFE
Length – l (mm)	113
Porosity ^m	0.45
Mean pore size ^m - D_m (μm)	0.1373
Inner diameter ^s - d_i (mm)	4.3
Outer diameter ^s - d_o (mm)	6

Table 3-2: Hollow fiber characteristics. Note: (m) denotes measured characteristics while (s) denotes those specified by the supplier

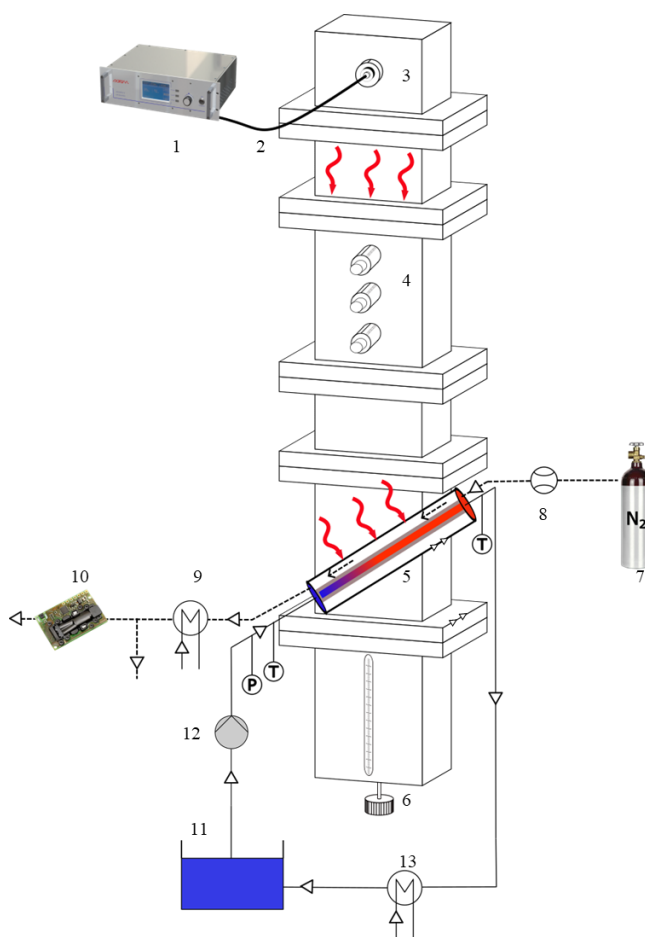


Figure 3-6: Experimental set-up for MW-assisted CO₂ desorption from 30%ETA solvent in a hollow fiber. 1: microwave generator; 2: coaxial cable; 3: coaxial line - waveguide transition; 4: automatic three-stub impedance tuner; 5: microwave applicator; 6: sliding short circuit; 7: N₂ bottle; 8: flow meter; 9: condenser; 10: CO₂ sensor; 11: solvent reservoir; 12: peristaltic pump; 13: heat exchanger

A stream of 30%wt. ETA solution (Sigma Aldrich $\geq 99.7\%$) with a predetermined CO₂ loading was made to circulate through the applicator in a closed loop configuration by action of a peristaltic pump connected to a reservoir of volume (500 mL). The solvent is introduced into the MW applicator through the fiber lumen as shown in Figure

3-7, when inside the cavity it would absorb microwave irradiation, consequently temperature increases favors chemical desorption of CO₂. The incident MW power was adjusted manually to achieve a specific outlet temperature of the solvent. The exiting stream is recirculated back to the reservoir after passing by a water cooler that lowers its temperature to ambient levels. The system therefore operates in a near steady-state regarding the temperature of the solvent throughout the circuit. The CO₂ load of the solvent in reservoir decreases with time due to continuous desorption, however the decrease was minor over the duration of the experiment (10 - 20 mins). Solvent temperature was recorded before entry into the cavity and right after exiting using two thermocouples. The N₂ flow on the annular side sweeps the CO₂ desorbed from the solvent Figure 3-8– similarly to a sweeping gas membrane distillation configuration [5]. The N₂ flowrate supplied by a bottle (Air Liquide – purity ≥ 99.8%), was measured by a rotameter of detection range (1.5 - 500 ± 0.15 mL/s). Water vapor contained in the outlet gas stream was condensed thanks to water cooled before analyzing its CO₂ content using an infrared analyzer (Sensirion SCD30, measurement range [400-40000] ± 30 ppm). The CO₂ desorption flux (J_{CO_2} – mol / m² s) was calculated from equation (1.36); N_{N_2} being the molar flow rate of N₂-gas (mol/s), (d_i) being the internal diameter of the fiber (m), and (l) the fiber length in (m), (Y) is the mole fraction of CO₂ in the gas phase relative to the inert species and is expressed in terms of the mole fraction (y_{CO_2}), measured by the CO₂ sensor, shown in (3.33). The molar flow rate (N_{N_2}) was calculated according to the ideal gas law in (3.34), with (P) being the ambient pressure (bar), (\dot{V}) the N₂ volumetric flow rate (L/s), (R) is the ideal gas constant (atm.L/mol.s) , and (T) is the gas temperature (K).

$$J_{CO_2} = [(Y_{out} - Y_{in})N_{N_2}/(\pi d_i l)] \quad (3.32)$$

$$Y = y/(1 - y) \quad (3.33)$$

$$N_{N_2} = P\dot{V} / (RT) \quad (3.34)$$

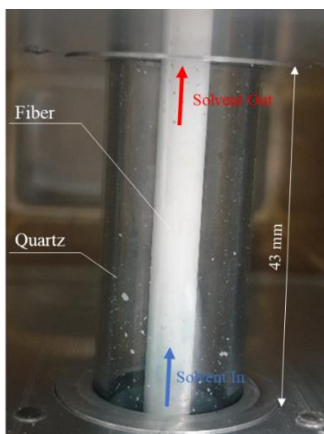


Figure 3-7: MW applicator containing hollow fiber placed concentrically with respect to the quartz tube and parallel with respect to the incident E-field // smaller dimension of the waveguide (43 mm).

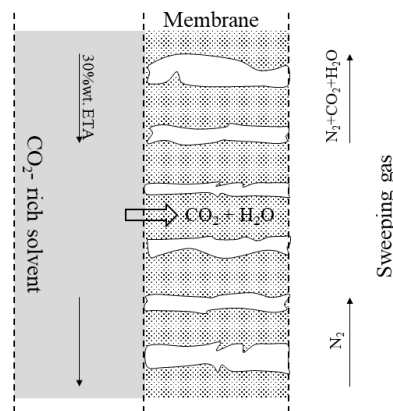


Figure 3-8: Schematic of the CO₂ desorption in the liquid phase, gas phase, and the porous membrane

Choice of fiber diameter

One characteristic of MW irradiation is their selective nature in targeting lossy materials that possess a high dielectric loss factor. Mediums with high dielectric loss factors (ϵ'') tend to dissipate MW irradiation in the form of heat, while others possessing low loss factors allow MW to propagate herein with little to no attenuation. The penetration depth (D_p) is the propagation distance of a plane EM wave in a material to reduce its E-field norm to 37% its initial value. It is a good indicator of the interactivity of a medium with MWs. i.e. lower penetration depths are the result of a high wave attenuation in the material and vice versa. The MW penetration depth in low-absorbing Quartz-glass, and poly-tetrafluoroethylene (PTFE) at 2450MHz are 3.5 and 920 meters respectively which is quite high with respect to that of moderately absorbing liquids such as water -1.4 cm [6]. The MW penetration depth for 30%wt. ETA at 2450 MHz is ($D_p \sim 2$ mm) for a carbonation ratio ($\alpha=0.55$) at 80°C. This quantity limits the choices of the fiber inner radius to be in the neighborhood of (2 mm): larger diameters will experience high non-homogeneities as waves will get absorbed in a small thickness of the solvent, on the other hand, smaller diameters will pose difficulty in power absorption as waves will traverse them without getting fully absorbed. It should be kept in mind that the penetration depth serves as a general guideline to achieving MW heating homogeneity, its accuracy should not be overestimated as MW heating is usually performed using guided waves instead of unguided ones. For more details on penetration depth and dielectric properties of 30%wt. ETA, refer to section (chapter 0).

The fiber used in this work is of greater diameter than the ones used in typical membrane modules in industrial applications or even in literature [7], those are the in the order of a fraction of a millimeter. The relatively great dimension of the fiber used in this work is to avoid the inconvenience of low surface area for desorption, and subsequently CO₂ concentrations that are below the lower measurement limit of the CO₂ analyzer employed. It was not possible to know a priori the experimental desorption rates of CO₂ at a given set of conditions, therefore literature data on desorption under similar conditions provided an estimate. One way to situate the adjust the outlet CO₂ concentration was by altering the sweeping gas flow rate.

Solvent-fiber compatibility:

It is well known that one of the main problems that hinder the employment of gas absorption membranes for carbon capture is membrane wetting [8]. Membrane wetting occurs with the penetration of the liquid phase into the porous structure. The wetting of membrane material can be predicted by the Laplace-Young equation therefor if the transmembrane pressure exceeds the LEP, then the wetting will occur. The prevention of wetting dictates using a solvent with a high interfacial tension and contact angle, and a porous structure that with small pore diameters. In this work, the porous fiber used in the lab-scale desorption tests is made from porous PTFE, as this material has shown a greater ability to conserve its surface properties in comparison to PP, PVDF and nylon materials; PTFE has proven to maintain its hydrophobicity upon prolonged periods of exposure to 30%wt. ETA [9, 10]. It is known that ETA – the reference solvent for chemical absorption – has the highest surface tension [11] in comparison to other alkanolamines (DEA, MDEA, AMP), consequently it presents the lowest risk of membrane wetting [12].

3.3.2 Applicator design: fiber orientation

In general, microwave applicator designs are tailored to produce an impedance continuity between the waveguide and the applicator containing the product of interest [13]. The design of the applicator differs based on the geometry as well as the dielectric properties of the product. We propose two designs for the MW applicator in which the fiber assumes different orientations with respect to the incident E-field in a rectangular WR340 waveguide: parallel, or perpendicular. At a given orientation, a multitude of different fiber diameters were tested of varying internal diameter which represents the region where the solvent circulates.

3.3.2.1 Geometry and boundary conditions

Geometry

COMSOL[®] multiphysics (version 6.1) was used to simulate the 3-D E-field maps by solving the Maxwell's equations in the cavity domain at different orientations of the fiber: parallel and perpendicular with respect to the incident E-field. Figure 3-9 shows the parallel orientation of the fiber with respect to the E-field propagating along (\vec{a}_k) where the fiber length exposed to MW irradiation is 43mm. The perpendicular orientation on the hand (Figure 3-10) allows a greater exposure to MW irradiation (86mm) although this may not necessarily translate to greater power absorption: In the TE₁₀ mode, the E-field intensity is not uniform across waveguide section as shown in Figure 3-4.

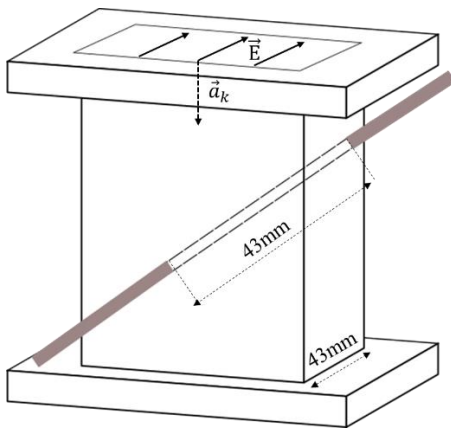


Figure 3-9: Fiber orientation parallel with respect to the polarization of incident E-field (\vec{E}) having a direction of propagation (\vec{a}_k)

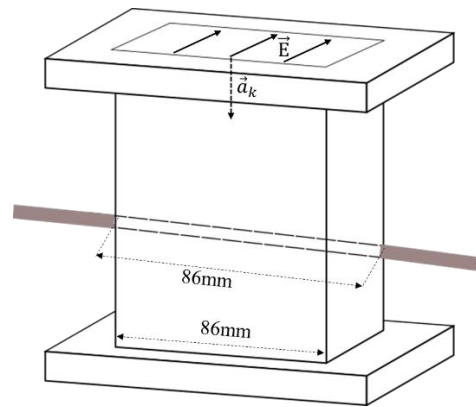


Figure 3-10: Fiber orientation perpendicular with respect to the polarization of incident E-field (\vec{E}) having a direction of propagation (\vec{a}_k)

The suitability of a given fiber-orientation and fiber diameter was evaluated by inspecting the ratio of reflected MW power (P_r) to incident one (P_i) as this is common criteria that is classically used by many authors. For a given applicator geometry, impedance matching was performed by increasing the distance between the MW cavity and the sliding short circuit (SSC) downstream– in order to simulate the action of a sliding short circuit. The obtained S_{11} parameter– shown in equation (3.35) in dB scale - was used to calculate the ratio of reflected to incident power as shown in equation (3.36) with $|E_i|$ and $|E_r|$ being the norms of the incident and the reflected E-field wave

respectively. The reflected power can be inferred by subtracting the dissipated power in the product from the incident MW power - ($P_r = P_i - P_{\text{absorbed}}$).

$$S_{11} = 20 \log_{10}(|E_r|/|E_i|) \text{ in (dB)} \quad (3.35)$$

$$P_r/P_i = (|E_r|/|E_i|)^2 = 10^{\frac{S_{11}}{10}} \quad (3.36)$$

Dielectric properties

The dielectric properties of the materials used in the model are shown in Table 3-3. We note that the apparent dielectric properties of porous PTFE fiber material were obtained using the Landau-Lifshiz-Looyenga [14] dielectric mixing law in conjunction with dielectric properties of PTFE. The properties of quartz and PTFE were obtained from [15]. The dielectric properties of the liquid in the lumen area of the fiber were varied between three cases as presented in Table 3-3 : DW and the 30%wt. ETA solvent at two experimental conditions. The properties of water were obtained from literature [16]; those of 30%wt. ETA at $[T, \alpha]$ conditions of $[20, 0.22]$ and $[80, 0.55]$ represent the conditions corresponding to the extremes of the dielectric loss factor (ϵ'') on the range of tested temperatures and carbonation ratios.

Material	$\epsilon' - j\epsilon''$
Quartz ^[15]	3.78
Porous PTFE ^[15]	1.42
DW [20°C] ^[17]	79.93-j10.44
30%ETA [20°C, 0.22] ^{This work}	56-j34.2
30%ETA [80°C, 0.55] ^{This work}	61.2-j78.4

Table 3-3: Dielectric properties at 2450MHz of different materials

Boundary conditions and meshing

The interior of the simulation domain was defined by the dielectric properties of each material: air, quartz, porous PTFE, and solvent. External surfaces of the geometry were defined as perfect electric conductors. Meshing was done automatically by COMSOL[®] all while taking care to achieve a good compromise between the solution time and independency of the solution on the mesh. The mesh was chosen amongst the options proposed by the software and mentioned in Table 3-4 along with the associated number of elements over the mesh. The solution becomes independent of the mesh size when using the mesh configuration “Fine”, and therefore it was adopted.

Type	Number of nodes
Normal	5214
Fine	15263
Finer	53221
Extra Fine	180431
Extremely Fine	519800

Table 3-4: tested mesh types

3.3.2.2 Numerical results

Fiber Orientation in MW applicator

The fraction of reflected power with respect to the incident power was calculated from the S_{11} parameter - equation (3.36) - at different fiber diameters ranging from 3 to 13 mm, and for the fiber oriented either in parallel (\parallel) or perpendicular (\perp) manner with respect to the incident E-field. The sliding short circuit (SSC) was varied over $[x, x + \lambda_g/2]$ by steps of 2 mm, which produces a curve of reflected power as a function of the SSC. The curve minimum represents the best possible impedance matching that could be achieved with the SSC.

Figure 3-11 shows the variations of the fraction of reflected power with the fiber diameter tested for both the two orientations (\parallel, \perp). The reported data correspond to the minimum of the reflected power fraction after optimizing the position of the SSC. Figure 3-11 shows that in the case of perpendicular orientation, the fraction of reflected power decreases with the fiber diameter, but still remains quite large at the largest diameter of 14 mm. In the case of parallel orientation, Figure 3-11 shows a tendency of increasing reflected powers at higher fiber diameters contrary to that of the (\perp) orientation. At small fiber diameters the levels of reflected powers are practically non-existent highlighting their suitability with this orientation.

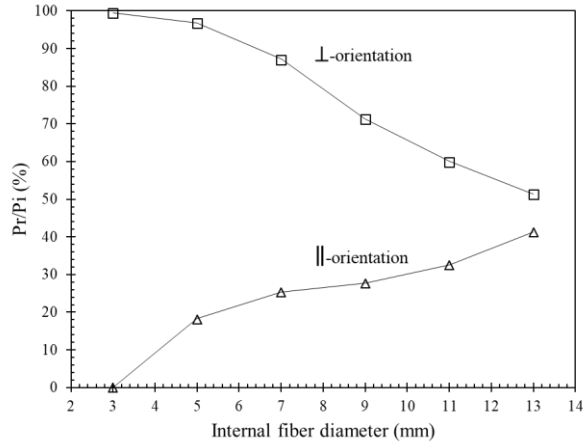


Figure 3-11: Microwave reflected power function of the internal diameter of the fiber filled with 30% wt. ETA at [0.55, 80°C]. (□): parallel orientation; (Δ): perpendicular orientation

E-field penetration with fiber diameter

As the parallel (∥) fiber-orientation was deemed appropriate, the E-field maps were plotted for cases of lowest and highest fiber diameters, with the aim of exploring the effect of the diameter on the distribution of the former. E-field maps are plotted in Figure 3-12 and Figure 3-13 for an internal fiber diameter of 3 mm and 13 mm respectively at optimal SSC position. Figure 3-12 shows that the near-homogenous E-field promises a uniform heating rate of the solvent. When the diameter increases to 13mm, the fiber dimension is considerably greater than the MW penetration depth, leading to less homogeneity in the E-field and a consequent greater disparity in the predicted heating rate profiles. As a reminder, rate of dissipation of EM energy into heat is dependent on the squared power of the E-field – equation (2.32). The E-field profile displayed for ($d_i= 3\text{mm}$) is preferred over that for ($d_i= 13\text{mm}$), because this allows a better long-term performance by the avoidance of hot-spots (regions of concentrated MW power).

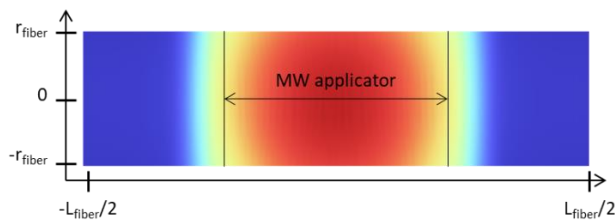


Figure 3-12: E-field map at 2450MHz in a hollow fiber ($d_i= 3\text{mm}$) at optimal SSC adaptation, 30% wt. ETA at [0.55, 80°C]

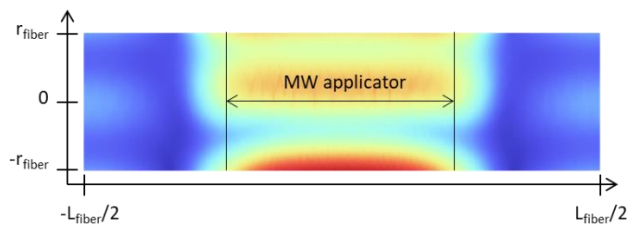


Figure 3-13: E-field map at 2450MHz in a hollow fiber ($d_i= 13\text{mm}$) at optimal SSC adaptation, 30% wt. ETA at [0.55, 80°C]

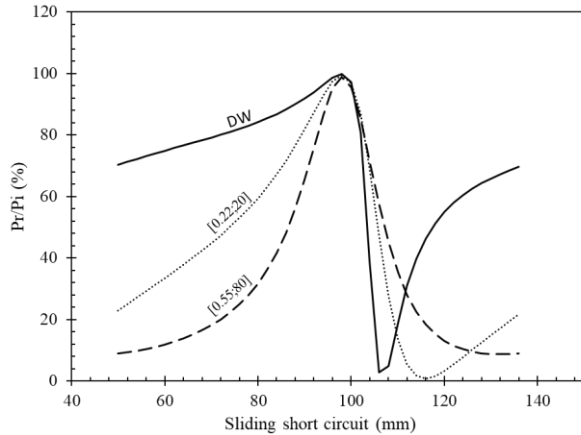


Figure 3-14: Reflected power fraction function of sliding short circuit position at 2450 MHz; ($d_i=3\text{mm}$) and parallel orientation. Simulated liquids are: distilled water (DW), 30% wt. ETA [0.22, 20°C], 30% wt. ETA [0.55, 80°C].

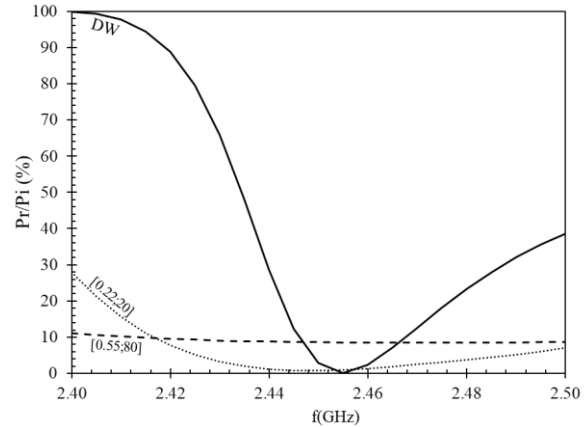


Figure 3-15: Reflected power fraction function of frequency at optimal SSC positions; ($d_i=3\text{mm}$) and parallel orientation. Simulated liquids are: distilled water (DW), 30% wt. ETA [0.22, 20°C], 30% wt. ETA [0.55, 80°C].

Reflected power function of sliding short circuit and frequency

Figure 3-14 displays the effect of the SSC on the reflected power fraction. The fiber was placed in the (II) orientation, and the dielectric properties of the fiber lumen were defined so as to simulate distilled water, and 30% wt. ETA solutions at different CO₂ loadings and temperature: [0.22, 20°C]; [0.55, 80°C]. The sliding short circuit was varied between $[x, x + \lambda/2]$ with λ being the guided wavelength (173mm) at 2450 MHz, and x being any arbitrary adaptation value. The figure shows that the cavity is well adapted for moderately absorbing liquids such as DW, to liquids with high absorbance such those of 30% wt. ETA with a high CO₂ load. In all three liquids, the SSC is sufficient to achieve very good levels of reflected power (<10 %), especially for the case of DW and 30% wt. ETA at [0.22, 20°C]. In the case of 30% wt. ETA at [0.55, 80°C], the reflected power function of the SSC is generally lower than that of the other liquids, however it experiences a minimum (10%) higher than those of the other liquids.

The reflected power as a function of frequency was plotted in Figure 3-15. The figure shows that the sensitivity of the liquids to frequency change decreases in the order: DW, 30%ETA [0.22, 20°C], 30% wt. ETA [0.55, 80°C]. Reflected power sensitivity with respect to frequency follows the same trend as that with respect to SSC position at the point of lowest reflected power, this is due to the fact that an increase in frequency is equivalent to shifting the SSC away from the MW cavity and vice versa.

3.3.3 Experimental design analysis

An experimental design approach was adopted to characterize the effects of different operating parameters on the CO₂ desorption rates from 30% wt. ETA under MW irradiation. Experimental design provides an organized framework through which minimal experimental work reveals important behavioral patterns of a system. It serves

as a useful tool in identifying the controlled variables with greatest effect on the system response, consequently controlled variables holding no effect can be discarded. In such a scheme, the controlled variables are denoted as “inputs”, while the experimental results are denoted as the “responses” of the system. In this work we adopt the (2^k) experimental design analysis, with “k” representing the number of controlled variables, while the base “2” represents the number of levels assigned to each input – “low” and “high”-, therefor (2^k) signifies the total number of experimental observations required. For more on experimental design, refer to the book entitled “Applied design of experiment and taguchi methods” [18].

The advantage of experimental design is that the levels of controlled variables are chosen methodically, so as to provide several estimations of the effect of each input on the response of the system. These estimations are averaged to obtain the mean effect on the response. Assuming a linear variation of the response within the experimental domain, the experimental response can be regressed with equation (3.37) for a system that depends on three controlled variables (X_i), with (R) being the response of the system, (β_0) the mean response, (β_{X_i}) the main effect of a given variable of (X_i), and ($\beta_{X_i X_j}$) interaction parameter between the controlled variables (X_i) and (X_j) and so on for ($\beta_{X_i X_j X_k}$). Experimental results for a three-input system are presented in the form of a cube as shown in Figure 3-16.

$$R(X_1, X_2, X_3) = \beta_0 + \beta_{X_1} X_1 + \beta_{X_2} X_2 + \beta_{X_3} X_3 + \beta_{X_1 X_2} X_1 X_2 + \beta_{X_1 X_3} X_1 X_3 + \beta_{X_2 X_3} X_2 X_3 + \beta_{X_1 X_2 X_3} X_1 X_2 X_3 \quad (3.37)$$

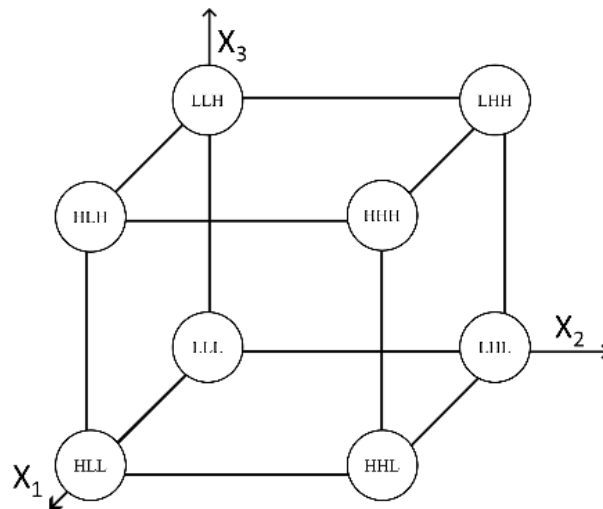


Figure 3-16: 2^k experimental design cube for a system-response dependent on three variables (X_1, X_2, X_3).

Each sphere designates the conditions on that experimental point under the form ($X_1 X_2 X_3$) with (H) and (L) accounting for “high” and “low” levels respectively.

The controlled variables primarily selected to account for the CO_2 desorption rates are: the carbonation ratio (α), the outlet temperature of the solvent (T_{out}), the volumetric liquid flow rate (v_l), and the sweeping gas flow-rate

(v_g). Each input variable being assigned two levels “high” and “low”, the total number of experimental points to be performed is (2^4). We choose however to divide the experiments into two campaigns, each at a different carbonation ratio with a (2^3) points performed per campaign. Each experiment was repeated three times and desorption fluxes were averaged at each experimental point. Obtained desorption flux are regressed as per (3.38) which includes the controlled variables [\hat{T} , \hat{v}_1 , \hat{v}_g], the effect of single controlled variables [β_T , β_{v_1} , β_{v_g}], as well the effect of two-variable interactions [β_{TXv_1} , β_{TXv_g} , $\beta_{v_1Xv_g}$], and that of three-variable interactions [$\beta_{TXv_1Xv_g}$] on the system response (J).

$$J(T, v_1, v_g) = \beta_0 + \beta_T \hat{T} + \beta_{v_1} \hat{v}_1 + \beta_{v_g} \hat{v}_g + \beta_{TXv_1} (\hat{T} \hat{v}_1) + \beta_{TXv_g} (\hat{T} \hat{v}_g) + \beta_{v_1Xv_g} (\hat{v}_1 \hat{v}_g) + \beta_{TXv_1Xv_g} (\hat{T} \hat{v}_1 \hat{v}_g) \quad (3.38)$$

The controlled variables denoted by (\hat{X}_i) allows the interpolation at values of (X_i) between the “high” level (X_{i-h}) and “low” level (X_{i-l}). (\hat{X}_i) is defined in (3.39) relative to the average value of a given controlled variable (X_{i0}) and (X_{i-h}). The average value of the controlled parameter is calculated from the high and low levels as shown in (3.40).

$$\hat{X}_i = (X_i - X_{i0}) / (X_{i-h} - X_{i0}) \quad (3.39)$$

$$X_{i0} = (X_{i-h} + X_{i-l}) / 2 \quad (3.40)$$

The regression parameters in (3.38) can be calculated from equation (3.41) with the (c_n) being defined as the contrast associated to the main effects or interaction effects on the system response. The contrasts (c_n) are given in Table 3-5 but for clarity, explicit expressions for the calculation of the variables (\hat{X}_i) and regression parameters can be found in (3.6-Annex). When obtained, the regression parameters (β) can be plotted to quantify the main and interactive effects of the operating conditions on the average desorption flux (J).

$$\beta_{X_i} = \frac{1}{2^k} \sum_{n=1}^{2^k} c_n R_n \quad (3.41)$$

Contrast (c)								
Exp	T	v_1	v_g	TXv_1	TXv_g	v_1Xv_g	TXv_1Xv_g	Response
1	-1	-1	-1	+1	+1	+1	-1	J_1
2	+1	-1	-1	-1	-1	+1	+1	J_2
3	-1	+1	-1	-1	+1	-1	+1	J_3
4	+1	+1	-1	+1	-1	-1	-1	J_4
5	-1	-1	+1	+1	-1	-1	+1	J_5
6	+1	-1	+1	-1	+1	-1	-1	J_6
7	-1	+1	+1	-1	-1	+1	-1	J_7
8	+1	+1	+1	+1	+1	+1	+1	J_8

Table 3-5: Contrast coefficients of the 2^k experimental design plan on the CO₂ desorption rates at constant (α). Controlled variables are [T, v_l , v_g]

3.3.4 Energy balance on a circulating liquid

The correct determination of the incident MW energy from the generator is an important input into the MW-heating model on one hand, and a crucial parameter for characterizing the energy efficiency of the process on the other. The energy balance of the system is based on the comparison of the absorbed MW energy by the liquid, and the net incident MW power. Ideally, the net MW power introduced by the generator should equate the power absorbed by the liquid to validate the energy balance. This relies on the fact that the liquid is the only lossy element in the applicator (Figure 3-6), and no MW leakages from the waveguide persist as has been verified. The net incident MW power (absorbed or non-reflected power) can be obtained by subtracting the incident (P_i) and reflected (P_r) power. Two different estimations of the absorbed power are possible: either in-line measurements from the six-port reflectometer that is integrated into the automatic impedance three-stub tuner (AI3S), or from the dual-directional coupler integrated into the solid-state microwave generator. Both provide measurements of the incident microwave power coming out from the MW generator and the reflected one.

A six-port reflectometer measures the forward power and the complex reflection coefficient (Γ) of a certain device under test. One port of the reflectometer connects to the MW generator, the other to the device under test, and the remaining four to power detectors. The determination of the transmitted power can be given directly by a power detector, while the complex reflection coefficient (Γ) is obtained by solving three non-linear equations that originate from the (6x6) scattering matrix of the system [19]. A dual directional coupler is a 4-port device that consists of two transmission lines denoted as the principle line and the auxiliary line [20]. It operates by coupling the outputs of the ports in the auxiliary line to the direction of propagation of the wave in the principle line. As an example, a forward moving wave in the main line can be sampled at (port 3), hence (port 3) is coupled to waves that propagate in the forward direction. Similarly, (port 4) samples backward propagating waves hence is coupled to that direction of propagation.

Graphic removed to respect copyright

Graphic removed to respect copyright

Figure 3-17: Representation of a six-port reflectometer [19]

Figure 3-18:Representation of a dual directional coupler as a 4-port network device with ports 3, and 4 being [20]

To accredit the power absorption readings from the generator or the AI3S, they were compared with the true absorbed power acquired by the energy balance based on inlet and outlet liquid streams temperatures in the MW

cavity. The absorbed MW power by the liquid (P_{abs}) is calculated from the expression provided in Table 3-6, with (\dot{m}) being the liquid flow rate (g/s), C_p the specific heat (J/g/K), and ΔT being ($T_{out} - T_{in}$).

Two liquids were used to test the MW power balance, distilled water (DW) and 30% wt. ETA. The density and specific heat of latter were obtained from [21] and [22] respectively. The MW power was adjusted to guarantee an outlet temperature of (40°C) while the inlet one was kept at ambient conditions of (20°C), the liquid flow rate was varied from (2g/s) to (5g/s) by steps of (1g/s). To minimize reflected power, impedance matching was performed by adjusting the position of the SSC to achieve minimal levels of reflected power. The AI3S, although capable of complementing the SSC in achieving minimal levels of reflected power, was not used as it would render the modeled geometry of greater complexity to simulate.

Determination method	P_{abs} (W)	Uncertainty (Watt)
Heat balance	$\dot{m}C_p\Delta T$	$\dot{m}C_p\Delta T (U(\dot{m})/\dot{m} + U(\Delta T)/\Delta T)$
Generator reading	$P_i - P_r$	$0.01(P_i + P_r) + 6$
AI3S reading	$P_i - P_r$	$0.05P_i + P_r(0.05 + 0.1/\sqrt{P_r/P_i})$

Table 3-6: Determination of absorbed microwave power and the associated uncertainty

3.4 Results

3.4.1 Energy balance on a circulating liquid

The absorbed MW powers by DW and 30% wt. ETA are shown in Figure 3-19 and Figure 3-20 respectively. For the case of DW, it can be seen that all measurement techniques agree quite well by having very close proximity, such that the absorbed MW power by the liquid is equal to the difference between the incident and reflected MW powers measured by the generator and the AI3S. This validates the energy balance in the system.

The question remains as to which MW measurement technique provides better estimations of the incident, absorbed, or reflected power. It can be seen for the case of DW (Figure 3-19) that (P_{abs}) from thermal balance and from generator readings are quite similar with overlapping error bars, but values obtained from AI3S readings are greater with increasing deviation when higher MW powers are applied. It may be that the AI3S provides good estimations of the net incident MW power while both the generator reading and energy balance calculations experience errors. It is important to mention that for the case of DW, the optimal experimental position of the SSC is 107.5mm, a value of extreme proximity to that theoretically obtained section (3.3.2.2) from numerical simulations - 106 mm. Therefore, it is very likely that the values of reflected power given by the model are representative of reality, and as the AI3S measures no reflected power, it stands in conformity with the model and thus provides a reliable source for measurements of MW power.

For the case of 30% wt. ETA as the circulating liquid, the absorbed MW powers are shown Figure 3-20 at different mass flow rates. In this figure, all readings agree quite well which validates the overall energy balance of the system. Readings of (P_{abs}) derived from the AI3S measurements agree better with those from the thermal balance than those of generator readings. Numerical simulations of MW-heating of 30% wt. ETA gave optimal SSC position

of 112 mm, a value that is completely identical to that obtained experimentally. As the simulation gave null levels of reflected powers (0.7%), the agreement of AI3S measurements with the former shows that it provides better accuracy than the generator readings.

In both cases of circulating liquid, the generator gave non-negligible readings of reflected power. The reason might be the imperfect impedance matches on the path between the MW generator up until the waveguide: junction between the generator and coaxial-cable, junction between the coaxial-cable and the waveguide. In comparison, the AI3S has the form of a waveguide section providing in-situ measurements of MW powers inside the waveguide thus eliminating any connector problem for power measurements.

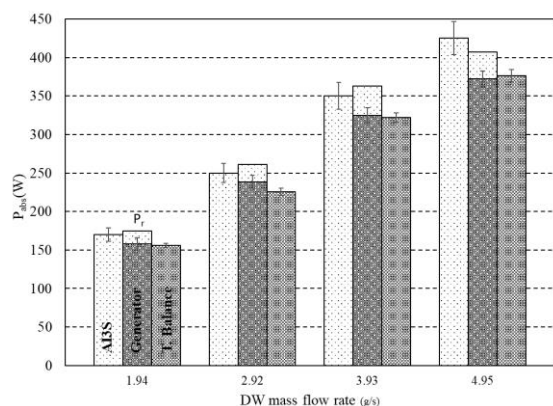


Figure 3-19: Different measurements of absorbed MW power by DW circulating in a hollow fiber at different mass flow rates. Automatic impedance 3-stub tuner (AI3S); MW generator; thermal balance on DW.

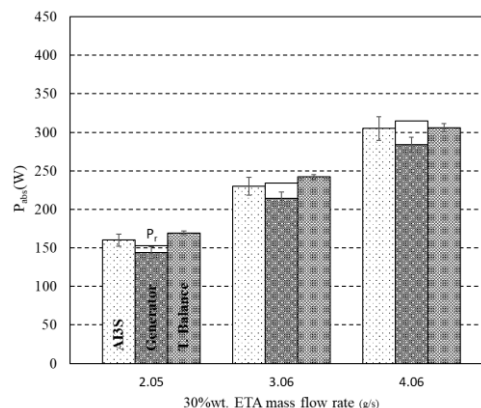


Figure 3-20: Different measurements of absorbed MW power by pure ETA circulating in a hollow fiber at different mass flow rates. Automatic impedance 3-stub tuner (AI3S); MW generator; thermal balance on ETA.

3.4.2 System dynamics: desorption rates and temperature profiles

Figure 3-21 presents the inlet and outlet temperature profiles as well as the CO₂ desorption flux from CO₂-enriched aqueous 30% wt. ETA solvent as a function of time. Solvent temperature at cavity exit as well as solvent volumetric flow rates were varied across the different subfigures of Figure 3-21, while the sweeping gas flow-rate was kept constant at (3.33mL/s), and the carbonation ratio was assumed constant ($\alpha=0.55$) due to small desorption rates in comparison to the volumetric flow rate of the solvent. Experiments were preceded by doing a blank run where no liquid was made to circulate in the cavity and the (N₂ gas) flow rate was set (3.33mL/s): recorded CO₂ concentrations were in the orders of few tens of ppm. For the sake of brevity, the desorption and temperature profiles were presented only for 4 experiments out of 16; the remaining can be found in the annex of this chapter.

Figure 3-21-(a) shows that at the start of the experiment, the desorption flux was minimal. Increasing the MW power led to the creation of a longitudinal temperature gradient between the liquid inlet and outlet, thus activating the chemical desorption reaction. Steady-state condition was achieved by manually adjusting MW power to achieve a constant outlet temperature of 40 °C, as is the case between t=300 and t=500 seconds, and the CO₂ desorption flux (J) was averaged over this region as per (3.42). The end of the experiment is marked by the drop of the outlet

temperature when the MW power was decreased, accompanied by a decrease in the CO₂ desorption flux. The inlet temperature profile was kept constant along the whole experiment duration thanks to the integrated cooling system in the solvent recycle loop.

$$J_{\text{avg}} = \frac{1}{t_2 - t_1} \int_{t_1}^{t_2} J(t) dt \quad (3.42)$$

The operating conditions of the CO₂ desorption profile in Figure 3-21-(b) are similar to that of (a), with the exception of the T_{out} being increased to 60°C. It can be seen that the desorption flux at T_{out}=60°C is superior to that at T_{out}=40°C for the most part due to the greater temperature gradients which contribute to higher driving force for mass transfer as can be concluded from vapor-liquid equilibrium data charts of 30% wt. ETA with CO₂ [23, 24], and from enhanced reaction rates. In subfigure-(b), setting (T_{out}) at exactly 60°C by controlling the MW power proved to be a challenge, therefore steady-state was achieved at any two temperatures in proximity to 60°C which allows to interpolate the desorption flux as a function of temperature in the neighborhood of 60°C. The heightened sensitivity of (J) to (T_{out}) motivated this approach. Subfigure-(b) shows that T=60⁺ and 60⁻ belong to the time lapse [600 - 800] seconds and at [1000 - 1200] seconds respectively.

Figure 3-21-(c) and (d) present the desorption rates at a higher liquid flow rate ($v_l=0.59\text{mL/s}$) for different outlet temperatures of 40°C and 60°C respectively. It should be noted that incident microwave powers (P_{inc}) were increased to account for the greater volumetric flow-rate of the solvent. It can be seen that subfigure (c) has a stable T_{out}-profile which leads to a stable desorption flux at steady state, in the neighborhood of 3×10^{-4} (mol/m²/s), higher than that obtained in subfigure (a). Subfigure (d) on the other hand experiences a lot of instability of the incident MW powers. Therefore, to obtain the desorption flux at 60°C we interpolated the fluxes surrounding at temperature that are slightly higher and lower denoted as 60⁺ and 60⁻. The inlet temperature increased with time due to the inability of the cooling system to evacuate the high input MW powers (~160W) relative to other experimental runs. This prevents prolonged experimentation times as (T_{in}) would no longer become a controlled parameter of the experiment.

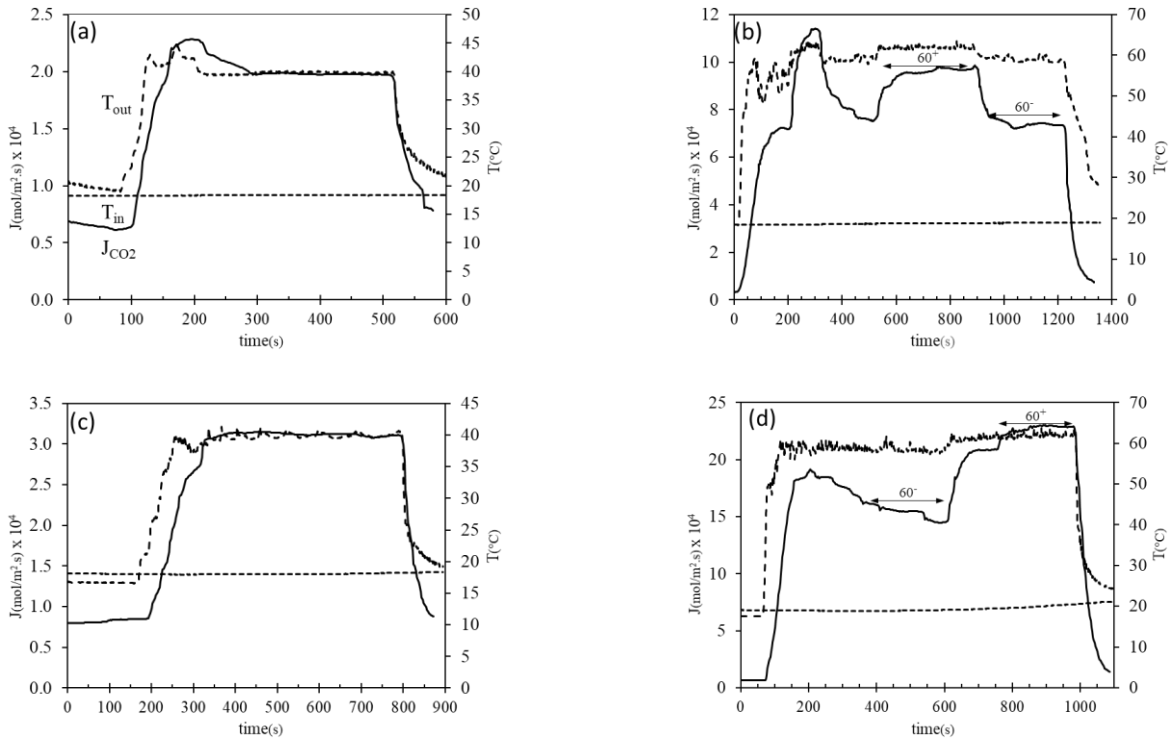


Figure 3-21: CO₂ desorption flux under MW irradiation from 30% wt. ETA circulating in a hollow fiber. For all figures, $T_{in}=20^{\circ}\text{C}$, $\alpha=0.55$, and $v_{N_2}=3.33\text{mL/s}$. The couple $[T_{out} (^{\circ}\text{C}); v_{liq} (\text{mL/s})]$ varies for each figure. (a)- $[40; 0.2]$, (b)- $[60; 0.2]$, (c)- $[40; 0.59]$, (d)- $[60; 0.59]$.

3.4.3 Influence of operating parameters on desorption flux

The total number of experimental points was determined to be (2^3) , which is all the of the possible combinations between “low”, and “high” level values for the chosen controlled variables $[T_{out}, v_l, v_g]$. The effect of the carbonation ratio (α) was studied, however it was not included in the regression equation, instead the equation was regressed individually to sets of data corresponding to “low” or “high” alpha. The “low” and “high” levels of all controlled variables, following the (2^k) experimental design plan, are given in Table 3-7 with different experimental values for chosen conditions at each carbonation ratio. The low level of (T_{out}) was increased from 40°C to 50°C between ($\alpha_h=0.55$) and ($\alpha_l=0.44$) respectively, in a similar manner the high level of (v_g) was decreased from 33.3mL/s to 6.66mL/s . This allowed achieving outlet CO₂ concentrations at lower (α) in the detection range of the CO₂ analyzer. Similarly, the “high” level of the N₂-flow rate was decreased from to 33.3 mL/s at (α_h) to 6.66 ml/s at ($\alpha_l=0.44$) to obtain outlet CO₂ concentrations in the detection range of the infrared CO₂ analyzer. Each experiment was repeated three times, the obtained average and standard deviations are shown in Table 3-7. For ease of reference, the experimental points were numbered from 1-8 ($\alpha=0.55$), and 9-16 for ($\alpha=0.44$).

Experiment number	α_{in}	$T_{out}(^{\circ}C)$	v_l (mL/s)	v_g (mL/s)	Average-J (mol/m ² .s)	σ (mol/ m ² .s)
1	0.55	40	0.2	3.33	1.90 E-04	1.00 E-05
2	0.55	60	0.2	3.33	7.90 E-04	6.00 E-05
3	0.55	40	0.59	3.33	3.20 E-04	4.00 E-05
4	0.55	60	0.59	3.33	1.76 E-03	8.00 E-05
5	0.55	40	0.2	33.3	2.70 E-04	1.00 E-05
6	0.55	60	0.2	33.3	7.50 E-04	6.00 E-05
7	0.55	40	0.59	33.3	3.20 E-04	1.00 E-05
8	0.55	60	0.59	33.3	2.26 E-03	1.10 E-04
9	0.44	50	0.2	3.33	7.79 E-05	9.77 E-06
10	0.44	60	0.2	6.66	1.94 E-04	4.42 E-05
11	0.44	50	0.59	3.33	1.05 E-04	1.95 E-05
12	0.44	60	0.59	6.66	3.98 E-04	7.89 E-05
13	0.44	50	0.2	3.33	8.14 E-05	1.73 E-05
14	0.44	60	0.2	6.66	2.24 E-04	4.48 E-05
15	0.44	50	0.59	3.33	1.38 E-04	2.83 E-05
16	0.44	60	0.59	6.66	3.53 E-04	1.08 E-04

Table 3-7: Average desorption flux obtained at operating conditions within the framework of the (2^k) experimental design approach

A better representation of the experimental CO₂ desorption fluxes at different conditions of [T_{out} , v_l , v_g] and for different values of ($\alpha=0.55$) and ($\alpha=0.44$) are presented in Figure 3-22 and Figure 3-23 respectively in the form of an Experimental design cube.

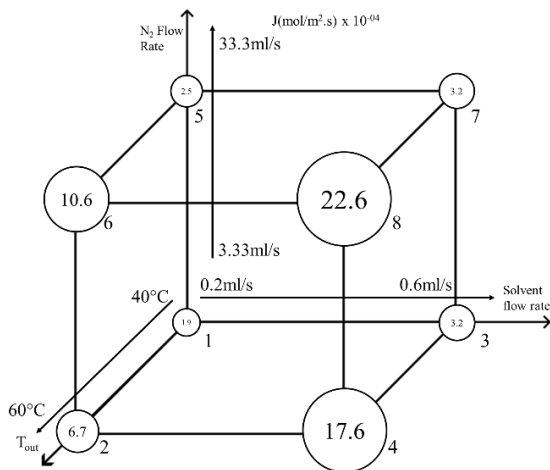


Figure 3-22: CO₂ desorption flux at ($\alpha=0.55$), represented according to the 2^k Experimental design scheme.

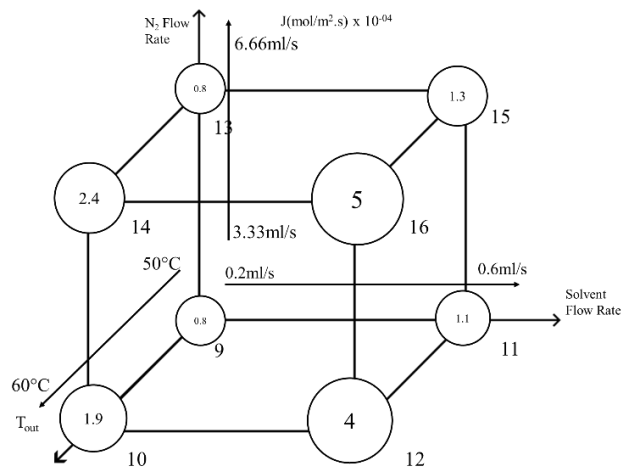


Figure 3-23: CO₂ desorption flux at ($\alpha=0.44$), represented according to the 2^k Experimental design scheme.

3.4.3.1 Temperature influence

For ($\alpha=0.55$) it can be seen that the desorption is incentivized by higher outlet temperatures, i.e. the desorption flux obtained at points (2; 4; 6; 8) at high T_{out} is greater than that obtained at points (1; 3; 5; 7) at low T_{out} respectively.

Similar tendencies are noticed for ($\alpha=0.44$) when comparing results at (9;11;13;15) to (10;12;14;16) respectively. The reason for increased CO₂ desorption is that higher temperatures increase the partial pressure of CO₂ in equilibrium with the liquid phase, which contributes to a higher driving force for mass-transfer as can be inferred from the vapor-liquid equilibrium data of CO₂ with 30% wt. ETA presented in Figure 3-24. Similar results are widely obtained from literature.

Another effect of temperature is the increase of CO₂ desorption kinetics as the rate for carbamate dissociation into molecular CO₂ increases. A detailed kinetic modeling of CO₂ desorption from different alkanolamine solvents was undertaken by Jamal [25] where he fitted the reaction rate constants of the model to Experimental data through an Error-minimizing scheme. He observed an increase of the rate for carbamate dissociation reaction with temperature. This can be reflected by the increase of the Equilibrium constant of the dissociation reaction of carbamate in reaction [26, 27]. This motivates the regeneration to take place at higher temperatures which was not our case as temperatures higher than ($T > 70^{\circ}\text{C}$) damaged the fiber structure.

It is important to clarify that the use of a single value to describe temperature (T_{out}) does not in any way imply its uniformity throughout the fiber. Temperature gradients are prone to Exist along the longitudinal, radial and the tangential direction of the fiber. The longitudinal distribution relates to the residence time in the fiber, while the radial and tangential gradients relates to the uniformity of the E-field in the liquid as well its velocity field of flow. Such temperature gradients have already been Encountered by others [28, 29] for the case of a laminar flow in a circular conduit with a parallel orientation with respect to the incident E-field. The principle characteristic of these T-profiles is that high temperatures occur at the boundary of the liquid flow and decrease when moving inwards along the radial direction of the flow.

3.4.3.2 Carbonation-ratio influence

Generally speaking, the desorption flux is higher at Experimental points (1-8) at (α_h) in comparison to those (9-16) at (α_l) respectively, but due to a lack of the homogeneity of Experimental conditions between both sets of data, the only viable comparisons of flux between (α_h) and (α_l) are at points (2;4) in comparison to points (10;12) respectively. It can be seen that the desorption flux at (α_h) is much greater than that at (α_l), owing to the positive correlation of the carbonation ratio with the partial pressure of CO₂ as observed in Figure 3-25, and the greater desorption rate when carbamate concentration increases. For reference we cite some sources who obtained similar results for the Effect on (α) on the desorption flux from 30% wt. ETA [25, 30, 31].

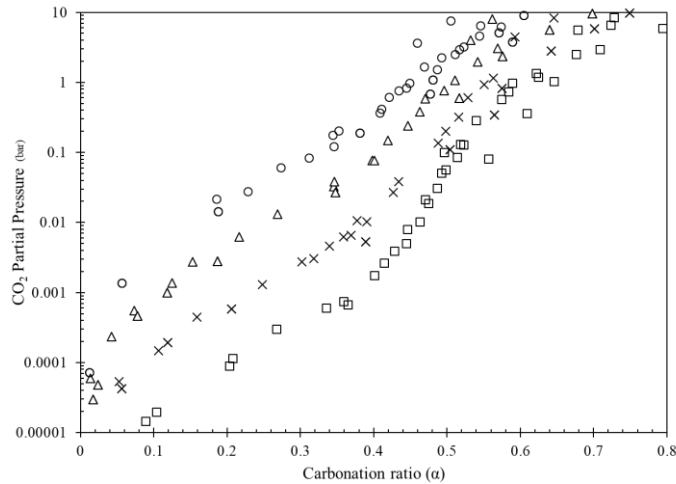


Figure 3-24: vapor-liquid Equilibrium for 30% wt. ETA function of carbonation ratio at different temperatures: (\square)-40°C; (\times)-60°C; (Δ)-80°C; (\circ)-100°C. [23, 24, 26, 32, 33]

3.4.3.3 Solvent flow rate influence

Figure 3-22 shows that the increase in the volumetric flow rate of the liquids contribute to the increase of the desorption flux. The respective comparison of the points (3; 4; 7; 8) at high level of flow to those at (1; 2; 5; 6) at low level shows that desorption flux is positively correlated to the liquid flow rate; similar observation can be drawn for the desorption at “low” carbonation ratio ($\alpha=0.44$). As the liquid flow rate increases, the thickness of the boundary stagnant film diminishes, thereby increasing the CO_2 concentration gradient and allowing for higher transfer rates [30, 34, 35]. This is usually the reason that Explains the increase in performance, however common desorption studies in hollow fibers are operated under isothermal conditions, whereas in our case temperature gradients are prone to Exist in our fiber. The particularity of MW heating is that temperature gradients are suspected to Evolve as the liquid flow rate and the applied MW power increases, all while keeping the same outlet temperature T_{out} . Therefore, we suspect that besides the decrease of the liquid boundary at higher liquid flow rates, an Extra thermal Effect at play that further boosts the desorption performance.

3.4.3.4 N_2 flow rate influence

The increased sweeping gas flow-rate does have some contribution on the desorption flux at α_h , although a minor one. For Experimental points having “low” temperature level, the increase of N_2 -gas flow rate has no Effect on desorption as can be seen by the respective comparison of points (1;3) and (5;7). When the temperature is set to “high”, the increase of N_2 gas flow incentivizes desorption as noticed upon comparing points (2;4) at low gas flow to (6;8) at high gas flow respectively. N_2 gas plays a role in increasing the driving force for mass transfer by diluting the desorbed CO_2 in the gas stream. Figure 3-25 presents the CO_2 concentration in the outlet gas stream at ($\alpha=0.55$) for all Experimental points. The figure shows that increasing N_2 flow is Effective at points (2;4) because the outlet concentration of CO_2 reaches relatively high values (1-2 %v). Outlet CO_2 concentration at points (1;3) are relatively

low, so further dilution of the CO₂ concentration by increasing N₂-flow would have little contribution on desorption. An additional Effect associated with higher flow rates of N₂-gas is the decrease of the stagnant gas-film on the outer surface of the fiber [5], although it never seems to pose a significant resistance to mass-transfer [30, 34] Especially when compared to that of the liquid phase [34].

For ($\alpha=0.44$), the increase of N₂-gas flow rate augments the desorption flux for points (13;14;15;16) in comparison to (9;10;11;12) respectively. This is different from the behavior at ($\alpha=0.55$) where not all cases Experience the increase higher desorption flux with increased N₂-gas. The suspected reason might be that the “high” level of N₂-flow at ($\alpha=0.44$) being (6.66 mL/s) is much lower than that at ($\alpha=0.55$) being (33.3 mL/s), consequently outlet CO₂ concentrations in these cases are higher, allowing the CO₂ analyzer to capture subtle changes in the desorption flux.

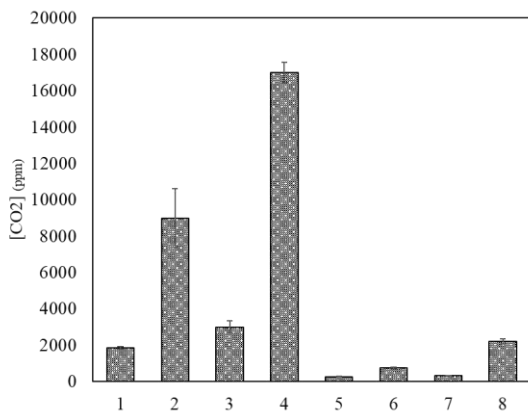


Figure 3-25: CO₂ concentration in outlet gas stream at different Experimental conditions and carbonation ratio ($\alpha=0.55$)

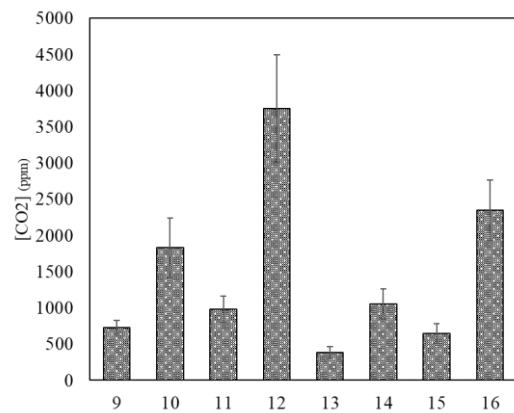


Figure 3-26: CO₂ concentration in outlet gas stream at different Experimental conditions and carbonation ratio ($\alpha=0.44$)

3.4.4 Regression of Experimental desorption flux

Equation (3.38) was fitted to the desorption flux of Experiments (1-8) and (9-16) for ($\alpha=0.55$) and ($\alpha=0.44$) respectively. The obtained coefficients from the fitting describe the Effects (β_{X_i}) of the controlled variable on the desorption flux, as well as those resulting from the interactions between the different controlled variables ($\beta_{X_i X_j}$, $\beta_{X_i X_j X_k}$) are presented in Figure 3-27 and Figure 3-28 for ($\alpha=0.55$) and ($\alpha=0.44$) respectively. Figure 3-27 shows that amongst the main Effects of the controlled variables, the temperature has the greatest contribution to the desorption flux followed by solvent flow rate, then the N₂-gas flow rate. Figure 3-28 shows the same rating of the main Effects of the controlled variables although with considerably lower absolute values such that ($\beta_{X_i}|_{0.55} > \beta_{X_i}|_{0.44}$). This is because higher carbonation ratios attribute greater sensitivities of the desorption flux vis-à-vis the controlled variables, in addition, the range between the high and low levels of controlled variables ($X_{i,h} - X_{i,l}$) varies between the two Experimental campaigns.

Regarding the Effects of interactions on the desorption flux, Figure 3-27 and Figure 3-28 show that the highest interaction is between the temperature and the solvent flow rate. It is suspected that usage of significantly higher MW powers Either by targeting a greater outlet temperature at a given flow rate, or the inverse, renders the temperature gradients stronger and having more of an impact on the desorption rate. Same Effect would occur when both controlled variables are increased, therefore, the interaction term (β_{TXv_l}) Expresses Explicitly the Effect of higher desorption kinetics, and driving force for mass transfer. Implicitly, it represents the Effects of inverted temperature gradients inside the fiber. The interactions of N_2 -flow with temperature and solvent-flow are of similar values and somewhat minute, and represents a greater dilution of CO_2 in the gas stream at increasing temperatures or liquid flow rates. It is worth pointing out that the sensitivity of desorption to sweeping gas flow depends highly on the tested range.

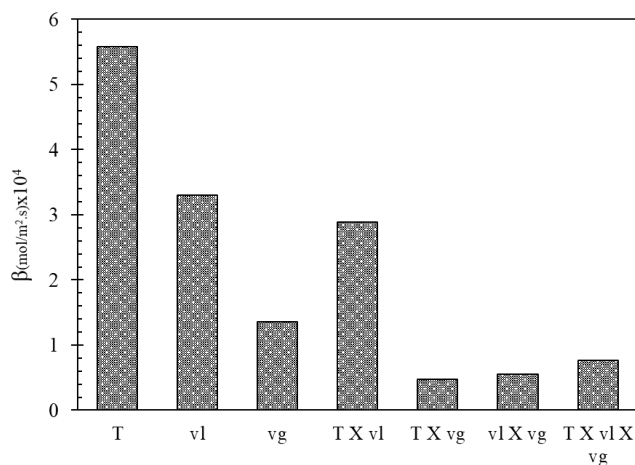


Figure 3-27: Regression coefficients based on the Experimental data of ($\alpha=0.55$)

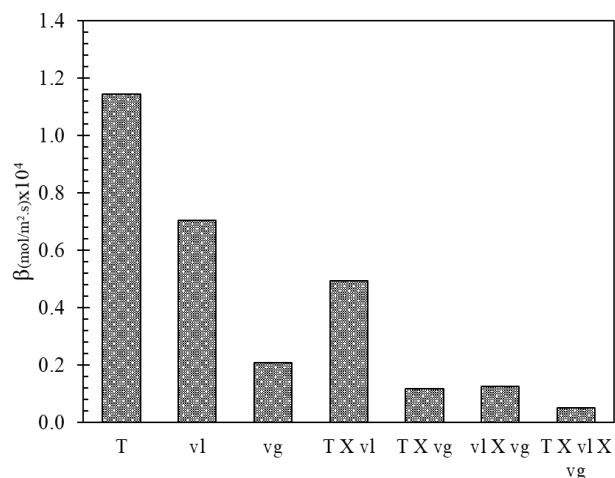


Figure 3-28: Regression coefficients based on the Experimental data of ($\alpha=0.44$)

3.4.5 Comparative analysis of desorption performances with literature

Table 3-8 presents the CO_2 desorption fluxes obtained in this work as well as others from literature operating. Cited works operate at isothermal conditions in which the solvent is preheated before entry into the hollow fiber membrane contactor. It is worth pointing that there exists a great number of parameters that influence the desorption flux, in addition there exists little availability of studies on CO_2 stripping in hollow fibers, thus the task of comparing MW regeneration technology to others is rendered difficult. For the sake of brevity, Table 3-8 does not present the full set of operating conditions of each study, but in fact aims to provide order of magnitude comparisons. It is important to point out that the use of certain polymeric materials for prolonged experimental campaigns may subject them to liquid wetting by intrusion or condensation mechanisms. This impairs the mass-transfer and leads to low desorption values that appear as a shortcoming of an applied technology when the problem could have been solved by using a membrane with a more stringent morphological structure or decreasing the severity of the operating conditions.

Regeneration mode	Temperature regime	Fiber material	Solvent	Temperature (°C)	CO ₂ -loading	J _{CO₂} × 10 ⁴ (mol/m ² s)	Reference
N ₂ -sweeping	MW heating	PTFE	30wt%. ETA	60	0.55	22.6	This work
N ₂ -sweeping	MW heating	PTFE	30wt%. ETA	60	0.44	5	This work
N ₂ -sweeping	Isothermal	Al ₂ O ₃	15% wt. ETA	80	0.45	24	[35]
N ₂ -sweeping	Isothermal	PVDF	3% wt. ETA	100	0.5	69.3	[30]
N ₂ -sweeping	Isothermal	PTFE	18% wt. ETA	100	0.45	30	[34]
Vacuum regeneration	Isothermal	PVDF // PP	20% wt. ETA	70	0.553	10.5 // 5.6	[36]
Vacuum regeneration	Isothermal	PP	30% wt. ETA	70	0.531	1.97	[37]
Vacuum regeneration	Isothermal	PP	20% wt. ETA	70	0.531	1.25	[38]
Vacuum regeneration	Isothermal	Al ₂ O ₃	30% wt. ETA	80	0.45	30	[39]

Table 3-8: Comparison of the CO₂ desorption flux from this work with those from literature

3.4.5.1 N₂-gas sweeping regeneration

As mentioned Earlier, N₂ is used commonly to study CO₂ desorption membrane processes as a sweeping gas, it serves to decrease the CO₂ partial pressure thus increasing the driving force for mass-transfer [5]. One objection to the use of N₂ sweeping gas is the difficulty in separating the CO₂ diluted in N₂ at the Exit of the process, as this represents capturing CO₂ from a flue gas stream by absorption only to release it into another flue gas stream. The reason for Employing this regeneration mode, is that it provides a simpler Experimental set-up as N₂ gas is Easy to work with and can Easily be replaced by feasible alternatives such as low-pressure steam when the technology reaches a greater maturity.

The CO₂ desorption flux in this work at [T, α] conditions of [60°C, 0.55] is almost identical to that obtained by Koonaphapdeelert [35] who operated at [80°C, 0.45]. As the temperature in this current work is lower than that Employed by the author, the higher carbonation ratio compensated the lower temperature and increased the CO₂ desorption flux. Our result at [60,0.44] is lower compared to that of [35] as both temperature and the carbonation ratio are inferior to those of the author. It is worth mentioning that high confidence can be accorded to the Experimental results of this article, as good modeling of the Experimental data was achieved under non-wetted membrane condition. More information on verification of wetting fraction by numerical modeling can be found in [40].

Rahim [30] obtained relatively higher values in comparison to the ones obtained in this work and to those from literature due to the Elevated operating temperature and carbonation ratio [100, 0.5]. We suspect that our result could reach that of the author in question by increasing the outlet temperature. Figure 3-21-(b) and (d) both demonstrate the sensitivity of the desorption to temperature as can be seen with the transition from T=60⁻ to T=60⁺.

The sensitivity in question is Estimated to be in the order of $(2 \times 10^{-04} \text{ [mol/m}^2 \text{ / s)]/}^\circ\text{C}$), therefore under the assumption of flux linearity the outlet temperature, a desorption flux similar to that of Rahim could be attained if desorption is operated at $T_{\text{out}}=80^\circ\text{C}$ in our system. It is worth mentioning that the absorbent Employed by the author had a very low alkanolamine concentration (3% wt.) relative to typical values (15-30% wt.). The lower amine concentration is said to have little Effect on the partial pressure of CO_2 for $(\alpha < 0.45)$ as implied by the correlation proposed by Weiland [41]; for carbonation ratios greater than (0.45) the partial pressure of CO_2 becomes positively correlated to the amine concentration in the solution [24].

The desorption flux by Khaisri [34] is of the same order of magnitude as that of Koonaphapdeelert[35] and our result at $(\alpha=0.55)$ despite the much lower regeneration temperature in this work. The author's result is markedly higher than our result at $(\alpha=0.44)$ given the higher temperature used to perform regeneration (100°C). It is worth mentioning that good confidence can be accorded to this reported result, as it represents the desorption flux at unwetted mode of operation.

3.4.5.2 Vacuum regeneration

Table 3-8 presents the desorption flux from vacuum regeneration of solvent from literature; it is important to point out that vacuum regeneration studies are not many, and some of them employ different solvents or membrane contactors in their studies. The reduced pressure on the shell/lumen side increases the driving force for mass transfer, and allows the regeneration to take place at lower temperatures. While some authors use low-pressure steam as a sweeping gas [31, 36–38, 42], others relied on the suction action of the vacuum pump to evacuate the desorbed CO₂ [39, 43].

The regeneration temperatures in [36–39] are somewhat low (60-70°C) in comparison to those employing sweeping-gas regeneration (80-100 °C), to compensate for the low temperature performance. The solvents employed in vacuum regeneration are characterized by a relatively high carbonation ratio (0.5-0.55) relative to the typical rich loading employed in a typical sweetening process ($\alpha=0.45$) [44]. Table 3-8 shows that the desorption flux obtained in this work at [60, 0.55] is much higher than that obtained by authors [36–38] that operated at a similar ETA concentration and carbonation ratios, but at higher temperatures than the one used in this work. While the liquid flowed on the lumen side of the porous fibers, the absolute pressure on the shell side was in the order of 10kPa in [36–38]. Comparison with our results highlights the advantages of microwaves in intensifying the regeneration in comparison to isothermal systems. The suspected reason is that MW heating leads to non-uniform temperature distributions that may intensify desorption.

The desorption flux of Lee [39] obtained at [80,0.45] is much higher in comparison to the results in this work at [60, 0.44] which may be due to the regeneration at higher temperature. Still, the carbonation ratio Employed by Lee is much lower in comparison to other vacuum regeneration data, and the study of Lee was performed by suction pressure of the pump while others Employed low pressure steam as a sweeping gas.

3.5 Conclusion

In this chapter CO₂ desorption from 30% wt. Ethanolamine was studied in a hollow fiber gas-liquid contactor under microwave irradiation. The solvent was circulated in a semi-continuous mode in a PTFE hollow fiber, and under exposure to microwave irradiation. Particular focus was placed on the design of the microwave cavity, where it was found through numerical simulations that placing the fiber in parallel with respect to the incident E-field allows for low levels of reflected MW powers and uniform Electric field distributions in the solvent.

The effect of microwave irradiation on the desorption flux from 30% wt. Ethanolamine solvent was studied at different operating conditions in the framework of a design of experimental plan. Results consisting of desorption flux as well as the outlet temperature of the solvent were plotted as a function of time. These plots show that desorption flux is extremely sensitive to temperature levels. The steady-state desorption fluxes were extracted from these plots and presented in the form of a 2^k Experimental-design cube. The regression coefficients were fitted to the experimental data to identify the extent of influence of each controlled parameter on desorption. It was

concluded that amongst the operating conditions, the outlet temperature had the highest effect on the desorption flux followed by the solvent flow rate. The effect of the interaction between temperature and increased solvent flow boosted the regeneration performance. The sweeping gas had very little effect on the desorption flux as the measured CO₂ concentration in the shell side were low such that any increase of the sweeping gas had little effect on increasing the driving force.

In the final part of this chapter, desorption fluxes obtained in this work were compared to those obtained from literature by different modes of regeneration: N₂-sweeping or vacuum regeneration. The difficulty in achieving identical Experimental conditions between this work and others from literature make it difficult to Evaluate the performance level of microwave regeneration technology with respect to others. Current Experimental results are on the same order of magnitude as those from literature that Employ N₂ sweeping gas, but those Employing vacuum decompression stripping of the solvent present inferior regeneration performance in comparison to this work, despite operating at greater temperatures.

While this chapter was focused on Experimental characterization of the desorption flux under microwave irradiation in a millimetric hollow fiber in a mono-mode cavity, the next chapter will focus on the modeling the desorption rates with the aid of multiphysics simulation.

3.6 Annex

3.6.1 Abbreviations

AI3S	Automatic impedance three stub tuner
AMP	2-amino-2-methyl-1-propanol
DEA	Diethanolamine
DW	Distilled Water
EM	Electromagnetic
ETA	Ethanolamine
MDEA	Methyldiethanolamine
MW	Microwave
PP	Polypropylene
PTFE	Polytetrafluorethylene
PVDF	Polyvinylidenedifluoride
SSC	Sliding short circuit
TE	Transverse Electric
TM	Transverse Magnetic

3.6.2 Symbols

E_s	Electric Field In Phasor Domain
E_0	Electric Field Magnitude
E_i	Incident Electric Field Magnitude
E_r	Reflected Electric Field Magnitude
S_{11}	Power Reflection Coefficient
θ	Phase Of Electric Field
k	Wavenumber
μ	Magnetic Permeability
ε	Electric Permittivity
σ	Direct Current Conductivity
β	Phase Constant
β'	Phase Constant In Vacuum
f_c	Cut-Off Frequency
λ_c	Cut-Off Wavelength
D_m	Mean Pore Size
d_i	Internal Fiber Diameter
d_o	Outer Fiber Diameter
ε'	Relative Permittivity
ε''	Dielectric Loss Factor
N	Molar Flow Rate
y	Molar Fraction
\dot{V}	Gaseous Flow Rate
P	Pressure
R	Ideal Gas Constant
L_{fiber}	Fiber Length
C_p	Specific Heat
J	Molar Flux
Al_2O_3	Alumina
\dot{m}	Mass Flow Rate

3.6.3 Effect of controlled variables and their interactions:

The regression pertaining to the 2^k design of Experimental plan is presented in Equation (3.38). The Effects of controlled variables (β_{X_i}) as well as those of interactions of controlled variables ($\beta_{X_i X_j}$) are Explicitly written in (3.43) to (3.49) following the Equation of (3.41) and Employing the contrast coefficients of Table 3-5. Equation (3.50) present the controlled used in the regression Equation in (3.38).

$$\beta_T = [-J_1 + J_2 - J_3 + J_4 - J_5 + J_6 + J_7 + J_8]/2^3 \quad (3.43)$$

$$\beta_{v_1} = [-J_1 - J_2 + J_3 + J_4 - J_5 - J_6 + J_7 + J_8]/2^3 \quad (3.44)$$

$$\beta_{v_g} = [-J_1 - J_2 - J_3 - J_4 + J_5 + J_6 + J_7 + J_8]/2^3 \quad (3.45)$$

$$\beta_{TXv_1} = [+J_1 - J_2 - J_3 + J_4 + J_5 - J_6 - J_7 + J_8]/2^3 \quad (3.46)$$

$$\beta_{TXv_g} = [+J_1 - J_2 + J_3 - J_4 - J_5 + J_6 - J_7 + J_8]/2^3 \quad (3.47)$$

$$\beta_{v_1 X v_g} = [+J_1 + J_2 - J_3 - J_4 - J_5 - J_6 + J_7 + J_8]/2^3 \quad (3.48)$$

$$\beta_{TXv_1 X v_g} = [-J_1 + J_2 + J_3 - J_4 + J_5 - J_6 - J_7 + J_8]/2^3 \quad (3.49)$$

$$\hat{T}; \hat{v}_1; \hat{v}_g = \left[\frac{T - T_0}{T_h - T_0} \right]; \left[\frac{v_1 - v_{10}}{v_{1-h} - v_{10}} \right]; \left[\frac{v_g - v_{g0}}{v_{g-h} - v_{g0}} \right] \quad (3.50)$$

3.6.4 Complementary data: Influence of operating parameters on desorption

The temperature profiles and the desorption fluxes for ($\alpha=0.55$) are presented in Figure 3-29 at sweeping gas flow rate of 33.3 ml/s and at different solvent outlet temperatures and flow rates. Experiments subfigures (a)-(d) correspond respectively to the Experiments numbered (5-8) in the Experimental-design cube of Figure 3-22, i.e. they represent desorption at the “high” level of sweeping-gas flow rate.

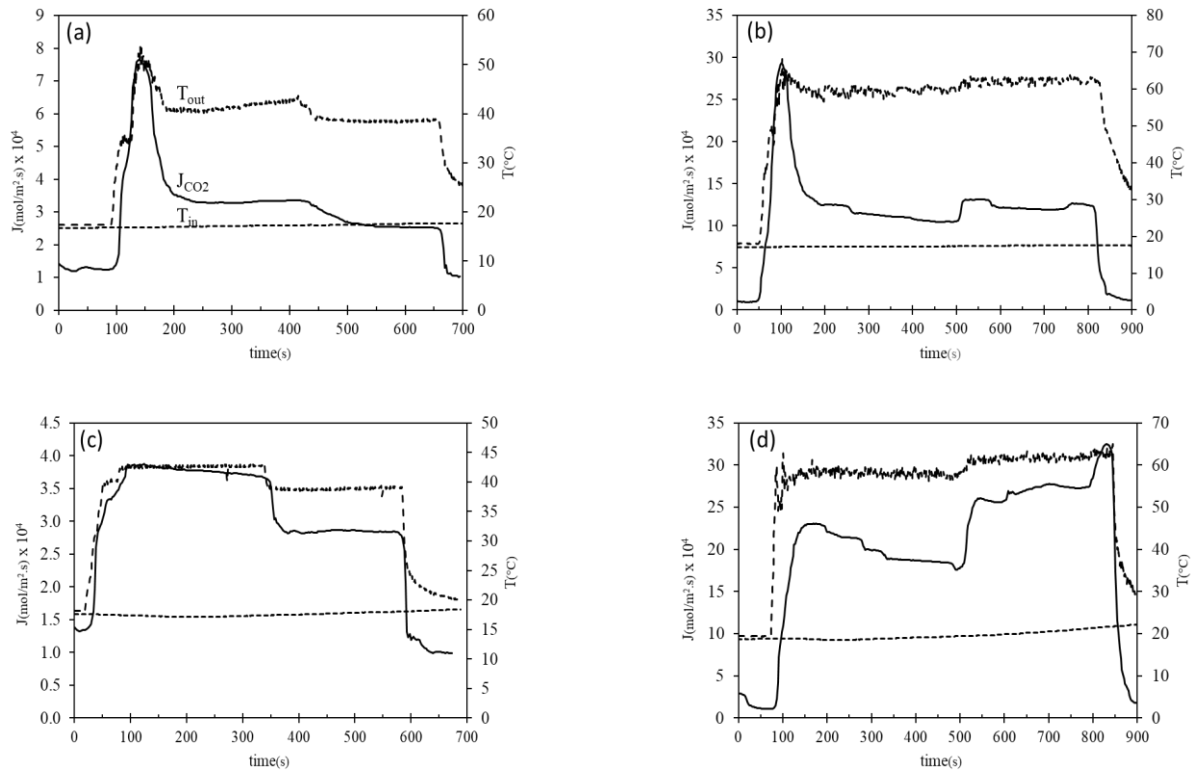
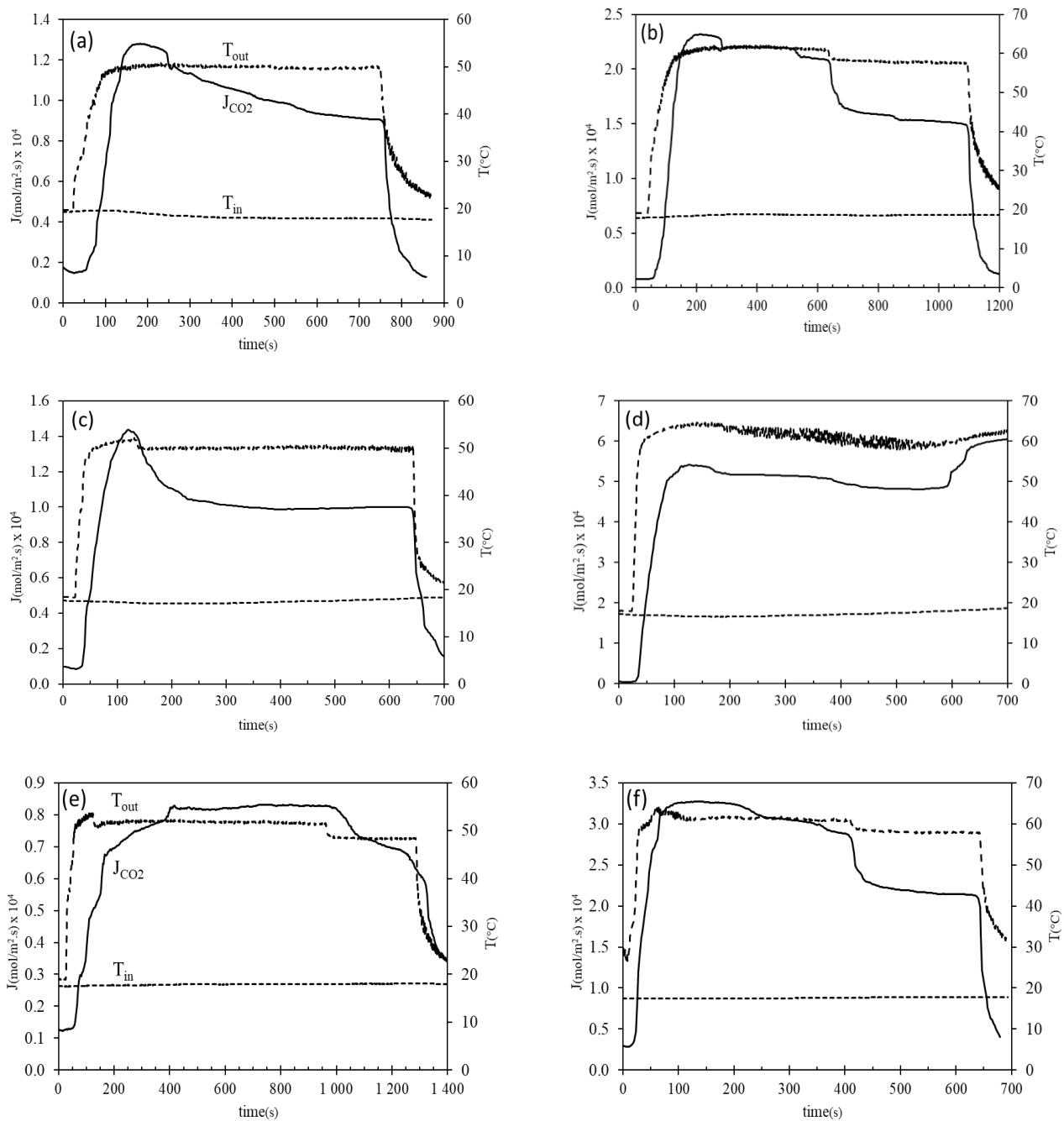


Figure 3-29: CO₂ desorption flux from 30% wt. ETA circulating in a hollow fiber under MW irradiation, $T_{in}=20^{\circ}C$, $\alpha=0.55$. The Experimental conditions of $[T_{out}(^{\circ}C), v_l (ml/s), v_g(ml/s)]$ are as follows: a-[40, 0.2, 33.3], b-[60, 0.2, 33.3], c-[40, 0.59, 33.3], d-[60, 0.59, 33.3]

The temperature profiles and the desorption fluxes for the Experimental campaign at ($\alpha=0.44$), complementing that performed at ($\alpha=0.55$), are presented in Figure 3-30 for different operating conditions of outlet temperature of liquid, liquid flow rate, and sweeping gas flow.



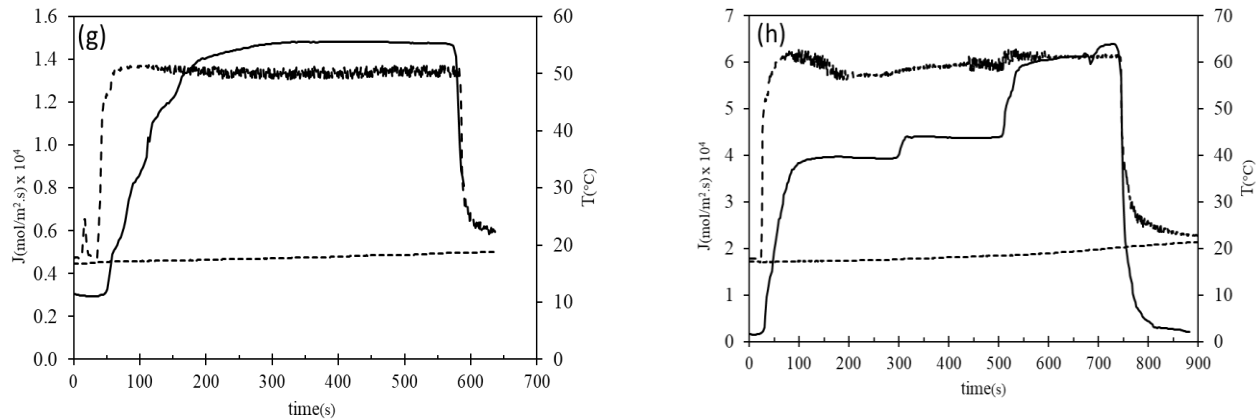


Figure 3-30: CO₂ desorption flux from 30% wt. ETA circulating in a hollow fiber under MW irradiation, $T_{in}=20^{\circ}\text{C}$, $\alpha=0.44$. The Experimental conditions of [$T_{out} (^{\circ}\text{C})$, v_l (ml/s), v_g (ml/s)] are as follows: a-[50, 0.2, 3.33], b-[60, 0.2, 3.33], c-[50, 0.59, 3.33], d-[60, 0.59, 3.33], E-[50, 0.2, 6.66], f-[60, 0.2, 6.66], g-[50, 0.59, 6.66], h-[60, 0.59, 6.66].

3.7 References

1. Sadiku, Matthew N. O. 2001. *Elements of electromagnetics*. 3rd ed. Oxford Series in Electrical and Computer Engineering. New York: Oxford University Press New York.
2. Kumar Baghel, Pushp. 2023. Application of microwave in manufacturing technology: A review. *Materials Today: Proceedings*: S2214785323005266. <https://doi.org/10.1016/j.matpr.2023.02.008>.
3. Pielak, Marlena, Ewa Czarniecka-Skubina, and Ingrida Kraujutienė. 2022. Microwave heating process – characteristics, benefits, hazards and use in food industry and households – a review ©. *Postępy Techniki Przetwórstwa Spożywczego* nr 1: 152–167.
4. Stefanidis, Georgios D., Alexander Navarrete Muñoz, Guido S.J. Sturm, and Andrzej Stankiewicz. 2014. A helicopter view of microwave application to chemical processes: reactions, separations, and equipment concepts. *Reviews in Chemical Engineering* 30. <https://doi.org/10.1515/revce-2013-0033>.
5. Alkhudhiri, Abdullah, Naif Darwish, and Nidal Hilal. 2012. Membrane distillation: A comprehensive review. *Desalination* 287: 2–18. <https://doi.org/10.1016/j.desal.2011.08.027>.
6. Bogdal, D., S. Bednarz, and K. Matras-Postolek. 2017. Microwave-Assisted Polymerization ☆. In *Reference Module in Materials Science and Materials Engineering*, B9780128035818103054. Elsevier. <https://doi.org/10.1016/B978-0-12-803581-8.10305-4>.
7. Gabelman, Alan, and Sun-Tak Hwang. 1999. Hollow fiber membrane contactors. *Journal of Membrane Science*: 46.
8. Zhao, Shuaifei, Paul H.M. Feron, Liyuan Deng, Eric Favre, Elodie Chabanon, Shuiping Yan, Jingwei Hou, Vicki Chen, and Hong Qi. 2016. Status and progress of membrane contactors in post-combustion carbon capture: A state-of-the-art review of new developments. *Journal of Membrane Science* 511: 180–206. <https://doi.org/10.1016/j.memsci.2016.03.051>.
9. Porcheron, Fabien, Daniel Ferré, Eric Favre, Phuc Tien Nguyen, Olivier Lorain, Régis Mercier, and Laurent Rougeau. 2011. Hollow fiber membrane contactors for CO₂ capture: From lab-scale screening to pilot-plant module conception. *Energy Procedia* 4: 763–770. <https://doi.org/10.1016/j.egypro.2011.01.117>.
10. Nishikawa, N., M. Ishibashi, H. Ohta, N. Akutsu, H. Matsumoto, T. Kamata, and H. Kitamura. 1995. CO₂ removal by hollow-fiber gas-liquid contactor. *Energy Conversion and Management* 36: 415–418. [https://doi.org/10.1016/0196-8904\(95\)00033-A](https://doi.org/10.1016/0196-8904(95)00033-A).
11. Pereira, Luís M.C., Fèlix Llovel, and Lourdes F. Vega. 2018. Thermodynamic characterisation of aqueous alkanolamine and amine solutions for acid gas processing by transferable molecular models. *Applied Energy* 222: 687–703. <https://doi.org/10.1016/j.apenergy.2018.04.021>.
12. Lv, Yuexia, Xinhai Yu, Shan-Tung Tu, Jinyue Yan, and Erik Dahlquist. 2010. Wetting of polypropylene hollow fiber membrane contactors. *Journal of Membrane Science* 362: 444–452. <https://doi.org/10.1016/j.memsci.2010.06.067>.

13. Liu, Man, Danfeng Zhou, Yu Peng, Zhengming Tang, Kama Huang, and Tao Hong. 2023. High-efficiency continuous-flow microwave heating system based on metal-ring resonant structure. *Innovative Food Science & Emerging Technologies* 85: 103330. <https://doi.org/10.1016/j.ifset.2023.103330>.
14. S. O. Nelson. 1992. Correlating Dielectric Properties of Solids and Particulate Samples Through Mixture Relationships. *Transactions of the ASAE* 35: 625–629. <https://doi.org/10.13031/2013.28642>.
15. Von Hippel, A.R., and A.S. Labounsky. 1995. *Dielectric materials and applications*. Artech House Microwave Library. Artech House.
16. Buchner, Richard, Glenn T. Hefter, and Peter M. May. 1999. Dielectric Relaxation of Aqueous NaCl Solutions. *The Journal of Physical Chemistry A* 103: 1–9. <https://doi.org/10.1021/jp982977k>.
17. STOGRYN, A. 1971. Equations for Calculating the Dielectric Constant of Saline Water 19: 733–736. <https://doi.org/10.1109/TMTT.1971.1127617>.
18. St, Cahyono. 2022. *Applied design of experiment and taguchi methods*.
19. Bilik, Vladimir. SIX-PORT MEASUREMENT TECHNIQUE: PRINCIPLES, IMPACT, APPLICATIONS.
20. *Microwave Engineering: Concepts and Fundamentals*. 2014. 1st ed. CRC Press.
21. Abdulkadir, Abdurahim, Aravind V. Rayer, Dang Viet Quang, Nabil El Hadri, Abdallah Dindi, Paul H.M. Feron, and Mohammad R.M. Abu-Zahra. 2014. Heat of Absorption and Specific Heat of Carbon Dioxide in Aqueous Solutions of Monoethanolamine,3-piperidinemethanol and Their Blends. *Energy Procedia* 63: 2070–2081. <https://doi.org/10.1016/j.egypro.2014.11.223>.
22. Weiland, Ralph H., John C. Dingman, D. Benjamin Cronin, and Gregory J. Browning. 1998. Density and Viscosity of Some Partially Carbonated Aqueous Alkanolamine Solutions and Their Blends. *Journal of Chemical & Engineering Data* 43: 378–382. <https://doi.org/10.1021/je9702044>.
23. Shen, Keh Perng, and Meng Hui Li. 1992. Solubility of carbon dioxide in aqueous mixtures of monoethanolamine with methyldiethanolamine. *Journal of Chemical & Engineering Data* 37: 96–100. <https://doi.org/10.1021/je00005a025>.
24. Aronu, Ugochukwu E., Shahla Gondal, Erik T. Hessen, Tore Haug-Warberg, Ardi Hartono, Karl A. Hoff, and Hallvard F. Svendsen. 2011. Solubility of CO₂ in 15, 30, 45 and 60 mass% MEA from 40 to 120°C and model representation using the extended UNIQUAC framework. *Chemical Engineering Science* 66: 6393–6406. <https://doi.org/10.1016/j.ces.2011.08.042>.
25. Jamal, Aqil, Axel Meisen, and C. Jim Lim. 2006. Kinetics of carbon dioxide absorption and desorption in aqueous alkanolamine solutions using a novel hemispherical contactor—II: Experimental results and parameter estimation. *Chemical Engineering Science* 61: 6590–6603. <https://doi.org/10.1016/j.ces.2006.04.047>.
26. Jou, Fang-Yuan, Alan E. Mather, and Frederick D. Otto. 1995. The solubility of CO₂ in a 30 mass percent monoethanolamine solution. *The Canadian Journal of Chemical Engineering* 73: 140–147. <https://doi.org/10.1002/cjce.5450730116>.
27. Li, Meng-Hui, and Bei-Chia Chang. 1994. Solubilities of Carbon Dioxide in Water + Monoethanolamine + 2-Amino-2-methyl-1-propanol. *Journal of Chemical & Engineering Data* 39: 448–452. <https://doi.org/10.1021/je00015a010>.
28. Zhang, Chun, Junqing Lan, Tao Hong, Tushar Gulati, Huacheng Zhu, Yang Yang, and Kama Huang. 2016. Dynamic analysis and simulation on continuous flow processing of biodiesel production in single-mode microwave cavity. *International Journal of Applied Electromagnetics and Mechanics* 51: 199–213. <https://doi.org/10.3233/JAE-160007>.
29. Yang, Fengming, Huacheng Zhu, Yang Yang, and Kama Huang. 2022. High-Efficiency Continuous-Flow Microwave Heating System Based on Asymmetric Propagation Waveguide. *IEEE Transactions on Microwave Theory and Techniques* 70: 1920–1931. <https://doi.org/10.1109/TMTT.2021.3123400>.
30. Rahim, Nihmiya Abdul, Nayef Ghasem, and Mohamed Al-Marzouqi. 2014. Stripping of CO₂ from different aqueous solvents using PVDF hollow fiber membrane contacting process. *Journal of Natural Gas Science and Engineering* 21: 886–893. <https://doi.org/10.1016/j.jngse.2014.10.016>.
31. Wang, Kun, Feng Wang, Yu Hai Guo, Hong Yan Tang, and Hua Peng Zhang. 2015. Regeneration of the Absorbent by the PTFE Hollow Fiber Membranes Using Vacuum Membrane Regeneration Technology. *Key Engineering Materials* 671: 300–305. <https://doi.org/10.4028/www.scientific.net/KEM.671.300>.
32. Jamal, Aqil. ABSORPTION AND DESORPTION OF CO₂ AND CO IN ALKANOLAMINE SYSTEMS: 380.
33. Lee, J. I., F. D. Otto, and A. E. Mather. 1974. The solubility of H₂S and CO₂ in aqueous monoethanolamine solutions. *The Canadian Journal of Chemical Engineering* 52: 803–805. <https://doi.org/10.1002/cjce.5450520617>.

34. Khaisri, Sakarin. 2011. CO₂ stripping from monoethanolamine using a membrane contactor. *Journal of Membrane Science*: 9.
35. Koonaphapdeelert, Sirichai, Zhentao Wu, and K. Li. 2009. Carbon dioxide stripping in ceramic hollow fibre membrane contactors. *Chemical Engineering Science* 64: 1–8. <https://doi.org/10.1016/j.ces.2008.09.010>.
36. Wang, Zhen, Mengxiang Fang, Qinhui Ma, Zhun Zhao, Tao Wang, and Zhongyang Luo. 2014. Membrane Stripping Technology for CO₂ Desorption from CO₂-rich Absorbents with Low Energy Consumption. *Energy Procedia* 63: 765–772. <https://doi.org/10.1016/j.egypro.2014.11.085>.
37. Fang, Mengxiang, Zhen Wang, Shuiping Yan, Qigang Cen, and Zhongyang Luo. 2012. CO₂ desorption from rich alkanolamine solution by using membrane vacuum regeneration technology. *International Journal of Greenhouse Gas Control* 9: 507–521. <https://doi.org/10.1016/j.ijggc.2012.05.013>.
38. Fang, Mengxiang, Shuiping Yan, Zhongyang Luo, Mingjiang Ni, and Kefa Cen. 2009. CO₂ chemical absorption by using membrane vacuum regeneration technology. *Energy Procedia* 1: 815–822. <https://doi.org/10.1016/j.egypro.2009.01.108>.
39. Lee, Hong Joo, Min Kwang Kim, and Jung Hoon Park. 2020. Decompression stripping of carbon dioxide from rich monoethanolamine through porous hydrophobic modified ceramic hollow fiber membrane contactor. *Separation and Purification Technology* 236: 116304. <https://doi.org/10.1016/j.seppur.2019.116304>.
40. Mavroudi, M., S.P. Kaldis, and G.P. Sakellariopoulos. 2003. Reduction of CO₂ emissions by a membrane contacting process☆. *Fuel* 82: 2153–2159. [https://doi.org/10.1016/S0016-2361\(03\)00154-6](https://doi.org/10.1016/S0016-2361(03)00154-6).
41. Weiland, R. H., M. Rawal, and R. G. Rice. 1982. Stripping of carbon dioxide from monoethanolamine solutions in a packed column. *AIChE Journal* 28: 963–973. <https://doi.org/10.1002/aic.690280611>.
42. Lu, Jian-Gang. 2013. CO₂ capture by membrane absorption coupling process Experiments and coupling process evaluation. *Journal of Membrane Science*: 10.
43. Ahn, Hyoseong, Jeonghoon Kim, and Jeong-Hoon Kim. 2013. Low-temperature vacuum stripping of CO₂ from aqueous amine solutions using thin-film silicalite-filled PDMS composite membranes. *International Journal of Greenhouse Gas Control* 18: 165–172. <https://doi.org/10.1016/j.ijggc.2013.07.004>.
44. Freguia, Stefano, and Gary T. Rochelle. 2003. Modeling of CO₂ capture by aqueous monoethanolamine. *AIChE Journal* 49: 1676–1686. <https://doi.org/10.1002/aic.690490708>.

4 Numerical modeling of chemical desorption under MW irradiation – Hollow fiber scale

4.1 Introduction

Previous chapters have dealt with the dielectric characterization of aqueous ethanolamine solution at different temperatures and carbonation ratios, and the experimental characterization of carbon dioxide desorption under microwave irradiation across a porous millimetric hollow fiber. The current chapter deals with the numerical modeling of the desorption process.

In this chapter, we present the conception of a multi-physical model that simulates chemical desorption of CO₂ from an alkanolamine solution in a millimetric hollow fiber exposed to microwave irradiation. We start by modeling the propagation of the electromagnetic fields in the microwave applicator. Afterwards, heat and momentum transfers were integrated into the 3D model to simulate the microwave heating process of a laminar flow of the solvent in a hollow fiber. Mass transfer and chemical reaction phenomena were described according to the double film theory, accounting for temperature dependent variables, and the partial wetting of the porous matrix. At last, the overall modeling approach incorporates the interactions between electromagnetic fields, heat-transfers and fluid mechanics coupled with mass-transfers accounting for chemical equilibrium and possible partial membrane wetting. The model was implemented using an in-house code, and describes the axial species concentration profiles as function of averaged axial temperature and liquid velocity profiles - derived from the 3D simulation approach. The layout of this chapter is as follows:

4.2 Modeling EM fields in a mono-mode applicator: In this section, the electromagnetic fields were modeled in the microwave applicator and levels of reflected power were compared with those obtained experimentally. The electric field distribution in the solvent allows the estimation of the dissipated microwave power herein

4.3 Coupling of EM propagation to fluid mechanics and heat transfer physics: The heat transfer and momentum transfer equations were solved to obtain the temperature maps in the unloaded solvent. After validating the numerical model, the sensitivity of temperature maps was tested with respect to several operating conditions, and fiber properties.

4.5 Modeling of CO₂ desorption across a single hollow fiber: To simulate desorption under microwave fields, previously obtained temperature maps were integrated into a 1D transfer model, assuming the effect of the reaction enthalpy as negligible (athermal reaction). The latter is based on the resistance-in-series approach with an enhancement factor to account for chemical reaction on desorption. Main results include the profiles of desorption flux along the axial direction of the fiber. Complementary studies were also performed to explore the effect of operating conditions and fiber geometries on desorption flux.

4.7 Sensitivity analysis of CO₂ desorption rates: In the last part of this chapter, a sensitivity analysis was undertaken with respect to the properties of the porous membrane, the physical and equilibrium properties of the solvent, as well as the operating conditions. Such a study was important in determining the accuracy to estimate solvent properties, as well as highlighting the main drivers of improvement of desorption performance.

4.2 Modeling EM fields in a mono-mode applicator

4.2.1 Maxwell's Equations

To describe the propagation of the electromagnetic fields in the cavity, Maxwell's equations need to be solved over the domain representative of the microwave cavity system. Maxwell's equations are reminded in equations (4.1) – (4.4) for ease of reference, with (\vec{E}_s) and (\vec{H}_s) being the electric and magnetic field intensities represented in phasor form, (ϵ) being the electric permittivity, (μ) the magnetic permeability, (σ) being the direct current (DC) electrical conductivity of the material, and (ω) being the angular frequency.

$$\text{Gauss's law} \quad \nabla \cdot \vec{E}_s = 0 \quad (4.1)$$

$$\text{Magnetic monopole} \quad \nabla \cdot \vec{H}_s = 0 \quad (4.2)$$

$$\text{Faraday's law} \quad \nabla \times \vec{E}_s = -j\omega\mu\vec{H}_s \quad (4.3)$$

$$\text{Ampere-Maxwell law} \quad \nabla \times \vec{H}_s = (\sigma + j\omega\epsilon)\vec{E}_s \quad (4.4)$$

Maxwell's equations can be expressed in the form of the Helmholtz equation (4.5), with (ϵ') and (ϵ'') being the real and the imaginary dielectric constants relative to vacuum, and (k_0) the unguided wave number in vacuum.

$$\nabla \times \nabla \times \vec{E} + k_0^2(\epsilon' - j\epsilon'')\vec{E} = 0 \quad (4.5)$$

4.2.2 Geometry and Boundary conditions

The simulated domain representative of the part of the experimental apparatus used to investigate the CO₂ desorption process at the fiber scale is shown in Figure 4-1. It includes the MW entry port, the applicator and the sliding short circuit (SSC). The microwave applicator is composed of a PTFE hollow fiber oriented in parallel with respect to the incident E-field at the entry port. The fiber is placed concentrically with respect to a surrounding quartz tube where desorbed CO₂ is collected and diluted in the nitrogen sweeping gas flowing.

The propagation of electromagnetic fields was simulated using the software Comsol[®] Multiphysics (6.1). The physical module "Radio Frequency" was used to simulate EM field propagation over the entire modeled domain by solving Maxwell's equations. Figure 4-2 shows the model geometry, the port is excited by a (TE₁₀), the dimensions of the applicator were reproduced without over-complexify or over-simplify the geometry. The walls of the waveguide are assumed to be a perfect electric conductor (PEC), hence the tangential component of the E-field cannot exist in that neighborhood – as implied by (4.6). The operation of the SSC was simulated by varying the distance from the bottom perfectly conducting boundary layer as shown in Figure 4-1.

Position	Type	Equation	
Entry port	Waveguide excitation TE ₁₀	-	-
Waveguide Walls	PEC	$\vec{n} \times \vec{E} = 0$	(4.6)
SSC	PEC	$\vec{n} \times \vec{E} = 0$	(4.7)

The dielectric properties of the materials used in the simulation environment are given in Table 4.1. The dielectric properties of fused quartz and PTFE were obtained from the book of Von Hippel [1], while those of the porous fiber were derived by using the Landau-Lifshitz-Looyenga dielectric mixing law [2]. The properties of

distilled water and unloaded 30%wt. ETA are obtained from the correlation of Stogryn [3] and from local measurements respectively. These liquids were used in the validation of the numerical model. Details regarding the computation of the dielectric data of the system components can be found in the Annex.

Fused Quartz [1]	3.78
PTFE [1]	3.15
Porous PTFE	1.44
Distilled water [3]-20°C	78.62-j10.53
30%wt. ETA*-25°C	61.5-j18.8

Table 4.1: complex permittivity of materials used in the simulation environment at 2450MHz.

4.2.3 Meshing and resolution scheme

To achieve a mesh-independent solution, the distance between the nodes should be enough close so as to minimize interpolation errors. The distance between the nodes in a dielectric is recommended to be less than $(\lambda/5)$ with (λ) being the unguided wavelength of the EM irradiation in the dielectric [4]. The wavelength in a given dielectric depends solely on the relative permittivity as demonstrated in equation (4.8), with (c) being the speed of light in vacuum, (f) the frequency, and (ϵ') the relative permittivity.

$\lambda = c / (f\sqrt{\epsilon'})$	(4.8)
-------------------------------------	-------

Meshing the geometry was done using the built-in mesh generator in the software. Air, quartz and fiber-thickness domains were meshed with the presetting (Fine), Only the solvent domain was tested for different mesh settings as it is the only lossy dielectric in the simulation environment. It is important to well represent the E-field on the solvent domain as this directly affects the simulated levels of absorbed powers. Three different mesh configurations were tested herein: Finer, Extra Fine, and Extremely Fine as detailed in Table 4.2.

Type	Nodes	Avg. size (mm)	Max size(mm)	Average E-field (V/m)
Finer	3067	1.324	2.11	11571
Extra Fine	10819	0.931	1.43	11573
Extremely Fine	28777	0.678	1.18	11574

Table 4.2: Characteristics of different mesh types on the solvent domain

Table 4.2 shows that the average size for all three meshes satisfies the requirements of good meshing, i.e. the average element size is lower than or equal to one-fifth of the wavelength of the EM irradiation in the solvent domain ($\lambda= 1.38$ cm for distilled water). It is partly for this reason that the average E-field on the solvent domain is independent from the mesh. The meshed geometry of the MW applicator is shown in Figure 4-2, with an emphasis on the meshing of the solvent region inside the fiber lumen.

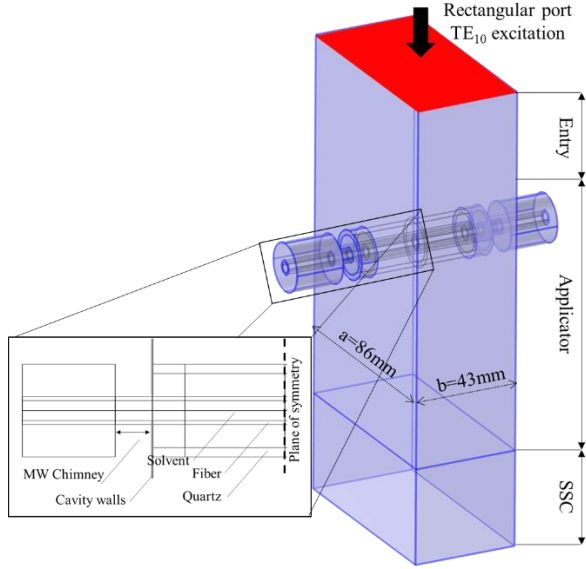


Figure 4-1: Representation of MW-assisted desorption set-up in Comsol multi-physics.

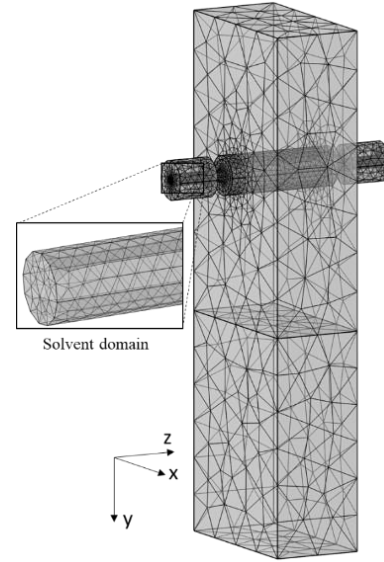


Figure 4-2: Meshed geometry of waveguide, and the solvent domain in the fiber lumen region.

4.2.4 Results

4.2.4.1 Model validation: comparison of reflected power spectra

In order to validate the modelling of the electromagnetic phenomenon, simulated and real levels of reflected powers were compared. If both data sets agree, this means that the simulation was able to well-predict the rate of absorbance of MW energy, hence the E-field maps inside the lossy material. Comparison was performed by either varying the position of the SSC, or by varying the frequency of the EM irradiation. It should be highlighted that both methods of validation are equivalent, as a change in frequency is equivalent to a change in the position of the SSC and vice versa.

A vector network analyzer (ENA 5062A, Agilent Technologies, Malaysia) was connected to the waveguide transition instead of the microwave generator. The VNA is able to generate low power EM waves and to record the norm of reflected E-field waves, in order to obtain the (S_{11}) spectrum over [2400-2500 MHz]; the SSC was used to set minimal levels of reflected powers at $f=2450$ MHz. The (S_{11}) parameter is defined in (4.9), with (E_r) being norm of the reflected E-field wave, (E_i) that of the incident wave, while (θ) is the phase difference. We define the optimum SSC position, as that which places the minima of the reflected power spectrum at $f=2450$ MHz.

$$S_{11} = |E_r|/|E_i| \angle \theta \quad (4.9)$$

The (S_{11}) parameter is usually represented in (dB) scale as shown in (4.10).

$$S_{11}(\text{dB}) = 20 \log_{10}[E_r/E_i] \quad (4.10)$$

The ratio of reflected to incident power is presented in (4.11).

$$[P_r/P_i] = [E_r/E_i]^2 \quad (4.11)$$

Case of distilled water flowing into the fiber

The model was validated by comparing the simulated and experimental reflected powers spectra when distilled water (DW) - that acts as absorbents of EM irradiation- circulated in the lumen region of the hollow fiber. Figure 4-3 presents both the experimental and computed (S_{11}) spectra: the experimental (VNA) results, the simulated data at the experimental optimum SSC position minimizing the experimental reflected powers at 2450MHz, as well simulated reflection at the simulated optimum SSC position.

Results show that experimental and simulated curves have similar tendencies, but the simulated curve corresponding to the real position of the SSC is shifted to higher frequencies. This can be explained by many reasons: errors in the estimation of dielectric properties, or in the geometrical dimensions of the applicator and waveguide, error in calibrating the VNA, as well as other simplifying assumptions. By slightly changing the position of the SSC in the model from 103.8 mm to 107 mm, the minimum of the simulated (S_{11}) spectrum is placed at 2450MHz. The simulated curve fits far better the experimental data, with the exception of the seemingly large difference of the minima. The large difference in minima is not to be seen as a deviation of the model, but rather due to the use of the logarithmic scale. As an example: an S_{11} value of -15 dB signifies (~3.1%) of reflected power relative to the incident one; conversly an S_{11} value of -25 dB signifies a reflected portion of (~0.31%). Despite large differences in S_{11} values, little difference persists in the actual reflected powers.

Figure 4-4, derived from Figure 4-3, presents the variations of the reflected power fraction as a function of frequency. The figure shows that the variations of the fractions of reflected power are closed to the measured values provided that the SSC position is slightly adjusted from 103.8 mm to 107 mm. The average error over the spectrum [2.4 - 2.5 GHz] is in the order of (~5.5 %).

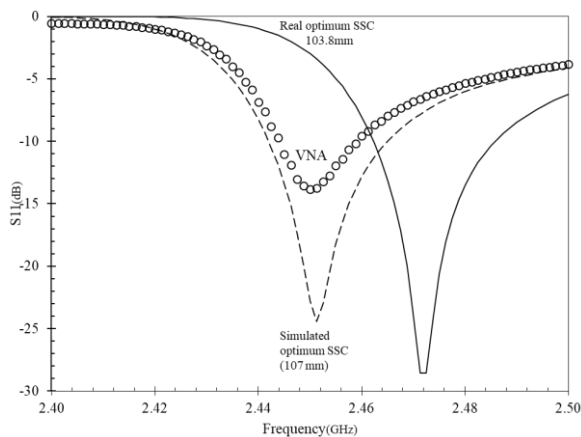


Figure 4-3: (S_{11}) spectrum with distilled water ($T=20^{\circ}\text{C}$) occupying the lumen region.

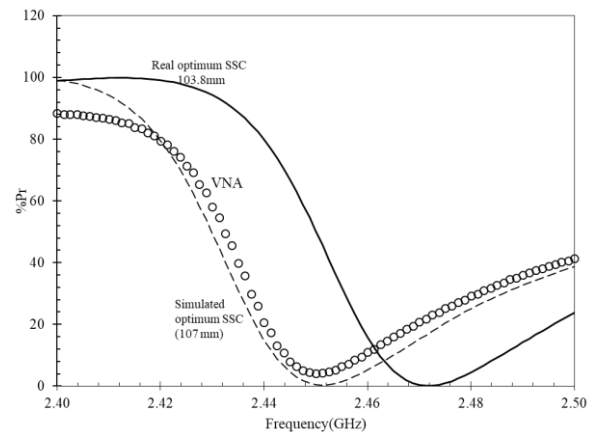


Figure 4-4: Reflected power spectrum with distilled water ($T=20^{\circ}\text{C}$) occupying the lumen region.

Case of 30%wt. ETA in the fiber

(S_{11}) as well as ($\% P_r$) spectra are plotted in Figure 4-5 and Figure 4-6 respectively as a function of frequency, in the case where distilled water is replaced by 30%wt. ETA flowing inside the fiber under ambient conditions.

Both figures demonstrate that thanks to the adjustment of the SSC position, that was moved to 112 mm in the simulation whereas the real position was 108mm, a quite good predictive capability of the model can be obtained, Figure 4-6 shows the almost perfect agreement obtained with the experimental reflected power fraction at 2450MHz, as well as in the above frequency domain.

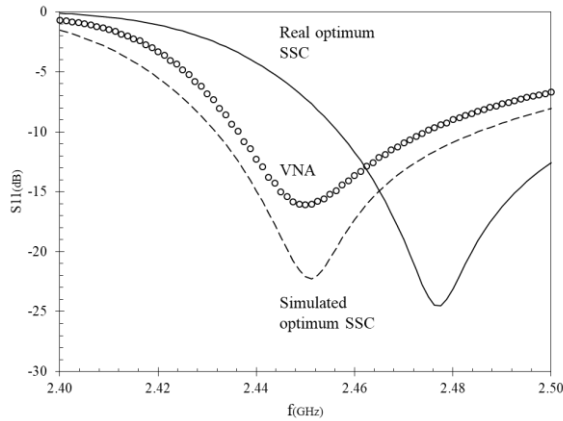


Figure 4-5: S11 spectrum with 30% wt. ETA (25°C) in the lumen region: experimental results using the VNA, simulated data at the real position of the SCC, and simulated data at the simulated optimal SSC position

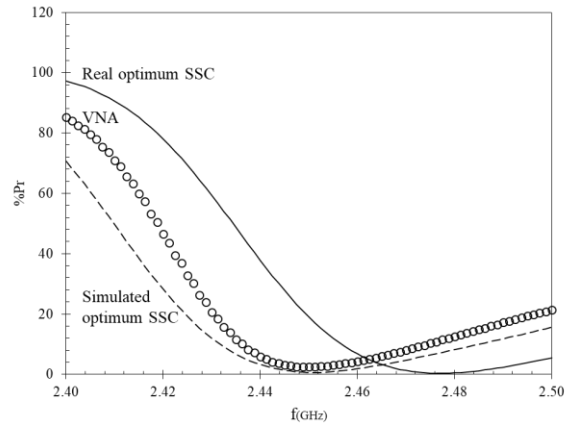


Figure 4-6: S11 spectrum with 30% wt. ETA (25°C) in the lumen region: experimental results using the VNA, simulated data at the real position of the SCC, and simulated data at the simulated optimal SSC position

4.2.5 Sensitivity analysis of power reflection

The sensitivity of the reflected power was studied with respect to the model parameters: dielectric properties of the system components: distilled water, quartz and Teflon fiber, as well as the dimensions of the fiber. In all cases, the position of the SSC was adjusted so that the experimental and computed minima of the (S_{11}) curves match at 2450 MHz. It is worth mentioning that the use of distilled water instead of 30% wt. ETA was motivated by the very well documented dielectric properties of the former, whereas data on the properties of the latter are practically non-existent.

Influence of the dielectric properties

Results show that the fraction of reflected power is insensitive to $\pm 10\%$ changes in the dielectric properties of the quartz tube or the Teflon. When the relative permittivity and loss factor of distilled water are varied in the range of $[-10\% - +10\%]$ with a step size of 5%, the reflected power spectrum experiences little variations as shown in Figure 4-7. These results are useful in providing an estimation of numerical error induced by an error in the estimation of the component dielectric properties. They also indicate that the presence of some impurities in the liquid, or minor temperature changes should not greatly affect the EM field propagation.

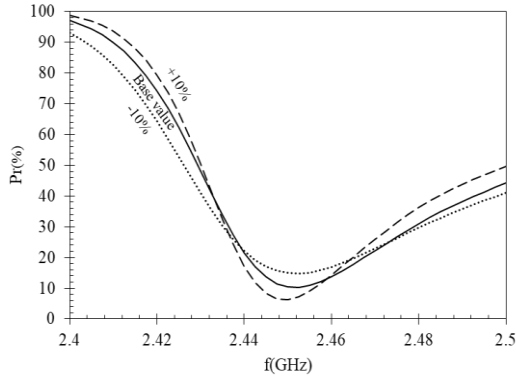


Figure 4-7: sensitivity of reflected power with respect to the relative permittivity (ϵ') of distilled water. Base value of relative permittivity at $f=2450$ MHz is set as ($\epsilon'_{H_2O}=78.67$).

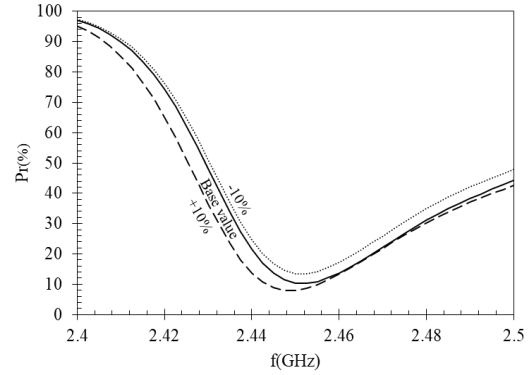


Figure 4-8: Sensitivity of reflected power with respect to the dielectric loss factor of distilled water. Base value of dielectric loss factor at $f=2450$ MHz is set as ($\epsilon''_{H_2O}=10$).

Influence of fiber dimensions

It is suspected that with the fiber ageing, the lumen radius may change under the effect of thermal stresses. It is for this reason that we evaluate the sensitivity of the model with respect to this parameter. In Figure 4-9, we compare simulated power fraction curves varying the lumen size by $\pm 7.5\%$ with a step size of 2.5%. The fraction of reflected power is shown to increase with the fiber radius over the most of the tested frequency range. In general, if the product increases in dimensions it disturbs the propagation of the EM, thus inducing a greater reflection, similarly small products would not absorb microwaves sufficiently and would lead to the same result.

Figure 4-10 presents the sensitivity of reflected power to the discussed parameters at $f=2450$ MHz. It is clear that accurate knowledge of fiber dimension is crucial, however power reflection is less sensitive to other parameters, hence they can be determined mildly determined without a considerable loss in accuracy.

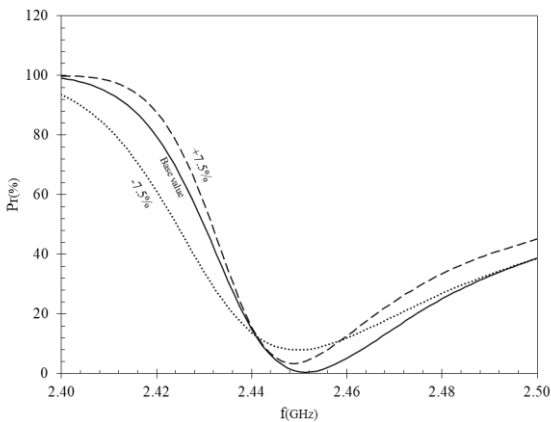


Figure 4-9: Sensitivity of reflected power to the internal radius of the fiber. Base value of fiber radius is set at 2.15 mm.

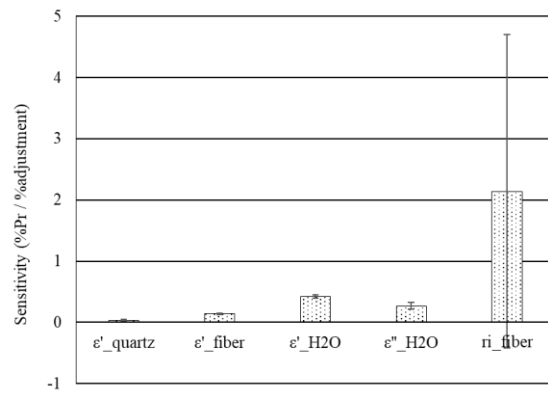


Figure 4-10: Sensitivity of optimal reflected power at $f=2450$ MHz

4.2.6 Simulation of EM fields: case of 30% wt. ETA enriched with CO₂

After experimentally assessing the accuracy of the simulated EM propagation inside the contactor using either DW or unloaded 30% wt. ETA, we attempt to model the system when 30% wt. ETA enriched with CO₂ flows into

the fiber lumen. This step subscribes to the methodology of progressive complexification of the numerical model, it will be followed by the incorporation of the physical phenomena of heat and momentum transfers.

4.2.6.1 Optimal SSC position

Before attempting to analyze the E-field maps in the solvent domain, optimal position of the sliding short circuit needs to be determined. Till now, the optimal SSC position was determined considering the measured experimental adaptation settings. For the case of EM simulations involving liquids that were not tested experimentally, the optimal position needs to be found numerically by plotting the reflected power as a function of the SSC position. The SSC is varied over the interval $[x, x+\lambda_g/2]$ with ($\lambda_g \sim 173$ mm) being the guided wavelength of the EM wave at $f=2450$ MHz in vacuum. A multi-step procedure was used to find the optimal SSC position corresponding to minimal reflected power, the step size of the variation of the SSC was progressively tightened at the position of the minimum.

Figure 4-11 presents the fraction of reflected power while varying the SSC position by steps of 10 mm, for the case of 30% wt. ETA at a carbonation ratio ($\alpha=0.44$) at $T=20, 60, 80^\circ\text{C}$. Figure 4-11 shows that the reflected powers at different temperatures are very similar which is surprising considering the high sensitivity of the dielectric properties of the solvent relative to it. The maxima of the reflected power curves are located at identical SSC position due to the fact that when nearly total reflection occurs, the EM field does not interact with the lossy dielectric, thereby the distribution of the E-field is independent of the properties of the solvent.

As Figure 4-11 shows that the minima of reflected power are computed at SSC positions in the range [110 - 150 mm], Figure 4-12 focuses in this region while applying a tighter step size of 2 mm to determine the minimal reflected power with greater accuracy. The analysis of the E-field produced at the minima of the power reflection in Figure 4-12 is examined in the sections below.

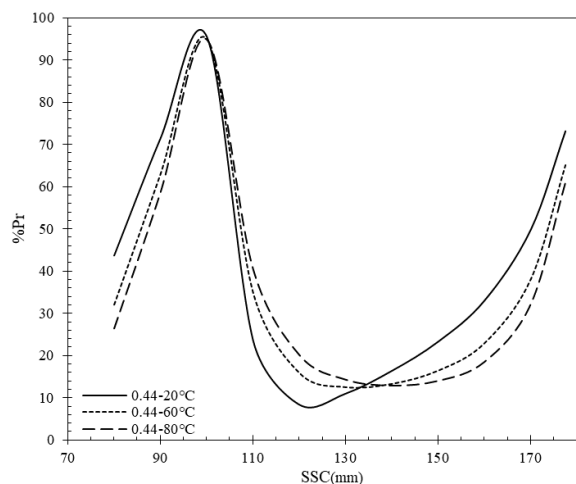


Figure 4-11: Simulated reflected power (% Pr) function of SSC position at 2540MHz - SSC step size (10 mm). Solvent used is 30% wt. ETA at ($\alpha=0.44$) and $T=20,60,80^\circ\text{C}$

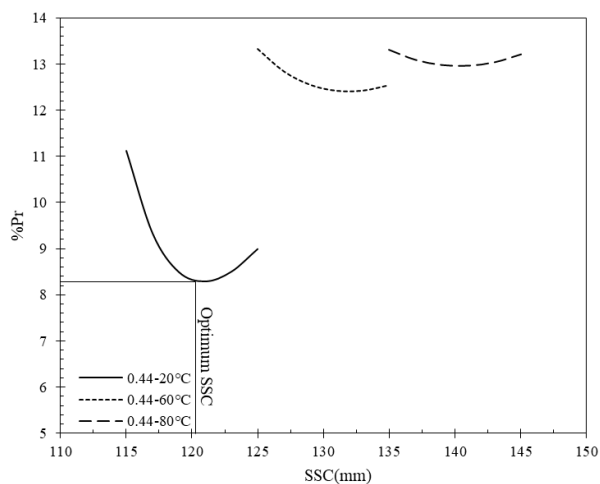


Figure 4-12: Simulated reflected power (% Pr) function of SSC position at 2540MHz - SSC step size (2 mm). Solvent used is 30% wt. ETA at ($\alpha=0.44$) and $T=20,60,80^\circ\text{C}$

4.2.6.2 Electric-field maps

Waveguide and applicator

The E-field map was plotted in Figure 4-13 along the waveguide, and the hollow fiber whose lumen region is occupied with 30%wt. ETA at ($\alpha=0.44$) and ($T=60^{\circ}\text{C}$). The incident power at the entry port was chosen arbitrarily, thus Figure 4-13 serves only as a qualitative representation that is independent from the set value of the incident MW power. The planar representation is sufficient given that in the (TE_{10}) mode, the E-field is invariant with respect to the small dimension ($b=43\text{ mm}$) of the waveguide.

Figure 4-13 shows that the E-field norm is stronger upstream the cavity than downstream. The variations of energy densities between the two regions imply that most of the EM power was absorbed upon first contact with the product. Part of the incident power, which is reflected back to the entry port, resonates with the incident E-field; the unabsorbed part of the energy bypasses the solvent and reaches the sliding short circuit where it gets reflected back towards the cavity.

To obtain a more quantitative assessment, the E-field norm was plotted in Figure 4-14 along a cut-line that traverses the waveguide for cases where solvent temperature (20, 60, 80 °C) was varied at a constant carbonation ratio ($\alpha=0.44$). To achieve similar power absorption in all the three cases, the incident MW power was adjusted in such a manner to account for the levels of reflected power. Figure 4-14 shows that the different E-field curves are “in-phase” upwind of the “product” and displaced from one another towards the SSC, this is due to the different set values of SSC used to reach optimal adaptation. The increased E-field norm upwind of the applicator is the consequence of using higher MW entry powers to compensate for the increased power reflection. It is interesting to note that in Figure 4-14, the E-field in the solvent is in the same order of magnitude as its surroundings despite having a much higher dielectric constant, the reason is partly attributed to the superposition of the forward and backward traveling E-field waves.

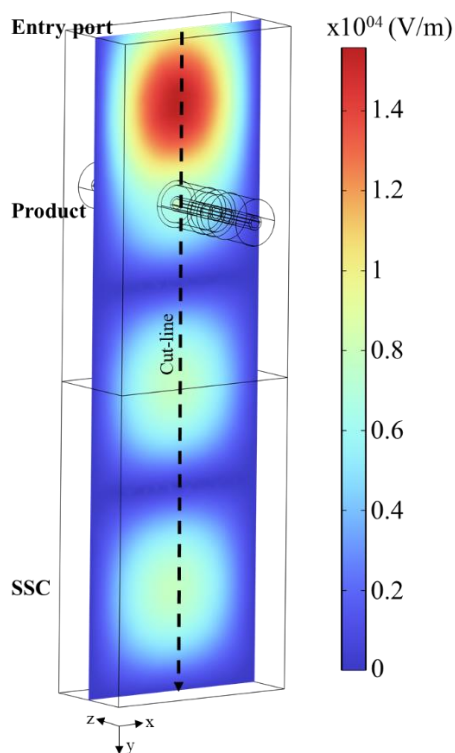


Figure 4-13: E-field maps in waveguide ($f=2450$ MHz) - case of 30% wt.ETA, $\alpha=0.44$, $T=60^\circ\text{C}$.

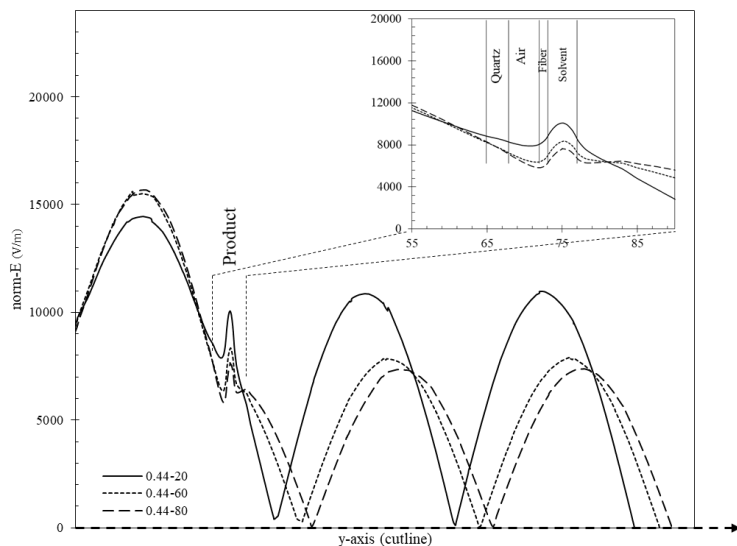


Figure 4-14: Plot of E-field norm on cut-line along the length of the waveguide ($f=2450\text{MHz}$). Case 30% wt. ETA ($\alpha=0.44$), $T=20^\circ\text{C}$, 60°C , 80°C .

Another E-field map is presented in Figure 4-15 focusing on the “product” region in the cavity. For a better representation, the E-field is plotted in a logarithmic scale (base “e”). It can be seen that the E-field is homogenous in the neighborhood of the solvent region, while it vanishes outside the cavity as it is obstructed at the MW chimney. The abrupt change in geometry causes an intensified E-field applied on the fiber material at the externals of the cavity walls. Such observations further justifies the use of low dissipation polymers such as (PTFE). Other polymers, such as(PCV) are actually prone to experience high absorbance of MW irradiation, especially at temperatures superior to glass transition T_g [5, 6].

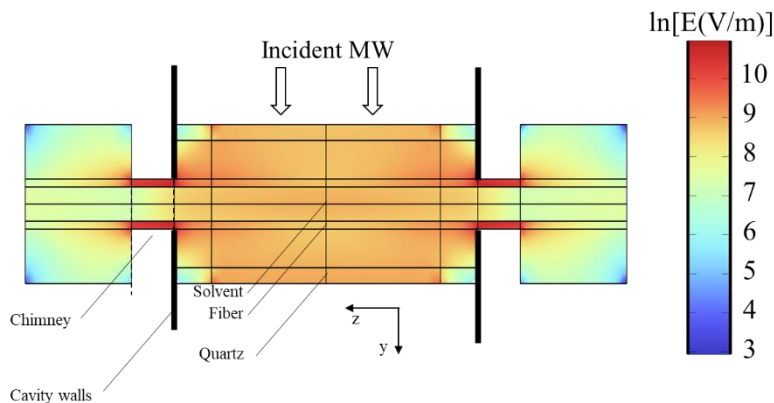


Figure 4-15: E-field map in the MW cavity ($f=2450$ MHz). Case of 30% wt. ETA, $\alpha=0.44$, $T=60^\circ\text{C}$

Fiber lumen: solvent domain

In this section, we examine the E-field distributions within the lumen volume of the fiber. Figure 4-16 presents the E-field maps computed within the solvent domain filling the lumen side. The figure demonstrates that the E-field is constant in the solvent domain inside the MW cavity. This can be attributed to the lumen radius being considerably lower than the penetration depth of EM waves. Uniform E-fields may induce a uniform EM dissipation rate, although the consideration of the flow velocity maps is likely to give a non-uniform T-distribution. Figure 4-16 also shows that the E-field norm is not constant across the three simulated cases despite equal dissipation of EM power: Increased temperature raises the dielectric loss factor of the solvent by ionic conduction, hence at higher temperature, a lower E-field norm is required to dissipate a same amount of EM energy.

Figure 4-17 presents the E-field maps across the radial cross-section of the fiber at different conditions $[T, \alpha]$: $[20^\circ\text{C}, 0.44]$, $[60^\circ\text{C}, 0.44]$, and $[80^\circ\text{C}, 0.44]$. It is interesting to observe that the E-field is more concentrated at the center of the fiber, this results from the superposition of forward and backward EM waves.

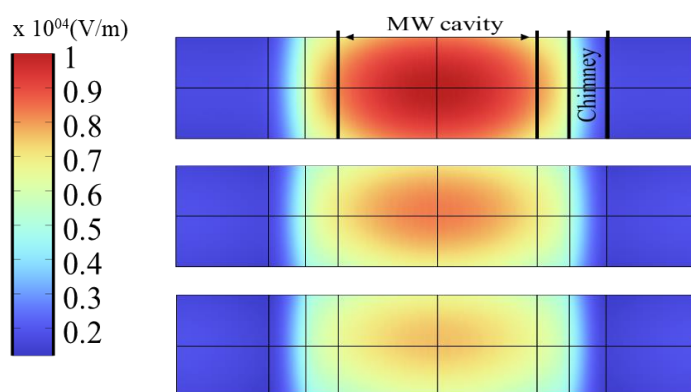


Figure 4-16: E-field in the longitudinal cross-section of the solvent domain at different conditions $[T, \alpha]$: $[20^\circ\text{C}, 0.44]$, $[60^\circ\text{C}, 0.44]$, $[80^\circ\text{C}, 0.44]$.

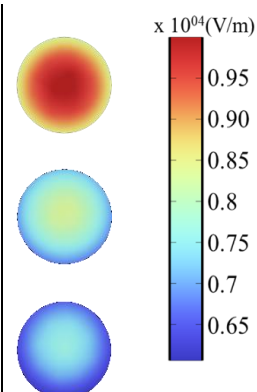


Figure 4-17: E-field in the radial cross-section of the solvent at mid-cavity

4.3 Coupling EM wave propagation to energy and momentum balances

In the previous part, the model was verified to be capable of simulating the propagation of the electromagnetic waves along the waveguide and within the applicator, which allows the visualization of the E-field maps in the solvent. In this part, the resolution of the energy and momentum balances was incorporated in the model to allow for the simulation of microwave heating of the solvent and the determination of temperature maps herein. The latter are necessary elements for modeling chemical desorption at non-isothermal condition.

4.3.1 Energy and momentum conservation equations

The liquid flow hydrodynamics was described according to the Naviers-Stokes balance equation, assuming its Newtonian behavior (eq. 1.13). The energy balance was expressed assuming that the volumetric dissipation rate of EM energy (Q) was integrally transferred to the lumen side to heat the liquid phase (eq. 1.14). The accumulation of

heat within the other components of the system, including the porous membrane, the quartz tube and the gas flow were assumed as negligible given their poor dielectric properties.

$$\text{Naviers-Stokes Equation} \quad \rho(\vec{u} \cdot \nabla)\vec{u} = \rho\vec{g} - \nabla P + \mu\nabla^2\vec{u} \quad (4.12)$$

$$\text{Energy Balance} \quad \rho C_p(\vec{u} \cdot \nabla T) - \nabla \cdot (k\nabla T) = Q \quad (4.13)$$

$$\text{EM dissipation rate} \quad Q_{W/m^3} = \omega \epsilon'' \epsilon_0^* E^2 \quad (4.14)$$

In equation (4.12), (ρ) is the density of the fluid, (u) is the velocity vector, (g) is the gravitational acceleration, (P) is the pressure, and (μ) is the fluid viscosity. In (4.13), (C_p) is the specific heat of the fluid, (T) is the temperature, (k) is the thermal conductivity, and (Q) is the volumetric dissipation rate of EM energy. (Q) is computed according to (4.14) with (ω) being the angular frequency, (ϵ'') the dielectric loss factor, (ϵ_0^*) the permittivity of free space and (E) is the rms-value of the electric field.

Figure 4-18 illustrates the multi-physical modeling approach under steady state conditions, pointing out the coupled phenomena and inter-related physical variables. The interaction between EM propagation and heat transfer is such that, the temperature of the solvent influences its dielectric properties, while change in dielectric properties influences the E-field maps and hence the volumetric dissipation rate. The interaction of fluid mechanics with heat transfer is that the velocity fields influence convective rate of heat exchange, consequently the change in temperature influences the physical properties of the solvent (ρ, μ).

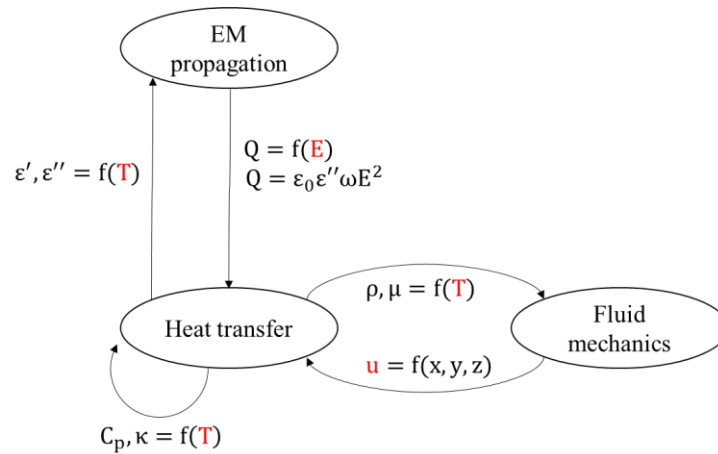


Figure 4-18: Schematic of the equation coupling to model solvent heating by microwave irradiation at steady state.

4.3.2 Boundary conditions

The boundary conditions of the fluid mechanics and heat-transfer physical phenomena are presented in Table 4.3, while those related to the EM phenomenon are identical to those given in section 4.2.

	Coordinates	Type	Equation
Momentum balance	$z=0$	solvent outlet	Constant mass flow
	$z=L$	solvent inlet	Constant pressure condition
	$0 < z < L; r = r_i$	Radial boundary	Liquid velocity is null at the membrane wall (No-slip condition)
			$m_{in} = \int \rho(\vec{u} \cdot \vec{n}) dS$
			$P = 0$
			$\vec{u} = 0$
Energy balance	$z=0$	(solvent inlet)	Fixed temperature
	$z=L$	(solvent outlet)	Heat transfer by conduction is null
	$0 < z < L; r = r_i$	(Radial boundary)	Heat transfer between the liquid flow and the membrane was neglected (thermal insulation)
			$T = T_{in}$
			$-\vec{n} \cdot \vec{q} = 0$
			$-\vec{n} \cdot \vec{q} = 0$

Table 4.3: Boundary conditions for fluid mechanics and heat transfer applied on fiber lumen

In Table 4.3 (r_i) stands for the internal radius of the fiber, (L) its length, (\vec{n}) normal vector to the surface, (P) pressure, (\vec{u}) the velocity vector of the fluid flow, and (\vec{q}) the heat flux.

It was assumed that the lateral surfaces of the fiber behave as insulator, this is because of the thickness of the PTFE fiber (1 mm) and the minimal sweeping gas flow rate (3.33-6.66 mL/s) used in experiments (9-16). The validity of this assumption is demonstrated in subsection (4.4.2.5). The dielectric properties of the solvent were assumed to be invariant with CO₂ loading along the length of the fiber as the regeneration rate ($\Delta\alpha = \alpha_{in} - \alpha_{out}$) was experimentally found to be very small, hence the dielectric properties are solely dependent on temperature. It is important to point out that the lumen is assumed to be completely filled with the liquid phase solvent: this may not be true as evaporation may be induced by hot-spots within the fiber, or the creation of CO₂ bubbles during desorption.

4.3.3 Resolution and Meshing

The coupling between the physical phenomena related to the electromagnetic field, heat transfers and fluid mechanics was implemented using the multi-physics branch in COMSOL[®] which includes the “Non-isothermal Flow” option that couples heat transfer physics to fluid mechanics, in addition to the “Electromagnetic heating” option that couples EM phenomenon with heat transfer. The resolution of the equation set enables 3D map computation of the electromagnetic field, E, temperature T and local liquid velocity U. The EM phenomenon and fluid mechanics were solved using the (GMRES) solver while energy balance equation was solved using the (PARDISO) algorithm.

Resolution of the system is done by a two-step procedure: in step one, the Navier-Stokes equation was exclusively solved to initialize the computation of the velocity field. In step 2, the model solves the whole set of

equations taking as initial guess the velocity field calculated in step 1. This procedure was found to reduce the computation time greatly. The model iterates until the error between two successive iterations (on E-field, velocity, and T) is inferior to a value fixed at (0.1%).

With regards to meshing, several configurations were tested with the aim of reaching an independency of the solution on the used mesh, and an acceptable computation time. In all tested meshes, the setting “Fine” -preset by Comsol®- was used to mesh the entire simulated domain with the exception of the solvent. The latter was meshed in various manners as shown in Table 4.4, the mesh was either pre-defined in Comsol® (Fine-Extremely Fine), or was adjusted by adding several boundary layers (Custom 1- Custom 2), the difference between meshing schemes is shown in Figure 4-19.

Type	Fine	Finer	Extra Fine	Extremely Fine	Custom 1	Custom 2
Number of vertices	457	3176	10828	28836	8684	35828
Maximum size (mm)	3.77	2.11	1.47	1.13	2.48	1.37
Number of boundary layers	-	-	-	-	3	5

Table 4.4: Meshing configuration of the fiber lumen domain (solvent)

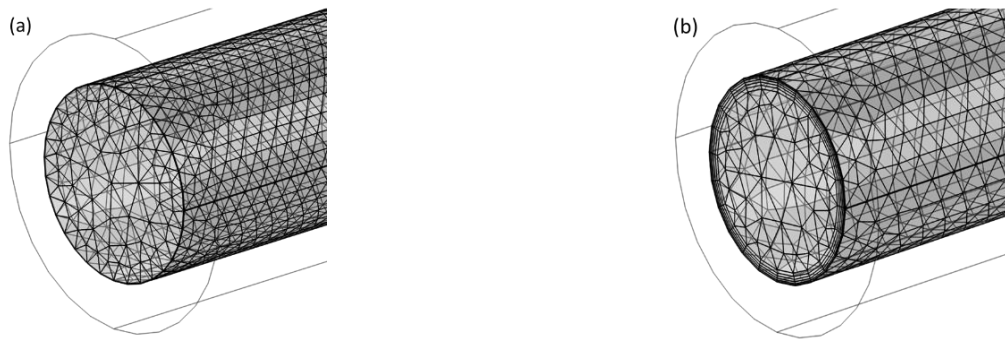


Figure 4-19: Meshing of the fiber lumen domain using two different configurations: (a)-Extremely Fine; (b)-Custom 2.

At identical simulation settings, the electric field, velocity, and temperature data were averaged over the fiber domain for different meshing configurations and are shown in Table 4.5. Overall the solution is fairly independent from the meshing used, for this reason the mesh (Custom 1) was chosen as it presents a very acceptable computation time.

Average	Fine	Finer	Extra Fine	Extremely Fine	Custom 1	Custom 2
\bar{E} (V/m)	12474	12483	12487	12491	12479	12488
\bar{u} (cm/s)	7.94	7.97	7.97	7.97	7.97	7.97
\bar{T} (°C)	42.79	43.94	44.51	44.79	44.26	44.75
Solution time (mm:ss)	00:38	01:16	02:55	07:40	02:52	11:55

Table 4.5: Averaged quantities over the fiber domain at different fiber configurations for the case of microwave heating of distilled water

4.4 Numerical results

4.4.1 Validation of MW-heating model

4.4.1.1 MW-heating of distilled water (DW)

In order to validate the numerical model, MW heating experiments using distilled water were performed. Distilled water was made to circulate inside the hollow fiber at different mass flow rates (2-5 ml/s) by steps of 1 ml/s. The MW power incident from the generator was adjusted so as to maintain an outlet temperature in the neighborhood of 40°C, whilst the inlet temperature was 20°C. The incident power from the generator was measured using the six-port reflectometer and was considered as the input power in the model. The use of distilled water was motivated by its well-known physical, dielectric and thermal properties, which is not the case of aqueous ethanalamine solutions, especially when loaded with CO₂. The properties of DW are reported in the Annex.

Figure 4-20 compares the simulated and the experimental outlet temperatures (T_{out}) of distilled water at different mass flow rates. Figure 4-20 shows that the model is able to predict (T_{out}) with a very high accuracy for the different tested mass flowrates, the deviations observed being in average of 0.32°C. It is worth mentioning that the real and simulated optimal SSC positions were in this case 21 and 21.5 mm respectively.

To further assess the predictive ability of the model a supplementary validation of outlet temperature was performed using 30%wt. ETA solution unloaded with CO₂. Similar experiment tests were conducted varying the mass flow rates in the same range, considering the solvent properties as specified in the Annex. The results are presented in Figure 4-21, and show that the strong agreement between the experimental and numerical data. It is worth mentioning that in this case, the real and simulated positions of the SSC were identical.

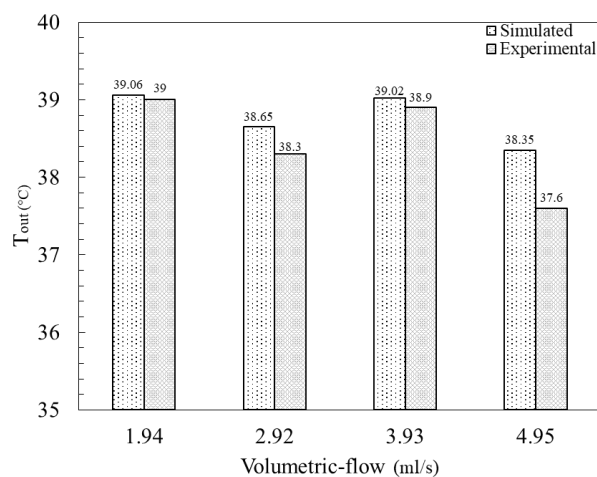


Figure 4-20: Comparison of simulated and experimental outlet temperatures of MW heating of distilled water.

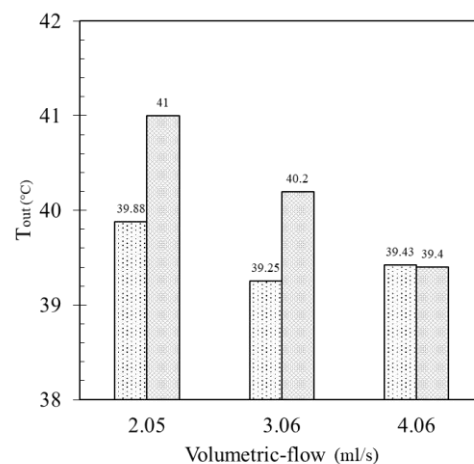


Figure 4-21: Comparison of simulated and experimental outlet temperatures of MW heating of 30% wt. ETA – unloaded.

4.4.2 MW-heating of 30% wt. ETA enriched with CO₂

MW heating of CO₂ loaded 30% wt. ETA solutions was simulated at the operating conditions of experiments (9-12) of the experimental design: volumetric flow rate of solvent at 0.2 and 0.6 mL/s, (T_{out}) at 50 and 60°C, carbonation ratio was fixed at ($\alpha=0.44$). As the lateral surfaces of the fiber were assumed to be adiabatic, the sweeping gas flow rate holds no effect on the temperature maps, hence it is only necessary to simulate experiments (9-12), to the exemption of (13-16). As the CO₂ desorption rates were very low in the experimental tested conditions, endothermal effect induced by the desorption reaction was not accounted for and the solvent mass flowrate was assumed as constant. As a reminder, the operating conditions of the experimental design are included in Table 4.6.

Experiment	$u_g(\text{mL/s})$	$V_l(\text{mL/s})$	$T_{out}(\text{°C})$
9	3.33	0.2	50
10	3.33	0.2	60
11	3.33	0.6	50
12	3.33	0.6	60
13	6.66	0.2	50
14	6.66	0.2	60
15	6.66	0.6	50
16	6.66	0.6	60

Table 4.6: Operating conditions at experiments (9-16) of the experimental design

4.4.2.1 2D/3D temperature maps in the fiber

In Figure 4-22, computed temperature maps are shown over the solvent flow region along the longitudinal section, for the experiments (9-12). Local axial and radial temperature variations are observed, with hotspots located close to the membrane wall, in the region of exit flow, thus the region near the liquid entry is deemed “cold” with respect to that near the liquid exit. The magnitude of the local temperature variations is clearly related with the solvent flowrate: the larger the liquid flowrate, the higher the local temperature rises close to the membrane walls at the same mean outlet temperature.

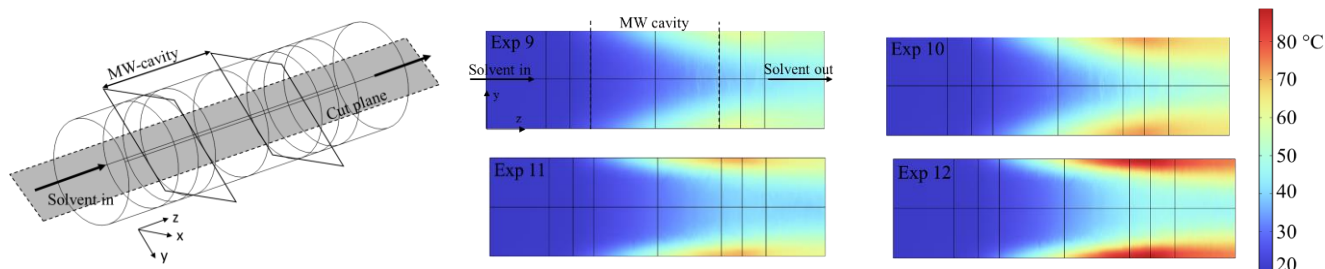


Figure 4-22: Simulated temperature maps on the longitudinal (ZY) cross-section of the fiber for different experiments [v_l , T_{out}]: Exp 9 - [0.2, 50]; Exp 10 - [0.2, 60]; Exp 11 - [0.6, 50]; Exp 12- [0.6, 60]

To explain the occurrence of local high temperature rises close to the membrane wall, the velocity field and the E-field of experiment (12) were plotted in Figure 4-23 and Figure 4-24 respectively. The velocity field displays

a typical laminar flow, with the velocity profile being parabolic and having its maxima at the fiber center and its minima at the fiber boundary. While the flow stagnates at the boundary of the fiber lumen (stagnant film region), the E-field does not experience radical changes between its center and boundary. The energy dissipation rate so appears uniform over the fiber cross section, therefore local temperature variations appear to be dictated by the distribution in the convective transport velocities of the liquid. The energy absorbed at the fiber center is easily evacuated due to large local solvent flow velocities, whereas the film region accumulates more heat in light of the similar dissipation rate, and less convective transport which leads to higher temperature levels. For a constant carbonation ratio, increased volumetric flow rate requires the use of higher MW powers that increase the accumulation of thermal energy at the fiber boundaries and thus an increase of local temperatures. This effect can be further compounded with higher dielectric loss factor in the film region which incentivizes greater energy dissipation.

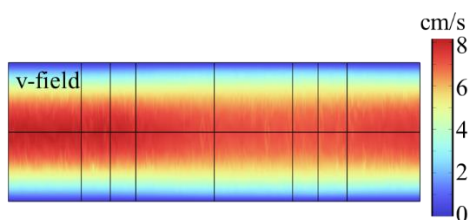


Figure 4-23: Velocity map in fiber lumen at operating conditions of Exp 12: $v_i = 0.6 \text{ mL/s}$, $T_{\text{out}} = 60^\circ\text{C}$, $\alpha = 0.44$.

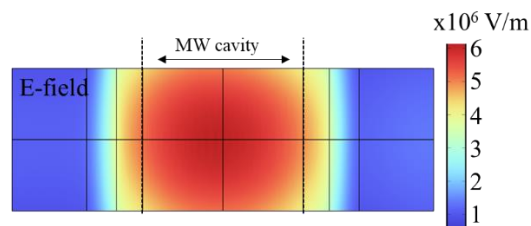


Figure 4-24: Electric field map in fiber lumen at operating conditions of Exp 12: $v_i = 0.6 \text{ mL/s}$, $T_{\text{out}} = 60^\circ\text{C}$, $\alpha = 0.44$.

4.4.2.2 Radial and tangential temperature profiles in the fiber

The radial and tangential temperature profiles were plotted in Figure 4-25 and Figure 4-26 respectively, the temperatures were plotted on the paths shown in Figure 4-27. Figure 4-25 shows that at the fiber boundaries, the temperature reaches high values then drops swiftly as we move further towards the bulk. In experiments 11 and 12, corresponding to the highest solvent flowrate, the bulk flow is characterized by a temperature plateau. Figure 4-26 presents the tangential T-profiles, it serves in showing the heating homogeneity, it shows that MW irradiation is being dissipated uniformly over all surfaces of the fiber: that facing the SSC, facing the MW entry port, and the lateral surfaces.

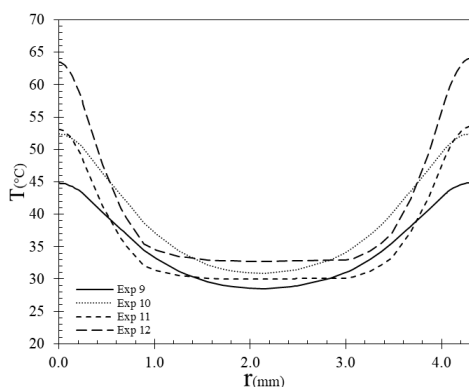


Figure 4-25: Radial temperature profiles at “mid-cavity” position for experiments (9-12)

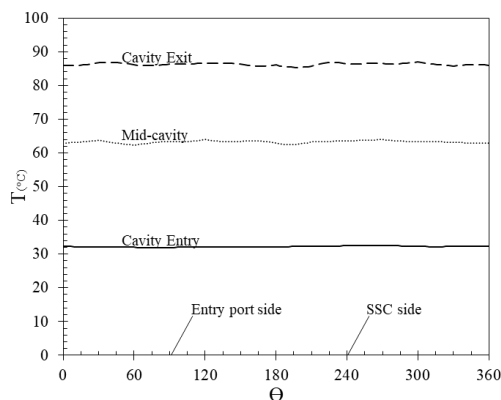


Figure 4-26: Tangential temperature profiles at $r=r_i$ and for $0<\Theta<360^\circ$ at operating conditions of experiment 12 [0.6 mL/s, $T_{out}=60^\circ\text{C}$].

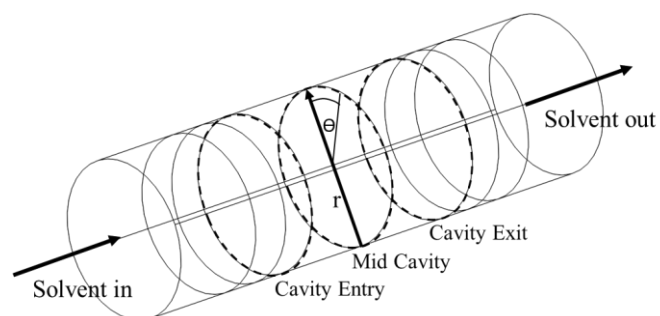


Figure 4-27: Schematic showing the paths over which temperature was evaluated.

4.4.2.3 Dielectric property maps

The evolution of the dielectric properties (ϵ'), and (ϵ'') of the solvent with respect to temperature are presented in Figure 4-28 and Figure 4-29 respectively at the operating conditions of experiment 12. Figure 4-28 shows that (ϵ') does not experience very strong variations over the fiber lumen, it displays similar distributions as the 3D-temperature maps, with higher values in the region of the stagnant liquid film. The large temperature gradients in the solvent are such that each point experiences a unique dielectric relaxation characterized by static dielectric

constant, relaxation time, and distribution of relaxation times. Therefore, the observed variations on (ϵ') cannot be explained in a straightforward manner as they are the result of several parameters at play.

The loss factor (ϵ'') is more straightforward to explain, it is plotted in Figure 4-29. Its distribution is shown to match those of the temperature maps, i.e. it is highest at positions of high temperatures and vice versa. This is related to the increase of the dielectric-loss by ionic conduction and dipolar rotation mechanisms. At higher temperatures, ionic compounds experience greater mobilities and thus are able to interact with the E-field. As the molecular dipoles, contribute less to dielectric loss at larger temperatures the increase in ionic activity mainly contributes to these variations. The evolution of the dielectric properties of aqueous ethanolamine is discussed in greater details in (insert chapter reference)

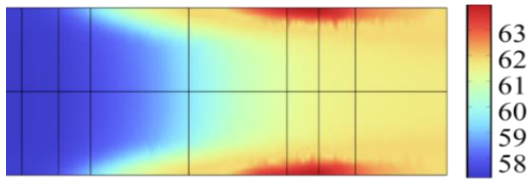


Figure 4-28: Relative permittivity (ϵ') in fiber lumen at $f=2450$ MHz and at conditions of experiment (12), [α, v_l, T_{out}] = [0.44, 0.6mL/s, 60°C].

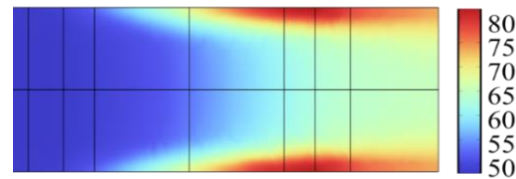


Figure 4-29: Dielectric loss factor (ϵ'') in fiber lumen at conditions of experiment 12, [α, v_l, T_{out}] = [0.44, 0.6mL/s, 60°C]

4.4.2.4 Effect of operating conditions on temperature distributions

It would be interesting to study the impact of operating conditions on the temperature distribution in the hollow fiber, this would serve to be useful when optimizing desorption in hollow fibers as the latter is temperature dependent. The evolution of the maximum temperature (T_{max}) determined at the membrane internal surface was examined as a function of the solvent flow rate (v_l), the carbonation ratio (α), and the average outlet temperature (T_{out}), as shown in Figure 4-30, Figure 4-31, and Figure 4-32 respectively. It is shown that the solvent mass flowrate as well as the outlet temperature affect the temperature rises in the liquid film: the larger the flowrate or the outlet temperature, the larger the local temperatures deviations. On the contrary, an increase in the carbonation ratio has no effect on T_{max} .

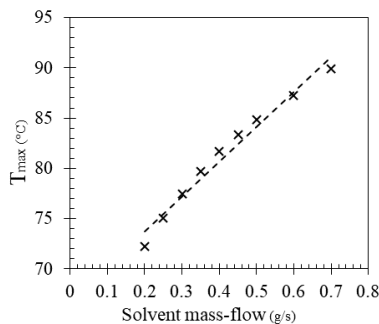


Figure 4-30: Influence of solvent v_l rate on T_{max} inside the fiber. [α, T_{out}] = [0.44, 60°C]

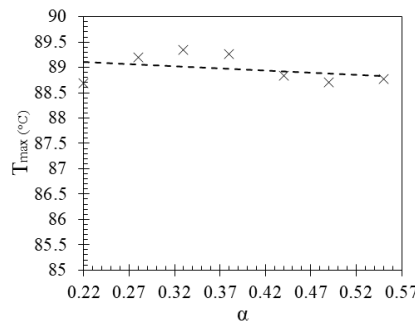


Figure 4-31: Influence of carbonation ratio (α) on T_{max} inside the fiber. [v_l, T_{out}] = [0.6 mL/s, 60°C]

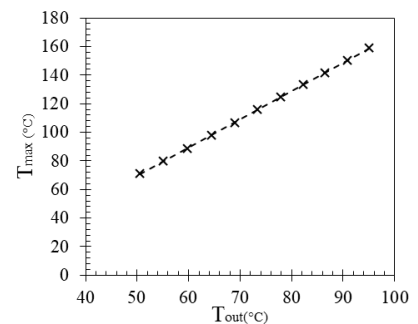


Figure 4-32: Influence of the outlet temperature of the solvent on T_{max} inside the fiber. [v_l, α] = [0.6 mL/s, 0.44]

4.4.2.5 Effect of heat losses across the membrane

To simplify the modeling approach, it was assumed that the fiber was adiabatic so that heat losses by conduction across the wall were considered negligible. In this part, we test the test the correctness of this assumption on experiments (9-16) by considering the heat transfers from the solvent across the membrane to the surrounding gas phase.

The thermal conductivity of the porous membrane (κ_m) was determined from equation (4.15), (κ_s) and (κ_g) being the thermal conductivity (W/m K) of PTFE and nitrogen respectively, computed from [7] and [8], and (ξ) the porosity of the membrane. The subscripts (s), (g) and (m) stand for solid PTFE, N₂ gas, and membrane respectively. Equation (4.15) was obtained from [9] and assumes a parallel resistances to heat transfer with no interaction between PTFE matrix and N₂ gas filling the pores.

$$\kappa_m = \xi \kappa_g + (1 - \xi)\kappa_s \quad (4.15)$$

The specific heat of the membrane (C_p) was determined from (4.16), where (ρ_s , ρ_g , ρ_m) are the densities of PTFE, nitrogen and of the porous membrane. ($C_{p,s}$) and (ρ_s) were obtained from [7]. Thermal and physical properties of N₂ gas were taken from Comsol[®] library of materials.

$$C_p = [(1 - \xi)\rho_s C_{p,s} + C_{p,g}\xi\rho_g]/\rho_m \quad (4.16)$$

A flow velocity boundary condition was applied on the gas inlet, and a static pressure condition was set at the gas outlet. The sweeping gas region was meshed with the preset “Fine” - performed by the software.

Results

Simulated temperature maps are shown in Figure 4-33 and Figure 4-34 for operating conditions of experiment (12) and experiment (16) respectively. Figure 4-33 shows that the at entry N₂-gas is heated by the exiting hot solvent, but as it moves in a counter current-manner, it contacts the cooler solvent region so that its temperature drops to reach a value equal to its inlet temperature ($T= 20^\circ\text{C}$). The low gas flow rate renders its thermal inertia very small with respect to the solvent stream, therefor heat is being recirculated from the hot side to the cold side of the fiber. The heat transfer to N₂-stream has no effect on the solvent temperature distribution within the internal fiber as the evacuated thermal power is in the order of (~0.1%) with respect to the incident microwave power. Increasing the gas flow rate in experiment (16), lower temperatures are encountered throughout the gas phase, as shown in Figure 1-36. Considering heat exchange between the gas and liquid phases, the values of (T_{\max}) reached in the solvent region deviate by less than (1 °C) compared to adiabatic conditions. The reader can refer to Figure 4-22 to examine the T-distribution at adiabatic condition of the fiber.

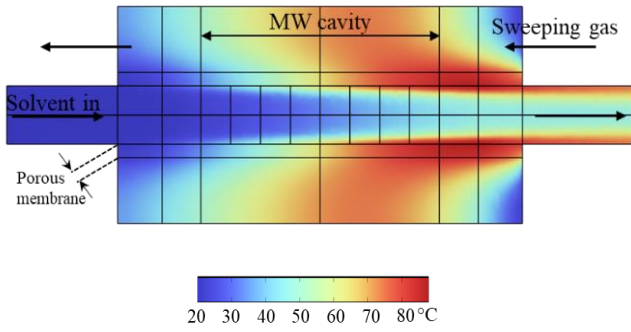


Figure 4-33: Temperature distribution in the gas, membrane and solvent regions. Operating conditions of experiment (12) were used: $T_{out}=60\text{ }^{\circ}\text{C}$, solvent $v_l=0.6\text{ mL/s}$, $v_g=3.33\text{ mL/s}$, $\alpha_{in}=0.44$.

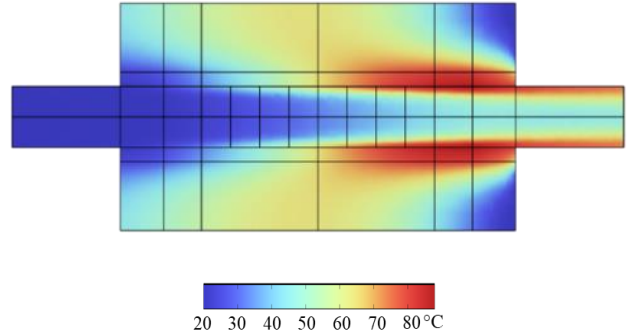


Figure 4-34: Temperature distribution in the gas, membrane and solvent regions. Operating conditions of experiment (16) were used: $T_{out}=60\text{ }^{\circ}\text{C}$, solvent $v_l=0.6\text{ mL/s}$, $v_g=6.66\text{ mL/s}$, $\alpha_{in}=0.44$.

In conclusion, the assumption of thermal insulation of the fiber walls is valid for the prediction of the local liquid temperature variations in the tested operating conditions. However, it should be said that a reevaluation is in order when using lower liquid flow rates or higher N_2 -gas flow rates.

4.5 Modeling of CO_2 desorption across a single hollow fiber

Previous parts have focused on the coupling of several physical phenomena of the system: electromagnetic propagation in the waveguide, heat transfer and momentum transfer in the fiber lumen. This part focuses on the theoretical description of mass-transfer combined with chemical desorption reaction described by the resistance-in-series model. First, a theoretical background regarding reactive mass-transfer phenomena are laid-out, for conditions of wetting and non-wetting of the membrane material. The model simulating the desorption process in isothermal conditions was first established with experimental data from the literature. This model was afterwards extended to describe the chemical desorption process assuming axial temperature variations in both the liquid film and bulk flow. The axial temperature profiles were then derived from the simulation data provided by the 3D model describing solvent flowing and microwave heating into the fiber lumen.

4.5.1 Resistance in series for modeling mass-transfer

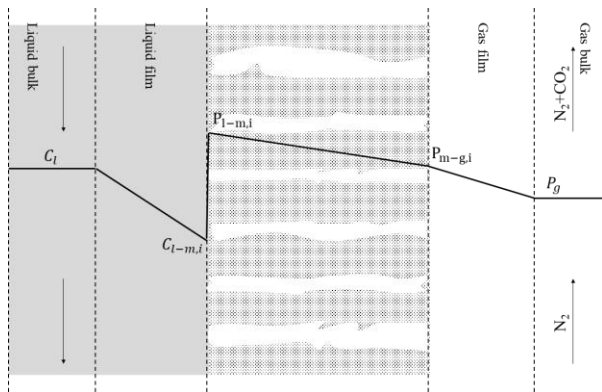


Figure 4-35: Schematic of the resistance in series model for mass-transfer, gas filled membrane

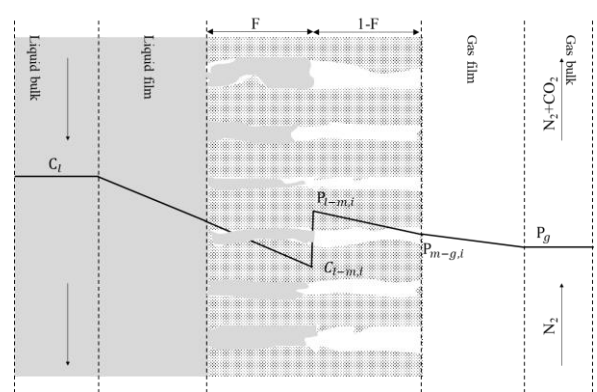


Figure 4-36: Schematic of the resistance in series model for mass-transfer, partially wetted mode of operation.

In a membrane process, mass-transfer takes place between the liquid and the gas bulk bulks. When only physical transfer takes place, the solute is supposed to be transported by the convective flow and to diffuse radially along the fiber. Over an elementary volume of the fiber, three transport resistances are accounted for, as shown in Figure 4-35.

1. Liquid film: The bulk of the liquid is considered to be well-mixed and hence is represented by a single composition, on the other hand, the liquid film adjacent to the internal membrane surface is stagnant. The solute diffusion across the liquid film is modeled using the Fick's law, therefor a concentration gradient is formed across the stagnant film. When reaching the liquid-membrane interface, the solute is supposed to become volatile. At the point where a change of phase occurs, it is common to assume equilibrium and use a partition coefficient (Henry's law) to describe the concentration distribution between the liquid and the gas phases.
2. Porous membrane: The volatile component transverses the gas-filled pores of the polymer matrix. The obstruction of the transfer of the volatile component by the stagnant gas filling the pores, as well as the tortuosity of the traveled path poses a resistance to mass-transfer. Equal pressures on both sides of the membrane dictate that diffusive transfer takes place via the molecular and the Knudsen diffusions.
3. Gas film: The thin film in contact with the outer surface of the membrane induces a supplementary mass transfer resistance. The solute diffusion across the gas film is described according to the Fick's law, whilst the gas bulk is assumed to be well-mixed over the elementary volume.

The resistance-in-series model is useful in order to calculate the overall mass transfer coefficient across all three resisting phases, starting from partial mass transfer coefficients in the liquid, membrane, and gas films, which are presented in equations (4.17), (4.18), and (4.19) respectively. In these equations the subscripts (l), (m), and (g) stand for liquid, membrane and gas respectively while subscript (i) stands for interface, (N) is the solute transfer rate, (A) is the surface area of gas-liquid contact, (k) is the partial mass transfer coefficient, and (C) is the concentration of physically dissolved volatile species.

$$N_l = A_l k_l (C_l - C_{l-m,i}) \quad (4.17)$$

$$N_m = A_m k_m (P_{l-m,i} - P_{m-g,i}) \quad (4.18)$$

$$N_g = A_g k_g (P_{m-g,i} - P_g) \quad (4.19)$$

Rearranging and using the partition coefficient ($He_c = P/C^*$), equations (4.17)-(4.19) become (4.20)-(4.22), with the superscript (*) designating the hypothetical concentration of a liquid phase at equilibrium with the partial pressure of the solute (or volatile component) in the gas phase.

$$(C_l - C_{l-m,i}) = N_l / (A_l k_l) \quad (4.20)$$

$$(C_{l-m,i}^* - C_{m-g,i}^*) = N_m / (A_m k_m He_c) \quad (4.21)$$

$$(C_{m-g,i}^* - C_g^*) = N_g / (A_g k_g He_c) \quad (4.22)$$

Adding equations (4.20)-(4.22), and applying the conservation of transfer rate ($N_l = N_m = N_g$), we get the expression of the mass transfer rate in equation (4.23).

$$N = \frac{C_l - C_g^*}{\frac{1}{A_l k_l} + \frac{1}{A_m k_m He_c} + \frac{1}{A_g k_g He_c}} \quad (4.23)$$

The mass-transfer rate is expressed in (4.24) with respect to the driving force for mass transfer, the over-all mass-transfer coefficient with respect to the liquid phase (K_L), and the surface area of exchange (A_1) of the fiber lumen.

$$N = (C_l - C_g^*) K_L A_1 \quad (4.24)$$

It can be found easily that by equating (4.23) and (4.24), and substituting the expressions of the transfer areas ($A = \pi d$), with (d) being the fiber diameter, we get the expression of (K_L) is given in (4.25). The inverse of (K_L) represents the total resistance to mass-transfer, and hence each term of (4.25) represents the partial resistance of each phase.

$$\frac{1}{K_L} = \frac{1}{k_l} + \frac{d_i}{d_{ln} k_m} \text{He}_c + \frac{d_i}{d_o k_g} \text{He}_c \quad (4.25)$$

4.5.1.1 Liquid phase mass-transfer coefficient

The liquid phase mass transfer correlation (k_l) was first derived by Graetz [10] for a 2D-problem of heat transfer of a fluid flowing into a cylinder under laminar regime. This correlation was then extended to mass transfer by L eveque [11] and consequently verified by Sherwood [12]. The correlation is expressed in equation (4.26) with (d_i) and (l) being the diameter and the length of the fiber, (Sh) the Sherwood number, (Re) the Reynold's number, and (Sc) being the Schmidt number. The expressions of the dimensionless numbers are given in (4.27), with (D_1) being the diffusivity of the solute in the liquid phase, (u) the average velocity of the solvent in the fiber lumen, (μ) the solvent viscosity.

$$Sh = 1,615 \left(Re \cdot Sc \cdot \frac{d_i}{l} \right)^{\frac{1}{3}} \quad (4.26)$$

$$Sh = \frac{k_l d_i}{D_1} // Re = \frac{\rho d_i u}{\mu} // Sc = \frac{\mu}{\rho D_1} \quad (4.27)$$

We substitute (4.27) in (4.26) to get the expression of the physical mass-transfer coefficient in the hollow fiber lumen in (4.28).

$$k_l = 1,615 \left(\frac{u}{l} \cdot \frac{D_1^2}{d_i} \right)^{\frac{1}{3}} \quad (4.28)$$

The expression of the diffusivity of CO_2 in carbonated 30% wt. ETA can be found in the Annex of the current chapter.

4.5.1.2 Membrane mass-transfer coefficient

The resistance to mass-transfer in the membrane depends on the operating conditions, such that high operating trans-membrane pressure may lead to the intrusion of the liquid phase into the pores [13]. The membrane wetting is known to have adverse effects on mass-transfer performance, as the diffusivity of the solute in the wetted pores is a few orders of magnitude lower than in gas-filled ones. We note that other wetting mechanisms can occur such as condensation wetting which may take place when the solute vapors cool down and condenses inside the membrane pores. The membrane mass-transfer coefficient is estimated considering either non-wetting or partially wetted modes.

Non-wetted mode

In the non-wetted mode, the mass transfer coefficient – (k_m) (m/s) - is calculated from (4.29) [14]. (τ) being the tortuosity and expressed in (4.30) and obtained from [15, 16], ($D_{g,eff}$) is the solute effective diffusivity in the pores filled with the gas phase (m^2/s), (δ) being the membrane thickness (m), and (ξ) is the connected porosity of the membrane.

$$k_M = [D_{g,eff} \xi] / [\tau \delta] \quad (4.29)$$

$$\tau = 1/\xi^2 \quad (4.30)$$

When the solute diffuses through the membrane pores it encounters resistances originating from collisions with gas molecules (molecular diffusion), and collisions with the pore walls (Knudsen diffusion). The effective diffusivity ($D_{g,eff}$) is calculated as per (4.31) [17–19], with (D_g) accounting for the molecular diffusion of the solute in the gas phase, while (D_{kn}) accounts for the Knudsen diffusion.

$$\frac{1}{D_{g,eff}} = \frac{1}{D_g} + \frac{1}{D_{kn}} \quad (4.31)$$

The molecular diffusivity of CO_2 is given in the appendix, while the Knudsen diffusivity is expressed according to equation (4.32) with r being the mean pore size in (cm), M the molar mass of CO_2 (g/mol), and R the ideal gas constant (J/mol. K).

$$D_{kn} = \frac{2}{3} r \sqrt{[8RT/\pi M_{CO_2}]} \quad (4.32)$$

Partially wetted mode

When the membrane pores are partially wetted, the membrane mass transfer coefficient is greatly reduced, as observed by many authors [16, 20–24]. Reduction in mass transfer rates resulting from the diffusivity of the liquid filling the pores is about a few orders of magnitude higher compared when no wetting takes place. The physical mass transfer coefficient in partially wetted membrane pores is expressed according to equation (4.33) [22, 23, 25] with (F) being the wetted fraction of the pores thickness as represented in Figure 4-36, ($D_{g,eff}$) the effective diffusivity of the solute in the gas filling the pores of the membrane, (D_l) the diffusivity of the solute in the liquid phase, and (He_c) is the gas-liquid partition coefficient.

$$\frac{1}{k_m} = \frac{\delta \tau (1 - F)}{D_{g,eff} \xi} + \frac{\delta \tau (F) He_c}{D_l \xi} \quad (4.33)$$

The first term of equation (4.33) accounts for resistance in the non-wetted region of the membrane, while the second accounts for that in the wetted region of the membrane.

4.5.1.3 Effect of chemical reaction on liquid phase mass-transfer coefficient

Chemical desorption involves the release of chemically bound CO_2 by the dissociation of carbamate ion ($ETACOO^-$) to produce CO_2 and ETA molecules as per reaction (4.34).



There exists different levels of complexity in modeling chemical absorption of CO₂, it can be as tedious as kinetic modeling with the whole set of chemical reactions being assigned forward and reverse reaction rates, and it can be as convenient as assuming the absorption reaction to be irreversible as implied by the pseudo-first order assumption [26]. Within the framework of the resistance-in-series model, it is possible to account for the effect of the chemical acceleration of the desorption through the inclusion of an enhancement factor (E) as introduced in equation (4.35).

$$\frac{1}{K_L} = \frac{1}{E_{rxn}k_l} + \frac{d_i}{d_{lm}k_m He_c} \quad (4.35)$$

Therefore, the desorption rate results from two contributions: the diffusion of CO₂ from the liquid bulk to the gas bulk, or the generation of CO₂ in the liquid film by dissociation of carbamate ion. In our work we chose the expression of the enhancement factor as derived by Astarita [27] and used by others [16, 18, 28, 29]. The analytical derivation of the enhancement factor is based on the following assumptions:

- The dissociation of the carbamate species is described by a single chemical reaction (4.34)
- Instantaneous chemical equilibrium is achieved in the liquid film
- Applicability of physical equilibrium at liquid-gas interface (Henry's law)
- Transfer by molecular diffusion in both the liquid and gas films

The expression of the enhancement factor is given in (4.36), where (D_p) is the diffusivity of the carbamate ion, (D_{CO_2}) is the diffusivity of CO₂ in the solvent phase, (C_{ETA}) is the concentration of free unreacted ethanolamine in the liquid bulk (mol/m³) expressed in (4.37), (D_{ETA}) is the diffusivity of ethanolamine in the aqueous solvent, (c_t) is the total concentration of the solvent components (mol/m³), ($x_{f,i}^*$) is the mole fraction of free unreacted CO₂ at the liquid-membrane interface, ($x_{f,l}$) is the mole fraction of free unreacted CO₂ in the liquid bulk. Free CO₂ is dissolved in its molecular form in the liquid bulk phase and is represented by the subscript (f), this comes contrary to the chemically dissolved CO₂ that is under the form of carbamate ions.

$$E_{rxn} = 1 + \frac{\frac{D_p}{D_{CO_2}} \sqrt{K} C_{ETA}}{\left[1 + 2 \frac{D_p}{D_{ETA}} \sqrt{K} (c_t x_{f,i}^*) \right] \left[\sqrt{c_t x_{f,l}} + \sqrt{c_t x_{f,i}^*} \right]} \quad (4.36)$$

$$C_{ETA,f} = C_{ETA,0} (1 - 2\alpha) \quad (4.37)$$

The equilibrium constant of the reaction (K) is presented in (4.38) with respect to the absorption reaction of CO₂ in ETA, with (α) being the carbonation ratio and ($C_{CO_2,f,l}$) being the free CO₂ concentration in the liquid bulk.

$$K = \frac{[\alpha C_{ETA0}]^2}{C_{CO_2,f,l} \cdot [(1 - 2\alpha) C_{ETA0}]^2} = \frac{1}{C_{CO_2,f,l}} \left[\frac{\alpha}{1 - 2\alpha} \right]^2 \quad (4.38)$$

4.5.2 Modeling chemical desorption along a porous fiber at isothermal conditions

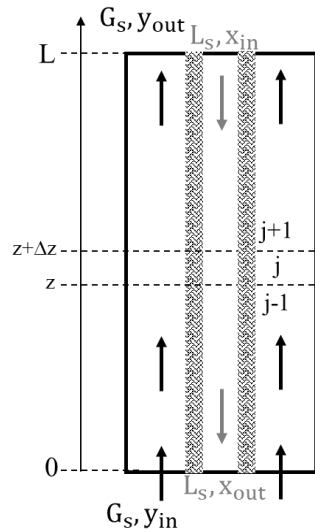


Figure 4-37: Schematic of a chemical desorption across a single hollow fiber

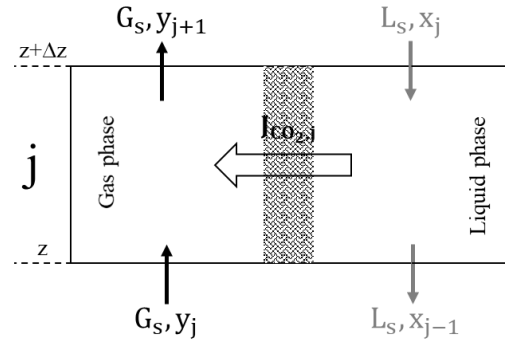


Figure 4-38: Mass balance across a differential element of the hollow fiber

The CO_2 desorption process along the hollow fiber is represented in Figure 4-37, where the solvent circulates in the lumen side and the sweeping gas in the shell side in a counter-current manner. The overall mass balances derived for the fiber are similar to the ones of a classical packed column: at ($z=0$) marks the section of sweeping-gas entry, and ($z=L$) – the section of solvent entry.

The nomenclature of the different streams throughout the cross section of an elementary volume are presented in Figure 4-38. To model the chemical desorption rates of CO_2 along the hollow fiber, the set of differential mass balance equations accounting for instantaneous chemical equilibrium in the liquid film was solved to predict the average CO_2 flux across the hollow fiber (J_{CO_2}). The numerical model consists of solving a set of 4 main equations on each elementary volume of the fiber, to produce a solution vector $[x, x_{f,i}, x_{f,i}^*, y] = f(z)$.

4.5.2.1 Model equations: analytical form

Operating line

The operating line is a mass-balance between the bottom section of the fiber ($z=0$) and that at a given height (z). The equation of the operating line is presented in its simplest form in (4.39), with (Y) being the molar ratio of CO_2 in the gas phase with respect to inert species (N_2), (X) the molar ratio of CO_2 with respect to all non-volatile species in the liquid phase (H_2O , ETA), (L_s) and (G_s) are the molar flow rates (mol/s) of the inert components in the liquid phase and the gas phase respectively. It should be mentioned that water was assumed non-volatile for the reason that during experimental desorption runs of chapter 3, the condensed water from the outlet gas stream was

next to negligible after operating for many hours. Evaporation, therefore, is not expected to influence temperature maps in the solvent.

$$Y = Y_{in} + L_s/G_s \cdot (X - X_{out}) \quad (4.39)$$

The molar ratios of CO₂ in the gas and liquid phases are presented in (4.40) with respect to the mole fractions, denoted as (x) and (y) in the liquid and gas phases respectively.

$$Y = y/[1 - y] // X = x/[1 - x] \quad (4.40)$$

Substituting (4.40) in (4.39) we get the expression of the operating line as presented in (4.41). This expression relates the mole fractions of CO₂ in both phases with the inert flow rates of liquid and gas phases. The advantage of such a formulation is that variations of total molar flow rates are accounted so that the assumption of the linearity of the operating line is not necessary.

$$y = \left[\frac{y_{in}}{1 - y_{in}} + \frac{L_s}{G_s} \left(\frac{x}{1 - x} - \frac{x_{out}}{1 - x_{out}} \right) \right] / \left[1 + \frac{y_{in}}{1 - y_{in}} + \frac{L_s}{G_s} \left(\frac{x}{1 - x} - \frac{x_{out}}{1 - x_{out}} \right) \right] \quad (4.41)$$

Differential mass balance

The general form of the differential mass-balance equation is presented in (4.42), with (K_L) being the overall mass-transfer coefficient (m/s) with respect to the liquid-phase, (a) the surface density of exchange at the fiber interior per unit length (m²/ m), (c_{f,l}) is the free concentration of the volatile species (CO₂) in the liquid bulk (mol/m³), (c_g^{*}) is the concentration of CO₂ in a hypothetical liquid phase at equilibrium with the CO₂ in the gas bulk (mol/ m³).

$$L_s \frac{dX}{dz} = K_L a (c_{f,l} - c_g^*) \quad (4.42)$$

The free concentration of CO₂ in the liquid bulk can be presented in terms of its mole fraction (x_{f,l}), and the total concentration in the liquid (c_t) as given by (4.43). The total concentration was obtained from equation (4.44) with (ρ) being the density of 30%wt. ETA loaded with CO₂, and \overline{MW} its average molecular weight.

$$c_{f,l} = c_t x_{f,l} \quad (4.43)$$

$$c_t = \rho(T, \alpha) / \overline{MW} \quad (4.44)$$

The concentration of free CO₂, in the solvent phase supposed in equilibrium with the gas bulk, can be obtained by applying Henry's law as shown in (4.45), with (He) being the solubility of CO₂ in 30% wt. ETA at ambient pressure.

$$c_g^* = y/He \quad (4.45)$$

Combining (4.40), (4.43) and (4.45) with (4.42) we get a modified expression of the differential mass balance given in (4.46) on a section of the hollow fiber.

$$\frac{L_s}{(1 - x)^2} \frac{dx}{dz} = K_L a c_t \left(x_{f,l} - \frac{y}{He c_t} \right) \quad (4.46)$$

Vapor-liquid equilibrium

The dissolved CO₂ in the solvent is either chemically bound under the form of carbamate ions (ETACOO⁻), or exists in its molecular form (physically dissolved). While the concentration of chemically bound carbon in the liquid bulk can be easily derived from the carbonation ratio (α), that of free carbon – although much less considerable- is

less straightforward to determine. By using a VLE model, it is possible to plot the chemical speciation with respect to operating conditions, the free CO₂ included. This method however is not preferred as VLE data have low accuracy as reported in [30–34]; it is for this reason that the free concentration is determined in another manner.

Starting from the carbonation ratio and temperature, the mole fraction of CO₂ in a hypothetical gas phase in equilibrium with the solvent can be calculated using chemical equilibrium relation in (4.47). Several correlations for vapor-liquid equilibrium for H₂O-ETA-CO₂ are proposed in literature such as those given by Weiland [28] or by Koonaphapdeelert [29]. For greater accuracy, it was preferred to describe chemical equilibrium from real experimental data extracted from literature instead of correlations. Figure 4-39 presents experimental equilibrium data for 30% wt. ETA as a function of carbonation ratio and at different temperatures collected from different sources. Interpolation of data was applied to determine the partial pressure at intermediate carbonation ratios or temperatures.

$$y = f(\alpha, T) \quad (4.47)$$

The obtained mole fraction of CO₂ in the gas phase is then used in conjunction with Henry's law to find the concentration of free molecular CO₂ in the liquid phase, i.e. by using relation (4.45). The mole fraction ($x_{f,i}$) can then easily be computed and introduced in the differential mass-balance.

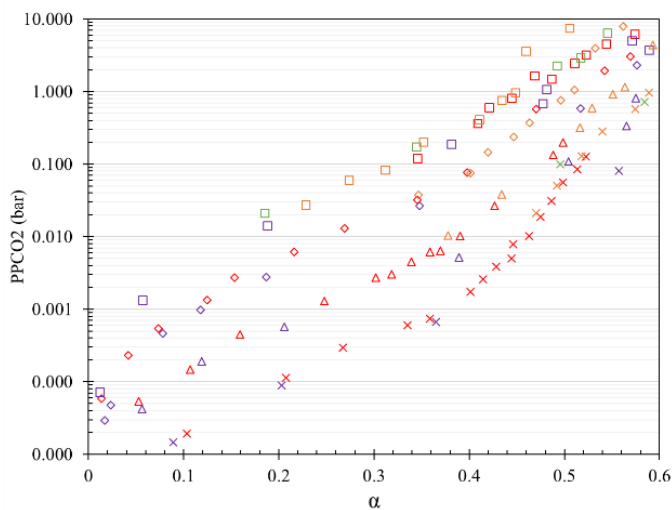


Figure 4-39: Vapor-liquid equilibrium plot of CO₂ with 30% wt. ETA as a function of the carbonation ratio at different temperatures: (x)-40°C, (Δ)-60°C, (□)-80°C; (◇)-100°C. Colors indicate the source of each data set: Red-[34], Violet-[33], orange-[35], green-[36].

Flux Continuity

The calculation of the enhancement factor - accounting for the effect of chemical reaction on mass transfer - necessitates the knowledge of the mole fraction of free unreacted CO₂ at the membrane-liquid interface, $x_{f,i}^*$. This value can be calculated by equating CO₂ desorption rates between the liquid phase and the gas phase in permanent regime. The transfer rate of the liquid and gas phases are presented in (4.48) and (4.49) respectively.

$$N_l = a_l L k_l E_{rxn} c_t (x_{f,l} - x_{f,i}^*) \quad (4.48)$$

$$N_m = a_m L k_m c_t \text{He}_c \left(x_{f,i}^* - \frac{y}{c_t \text{He}} \right) \quad (4.49)$$

Equating liquid and membrane fluxes and substituting the enhancement factor in equation (4.36) , we get equation (4.50). (a_l) represents the mass-transfer area per unit length of the fiber at the internal diameter of the fiber, and (a_m) being the mass-transfer area computed from the logarithmic mean diameter of the fiber.

$$a_l k_l \left[1 + \frac{(D_p/D_{CO_2}) \sqrt{K} C_{ETA}}{[1 + 2(D_p/D_{am}) \sqrt{K} (c_t x_{f,i}^*)] [\sqrt{c_t x_{f,l}} + \sqrt{c_t x_{f,i}^*}]} \right] c_t (x_{f,l} - x_{f,i}^*) - a_m k_m (c_t \text{He} x_{f,i}^* - y) = 0 \quad (4.50)$$

4.5.3 Coupling MW heating with chemical desorption of CO₂

Chemical desorption being described from the resistance-in-series model, accounts for convective and diffusive transport phenomenon on the radial and tangential directions; the model is 1D along the axial length of the fiber. In order to perform the coupling between the 1D mass-transfer model and the 3D temperature and velocity maps derived from the modeling of the microwave heating process, the variable profiles were averaged over the internal cross-sectional areas along the fiber.

Just as the mass-transfer model is based on the bulk and interfacial quantities, in a similar manner we distinguish two flow regions, the liquid film region and the bulk region. At a given length of the fiber, the radial cross-section was divided into two regions, the film region is that occupied by the stagnant liquid film defined arbitrarily by the criteria ($u < 5\% u_{max}$), the bulk region is the core cross-section delimited by the surrounding film, as described in Figure 4-40.

Upon averaging the 3D temperature maps over each region of the cross section, we obtain two 1D axial temperature. The homogeneity of MW power absorption throughout the fiber surface ensures a near-uniform radial temperature for a given radius ($r=r_i$) at a constant (z) value. For this reason, the film T-profile is an accurate representation of boundaries of the lumen region.

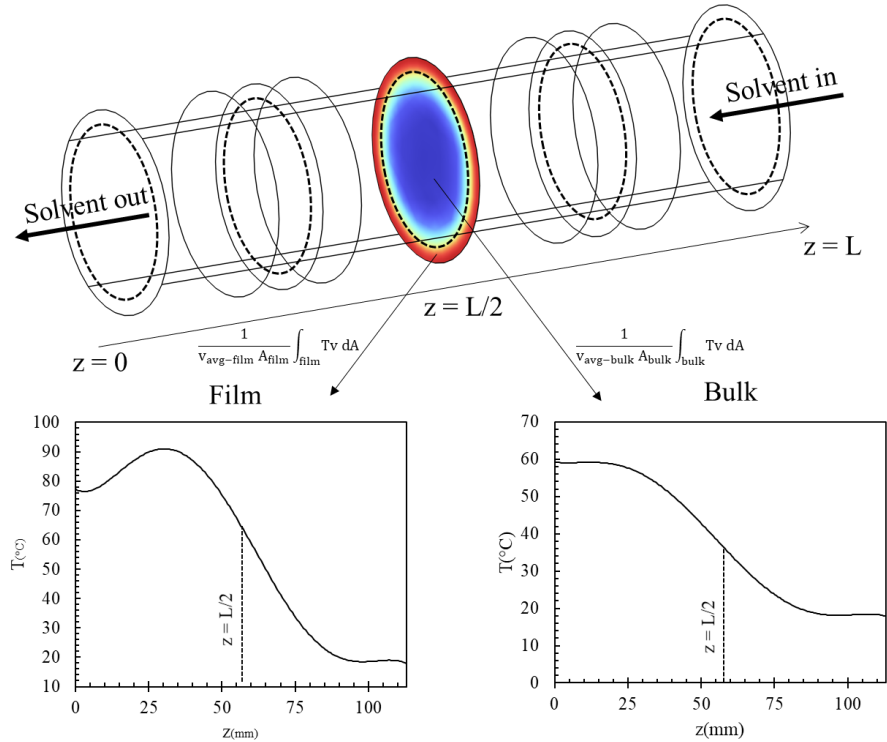


Figure 4-40: Transformation of a 3D T-maps into bulk and film T-profiles.

The derived bulk and film temperature axial profiles are plotted in Figure 4-41 and Figure 4-42 respectively, for experiments (9-12) of the experimental design. Figure 4-41 shows that the bulk temperature profile has a linear increase from ($T_{\text{in}} = 20^\circ\text{C}$) at the cavity entrance till (T_{out}) at the exit, irrespective of the solvent mass flow-rate. The reason is related to the uniform EM power loss density as mentioned earlier in section (4.4.2). In Figure 4-42, the film temperature increases before the liquid exit region are significant compared to (T_{out}).

The axial temperature profiles were fitted with a polynomial of the fifth degree – i.e. ($T=f(z)$), and integrated into the non-isothermal mass transfer model such that each position along the hollow fiber has a unique temperature couple [$T_{\text{bulk}}(z)$, $T_{\text{film}}(z)$]. Consequently, all physical, transfer and chemical properties of the system are evaluated as function of temperature in each region of the liquid flow to compute variations of local desorption flux along the fiber. MW-assisted chemical desorption can hence be simulated as per the schematic in Figure 4-43.

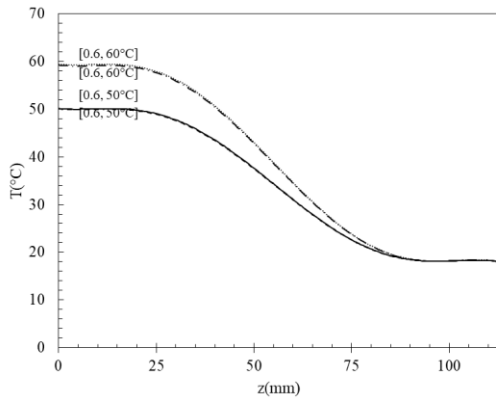


Figure 4-41: Longitudinal temperature profiles of the bulk region at operating conditions [mass flow-rate, T_{out}] of experiments (9-12): Exp(9)-[0.2, 50]; Exp(10)-[0.6, 50]; Exp(11)-[0.2, 60]; Exp(12)-[0.6, 60].

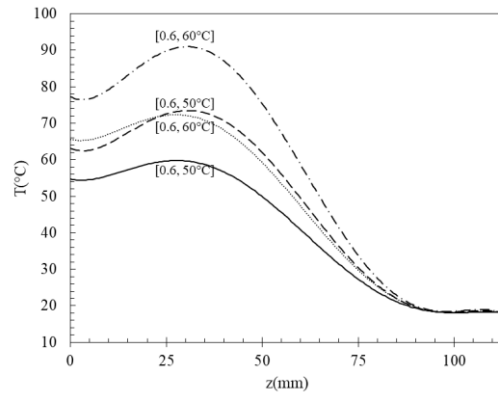


Figure 4-42: Longitudinal temperature profiles of the film region at operating conditions [mass flow-rate, T_{out}] of experiments (9-12): Exp(9)-[0.2, 50]; Exp(10)-[0.6, 50]; Exp(11)-[0.2, 60]; Exp(12)-[0.6, 60].

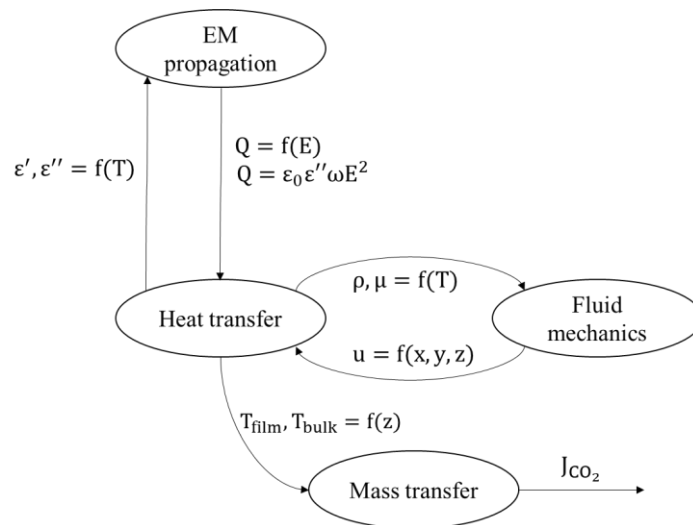


Figure 4-43: Schematic of mass-transfer coupling to MW heating to simulate MW-assisted chemical desorption

Till now, we have described the coupling of MW-heating and mass-transfer with chemical reaction, although there more to be said. One important detail is to determine based on which temperature profile should a quantity be evaluated. Table 4.7 elaborates the choice of temperature regions that were considered to evaluate the main quantities of the model, i.e. those which are used to calculate the mass transfer coefficients (k_i , k_m , E , K_L) or the driving force ($x_{f,i}^* - y/(c_t He)$).

Quantity	Region	Justification
VLE	bulk	○ VLE relation is used for calculation of molecular CO ₂ in the liquid bulk.
He	bulk/film	○ Bulk temperature is used to determine the free unreacted CO ₂ in the liquid bulk. ○ Film temperature is used to determine free unreacted CO ₂ in equilibrium with gas phase.
D _{ETA} in 30%wt. ETA+CO ₂	film	○ D _{ETA} determines the transfer rate of ETA out of the reacting film. Hence it is dependent on the film temperature.
D _{CO2} in 30%wt. ETA+CO ₂	film	○ D _{CO2} determines the transfer rate of CO ₂ across the liquid film to reach the liquid-gas interface. Hence it is dependent on the film temperature. ○ For cases of membrane wetting by solvent, D _{CO2} is calculated from the film temperature.
D _{CO2} in N ₂	film	○ The porous membrane has been shown to have similar temperature as the hot liquid film.
D _{CO2-knudsen}	film	○ The porous membrane has been shown to have similar temperature as the hot liquid film.

Table 4.7: Choice of T-profile in calculating physical and equilibrium properties in the non-isothermal chemical desorption model

4.5.4 Resolution and boundary conditions

The fiber, having a length of 113 mm, was uniformly divided into 400 elements. Over each element, equations (4.41),(4.46),(4.47),(4.50) were solved using finite difference method to produce the solution vector $[x, x_{f,l}, x_{f,i}^*, y] = f(z)$. The equations were implemented in a Matlab® code. Model inputs are membrane properties, inlet solvent composition, as well as the operating conditions which include gas and liquid volumetric flow rates (u_g) and (u_l) respectively, in addition to bulk and film axial temperature profiles given in the form of a fifth-degree polynomial corresponding to the tested conditions in experiments (9-12).

The model calculates the composition profiles on each elementary volume, starting from one end and moving towards the other. Only the compositions of inlet gas and liquid streams are known (x_{in}, y_{in}) therefor, in a counter-current operation, it is necessary to introduce an iteration loop in order to compute the composition of the gas at the solvent entrance section. The overall mass balance equation is used to test the goodness of the approximation of the initialized ($y_{out,g}$) value. For a co-current mode of operation, such an iteration loop is not necessary.

The resolution of the equation set is schematically given in Figure 4-44. Inert molar flow rates (L_s, G_s), as well as composition variables at $z=0$ are first computed, as well as temperature dependent diffusivities and equilibrium data in order to derive the partial mass transfer coefficients and the chemical enhancement factor. The “flux-continuity” equation is solved to obtain the CO₂ molar fraction at the interface between the film and the membrane ($x_{f,l,j-1}^*$). The differential mass balance is then resolved after an explicit discretization scheme in order to compute the fraction of CO₂ dissolved at the exit of the first elementary volume. The corresponding CO₂ fraction present in the gas entering in counter-current flow into the elementary volume is deduced from the operating curve whilst the

free unreacted CO₂ molar fraction in the liquid bulk phase and liquid film is calculated from the equilibrium data. The model then iterates along the fiber length until reaching the fiber length corresponding the exit solvent section.

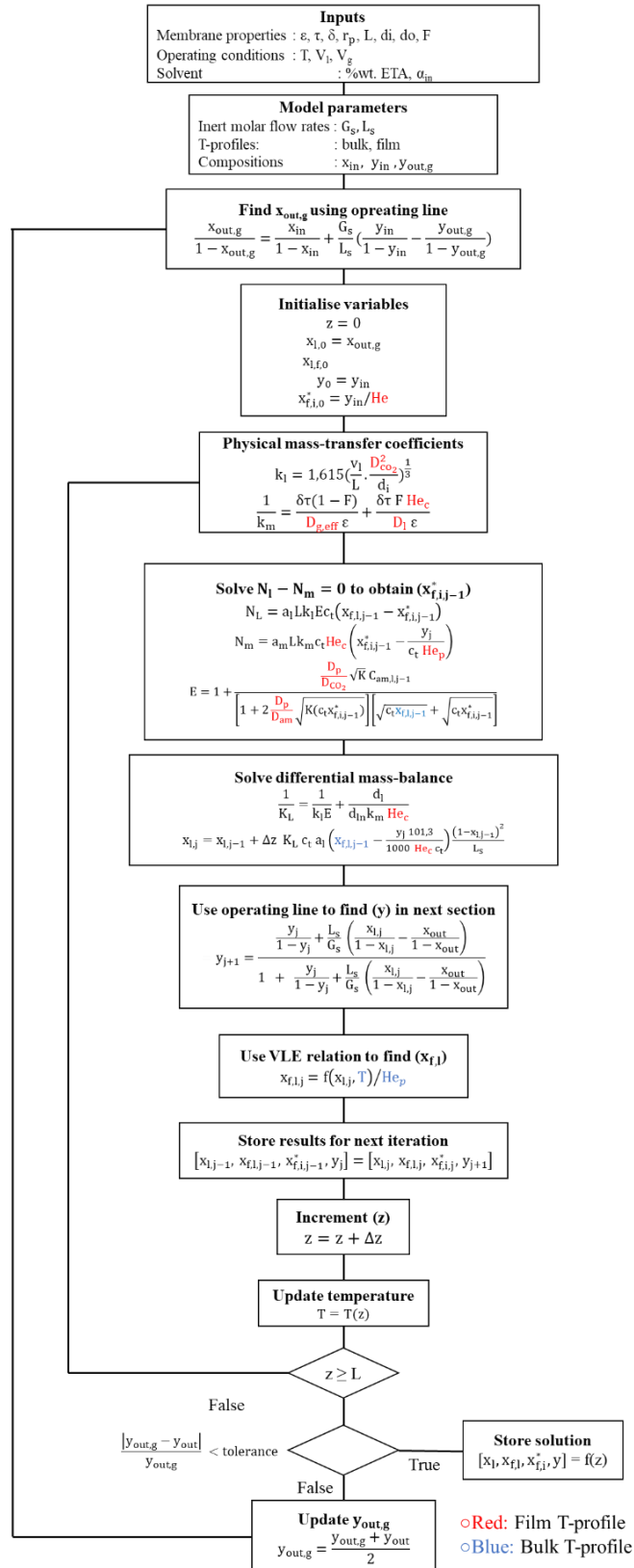


Figure 4-44: Resolution of microwave-assisted CO₂ desorption model

4.6 Results

4.6.1 Model Validation: chemical desorption in a hollow fiber at isothermal conditions

Before attempting to model MW-assisted chemical desorption, the modeling of mass-transfer phenomena with chemical reaction is to be validated independently from other phenomena. For this reason, chemical desorption was simulated at isothermal conditions, and results were compared with those experimentally obtained by Koonaphadeelert [29]. The author performed CO₂ desorption with N₂ gas sweeping from 15% wt. ETA solution using a module composed of surface modified ceramic hollow fibers, maintained in isothermal conditions.

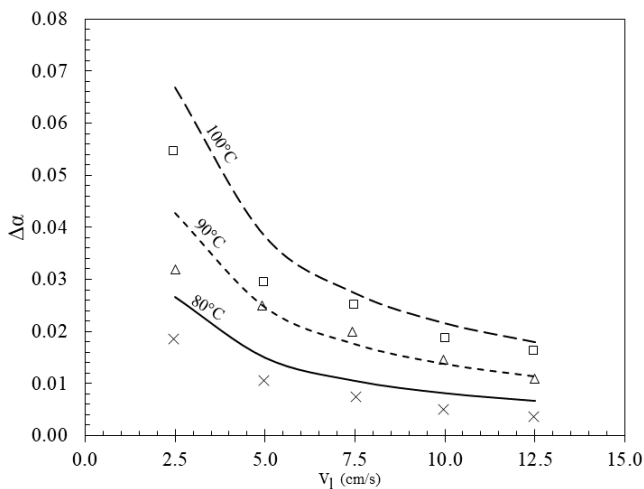


Figure 4-45: Isothermal regeneration of 15% wt. ETA at varying temperatures and liquid velocities: comparing the simulated results to experimental data of [29]. (Lines)- predictions from numerical model; (symbols)- experimental data.

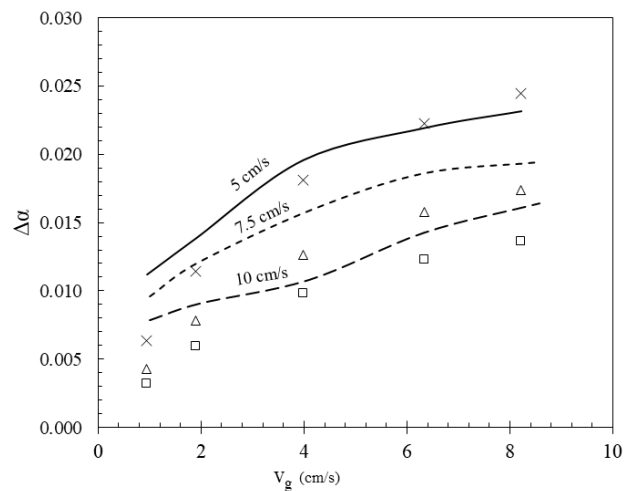


Figure 4-46: Isothermal regeneration of 15% wt. ETA at varying liquid and gas velocities: comparing the simulated results to experimental data of [29]. (Lines)- predictions from numerical model; (symbols)- experimental data.

Figure 4-45 shows the experimental and simulated regeneration extent ($\Delta\alpha = \alpha_{in} - \alpha_{out}$) of 15% wt. ETA solution as a function of liquid velocity at different temperatures. Figure 4-45 shows that the predicted values, assuming no membrane wetting, are fairly close to those observed from the experimental data, the allure of both sets of data are very similar. The good agreement between both sets of data accords confidence in the mass transfer model coupled with the chemical desorption reaction and supposes the correctness of its underlying assumptions, its implementation, and input data such as correlations of physical and transfer properties.

Observed discrepancies may arise from several reasons, on the part of the author this includes:

- Deviation from isothermal conditions
- Inaccurate measurement of CO₂ loading
- Occurrence of membrane wetting

On the part of the numerical model errors may arise from:

- Inaccurate estimation of transfer properties
- Assumption of infinitely fast chemical reaction

Figure 4-46 presents the experimental and predicted regeneration rates as a function of gas velocity at different liquid flow rates. The figure shows a general agreement between both sets of data with higher deviations at low gas velocities; this is due to the contribution of the mass-transfer resistance in the gas phase which the model does not account for.

4.6.2 Results: MW-assisted chemical desorption

4.6.2.1 Effect of temperature profile assumptions

As mentioned in section (4.5.3), coupling microwave heating to mass-transfer and chemical reaction is achieved by integrating two longitudinal temperature profiles in the 1D reactive mass-transfer model. The question of which axial temperature profiles to use was addressed earlier, but we deemed it interesting to analyze the behavior of the desorption flux assuming not dual but single T-profiles in the liquid: either that of the bulk flow or that of the stagnant film- or a mixed bulk and film method. As a reminder, the operating conditions of experiments (9-16) of the experimental design are mentioned in Table 4.8.

Experiment	$U_g(\text{mL/s})$	$V_l(\text{mL/s})$	$T_{\text{out}}(^{\circ}\text{C})$
9	3.33	0.2	50
10	3.33	0.2	60
11	3.33	0.6	50
12	3.33	0.6	60
13	6.66	0.2	50
14	6.66	0.2	60
15	6.66	0.6	50
16	6.66	0.6	60

Table 4.8: Operating conditions at experiments (9-16) of plan of experimental design

We start by examining the variations in the average desorption rates assuming uniform temperature over the internal fiber cross section area and axial variations according to the ones computed for the film. Results in Figure 4-47 show that the model overestimates the experimental average CO_2 desorption rate by a factor of five, this indicates that the exclusive use of the film temperature is not suitable to produce accurate results. It can be suspected that the large discrepancy could also be caused by partial membrane wetting. To test this hypothesis, desorption was simulated considering different fractions of wetting in the membrane as shown in Figure 4-48. The figure shows that despite the huge decrements of the computed desorption flux, the allure of the curves remains independent of the wetting fraction used. This shows that the occurrence of membrane wetting cannot account for the deviations observed in Figure 4-47, especially corresponding to the experimental points (11), (12), (15) and (16). In conclusion the exclusive use of film T-profile in the numerical model is not appropriate to simulate MW-assisted desorption.

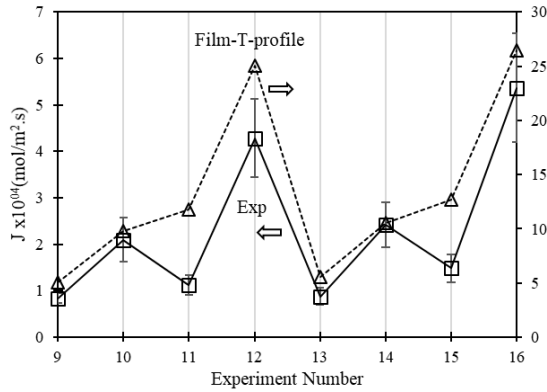


Figure 4-47: Comparison of experimental desorption flux with the numerical model utilizing the “film” temperature profile and F=0%

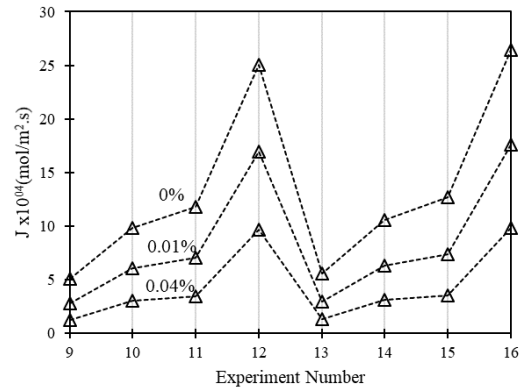


Figure 4-48: Desorption flux with model utilizing “film” T-profile at different wetting fractions

Figure 4-49 compares the experimental desorption flux to that predicted by the model utilizing the “bulk” temperature profile. The figure shows that the predicted flux is of the same order of magnitude as the experimental, albeit it cannot correctly account for variations observed in the different operating conditions. The model is unable to account for the effect of the inversed radial temperature gradient in the fiber, consequently the jump in the desorption flux at experiments (12) or (16) is vastly underestimated by the numerical model. This demonstrates that the use of “bulk” profile is insufficient to simulate MW-assisted desorption.

Figure 4-50 presents the simulated average desorption flux when considering the two distinct T-profiles (Bulk & film) and no membrane wetting, in the manner previously highlighted in section (4.5.4). Despite the overestimation of the simulated data, the effects of the operating parameters on relative variations of the desorption flux appear better represented, especially at points (12) and (16). As a conclusion, the use of both temperature profiles is deemed appropriate, as the effect of inverted radial temperature gradients is accounted for.

It is noteworthy to say that in this work we presented a first approach in obtaining 1D T-profiles from 3D maps; the choice of the film and bulk regions of the fiber was made in an intuitive manner. It remains important to establish some physical reasoning that demarks in a precise manner the film and the bulk regions.

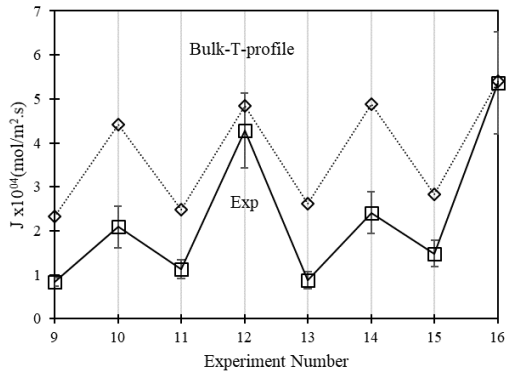


Figure 4-49: Comparison of experimental desorption flux with the numerical model utilizing Bulk T-profile

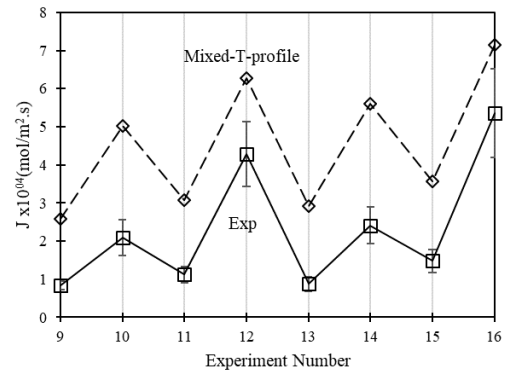


Figure 4-50: Comparison of experimental desorption flux with the numerical model utilizing both bulk and film T-profiles.

4.6.2.2 Effect of partial membrane wetting

In the previous section, it was demonstrated through numerical modeling that the use of both temperature profiles is necessary to replicate the evolution of the desorption flux measured at different experimental conditions, deviations from experimental data persisted nonetheless. It is suspected that membrane wetting may cause a drop in the experimental performances beyond the values predicted by the model. In this part, the sensitivity of the model towards the partial membrane wetting is examined.

The influence of wetted fraction on desorption is presented in Figure 4-51, assuming dual film-bulk temperature profiles. It is revealed that with even very low wetting fractions, the global desorption rates experiment significant decrements. In addition, the model sensitivity towards operating conditions decreases with this parameter. This is explained because the membrane actually constitutes the principle resistance to mass-transfer.

The relative contributions of the liquid film and membrane resistances according to different fractions of wetting are plotted in Figure 4-52. It shows that the membrane resistance dominates at all experimental conditions, under wetted or non-wetted modes. It should be pointed out the even at no wetting the membrane has a thickness of 1 mm, this is higher than what is usually employed in membrane modules [37].

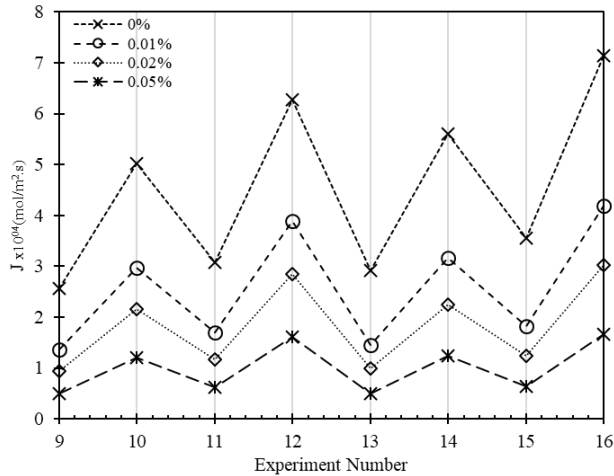


Figure 4-51: Fitting numerical desorption flux to experimental values by adjusting the wetted fraction (F) of the membrane.

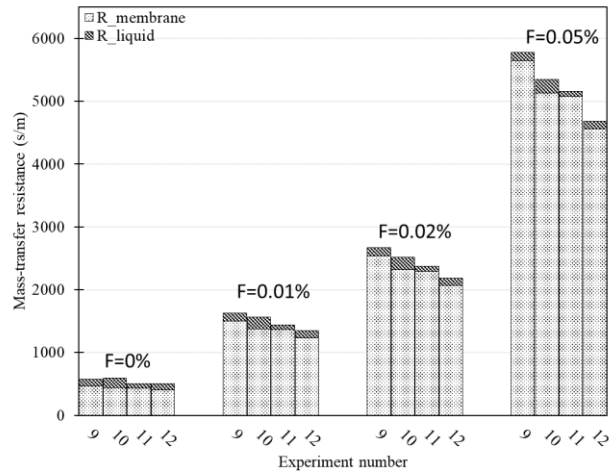


Figure 4-52: Evolution of the resistance in the membrane and the liquid phase at different wetting fractions (F).

The wetting fraction to produce the best fit with experimental desorption data is (F=0.01%), shown in Figure 4-53. The predicted desorption seems to provide reasonably accurate estimation of the experimental desorption, but it is difficult to assert the degree to which the model well predicts the experimental data, given that the latter possess a considerable uncertainty. In addition, in this study we assume the wetted fraction to be independent from the operating conditions, which may be untrue. Still, assuming an experiment-dependent value of (F) is surely to give an excellent agreement at each experimental point; this is to the detriment of extrapolating the numerical data to cases that aren't tested experimentally.

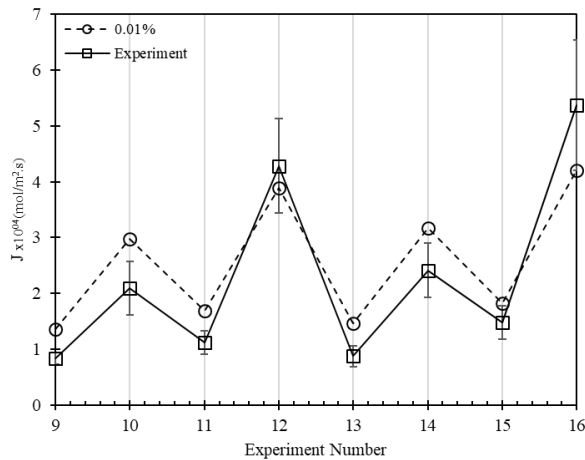


Figure 4-53: Experimental and simulated desorption flux at different experiments. Used wetting fraction in numerical model is (F=0.01%)

4.6.2.3 Local desorption flux

As the solvent temperature varies substantially in the radial and axial directions of the fiber, it affects the desorption rates along the fiber. Figure 4-54 shows the axial variations of the desorption rates computed along the whole fiber length which appear to be negligible in the first half of the microwave cavity region. Around the mid-

cavity, desorption rates steeply increase and plateaus outside the microwave cavity, at the solvent exit region. This indicates that in the tested conditions, the working surface area corresponds to nearly the half of the whole fiber length being (113mm). This is related to the solvent heating rate resulting in the formation of dead surface areas where temperature is not high enough to overcome the equilibrium conditions with the gas phase.

The cumulated desorption rates were plotted as function of the total surface area fraction in Figure 4-55. The figure shows that cumulated desorption rates are identical for all experiments, and that 40% of the fiber mass-transfer area is actually responsible for the total desorbed quantity. This result raises the question as to over which surface area should the average desorption flux be estimated, a question that is exclusive to microwave regeneration. Consideration of entire exchange area would negatively impact the estimation of the average desorption flux, thus clouding any advantages that this novel regeneration method might promise. This question was not explored any deeper, hence we base our estimations of average desorption flux on the entire surface of exchange including the sections outside the microwave cavity.

It is important to point out that, in general, isothermal membrane regeneration studies employ different operating conditions which makes it challenging to draw out clear conclusions as to which membrane, solvent, or process configuration are more efficient. When employing MW irradiation as a regeneration method, efficiency and performance stability is not only tied to the aspects of isothermal mode but extends to include the design of the MW cavity – an aspect of the process that is difficult to normalize.

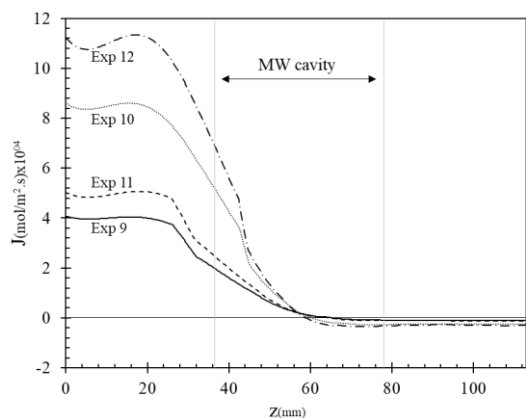


Figure 4-54: CO₂ desorption profile as a function of the fiber position (Exp 9-12)

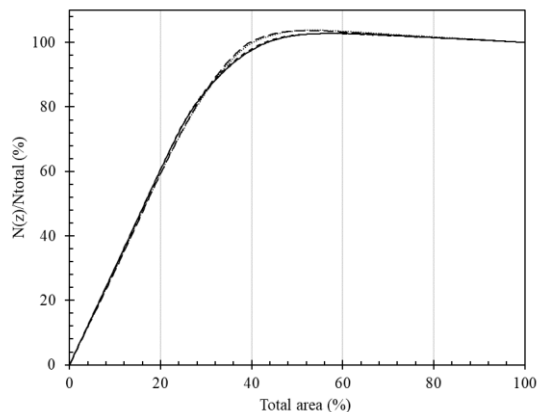


Figure 4-55: Accumulated desorption rate function of the area for mass-transfer (Exp 9-12)

Upon further consideration of the desorption profiles in Figure 4-54, we notice that the flux has negative values for ($z > 60\text{mm}$). This shows that on the cold side of the fiber, chemical absorption takes place, this can be explained by the fact that the sweeping gas and the liquid flow in a counter-current manner. Upon entering, the sweeping gas -being poor in CO₂- contacts the hot solvent and thus desorption takes place; as it progresses along the fiber length it gets more and more enriched, simultaneously, the solvent temperature is decreasing as shown in Figure 4-56. At some given point in the fiber, the partial pressure of CO₂ surpasses that in equilibrium with the solvent, thus chemical absorption occurs.

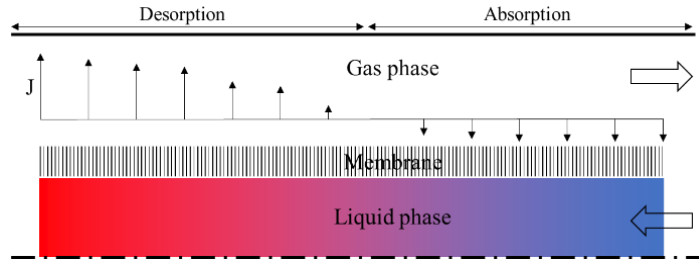


Figure 4-56: Schematic representation of the evolution of the direction of mass-transfer in counter-current mode of operation.

4.6.2.4 Overall mass-transfer coefficient and enhancement factor

Desorption profiles observed in Figure 4-54 depend on the driving force of mass-transfer and on the overall mass-transfer coefficient. We plot in Figure 4-57 the profile of the overall transfer coefficient as function of the fiber length. For brevity of presentation, only results of experiments (9-12) are shown. The overall mass transfer coefficient does not experience great variations throughout the fiber length, it is higher at the “hot” side of the fiber. It is interesting to note that variations of the overall mass transfer coefficient show a high degree of similarity to the film T-profile, but differs in the position of its maxima being found inside the MW cavity as opposed to that of the film temperature being outside.

The liquid and membrane mass transfer coefficients as well as the enhancement factor profiles were plotted in Figure 4-58 at the operating conditions of experiment (12). The transfer coefficients (k_l , k_m) are higher at the hot side of the fiber, this is normal as they depend on the diffusivity of CO_2 in alkanolamine solution (when membrane is wetted). This in part explains the higher overall transfer coefficient at the hot fiber side. In a contrary manner, the enhancement attains high values at the cold side of the fiber and low values at the “hot” side, this is because as ($\Psi = x_{f,i}^*/x_{f,l}$) tends to zero, the enhancement factor converges to the quantity given in (4.51).

$E = 1 + \frac{D_{\text{ETA}} C_{\text{ETA},f}}{D_{\text{CO}_2} (C_{\text{CO}_2,l} - C_{\text{CO}_2,i}^*)}$	(4.51)
---	--------

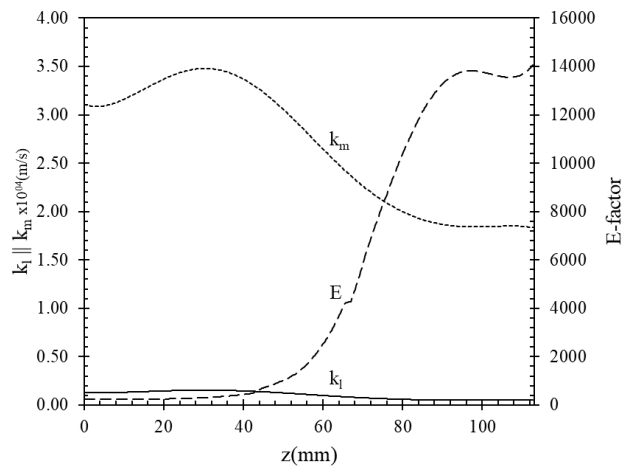
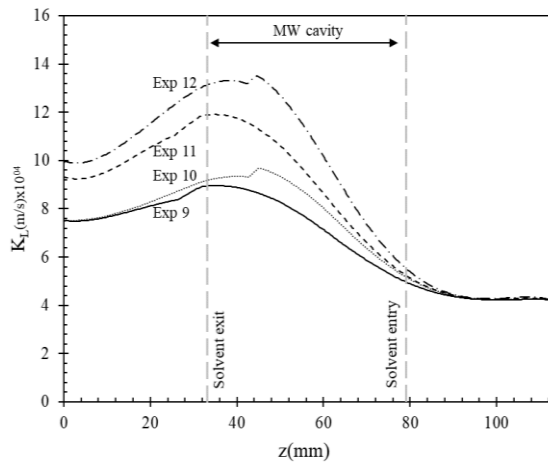


Figure 4-57: Profile of overall transfer coefficient (K_L) function of the fiber length, ($F=0.01\%$)

Figure 4-58: Simulated profiles of transfer coefficients of liquid (k_l), membrane (k_m) and enhancement factor of experiment (12), ($F=0.01\%$)

4.6.2.5 Driving force for mass-transfer

The profile of the driving force, expressed as $(x_{f,l} - x_{f,g}^*)$, is the difference between the mole fraction of free molecular CO_2 in the liquid bulk and that in equilibrium with the gas bulk. The driving force was plotted in Figure 4-59 for experiments (9-12), the driving force becomes significant at ($z < 60$ mm) which explains why desorption becomes active in this region. At the region of solvent entry, the driving force is negative indicating a CO_2 flux from the gas to liquid phases, hence chemical absorption. The discontinuities observed in the curves are caused by the interpolations on experimental VLE data.

The driving force follows very similar tendencies than bulk temperature profiles that we plot again in Figure 4-60 for ease of reference. This ensues as $(x_{f,l})$ was taken to be dependent on (T_{bulk}) , on the other hand, $(x_{f,g}^*)$ was taken to be dependent on (T_{film}) , however its influence is much less significant as it was calculated using Henry's law. The latter follows a linear increase with respect to temperature instead of a logarithmic one as with VLE.

Under the assumption of a uniform EM-dissipation in the solvent domain bounded by the MW cavity and as long as (T_{out}) is maintained constant, (T_{bulk}) is expected to be invariant at different fiber geometries or different solvent hydrodynamics as can be shown in Figure 4-60 (experiments 9,11 or 10,12). Therefore, with regards to the driving force for mass-transfer no enhancement of this quantity is expected. This highlights that any potential of intensification proposed by this technology would mainly target the transfer coefficient, a conclusion that is subjected to the assumption of chemical desorption being influenced only by thermal considerations (temperature) instead of a non-thermal one.

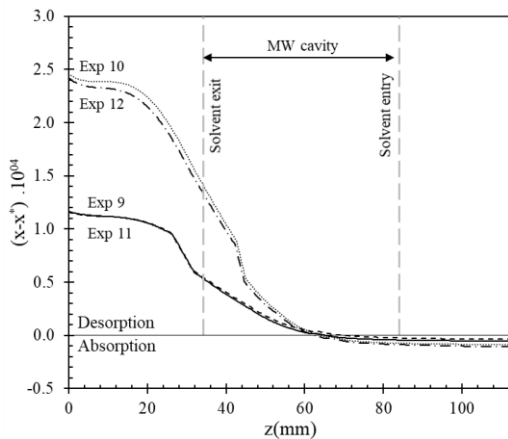


Figure 4-59: Driving force for mass transfer ($x_{f,l} - x_{f,g}^*$) function of fiber length. Wetting fraction $F=0.01\%$

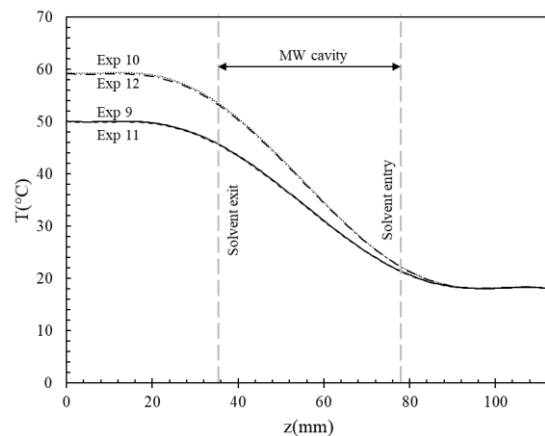


Figure 4-60: Bulk temperature profile, experiments (9-12)

We deemed it interesting to perform a comparison of the driving force between isothermal and non-isothermal regeneration (using MW irradiation). We plot both the operating line and the equilibrium curve in Figure 4-61 and 1-66, corresponding respectively to the isothermal conditions. In isothermal regeneration the fiber volume was

maintained at constant temperature which is the outlet temperature of the solvent from the microwave cavity ($T_{out}=60^{\circ}\text{C}$).

Figure 4-61 shows that a considerable driving force exists along the entire fiber length, even at the solvent entry. This is not the case for the non-isothermal mode where driving force becomes substantial after MW cavity midway. Towards the solvent exit region, the driving force increases in both modes and reach similar values. We point out that the use of experimental instead of correlated VLE data, can cause some discontinuities in the equilibrium curve as observed in Figure 4-61.

In isothermal mode, the equilibrium curve and the operating line cannot intersect, as shown in Figure 4-61. For conditions of non-isothermal regeneration, because of solvent temperature variations along the fiber the operating line and the equilibrium curve intersect. Towards the region of solvent entry, solvent temperature drops decrease the theoretical partial pressure of CO_2 in equilibrium with the liquid phase, resulting in chemical absorption on the cold side of the fiber, although to a very low extent. Still, there is the possibility that negative driving force may be a numerical error caused by inaccurate equilibrium data, even if the data were collected from several sources.

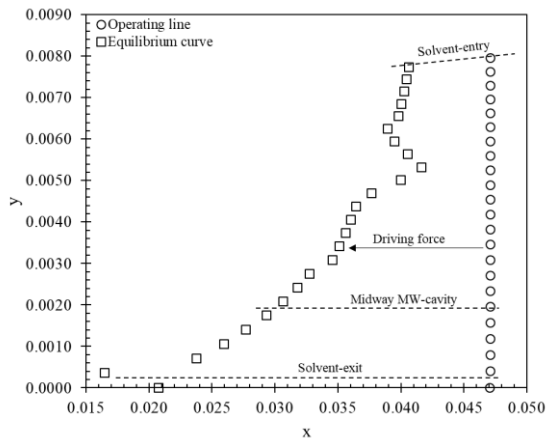


Figure 4-61: Driving force diagram, case of isothermal regeneration at operating conditions of experiment (12), ($F=0.01\%$)

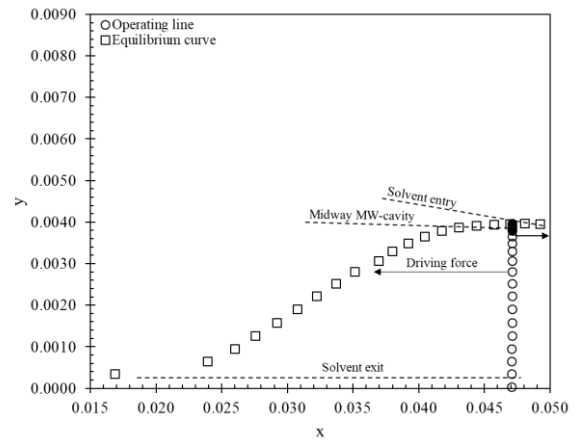


Figure 4-62: Driving force diagram, case of microwave regeneration at operating conditions of experiment (12), ($F=0.01\%$)

4.6.2.6 Power consumption for chemical desorption reaction

The dissociation of carbamate ions (ETACOO^-) to produce molecular CO_2 is an endothermic reaction, which is characterized by the enthalpy of desorption, or the energy needed to desorb 1 mol CO_2 from the 30% wt. ETA solvent (ΔH_{abs}). Assuming that carbamate dissociation is the dominant chemical reaction in the system [28], the rate of energy utilized for desorption along the fiber length can be presented as follows:

$P_{des} = J(z) \cdot \Delta H_{abs}(T_{film}, \alpha)$	(4.52)
---	--------

Figure 4-63 shows the estimated MW power for the dissociation of the carbamate ions along the fiber length for experiments (9-12). The figure shows that the larger fraction of the desorption energy is consumed at the “hot” section of the fiber where desorption is most active. It can be observed that desorption energy curves follow similar trends to axial desorption profiles at different experimental points. The observed discontinuities are related to those

observed for axial desorption profiles, or due to the discontinuities of interpolation starting from experimental data - taken from [38, 39].

One assumption of the numerical model of for the MW heating of the solvent is that only a negligible portion of the absorbed MW power is consumed by the carbamate dissociation reaction. This signifies that the endothermic desorption reaction has no cooling effect on the solvent flow. In a similar manner, the endothermic evaporation of water evaporation has no cooling effect, as the evaporated quantities were found to be negligible over prolonged periods of operation. In Figure 4-64 we display the percentage of MW power consumed for chemical desorption with respect to the incident one. Figure 4-64 shows that the power diverted for desorption is negligible, hence justifying our assumption.

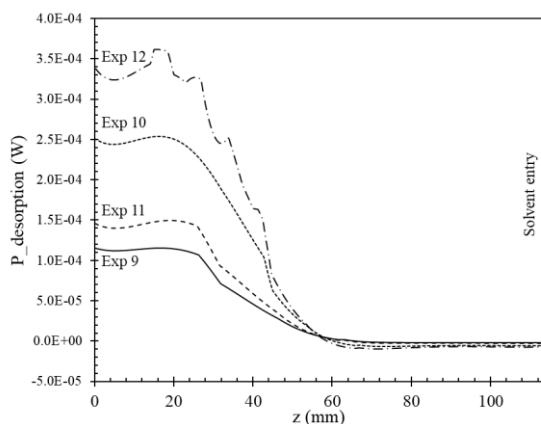


Figure 4-63: Profile of MW power used for chemical desorption reaction, experiments (9-12).

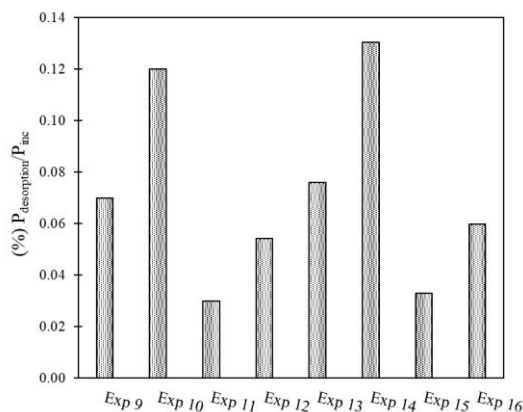


Figure 4-64: Percentage of incident MW power used for chemical desorption reaction, experiments (9-16)

4.6.3 MW-assisted desorption versus isothermal desorption

In order to evaluate the efficiency of MW regeneration, desorption fluxes were compared to those that would be obtained in an isothermal mode of operation, assuming a uniform temperature equal to that of the solvent stream outlet.

Figure 4-65 presents the CO₂ flux simulated in isothermal and non-isothermal conditions, as well as the experimental non-isothermal data, for a wetted fraction of membrane taken at (F=0.01%). The figure shows that the simulated isothermal regeneration outperforms that of MW irradiation at all experimental points, to elaborate this observation, the desorption profiles of experiment (12) were plotted at isothermal and non-isothermal regeneration in Figure 4-66. In isothermal regeneration, the desorption flux is nearly constant along the fiber length, whereas under microwave irradiation, it is significant in the hot region where it outperforms that of the isothermal model.

It is worthy to note that the present observations are exclusive to this experimental setup, as the latter was designed to produce exploratory results and not optimized ones. A better configuration of the current set-up would be to decrease the fiber length at solvent entry, and increase that at the solvent exit side; so that advantage is taken from the film local temperature rises obtained in the non-isothermal mode.

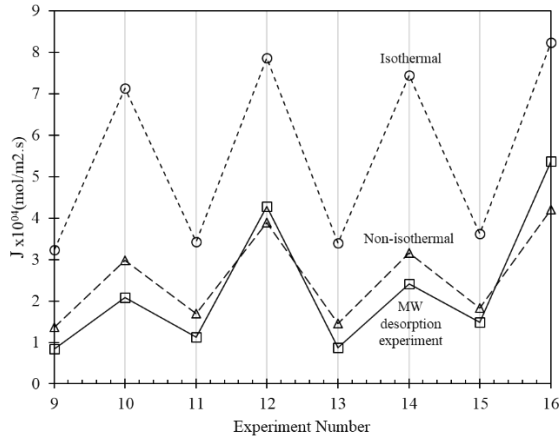


Figure 4-65: Comparison of desorption flux under isothermal - ($T=T_{out}$) and non-isothermal regeneration - $T=f(z)$. Wetting fraction ($F=0.01\%$)

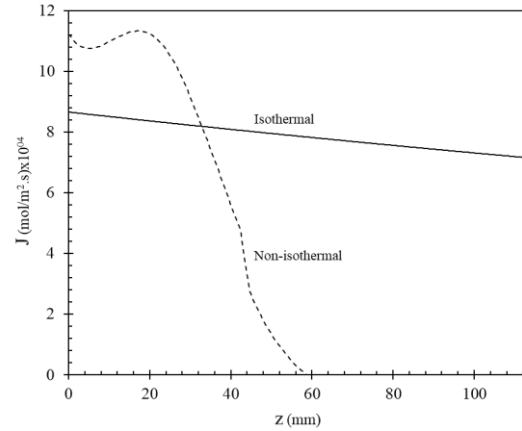


Figure 4-66: Simulated desorption profile: isothermal - ($T=T_{out}$) vs non-isothermal regeneration. Operating conditions of experiment 12. Wetting fraction ($F=0.01\%$)

4.6.4 Effect of solvent preheating on desorption

It has been shown that the average desorption rates correlated positively with the solvent outlet temperature (T_{out}) and flow rate. In order to explore potential parameters that may improve desorption rates under non-isothermal mode, the impact of (T_{in}) on the performance of MW-desorption was explored.

Effect of (T_{in}) on liquid film temperature rises

The inlet temperature (T_{in}) of the solvent was varied between [10- 50°C] by steps of 10°C, other operating conditions were held constant at those of experiment (12). It was not found necessary to plot the bulk temperature profiles, as they show a uniform increase while traversing the microwave cavity; film T-profiles on the other hand are of interest and are plotted in Figure 4-67 function of (T_{in}). Figure 4-67 shows that as T_{in} decreases, the “cold” side of the fiber becomes colder leading to lower film temperatures; the “hot” side of the fiber becomes hotter leading to increased film temperatures. It appears as well that all curves have similar shapes, with temperature maxima located at the same position. Another observation is that all film T-profiles intersect at mid-cavity, independently from (T_{in}).

In Figure 4-68 (T_{max}) is plotted as a function of (T_{in}), and for different solvent flow rates while keeping ($T_{out} = 60^\circ\text{C}$). Figure 4-68 shows that irrespective of the flowrate of the solvent, lower solvent entry temperatures lead to greater maximal film temperature rises (T_{max}), hence larger local temperature deviations from the bulk. When the solvent mass flow increases, the local temperature variations are intensified, although this is less pronounced when (T_{in}) is close to (T_{out}).

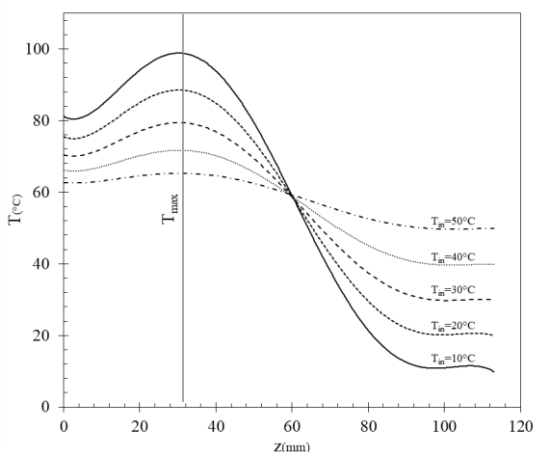


Figure 4-67: Film T-profiles along the fiber for 30% wt. ETA solvent flow rate (0.6mL/s) at different entry temperature $T_{in} = [10, 50]$, and T_{out} fixed at 60°C

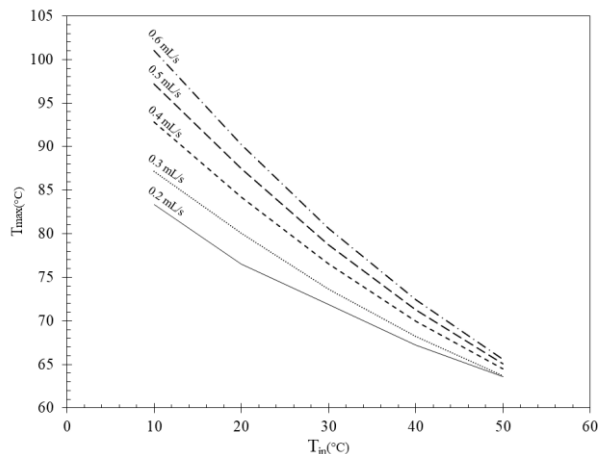


Figure 4-68: Film T-profiles along the fiber for 30% wt. ETA solvent flow rate (0.6mL/s) for different entry temperature $T_{in} = [10, 50]$, and $T_{out} = 60^{\circ}\text{C}$

Effect of (T_{in}) on desorption flux

The average desorption flux was simulated for different values of (T_{in}) and plotted in Figure 4-69, experimental conditions are held similar to those of experiment (12). Figure 4-69 shows that for ($10^{\circ}\text{C} < T_{in} < 30^{\circ}\text{C}$), global desorption rates are constant: lower entry temperatures do not impact desorption neither negatively, nor positively. As (T_{in}) approaches ($T_{out} = 60^{\circ}\text{C}$), the desorption flux increases up to the point where ($T_{in} = T_{out}$) at which isothermal regeneration takes place.

To understand the evolution of (J_{avg}), the axial variations of the desorption flux were plotted in Figure 4-70, for different values of (T_{in}). The figure shows that greater variations are observed when (T_{in}) is lower, i.e. for $T_{in} = 10^{\circ}\text{C}$, chemical absorption takes place on the “cold” side of the fiber. On the hot side, the local desorption flux is superior to all other cases. The observed decrease and increase in axial desorption rates along the fiber balance out such that on average, no change in global desorption performance is observed. Figure 4-70 also shows that as T_{in} increases, desorption profiles start to flatten until reaching the isothermal case representing an almost constant desorption profile.

As a conclusion, adjusting the entry temperature of the solvent will not produce a marked improvement; Isothermal regeneration has still a superior performance to microwave regeneration in the current experimental set-up.

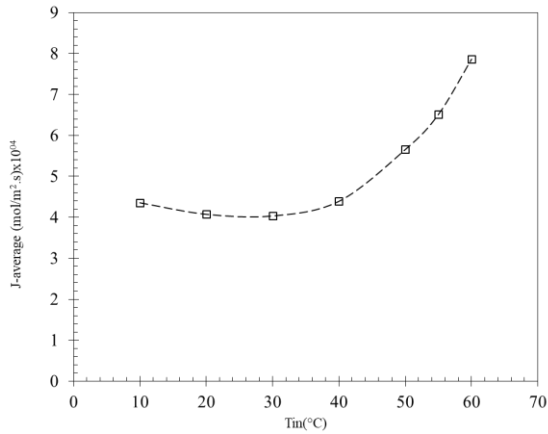


Figure 4-69: Average desorption flux function of solvent entry temperature (T_{in}). $F= 0.01\%$, $T_{out}= 60^{\circ}\text{C}$, solvent vl= 0.6mL/s

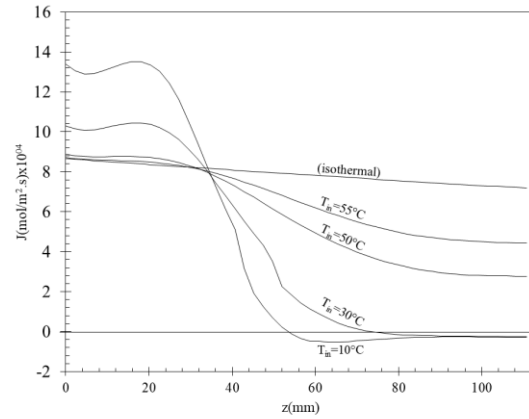


Figure 4-70: Variations of local desorption rates along the fiber length for different entry temperature. $F= 0.01\%$, $T_{out} = 60^{\circ}\text{C}$, solvent vl = 0.6mL/s .

4.6.5 Effect of fiber radius on desorption flux

The hollow fiber used for desorption tests is of millimetric diameter (4.3mm), which is large in comparison to those used in hollow fiber membrane contactors. In order to take full advantage of polymeric gas-liquid membrane contactors, the diameter of the fiber needs to be small in order to have greater interfacial surface density. It is highly probable that if MW-assisted desorption is to be feasible on the contactor scale, it should utilize fibers with a much lower diameter. For this reason, the effect of the fiber size on the process performance needs to be explored.

Figure 4-71 displays the T-maps of the solvent obtained with different fiber radii being: 1, 1.25, 1.5, 1.75, 2.15, 2.5, 2.75, and 3 mm. For all tested cases, inlet and outlet temperatures were held constant at ($T_{in}= 20^{\circ}\text{C}$) and ($T_{out}= 60^{\circ}\text{C}$) respectively, the solvent flowrate per cross-sectional unit area was held constant as well. Figure 4-71 shows that at lower fiber radius, a greater uniformity in the temperature maps is observed; on the contrary as the radius increases, more heterogeneities ensue leading to stronger T-gradients.

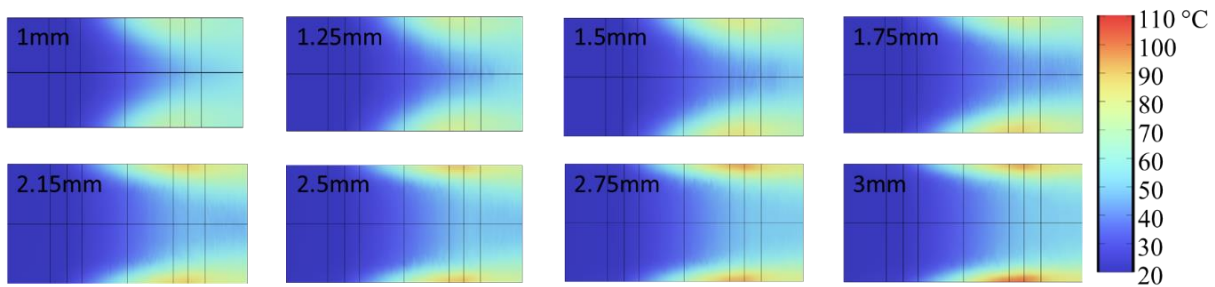


Figure 4-71: T-maps in fiber lumen for different internal radii of the hollow fiber. For all cases, $T_{in}=20^{\circ}\text{C}$, $T_{out}=60^{\circ}\text{C}$ and solvent mass-flux= $4.9\text{g/cm}^2.\text{s}$

The corresponding bulk and film temperature profiles - presented in Figure 4-72 – show that with increasing fiber radius, bulk temperature profile remains unchanged, the film region on the other hand experiences stronger temperature gradients. To understand the evolution of local temperature variations with fiber diameter, T_{max} was

plotted as a function of the fiber radius in Figure 4-73. The figure shows that the maximal film temperature follows a linear increase as a function of the internal radius of the fiber.

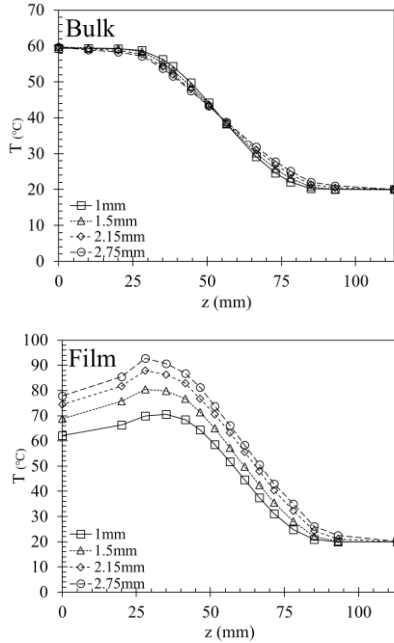


Figure 4-72: Bulk and film temperature profiles for different internal radii of the fiber. For all cases, $T_{in}=20^{\circ}\text{C}$, $T_{out}=60^{\circ}\text{C}$, mass-flux = $4.9 \text{ g/cm}^2.\text{s}$

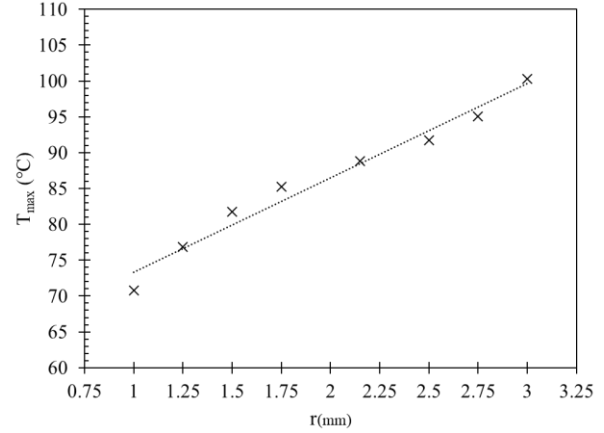


Figure 4-73: Maximal solvent temperature for different internal radii of the fiber. $T_{in}=20^{\circ}\text{C}$, $T_{out}=60^{\circ}\text{C}$, mass-flux = $4.9 \text{ g/cm}^2.\text{s}$

The average desorption flux (J) was plotted as a function of the internal radius (r) in Figure 4-74. Examining

the global desorption flux variations shows that the larger the radial dimension of the fiber, the larger is the desorption flux. It can be seen that the global desorption rate increases almost linearly with respect to the fiber radius. This performance is limited to the scale of a single fiber, and is no way representative of the performance of a membrane module.

In order to assess performance of gas-liquid contactors, the height of transfer unit is a good indicator of the volumetric performance of the equipment. Starting from the differential mass-balance, equation (4.53) can be easily established.

$$\int_{x_{out}}^{x_{in}} \frac{dx}{(1-x_l)^2(x_{f,l} - x_{f,g}^*)} = \frac{a_1}{L_s} \int_{z=0}^{z=1} K_L c_t dz \quad (4.53)$$

From (4.53), we can deduce the expressions of the height of the transfer unit (HTU) and the number of transfer units (NTU), as expressed in (4.54) and (4.55) respectively.

$$\text{HTU} = \frac{L_s}{a_1(K_L c_t)_{avg}} \quad (4.54)$$

$$\text{NTU} = \int_{x_{out}}^{x_{in}} \frac{dx}{(1-x_l)^2(x_{f,l} - x_{f,g}^*)} \quad (4.55)$$

Equation (4.54) can be modified to reach (4.56) where the (HTU) is expressed in terms of the average solvent velocity (v_l) over the entire section of the module, (K_L), and the interfacial area of exchange per unit volume of the contactor (a_v).

$$HTU = v_1/K_L a_v \quad (4.56)$$

The volumetric density of interfacial area -obtained from [21]- is expressed in (4.57) with (d_i) and (d_o) being the inner and outer diameters of the fiber, while (ϕ) is the volumetric fraction of the hollow fibers in the membrane module. In our case the ensemble of the fiber and the surrounding quartz tube constituted the membrane contactor.

$$a_v = (4\phi d_i)/d_o^2 \quad (4.57)$$

The HTU is plotted as a function of the fiber radius in Figure 4-75: The figure shows that increasing the radius of the fiber increases the height of the transfer unit, thus decreasing the volumetric desorption efficiency of the module. This shows that the improvement of the desorption transfer rate per unit of surface area resulting from enlargement of the fibers is outweighed by the loss in the volumetric density area. Hence, we concluded that using fibers of large size would not lead to the intensification of MW-assisted desorption.

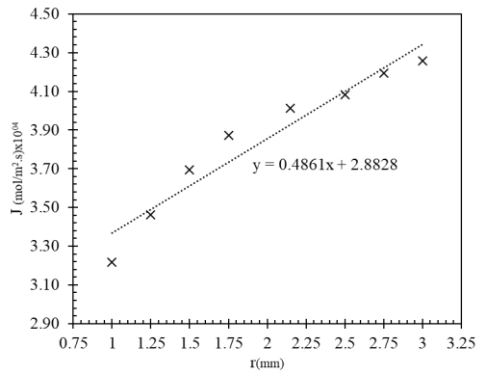


Figure 4-74: Average desorption flux function of the internal radius of the fiber. For all cases, $T_{in}=20^{\circ}C$, $T_{out}=60^{\circ}C$, mass-flux = $4.9 \text{ g/cm}^2.s$, and $F=0.01\%$

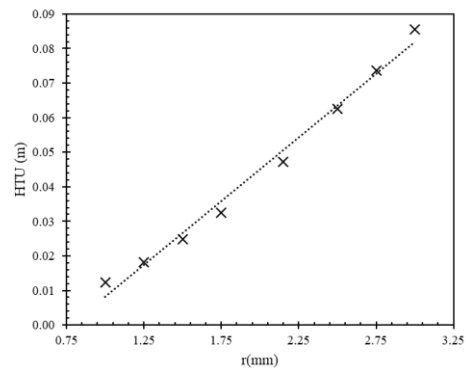


Figure 4-75: Height of transfer unit function of the internal radius of the fiber. For all cases, $T_{in}=20^{\circ}C$, $T_{out}=60^{\circ}C$, mass-flux = $4.9 \text{ g/cm}^2.s$, and $F=0.01\%$, $\phi=0.85$.

4.6.6 Effect of sliding short circuit (SSC) on temperature maps

So far, the SSC was treated as a secondary element in the analysis of the desorption process, however, it carries a great importance. The SSC is responsible for placing the E-field inside the product, which results in the dissipation of the EM energy in the form of heat, and minimization of reflected power. Minimizing reflected power is necessary for improving the energetic performance of the process although it is not sufficient, a very important criteria is the uniform dissipation of EM energy across all surfaces of the fiber.

As the demonstration, the electric field as well as the resulting temperature maps were plotted in Figure 4-76 at different positions of the SSC. The figure shows that the SSC can shift the position of the E-field to the fiber boundary, or center it at the middle. The shifted E-field entails a non-uniform volumetric dissipation rate, hence the preferential heating of one side as shown in the corresponding temperature maps. Non-uniform heating of one side risks formation of hot spots leading to solvent boiling, thermal attack on the fiber matrix, and a decrease in operating efficiency.

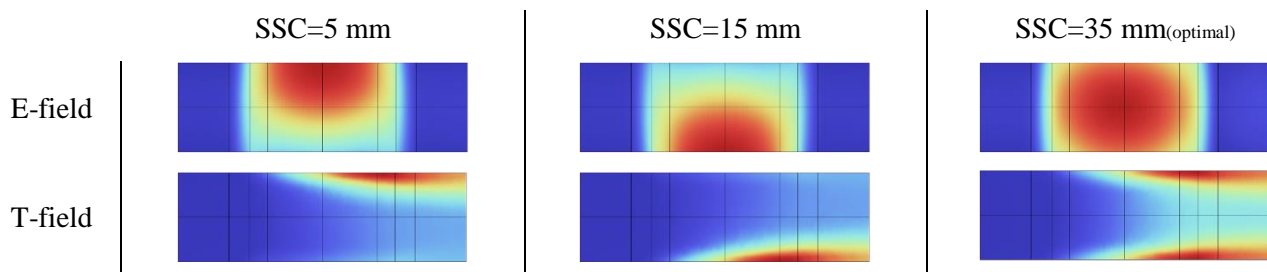


Figure 4-76: Electric and temperature field maps at different SSC positions. Solvent 30% wt. ETA ($\alpha=0.44$), $T_{in}=20^{\circ}\text{C}$, mass flow=0.6mL/s, $r_i=2.15\text{mm}$.

4.6.7 Co-current versus Counter-current operation

It is well known that counter-current operation produces a better performance in gas-liquid contactor, however this is particular to isothermal systems and does not necessarily extend to non-isothermal ones. In this part, MW-assisted desorption was simulated for the case where the solvent was flowing co-currently relative to that of the N_2 sweeping gas. One important observation from counter-current mode of operation, is that both chemical desorption and chemical absorption occur along the fiber length. It would be interesting to observe if this phenomenon is a characteristic of co-current mode as well.

In Figure 4-77 we plot the desorption flux along the fiber length, for both co-current and counter-current modes of operation. The co-current mode shows a very similar profile to the counter-current one. It is suspected that because the CO_2 concentration at gas outlet is very low, therefore changing the flow configuration of the gas phase would have no effect in the tested experimental conditions. Co-current flow has a major difference from the counter-current one, it is only possible for desorption to occur instead of a mixed absorption-desorption process. The reason is that in co-current operation, the sweeping gas contacts an ever-hotter solvent as shown in Figure 4-78.

It is true that, in counter-current operation, total absorbed quantity CO_2 on the “cold” side of the fiber is almost negligible in comparison with that desorbed. Nonetheless, this is only exclusive to our work which involves a single fiber, operating at a relatively low temperature, and a small contact area. When operating a membrane contactor in counter-current mode, the sweeping gas phase should be highly enriched in CO_2 when passing the “hot” side of the contactor. Consequently, the CO_2 absorption is expected to take place on the “cold” side of the contactor due to a greater partial pressure of CO_2 than that at the equilibrium with the “cold” liquid. This is expected to penalize the desorption efficiency.

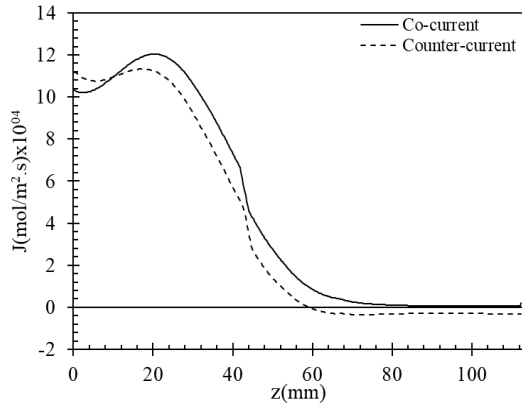


Figure 4-77: Evolution of desorption flux along fiber length, co-current Vs counter-current mode at operating conditions of experiment 12. $T_{out}=60^{\circ}\text{C}$, solvent $v_l=0.6\text{mL/s}$, $\alpha_{in}=0.44$, gas flow= 3.33 mL/s .

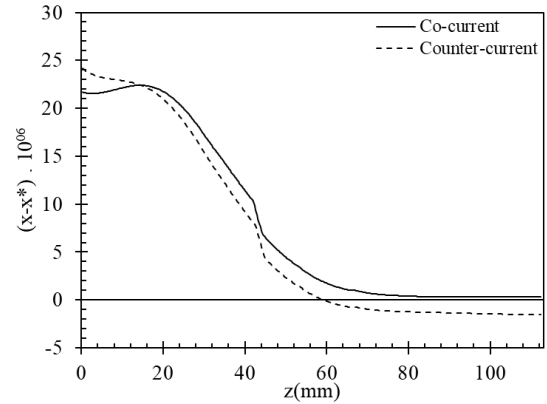


Figure 4-78: Evolution of driving force for mass transfer along fiber length, Co-current Vs counter-current mode at operating conditions of experiment 12. $T_{out}=60^{\circ}\text{C}$, solvent $v_l=0.6\text{mL/s}$, $\alpha_{in}=0.44$, gas flow= 3.33 mL/s .

The average desorption flux for co-current and counter current modes are shown in Figure 4-79. Overall the co-current mode achieved a better performance as only chemical desorption seems to be taking place. It is worth noting that the T-profiles for co-current and counter-current operation are identical and hence can be found in section (4.5.3).

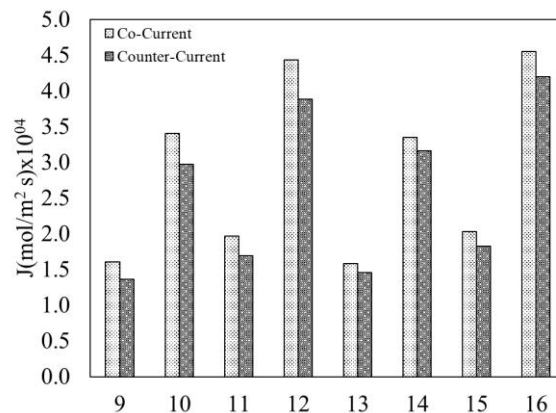


Figure 4-79: Comparison of desorption performance between two modes of operation: co-current vs counter-current operation for solvent and sweeping gas flows

4.7 Sensitivity analysis of CO_2 desorption rates

4.7.1 Objectives and motivation

It has been established that the proposed model is able to predict fairly well the chemical desorption process under MW irradiation. Despite its relatively primitive state and simplifying assumptions, it displays a good qualitative agreement with experimental desorption data. Therefore it can serve as a sensitivity analysis tool regarding the parameters presented in Table 4.9 which pertain to: membrane properties, physical properties, and operating conditions. Sensitivity study of these parameters would help to reveal in what manner should a given

operating variable be adjusted to ensure better regeneration performance. Another advantage of conducting this analysis is to establish the sought-out degree of accuracy to tolerate when estimating physical, chemical, and transfer properties.

One particularity of microwave regeneration is that fiber and operating parameters influence the temperature maps. Changes of fiber dimensions, solvent flow velocity, and solvent carbonation ratio evoke changes in T-maps, hence in the desorption flux. In the following sensitivity study, it was assumed that each parameter was changed in a near infinitesimal manner so as to not affect the T-maps; otherwise the analysis would drastically be more complex.

Membrane properties include those pertaining to the morphology of the porous media, and fiber dimensions which influence mass-transfer as well as hydrodynamic conditions respectively. Operating conditions include average liquid (v_l) or gas (v_g) volumetric flow rates, carbonation ration at entry (α_{in}), composition of the sweeping gas at entry (y_{in}), as well as bulk (T_b) and film (T_f) profiles. The physical properties pertain to the general transfer properties of the solvent, as well as multiphase equilibrium of CO_2 . These quantities include the diffusivities of CO_2 in the solvent and membrane presented by (D_{CO_2-l}) and ($D_{CO_2_eff_g}$) respectively, the diffusivity of ETA in the solvent (D_{ETA-l}), physical solubility of CO_2 in the solvent (He). The quantities (E) and (k_l), although completely dependent on other physical or quantities operating conditions, were tested as this puts in question the assumptions in deriving the numerical expressions.

membrane properties	Physical properties	operating conditions
ξ	D_{CO_2-l}	v_l
τ	D_{ETA-l}	v_g
r_i	$D_{CO_2_eff_g}$	α_{in}
d_o	VLE	y_{in}
d_i	He	T_{film}
	E	T_{bulk}
	k_l	

Table 4.9: quantities used to evaluate the sensitivity of the desorption flux

4.7.2 Methodology and equations

The sensitivity of the desorption flux was evaluated by applying a perturbation to each tested quantity. Each quantity was changed in the range [-10%, +10%] with respect to the base value, and with a step of 2% to give a total of 11 points. This procedure was performed over all experiments (9-16), which results in a total of (8x11) average desorption flux data.

The relative desorption rate (J_{avg_R}) was calculated relative to the base case as per (4.58). (J_{avg}) is the average desorption flux over the fiber surface, (P) being the factor that adjusts the value of a given quantity. The subscript (R) stands for relative, i.e. relative to the base case. As an example, ($P=1$) is the case where the tested parameter is

not varied from the reference case, (P=1.1) represents an increase of 10% relative to the base value of that parameter. For ease of presentation, variations in the flux (J) were normalized with respect to the base case (P=1) and expressed in percentage points.

$$J_{\text{avg_R}}|_{\text{Exp}(i),P} = \frac{J_{\text{avg}}|_{\text{Exp}(i),P} - J_{\text{avg}}|_{\text{Exp}(i),P=1}}{J_{\text{avg}}|_{\text{Exp}(i),P=1}} \times 100 \quad (4.58)$$

For a given parameter and value of (P), the mean relative average desorption flux $\bar{J}_{\text{avg_R}}$ was obtained from the eight experiments (9-16) as expressed in (4.59).

$$\bar{J}_{\text{avg_R}}|_P = 1/8 \sum_{i=9}^{i=16} \Delta J_{\text{avg_R}}|_{\text{Exp}(i), P} \quad (4.59)$$

The local sensitivity of the mean average relative flux at (P) with respect to a given parameter, is denoted by $(\bar{\Delta}J_{\text{avg_R}}|_P)$ as expressed in equation (1.60). This formulation gives 9 estimations of the local sensitivity, however in this formulation, P belongs to the range [0.92 - 1.08] as the sensitivity cannot be determined at points (P=0.9) and (P=1).

$$\bar{\Delta}J_{\text{avg_R}}|_P = \frac{\bar{J}_{\text{avg_R}}|_{P+0.02} - \bar{J}_{\text{avg_R}}|_{P-0.02}}{0.04 \times 100} \quad (4.60)$$

The total average relative sensitivity $(\bar{\Delta}J_{\text{avg_R_t}})$ with respect to a parameter can be calculated as shown in (4.61) by averaging the obtained estimations of the local sensitivities at different perturbations.

$$\bar{\Delta}J_{\text{avg_R_t}} = 1/9 \sum_{P=0.92}^{1.08} \bar{\Delta}J_{\text{avg_R}}|_P \quad (4.61)$$

4.7.3 Desorption Sensitivity

4.7.3.1 Membrane properties

The sensitivity to membrane properties is presented in Figure 4-80, where the mean relative flux ($\bar{J}_{\text{avg_R}}$) was plotted with respect to the factor (P). Figure 4-80 shows that membrane porosity is the most influential parameter, i.e. an increase of (10 %) increases the desorption flux by (17%) relative to the base value. The internal diameter (d_i) influences the liquid phase mass transfer coefficient, while (r_p) holds the lowest influence as it is responsible for decreasing the effective diffusivity of CO₂ in the porous media. The tortuosity is shown to have a negative influence on desorption as it increases the path traveled by CO₂ molecule to reach the sweeping gas.

4.7.3.2 Transfer and equilibrium properties

The mean relative flux ($\bar{J}_{\text{avg_R}}$) with respect to liquid mass transfer coefficient, physical solubility and vapor-liquid equilibrium properties is shown in Figure 4-81. The vapor-liquid equilibrium is shown to have the greatest influence followed by the effective diffusivity of CO₂ in the gas phase ($D_{\text{CO}_2\text{-eff}}$). This is not surprising as even under non-wetted condition, the membrane presents the biggest resistance to mass-transfer. Increase in CO₂ diffusivity in

the liquid phase is found to negatively impact desorption performances, because as diffusivity increases, CO₂ concentration in the reactive film becomes similar to that in the bulk of the solvent thus chemical desorption reaction is less active. Increased diffusivity of ETA has a positive impact on desorption, this is due to the fact that the liquid film is richer in ETA than the liquid bulk, consequently greater diffusivity of ETA helps evacuate the produced ETA which helps shift the chemical reaction to the products side. It is also worth noting that, in the numerical model, the diffusivities of ETAH⁺ and ETACOO⁻ were assumed identical to that of ETA. Therefore, increased diffusivity allows faster diffusion of these reactants from the solvent bulk into the reactive film. Figure 4-81 also shows that desorption has negligible sensitivity to Henry's law, however it is very sensitive with respect to the equilibrium of 30%wt. ETA-CO₂ system.

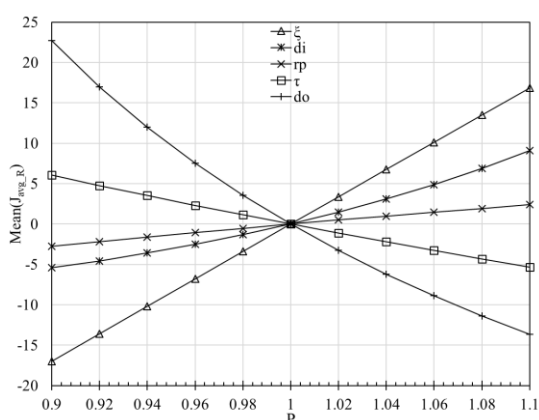


Figure 4-80: Sensitivity curves of the desorption flux with respect to the change in membrane properties

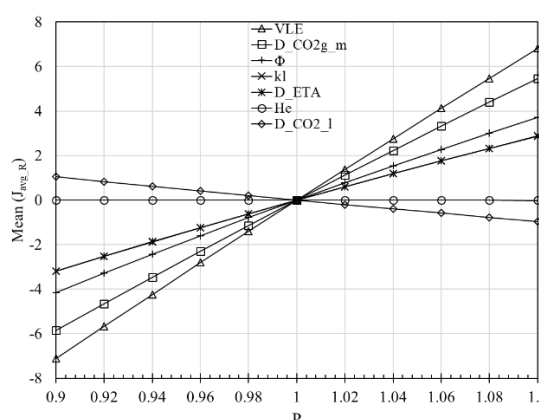


Figure 4-81: Sensitivity curves of the desorption flux with respect to the change in physical or equilibrium properties

4.7.3.3 Operating conditions

The mean relative change in desorption flux is plotted in Figure 4-82 with respect to changes in the operating conditions. The carbonation ratio holds the greatest effect on desorption rates, it is followed by bulk temperature as it increases the concentration of free CO₂ in the bulk. The film temperature on the other hand - used for calculation of transfer properties, transfer coefficients and enhancement factor – follows the same trend as the bulk temperature but with a lower impact.

These results indicate that the carbonation ratio needs to be determined with a high degree of accuracy. They also show the importance of careful prediction of (T_{bulk}) profiles, and the necessity of precise modeling of heat transfer in a microwave cavity. Liquid and gas flow rates have little contribution on desorption performance in comparison to other quantities, liquid velocity only contributes to the liquid mass transfer coefficient, but in a small manner as it is raised to the power of (1/3) in the Graetz-Lévêque correlation.

4.7.3.4 Recommendations

The overall mean parameter sensitivities were calculated and plotted in Figure 4-83. With regards to the membrane properties, it is recommended to choose a highly porous membrane material with small pore sizes as this would prevent liquid intrusion all while ensuring a good regeneration performance. With regards to the solvent properties, accuracy in determining (H_e) can be neglected as this has little impact on desorption, while (D_{CO_2-l}) and (D_{CO_2-g}) can be estimated with mild accuracy. In view of the moderate effect of VLE, data can be estimated with mild accuracy. Still, VLE data experience logarithmic variations with carbonation ratio or with temperature, therefore it holds the greatest effect on desorption rates amongst the other physical quantities. These indications not only define the acceptable accuracy of physical correlations and VLE data, but they also serve to highlight that the key characteristics of a solvent that would replace the 30% wt. ETA; namely its chemical equilibrium behavior.

Examination of sensitivity with respect to the operating conditions underlines the great improvement of desorption performance using high solvent carbonation ratios at entry. Figure 4-83 reveals that desorption is highly sensitive to (T_{bulk}) , hence derivation of the mean axial bulk T-profiles from 3D T-maps requires to be done in a rigorous manner. The film temperature on the other hand depends on several parameters mainly on the solvent flow rate and fiber diameter. Higher solvent flow rates may result in a greater desorption flux at the expense of a lesser regeneration extent. On the other hand, larger fiber diameters increase the HTU making a potential membrane module less efficient.

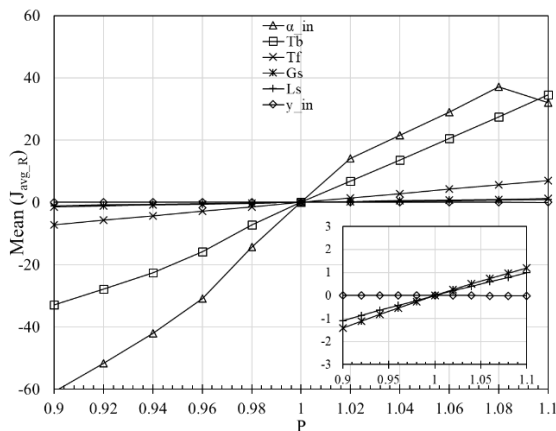


Figure 4-82: Sensitivity curves of the global desorption flux with respect to operating conditions

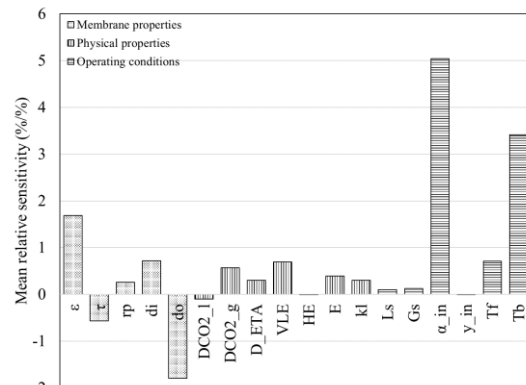


Figure 4-83: mean sensitivity of the desorption flux with respect to quantities pertaining to membrane properties, physical properties of the solvent, and operating conditions

4.8 Conclusion

In this chapter, a multi-physical model was conceived to simulate sweeping-gas desorption of CO_2 from a laminar flow of 30% wt.ETA in the lumen of a porous PTFE hollow fiber membrane. The hollow fiber was placed concentrically in a quartz tube and the ensemble was placed in a mono-mode microwave cavity. A progressive complexification approach was adopted in which several physical phenomena were simulated and verified one at a

time. Numerical modeling of the electromagnetic fields in the microwave cavity shows the electric field to be homogeneous. To simulate the dissipation of microwaves in the solvent stream, heat and momentum transfer were integrated into the model which allows the obtention of the 3D T-maps. The latter highlight the strong temperature gradients in the region close to the membrane wall of the hollow fiber.

Mass-transfer modeling in a hollow fiber membrane was based on the 1D resistance-in-series model which accounts for the effects of chemical reactions of the solvent and CO₂, and the decrement of desorption rates due to partial wetting of the membrane. The model simulates the local desorption rates along the axial direction of the hollow fiber as temperature levels vary. To simulate microwave desorption, the 3D temperature maps obtained in the MW cavity were transformed into two 1D temperature profiles that represent the variations of temperature along the fiber length in both the liquid film and bulk.

Desorption fluxes along the axial direction of the fiber show that desorption onsets at high temperatures, leading to negligible desorption rates across 60% of the fiber area. Supplementary studies suggest that contrary to conventional processes co-current mode of operation is more advantageous than the counter-current due to the occurrence of CO₂ absorption at cold regions of the fiber. In an attempt to characterize the performance of microwave regeneration, it is compared to numerical desorption data at isothermal mode. Microwave regeneration is shown to be more efficient in the “hot” side of the fiber, however the isothermal mode is more efficient on the whole.

Complementary studies highlight that increased fiber diameters augment desorption flux, however it does so at the expense of lower volumetric efficiency. Lower temperatures of the solvent at entry of the microwave cavity have no effect on the overall desorption, as long as the average outlet temperature of the solvent is fixed. Increasing the solvent flow rate improves desorption rates mainly due to the formation of stronger temperature gradients, however this happens at the expense of a lower residence time in the membrane. A sensitivity study of desorption shows that a mild sensitivity with respect to transfer, and physical properties of the solvent as well as fiber geometries. Very high sensitivities of bulk temperature of the solvent and its carbonation ratio are found to be the main drivers for chemical desorption.

4.9 Annex: correlations used for the estimation of properties of the simulated systems

4.9.1 Notations

E	Electric field intensity (V/m)
H	Magnetic field intensity (A/m)
ω	Angular frequency (rd/s)
μ	Magnetic permeability (H/m)
ϵ	Electric permittivity (F/m)
ϵ'	Relative permittivity
ϵ''	Dielectric loss factor
σ	Electrical conductivity (S/m)
c	Speed of light in vacuum (m/s)
f	Frequency (Hz)
λ	Wavelength (m)
S_{11}	Reflected power coefficient (dB or %)
P	Power (W) or pressure (kPa)
α	Carbonation ratio
	Fiber radius (mm)

r

a	Width of WR340 waveguide (43 mm)
b	Length of WR340 waveguide (86 mm)
ρ	Fluid density (g/mL)
v	Fluid velocity (m/s)
g	Gravitational acceleration (m/s ²)
μ	Viscosity (cP)
C_p	Specific heat (J/g K)
T	Temperature (°C)
Q	Volumetric heating rate (W/m ³)
ϵ_0^*	Permittivity of free space (F/m)
\vec{n}	Normal vector
C	Concentration (mol/m ³)
N	Mass-transfer rate (mol/s)
A	Mass-transfer area (m ²)
He_c	Partition coefficient
He	Henry's law (kPa m ³ / mol)
d	diameter (m)
K	overall mass-transfer coefficient (m/s)
L	Fiber length (m)
ξ	Fiber porosity
Re	Reynold's number
Sc	Schmidt number
Sh	Sherwood number

4.9.2 Abbreviations

MW	Microwaves
EM	Electromagnetic
SSC	Sliding short circuit
TE	Transverse electric
PTFE	Polytetrafluoroethylene
DW	Distilled water
ETA	Ethanolamine
Max	Maximal
VNA	Vector Network Analyzer
CO ₂	Carbon dioxide
N ₂	Nitrogen
eff	Effective
kn	Knudsen
Exp	Experiment

4.9.3 Subscripts

Superscripts

s	Phasor domain
r	Reflected
i	Incident, or at gas-liquid interface
*	In equilibrium with vapor phase
l	liquid
g	Gas
m	membrane
k	mass transfer coefficient (m/s)
t	total
f	free
0	at initial conditions
R	Relative
s	Phasor domain
r	Reflected
i	Incident, or at gas-liquid interface
*	In equilibrium with vapor phase
l	liquid
g	Gas

D	Diffusivity (m ² /s)
τ	Tortuosity
δ	Membrane thickness (m)
M	Molar mass (g/mol)
R	Ideal gas constant (J/mol K) or mass-transfer resistance (s/m)
F	Wetting fraction
E _{rxn}	Enhancement factor
K	Equilibrium constant of CO ₂ with ETA
G _s	Inert gas flow rate (mol/s)
L _s	Inert liquid flow rate (mol/s)
x	mole fraction in liquid phase
y	mole fraction in gas phase
J	CO ₂ desorption flux (mol/m ² s)
X	Mole fraction relative to inert species in liquid phase
Y	Mole fraction relative to inert species in gas phase

4.9.3.1 Dielectric properties of porous PTFE fiber

The relative permittivity of porous PTFE fiber is determined using the Landau-Lifshitz-Looyenga dielectric mixing law [40]; the law is used to calculate the apparent dielectric properties of a dispersed phase in a continuous phase. The equation is given in (4.62) with (ϵ^*) being the complex permittivity of the mixture, (ϵ_1^*) complex permittivity of the continuous phase, (ϵ_2^*) complex permittivity of the dispersed phase, and (v) being the volumetric fraction ($v_1 + v_2 = 1$).

$$(\epsilon^*)^{1/3} = v_1(\epsilon_1^*)^{1/3} + v_2(\epsilon_2^*)^{1/3} \quad (4.62)$$

4.9.3.2 Dielectric properties of distilled water

The Debye model was used for calculation of the dielectric properties of distilled water. The dispersion parameters function of temperature were obtained from previous authors [41]. Validity of these parameters are for $T \in [0, 55] \text{ }^\circ\text{C}$ and in the frequency range $f < 20.05 \text{ GHz}$. The complex permittivity is given by the Debye model:

$$\epsilon' - j\epsilon'' = \epsilon_\infty + \frac{\epsilon_0 - \epsilon_\infty}{1 - i2\pi\tau f} + \frac{i\sigma}{2\pi\epsilon_0^* f} \quad (4.63)$$

-The relative static dielectric constant is given by the following expression:

$$\epsilon_0 = 87,85306 \exp(-0,00456992 T) \quad (4.64)$$

-The relaxation time is given by:

$$\tau(\text{ps})^{-1} = 5.631 \cdot 10^{-02} + 2.12 \cdot 10^{-03}T + 1.86 \cdot 10^{-05}T^2 \quad (4.65)$$

-The optical relative dielectric constant is given by:

$$\epsilon_\infty = 6,49 - 0,025 T(^\circ\text{C}) \quad (4.66)$$

4.9.3.3 Dielectric properties of 30% wt.ETA

The dielectric properties of 30% wt. ETA used in the MW heating model are displayed in Table 4.10 over the temperature range [20-80 °C], and the carbonation ratio [0.2- 0.55]. The aforementioned data were measured experimentally using the open-ended coaxial technique, for more details refer to (insert chapter reference). Linear interpolation was used to estimate the properties within and outside the measurement ranges of temperature and carbonation ratio.

α	T(°C)	ϵ'	ϵ''
0	20	61.5	18.8
0	60	56.9	9.1
0.22	20	56.04	34.19
0.22	30	57.29	34.33
0.22	40	57.95	35.45
0.22	50	58.27	37.49
0.22	60	57.78	39.79
0.22	70	56.92	42.71
0.22	80	55.94	46.78
0.33	20	56.54	39.68
0.33	30	58.27	41.52
0.33	40	59.33	44.42
0.33	50	59.69	47.73
0.33	60	59.33	52.27
0.33	70	58.88	56.62
0.33	80	56.44	59.48
0.44	20	57.04	45.66
0.44	30	58.64	48.43
0.44	40	60.22	53.51
0.44	50	60.93	58.26
0.44	60	61.18	63.50
0.44	70	61.01	68.96
0.44	80	61.54	74.43
0.55	20	56.42	50.92
0.55	30	58.53	55.29
0.55	50	59.12	64.84
0.55	60	59.08	69.10
0.55	70	61.59	74.29
0.55	80	61.23	78.43

Table 4.10: relative permittivity (ϵ') and loss factor (ϵ'') of 30% wt. ETA at 2.45GHz.

4.9.3.4 Thermal conductivity of 30% wt. ETA

The thermal conductivity of 30% wt. ETA was fitted by Ghasem [42] using the Filippov equation of a binary mixture presented in (4.67). (λ) is the thermal conductivity of pure component in (W/m K), (w_1) and (w_2) are the weight fractions of ethanolamine and water respectively, (K) is a fitting constant taken as ($K=0.72$) for aqueous

ethanolamine solution. The correlation is valid for a molar fraction ($x_{\text{ETA}} < 0.1$) and at $T = 25^\circ\text{C}$. Despite its limited validity, it was used in the current multi-physical model due to lack of better data.

$$\lambda_m = w_1\lambda_1 + w_2\lambda_2 - Kw_1w_2(\lambda_2 - \lambda_1) \quad (4.67)$$

The thermal conductivity of pure ETA is determined from the correlation proposed by Shokouhi [43] and presented in (4.68) for a validity range of $30 < T < 80^\circ\text{C}$.

$$\lambda_{\text{MEA}} = -0,1711T + 291,2846 \quad (4.68)$$

The thermal conductivity of DW is determined from correlation (4.69), taken from [44].

$$\lambda' = -1,48 + 4,12T^2 - 1,63T^2 \quad (4.69)$$

4.9.3.5 Specific heat of 30% wt. ETA solution

The specific heat of aqueous ethanolamine was calculated from the correlation of Kim[45] for loaded and fresh solutions of aqueous ethanolamine. The expression of the specific heat is given in (4.70), and the pertaining constants are listed in Table 4.11 for different ETA mass fractions, and carbonation ratios. Equation (4.70) is valid for $30^\circ\text{C} < T < 80^\circ\text{C}$, for temperatures outside this range linear extrapolation was used. Linear interpolation was used to determine the specific heat at carbonation ratios bounded by $\alpha = 0$ and $\alpha = \alpha_{\text{max}}$.

$$C_p (\text{J} \cdot \text{g}^{-1} \cdot \text{K}^{-1}) = a + bT \quad (4.70)$$

% wt. ETA	Carbonation ratio	a	b x 10 ⁰³
20	Fresh Solution	3.1315	2.8479
	0.634	2.247	4.4044
22.5	Fresh Solution	3.0666	2.8945
	0.616	2.1374	4.5492
25	Fresh Solution	2.9523	3.1530
	0.597	1.9983	4.8434
30	Fresh Solution	2.5661	4.1847
	0.581	1.8252	5.0097

Table 4.11: parameters for the calculation of specific heat of aqueous ethanolamine solutions

It is worth mentioning that as we rely on interpolating, data this is not without justification. To our knowledge, the only other author who reported the specific heat of aqueous ETA solution at different carbonation ratios, was Weiland [46]; unfortunately, his data are limited to ambient temperatures thus limiting their utility.

4.9.3.6 Density of 30% wt. ETA solution

Weiland [47] measured the density of aqueous solutions of single and blended alkanolamine aqueous solutions at different temperatures and carbonation ratios. The author used experimental data along with data collected from ten different sources to establish the density correlation valid for several amines, over the temperature range $[273-398 \text{ K}^\circ]$ and the carbonation ratio ($\alpha < 0.6$).

The density is presented in (4.71) with subscript (AM) representing amine, (x) is the mole fraction, (M) is the molar mass, (V) is the molar volume of the solution.

$$\rho = [x_{\text{AM}}M_{\text{AM}} + x_{\text{H}_2\text{O}}M_{\text{H}_2\text{O}} + x_{\text{CO}_2}M_{\text{CO}_2}]/V \quad (4.71)$$

The molar volume of the solution (mL/mol) is expressed in (4.72) with (V^*) being null for the case of ETA, while (V^{**}) being the excess molar volume from two component interactions is expressed in (4.73) for ETA. The constants “e”, and “d” are found in Table 4.12.

$$V = x_{AM}V_{AM} + x_{H_2O}V_{H_2O} + x_{CO_2}V_{CO_2} + x_{AM}x_{H_2O}V^* + x_{AM}x_{CO_2}V^{**} \quad (4.72)$$

$$V^{**} = d + ex_{AM} \quad (4.73)$$

The molar volume of amine is presented in (4.74), with (V_{AM}) expressed in (mL/mol), (T) is in K° , with the constant “a”, “b”, “c” being expressed in Table 4.12.

$$V_{AM} = M_{AM}/[a T^2 + bT + c] \quad (4.74)$$

The molar volume of H_2O (mL/mol) was calculated from (4.75) and has a validity range [273-648 K°]. The constants A, B, C, D are presented in Table 4.12.

$$\rho_{H_2O} = a/b^{1+(1-\frac{T}{c})^d} \quad (4.75)$$

	MEA	DEA	MDEA	H ₂ O
a	-5.35E-07	-6.91E-07	-4.68E-07	0.14395
b	-4.51E-04	-2.07E-04	-4.25E-04	0.0112
c	1.194	1.217	1.205	649.727
d	0	0	12.983	0.05107
e	0	0	397.72	-

Table 4.12: constants for calculation of molar and excess volumes

4.9.3.7 Viscosity of 30%wt. ETA solution

The viscosities of partially carbonated aqueous amine solutions were measured and correlated in [47] according to equation (4.76). The validity of this correlation extends to the temperature range [273-398 K°], a carbonation ratio ($\alpha < 0.6$), and for an amine mass fraction ($\Omega < 40\%$). The constants in equation (4.76) are presented in Table 4.13 for three different alkanolamines.

$$\frac{\mu_{soln}}{\mu_{H_2O}} = \exp\left[\frac{(a\Omega + b)T + (c\Omega + d)}{\alpha(e\Omega + fT + g) + 1}\Omega/T^2\right] \quad (4.76)$$

	ETA	DEA	MDEA
a	0	-0.0724	-0.1944
b	0	-3.4363	0.4315
c	21.186	54.319	80.684
d	2373	3628	2889.1
e	0.01015	-0.0015	0.0106
f	0.0093	0	0
g	-2.2586	0.204	-0.2141

Table 4.13: fitting constants for the viscosity of amine solvents

The viscosity of H₂O is given by correlation (4.77) obtained from [48], where (μ) is in (mPa.s), while T in (K°).

$$\mu_{\text{H}_2\text{O}} = A \cdot 10^{B/T-C} \quad (4.77)$$

4.9.4 Model parameters: Mass-transfer modeling

1.1.1.1 CO₂ diffusivity in 30% wt. ETA

It is difficult to determine the diffusivity of CO₂ in 30% wt. ETA, due its reactive nature in the solvent. This renders common determination techniques unsuitable. One way of determining this data is by using the N₂O analogy. This analogy - first proposed by Ladda [49] and verified by Joosten [50]– is based on the similarity of molecular sizes between carbon dioxide and dinitrogen monoxide, and states that the ratios of diffusivity and solubility between these molecules is constant irrespective of the solvent. Given that (N₂O) does not react with ethanolamine, this relation can be used to estimate the diffusivity of acid gas in a reactive medium as given in (4.78).

$$\left[\frac{D_{\text{CO}_2}}{D_{\text{N}_2\text{O}}} \right]_{\text{H}_2\text{O}} = \left[\frac{D_{\text{CO}_2}}{D_{\text{N}_2\text{O}}} \right]_{30\% \text{ETA}} \quad (4.78)$$

The diffusivity of CO₂ and N₂O in H₂O were correlated by [51]. They are presented in (4.79) and (4.80) respectively with (T) being the temperature, for a validity range of [273-353 K].

$$D_{\text{CO}_2-\text{H}_2\text{O}} = 3,7191 \cdot 10^{-06} \exp(-2257.9/T) \quad (4.79)$$

$$D_{\text{N}_2\text{O}-\text{H}_2} = 5,2457 \cdot 10^{-06} \exp(-2388.9/T) \quad (4.80)$$

Experimental data on the diffusivity of N₂O in aqueous ETA solutions at different temperatures and carbonation ratios are rather very limited and cover the temperature range encountered in the absorption step of carbon capture at null carbonation ratio [33, 52, 53]. It is for this reason that the diffusivity of N₂O in 30% wt. ETA was determined from the modified Stokes-Einstein equation as shown in (4.81). The exponent value 0.8 was proposed by [51] by fitting experimental data from literature; correlation errors are of the order of 20% in comparison to experimental data [53].

$$D_{\text{N}_2\text{O}-30\% \text{ETA}} \cdot \mu_{30\% \text{ETA}}^{0.8} = D_{\text{N}_2\text{O}-\text{H}_2\text{O}} \cdot \mu_{\text{H}_2\text{O}}^{0.8} \quad (4.81)$$

4.9.4.1 ETA diffusivity in 30% wt. ETA solution

The diffusivity of ETA in aqueous 30% wt.ETA solution was determined from modified Stokes-Einstein correlation presented in (4.82).

$$D_{am}\mu^{0.6}|_{H_2O} = D_{am}\mu^{0.6}|_{soln} \quad (4.82)$$

The correlation was fitted by Versteeg [51] to experimental data from literature at 25°C for different alkanolamines including ETA, (α) was fitted to be 0.6. The diffusivity of the amine in pure water was determined from the Wilke-Change [54] correlation presented in (4.83), with (x) being the molecular weight adjustment factor (1.6 for water), (M) molecular weight of H₂O, (T) is the temperature in K°, (μ) is the viscosity of water (mPa.s), and (V) is the molar volume of the solute at its normal boiling point (for ETA 170°C).

$$D = 7,4 \cdot 10^{-8} [[xM]^{0.5} T / \mu V^{0.6}] \quad (4.83)$$

Snijder [55] measured the diffusivities of alkanolamines in several aqueous alkanolamine solutions at T=[25-60°C] and that the correlation of Versteeg gave an average error of 7% and a maximal error of 25%, while Jamal [53] and Glasscock [56] used the correlation in their studies.

4.9.4.2 Solubility of CO₂ in aqueous ETA solution

Versteeg [51] used the N₂O analogy for calculation of CO₂ solubility in a reactive medium based on the works of Laddah[49] who found a ratio of solubility between CO₂ and N₂O in different organic solvents, and Haimour [57] who verified the validity of the N₂O analogy in aqueous MDEA solution.

The solubility of CO₂ and N₂O in pure water were measured and correlated by Jamal [53]. The correlations are shown (4.84), and (4.85) and have a validity range of [273-523 K], as well as [278-393 K] respectively.

$$H(CO_2 - H_2O) = 10^{(69,395 - 3557,79/T - 22,29 \log(T) + 0,0039T)} \quad (4.84)$$

$$H(N_2O - H_2O) = 10^{(85,84 - 4373,35/T - 27,71 \log(T) + 0,0033T)} \quad (4.85)$$

The ratio of both solubilities is constant as per the N₂O analogy shown in equation (4.86).

$$(H_{CO_2}/H_{N_2O})_{H_2O} = (H_{CO_2}/H_{N_2O})_{solvent} \quad (4.86)$$

Wang [58] measured the solubility of N₂O in pure alkanolamines at the temperature range [20-95°C]. The experimental findings were correlated by (4.87), while coefficients (b₁, b₂) are presented in Table 4.14 for several pure alkanolamines.

$$H_{N_2O-am} = b_1 \exp(b_2/T) \quad (4.87)$$

	b1	b2	σ (%)
AMP	86480	-1205.2	1.55
MEA	120700	-1136.5	1.39
DEA	163800	-1174.6	2.43
TEA	482500	-1572.2	0.3
MDEA	152400	-1312.7	0.9
DIPA	101000	-1187.9	1.85

Table 4.14: Coefficients for solubility of N₂O in pure alkanolamines

The solubility of CO₂ in pure alkanolamines can then be calculated using the N₂O analogy.

The solubility of CO₂ in a mixture can be determined by (4.88), with (H_{CO₂,m}) being the solubility in unloaded solvent mixture, (\emptyset_i) being the volumetric fraction of pure solvent (i) in the mixture, (H_{CO₂,i}) is the solubility of CO₂ in the pure solvent (i), and R is the excess solubility due to the interaction between the different molecules in the mixture.

$$\ln H_{\text{CO}_2,m} = \sum \phi_i \ln H_{\text{CO}_2,i} + R \quad (4.88)$$

The volume fraction of each solvent in the mixture is presented in (4.89), with v_i being the molar volume, and (x_i) the molar fraction.

$$\phi_i = \frac{x_i v_i}{\sum x_i v_i} \quad (4.89)$$

The excess term (R) was taken from [59, 60] and is expressed in (4.90) with (α_{12}) being a temperature-dependent empirical parameter obtained from Jamal [53] and valid over the range [20-120 °C].

$$R = \phi_1 \phi_2 \alpha_{12} \quad (4.90)$$

$$\alpha_{12} = a_1 + a_2/T \quad (4.91)$$

To calculate the solubility of 30%wt. ETA, equation (4.88) can be used. The solubility of CO₂ in a solution containing ionic species such as loaded ETA solution, is calculated using (4.92). Here, ($H_{\text{CO}_2,m}$) is the solubility in 30%wt. ETA solution with no ionic content, $H_{\text{CO}_2,m}^*$ is the solubility of CO₂ in a similar solution but with CO₂ loading, h is the Van-Krevlen coefficient, and (I) is the ionic strength.

$$\log(H_{\text{CO}_2,m}^*/H_{\text{CO}_2,m}) = hI \quad (4.92)$$

The Van-Krevlen coefficient is expressed in (4.93), with (h_+) is the sum of coefficients of cationic species, (h_-) that of the anionic species, and (h_g) that of dissolved but unreacted gases, i.e. CO₂. Coefficients pertaining to the ionic and cationic species were obtained from [61] while that of CO₂ was obtained from [62].

$$h = h_+ + h_- + h_g \quad (4.93)$$

The ionic strength (I) is expressed in (4.94) with c_i being the concentration of the ionic species, (Z_i) being the charge of the ionic species. Concentrations of ionic species were obtained from Kent-Eisenberg [63] vapor-liquid equilibrium model at 50°C and were used.

$$I = 1/2 \sum c_i Z_i^2 \quad (4.94)$$

1.1.1.2 Diffusivity of CO₂ in N₂ gas

The diffusivity of CO₂ in N₂ gas is calculated from equation (4.95) used by Khaisri [18] with “A” denoting CO₂, “B” denotes N₂ gas, (M) is the molar mass (g/mol), (T) is the temperature in (°K), (P) is the total pressure (bar), (σ_{AB}) is the mean collision diameter (Å), (Ω) is the collision integral (unitless). In what follows all expressions and properties were obtained from [64].

$$D_{AB} = \left[0,001858 T^{\frac{3}{2}} (1/M_A + 1/M_B)^{\frac{1}{2}} \right] / [P \sigma_{AB}^2 \Omega_D] \quad (4.95)$$

The collision diameter is expressed in (4.96) with (σ_A) and (σ_B) corresponding to the molecular diameter of CO₂ and N₂ respectively. The latter can be calculated from the critical temperature and pressure (T_c), and (P_c).

$$\sigma_{AB} = [\sigma_A + \sigma_B]/2 \quad (4.96)$$

$$\sigma_A = 2,44(T_c/P_c)^{1/3} \quad (4.97)$$

The collision integral (Ω) is defined as in equation (4.98), with (κ) being the Boltzmann constant ($1.38 \cdot 10^{-16}$), and (ϵ_{AB}) being the energy of molecular interaction for non-binary system defined in (4.99) and (4.100). (T_b) is the normal boiling point in kelvin (K°).

$$\Omega = f(\kappa T/\varepsilon_{AB}) \quad (4.98)$$

The collision integral is identified by the curve shown in Figure 4-84.

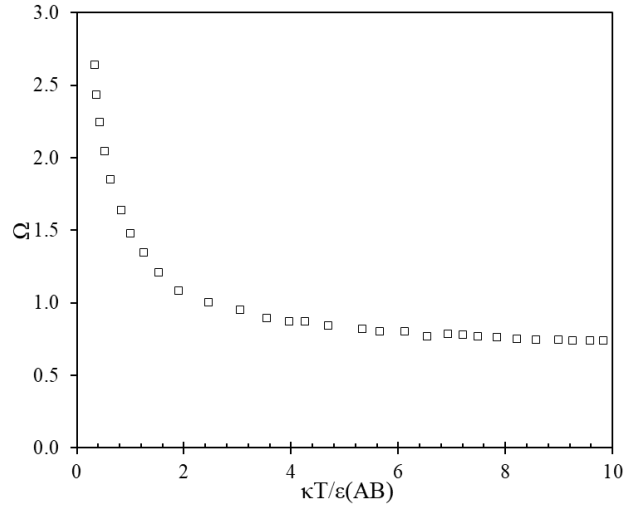


Figure 4-84: collision integral for CO₂-N₂ mixture (Ω)

(ε_{AB}) is defined in (4.99), while the individual constants (ε_A , ε_B) are calculated as per (4.100) with T_b being the normal boiling point in (K°)

$$\varepsilon_{AB} = \sqrt{\varepsilon_A \varepsilon_B} \quad (4.99)$$

$$\varepsilon_A/\kappa = 1,15 T_{b,A} \quad (4.100)$$

4.9.4.3 Evaluating the Knudsen diffusivity

The Knudsen diffusivity was calculated as per the expression from [17–19] and presented in (4.101). “r” is the average pore radius (cm), R is the ideal gas law (8.314 Pa.m³/mol K), T is the temperature (K°), M is the molar weight of CO₂.

$$D_{kn} = \frac{2}{3} r \sqrt{8RT/(\pi M_A)} \quad (4.101)$$

Expression (4.101) can be simplified to obtain that more commonly used equation (4.102).

$$D_{kn} = 0,97 r_{pore} \sqrt{T/M_A} \quad (4.102)$$

4.9.5 References

1. Von Hippel, A.R., and A.S. Labounsky. 1995. *Dielectric materials and applications*. Artech House Microwave Library. Artech House.
2. S. O. Nelson. 1992. Correlating Dielectric Properties of Solids and Particulate Samples Through Mixture Relationships. *Transactions of the ASAE* 35: 625–629. <https://doi.org/10.13031/2013.28642>.
3. STOGRYN, A. 1971. Equations for Calculating the Dielectric Constant of Saline Water 19: 733–736. <https://doi.org/10.1109/TMTT.1971.1127617>.
4. RF module- User's guide Comsol.
5. Ito, M., K. Ushida, N. Nakao, N. Kikuchi, R. Nozaki, K. Asai, and M. Washio. 2006. Dechlorination of poly(vinyl chloride) by microwave irradiation I: A simple examination using a commercial microwave oven. *Polymer Degradation and Stability* 91: 1694–1700. <https://doi.org/10.1016/j.polyimdegradstab.2005.12.003>.
6. Minobe, Tomio. CHLORIDE USING MICROWAVES.
7. Overview of materials for Polytetrafluoroethylene (PTFE), Extruded.
8. Jönsson, Ann-Sofi, Roland Wimmerstedt, and AC Harrysson. 1985. Membrane distillation - A theoretical study of evaporation through microporous membranes. *Desalination* 56. Elsevier: 237–249. [https://doi.org/10.1016/0011-9164\(85\)85028-1](https://doi.org/10.1016/0011-9164(85)85028-1).
9. Smith, David S., Arnaud Alzina, Julie Bourret, Benoît Nait-Ali, Fabienne Penneç, Nicolas Tessier-Doyen, Kodai Otsu, Hideaki Matsubara, Pierre Elser, and Urs T. Gonzenbach. 2013. Thermal conductivity of porous materials. *Journal of Materials Research* 28: 2260–2272. <https://doi.org/10.1557/jmr.2013.179>.
10. Graetz, L. 1885. Ueber die Wärmeleitungsfähigkeit von Flüssigkeiten. *Annalen der Physik* 261: 337–357. <https://doi.org/10.1002/andp.18852610702>.
11. Lévêque André. *Lévêque, André. 1928. Les Lois de la transmission de chaleur par convection, par André Lévêque. Paris: Dunod.*
12. Linton, W.H., and T.K. Sherwood. 1950. Mass transfer from solid shapes to water in streamline and turbulent flows 46: 258–264.
13. Ibrahim, Mohamed H, Muftah H El-Naas, and Zhien Zhang. CO₂ Capture using Hollow Fiber Membranes: A review of membrane wetting: 58.
14. Kreulen, H., C.A. Smolders, G.F. Versteeg, and W.P.M. van Swaaij. 1993. Microporous hollow fibre membrane modules as gas-liquid contactors. Part 1. Physical mass transfer processes. *Journal of Membrane Science* 78: 197–216. [https://doi.org/10.1016/0376-7388\(93\)80001-E](https://doi.org/10.1016/0376-7388(93)80001-E).
15. Alkhubiri, Abdullah, Naif Darwish, and Nidal Hilal. 2012. Membrane distillation: A comprehensive review. *Desalination* 287: 2–18. <https://doi.org/10.1016/j.desal.2011.08.027>.
16. Fang, Mengxiang, Zhen Wang, Shuiping Yan, Qigang Cen, and Zhongyang Luo. 2012. CO₂ desorption from rich alkanolamine solution by using membrane vacuum regeneration technology. *International Journal of Greenhouse Gas Control* 9: 507–521. <https://doi.org/10.1016/j.ijggc.2012.05.013>.
17. Khayet, M., M. P. Godino, and J. I. Mengual. 2001. Modelling Transport Mechanism Through A Porous Partition. *Journal of Non-Equilibrium Thermodynamics* 26: 1–14. <https://doi.org/10.1515/JNETDY.2001.001>.
18. Khaisri, Sakarin. 2011. CO₂ stripping from monoethanolamine using a membrane contactor. *Journal of Membrane Science*: 9.
19. Li, K, Jianfeng Kong, and Xiaoyao Tan. 2000. Design of hollow fibre membrane modules for soluble gas removal. *Chemical Engineering Science*.
20. Dindore, V.Y., D.W.F. Brilman, P.H.M. Feron, and G.F. Versteeg. 2004. CO₂ absorption at elevated pressures using a hollow fiber membrane contactor. *Journal of Membrane Science* 235: 99–109. <https://doi.org/10.1016/j.memsci.2003.12.029>.
21. Nishikawa, N., M. Ishibashi, H. Ohta, N. Akutsu, H. Matsumoto, T. Kamata, and H. Kitamura. 1995. CO₂ removal by hollow-fiber gas-liquid contactor. *Energy Conversion and Management* 36: 415–418. [https://doi.org/10.1016/0196-8904\(95\)00033-A](https://doi.org/10.1016/0196-8904(95)00033-A).
22. Chabanon, Elodie. Contacteurs à membranes composites et contacteurs microporeux pour procédés gaz-liquide intensifiés de captage du CO₂ en post-combustion: expérimentation et modélisation: 217.

23. Mavroudi, M., S.P. Kaldis, and G.P. Sakellariopoulos. 2003. Reduction of CO₂ emissions by a membrane contacting process☆. *Fuel* 82: 2153–2159. [https://doi.org/10.1016/S0016-2361\(03\)00154-6](https://doi.org/10.1016/S0016-2361(03)00154-6).
24. Rezaei, Mohammad, David M. Warsinger, John H. Lienhard V, Mikel C. Duke, Takeshi Matsuura, and Wolfgang M. Samhaber. 2018. Wetting phenomena in membrane distillation: Mechanisms, reversal, and prevention. *Water Research* 139: 329–352. <https://doi.org/10.1016/j.watres.2018.03.058>.
25. Wang, R., D.F. Li, C. Zhou, M. Liu, and D.T. Liang. 2004. Impact of DEA solutions with and without CO₂ loading on porous polypropylene membranes intended for use as contactors. *Journal of Membrane Science* 229: 147–157. <https://doi.org/10.1016/j.memsci.2003.10.022>.
26. Kierzkowska-Pawlak, Hanna. 2012. Determination of Kinetics in Gas-Liquid Reaction Systems. An Overview. *Ecological Chemistry and Engineering S* 19: 175–196. <https://doi.org/10.2478/v10216-011-0014-y>.
27. Astarita, Gianni, and David W. Savage. 1980. Gas absorption and desorption with reversible instantaneous chemical reaction. *Chemical Engineering Science* 35: 1755–1764. [https://doi.org/10.1016/0009-2509\(80\)85011-1](https://doi.org/10.1016/0009-2509(80)85011-1).
28. Weiland, R. H., M. Rawal, and R. G. Rice. 1982. Stripping of carbon dioxide from monoethanolamine solutions in a packed column. *AIChE Journal* 28: 963–973. <https://doi.org/10.1002/aic.690280611>.
29. Koonaphapdeelert, Sirichai, Zhentao Wu, and K. Li. 2009. Carbon dioxide stripping in ceramic hollow fibre membrane contactors. *Chemical Engineering Science* 64: 1–8. <https://doi.org/10.1016/j.ces.2008.09.010>.
30. Zhu, Kai, Changhai Yue, Zhenhao Wei, Jingjing Huang, Meng Hu, Yufan Ji, Hanfei Liu, et al. 2022. Experimental and Thermodynamic Investigation on CO₂ Absorption in Aqueous MEA Solutions. Edited by Ghulam Rasool. *Advances in Materials Science and Engineering* 2022. Hindawi: 6278342. <https://doi.org/10.1155/2022/6278342>.
31. Barreau, A., E. Blanchon le Bouhelec, K.N. Habchi Tounsi, P. Mougin, and F. Lecomte. 2006. Absorption of H₂S and CO₂ in Alkanolamine Aqueous Solution: Experimental Data and Modelling with the Electrolyte-NRTL Model. *Oil & Gas Science and Technology - Revue de l'IFP* 61: 345–361. <https://doi.org/10.2516/ogst:2006038a>.
32. Li, Meng-Hui, and Keh-Perng Shen. 1993. Calculation of equilibrium solubility of carbon dioxide in aqueous mixtures of monoethanolamine with methyldiethanolamine. *Fluid Phase Equilibria* 85: 129–140. [https://doi.org/10.1016/0378-3812\(93\)80008-B](https://doi.org/10.1016/0378-3812(93)80008-B).
33. Jou, Fang-Yuan, Alan E. Mather, and Frederick D. Otto. 1995. The solubility of CO₂ in a 30 mass percent monoethanolamine solution. *The Canadian Journal of Chemical Engineering* 73: 140–147. <https://doi.org/10.1002/cjce.5450730116>.
34. Aronu, Ugochukwu E., Shahla Gondal, Erik T. Hessen, Tore Haug-Warberg, Ardi Hartono, Karl A. Hoff, and Hallvard F. Svendsen. 2011. Solubility of CO₂ in 15, 30, 45 and 60 mass% MEA from 40 to 120°C and model representation using the extended UNIQUAC framework. *Chemical Engineering Science* 66: 6393–6406. <https://doi.org/10.1016/j.ces.2011.08.042>.
35. Lee, J. I., F. D. Otto, and A. E. Mather. 1974. The solubility of H₂S and CO₂ in aqueous monoethanolamine solutions. *The Canadian Journal of Chemical Engineering* 52: 803–805. <https://doi.org/10.1002/cjce.5450520617>.
36. Shen, Keh Perng, and Meng Hui Li. 1992. Solubility of carbon dioxide in aqueous mixtures of monoethanolamine with methyldiethanolamine. *Journal of Chemical & Engineering Data* 37: 96–100. <https://doi.org/10.1021/jc00005a025>.
37. Zhang, Chun, Junqing Lan, Tao Hong, Tushar Gulati, Huacheng Zhu, Yang Yang, and Kama Huang. 2016. Dynamic analysis and simulation on continuous flow processing of biodiesel production in single-mode microwave cavity. *International Journal of Applied Electromagnetics and Mechanics* 51: 199–213. <https://doi.org/10.3233/JAE-160007>.
38. Kim, Inna, and Hallvard F. Svendsen. 2007. Heat of Absorption of Carbon Dioxide (CO₂) in Monoethanolamine (MEA) and 2-(Aminoethyl)ethanolamine (AEEA) Solutions. *Industrial & Engineering Chemistry Research* 46: 5803–5809. <https://doi.org/10.1021/ie0616489>.
39. Kim, Inna, Karl Anders Hoff, and Thor Mejdell. 2014. Heat of Absorption of CO₂ with Aqueous Solutions of MEA: New Experimental Data. *Energy Procedia* 63: 1446–1455. <https://doi.org/10.1016/j.egypro.2014.11.154>.
40. Reynolds, J A, and J M Hough. 1957. Formulae for Dielectric Constant of Mixtures. *Proceedings of the Physical Society. Section B* 70: 769–775. <https://doi.org/10.1088/0370-1301/70/8/306>.
41. Buchner, Richard, Glenn T. Hefter, and Peter M. May. 1999. Dielectric Relaxation of Aqueous NaCl Solutions. *The Journal of Physical Chemistry A* 103: 1–9. <https://doi.org/10.1021/jp982977k>.
42. Nayef Ghasem, Nihmiya Abdul Rahim, and Mohamed Al-Marzouqi. 2016. Thermal Conductivity of Aqueous Solvents Used in CO₂ Capture. *Journal of Chemical Engineering Research Updates* 3: 25–30. <https://doi.org/10.15377/2409-983X.2016.03.01.2>.

43. Shokouhi, Mohammad, Amir Hossein Jalili, Farid Samani, and Masih Hosseini-Jenab. 2015. Experimental investigation of the density and viscosity of CO₂-loaded aqueous alkanolamine solutions. *Fluid Phase Equilibria* 404: 96–108. <https://doi.org/10.1016/j.fluid.2015.06.034>.
44. Thermal conductivity of distilled water.
45. Yun, Soung Hee, Young Eun Kim, Jeong Ho Choi, Sung Chan Nam, Jaeon Chang, and Yeo Il Yoon. 2016. CO₂ absorption, density, viscosity and vapor pressure of aqueous potassium carbonate+2-methylpiperazine. *Korean Journal of Chemical Engineering* 33: 3473–3486. <https://doi.org/10.1007/s11814-016-0210-7>.
46. Weiland, Ralph H., John C. Dingman, and D. Benjamin Cronin. 1997. Heat Capacity of Aqueous Monoethanolamine, Diethanolamine, *N*-Methyldiethanolamine, and *N*-Methyldiethanolamine-Based Blends with Carbon Dioxide. *Journal of Chemical & Engineering Data* 42: 1004–1006. <https://doi.org/10.1021/je960314v>.
47. Weiland, Ralph H., John C. Dingman, D. Benjamin Cronin, and Gregory J. Browning. 1998. Density and Viscosity of Some Partially Carbonated Aqueous Alkanolamine Solutions and Their Blends. *Journal of Chemical & Engineering Data* 43: 378–382. <https://doi.org/10.1021/je9702044>.
48. Viscosity of pure water.
49. Laddha, S.S, J.M Diaz, and P.V Danckwerts. 1981. The N₂O analogy the solubilities of CO₂ and N₂O in aqueous solutions of organic compounds: 228.
50. Joosten, Geert E. H., and Peter V. Danckwerts. 1972. Solubility and diffusivity of nitrous oxide in equimolar potassium carbonate-potassium bicarbonate solutions at 25.deg. and 1 atm. *Journal of Chemical & Engineering Data* 17: 452–454. <https://doi.org/10.1021/je60055a016>.
51. Versteeg, Geert F., and Wim P. M. Van Swaaij. 1988. Solubility and diffusivity of acid gases (carbon dioxide, nitrous oxide) in aqueous alkanolamine solutions. *Journal of Chemical & Engineering Data* 33: 29–34. <https://doi.org/10.1021/je00051a011>.
52. Sada, Eizo, Hidehiro Kumazawa, and M. A. Butt. 1978. Solubility and diffusivity of gases in aqueous solutions of amines. *Journal of Chemical & Engineering Data* 23: 161–163. <https://doi.org/10.1021/je60077a008>.
53. Jamal, Aqil. ABSORPTION AND DESORPTION OF CO₂ AND CO IN ALKANOLAMINE SYSTEMS: 380.
54. Wilke, C. R., and Pin Chang. 1955. Correlation of diffusion coefficients in dilute solutions. *AIChE Journal* 1: 264–270. <https://doi.org/10.1002/aic.690010222>.
55. Snijder, Erwin D., Marcel J. M. te Riele, Geert F. Versteeg, and W. P. M. van Swaaij. 1993. Diffusion coefficients of several aqueous alkanolamine solutions. *Journal of Chemical & Engineering Data* 38: 475–480. <https://doi.org/10.1021/je00011a037>.
56. Glasscock, Davide.A. 1990. Modelling and experimental study of carbon dioxide absorption into aqueous alkanolamines. The university of Texas at Austin.
57. Haimour, Noman, and Orville C. Sandall. 1984. Absorption of carbon dioxide into aqueous methyldiethanolamine. *Chemical Engineering Science* 39: 1791–1796. [https://doi.org/10.1016/0009-2509\(84\)80115-3](https://doi.org/10.1016/0009-2509(84)80115-3).
58. Wang, Y.W., S. Xu, F.D. Otto, and A.E. Mather. 1992. Solubility of N₂O in alkanolamines and in mixed solvents. *The Chemical Engineering Journal* 48: 31–40. [https://doi.org/10.1016/0300-9467\(92\)85004-S](https://doi.org/10.1016/0300-9467(92)85004-S).
59. Boublík, T., and E. Hála. 1966. Solubility of gases in mixed solvents. *Collection of Czechoslovak Chemical Communications* 31: 1628–1635. <https://doi.org/10.1135/cccc19661628>.
60. Schneider, G. M. 1970. J. M. Prausnitz: Molecular Thermodynamics of Fluid Phase Equilibria. International Series in the Physical and Chemical Engineering Sciences. Prentice-Hall Inc., Englewood Cliffs, New Jersey, 1969. 523 Seiten Preis: 145 s. *Berichte der Bunsengesellschaft für physikalische Chemie* 74: 308–308. <https://doi.org/10.1002/bbpc.19700740327>.
61. Browning, Gregory J., and Ralph H. Weiland. 1994. Physical Solubility of Carbon Dioxide in Aqueous Alkanolamines via Nitrous Oxide Analogy. *Journal of Chemical & Engineering Data* 39: 817–822. <https://doi.org/10.1021/je00016a040>.
62. Onda, Kakusaburo, Eizo Sada, Takeshi Kobayashi, Shigeharu Kito, and Kunimitsu Ito. 1970. SALTING-OUT PARAMETERS OF GAS SOLUBILITY IN AQUEOUS SALT SOLUTIONS. *JOURNAL OF CHEMICAL ENGINEERING OF JAPAN* 3: 18–24. <https://doi.org/10.1252/jcej.3.18>.
63. Kent, R.L., and B. Eisenberg. 1976. Better data for amine treating: 87–90.
64. Welty, J.R, R.E Wilson, and G Rorrer. 2001. *Fundamentals of Momentum, Heat and Mass Transfer*. John Wiley & Sons.

5 MW-assisted regeneration in membrane contactor

5.1 Introduction

Up until this point in this work, chemical desorption has been studied on the scale of a single fiber, either experimentally, or numerically. Principle results have shown the formation of T-gradients along the radial direction of the fiber thus promising improvements in the desorption performance. The study was conducted using a fiber of rather great dimensions with respect to common sizes, in addition, the electric field which was responsible for heating the solvent in the hollow fiber was of uniform character at the fiber, which is merely a special case. The use of fiber modules containing great numbers of fibers and spanning greater lengths in a cavity instead of a single fiber will most probably lead to non-uniformities in the electric field distributions which may endanger its operational stability on the long-term at best and short-term at worst.

In this chapter we discuss the upscaling of regeneration from a single fiber to the scale of a membrane module through the conception of a prototype unit for MW-assisted regeneration of solvent in a hollow fiber membrane module. The core of this process are two microwave cavities that are custom designed for the isothermal and non-isothermal (MW-assisted) regeneration of the solvent. A MW cavity was used to preheat the solvent before entering the membrane module, while non-isothermal mode relies on heating the solvent while it traverses the membrane module, i.e. the latter is housed inside the custom designed MW cavity. With the bulk of this chapter focusing on the design of the named microwave cavities - especially for non-isothermal regeneration – and the operation of the prototype unit, the performance of the prototype was not fully explored and remains the objective of future works.

The layout of this chapter is as follows:

5.2-Design of single-mode microwave applicators: A brief introduction of the design of cylindrical mono-mode applicators, main considerations should be given to the orientation of the product with respect to the incident electric field, length and diameter of the cavity, as well as the length of the iris for optimal impedance matching.

5.3-Microwave cavity for solvent preheating: In this part we expose the methodology, numerical and experimental results associated with the cavity used to preheat the solvent before performing chemical desorption in the membrane module. Main results are presented under the form of S_{11} spectra and power dissipation maps in the solvent flow.

5.4- MW cavity for non-isothermal regeneration of solvent: A second cavity was designed to heat the solvent by MW while it circulates directly inside the membrane module. This necessitates housing the membrane module inside the cavity. The cavity design methodology is similar to that of the preheating cavity, however the main focus of this part is the correct assessment of the dielectric properties of the solvent filled membrane module, which largely influence the analysis of E-field power dissipation maps throughout.

5.5-Conception of the prototype unit: A prototype-scale process of MW-assisted desorption in a membrane module was conceived. The prototype permits the regeneration of solvent under isothermal or non-isothermal conditions in the membrane module. The gas side of the membrane module on the other hand can be occupied by a sweeping gas configuration or can be placed under vacuum.

5.2 Design of single-mode microwave applicators

The design of single-mode cavity is based on two main considerations: minimizing the reflected microwave power, and ensuring a good heating homogeneity in the product. This is achieved by careful choice of three characteristics: iris dimensions, the position of the sliding short circuit, and the cavity diameter. The impedance of a waveguide may not consistently align with its load devices, this discrepancy leads to standing waves, power loss, decreased power-handling capacity, and heightened frequency sensitivity. The sliding short circuit, iris and stub tuners are elements that adjust the impedance of the product to that of the waveguide in such a manner to decrease the E-field reflection coefficient defined in (5.2.1) with (Γ) being the complex reflection coefficient, (Z_L) being the load impedance, and (Z_0) being the characteristic impedance of the line, (E) and the (θ) being the phase of the E-field, and subscripts (r) and (i) correspond to the reflected and the incident waves.

$$\Gamma = \frac{Z_L - Z_0}{Z_L + Z_0} = \frac{E_r \angle \theta_r}{E_i \angle \theta_i} \quad 5.2.1$$

An iris is a metal plate that is situated in the transverse plane, acts as a shunt capacitive or inductive element which both can be either symmetrical or asymmetrical. The capacitive and the inductive irises are shown in Figure 5-1 and Figure 5-2 respectively: the width of the opening in both types of irises allows the calculation of the susceptance (Y_0) at a given waveguide dimensions, and EM frequency that determines the guided wavelength [1]. In more practical terms, the iris reflects part of the incident E-field that is 180° out of phase with that reflected from the load thus eliminating reflected power [2].

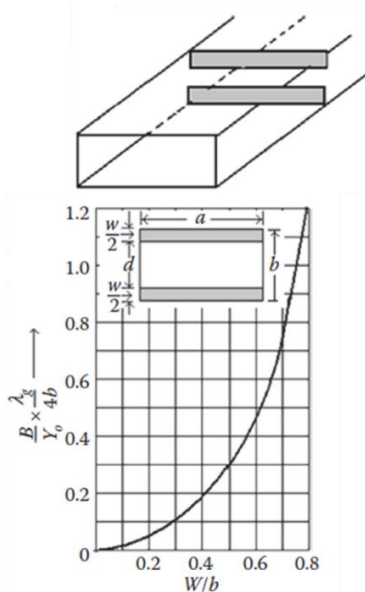


Figure 5-1: The susceptance (Y_0) of the capacitive iris for impedance matching. (Reproduced with permission from [1])

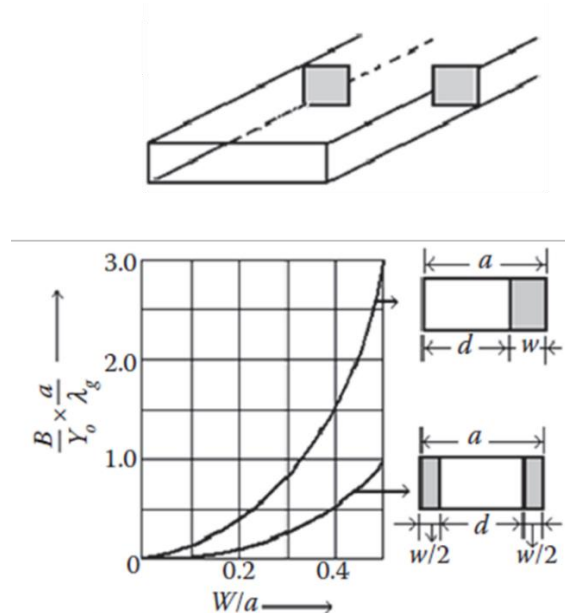


Figure 5-2: The susceptance (Y_0) of an inductive iris for impedance matching. (Reproduced with permission from [1])

While cavity design can influence the homogeneity of MW power absorption energy through the surface of the product, the constraint of the penetration depth of the wave in the product poses a physical constraint on the

attainable heating homogeneity in the depth of the product, independently from the engineering work of the microwave cavity. Other aspects that influence homogeneity are the shape of the product and the choice of the EM frequency for heating.

The orientation of the product with respect to the incident E-fields is of extreme importance; in a TE_{10} mode the E-field follow the direction of the smaller dimension of the waveguide. The three principle orientations product in a single-mode cavity are: parallel, perpendicular and what we choose to call as longitudinal. The three configurations are presented in Figure 5-3, Figure 5-4, and Figure 5-5 respectively for the case of a heating of a continuous flow through a mono-mode cavity. Principally, the cavity dimensions such as diameter, length, and iris should be adjusted with the aim of achieving a compromise minimizing reflected powers and achieving a good heating homogeneity. Experience has shown that parallel orientation is recommended for products that are of small dimensions, perpendicular orientation is useful for products with great dimensions, while longitudinal configuration prevents the penetration of the EM waves. The size of the product also influences the choice of frequency, products with larger dimensions are usually heated at 915 MHz given the considerable upscale of equipment size relative to those at 2450 MHz.

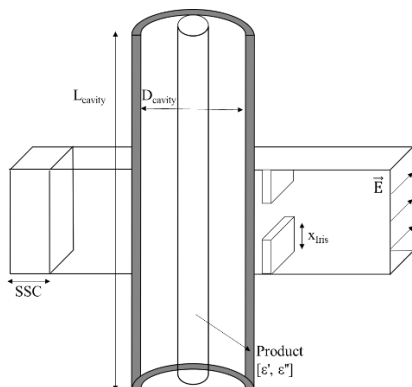


Figure 5-3: Perpendicular orientation of the product with respect to the incident E-field

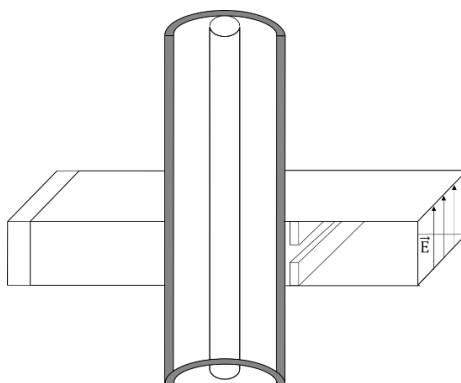


Figure 5-4: Parallel orientation of the product with respect to the incident E-field

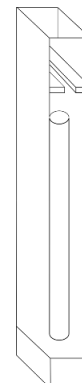


Figure 5-5: Longitudinal orientation of the product in the waveguide

5.3 MW cavity for solvent preheating

5.3.1 Methodology: empirical approach for cavity design

To ensure chemical desorption under isothermal operation, the solvent needs to be preheated to the desired temperature before entering the membrane module. One way to do this is by passing the solvent flow through a microwave cavity to continuously heat it before it enters the membrane module. The CO_2 -enriched solvent passes through a quartz tube inside the MW cavity; the latter is positioned in a perpendicular manner with respect to the E-field at the entry port, and follows the longitudinal direction cavity. It is true that a similar result could have been obtained whilst using a resistive element, but we chose to design this cavity due to advantages of accurate power

control and adaptability to different products. Its advantage over a resistant element is the ease with which energy transfer can be controlled. This cavity may be referred to as the “preheating cavity” in the remainder of the chapter.

The E-field distribution in the cavity was obtained by solving the Maxwell’s equations using the software CST Studio Suite® (Dassault Systèmes, France). Modelling the E-field distribution inside the solvent allows the determination of the fraction of the power absorbed and the fraction that is reflected back to the entry port – the latter expressed as (S_{11}) as shown in 5.3.1.

$$S_{11} = 10\log_{10} \left(\frac{P_r}{P_i} \right) \quad 5.3.1$$

The specifications of the MW cavity (diameter, iris) are to be empirically determined through examination of the corresponding levels of reflected power, in light of the dimensions and the dielectric properties that are attributed to the product. Although the dielectric properties of 30%wt. ETA have been well characterized, the desired versatility of this cavity requires that it should be adapted to a large range of dielectric properties for other liquids. The frequency of the EM irradiation was chosen as a parameter as the MW frequency change (within fixed lower and upper bounds in the neighborhood of the central frequency 2.45GHz) simulates impedance adaptation in a similar way as sliding short circuit adaptation. For solid-state generators operating at 2.45 GHz, the frequency range is in the order of (± 50 MHz), for those operating at 915MHz the adaptation range is (± 13 MHz), in compliance with the frequency band allocated by the Federal Communications Commission (FCC) for industrial, scientific, and medical (ISM) applications [3].

The ‘parametric sweep’ option in CST Studio Suite® was used to vary simultaneously the following parameters:

- Relative permittivity (ϵ') of the product.
- Dielectric loss-factor (ϵ'') of the product.
- SSC adaptation
- MW frequency
- iris dimensions
- Cavity diameter

5.3.2 Geometry, meshing and boundary conditions

Geometry

The geometry of the preheating cavity is shown in Figure 5-6, the solvent occupies the interior of the quartz tube, and the latter is oriented parallel to the longitudinal direction of the cylindrical cavity. Due to the disproportionate length of the cylindrical cavity with respect to its other dimensions, the entire cavity length is not completely shown in Figure 5-6.

Boundary conditions

The entry port is excited at a frequency range belonging to [2.425-2.475] GHz at the TE₁₀ mode. All the outer surfaces of the displayed geometry are supposed perfect electric conductors (PEC) meaning that the tangential component of the E-field (E_t), vanishes at the boundaries. The product was accorded different dielectric properties – either those of 30% wt. ETA or others. It is interesting that the entire geometry is symmetrical with respect to the ZY and XY planes, although such a condition was not used despite its ability to decrease the calculation time by around 50%.

Meshing and resolution

The 3D geometry is meshed using hexahedral elements for a total count of 53 047 elements with an average element quality of 0.7805. The minimum and maximum distances between two elements are 1.543 mm and 33.31 mm respectively. The option of ‘adaptive mesh refinement’ was implemented to achieve independency of the solution on the mesh, the mesh was refined until the error on (S_{11}) was less than a set value of 2%. The frequency domain solver was used to find the solution of Maxwell’s equations using the finite element method (FEM), although the usage of the time domain solver was possible with the latter employing the finite difference time domain (FDTD) method.

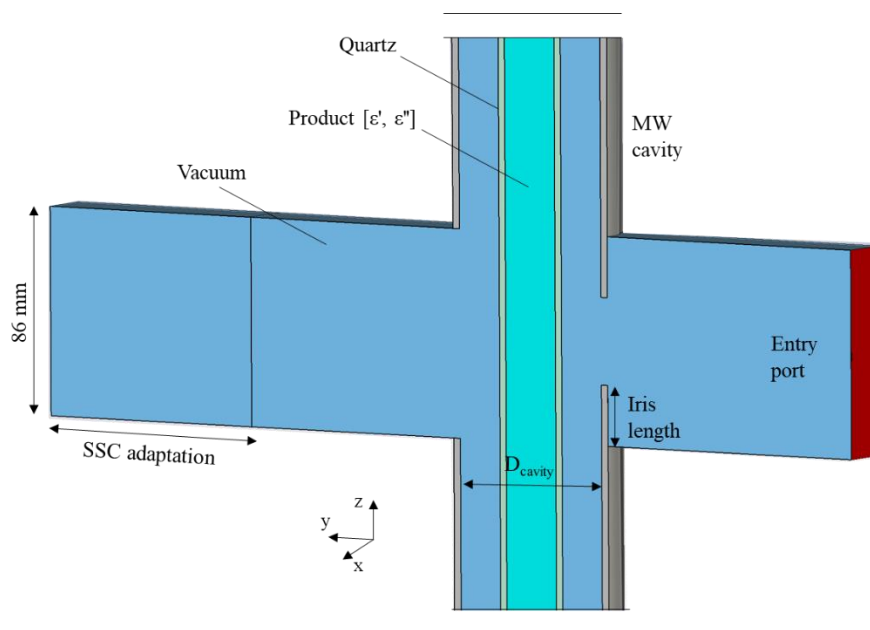


Figure 5-6: Cross-section view of the 2.45 GHz MW cavity for preheating 30% wt. ETA. drawn in CST Studio Suite®

5.3.3 Numerical results

1.1.1.3 Simulation run #1

The geometrical parameters of the cavity (diameter, iris), along with the dielectric properties of the solvent (ϵ' , ϵ''), and impedance matching tools (SSC, frequency) were varied in the range shown in Table 5-1. Variations were made following a classical parametric sweep configuration where one parameter is varied at a time. The dielectric

properties especially $[\epsilon', \epsilon''] = [55, 70]$ represent the solvent's properties at ($\alpha=0.44$) and ($T= 50\text{ }^\circ\text{C}$). The total number of simulated cases equate to 8636 cases excluding the frequency variations.

In order to decrease the number results to a reasonable level, cases of minimal power reflection across the SSC range, and across the frequency adaptation range, were extracted. The optimal reflection coefficients were then averaged over all tested dielectric properties, to give a representation of the overall performance of the cavity at a given diameter, and iris dimension. The cavity length was fixed by the quartz tube to 600 mm.

Parameter	Range
D_{cavity}	[70-130 mm], 20 mm step
iris length	[0-25 mm], 3.5 mm step
ϵ' product	10, 25, 55
ϵ'' product	10, 30, 50, 70
Sliding short circuit	[10-97 mm], 3 mm step
Frequency	2425-2475 MHz, 1 MHz step

Table 5-1: Ranges of geometrical parameters, frequency and dielectric properties simulated

Figure 5-7 shows the average optimal value of the (S_{11}) reflection coefficient, as a function of the iris positions, at different cavity diameters. Although many dielectric properties were tested, Figure 5-7 shows only the average of the optimal S_{11} coefficients at a given geometrical configuration. The figure shows that diameters: 70, 90, and 110 mm have similar tendencies, the average reflection experiences a minimum that occurs at increasing iris value as the diameter increases. For cavity diameter of 130 mm, minimal reflection occurs at minimal to no iris dimensions, which is a good advantage for cost of the cavity due to its ease of fabrication. As cavity diameters 90 and 110mm result in greater reflected powers, their counterparts (70 and 130 mm) will be considered for greater evaluations. For a given cavity diameter, it was found that the optimal SSC positions had a range of variations of 3 mm.

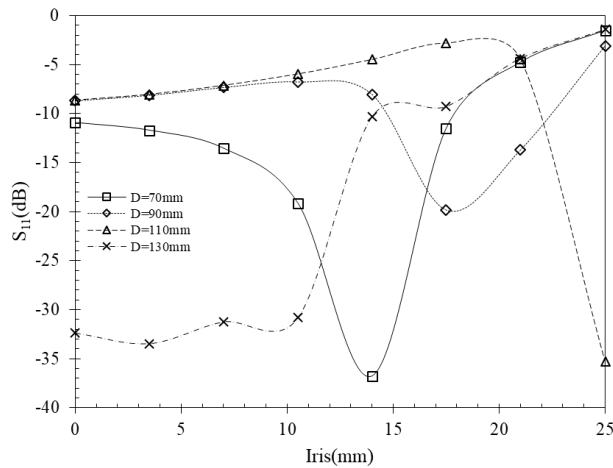


Figure 5-7 : Average optimal power reflection coefficients as a function of iris aperture for all tested diameters.

The optimal reflected powers over the simulated frequency range and SSC positions were plotted in Figure 5-8 for some dielectric properties of the solvent. Values are plotted to compare the performance of the diameters (70 mm, 130 mm) with iris values of 14 and 3.5 mm respectively. Figure 5-8 displays the excellent impedance adaptation performance at all tested properties, including some properties of interest [55, 50] that represent the 30 %wt. ETA solution at $[\alpha, T]$ of $[0.22, 20^\circ\text{C}]$ and $[0.55, 20^\circ\text{C}]$ respectively. However, it remains difficult to decisively choose the cavity dimensions as both configurations present very comparable results.

It might be interesting to evaluate the robustness of the cavity's performance. This was done by applying a small perturbation of (1.5 mm) on the optimal position of the SSC, obtained reflections are plotted in Figure 5-9. The figure shows the smaller diameter of the cavity maintains its excellent performance, while that of 130 mm experiences some increase in reflected power but remains nonetheless quite acceptable.

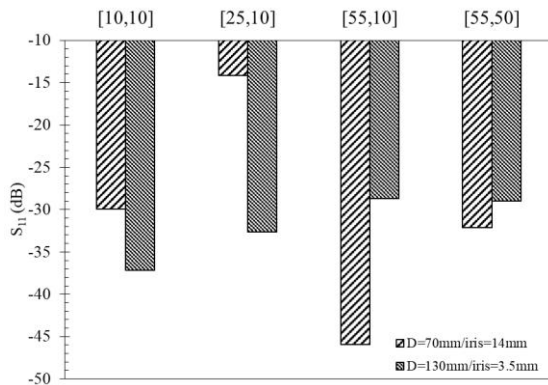


Figure 5-8: Comparison of optimal (S_{11}) at two cavity configurations for different dielectric properties $[\epsilon', \epsilon'']$

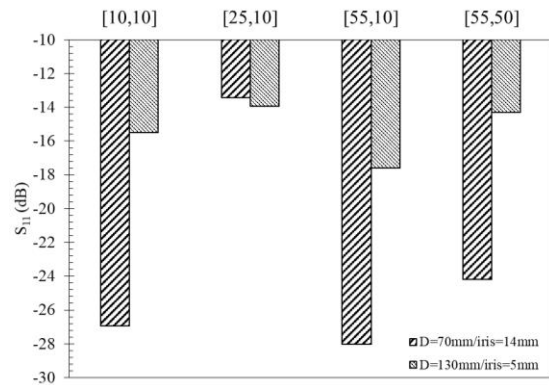


Figure 5-9: Comparison of optimal (S_{11}) at two cavity configurations for different dielectric properties $[\epsilon', \epsilon'']$ – a perturbation of 1.5mm was applied at the optimal SSC position.

5.3.3.1 Simulation run #2

Having chosen the appropriate cavity diameter to be 70 mm, another parametric sweep is performed with tighter step-sizes on the iris and the SSC variations. The varied parameters are shown in Table 5-2: cavity diameter is kept constant at 70 mm, variations on the iris dimensions are in the neighborhood of 14mm, and the SSC is varied in steps of 3 mm in the neighborhood of the optimal SSC position obtained previously.

Parameter	Range
Cavity diameter	70 mm
iris	12, 13, 14, 15, 16 mm
ϵ'	10, 25, 55
ϵ''	10, 30, 50, 70
SSC	45, 48, 51, 54 mm
Frequency	2425-2475 MHz, step 1MHz

Table 5-2: Refined ranges of the parameters to optimize the solvent preheating MW cavity

As has been previously done, the optimal (S_{11}) values over the frequency and the SSC were averaged, and are plotted as a function of the iris position in Figure 5-10. We plot as well the average sensitivity defined as the average change (ΔS_{11}) due to change in the optimal SSC position by (± 1.5 mm) all while implementing a frequency adaptation. Obtained sensitivities ($\Delta S_{11} / 1.5$ mm) are averaged over all simulated cases of the dielectric properties [ϵ', ϵ''] as shown in (5.1).

$$S_{11_avg}|_{D_{cavity}, Iris} = \sum_{i=1}^3 \sum_{j=1}^4 \frac{S_{11,ssc_opt+1.5mm} + S_{11,ssc_opt-1.5mm}}{2} \Big|_{[\epsilon'_i, \epsilon''_j]} \quad (5.1)$$

It can be observed that an iris position of (14 mm) is the optimal value to achieve lowest reflected power. Moreover, the S_{11} sensitivity shows that the even with disturbances or imperfect adaptation the cavity will still perform quite well; hence, we fix the diameter and iris to 70 and 14 mm respectively.

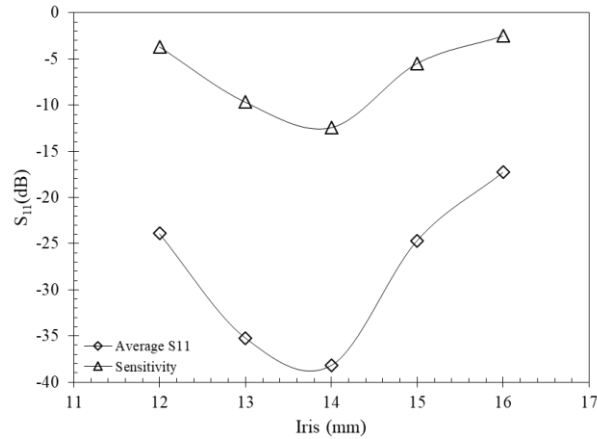


Figure 5-10: Average (S_{11}) value as a function of the iris dimension for a cavity diameter (70 mm).

5.3.3.2 E-field and power-loss maps

3D map of the average E-field was plotted in Figure 5-11 for the case of $[\epsilon', \epsilon''] = [50, 77]$. The figure shows that the average E-field on the entry port is uniform along the direction of the waveguide due to the progressive nature of the MW, while that near the SSC is stationary. Further emphasis can be made on this idea when regarding Figure 5-12 where we plot the E-field on the cut-line that spans the entire length of the waveguide.

Figure 5-11 shows that following longitudinal direction of the cavity we notice the existence of a standing wave, formed by the superposition of the forward traveling wave and that reflected by the MW chimney at the cavity end. It is interesting to note distance between maxima is ($\sim 90\text{mm}$), a value very closely to that in a waveguide WR340 ($\lambda_g/2 \sim 88 \text{ mm}$) operating at 2450 MHz.

The local MW volumetric heat dissipations are plotted in Figure 5-13 along circular paths on the outer surface of the solvent at different heights along the cavity. The figure shows the heating rates to decrease as the wave becomes attenuated with increasing height. The profile of local MW absorbed power however changes with height. At ($z=0$) the side facing the SSC was heavily heated in comparison to all other sides. At ($z=122 \text{ mm}$), the lateral sides are more heated than those facing the SSC and the entry port. It should be noted that the magnitudes of the E-field or local MW absorbed power are not important as an absolute value because they vary with incident levels of MW power. Instead, the values should be regarded in a relative manner with respect to one another as increasing the microwave power will increase scale the E-field maps by an easily determined value.

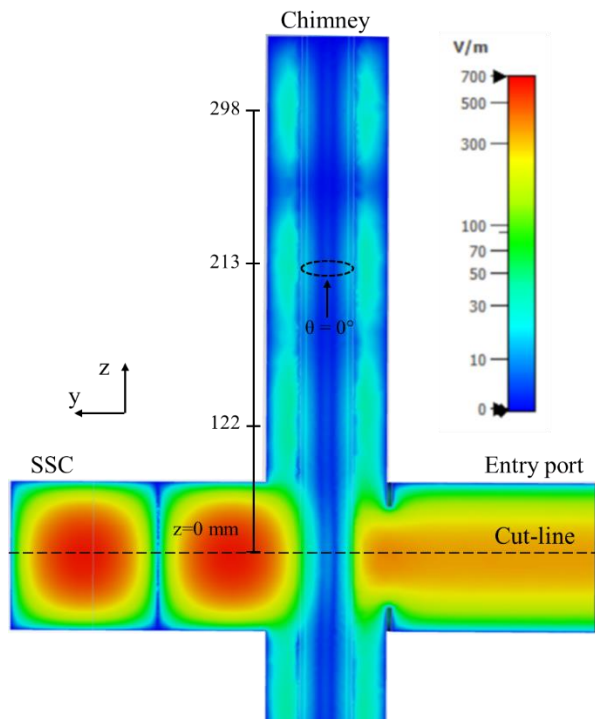


Figure 5-11: Average E-field distribution in the preheating cavity at ($f=2.4699 \text{ GHz}$), optimal SSC position (48 mm), $[\epsilon', \epsilon'']$ of the solvent are $[55, 70]$.

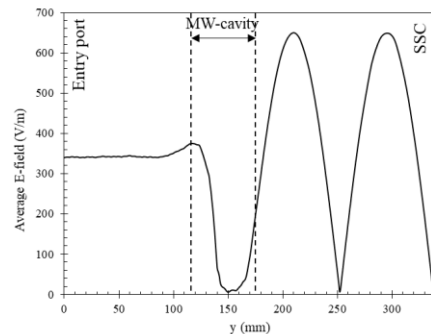


Figure 5-12: Average E-field plot along the waveguide length at ($f=2.4699 \text{ GHz}$), optimal SSC position, $[\epsilon', \epsilon'']$ of the solvent are $[55, 70]$.

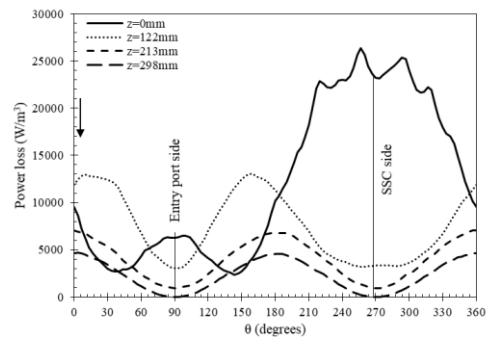


Figure 5-13: Power loss density over a circular path on the outer surface of the solvent, and at different heights (z). The

values of θ at 90° and 260° represent the sides facing the entry port and the sliding short circuit respectively.

5.3.4 Experimental validation of reflected power spectra

5.3.4.1 Materials and methods

The S_{11} spectra were measured using a VNA with liquids of various dielectric properties circulating at ambient conditions inside the preheating cavity. The VNA was calibrated in waveguide mode over the frequency range [2400-2500] MHz by fixing three types of charges: open circuit, closed circuit, and a perfectly matched load. The MW circuit of the set-up, is composed of a VNA (Rhode and Schwartz ZVL network analyzer 9kHz-3GHz), a coaxial cable, a type N-coaxial to waveguide transition, a 3-stub tuner (SAIREM-AI3SMWR340 NG) used for secondary impedance adaptation, the microwave applicator, and a sliding short circuit (SAIREM-PCCMW340L130PUMRIPE-B) for impedance adaptation. The hydrodynamic circuit of the set-up is composed of a peristaltic pump (Watson Marlow 520U) operating with a suction tube (Watson Marlow-Bioprène 8mm) connected to the quartz tube placed inside the MW cavity. The liquid circulates continuously through the quartz tube in a closed circuit. Care was taken to ensure that no air bubbles were trapped in the horizontally placed cavity which would otherwise greatly perturb the measurements.

5.3.4.2 Simulating the dielectric properties of 30%wt. ETA

Keeping in mind the final application of this cavity, it is of utmost importance that the characterization tests be conducted by using the solvent of choice (30%wt. aqueous ETA solution charged with CO_2), at varying temperatures and CO_2 charges. Due to practicality it was not possible to generate CO_2 -loaded ethanolamine solutions. To test their performance, one practical alternative was to simulate the dielectric properties of the solvent by using solutions of varying degrees of salinity or sweetness. Concentration of soluble (NaCl) increases the dielectric loss factor due to ionic conduction [4], while saccharose ($\text{C}_{12}\text{H}_{22}\text{O}_{11}$) causes a decrement of relative permittivity and loss factor by increasing the viscous forces in the solution [5].

Two saline solutions of compositions (48 g/L) and (68 g/L) were prepared by weighing NaCl (95.5%wt. Sigma-Aldrich) and deionized water. Additional solutions of (Water + ethanol) were used to test the versatility of the MW cavity when dealing with moderately absorbing liquids with varying relative permittivity. Three ethanol/water solutions (0%v, 30%v, 60%v) were prepared by weighing ethanol (95%v. Sigma-Aldrich) and deionized water. Figure 5-14 shows the dielectric dispersion diagram where we find the measured properties of: the solvent (30%wt. ETA), the design properties (accorded to the product when designing the preheating cavity), and those of the tested liquids. For water/ethanol mixtures, the decrement in the relative permittivity can be easily controlled by increasing the alcohol proportion [6]. The compositions of the discussed liquids are presented in Table 5-3.

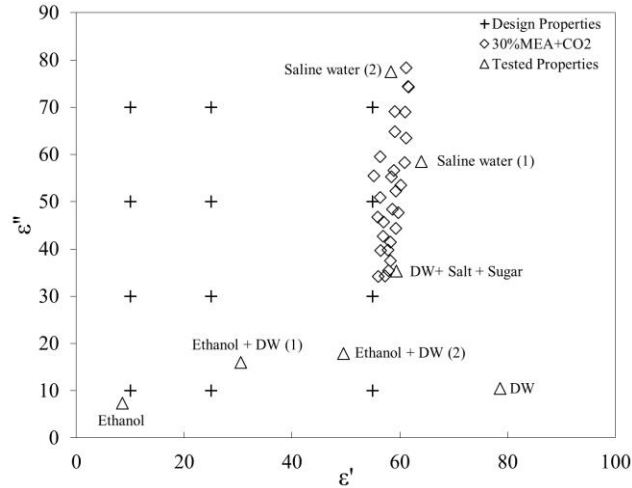


Figure 5-14: Dielectric dispersion diagram showing the design properties, those of 30% wt.ETA over $\alpha = [0.22-0.55]$ and $T = [20-80 \text{ }^\circ\text{C}]$, and the tested properties

Liquid	Composition	T(°C)	ϵ'	ϵ''
DW	Pure	18,8	78.62	10.53
Ethanol	95% volume	19,2	8.5	7.37
Saline water (1)	48g/L salt	18,6	63.99	58.55
Saline water (2)	68g/L salt	19,5	58.33	77.57
Ethanol + DW (1)	30% v. H2O	26.5	30.5	16
Ethanol + DW (2)	60% v. H2O	26.5	49.59	17.85
DW+ Salt + Sugar	30g/L NaCl, 300g/L Sugar	20	59.4	35.36

Table 5-3: Dielectric properties of the liquids used to validate the performance of the preheating cavity ($f=2450 \text{ MHz}$)

5.3.4.3 Results

Once the cavity was fabricated it is important to validate its performance experimentally and numerically. The agreement between both types of spectra validates the predicted E-field and power loss maps issued from simulation, in addition, it accords greater confidence to all design properties that were not experimentally tested. The fabricated cavity is shown in Figure 5-15, while Figure 5-16 presents the entry port with the iris and the quartz tube are clearly shown.



Figure 5-15: Microwave cavity for solvent preheating

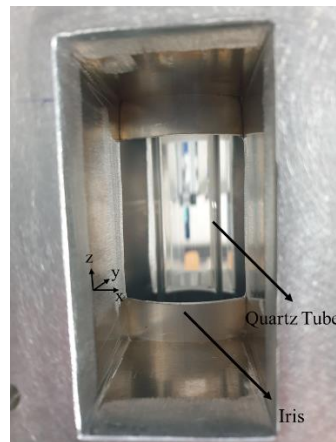


Figure 5-16: Microwave entry port of the solvent preheating cavity

Experimental characterizations of the cavity using a VNA are shown in Table 5-4, where we notice the excellent degree of adaptation of the cavity with liquids of various dielectric properties.

	Minimal S_{11} (dB)	Max(S_{11}) 2450 ± 10 MHz
DW	-20.24	-14.45
Ethanol	-24.64	-18.37
Saline water (1)	-25.71	-18.30
Saline water (2)	-26.41	-19.18
Ethanol + DW (1)	-27.78	-18.97
Ethanol + DW (2)	-21.25	-17.04
DW+ Salt + Sugar	-47.78	-17.92

Table 5-4: Preheating cavity characterization using a VNA at $f=2450$ MHz

The first four liquids of Table 5-4 were numerically simulated in the cavity, the comparison of numerical and experimental S_{11} spectra are presented in Figure 5-17 and Figure 5-18 for the cases of pure ethanol and saline water (68g/L) respectively. The figures show to what point the simulation is accurate where errors in reflected power are less than 1%. The optimal SSC positions are almost identical as shown in Figure 5-19 which demonstrates the accuracy with which the system is modeled. For the case of ethanol, the error between the simulated and real optimal SSC position is due to the presence of moisture in the ethanol solution (5% wt. H_2O).

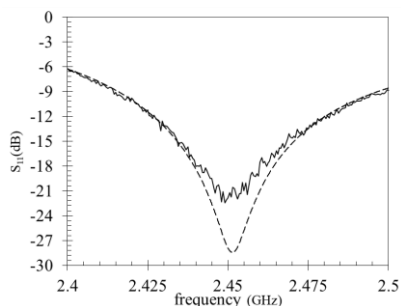


Figure 5-17 Experimental and simulated S_{11} spectra for case of pure Ethanol.

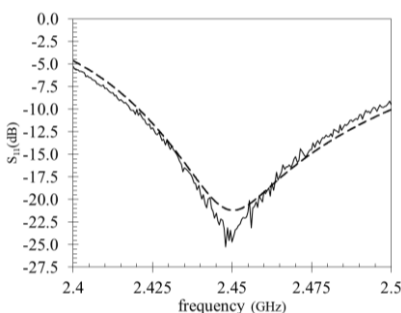


Figure 5-18 Experimental and simulated S_{11} spectra for case of Saline water (2) - 68g/L NaCl.

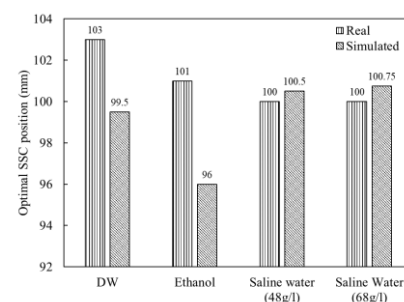


Figure 5-19: comparison of optimal SSC position (min S_{11} at 2450)

5.4 MW cavity for non-isothermal regeneration of solvent

To achieve non-isothermal regeneration, chemical desorption should take place directly under the influence of MW irradiation. This can be rendered possible by placing the membrane module inside the MW cavity, i.e. as the solvent traverses the module, it absorbs MW energy which incentivizes desorption through temperature increase. The proposed idea is of similar tone as placing a single fiber in a mono-mode cavity, however the transition from laboratory to prototype scale makes the use of 915 MHz more desirable. The proposed cavity operating at 915 MHz and housing a membrane module, will be referred to as the “in-situ” cavity from here on out.

5.4.1 Challenges

It is important to understand that placing a membrane module (MM) in an EM field poses many challenges to the long-term performance of the module, and to the cavity design.

5.4.1.1 Performance stability

It is essential that all parts of the MM (to the exclusion of the solvent) be inert with respect to MW irradiation, i.e. the porous fiber material, shell material, and the potting glue at the extremities. The membrane module used in this study (Hydroblue, China) has porous PTFE fibers which do not absorb microwaves. The potted ends of the membrane module have unknown dielectric behavior, and hence are made to protrude from the MW-cavity and with that the length of the MW cavity is fixed to the length of the hollow fibers of the module. The shell side material of the module was initially made of PVC which may cause problems at elevated temperatures: at low temperatures, PVC is a very poor absorbent of microwaves, however if it heats up by conduction or convection it experiences a runaway effect under MW, i.e. temperature rise increases absorptivity and vice versa. Our experience shows in Figure 5-20 that the PVC shell material of the MM became damaged at the middle of the module when placed in a mono-mode cavity. In order to prevent such reoccurrence, the shell side of the original module was removed and replaced with a housing made of quartz. The fibers of the membrane module are displayed in Figure 5-21 after removing the PVC shell material and before insertion into the new quartz housing.



Figure 5-20: Damaged membrane module after placing it in a microwave cavity (center)



Figure 5-21: Hollow fibers of membrane module after stripping the PVC shell material

5.4.1.2 Difficulty in cavity optimization

Another level of complexity is added by the fact that the dielectric properties of membrane module are unknown. The membrane module is not a continuous medium, and hence its dielectric properties cannot be

characterized by classical methods such as resonant cavity or dielectric probe. On the other hand, even if the solvent properties are known, simulating the real geometry membrane module is not a feasible approach: the great number of fibers, and their small diameters makes it difficult and computationally demanding. One way to circumvent this problem is through employing dielectric mixing laws that allow for a complex heterogenous medium to be presented as a continuum. The latter would have apparent dielectric properties that translate to a similar interaction with MW fields as with the complex heterogenous medium.

5.4.2 Apparent dielectric properties of membrane contactor

Dielectric mixing laws are used to predict the apparent dielectric properties of mixtures based on those of the parent components, and the mixing ratios. Mixing laws are important in alleviating the need to experimentally characterize and document countless mixtures of varying compositions such as solvent [7], air-particle, biomass [8], or foods [9] mixtures.

Different dielectric mixing laws treat a dispersion of particles of a non-continuous phase in a continuum such as solid particles in a liquid phase, or powders. The multitude of available laws are the result of many criteria that govern the global dielectric behavior of a medium such as the shape of the dispersed media (non-continuous) , orientation with respect to the incident E-field, the concentration levels of the dispersed phase, along with other assumptions. Equations (5.2) and (5.3) form the bases of all dielectric mixing laws, with (\bar{D}) being the mean electric flux density, (\bar{E}) the mean electric field intensity, (ϕ) the volume fraction, and the subscripts (1) and (2) designate the dispersed phase and the continuous phase respectively.

$$\bar{D} = \phi_1 \bar{D}_1 + \phi_2 \bar{D}_2 \quad (5.2)$$

$$\bar{E} = \phi_1 \bar{E}_1 + \phi_2 \bar{E}_2 \quad (5.3)$$

Manipulation of (5.2) and (5.3), then substituting ($D = \epsilon E$) would give the expression shown in (5.4), with (ϵ) being the relative permittivity, the subscript (m) stands for mixture, while (f_1) is defined as (\bar{E}_1/\bar{E}) with (\bar{E}) being the average electric field intensity

$$\epsilon_m = \epsilon_2 + (\epsilon_1 - \epsilon_2)\phi_1 f_1 \quad (5.4)$$

The common basis from which all dielectric mixing laws are derived is equation (5.4). The particle shape and orientation, as well as the choice of the electric field in the continuous medium allow for different determinations of the fraction (f_1) [10]. The orientation is angle made between the main axis of the particle geometry and the polarization of the E-field. We cite some of the most popular mixing laws in Table 5-5. It is important to reiterate that, in this study, the usage of dielectric mixing laws aims not to provide an accurate estimate of the apparent properties of the model, but to provide an order of magnitude estimation around which the in-situ cavity could be designed. It is important to highlight that our approach is purely empirical, hence the suitability or non-suitability of a dielectric law in modeling the properties of the module is out of the scope of this section.

Law	Equation	Shape of dispersed phase	Orientation
Refractive index	$\varepsilon^{1/2} = v_1 (\varepsilon_1^{1/2}) + v_2 (\varepsilon_2^{1/2})$	None	None
Landau-Lifshitz-Looyenga	$\varepsilon^{1/3} = \phi_1 \varepsilon_1^{1/3} + \phi_2 \varepsilon_2^{1/3}$	None	None
Lichtenecker	$\ln(\varepsilon) = \phi_1 \ln(\varepsilon_1) + \phi_2 \ln(\varepsilon_2)$	None	None
Wienar (1)	$\varepsilon = \varepsilon_1 \phi_1 + \varepsilon_2 \phi_2$	Lamellae	90°
Wienar (2)	$\frac{1}{\varepsilon} = \frac{\phi_1}{\varepsilon_1} + \frac{\phi_2}{\varepsilon_2}$	Lamellae	0°
Bruggemann (1)	$\phi_1 \left(\frac{\varepsilon_1 - \varepsilon}{\varepsilon_1 - 2\varepsilon} \right) + \phi_2 \left(\frac{\varepsilon_2 - \varepsilon}{\varepsilon_2 + 2\varepsilon} \right) = 0$	Sphere	Random
Bruggemann (2)	$\phi_1 \left(\frac{\varepsilon_1 - \varepsilon}{\varepsilon_1 + \varepsilon} \right) + \phi_2 \left(\frac{\varepsilon_2 - \varepsilon}{\varepsilon_2 + \varepsilon} \right) = 0$	Cylinder	45°
Botchner	$\left(\frac{\varepsilon - \varepsilon_2}{3\varepsilon} \right) - \phi_1 \left(\frac{\varepsilon_1 - \varepsilon_2}{\varepsilon_1 + 2\varepsilon} \right) = 0$	Sphere	Random
Wagner	$\frac{\varepsilon - \varepsilon_2}{3\varepsilon_2} = \phi_1 \frac{\varepsilon_1 - \varepsilon_2}{\varepsilon_1 + 2\varepsilon_2}$	Sphere	Random
Rayleigh	$\frac{\varepsilon - \varepsilon_2}{\varepsilon + \varepsilon_2} = \phi_1 \frac{\varepsilon_1 - \varepsilon_2}{\varepsilon_1 + \varepsilon_2}$	Cylinder	45°
Lorentz	$\frac{\varepsilon - \varepsilon_2}{\varepsilon + 2\varepsilon_2} = \phi_1 \frac{\varepsilon_1 - \varepsilon_2}{\varepsilon_1 + 2\varepsilon_2}$	Sphere	Random

Table 5-5: Dielectric mixing laws for the estimation of the dielectric properties of the solvent filled membrane module. Subscript (1) and (2) stand for both the dispersed and continuous phases respectively

The properties we seek to obtain are those of the interior of the membrane module containing: 30%wt. ETA solvent, PTFE hollow fibers, and air separating the fibers with volume fractions shown in Table 5-6. The multitude of the mixing laws makes it difficult to perform an examination of the underlying assumptions and their adaptability to represent the properties of the solvent-filled module, instead we rely on intuition to qualify whether a law produces credible results or not.

Length of fibers (mm)	500
Number of fibers	240
Diameter of MM	40
Fiber id (mm)	0.8
Fiber od (mm)	1.6
Porosity (%)	42

Table 5-6: characteristics of membrane module (Hydroblue, China)

The apparent dielectric properties of the membrane module obtained using the dielectric mixing law are shown in Figure 5-22. The figure shows that the laws of Wiener (2), Wagner, Lichtenecker, and Lorentz gave negligible

dielectric loss factors indicating a near impossibility of absorbing MW-irradiation. The laws of refractive index and Landau-Lifshitz-Looyenga gave low permittivity and loss factor, while those of Wiener (1), Bruggemann (1) and the Botchner were very elevated in comparison to others. Some mixing laws such as Rayleigh or Bruggemann (2) gave non-physical results where the relative permittivity of the module is equal to or lower than that of vacuum ($\epsilon' = 1$). Among all the tested laws, we chose those that gave the high dielectric loss factor as the basis for the design of the microwave cavity, with that said the dielectric properties used for the design of the in-situ cavity would be on the same order of magnitude as the results from the Wiener (1), Bruggemann (1) and Botchner dielectric mixing laws.

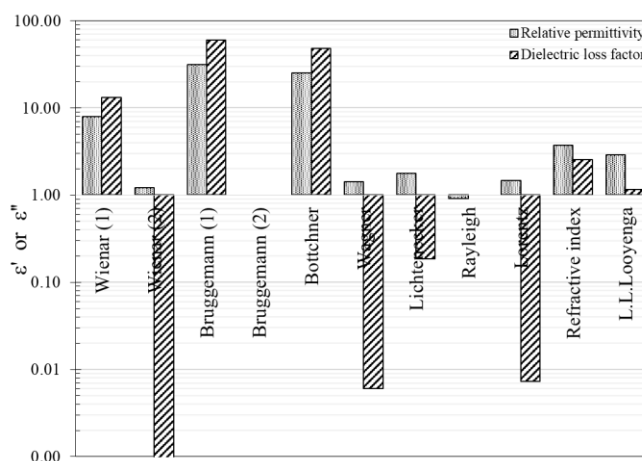


Figure 5-22: Prediction of the apparent dielectric properties of the membrane module by the dielectric mixing laws, $f=915\text{MHz}$. Module is filled with 30% wt. ETA at ($\alpha=0.44$), and ($T=60^\circ\text{C}$)

5.4.3 Geometry, meshing and boundary conditions

Geometry

The geometry of the modeled cavity is shown in Figure 5-24 where the hollow fiber membrane is placed in a perpendicular manner with respect to the incident E-field within the waveguide. The shell of the MM is accorded to the dielectric properties of quartz ($\epsilon' = 3.78$), the interior module of the module is accorded to the design dielectric properties that were inspired from the Wiener, Bruggemann and Botchner dielectric mixing laws. It is very important to state that the dielectric properties were considered to be uniform over the MM domain, but in real operation the formation of radial and axial T-gradients, as well as the change of the CO_2 loading of the solution, cause spatial variations of the dielectric properties of the solvent, and hence the MM.

Boundary conditions

The entry port is excited at the frequency range [902-928] MHz at the TE_{10} mode. All the outer surfaces of the displayed geometry are supposed perfect electric conductors (PEC) meaning that the (E_t), tangential component of the E-field, vanishes at the geometry boundaries. The upper and lower extremities of the MM are assumed PECs, in practice this region will be covered by what is called a MW chimney that prevents EM leakages. The geometry

is symmetrical with respect to the (ZY) and (XY) planes due to assumption of constant properties of the module; the latter assumption is rendered invalid under real operating conditions.

Meshing and resolution

The geometry is meshed using hexahedral elements for a total count of 10 243 elements with an average element quality of 0.66. The minimum and maximum distances between two elements are 4.2 mm and 93.89 mm respectively. The option of ‘adaptive mesh refinement’ was implemented with a tolerance on the absolute (S_{11}) value of 2%. The frequency domain solver was used to obtain the solution of the Maxwell’s equations, and the “parametric sweep” was used to vary the parameters of interest.

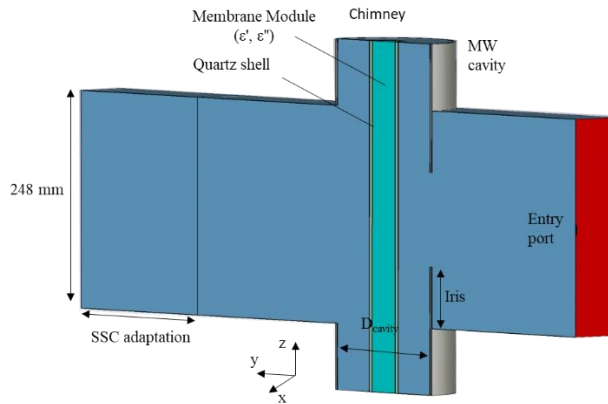


Figure 5-23: Cross-section view of the in-situ MW cavity that operates at a frequency 915MHz. Drawn in CST microwave-studio.

5.5 Results: cavity for non-isothermal regeneration

5.5.1 MW reflected power: Simulation run #1

The geometrical parameters of the cavity (diameter, iris) along with the dielectric properties of the membrane module (ϵ' , ϵ''), and impedance matching tools (SSC, frequency) were varied in the range shown in Table 5-7. The dielectric properties were chosen to represent the dielectric mixing laws of Wiener, Bruggemann, and Botchner discussed earlier. The range of cavity diameters was constrained by the lower limit of (124 mm) which is the smaller dimension of the (WR975) waveguide. The frequency range was set to [902-928] MHz representing the tuning capability of the solid-state microwave generator to be used in the final prototype.

Parameter	Range
Cavity diameter	160, 180, 200, 220 mm
iris	0, 45, 50, 55, 60, 65, 70 mm
ϵ'	5, 15, 30
ϵ''	10, 35, 50
Sliding short circuit	[100-200] step of 5mm
Frequency	902 - 928 MHz, 0.1 MHz step

Table 5-7: varied parameters for the design of in-situ cavity

The total number of simulated cases are close to 3300 cases (excluding frequency adaptation): In order to decrease the number of results to a reasonable level, cases of minimal power reflection across the SSC range of adaptation, and across the frequency adaptation range, were extracted. The optimal reflection coefficients were then averaged for all tested cases of the apparent dielectric properties of the membrane, that is to give a representation of the cavity's performance at a given diameter, and iris dimension.

The averaged resulting S_{11} parameters are shown in Figure 5-24 at different cavity diameters and iris dimensions. The figure shows that reflected power is not very sensitive to changes in diameter: 160 and 180 mm perform in better manner than at 200 or 220 mm. The standard deviations of (S_{11}) at iris dimension of 70 mm (ideal adaptation) are: 9.7, 4.9, 2.5, and 0.9 dB at diameters of 160, 180, 200, and 220 mm respectively. Further studies on the 160 and 180 mm reveal that even with regards to homogeneity of heating not many differences can be concluded. Therefore for reasons of compacity the smaller diameter between the two was chosen for further examination.

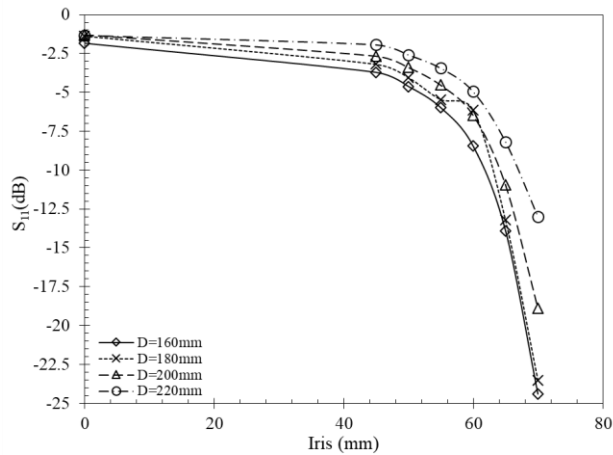


Figure 5-24: Average power reflection coefficient as a function of the size of the iris, and at different cavity diameters

5.5.2 MW reflected power: Simulation run #2

A second simulation run has been performed over the parameters shown in Table 5-8. The range of variation of the iris, SSC were narrowed down and cavity diameter was fixed to 160mm.

Parameter	Range
Cavity diameter	160 mm
iris	68, 70, 72, 74, 75 mm
ϵ'	5, 15, 30
ϵ''	10, 35, 50
Sliding short circuit	[140-190], step of 5 mm
Frequency	902 - 928 MHz, 0.1 MHz step

Table 5-8: varied parameters for in-situ cavity design, simulation run #2

Resulting power reflections are shown in Figure 5-25 for the average optimal S_{11} parameter – averaged over the tested dielectric properties $[\epsilon', \epsilon'']$ - as a function of the iris dimension. The figure shows the optimal iris dimension to be that at 74 mm. Further inspection of power reflection and sensitivity (Figure 5-26) at several dielectric properties demonstrates the good performance and stability at a cavity diameter of 160 mm and iris dimension of 74 mm. The sensitivity of Figure 5-26 is defined as the change of the optimal (ΔS_{11}) to a perturbation of 5 mm (± 2.5 mm) on the optimal SSC position, averaged for all cases of tested dielectric properties, all while allowing frequential adaptation over the range of [902-928 MHz]. The average sensitivity of reflected power is presented in (5.5), and the resulting unit is (dB /2.5 mm).

$$S_{11_avg}|_{D_{cavity}, Iris} = \sum_{i=1}^3 \sum_{j=1}^3 \frac{S_{11,ssc_opt+2.5mm} + S_{11,ssc_opt-2.5mm}}{2} \Big|_{[\epsilon'_i, \epsilon''_j]} \quad (5.5)$$

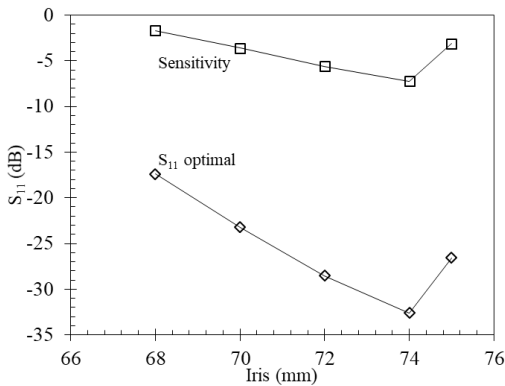


Figure 5-25: optimal (S_{11}) parameter as a function of the iris dimension

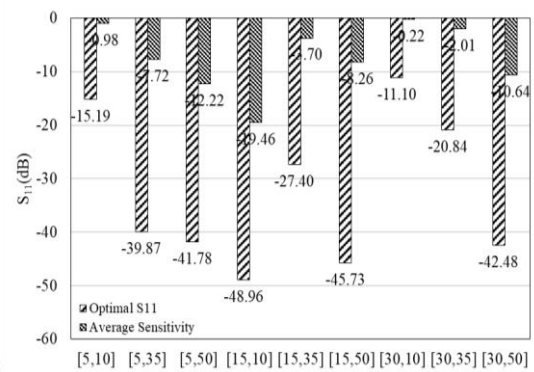


Figure 5-26: optimal reflected power and its sensitivity for different dielectric properties of the membrane module, D=160mm, iris dimension=74 mm

5.5.3 Power dissipation fields in membrane module

Evaluating the heating homogeneity inside the membrane module is of high importance as uniform energy distribution across the hollow fibers would lead to a stable performance. On the contrary, a concentration of volumetric MW power dissipation in certain zones of the membrane module may lead to the formation of hot spots that may entail damage to the polymer material, or cause the solvent to boil inside. The task of determining accumulated power absorption by a capillary across the length of the MM would shed more light onto the long-term performance of the module. The microwave cavity design was fitted to a great range of dielectric properties

during the design phase, still to evaluate the heating uniformity we consider the two most extreme cases among in the considered range. The membrane module has the dielectric properties of $[\epsilon', \epsilon''] = [5, 10]$ as the case of lowest permittivity and lossy character, and $[\epsilon', \epsilon''] = [35, 50]$ where the membrane module has the highest tested permittivity and loss factor.

5.5.3.1 Case of low dielectric properties of the membrane module

The power dissipation maps for the case $[\epsilon', \epsilon''] = [5, 10]$ is shown in Figure 5-27 for a longitudinal section in the membrane module. Figure 5-27 shows heating to take place principally along the center of the membrane module and decreases towards its ends. To have a greater understanding of the distribution of the heating patterns in the membrane, we plot in Figure 5-28 the power loss density across radial cross-sections of the membrane module at different heights. Only the upper part of the membrane was inspected for reasons of symmetry with respect to the XY plane.

The radial section right across from the microwave shows an acceptable homogeneity regarding the MW absorbed power. At ($z=0\text{mm}$) the side facing the microwave entry is heated in a greater manner than that facing the SSC. The rates are found to decrease as we move gradually towards the top/bottom of the membrane module, i.e. the solvent will remain cold in the membrane for $120 < z < 200 \text{ mm}$. It should be pointed out that for ($z > 80 \text{ mm}$) heating seems to be concentrated on the lateral side of the membrane module, i.e. those that are not facing the entry port of the SSC.

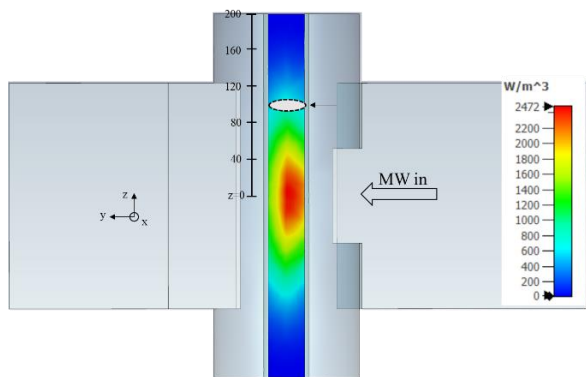


Figure 5-27: Power loss distributions in the hollow fiber module. Dielectric properties of the membrane module are $[\epsilon', \epsilon''] = [5, 10]$

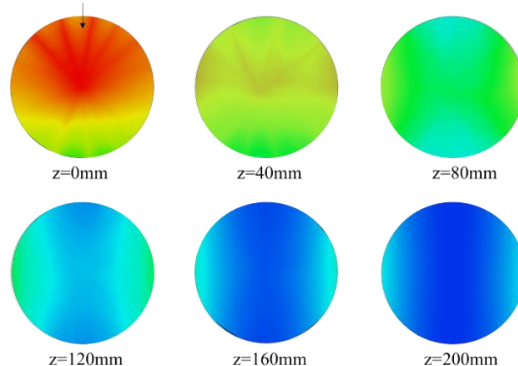


Figure 5-28: Power loss distributions in the hollow fiber module. Dielectric properties of the membrane module are $[\epsilon', \epsilon''] = [5, 10]$

5.5.3.2 Case of elevated properties of the membrane module

Figure 5-29 shows that the dissipation rates in the membrane module when the latter is accorded the dielectric properties $[\epsilon', \epsilon''] = [35, 50]$. The figure shows heating to be less homogenous along the radial direction of the module. This is caused in principle on the increase of the relative permittivity that decreases the wavelength in the solvent medium, leading to the observed ripple effect shown. Moreover, the elevated loss factor would lead to penetration depths in the order of ($\sim 7 \text{ mm}$ at 915MHz). To have better vision of the 3D distribution of the MW power dissipation we plot in Figure 5-30 the power loss density across different sections of the membrane module.

The very high permittivity and loss factor lead to poor absorption at ($z=0$) where a small fraction of the incident power is absorbed. As we move towards the top greater power absorption takes place: at ($z=80$ mm) the maximum power absorption occurs on the lateral sides of the membrane module. In practice this amounts to very strong heterogeneity that threatens to compromise the feasibility of the process.

It should be made clear again that the dielectric properties of the membrane module are not well known, and the purpose of using dielectric mixing laws is to have an order of idea of what might those be. In no manner are those properties well defined, and in reality, this analysis may be rendered obsolete as the membrane properties might be something completely different. Despite this, we still deemed necessary to investigate the membrane properties and the consequent heating maps.

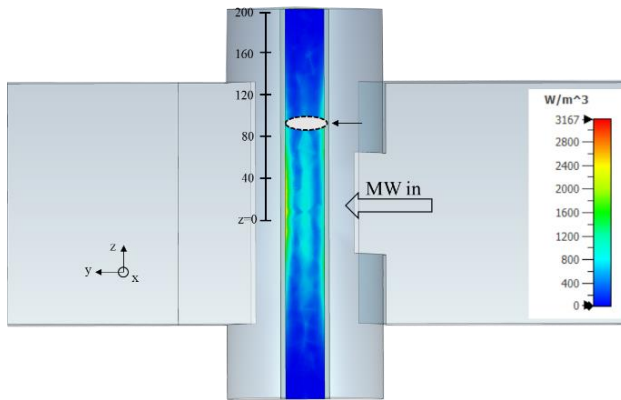


Figure 5-29: Power loss distributions along the hollow fiber module. Dielectric properties of the membrane module are $[\epsilon', \epsilon''] = [35, 50]$

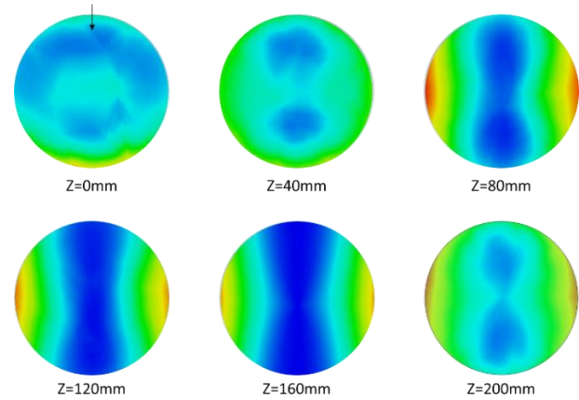


Figure 5-30: Power loss distribution at radial sections of the membrane module at different heights.

To quantitatively assess the MW power loss density, we summarize in Figure 5-31 and Figure 5-32, the results when the membrane has the dielectric properties of $[5, 10]$ and $[35, 50]$. In these figures are plotted the average power loss density at a radial cross-section of a given height, and the absolute relative standard deviation in (%). Figure 5-31 shows that at ($z=0$) - entry port level - the average power loss density was highest, and decreases gradually towards the top of the module. The absolute average deviation of power loss on a cross-section of the module increases with height. This signifies a greater non-homogeneity at the top of the module, although the lower power loss density does not pose a risk to the long-term operation of the module. Figure 5-32 shows that when the membrane module is accorded higher dielectric properties, the principle power absorption does not take place at the level of the entry port, and while the absolute deviation still follows an increasing tendency it is appreciably higher than the case of low dielectric properties of the module. This serves to qualitatively indicate the desirability of low dielectric properties of the module.

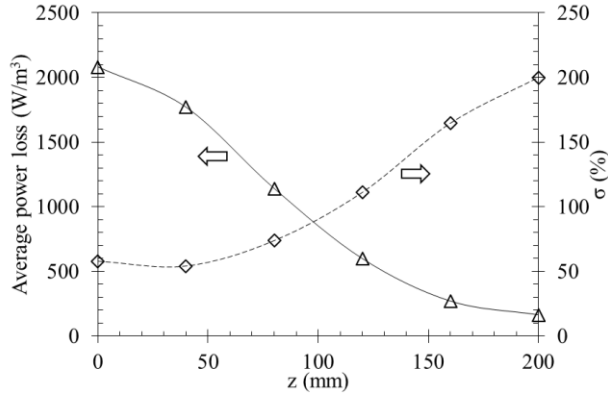


Figure 5-31: Power loss density in the membrane module at different heights. Dielectric properties of membrane are $[\epsilon', \epsilon''] = [5, 10]$, absolute average deviation presented in right axis

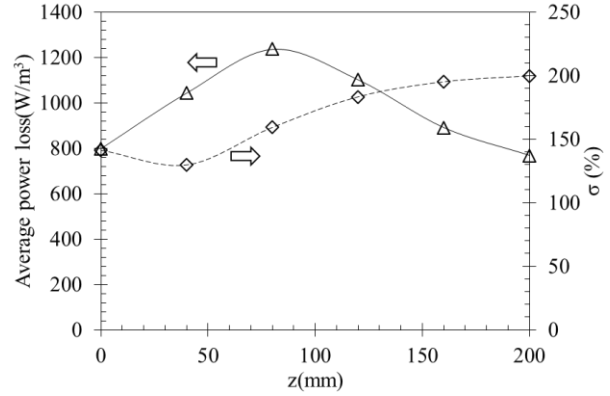


Figure 5-32: Power loss density in the membrane module at different heights. Dielectric properties of membrane are $[\epsilon', \epsilon''] = [35, 50]$, absolute average deviation presented in right axis

5.5.4 Experimental validation of reflected power profiles

5.5.4.1 Materials and methods

A mechanical drawing of the (in-situ) 915 MHz MW cavity is shown in Figure 5-33 along with the dimensions of the iris and the internal diameter. The cavity was equipped with two windows for fixing an IR camera, in addition it is made to have an adjustable length through the extension flanges as shown. To validate the performance of the cavity, the reflected power performance was tested using a vector network analyzer (VNA) as following the set-up in Figure 5-34. The set-up is composed of a VNA (Rhode and Schwartz ZVL network analyzer 9kHz-3GHz), waveguide transition (Sairem, TGCP WR975R), a manual 3-stub impedance tuner (Sairem, AI3SMWR975), the in-situ cavity in which the membrane module (Hydroblue, China) is placed, and an SSC (Sairem, PCCMWR9751230). A peristaltic pump (Series 530, Watson Marlow) was used to circulate fluid inside the membrane module, and the (S_{11}) spectrum was set to be (902-928 MHz).

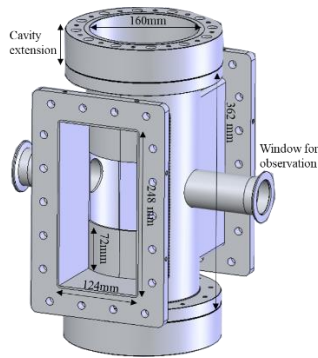


Figure 5-33: mechanical drawing of the microwave cavity at 915 MHz



Figure 5-34: Experimental characterization of reflected power in the in-situ desorption cavity

5.5.4.2 Results

Several liquids were made to circulate in the membrane module such as distilled water, and 30%wt. ETA uncharged with CO₂. Two mixtures of saline water at (48 g/L) and (68 g/L) of NaCl were tested as they represent the dielectric properties of 30% wt. ETA at conditions of [α , T] that equal [0.55, 50°C] and [0.55, 80°C] respectively. The resulting power reflection spectra for the tested liquids is shown Figure 5-35, adjustment of the SSC position and the frequency tuning are the only methods used for impedance matching. Figure 5-35 shows that experimental reflected powers are extremely high for the case of distilled water, and 30%wt. ETA. For the saline water mixtures, it appears that microwave absorption performance is superior to low absorbing liquids; still, considerable reflected powers persist in the order of (20-25%). It should be noted that metrology check of the VNA was due for the following month at the time of the measurements, this might explain the small positive values S_{11} values observed near $f=902\text{MHz}$, and the general noise levels observed in the signals.

Despite the great versatility with which this cavity was designed, experimental results show that its performance is not satisfactory when paired with the hollow fiber membrane module and 30% wt. ETA. This indicates that design properties, over which cavity optimization was made, were not representative of the true behavior of the membrane module under a MW field, the disparity in reflected powers is too great.

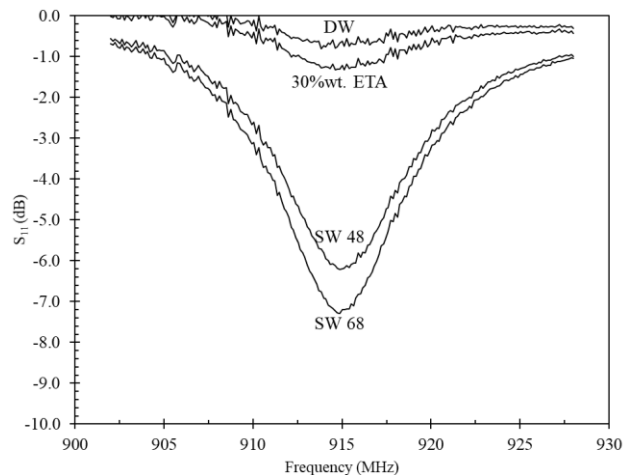


Figure 5-35: Experimental reflected power spectrum for different tested liquids: 30% wt. ETA, Distilled water, saline water (48g/L NaCl) and (68g/L NaCl) circulating through the lumen of the membrane module.

5.5.5 Dielectric characterization of membrane module through reverse technique

With some of the dielectric laws proving to provide erroneous results, it remains necessary to be able to determine the properties of the membrane module, as this would allow for a detailed visualization of the spatial MW absorbed power. The concept of the inverse method is to minimize the errors between the experimental and

the numerical S_{11} spectra, through the manual adjustment of the properties accorded to the membrane module. In this part we focus on reproducing the experimental spectrum obtained when saline water (48g/L NaCl) was made to occupy the lumen region of the MM. Before implementing the inverse method, it is of necessity to have a fixed narrow range that englobes the real dielectric properties of the membrane module. Hence, we refer once more to the entire array of dielectric mixing laws.

Mixing law	ϵ'	ϵ''
Wienar	7.13	13.56
Bruggemann	32.34	42.28
Botchner	25.90	33.99
Lichtenecker	1.69	0.12
Refractive index	3.60	1.87
La. Li. Looyenga	2.78	0.88

Table 5-9: Estimations of the dielectric properties of the membrane module using dielectric mixing laws. Membrane module is assumed to be filled with saline water (48g/L NaCl) at $T=20^{\circ}\text{C}$ which simulates the properties of 30% wt. ETA at $\alpha=0.44$ and $T=60^{\circ}\text{C}$.

Table 5-9 presents the properties obtained using the dielectric mixing laws while Figure 5-36 presents the experimental (S_{11}) curve along with those obtained numerically using the properties of different laws. The optimal SSC position was chosen to set the minima of the reflected power curve in the neighborhood of 915 MHz. Figure 5-36 shows that the majority of the dielectric mixing laws vastly overestimate the performance of absorbed power (>96%), contrary to the law of ‘‘Lichtenecker’’ that seems to underestimate it (~50%). It is clear that not a single dielectric law is capable of predicting with accuracy the properties of the membrane module, but these results serve as an indication that the real properties of the MM are in the range given by ‘‘Lichtenecker’’ or ‘‘La. Li. Looyenga’’, i.e. in the order of a few units.

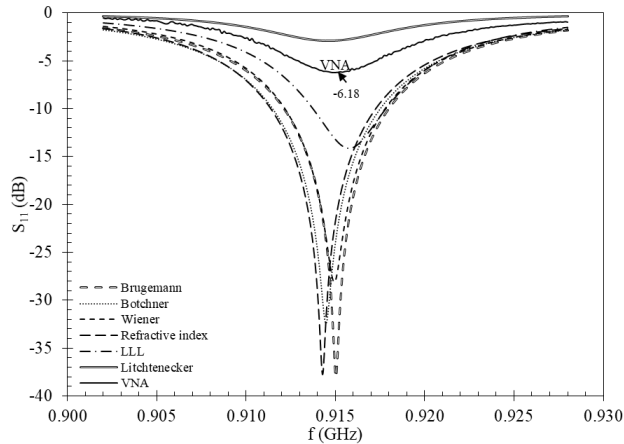


Figure 5-36: Simulated power reflection spectra whilst using different dielectric mixing laws to represent the properties of the membrane module. The latter is filled with saline water (48g/L) at 20°C to simulate 30% wt. ETA ($\alpha=0.44$, $T=60^{\circ}\text{C}$)

A parametric sweep was performed by varying the relative permittivity and the loss factor on the ranges of [1.1- 4] and [0.05- 4] with steps of 0.25 and 0.33 respectively. The SSC and the frequency of the MW were varied to reach the optimal position for low MW reflected power, which leads to simulating a total of (~1700) cases excluding frequency optimization. A case-by-case comparison of numerical (S_{11}) curve with the experimental one would consume a lot of time, instead we divided the data into groups depending on the values of the optimal reflected power.

We enumerate five groups depending on the range to which the S_{11} values subscribe to: values of order [-3, 0] dB signify a high reflection of MW power, [-6, -3] bad power absorption, [-9, -6] a mediocre performance, [-12, -6] good absorption, [-∞, -12] for perfect impedance matching. In Figure 5-37 we plot the dielectric dispersion of the tested membrane properties, the symbol of each point on the diagram communicates the range of the numerical S_{11} minima obtained at each simulated case. The diagram shows that to obtain the optimal (S_{11}) in the range of -6 dB, the relative permittivity of the module needs to have low to moderate values while the loss factor needs to have elevated values; another possibility is for (ϵ') being very high while (ϵ'') has low loss values.

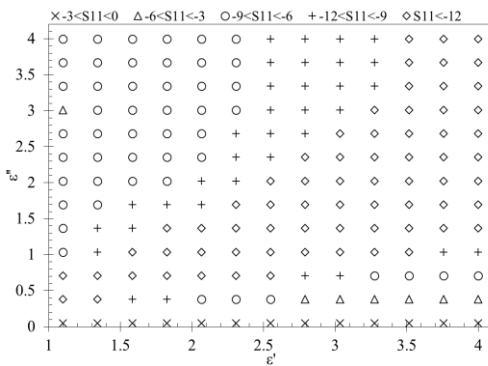


Figure 5-37: Dielectric dispersion diagram for the simulated dielectric properties of the membrane module. Data are divided into groups based on the value of the resulting (S_{11}). (x): $-3 \text{ dB} < S_{11}$; (Δ): $-6 \text{ dB} < S_{11} < -3 \text{ dB}$; (o): $-9 \text{ dB} < S_{11} < -6 \text{ dB}$; (+): $-12 \text{ dB} < S_{11} < -9 \text{ dB}$; (\diamond): $S_{11} < -12 \text{ dB}$

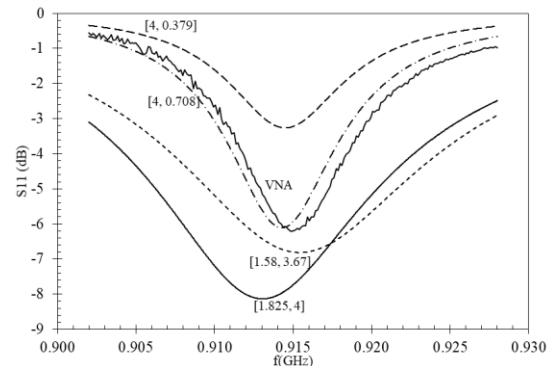


Figure 5-38: Comparison between the experimental spectrum of saline water (48g/L NaCl) and those obtained numerically at different dielectric properties of the membrane

Several potential properties of the membrane module were selected from Figure 5-37, the consequent S_{11} power curves were compared with that obtained using a VNA as shown in Figure 5-38. The figure shows that the tested properties are all of relative proximity to the experimental curve, however only the property [ϵ' , ϵ''] = [4, 0.708] was able to produce a spectrum with a similar optimal (S_{11}) value and identical tendencies, and hence we can assign the membrane module those apparent dielectric properties. It should be kept in mind that throughout all of our analysis we assume isothermal conditions inside the MM contactor, the module is filled with saline water mixture (48g/L NaCl) representing the properties of 30% wt. ETA at $T=60^\circ\text{C}$ and $\alpha=0.44$. During real operation, temperature variations and change in CO_2 loading will occur along the length of the module, thus causing deviations in dielectric behavior that prevent assigning a single dielectric behavior to the entire MM. The inverse method, although empirical and easy to implement, may raise the question of the uniqueness of the dielectric properties. One

question that we can pose is: can two different sets of dielectric properties lead to identical S_{11} spectra? This discussion extends beyond the scope of this manuscript, however, if proven to be so, then our approach could be undermined.

5.5.6 Power dissipation maps in membrane module

As the properties of the membrane module have been obtained by the inverse method - [4, 0.708], it is important to re-evaluate the power dissipation maps therein. Figure 5-39 presents the power loss in longitudinal direction of the membrane module, the figure shows that power dissipation is concentrated in the center, while no dissipation persists near the extremities of the MM. To obtain a better visualization of the heating homogeneity, power loss maps across a radial cross-section of the MM are presented in Figure 5-40. The figure shows the existence of an acceptable heating homogeneity at different radial sections of the MM which promise a good power distribution. This is further emphasized by the relatively low absolute deviation with respect to previous observations (Figure 5-32) from the average as plotted in Figure 5-41.

The low apparent properties of the membrane module can be considered to be an advantage as they allow for greater homogeneity of heating and as a result permit greater performance stability on the long run. These results reinforce the notion that chemical desorption in MMs is compatible with MW technology. Albeit, this remains ultimately tied to MW cavity specifications and the membrane module characteristics (diameter, void fraction, fiber materials ...)

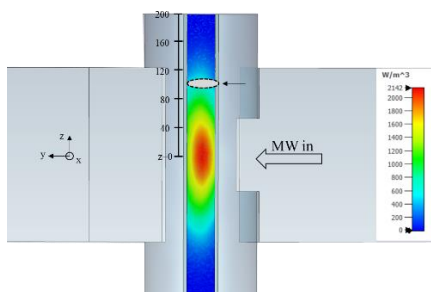


Figure 5-39: Power dissipation along a longitudinal cross-section of the membrane module. Dielectric properties of MM are $[\epsilon', \epsilon''] = [4, 0.708]$

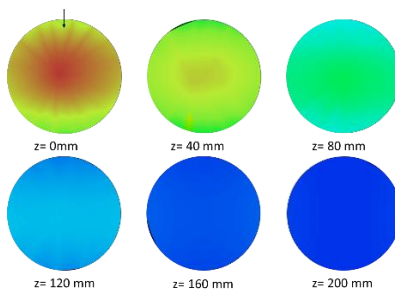


Figure 5-40: Power dissipation on different radial cross-sections of the membrane module. Dielectric properties taken of MM are $[\epsilon', \epsilon''] = [4, 0.708]$

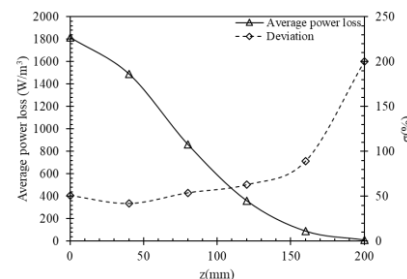


Figure 5-41: Averaged MW absorbed power and deviation at different radial cross sections of the membrane module. Dielectric properties of the MM are $[\epsilon', \epsilon''] = [4, 0.708]$

5.6 Prototype for MW-assisted regeneration

Initial conceptions of the process for microwave-assisted solvent regeneration were focused on the entire process of chemical absorption in both of its stages. The aim was to allow a great deal of operational flexibility, and to allow individual testing of either the absorption stage in a membrane module, or the desorption stage at different process conditions. The initial process conception was deemed too ambitious in light of budgetary limitations, prolonged durations for assembly and process startup, in addition to the project time constraints that prevent

utilizing the prototype to its full potential. Therefore, the initial design was downsized to account only for chemical desorption in hollow fiber module. The reader is referred to the annex for more details on the full process design.

5.6.1 MW-assisted regeneration at the desorption stage

To test the performance of the MW-assisted regeneration of CO₂-rich solvent we present the prototype in Figure 5-42. Regarding the solvent line, it is composed of CO₂-rich solvent tank, centrifugal pump, a solid-state microwave generator at (2450 MHz) (Sairem, model GMS1000) (3), the microwave cavity for preheating the solvent (4), a second solid-state microwave generator (915MHz) (Sairem, GLS1500), MW cavity for in-situ regeneration of the solvent, the hollow fiber membrane module (Hydroblue, China) which was placed inside the microwave cavity, a multiway valve, lean solvent tank and a cooler. With regards to the gas line, main elements include an N₂ bottle, a mass-flow controller, a rotameter, needle valve and a vacuum pump.

The operation of chemical desorption takes place as follows: solvent is pumped from the rich solvent tank through two microwave cavities operating at different frequencies. The two associated microwave generators cannot be run simultaneously, the solvent can be preheated in the cavity ($f=2450$ MHz), then introduced into the MM to achieve desorption under isothermal condition. Alternatively, it can be heated in the in-situ cavity whilst traversing the membrane module to achieve non-isothermal condition. The solvent pressure is controlled through a needle valve placed at the liquid exit. The exiting solvent can be circulated either to the lean solvent tank to simulate steady-state desorption, or it can be diverted to the rich solvent tank to simulate transient desorption. In the latter case, a water cooler is placed on the solvent return line to bring the solvent temperature back to ambient levels. On the shell side of the MM, (N₂) gas is made to flow to decrease, through convection, the partial pressure of CO₂. Another possibility would be to apply a vacuum to the shell of the module, controlled by a needle valve at the exit of the membrane module.

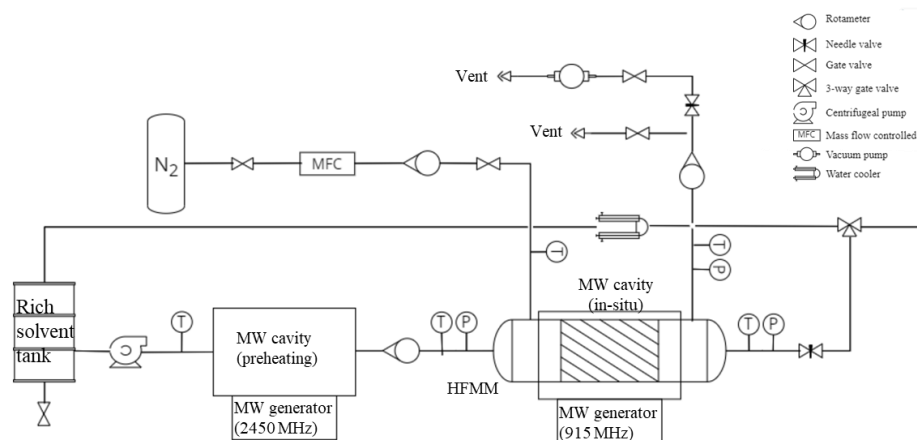


Figure 5-42: Process flow diagram for microwave-assisted regeneration of amine solution in hollow fiber module.

Unfortunately, the time allocated for this entire work has reached its end before any meaningful exploitation can take place. The set-up although functional, and with preliminary testing showing a stable performance, no

presentable experimental data were generated. A photo of the experimental set-up is shown in Figure 5-43, while in Figure 5-44 a photo of the MW cavity is shown.

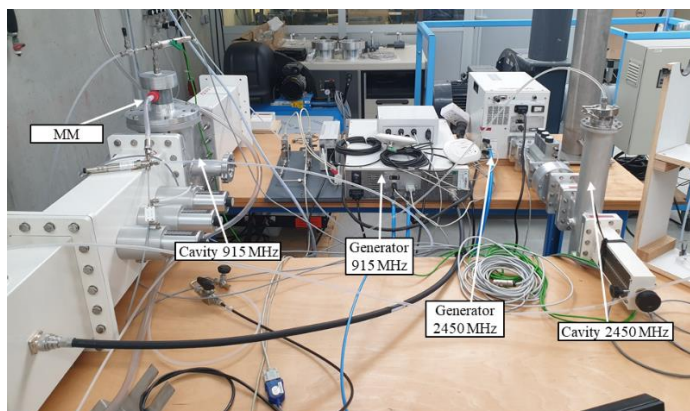


Figure 5-43: Experimental set-up for MW-assisted desorption in a HFMM

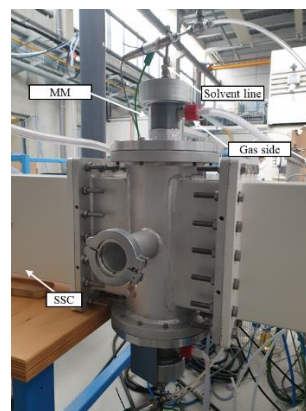


Figure 5-44: HFMM fixed inside the MW cavity (915 MHz)

5.7 Conclusion

In this chapter the conception of prototype unit for MW-assisted regeneration of 30% wt. ETA was explored. The original conceived process allowed for much operational flexibility, however the budgetary limitations and duration of assembly motivated the downscale of the process. The realized process prototype focuses solely on the desorption step, it allows for different temporal schemes and different modes of regeneration, sweeping gas Vs vacuum regeneration or isothermal vs non-isothermal modes. While the gas-side condition of the membrane module can be easily implemented, achieving temperature condition is not straightforward, hence most of this chapter has dealt with this problematic.

Isothermal regeneration in membrane module is achieved by preheating the solvent before entering the gas-liquid contactor. The cavity, deemed preheating cavity, was designed following an empirical methodology that aims to minimize MW reflected power. The cavity was designed to fit a wide array of dielectric properties of the product, i.e. simulated levels of reflected power are in the range of a few percent, as also verified experimentally.

Non-isothermal regeneration can be achieved by heating the solvent in-situ within the desorption membrane module, hence this is deemed possible by placing the latter inside the custom microwave cavity – called in-situ cavity. The design of this equipment was less straightforward as the main challenge was the unknown value of the dielectric properties of the 30% wt. ETA-filled membrane module. To circumvent this problem, dielectric mixing laws were used to design the cavity. However experimental measurements allowed us to conclude that most dielectric mixing laws over-estimated the real properties of the solvent filled module. The correct estimation of the apparent dielectric properties of the module are necessary to obtain the EM dissipation rates, and hence we used the inverse method to fit the simulated S_{11} spectra to the experimental one. Associated power dissipation maps show

very good homogeneity following a radial cross-section, which in turn promises a good stability of performance on the long-term.

5.8 Annex

5.8.1 Nomenclature

MW	Microwave
ETA	Ethanolamine
DW	Distilled water
SW	Saline water
MM	Membrane Module
SSC	Sliding short circuit
VNA	Vector Network Analyzer
PEC	Perfect Electric conductor
PTFE	Polytetrafluoroethylene
PVC	Polyvinylchloride
id	Internal diameter
od	Outer diameter
FEM	Finite element method
FDTD	Finite-difference Time-Domain
Preheating cavity	Cavity to preheat the solvent before entry into the membrane module
In-situ cavity	Cavity to heat the solvent while circulating in the membrane module

5.8.2 Symbols

S_{11}	Reflected power
ϵ'	Relative permittivity
ϵ''	Relative dielectric loss factor
\emptyset	Volume fraction
E	Electric field intensity(V/m)
D	Electric field flux (C/m^2)
T	Temperature ($^{\circ}C$)

5.8.3 Operation of prototype unit for mixed absorption/desorption operation

The process flow diagram of the process prototype is shown in Figure 5-45, it permits regeneration under different temporal schemes and operating conditions.

5.8.3.1 Operating modes:

The flexibility of process design is made possible by a carefully selected valve assembly. The latter allows for many possible regeneration schemes, placing focus on the absorption stage or on the desorption stage. We enumerate the operating modes below:

- **Chemical absorption at steady state:** The solvent passes once by the membrane module where absorption from synthetic flue gas takes place and is stored in a separate tank.
- **Chemical absorption at transient state:** The solvent is recirculated in a closed loop between the absorption membrane module and the lean solvent tank.
- **Chemical desorption at steady state:** The solvent is allowed a single pass in the desorption membrane module, then is stored in the lean solvent tank.
- **Chemical desorption at transient state:** The solvent circulates in a closed loop through the desorption membrane module and the rich solvent tank.
- **Chemical absorption and desorption at steady state:** This operation is most similar to classical chemical absorption processes. The solvent is pumped from the rich solvent tank towards the desorption module where it is regenerated and stored in the lean solvent tank. At the same time solvent from the lean tank is pumped into the absorption module where it is enriched then stored at the rich-solvent tank.

5.8.3.2 Isothermal Vs non-isothermal regeneration:

The employment of different heating strategies allows for the following regeneration modes:

- **Isothermal mode:** achieved by passing the solvent through the cavity preheating cavity. The solvent is then passed through the membrane module.
- **Non-isothermal mode:** achieved by passing the solvent through the membrane module while simultaneously being exposed to microwave irradiation. This is made possible by placing the membrane module inside the microwave cavity.

It should be noted that both microwave generators cannot be run simultaneously, the solvent is either preheated before entering the membrane module or directly inside the microwave cavity.

5.8.3.3 Vacuum versus sweeping gas regeneration:

The conditions on the shell side are very influential the regeneration performance, they aim at the reduction of the partial pressure of CO₂. one of two methods can be used:

- **Vacuum membrane regeneration:** A vacuum pump is connected to the shell side of the membrane which decreases the total pressure on the shell side, and that of CO₂ included. In the experimental set-up of Figure 5-45 a N₂-flow is used in conjunction with the vacuum pump, a better alternative would be the use of low-pressure steam. The low-pressure steam can be separated from the desorbed CO₂ through condensation.

- Sweeping gas regeneration:** N_2 can be used to decrease the partial pressure by evacuating the accumulated CO_2 in the shell side through convection. This operating scheme is easy to implement compared to the vacuum pump, and allows for a less complex experimental bench. The main associated disadvantage would be the impossibility of using this scheme on the industrial scale.

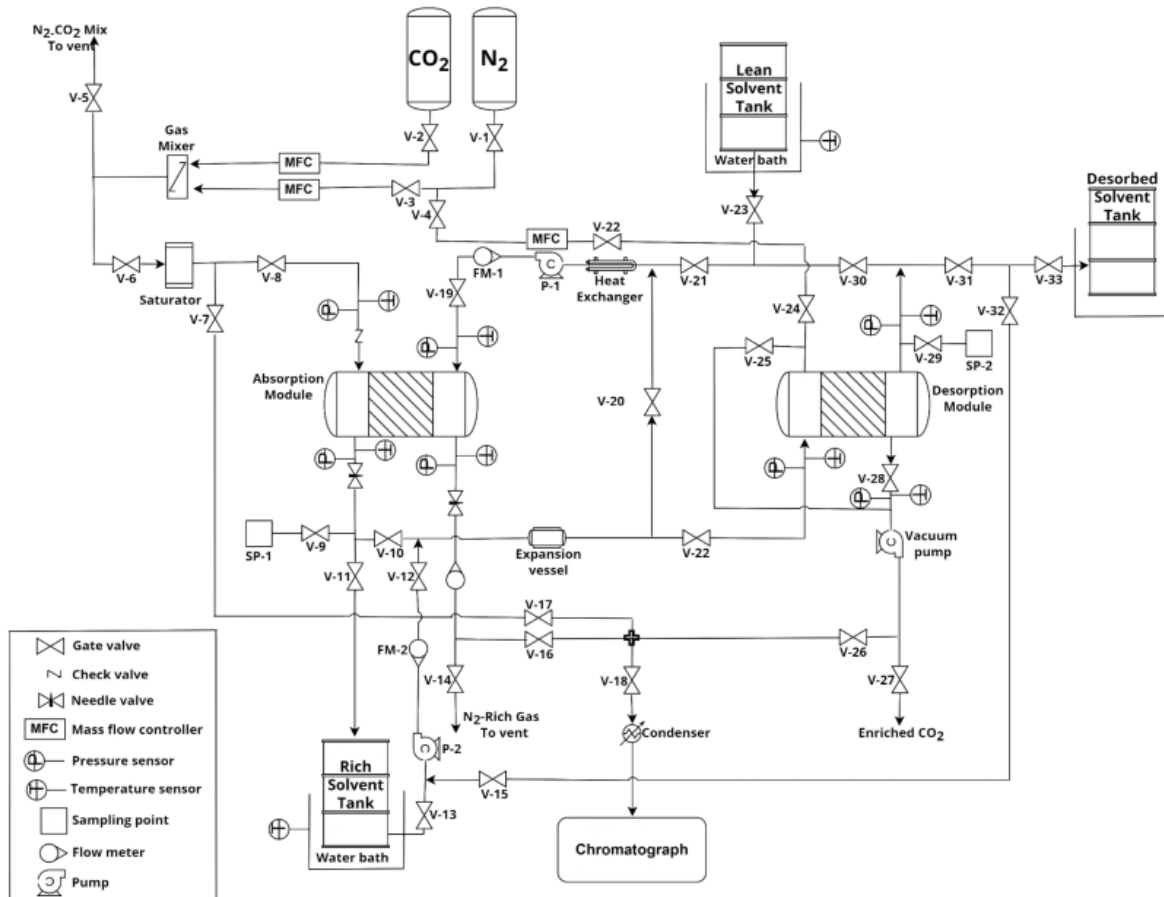


Figure 5-45: Process flow diagram for regeneration of amine rich solutions using hollow fiber membrane modules

5.9 References

- Microwave Engineering: Concepts and Fundamentals. 2014. 1st ed. CRC Press.
- Gyüre, B., B. G. Márkus, B. Bernáth, F. Murányi, and F. Simon. 2015. A time domain based method for the accurate measurement of Q-factor and resonance frequency of microwave resonators. *Review of Scientific Instruments* 86: 094702. <https://doi.org/10.1063/1.4929865>.
- Buffler, Charles R. 1993. *Microwave cooking and processing: engineering fundamentals for the food scientist*. Van Nostrand Reinhold New York.
- STOGRYN, A. 1971. Equations for Calculating the Dielectric Constant of Saline Water 19: 733–736. <https://doi.org/10.1109/TMTT.1971.1127617>.
- Bakam Nguenouho, O. S., A. Chevalier, B. Potelon, J. Benedicto, and C. Quendo. 2022. Dielectric characterization and modelling of aqueous solutions involving sodium chloride and sucrose and application to the design of a bi-parameter RF-sensor. *Scientific Reports* 12: 7209. <https://doi.org/10.1038/s41598-022-11355-w>.

6. Bao, Jian-Zhong, Mays L. Swicord, and Christopher C. Davis. 1996. Microwave dielectric characterization of binary mixtures of water, methanol, and ethanol. *The Journal of Chemical Physics* 104: 4441–4450. <https://doi.org/10.1063/1.471197>.
7. Lou, Jianfeng, T. Alan Hatton, and Paul E. Laibinis. 1997. Effective Dielectric Properties of Solvent Mixtures at Microwave Frequencies. *The Journal of Physical Chemistry A* 101: 5262–5268. <https://doi.org/10.1021/jp970731u>.
8. Ellison, Candice, Murat McKeown, Samir Trabelsi, and Dorin Boldor. 2017. Dielectric Properties of Biomass/Biochar Mixtures at Microwave Frequencies. *Energies* 10: 502. <https://doi.org/10.3390/en10040502>.
9. S. O. Nelson. 1992. Correlating Dielectric Properties of Solids and Particulate Samples Through Mixture Relationships. *Transactions of the ASAE* 35: 625–629. <https://doi.org/10.13031/2013.28642>.
10. Reynolds, J A, and J M Hough. 1957. Formulae for Dielectric Constant of Mixtures. *Proceedings of the Physical Society. Section B* 70: 769–775. <https://doi.org/10.1088/0370-1301/70/8/306>.

6 General conclusions

In accordance with the main objectives of this work, many tasks were undertaken. From the dielectric characterization of the solvent, passing by the experimental and modeling works of microwave-assisted desorption in hollow fiber and ending by the attempt to characterize the process at the pilot scale. The main takeaways from this work are presented in what follows.

The dielectric properties of 30% ethanolamine aqueous solutions with chemically dissolved CO₂ were measured and modeled using the Cole-Cole model in Chapter 2. The experimental data showed an elevated loss factor that increases with higher temperatures and carbonation ratios. Ionic conduction was identified as the dominant loss mechanism across the measured frequency range. Although extrapolations of the Cole-Cole model indicate that dipolar rotation dominates at the relaxation frequency. Due to the high absorbance of the CO₂-loaded solution, the calculated penetration depths were only a few millimeters and decrease with increasing frequency, temperature, and carbonation ratios. The results so obtained bring a better understanding of the solvent dielectric behavior as a function of temperature CO₂ loading.

In chapter 3 CO₂ desorption from a 30% wt. ethanolamine solution was investigated using a hollow fiber gas-liquid contactor under microwave irradiation in chapter 3. The solvent was circulated in a semi-continuous mode through a PTFE hollow fiber while being exposed to microwave irradiation. Special attention was paid to the design of the microwave cavity. Numerical simulations revealed that positioning the fiber parallel to the incident electric field results in low levels of reflected microwave power and uniform electric field distributions within the solvent.

The effect of microwave irradiation on the desorption flux from a 30% wt. ethanolamine solvent was investigated under various operating conditions using an experimental design approach. Results, including desorption flux and outlet temperature of the solvent, were plotted over time. These plots demonstrated that desorption flux is highly sensitive to temperature. Steady-state desorption fluxes were extracted from these plots and presented in a 2^k experimental-design cube. Regression coefficients were fitted to the data to assess the influence of each controlled parameter on desorption. It was found that outlet temperature has the most significant effect on desorption flux, followed by solvent flow rate. The interaction between temperature and increased solvent flow further enhances regeneration performance. The sweeping gas flowrate has minimal impact on desorption flux because of flow CO₂ concentration on the shell side.

In the final part of this chapter, the desorption fluxes obtained were compared to those reported in the literature using different regeneration modes: N₂-sweeping and vacuum regeneration. The challenge of achieving identical experimental conditions as those tested in the literature makes difficult to accurately evaluate the performance of

microwave regeneration technology relative to other modes. The measured desorption flux was found in the same order of magnitude than those obtained using N₂ sweeping gas at higher bulk temperature. However, methods employing vacuum decompression stripping of the solvent showed inferior regeneration performance compared to this study, despite operating at higher temperatures.

In chapter 4, a multi-physical model was developed to simulate the sweeping-gas desorption of CO₂ from a laminar flow of 30% wt. ethanolamine in the lumen of a porous polytetrafluoroethylene hollow fiber membrane under microwaves. Numerical modeling of the electromagnetic fields in the microwave cavity demonstrated a homogeneous electric field. To simulate the dissipation of microwaves in the solvent stream, heat and momentum transfer were integrated into the model, allowing for the generation of 3D temperature maps. These maps revealed significant temperature gradients near the membrane wall of the hollow fiber resulting from the laminar flow regime.

Mass-transfer modeling in a hollow fiber membrane was based on a 1D resistance-in-series model, which accounts for the chemical reactions between the amine compound and CO₂, as well as for the reduction in desorption rates due to partial wetting of the membrane. This model simulates the local desorption rates along the axial direction of the hollow fiber as temperature levels vary. To simulate microwave desorption, the computed 3D temperature maps were converted into two 1D temperature profiles. These profiles represent the temperature variations along the fiber length in both the liquid film and the bulk flow.

Desorption fluxes along the axial direction of the fiber indicate that desorption begins at a temperature that should be high enough, resulting in negligible desorption rates across 60% of the fiber area. Additional investigations suggest that contrary to conventional processes, operating in co-current mode is more advantageous than counter-current due to CO₂ absorption occurring in colder regions of the fiber. In efforts to assess microwave regeneration performance, the desorption process was simulated assuming operating under isothermal conditions. Microwave regeneration was found to be more efficient at the "hot" side of the fiber, near the cavity exit. The desorption process was better performing in isothermal mode as the region corresponding to the solvent flow heating until reaching the regeneration temperature was removed.

Additional studies indicate that larger fiber diameters increase desorption flux, albeit with reduced volumetric efficiency. Solvent entry temperatures into the microwave cavity have minimal impact on desorption rates, provided that the average outlet temperature remains constant. Increasing solvent flow rates enhances desorption flux primarily by creating stronger temperature gradients, although this reduces residence time in the membrane. Sensitivity analysis of desorption process reveals mild sensitivity to transfer and physical properties of the solvent and fiber geometries. Notably, bulk solvent temperature and carbonation ratio exhibit the highest sensitivities on driving the chemical desorption processes.

In chapter 5, the development of a prototype unit for microwave-assisted regeneration of 30% weight ethanolamine (ETA) was investigated. The designed experimental set-up should offer significant operational flexibility. Because of assembly time considerations, the constructed prototype focuses on the desorption stage, allowing for varying temporal schemes and different regeneration modes such as sweeping gas versus vacuum regeneration, and isothermal versus non-isothermal modes. Implementing gas-side operating conditions for the membrane module is straightforward; however, achieving temperature control has proven challenging. As a result, much of this chapter has focused on addressing this issue.

To achieve isothermal regeneration in the membrane module, the solvent was preheated before entering the gas-liquid contactor. This preheating is facilitated by a specially designed cavity, referred to as the preheating cavity, which was developed considering minimizing reflected microwave power. The cavity's design accommodates a broad spectrum of dielectric properties found in the product. Simulated levels of reflected power typically range within a few percent, a finding that has been experimentally validated.

Non-isothermal regeneration can be achieved by heating the solvent directly within the desorption membrane module, facilitated by placing it inside a custom microwave cavity referred to as the *in-situ* cavity. Designing this equipment posed challenges, primarily due to uncertainties regarding the dielectric properties of the 30% weight ethanolamine (ETA)-filled membrane module. To address this, dielectric mixing laws were employed for cavity design. However, experimental measurements revealed that most mixing laws tended to overestimate the actual properties of the solvent-filled module.

To accurately determine the dielectric properties necessary for calculating electromagnetic (EM) dissipation rates, an inverse method was utilized. This involved fitting simulated S11 spectra to experimental data. The resulting power dissipation maps exhibit excellent homogeneity across radial cross-sections, suggesting robust long-term performance stability.

7 Perspectives

Despite the undertaken efforts, there is still much to be explored and studied and hence we think that future efforts for advancing microwave-assisted regeneration in hollow fibers should subscribe to what follows.

In the field of dielectric characterization, focus should be placed on expanding the range of measurements to incorporate: higher temperatures, different amine fractions, and even by changing the composition of the alkanolamine solvent, considering diethanolamine, piperazine, methyldiethanolamine. The existence of such a database would help authors to use dielectric properties to screen large number of solvents to find that which is compatible with microwaves.

In experimental regeneration, it is important to identify novel solvents that are compatible with microwaves. Similar experimental procedure to the one used in this work should be undertaken to perform solvent screening tests which should evaluate: testing of microwave heating rates, evaluating individual rates of absorption and desorption, in addition to performing absorption-desorption cyclic tests. In light of the membrane process requirements, long-term stability should also be tested against common porous membranes.

A 1D numerical model was modified so that it can accommodate 3D-temperature maps in the fiber to calculate the desorption. This can be considered a good achievement, although it remains necessary to double down on the modeling work and attempt simulating microwave regeneration with more rigorous models that are fundamentally true. Comparison between the two modeling approaches should give estimations of its accuracy and highlight its strength to what point our resistance-in-series model was accurate and what actions should be implemented to facilitate its use.

In this work, significant strides have been made in the design of the microwave regeneration prototype, considerable research is further warranted. Key areas for future investigation include comparing the performance between isothermal and non-isothermal modes of regeneration, as well as evaluating sweeping gas versus vacuum membrane regeneration methods. Additionally, leveraging the numerical model developed at the single fiber scale to predict membrane module performance is crucial; the observed uniform heating across the radial section allows for accurate representation of the module as a repeating unit of a single fiber. Long-term performance characterization of the membrane module, particularly under non-isothermal regeneration conditions, is essential for assessing durability and efficiency over extended operational periods. Furthermore, numerical modeling of local MW power absorption within the membrane module under non-isothermal conditions is pivotal for optimizing cavity design and predicting temperature profiles to enhance overall process efficiency. These future research directions are imperative for advancing the understanding and application of MW-assisted regeneration technologies.

Titre : Couplage des Microondes avec un processus de désorption du CO₂ à partir d'un solvant aminé : approches expérimentales et de modélisation

Mots clés : Absorption chimique, régénération micro-ondes, module à fibres creuses, MEA, caractérisation diélectrique

Alors que les besoins énergétiques mondiaux continueront d'être satisfaits par des sources d'énergie fossiles, une solution viable pour réduire les émissions de CO₂ serait de mettre en œuvre des technologies de captage du carbone. Le captage du CO₂ par absorption dans des solvants aminés fait partie des technologies les plus avancées mises en œuvre sur les unités de post-combustion. Son application reste néanmoins limitée aux grandes sources ponctuelles, et les petites sources restantes difficiles à décarboner. Récemment, le chauffage microondes a gagné en popularité en raison de ses caractéristiques de sélectivité, de nature volumétrique et de facilité de contrôle ; d'autre part, les contacteurs à membrane sont des contacteurs gaz-liquide prometteurs en raison de leur compacité, de leur flexibilité opérationnelle et de leur facilité d'évolutivité par rapport aux colonnes à garnissage. Dans ce travail, nous explorons le fonctionnement de la désorption chimique lors d'un contacteur à membrane à fibres creuses par chauffage par micro-ondes.

Une compréhension complète des interactions entre les champs microondes et les phénomènes de transfert est essentielle pour la conception, le fonctionnement et l'optimisation corrects d'un équipement à l'échelle industrielle. Ainsi, les taux de désorption du CO₂ ont été étudiés expérimentalement à l'échelle locale d'une seule fibre millimétrique, placée dans une cavité micro-onde monomode. La modélisation numérique de la fibre a permis de visualiser les gradients de température formés à l'intérieur du solvant, et les taux de désorption locaux correspondants. En parallèle, une unité à l'échelle prototype a été conçue pour la désorption du CO₂ à l'échelle d'un module à fibres creuses sous des champs microondes. À cette fin, nous avons conçu une cavité sur mesure pour abriter un module à membrane de telle manière que la désorption du CO₂ aurait lieu simultanément avec le chauffage électromagnétique.

Title : Coupling Microwave with a CO₂ desorption process from amine solvent: experimental and modeling approaches

Keywords: Chemical absorption, Microwave regeneration, hollow fiber module, MEA, dielectric characterization

As global energy needs will continue to be met by fossil-fuel based sources, a viable solution to reduce CO₂ emissions would be to implement carbon capture technologies. CO₂ capture by absorption in amine solvents ranks among the most advanced technologies to be implemented on post combustion units. Still, its application is remains constrained large point sources with small sources remaining difficult to decarbonize. Recently, microwave heating has gained in popularity due to its characteristics of selectiveness, volumetric nature, and ease of control; on the other hand, membrane contactors are promising gas-liquid contactors due to their compacity, operational flexibility, and ease scalability in comparison to packed columns. In this work we explore the operation of chemical desorption when a hollow fiber membrane contactor by microwave heating.

A comprehensive understanding of the interactions of microwave fields and transfer phenomena is essential for the correct design, operation, and optimization of an industrial scale equipment. Hence CO₂ desorption rates were experimentally studied at the local scale of a single millimetric fiber, placed in a mono-mode microwave cavity. Numerical modeling of the fiber allowed the visualization of the temperature gradients formed inside the solvent, and the corresponding local desorption rates. In parallel, a prototype-scale unit was designed for the desorption of CO₂ at the scale of a hollow fiber module under microwave fields. To this end we designed a custom-design cavity was made to house a membrane module in such a manner that CO₂ desorption would take place simultaneously with electromagnetic heating.